ANALYSIS AND MODELLING OF THE IMPACT OF ANOMALOUS PROPAGATION ON TERRESTRIAL MICROWAVE LINKS IN A SUBTROPICAL REGION, BASED ON LONG-TERM MEASUREMENTS

Volumes I and II

A. M. A. ABOUALMAL

Ph.D.

2015

ANALYSIS AND MODELLING OF THE IMPACT OF ANOMALOUS PROPAGATION ON TERRESTRIAL MICROWAVE LINKS IN A SUBTROPICAL REGION, BASED ON LONG-TERM MEASUREMENTS

Statistical analysis of long-term meteorological and signal strength measurements in a subtropical region and investigation of the impact of anomalous refractivity profiles on radio propagation in terrestrial microwave wireless systems

Volumes I and II

Abdulhadi Mahmoud Abdulaziz ABOUALMAL

BSc, MSc.

Submitted for the Degree of

Doctor of Philosophy

School of Engineering, Design and Technology

University of Bradford

2015

Abstract

ANALYSIS AND MODELLING OF THE IMPACT OF ANOMALOUS PROPAGATION ON TERRESTRIAL MICROWAVE LINKS IN A SUBTROPICAL REGION, BASED ON LONG-TERM MEASUREMENTS

Statistical analysis of long-term meteorological and signal strength measurements in a subtropical region and investigation of the impact of anomalous refractivity profiles on radio propagation in terrestrial microwave wireless systems.

Keywords: Propagation, Refractivity, k-factor, Super-refraction, Sub-refraction, Ducting, Microwave link, Received Signal Strength, Signal Fading, Radiosonde

Prevailing propagation phenomena in certain areas play a vital role in deciding terrestrial wireless systems performance. Vertical refractivity profile below 1 km is a critical parameter for designing reliable systems; noting that there is a shortage of upper-air data worldwide. Anomalous phenomena may cause severe signal fading and interference beyond the horizon.

The objectives of this thesis are to investigate dominant refractive conditions in the subtropical Arabian Gulf region, develop new approaches and empirical models for evaluating vertical refractivity profiles and relevant propagation parameters in the low troposphere, and to examine the impact of frequently experienced anomalous phenomena on terrestrial microwave links. Twenty-three years of meteorological measurements, from 1990 to 2013, are utilized using spatially separated surface stations and a single radiosonde in the United Arab Emirates (UAE). Profiles of sea level, surface and upper refractivity components are statistically analysed. Three major atmospheric layers; namely 65 m, 100 m and 1 km above the ground are studied to analyse relevant propagation parameters such as sub-refraction, super-refraction, anomalous propagation probability parameter β_0 and point refractivity gradient not exceeded for 1% of time. The effective earth radius factor k is investigated using a new weighted averaged approach. In addition, the seasonal structure of atmospheric ducting is dimensioned within 350 m layer above ground. Finally, microwave measurement campaign is conducted using multiple radio links operating in UAE using various frequency bands. The link budget simulations are compared with the signal strength measurements. Fading scenarios are studied against the observed anomalous conditions and several recommendations are concluded.

Table of Contents

Acknowledgement

The completion of this report would not have been possible without the help and support of the following people. First and foremost, I would like to introduce all the praises and thanks to the God, Allah, for guiding me and for all goodness he gave me "man is the slave of goodness made for him". Second, I would like to express my appreciation and gratitude to my supervisor Prof. R. A. Abd-Alhameed. He has been very generous in his time and always a source of encouragement and inspiration to me. Also, I would like to express my appreciation for supervision, support and invaluable guidance of Dr. S. M. R. Jones and Prof. Hussain Al-Ahmad throughout completion of this work.

Moreover, I extend my thanks to the United Arab Emirates (UAE) National Center of Meteorology and Seismology for providing the meteorological data used in this work. My thanks and gratitude are also expressed to the Emirates Telecommunication Corporation, Etisalat UAE, in particular Mr. Ali H. Alwan, and to the UAE Telecommunication Regulatory Authority, in particular Mr. Tariq A. Al-Awadhi, for their continuous help and valuable support.

I am indebted to my father, mother, wife and brothers for their continuous support and encouragement that I am always given.

Acronyms

ANN	Artificial Neural Networks
APM	Advanced Propagation Model
b-LOS	beyond - Line Of Sight
BW	Bandwidth
CAL-4	Calibration Machine for PTU Sensors
CDMA	Code Division Multiple Access
COFDM	Coded Orthogonal Frequency Division Multiplexing
DCS	Ducting Climatology Summary
DEC	Decimal Degree Coordinate System
DECT	Digital Enhanced Cordless Telecommunications
DVB-H	Digital Video Broadcasting-Handheld
DVB-T	Digital Video Broadcasting-Terrestrial
EDH	Evaporation Duct Height
EIRP	Effective Isotropic Radiated Power
EM Wave	Electromagnetic Wave
ETSI	European Telecommunications Standards Institute
FDMA	Frequency Division Multiple Access
GC25	Vaisala Ground Check Set of Radiosonde
GHz	Giga Hertz
GPON	Gigabit Passive Optical Network
GPS	Global Positioning System

GSM	Global System for Mobile Communications
ICS Telecom	Advance Wireless Planning Software
IDU	Indoor Unit
IEEE	Institute of Electrical and Electronic Engineers
ISS	Integrated Sensor Suite
ITU	International Telecommunication Union
ITU-R	International Telecommunication Union - Radiocommunication Sector
k-factor	Effective Earth Radius Factor
kHz	kilo Hertz
LAN	Local Area Network
LMDS	Local Multipoint Distribution System
LOS	Line Of Sight
Mbps	Mega Bits Per Second
MHz	Mega Hertz
MW	Microwave
NMS	Network Management System
ODU	Outdoor Unit
OS	Operating System
PC	Personal Computer
PE	Parabolic Equation Method
PMP	Point to Multipoint
PPS	Precise Positioning Service

PR	Received Power
PTP	Point to Point
PTU	Pressure, Temperature, and Relative Humidity
PWE	Parabolic Wave Equation
QAM	Quadrature Amplitude Modulation
QPSK	Quadrature Phase Shift Keying
RAM	Random Access Memory
RAOB	RAwinsonde OBservation program
RFC	Refractivity From Clutter
RO	Ray-Optics
RS92-SGP	Vaisala Radiosonde Model
RSSI	Received Signal Strength Indicator
RX Power	Received Power
SDS	Surface Duct Summary program
SFN	Single Frequency Network
SG	Study Group
SSF	Split-Step Fourier
TDMA	Time Division Multiple Access
TX Power	Transmission Power
UAE	United Arab Emirates
V-SAT	Very Small Aperture Terminal
WiFi	Wireless Fidelity

WiMAX	Worldwide Interoperability for Microwave Access
WP	Working Party
2G	Second Mobile Generation
3G	Third Mobile Generation
4G	Fourth Mobile Generation
3-D	Three Dimentions

List of Symbols

k-factor	Effective Earth radius factor
A_{fs}	Free space attenuation factor / loss
P_e	Transmitted EIRP
d	Distance between the transmitted and the receiver
A_e	Effective aperture area of the reception antenna
P_r	Received power strength
λ	Wavelength of the transmitted signal
G_e	Transmitting antenna gain
G_r	Receiving antenna gain
ΔN	Gradient of Refractivity at two points
ε	Atmospheric permittivity
ε_r	Relative permittivity
ε_o	Permittivity of free space
n	Atmospheric refractive index
N	Radio refractivity ($N = (n\text{-}1) \times 10^6$)
N_{dry} (N_D)	Dry refractivity component
N_{wet} (N_W)	Wet refractivity component
P	Atmospheric pressure (hPa)
e	Water vapour pressure (hPa)
T	Dry air temperature (K)

H	Relative humidity (%)
e_s	Saturation vapour pressure (hPa)
EF	Evaporation factor
EF_{water}	Water evaporation factor
t	Temperature (^oC)
T_d	Dewpoint temperature (K)
ρ	Water vapour density
$f(P)$	Enhancement factor at air pressure P (hPa)
N_1	Refractivity at height h_1
N_2	Refractivity at height h_2
N_0	Atmospheric refractivity extrapolated to sea level
h_0	Height coefficient (km)
N_s	Refractivity at the Earth's surface
h_s	Height of the Earth's surface above sea level (km)
β_0	Time percentage in which ΔN value, in the first 100 m of the Atmosphere, is less than or equal to -100 N/km
dN_1 ($dN_{1\%}$)	Point refractivity gradient at 65m above ground
N_1	Refractivity at 1 km height above ground
r	Radius of signal curvature
H	Height of signal above the ground
dn/dh	Rate of refractive index change with height
A	Horizontal angle of the path

A	Actual Earth's radius (a = 6371 km = 3440 nmi)
M	Modified refractivity parameter
$M(h)$	Modified refractivity parameter (M-units) of refractivity, $N(h)$, at certain height, h
$\overline{\Delta N}$	Average refractivity gradient
$\overline{N_s}$	Average surface refractivity
c	$c = \frac{1}{8 - h_s} \ln(\frac{N_1}{105})$
c_e	$c_e = \ln\left(\frac{N_s}{N(1\ km)}\right) = \ln\left(\frac{N_s}{N_s + \Delta N}\right)$
$N_{h\_(D+W)}$	Net of dry and wet components of N_h
$\Delta N_{(D+W)}$	Net of dry and wet components of ΔN
N_{1km}	Refractivity at 1 km altitude above the ground
$N_{0.1km}$	Refractivity at 100 m altitude above the ground
$N_{0.065km}$	Refractivity at 65 m altitude above the ground
ΔN_{1km}	Vertical ΔN of first kilometre atmospheric layer above the ground
$\Delta N_{0.1km}$	Vertical ΔN of first 100 m atmospheric layer above the ground
$\Delta N_{0.065km}$	Vertical ΔN of first 65 m atmospheric layer above the ground
N_{s_D}	Dry component of N_s
N_{h_D}	Dry component of N_h
N_{1km_D}	Dry component of N_{1km}
$N_{0.1km\_D}$	Dry component of $N_{0.1km}$
$N_{0.065km\_D}$	Dry component of $N_{0.065km}$

ΔN_{1km_D}	Dry component of ΔN_{1km}
$\Delta N_{0.1km\_D}$	Dry component of $\Delta N_{0.1km}$
$\Delta N_{0.065km\_D}$	Dry component of $\Delta N_{0.065km}$
N_{s_W}	Wet component of N_s
N_{h_W}	Wet component of N_h
N_{1km_W}	Wet component of N_{1km}
$N_{0.1km\_W}$	Wet component of $N_{0.1km}$
$N_{0.065km\_W}$	Wet component of $N_{0.065km}$
ΔN_{1km_W}	Wet component of ΔN_{1km}
$\Delta N_{0.1km\_W}$	Wet component of $\Delta N_{0.1km}$
$\Delta N_{0.065km\_W}$	Wet component of $\Delta N_{0.065km}$
$N_{0.065\&0.1km}$	Combined net component of two layers refractivity of $N_{0.065km}$ and $N_{0.1km}$ (at 65m and 100 m altitudes above the ground)
D	Duct Thickness (m)

List of Figures

List of Tables

Chapter 1

INTRODUCTION

1.1 Overview

The increasing demand for high data rate connectivity is one of the pillars that drives the development of communication technologies. This also urges the telecommunication industry to design and manufacture systems with enough capabilities to satisfy such a growing requirement. The telecommunication service providers have to regularly survey the latest broadband technologies and high bandwidth solutions to meet current and future demands.

Wireless technologies are essential to provide connectivity for communication services in places where cable infrastructure does not exist. The wireless electromagnetic waves are seriously impacted by atmospheric conditions which may cause the signal to be attenuated or bent while propagating through the air. Anomalous propagation phenomena may seriously degrade the performance of wireless communication systems and cause harmful interference across national borders.

Accurate modelling of local propagation conditions based on the analysis of local meteorological data assists designers of wireless systems to predict their performance. The proper estimation of different design parameters is crucial to provide reliable broadband wireless solutions and to avoid unexpected interruption to the services provided over course of the year.

The Arab Gulf region, in particular United Arab Emirates (UAE), is selected as a unique location for conducting several real time experiments in this study due to its special subtropical climate. Although such climatic regions suffer from severe propagation conditions due to the rapid variations of some atmospheric factors which are difficult to predict and control, very few studies are available for this part of the world. One of the most critical parameters in such humid climates is the refractive index of vertical and horizontal atmospheric layers, in particular where the rain precipitation is considerably small.

The refractive index parameter of the air can be measured or calculated from local meteorological data. The thorough study of vertical refractivity profile is essential for predicting and analysing signal fading and interference between radio signals. In the case of abnormal refractivity conditions, where the signal can be trapped within two atmospheric layers forming a semi- waveguide, the leakage of propagating energy cannot be completely controlled.

The measurements of meteorological data and received signal strength indicator (RSSI) data are gathered from various weather stations and point-to-point (PTP) microwave (MW) links, respectively, which are located in places with different atmospheric conditions all over the country. The microwave links operate with different specifications in different frequency bands. The actual received signal levels are compared with the predicted values, which are calculated using a commercial software for wireless system design and link budget simulation. The existing propagation phenomena and their contribution to the variation of the propagating signal strength are analysed taking into consideration the various recommendations of the International Telecommunication Union (ITU).

1.1.1 UAE Location and Climate

The UAE is situated on the north-eastern part of the Arabian Gulf, along the tropic of cancer. Abu Dhabi, capital of the UAE, is located at 24.52º N latitude and 54.98º E longitude, with an altitude of 27 m above sea level. Abu Dhabi, Dubai, Sharjah, and Ras Al-Khaimah are four coastal cities located near by the Arabian Gulf where the climate is usually hot and humid. Al-Ain is an inland city with lower humidity, and finally Al-Fujairah is coastal city near the Oman Gulf that is again hot and humid but near the tropical zone where the gulf is opened to the Indian Ocean, which results in a special climate for this Emirate in comparison with other Emirates. The UAE map showing the locations of the six emirates is given in Figure 1.1.

Figure 1.1: UAE Map with Locations of the Six Airports' Sites [1]

The UAE climate is subtropical and arid due to its location within the northern desert belt, which is warm and sunny throughout the year. From May to September, the temperature and humidity are high with an average temperature above 40 °C and sandstorms occur intermittently. Winter can be windy with short and irregular rainfall.

1.1.2 Meteorological Data

Long-term meteorological data are being gathered from several weather stations spread over the UAE, and then analysed to identify the characteristics and occurrence probability of different propagation phenomena. The meteorological data are categorized into two types which are; surface based data and upper-air data up to 1 km of atmosphere above the ground. The limit of 1 km is selected in this work since it focuses on the impact of anomalous propagation conditions on terrestrial wireless systems. In addition, the evaluation of some important propagation parameters such as effective Earth radius factor,

k, are found to be based on the analysis of vertical refractivity and its gradient at 65 m, 100 m and 1 km layers. Automatic stations and manual observations are used to measure the surface meteorological data. The upper-air data are obtained from the radiosonde measurements and assist in studying the vertical profile of the atmosphere. A radiosonde is an airborne weather station coupled with a radio transmitter which makes measurements of temperature, air pressure, humidity, wind speed and direction, and transmits the measurements back to the ground. A Vaisala RS92 Radiosonde, which offers high level performance of meteorological measurements and GPS capabilities with a reliable telemetry link, has been used for gathering the upper-air meteorological data.

Automatic surface weather stations are available all over the county while six manual surface weather stations are located in six airports of the main UAE emirates. The manual data are obtained in the six sites of Abu Dhabi, Dubai, Sharjah, Ras Al-Khaimah, Fujairah and Al-Ain airports. Some additional meteorological parameters such as visibility, fog and other weather parameters can be measured manually by professional observers at the airports. Upper-air data exists only at Abu Dhabi city, the capital of UAE. The coordinates of the six sites locations are provided in Table 1-1.

Table 1-1: Locations of six UAE emirates

Emirate	Latitude	Longitude
Abu Dhabi	24.52ºN	54.98ºE
Dubai	25.26ºN	55.33ºE
Sharjah	25.33ºN	55.52ºE
Al Ain	24.33ºN	58.74ºE
Ras Al-Khaimah	25.79ºN	55.94ºE
Al Fujairah	25.13ºN	56.34ºE

The local meteorological measurements are taken from the national center of meteorology. It should be noted that some meteorological data can also be obtained from the global databases of the Wyoming University website.

Various types of weather instruments can be used for measuring the refractive index and meteorological data such as refractometer, fixed psychrometers and barometers, fixed surface weather stations that consist of multiple sensors, and radiosonde for gathering upper-air data. In this work, three types of weather stations are available in different locations, which are manual surface stations at airports, automatic surface weather stations in other locations all over the country and upper-air radiosonde station in Abu Dhabi.

1.1.3 Propagation Conditions

Propagation characteristics under clear air conditions are influenced by three basic phenomena, which are refraction, diffraction and scattering [2, 3]. The meteorological conditions in an area decide the radio-horizon, signal strength, trapping of radiowave, and anomalous propagation of radio waves. The Arab Gulf region is likely to experience

anomalous propagation due to its special climate which is hot and humid most of the year. In this regard, few studies are available for this region. The ITU maps and our initial analysis show that many factors will be varying considerably within the same country and even within a large city.

1.1.4 Signal Strength Measurements

The wireless technology of the PTP MW link is selected to conduct the wireless measurement experiments in this project. The received signal strength measurements of several terrestrial microwave links working with different configurations and within several frequency bands are gathered and analysed. The links are located all over the country in various atmospheric conditions. The existing commercial network of microwave links is utilized, which belong to the leading telecommunication operator in UAE: Etisalat. The company has a big fixed wireless network including fixed PTP microwave links operating in UAE, in addition to broadband access networks (WiMAX), earth-space links (V-SAT) and satellite earth stations as well. The microwave links could be used to backhaul stations of mobile or fixed broadband access technologies and to provide telecommunication services to fixed customers. Other new links with different specification and frequency spectrum might be procured in the future. Long-term field measurements might also need to be stored for further analysis. The measured signal levels are compared with the predicted values by reliable design and planning ICS Telecom software, ICS Telecom, which consider theoretical propagation models obtained from

various ITU-R recommendations (Radio-communication Sector of the International Telecommunication Union).

The microwave links should be connected to a network management system for the purpose of remote access and signal strength monitoring. Practically this task seems to be very complicated and time consuming due to the different specifications of the vendors, technological issues, availability and connectivity of monitoring Ethernet ports in the equipment. The existing microwave network works in multiple frequency bands with single and dual polarizations. The analysis in this thesis focuses on MW links that operate in 7GHz and 23GHz bands.

1.2 Problem Statement

The electromagnetic waves in the Arabian Gulf atmosphere experience considerable fading through their propagation. The signals also travel beyond the horizon due to non-standard refractive conditions causing interference to other systems across the national borders. There are multiple reasons causing these anomalous situations. One of the main reasons is the high variations of atmospheric parameters such as the temperature and humidity, which causes the refractive index to change rapidly in such atmosphere. The configurations of the operating wireless system have to be set carefully to either make use of certain conditions to transmit signals over long distances or to eliminate the harmful impact due to the unwanted attenuation or interference. The subtropical region of Arabian Gulf often suffers

from these severe propagation conditions when compared with regions of temperate climate.

The anomalous propagation phenomena have to be analysed through the gathering of long-term meteorological data and measurements of received signal strength from microwave links operating in the same or the surrounding areas, as practically as possible. The fading measurements could be correlated with variations of these propagation parameters in order to figure out the root causes of the signal attenuation. The current prediction methods for the signal strength can also be validated after being compared with real signal measurements. The seasonal variations of the anomalous propagation need to be thoroughly studied and the development of new accurate propagation models for this hot and humid subtropical climate may be required.

In addition, the analysis of several propagation parameters requires the dimensioning of vertical atmospheric profiles that are based on upper-air meteorological data. Due to cost implications and technical difficulties of the systems used to gather upper-air profiles, the number of locations with these data are much fewer when compared with surface weather stations. This makes it essential for the researchers to derive and develop algorithms and approaches with maximum possible accuracy to evaluate the vertical profiles from the widely available surface data in order to be able to statistically analyse the relevant propagation phenomena.

1.3 Work Motivation and Significance

Operational experience shows repeated outages and interference situations in the line of sight (LOS) point to point (PTP) microwave links operating in a sub-tropical region, such as the Arabian Gulf region. Also, there is a shortage of a complete studies for the anomalous propagation phenomena experienced in this region. This necessitated the requirement to conduct this work to assist the radio planners in accurately designing the microwave links operating in the region. From the literature, the refractive conditions and *k-factor* were investigated based on short-term data, for few years, in different places, which makes the results' accuracy questionable. Also, most of the studies were conducted in temperate regions while few of them were from tropical rainy regions and subtropical areas. There has always been a need for conducting thorough studies to precisely model the impact of different clear air propagation parameters on the operating microwave links in this subtropical region based on intensive long-term measurements of meteorological data and signal strength from multiple microwave links. This data could be gathered in the UAE, which is part of the Arabian Gulf region. The common anomalous propagation phenomena in the Gulf region and their impact on the signal attenuation are investigated to find possible approaches for improving the performance of wireless systems operating in such severe conditions.

1.4 Statement of Project Aim and Objectives

This research aims at modelling anomalous refractive conditions of clear air atmosphere and their fading impact on received signal strength levels of LOS microwave links

operating in regions with subtropical climate, using long-term meteorological data and received signal strength measurements. The variations of the effective Earth radius factor, point refractivity gradient, anomalous propagation conditions; such as sub-refraction, super-refraction, and different types of atmospheric ducts are investigated and statistically analysed. Existing models for evaluating the vertical atmospheric profiles are examined. The obtained results in this research work are compared with proposed reference values by radio communication sector of the International Telecommunication Union (ITU-R) for each of the analysed parameters in the area under study.

The main objectives of this work are:

- Utilize long-term meteorological measurements over twenty-three years for the analysis of dominant refractive conditions and relevant propagation phenomena in the subtropical Arabian Gulf region such as:
    - Surface refractivity and refractivity extrapolated to sea level,
    - Vertical refractivity profiles and refractivity gradients at 65 m, 100 m and 1 km above the ground, using linear and exponential models,
    - Anomalous propagation statistics including β_0 parameter, sub-refraction, super-refraction and atmospheric ducts,
    - Effective Earth radius factor, k,
    - Point refractivity gradient, dN_1, and
    - Height coefficient parameter of ITU exponential models at multiple altitudes and refractivity components.

- Develop new approaches, algorithms and empirical models for:
    - Evaluation of vertical refractivity profiles based on the analysis of dry, wet and net components,
    - Estimation of vertical refractivity from the analysis of surface data in the areas surrounding to a radiosonde location,
    - Deriving empirical curve-fitting models for vertical refractivity evaluation,
    - Weighted average approach for evaluating the effective earth radius factor, *k*-factor parameter, from the analysis of three atmospheric layers namely; 65 m, 100 m and 1 km,
    - Dimensioning of atmospheric ducts and their characteristics from the analysis of mean modified refractivity profiles, *M*, at given altitudes.

- Analyse the measurements of received signal strength for different microwave links in comparison with the link budget calculations and performance simulations,
- Investigate the impact of anomalous propagation phenomena on the performance of the microwave links and signal fading,
- Propose mitigation techniques to eliminate the harmful impact of some common anomalous propagation conditions for further consideration during the design of wireless systems operating in subtropical regions with similar climate.

1.5 Research Methodology

The field measurements of meteorological data and received signal strength will be gathered and analysed in order to study the vertical profiles of clear air atmosphere in the Arabian Gulf region, to evaluate the impact of different propagation conditions on the signal strength fading and to develop accurate propagation models for vertical refractivity and *k-factor* considering the local severe atmospheric conditions.

The microwave links and weather stations that belong to Etisalat and National Center of Meteorology and Seismology, NCMS, respectively, are used in this research, taking into account some limitations on the systems' configurations, since they are implemented to satisfy certain business requirements.

1.6 Report Organization

This report consists of eleven chapters followed by appendices. In chapter 1, an introduction is provided highlighting the problem, significance of the work and the research methodology. Background, literature review and results of previous research work and experiments conducted around the world are discussed in chapter 2. In chapter 3, specifications of radiosonde, surface weather station and wireless equipment used for gathering signal strength measurements, are provided. The step by step design and installation procedure of a microwave link is addressed based on our operational experience in the same chapter. The types of the meteorological data, the utilized software

and programs for data processing and analysis are presented in chapter 4. In chapter 5, initial analysis results of fourteen years' meteorological data from 1990 to 2003, statistics of refractive conditions in Abu Dhabi and comparison with ITU maps are provided. The selection criteria of candidate microwave links among the huge available network along with some limitation and challenges are presented. Anomalous propagation phenomena and β_0 parameter are statistically analysed in chapter 6, using meteorological data from 1997 to 2005. In chapter 7, seventeen years of high resolution surface and radiosonde meteorological data from 1997-2013 are studied to develop new approaches and algorithms for analysing the vertical atmospheric profile below 1 km. The vertical refractivity profile is derived from the analysis of dry and wet components of the surface one. New methodologies for refractivity predictions and derivation of certain propagation parameters at different atmospheric layers are presented in chapter 8. A new simplified approach is proposed to evaluate the vertical refractivity profile. Chapter 9 investigates the critical phenomena of three types of atmospheric ducts in the area under study. The path profiles and link budget calculations for candidate microwave links using reliable commercial design software, ICT Telecom, are presented in chapter 10. Some fading scenarios with respect to the dominant propagation conditions at certain times are also discussed. Chapter 11 gives the final conclusions and the recommendations. Finally, the references are provided followed by appendices with the list of publications and the radiosonde datasheet, which has been used in gathering the upper-air data.

Chapter 2

BACKGROUND AND LITERATURE REVIEW

2.1 Introduction

Radio waves propagation is affected by the atmospheric refractive index profile and its vertical variations. This profile is mainly decided by the temperature and moisture variations in the atmosphere.

Anomalous propagation phenomena occur regularly in the subtropical regions, in particular in the Arabian Gulf region, due to its special climate. The hot and humid climate generates special refractivity profiles across the region, which is important to be thoroughly studied for accurate evaluation of clear air effects on the propagating signals of the wireless systems operating in the low troposphere. Only few research works have been carried out to study the unique atmospheric conditions of this area. [4, 5]

The modelling of different propagation phenomena is a complicated process and some of them are difficult to predict. It is essential to study the impact of different severe conditions on the signal degradation in order to be able to derive the appropriate models for this subtropical climate.

2.2 Background

2.2.1 Fundamental of Meteorology and Characteristics of Earth Atmosphere [6]

The Earth's atmosphere is a collection of many gases together with suspended particles of liquid and solids. Excluding variable components such as water vapour, ozone, sulfur dioxide, and dust, the gases of nitrogen and oxygen occupy about 99 percent of the volume, with argon and carbon dioxide being the next two most abundant gases.

From the Earth's surface to an altitude of approximately 80 kilometres, mechanical mixing of the atmosphere by heat-driven air currents evenly distributes the components of the atmosphere. At about 80 kilometres, the mixing decreases to the point where the gases tend to stratify in accordance with their weights. The lower atmosphere, which is called the homosphere, is well-mixed while the higher, stratified portion is called the heterosphere. The bottom portion of the homosphere is called the troposphere. The troposphere extends from the earth's surface to an altitude of 8 to 10 kilometres at polar latitudes, 10 to 12 kilometres at middle latitudes, and up to 18 kilometres at the equator. It is characterized by a temperature decrease with height due to the decreasing atmospheric pressure with height. The point at which the temperature ceases to decrease with height is known as the tropopause. The average vertical temperature gradient of the troposphere varies between 6 and 7 degrees Celsius per kilometre. The concentrations of gas components of the troposphere vary little with height, except for water vapour. The water vapour content of

the troposphere comes from evaporation of water from oceans, lakes, rivers, and other water reservoirs. Differential heating of land and ocean surfaces produces vertical and horizontal wind circulations that distribute the water vapour throughout the troposphere. The water vapour content of the troposphere rapidly decreases with height. At an altitude of 1.5 kilometre, the water vapour content is approximately half of the surface content. At the tropopause, the content is only a few thousandths of what it is at the surface.

In 1925, the International Commission for Aeronavigation defined the international standard atmosphere as a hypothetical atmosphere having an arbitrarily selected set of pressure and temperature characteristics that reflect an average condition of the real atmosphere.

2.2.2 Wireless Communication Systems and Channels

The performance of a wireless system such as PTP MW link can be represented by the received signal strength and the quality of received signal represented by the signal to noise plus interference ratio. The performance depends on several internal and external factors. The internal factors refer to the system characteristics based on the design and specification from different manufacturers, which are essential pillars in deciding the overall system performance. These characteristics differ from a manufacturer to another, depending on the used technologies and standard. For example, the maximum throughput provided by a microwave link is related to maximum bandwidth of a channel and modulation schemes supported by the specific equipment. Also, the maximum distance per link is decided based

on the maximum power to be transmitted by the equipment and the sensitivity of the receiver which are manufacturer's specific characteristics. However, other external factors play important role in affecting the system performance as well, such as the atmospheric and propagation conditions in the area under study in addition to obstacles in the signal path. In this chapter, the components of a wireless system and some of these external factors that might affect the system performance are discussed. The equations to calculate the signal attenuation using the free space model is addressed and other reasons for attenuation are highlighted, which will be calculated using a commercial software in this work. [7]

2.2.2.1 Components of Wireless Communication System

The wireless communication system consists of major components which are transmitter, wireless channel, and receiver. The information bits are converted into a modulated electromagnetic signal at the transmitter side. The modulated signal has the capability to travel across the wireless medium for long distance. The characteristics of the wireless channel decide the behaviour of the transmitted signal. The electromagnetic wave can be attenuated while propagating through the channel due to propagation loss, shadowing, and multipath fading. The waveform of the received signal can be different from the transmitted one, due to multipath delay, the time/frequency selectivity of the channel, in addition to the unwanted noise and interference. At the receiver side, the signal is received and the information bits are recovered through the operations of equalization, demodulation, and channel decoding [8]. Figure **2.1** shows the communication system's components.

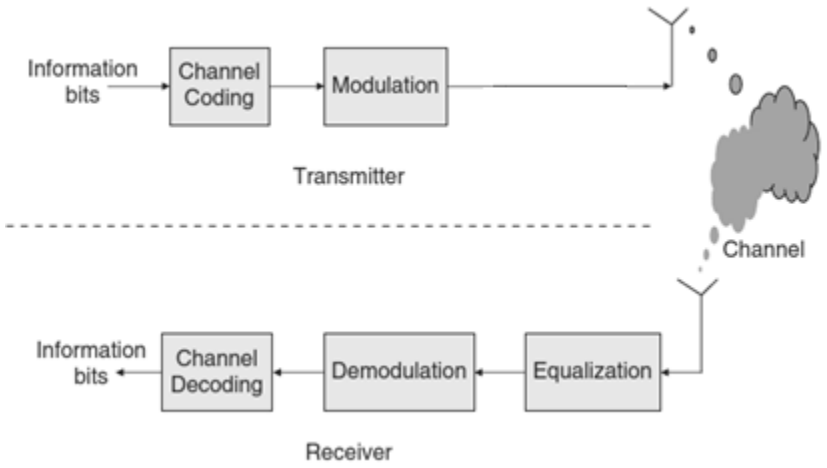

Figure 2.1: Block diagram of a Wireless Communication System [14]

2.2.2.2 Wireless Channel and Propagation Conditions

The channel is the medium between the transmitting and receiving antennas as shown in Figure 2.2. Many factors affect the wireless signal characteristics while it propagates through the atmosphere from the transmitter to the receiver. Some of these factors are related to the characteristics of atmospheric layers which mainly depend on their meteorological conditions such as temperature, humidity, rain, and pressure of the atmosphere. The channel characteristics are also affected by the distance between the two antennas, path(s) taken by the signal and the environment (buildings and other objects) around the path. The channel model is the model of the medium between the two antennas which is used to obtain the profile of received signal [9].

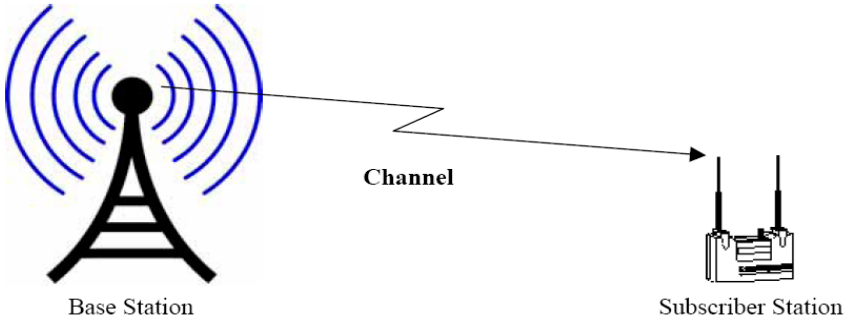

Figure 2.2: Wireless Channel [9]

The signals propagate through different channels such as free space channel and multipath channels. Objects may exist between the transmitting and receiving antennas such as buildings, trees and mountains. In LOS situations, where there is almost a clear path between the two antennas, the transmitted signal strength may be further attenuated during its spread around the transmitting antenna in addition to the free space loss. The propagating signal is attenuated due to several factors such as signal absorption, scattering, reflection and diffraction and might be lost in case of high attenuation. The reflected signals from the ground contribute to the reduction of the net received power level based on the phases of the received signals. Furthermore, shadowing phenomena may occur when the signal intersects with some objects through the path which probably has lognormal distribution [9]. The reflected signals from different objects take different paths and consequently each could have different amplitude and phase. This phenomenon is known as multipath, as displayed in Figure 2.3. These multiple received signals may increase or decrease the net power level. They could be totally destructive and cancel the transmitted signal if there is a phase shift of 180° from the main one [9]. The abnormal refraction

conditions may cause multipath within two atmospheric layers or with respect to the Earth surface in the case of ducting occurrence. Also, the non-standard propagation condition due to abnormal changes of vertical refractivity profile may result in bending the signals downward or upward and consequently losing part of the signal energy.

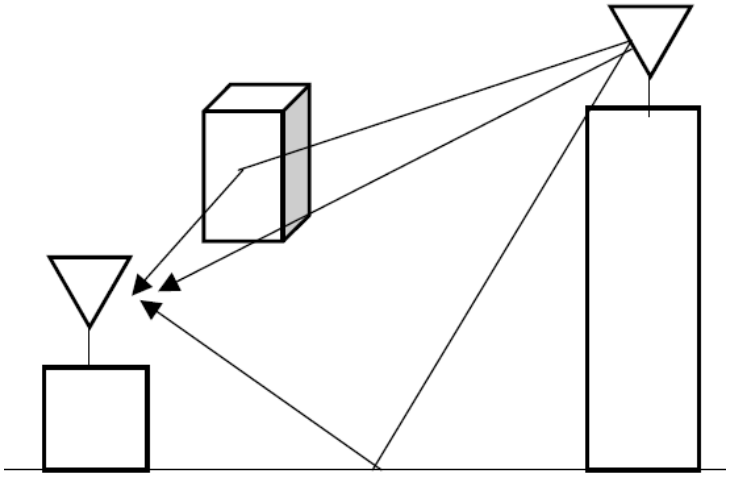

Figure 2.3: Multipath Propagation [9]

2.2.2.3 Free Space Loss Calculation

Several propagation models can be used to describe the signal behaviour. The power level of the transmitted signal degrades with distance due to several attenuation factors including rain, humidity, gas, diffraction by an obstacle and other air particles, until it reaches its destination. If the signal path is clear, only the meteorological conditions will affect the power degradation.

The free space loss and attenuation factor, A_{fs}, is calculated using free space model. However, other atmospheric conditions, such as multipath phenomenon, have to be taken into consideration to match with the measured received power. Also, additional attenuation factor might need to be added to the free space loss value depending on the existing climate at the experiment location and surrounding wireless environment. The free space loss depends on the distance between the transmitter and receiver in addition to the utilized frequency band as follows [10]:

$$P_r = (P_e . A_e) \,/\, (4\pi d^2) \tag{2.1}$$

where P_e is the transmitted effective isotropic radiated power, EIRP, d is the distance between the transmitter and the receiver, A_e is the effective aperture area of the reception antenna, and P_r is the received power strength. The P_r value has to be higher than a threshold level in order to achieve specific level of signal quality and accordingly data throughput. The received signal should also be above the noise level of the equipment with enough margin to guarantee that the signal is correctly received and decoded. The aperture area, A_e, for isotropic antenna which is measured in m^2, is calculated from:

$$A_e = \lambda^2 / (4\pi) \tag{2.2}$$

where λ is the wavelength of the transmitted signal in meter, m.

$$\lambda = c / f \tag{2.3}$$

where c is the speed of light in (m/s), and f is the frequency in Hz. Then, the free space attenuation, A_{fs}, factor can be calculated by the following equation:

$$\frac{1}{A_{fs}} = \frac{P_r}{P_e} = \frac{A_e}{4\pi d^2} \tag{2.4}$$

For isotropic antenna:

$$A_{fs} = \left(\frac{4\pi d}{\lambda}\right)^2, \tag{2.5}$$

or;

$$A_{fs} = 20 \log_{10}\left(\frac{4\pi d}{\lambda}\right), \tag{2.6}$$

The power level is measured by units of watt (W) or dBm[1]. On the other hand, the coverage area can be represented by the field strength, in units of dBu or dBμV/m, regardless the receiver parameters such as antenna gain.

[1] dBm (decibel-milliwatts) unit is the power ratio in decibels (dB) of the measured power referenced to one milliwatt (mW).

If the transmitting and receiving antennas have gains of G_e and G_r respectively, with respect to the isotropic radiator, where the gain unit is dBi, the free space attenuation will be:

$$\frac{1}{A_{fs}} = \frac{P_r}{P_e} = G_e \,.\, G_r \left(\frac{\lambda}{4\pi d}\right)^2 \tag{2.7}$$

$$A_{fs} = \frac{1}{G_e \,.\, G_r}\left(\frac{4\pi d}{\lambda}\right)^2 \tag{2.8}$$

Equation (8) can be expressed in decibels (dB) as follows:

$$A_{fs}\,[\text{dB}] = -10\log_{10}(G_e) - 10\log_{10}(G_r) + 20\log_{10}\left(\frac{4\pi d}{\lambda}\right) \tag{2.9}$$

2.2.3 Fundamentals of Refractivity and Relevant Propagation Parameters

The meteorological conditions play a vital role in affecting radiowave propagation in the lower and mid troposphere [11, 12]. Statistics of the signal refraction, reflection, and multipath propagation are important in properly predicting the behaviour of a propagating wave. An accurate knowledge of radio refractivity is essential for determining the propagation criteria [13], where its variability may cause bends in the signal path, ducting, and scintillation. Important issues regarding the inclusion of site-specific information of different propagation factors have been identified during the application of several ITU-R

Recommendations; such as ITU-R P.453 [12], P.452 [13] …etc, under the purview of Working Group 3J.

2.2.3.1 Atmospheric Refractive Index and Radio Refractivity

As a reference point, the ITU has defined a negative exponential "standard atmosphere" and published maps showing variations in refractive index at the Earth's surface [12]. The gradient of refractive index in N-units versus height (in km) at the surface is known as the surface lapse rate, ΔN. ITU maps [12] also provide ΔN data at specified altitudes.

Electromagnetic waves would travel in straight lines if the atmosphere was homogeneous but since the atmosphere and its permittivity (ε) are stratified, electromagnetic waves bend downward or upward according to the variations of the refractive index from layer to another. As a result, the atmosphere's refractive index, n, is related to the relative permittivity, ε_r, as follows:

$$n^2 = \varepsilon_r \tag{2.10}$$

where $\varepsilon_r = (\varepsilon / \varepsilon_o)$, and ε_o is the permittivity of free space.

The atmospheric radio refractive index, n, can be calculated by the formula [11, 12]:

$$n = 1 + N \text{ x } 10^{-6} \tag{2.11}$$

where N is the radio refractivity, which is usually used instead of n. The radio refractivity, N, is expressed by:

$$N = N_{dry} + N_{wet} = \frac{77.6}{T}\left(P + 4810\ \frac{e}{T}\right) \quad \text{(N-units)} \tag{2.12}$$

N consists of two components which are dry and wet refractivity components. The dry component contributes to more than 50% of the net refractivity. The dry term, N_{dry}, of the radio refractivity is given by:

$$N_{dry} = 77.6\ \frac{P}{T} \tag{2.13}$$

while the wet term, N_{wet}, is expressed by:

$$N_{wet} = 3.732 \times 10^{5}\ \frac{e}{T^{2}} \tag{2.14}$$

where P is atmospheric pressure (hPa), e is water vapour pressure (hPa), T is the absolute temperature (K). The index of refraction, and therefore refractivity, decreases normally with increasing altitude since the pressure and water vapour content of the atmosphere decrease rapidly with height while the temperature decreases slowly [14].

The ITU-R recommendation P.453-10 suggests that the error is less than 0.5% using the above refractivity expressions for all radio frequencies up to 100 GHz [12, 15]. The ITU provides maps and profiles of vapour content and density as a reference for areas without local reliable data [16, 17].

For given humidity measurements, the relationship between water vapour pressure, *e*, relative humidity, *H*, and saturation vapour pressure is given by [12]:

$$e = \frac{H \cdot e_s}{100} \tag{2.15}$$

where e is given in hPa, and the saturation vapour pressure, e_s, can be obtained from:

$$e_s = EF \cdot a \cdot \exp\left[\frac{\left(b - \frac{t}{d}\right) \cdot t}{t + c}\right] \tag{2.16}$$

In the Gulf region, the vapour pressure, *e*, evaporation factor, *EF*, and the coefficients *a*, *b*, *c* and *d* are selected with reference to water since the temperature is between –40 ^{o}C to +50 ^{o}C [12]. The water evaporation factor, EF_{water}, is expressed by:

$$EF_{water} = 1 + 10^{-4}\left\lfloor (7.2 + P \cdot (0.00320 + 5.9 \cdot 10^{-7} \cdot t^2)) \right\rfloor \tag{2.17}$$

where t is the temperature (^{o}C), P is pressure (hPa), and H is relative humidity (%).

e_s is saturation vapour pressure (hPa) at the temperature t (^{o}C) and the values of the constant coefficients a, b, c, and d for water are; a= 6.1115, b= 18.678, c= 257.14 and d= 234.5.

The relative humidity, H, can be calculated from the dry air temperature, t, and dewpoint temperature, t_d, using the following expression:

$$H = 100 \left(\frac{112 - 0.1\,t + t_d}{112 + 0.9\,t}\right)^{8} \tag{2.18}$$

2.2.3.2 Vapour Pressure Calculation

Several theoretical and empirical equations for have been developed for the relationship between vapour pressure, relative humidity, temperature and dewpoint, and an immense number of expressions have been proposed [18]. The atmospheric pressure and temperature are directly measured during the radiosonde balloon ascents, while the vapour pressure is derived from the given dewpoint temperature or water vapour density.

The vapour pressure, e, can be obtained from the water vapour density, ρ, using the equation [12]:

$$e = \frac{\rho\,T}{216.7} \tag{2.19}$$

where ρ is given in gm^{-3}. The ρ values are provided by the ITU recommendation [17]. When the dewpoint temperature is given instead of the relative humidity, the water vapour pressure, *e*, could be calculated from [19].

$$T_d = A \Big/ \left(\frac{B}{\log\left(\frac{e}{C}\right)} - 1 \right) \tag{2.20}$$

where the values of the constants *A*, *B*, and *C* are 240.71, 7.5892 and 6.1162, respectively.

Another model was proposed to calculate the saturation vapour pressure and actual vapour pressure as a function of temperature and site atmospheric pressure [20]. Accordingly, the authors considered that the saturation vapour pressure is a function of air temperature and site atmospheric pressure, whereas actual vapour pressure, *e*, is a function of dewpoint temperature, T_d, and site atmospheric pressure with respect to the water. The following equation was proposed for calculating the saturation vapour pressure, e_s:

$$e_s = 6.112 \ f(P) \,.\exp\left(\frac{17.62\, t}{243.12+t}\right) \tag{2.21}$$

where e_s is calculated with respect to the water at the air temperature *t* (°C), $f(P)$ is the enhancement factor at the air pressure *P* (hPa) and can be obtained from:

$$f(P) = 1.0016 + (3.15\text{x}10^{-6})P - 0.0074P^{-1} \quad (2.22)$$

Accordingly, the actual vapour pressure, *e*, can be expressed by:

$$e = 6.112\ f(P).\exp\left(\frac{17.62\ t_d}{243.12 + t_d}\right) \quad (2.23)$$

where t_d is the dewpoint temperature at the same air pressure *P* (hPa). Another logarithmic relationship between the vapour pressure and dewpoint was proposed [21].

$$t_d = \frac{B_1\ .\ \ln(\frac{e}{C_1})}{A_1 - \ln(\frac{e}{C_1})} \quad (2.24)$$

where the coefficients: A_1 = 17.625, B_1 = 243.04°C, and C_1 = 610.94 Pa. The water vapour pressure, *e*, can be calculated from the dewpoint temperature, t_d (°C) directly by replacing the dry temperature, *t*, in Equations (2.16) and (2.17) with the dewpoint temperature, t_d, and using the same constants' values.

$$e = EF \cdot a \cdot \exp\left[\frac{\left(b - \frac{t_d}{d}\right) \cdot t_d}{t_d + c}\right] \quad (2.25)$$

$$EF_{water} = 1 + 10^{-4}\left\lfloor (7.2 + P \cdot \left(0.00320 + 5.9 \cdot 10^{-7} \cdot {t_d}^2\right)) \right\rfloor \quad (2.26)$$

The analysis of meteorological data using the above vapour pressure models shows that they are similar. Any of these models can be adopted based on the available parameters for the study.

2.2.3.3 Refractivity Gradient and Refractivity as a function of height

The vertical refractivity gradient, ΔN, in the low troposphere is an important parameter for the estimation of propagation effects such as ducting and multipath on terrestrial line-of-sight links. In the standard atmosphere, *N* decreases exponentially with altitude since the total pressure drops off rapidly while temperature decreases with height [22]. Consequently, the vertical refractivity gradient usually has a negative value causing rays to bend downward from a straight line towards the Earth, and to propagate beyond the geometric horizon.

A standard gradient is characterized by a decrease of a typical *N* value per kilometre, which is assumed to be a decrement of 39 N/km for a temperate region over a typical year. A standard gradient will cause traveling Electromagnetic (EM) waves to bend downward from a straight line. Normal gradient conditions have similar effects to the standard gradient, but are found to vary in larger ranges that are different to those in the literature

due to the area and period under study, such as 0 to -100 N/km [12] or between 0 and -79 N/km [14].

If the gradient is less negative than usual, or even positive, sub-refraction occurs, where the ray bends less than usual towards the Earth, even bending upwards, in the case of a positive gradient and the range reduces. Sub-refraction occurs when temperature and humidity distribution creates increasing value of N with height, in a situation such that a warm moist air flows over a cool ocean surface or over a cooler air mass just above the ocean surface [23, 24]. The sub-refraction phenomenon infrequently occurs in nature [14], however, it needs to be considered when assessing the electromagnetic systems' performance.

If the gradient is more negative than in a standard or normal atmosphere, super-refraction takes place with the ray bending more than usual towards the earth and propagating further than in standard conditions. Super-refraction occurs when temperature increases and/or water vapour content decreases rapidly with height, where the signal propagates between the normal and critical gradient conditions. At a critical gradient value, ΔN = -157 N/km, the radius of curvature of the ray becomes equal to the Earth radius. The wave path approaches the Earth curvature and consequently the signal moves parallel to its surface [24]. Gradients more negative than this critical value lead to ducting, in which the signal becomes trapped in the boundary layer, propagating well beyond its usual range. Figure 2.4 shows the various refractive conditions explained above.

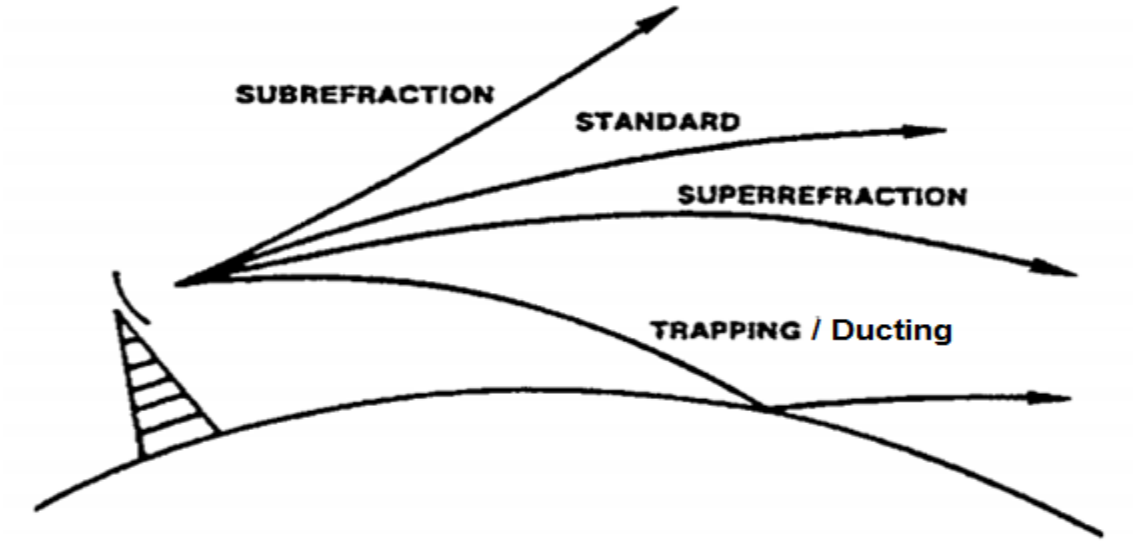

Figure 2.4: Refractive conditions [14]

In addition, Table 2-1 summarizes the limits considered for the refractive conditions considering the ITU-R values defined for anomalous propagation conditions [12].

Table 2-1: Summary of Refractive Propagation conditions

Refractive Conditions	**Gradients [N/km]**
Sub-refraction	> 0
No Refraction	0
Normal Refraction	0 to -100
Super-refraction	-100 to -157
Trapping or Ducting	< -157

Different linear and exponential models have been adopted to calculate the vertical refractivity gradient at specific altitudes from either one or two levels of refractive index per atmospheric layer. Other works have been conducted to study the possibility to estimate the vertical refractivity gradient near the ground from measurements of electromagnetic

wave strength and diffraction losses [25, 26], in particular when the upper-air data are not available.

2.2.3.3.1 Linear Model

The vertical exponential decrement of N within 1km from the ground allows the approximation of exponential function by a linear one [14]. The refractivity gradient can be obtained from two refractivity values, N_1 and N_2, with heights h_1 and h_2 using the following linear model [3, 27, 28]:

$$\Delta N = \frac{N_2 - N_1}{h_2 - h_1} \tag{2.27}$$

The radiosonde data may not be available at certain altitudes, in which case h_1 and h_2 are selected to be the nearest available point to the targeted heights. For example, the ΔN for first kilometre could be calculated from the first point with valid data (nearest to the surface) and the point nearest 1 km, where h_1<500 m, h_2<1500 m and h_2- h_1>500 m [3, 27]. These ranges will depend on the resolution of the available data. Initial statistics of surface refractivity and first kilometre refractivity gradient in Abu Dhabi were presented in [4, 5].

2.2.3.3.2 Exponential Model

The long-term average dependence of the refractive index, *n*, upon the height, *h*, is well expressed by an exponential law [12]:

$$n(h) = 1 + 10^{-6}\, N_o\, .\, \exp(-\frac{h}{h_o}) \tag{2.28}$$

where N_0 is the average value of atmospheric refractivity extrapolated to sea level, and h_0 is the height coefficient (km).

N_0 and h_0 can be determined statistically for different climates. For reference purposes a global mean of the height profile of refractivity, which applies only for terrestrial paths, may be defined by: $N_0 = 315$, $h_0 = 7.35$ km.

This reference profile may be used to compute the value of refractivity N_s at the Earth's surface from N_0 as follows [12]:

$$N_s = N_0 \exp(-h_s/h_0) \tag{2.29}$$

where h_s is height of the Earth's surface above sea level (km). The ITU contour maps of the monthly mean values of N_o were derived using a value of h_0 equal to 9.5 km [12] from a 5-year data set (1955-1959) from about 1000 surface stations. The last equation may also

be used for quick and approximate estimates of refractivity gradient near the Earth's surface and of the apparent bore-sight angle [12, 28].

2.2.3.4 β_0 Parameter and Vertical Gradient in the lowest 100 m of Atmosphere

β_0 is an important parameter in the studies of clear air propagation and interference since it is commonly used to indicate the relative incidence of anomalous propagation in the lowest troposphere. β_0 represents the time percentage in which ΔN value, in the first 100 m of the Atmosphere, is less than or equal to -100 N/km [12, 23, 29]. It is derived from ΔN statistics in the lowest 100 m of the atmosphere. The normal range of ΔN in the surface layer is between 0 and -100 N/km. Other references consider different values such as -79 N/km for the limit between the normal and non-standard propagation [24]. In this thesis, "anomalous propagation" is defined as that occurring outside this normal range. β_0 might relate, with reasonable accuracy, to the presence of ducting phenomenon. It was observed [23] that β_0 is correlated to the latitude of the area under consideration, showing higher values in the equatorial regions and lower toward the poles. In this work, β_0 is calculated from the occurrence probability of both super-refraction and ducting conditions.

2.2.3.5 Point Refractivity Gradient

The prediction of a microwave link's availability is related to the point refractivity gradient, dN_1 [30]. The parameter dN_1 needs to be calculated correctly for reliable design and

performance prediction of microwave links [13]. Estimated values of dN_1 are provided by ITU tables for different geographical locations whenever local data are not available [12].

2.2.3.6 Effective Earth Radius

The effective Earth radius has to be set carefully for accurate simulation and design of microwave links [13]. The effective Earth radius factor, *k*, is found to be directly related to the vertical gradient of refractivity in the low troposphere. The *k*-factor parameter is set to a global value of 4/3, assuming a standard atmosphere with an average refractivity gradient of around -39 N/km. This could be useful when local reliable data are not available [12].

Effective Earth radius is the radius of a hypothetical spherical Earth, without atmosphere, for which propagation paths are along straight lines. The heights and ground distances are considered to be the same as for the actual Earth in an atmosphere with a constant vertical refractivity gradient [31].

The *k*-factor can be derived from the vertical refractivity gradient, ΔN, in the first kilometre above the ground surface. If the linear equation is used to calculate, ΔN, then the two levels of refractivity are to be; N_s, surface refractivity, and N_1, refractivity at 1 km height above the ground [3]. The atmospheric refractive index can be obtained from the relative permeability as given in equation (2.10) above. The radius of the path curvature of a propagating signal through the air is proportional to the refractive index and its variation with height as follows [24]:

$$\frac{1}{r} = \frac{1}{n} \cdot \frac{dn}{dh} \cos \alpha \tag{2.30}$$

where r is the radius of the signal curvature, h is the height of the signal above the ground, dn/dh is the rate of refractive index change with height, and α is the horizontal angle of the path, which is known as the antenna elevation angle.

The k-factor parameter can be calculated from Snell's law in spherical geometry [24, 32]. The incident and refracted rays as well as the angles made at the point of refraction with the normal to the boundary is shown in Figure 2.5, as per the following relationship:

$$n_1 \sin \theta_1 = n_2 \sin \theta_2 \tag{2.31}$$

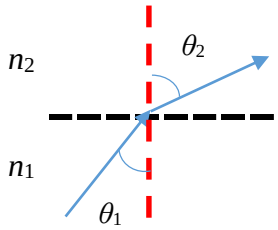

Figure 2.5: Angles of incident and refracted rays in Snell's Law

The relation between the radius of signal curvature, r, gradient of refractive index and the Earth radius, a, can be expressed by [12, 15, 30, 33, 34]:

$$\frac{r}{a} = k \cong \frac{1}{1 + a\,.\,(\frac{dn}{dh})} \tag{2.32}$$

This value must be multiplied by the actual Earth's radius, *a*, in order to plot the propagation paths as straight lines, as follows:

$$k = 1/(1 + a.(dn/dh)) \tag{2.33}$$

where *a* is given by unit of nmi rather than km (*a* = 6371 km = 3440 nmi) and d*n*/d*h* is the rate of change of the refractive index with height, knowing that $N = (n\text{-}1) \times 10^6$, the *k*-factor can be expressed in terms of *N* as follows [15, 35]:

$$k \cong \frac{1}{1 + (\frac{dN}{dh})/157} \tag{2.34}$$

Accordingly, monthly, yearly or long-term median *k*-factor may be calculated using the monthly, yearly or long-term median, Δ*N*, and the *k*-factor equation can be simplified by as follows [11]:

$$k = 157/(157 + \Delta N) \tag{2.35}$$

It should be noted that the above equation has also been used in the literature with replacing the addition sign in denominator to a subtraction sign [4, 13]. In such case, a modulus ΔN should be considered.

The classification of *k*-factor was proposed in [15] assuming that normal refraction conditions occur at the reference value of -39 N/km exactly. The *k*-factor value of 4/3 is then the edge between sub-refraction, when *k* has a positive value less than 4/3, and super-refraction, when positive *k* is larger than 4/3. Accordingly, ducting phenomena, where the waves bend downwards with a greater curvature than that of the Earth, are expected when the *k*-factor value is negative. However, other references consider a range for the normal refraction instead of just a value [13, 24].

In this research work, different values for the limits of the refractive conditions have been proposed assuming that the rate of vertical change in refractivity can be considered as normal in the range between -100 and 0 N/km, and considering that the long-term refractivity gradient in the first kilometre is found to be around -72.5 N/km. Accordingly, the refractive conditions have been categorized according to the values of effective earth radius factor, *k*, as follows:

- Sub-refraction: when *k*-factor is less than 1 ($0 < k < 1$),
- No refraction: when *k*-factor = 1,
- Normal refraction: when *k*-factor is between 1 and 2.75 ($1 < k < 2.75$),
- Super-refraction: when *k*-factor is larger than 2.75 ($k > 2.75$),
- Ducting: when *k*-factor is negative ($k < 0$)

2.2.3.7 Modified Refractivity and Atmospheric Duct

The tropospheric ducting phenomena occur due to abnormal vertical structures of the refractive index of the lower atmosphere. The rapid variations of meteorological parameters, such as temperature and humidity, result from processes such as surface heating (advection), radiation cooling and evaporation [36]. The unusual atmospheric conditions may cause the temperature to increase with height over some limited ranges, creating temperature inversion and atmospheric ducting, when warm dry air overlays the moist cool air mass near the surface [14, 37]. It has been noted that a sub-refractive condition may also occur in such cases with steep vertical refractivity gradients that cause the transmitted signals with large elevation angle to be lost in to space [37]. Consequently, a trapping layer is formed where propagating and the waves can propagate beyond the horizon in the such atmospheric ducts [38].

The vertical refractivity profile as well as the geometrical relationship of transmitter and receiver with respect to the duct have to be taken into account in order to assess the duct's effect at any particular frequency. In the duct channel, the electromagnetic energy can propagate over great ranges. However, the angle of incidence of the electromagnetic energy with respect to the duct must be small, usually less than 1 degree. Since the trapping of electromagnetic waves depend on their frequencies, the thicker ducts can support trapping of lower frequencies [14].

The duct acts as a waveguide, but energy is continually leaking from the duct since its boundaries can be penetrated except for the Earth's surface in case of surface based ducts. A real advantage of the ducting phenomena is the propagation beyond the horizon for several hundreds of kilometres, in addition to its effects within the horizon [38]. The normal lobe pattern as well as the relative phases and amplitudes of interfering direct and surface-reflected rays may be changed within the atmospheric ducts.

2.2.3.7.1 Modified Refractivity

The modified refractivity parameter, *M*, is commonly used in place of refractivity to examine the refractivity gradients and to describe their effect, such as atmospheric ducts. The modified refractivity is defined as [12]:

$$M(h) = N(h) + 157\,h \tag{2.36}$$

where *M(h)*, in M-units, is the modified parameter of refractivity, *N(h)*, at certain height, *h*, given in kilometre. The decreasing vertical refractivity gradients are equivalent to the increasing modified refractivity gradients with heights. The refractive conditions are revised in Table 2-2 in terms of modified refractivity gradients.

Table 2-2: Summary of refractive conditions in terms of modified refractivity gradients

Refractive Conditions	Modified Refractivity Gradients [M/km]
Sub-refraction	> 157
No Refraction	157
Normal Refraction	78 to 157
Super-refraction	0 to 57
Trapping or Ducting	< 0

2.2.3.7.2 Types of Atmospheric Ducts

The ducting phenomenon or signals' trapping occurs when the gradient of refractivity goes below the critical gradient such that the modified refractivity gradient is less than zero. The radius of wave curvature becomes smaller than the Earth's curvature striking the Earth and may undergo surface reflection [14]. There are four types of atmospheric duct. Three of them are surface based ducts, while the fourth one is elevated duct with a duct's base above the surface level. Surface based ducts occur when the air aloft is exceptionally warm and dry compared with the air at the Earth's surface and can be of three types based on their trapping layers' relationships to the Earth or sea surfaces, which are surface, elevated-surface and evaporation ducts. Several meteorological conditions may lead to the formation of surface-based ducts such as the situation where warm, dry continental air may be advected over a cooler water surface over the ocean and near land masses. While a temperature inversion occurs at the surface due to advection phenomenon, the moisture is added to the air by evaporation, producing a moisture gradient to strengthen the trapping gradient [14]. The elevated-surface ducts, where trapping layer rises from the surface, particularly over the open ocean. This tends to be on the leeward side of land masses and

may occur during the day or at night. This is associated with fair weather, where occurrence probability increases during the summer months towards equatorial latitudes while it decreases in the case of a well mixed troposphere, such as with high wind conditions. This duct type may extend over the ocean for several hundreds of kilometres and may last for several days.

The surface duct statistics can be derived by combining elevated-surface ducts with surface ducts in one group, due to rather few cases of elevated-surface ducts [12].

The evaporation duct is of great importance for overwater wave propagation that is created by the rapid decrease of relative humidity adjacent to the air-sea interface. The air in contact with the ocean's surface is saturated with water vapour, which is not usually the case for the air aloft with few meters' height. The water vapour pressure decreases rapidly well above the surface, causing the modified refractivity, *M*, to decrease with height until it reaches its minimum at a value known as evaporation duct height. *M* starts increasing with height again after reaching its minimum value. It has been observed that the duct height varies from a meter or two in northern latitudes during winter nights to as much as 40 meters in equatorial latitudes during summer days. On a world average, the evaporation duct height is approximately 13 meters. [14]

The elevated duct occurs when the duct base of the trapping layer is above the earth's surface. It can be formed by a layer of warm, dry air overlaying another cool, moist layer that is often called a marine boundary layer. This inversion may create a strong ducting

condition at the top of the boundary layer. Elevated ducts may vary from a few hundred meters above the surface at the eastern part of the tropical oceans to several thousand meters at the western part [14].

The ducting conditions may be present in hot climates, and over the sea, at almost all of the time, where they occur in the early evening as the Sun sets, due to rapid cooling of the ground, in temperate climates [37]. The meteorological conditions are similar for both elevated surface and elevated ducts. A surface-based duct may turn into an elevated duct as warm, dry continental air rises over cool, moist marine air. On the other hand the elevated duct may slope downward to elevated surface duct due to inversion intensification [14].

It is noted that multipath fading may occur through atmospheric duct where large number of rays interfere simultaneously at the receiver. The fading impact of atmospheric ducting can be eliminated by either using different antenna heights or applying vertical space diversity with enough separation [37].

2.2.3.8 Signal Attenuation Due to Refraction-Diffraction Fading (*k*-type Fading) and Multipath

The vertical rate of the refractive index and *k*-factor variations can cause fading to the propagating waves, which is considered in relation with diffraction fading and known as *k*-type fading. The probability of refraction-diffraction fading is related to the obstruction

attenuation for a given value of Earth radius factor. The value of *k*-factor is critical for predicting the fading due to refraction and diffraction interaction as follows:

- For low values of *k*-factor below 1, the propagation becomes "curved" and terrain irregularities, man-made structures and other objects in the path may intercept the Fresnel Zone[2].
- For high *k* values, above 1, the hypothetical Earth's surface gets approximately close to a plane surface and better LOS can be obtained with lower antenna height.

The probability of refraction-diffraction fading can be calculated based on cumulative distributions of the *k*-factor, since it varies according to the atmospheric conditions.

The attenuation of received signals due to multipath interference may result from two dominant destructive signals created by a significant reflection from ground or sea. Adjustment of antenna height may provide constructive interference in normal atmospheric conditions, where the magnitudes of in-phase signals enhance the received signal level. However, the time variability of *k*-factor causes differences in the effective path curvature in the case of the abnormal refraction conditions. The signal fading due to time variations of received signals should be taken into account by considering an adequate fade margin [37].

[2] The Fresnel Zone is the area around the visual line-of-sight, where the radio waves spread out, after they leave the transmitting antenna.

2.3 Literature Review

Several research works have been conducted to statistically analyse the existing propagation conditions in different climates all over the world such as the rain precipitation, gas attenuation and refractivity analysis. In a clear air atmosphere, special attention has been paid to the analysis of refractivity profile and the relevant propagation parameters such as β_0, ducting and effective Earth radius factor. Several studies related to the refractivity analysis are available [23, 29, 39-46].

Bean and Thayer [47] introduced two models to evaluate atmospheric radio refractive index in order to predict refraction effects from the index value at the transmitting point rather. Those models showed considerable improvements particularly for applications at long distances and high elevations in the atmosphere. The authors proposed a new method for predicting signal refraction at very low initial elevation angles which utilizes both the initial value and the initial height-gradient of the refractive index over roughly the first 100 meters above the Earth's surface. It was expected that the refractivity to decrease exponentially with height since the dry component of refractivity is proportional to Pressure/Temperature, which comprises at least 70 per cent of the total refractivity and is proportional to air density that is a well-known exponential function of height. The following two criteria were proposed to evaluate the usefulness of refractive index models:

a- relative agreement between the model and the average refractive index structure of the atmosphere, and

b- relative agreement between the amount of refraction (ray bending), predicted by the model and the amount actually calculated for observed refractive index profiles representing both mean and individual observations of extreme conditions from many geographically and climatically diverse locations.

The following equation was proposed for the relationship between surface refractivity, N_s, and refractivity gradient, ΔN, using least squares determination, for average conditions below the first kilometre of the lowest troposphere:

$$-\overline{\Delta N} = 7.32\ \exp(0.005577\ \overline{N_s}) \tag{2.37}$$

In the altitude range of 1 to 9 km, it was suggested that the refractivity, N, be represented by an exponential function of height which was given by the following equation:

$$N(h) = N_o\ .\ \exp(-\mathrm{b}h) \tag{2.38}$$

where b is constant but its value was provided. In order to develop the proposed models, the authors made the following assumptions to describe the effect of the atmospheric refraction:

1. An invariant model such as the 4/3 Earth radius model, which is near to the actual average conditions, was assumed to facilitate the signal strength calculation,
2. The approach of variable effective Earth's radius factor for the calculation of radio field strengths in various climatic regions.

3. Modifying the effective Earth's radius model considering a more realistic *N* structure in the regions where the original effective Earth's radius approach was inadequate.
4. An entirely new model of *N* structure guided by the average *N* structure of the atmosphere was assumed, allowing for seasonal and climatic changes of the average refractive index structure as in the assumption 3.

The first proposed refractivity model was based on the effective Earth's radius concept in the first kilometre and three equations were proposed for three layers of the atmosphere, namely below 1 km, from 1 km to 9 km and above 9 km. Refractivity, *N*, was assumed to decay linearly from the surface h_s to 1 km above the ground, h_s +1, as follows:

$$N(h) = N_s + (h - h_s)\,\Delta N, \qquad h_s \leq h \leq h_s + 1 \tag{2.39}$$

where

$$-\Delta N = 7.32 * \exp(0.005577\, N_s) \tag{2.40}$$

Then, it was assumed that *N* decreases exponentially from h_s+1 to 9 km above sea level, which was expected to have a constant refractivity value of 105 around the globe.

$$N = N_1 \,.\, \exp\{-c(h - h_s - 1)\}, \qquad h_s + 1 \leq h \leq 9\ km \tag{2.41}$$

where, N_1 was assumed to be the value of N at 1 km above the surface and c was calculated from:

$$c = \frac{1}{8 - h_s} \ln\left(\frac{N_1}{105}\right) \tag{2.42}$$

Above the altitude of 9 km, the following exponential expression was proposed:

$$N = 105 \exp\{-0.1424\,(h - 9)\}, \qquad h \geq 9\ km \tag{2.43}$$

On the other hand, the second proposed model assumed a single exponential distribution of the refractivity, N, as follows:

$$N = N_s \,.\, \exp\{-c_e\,(h - h_s)\} \tag{2.44}$$

where;

$$c_e = \ln\left(\frac{N_s}{N(1\ km)}\right) = \ln\left(\frac{N_s}{N_s + \Delta N}\right) \tag{2.45}$$

It was concluded that the average refractivity structure of the atmosphere could be represented by an exponential decrease with height than by the linear decrease inherent in the effective Earth's radius model, which indicated too little refraction between the Earth

and about 16 km, and too much refraction above that height. The refractivity was assumed to be approximately constant at an altitude of 9 km. It was suggested to improve the proposed methods by deriving individual regression lines of ΔN upon N_s for each station or climatic region and then, perhaps, presenting maps of the statistically determined constants of these regression equations. The paper referred to French reports on 1957 and 1958 on refractivity climatology, which indicated essential agreement in the relationship between ΔN and N_s for France, but some disagreement for North Africa. That disagreement indicated the need for some adjustment of the regression equation for tropical regions.

The refractivity of the lower atmosphere has been estimated using direct measurement from microwave refractometers [38], radiosonde [48] as well as Global Positioning System (GPS) measurements [49]. Other techniques were utilized such as in situ bulk measurements [50], and refractivity prediction from clutter [51, 52].

Otakar et al. [25] addressed the indirect refractivity estimation from the received strength measurement. The authors used artificial neural networks (ANN) to find the relationship between the vertical refractivity gradient and the measured electromagnetic wave strength, since previous studies using deterministic approaches [53], did not show any promising results. Signal strength measurements gathered from a microwave link with three receiving antennas in LOS with the transmitter, were used to estimate the vertical refractivity gradient. Estimated values were compared with the refractivity gradient derived from meteorological measurements. Other studies estimated the vertical gradient of radio refractivity from the diffraction attenuation measured on shadowed radio links [26, 54],

assuming that the vertical refractivity profile is linear after transforming the radio ray trajectory to a straight line above the Earth considering the Effective Earth radius. Refractivity gradient derived from diffraction losses showed promising results which confirmed that meteorological measurements might not properly represent the influence of atmospheric effect on radiowave propagation. Although results indicated that it might be possible to estimate the vertical refractivity gradient from measurements of received power strengths of multiple line-of-sight links at different heights, ANN could not be expected to give correct estimations at all times.

O. Jicha et al. [55] discussed the uncertainty of the indirect refractivity measurements from the meteorological parameters of pressure, temperature, and humidity, which is mainly due to the uncertainties of meteorological sensors. Although the uncertainty of each independent sensor could be negligible, however the combination of uncertainties through the refractivity calculation may lead to an undesirable significant uncertainty, which may affect the validity of the results. Different methods, techniques and instruments, which are used to derive the vertical refractivity profile, are generally highlighted in the paper such as refractometers, radars [56], GPS [57], indirect empirical calculation from meteorological data, and the time delay of the propagating wave between transmitter and receiver [58]. It was concluded that the uncertainty could be non-negligible and has to be addressed since uncertainty increases with temperature and humidity even in a temperate climatic zone, but could be unreliable in the tropical temperature zones. Based on the given assumptions, the refractivity measurement uncertainties were expected to be less than 3.5 N-units, with a median value of around 1.5 N-units and around 0.5 N-units during the cold days in a

temperate climate zone. However, it was expected that the uncertainty to be worse for hot and humid climates and in case of the vertical refractivity gradient measurement. It was proposed to use more than two meteorological sensors to measure indirectly the refractivity profile, filter the measured refractivity data within the time domain to remove the uncertainty arising from random effects, and to use appropriate level of space resolution to interpolate data using existing refractivity models.

In this thesis, the radiosonde is used to gather the vertical upper-air meteorological data where lots of vertical measurements are taken. The ROAB software, which is commonly used by meteorological centers all over the world, has been used to filter and interpolate the radiosonde raw data in order to obtain smooth reliable meteorological measurements at the required heights. Also, the radiosonde measurements at the ground have been compared with data gathered from other surrounding surface weather stations in order to study and compare the behaviour of the indirectly measured radio refractivity.

The influence of changing the parameters of the evaporation and surface based ducts on microwave path loss has been simulated by Sirkova et al. [59], using Advanced Propagation Model (APM) routines of the SPAWAR Systems Center. The path loss was assessed considering multiple scenarios of different frequencies, 2.5 and 5.8 GHz, different ranges of link distances, and different transmitting antenna heights above the duct height. In the case of the evaporation duct, a series of duct heights measured over 100 minutes period in Australia [60], were used to illustrate the influence of the evaporation duct height. In order to increase the accuracy of path loss prediction, particularly in coastal areas, it was

recommended to use range dependent refractivity profiles to improve the performance and eliminate the interference between links operating in the same region.

A.T. Adediji et al. [15] evaluated the variations of refractivity, refractivity gradient and k-factor using two years of meteorological data, from January 2007 to December 2008, measured by wireless weather stations (Integrated Sensor Suite, ISS). The sensors were positioned at five different height levels up to 200 m from the ground with steps of 50 m. The effective Earth radius factor was calculated from the refractive index gradient. The relation between the effective Earth radius factor and the anomalous propagation phenomena such as super-refraction and sub-refraction was addressed. It was considered that the common value of *k*-factor of 4/3, where the signal is assumed to travel through straight line along the Earth's surface, is given near the ground assuming an average radio refractive index gradient of -39 N/km. The super-refraction was expected to occur when k-factor is between 0 and 4/3, while its value could be between 4/3 to infinity when sub-refraction takes place. The average values of refractivity gradient were found to be -55.4 N-units/km and -50.1 N-units/km for the years 2007 and 2008, respectively, and the average *k*-factor was found to be 1.51 over the two-year period.

Experiments were conducted by Tjelta et al. [27] to study the impact of propagation phenomena on the performance of single carrier links of a gigabit capacity operating in the frequency band of 70/80 GHz. The paper addressed the effects of precipitation on links operating at 70-80 GHz, and provided a validation of precipitation attenuation methods. It was found that the method recommended by the International Telecommunication Union

gives results close to the observed data, but is slightly optimistic. The recommended ITU-R method for precipitation attenuation was not validated for real link design at frequencies above 40 GHz and the work highlighted another methodology to be used for a future refinement of the ITU-R method. It also addressed the requirement to derive a method to combine gaseous attenuation and precipitation attenuation distributions. It was concluded that attenuation due to clouds, fog and perhaps scintillation effects should more likely be included.

The results of some studies conducted around the world have been submitted to the Working Party 3J (WP-3J) of the Study Group 3 (SG-3) of the Radiocommunication Sector of International Telecommunication Union (ITU-R) by the member states. These contributions are being considered in developing the mathematical equations, maps, and tables of the ITU recommendations, which are related to the most common propagation phenomena in the areas under study such as rain fall rate and attenuation. Some of the submitted documents, with regards to the common propagation phenomena in the areas of the study, such as rain impact, are summarized in the following paragraphs.

In document 3J/170E from Spain [34, 61], Garcia-Rubia et al. conducted an experiment to study the rain attenuation impact on the Ka-band satellite applications. The instruments of rain gauge and a satellite beacon receiver were installed in Madrid. Four years of measurements from a tipping-bucket rain gauge and the satellite beacon receiver, operating in 19.7 GHz band, were gathered and processed. The results of annual statistics of rain fall

rate and rain attenuation showed a maximum rate was up to 70 mm/h and around 28 dB attenuation for 0.001 % of the average year.

Document 3J/178-E was submitted by the UK administration [62] for revising the sleet attenuation model. The predicted values were compared with the real data gathered from fixed links operating in 9, 15, 18, 26 and 38 GHz bands around the UK. The fade margins were calculated using Ofcom's frequency assignment software, which is used for processing the fixed link requests. It was found that the re-tuned sleet model reduced the predicted fade margin for some of the links while it enhanced it for the others. The expected values from the revised model were in good agreement with test results.

Different wave propagation methods and tools have been used to model wave propagation in a ducting channel. The parabolic equation method (PE) is commonly used for modeling ducting channels and anomalous propagation [63-66], which can be solved with numerical methods such as Split-Step Fourier (SSF) [38, 67, 68]. AREPS is a widely used tool [14, 38], which utilizes both SSF based PE and ray-optics (RO) methods. Analysis for beyond line of sight (b-LOS) sensor networks was performed using AREPS in [64] showing a high data rate employment of the atmospheric ducts. It was concluded that AREPS produces results consistent with experimental results. PETOOL is another promising tool, in particular for regions with irregular terrain conditions. This was utilized for the simulation of wave propagation in duct channels based on the PE method in [38], since it is a free online available tool that is calibrated with RO methods and AREPS [69].

The evaporation duct was analysed by Wayne L. Patterson [14]. It was highlighted that the long-term statistical frequency distribution of worldwide evaporation ducts has been readily available through the EREPS Surface Duct Summary (SDS) program or Ducting Climatology Summary (DCS) program. It was found that the evaporation duct is much weaker than surface-based ducts since the ability to trap energy is highly dependent on frequency. The evaporation duct was found to be strong enough to affect electromagnetic systems above 3 GHz only. It was also noted that the duct strength is a function of wind velocity, where stronger winds generally result in less propagation loss and stronger signal strengths, in the case of unstable atmospheric conditions. In addition, it has been observed that the world average height of the evaporation duct is approximately 13 meters and it varies from a meter or two in northern latitudes during winter nights to as much as 40 meters in equatorial latitudes during summer days. It was emphasized that the antenna should not always be located below evaporation duct height to have extended propagation, since the height relates to certain duct's strength or the ability of the duct to trap radiation. It was concluded that the assessment of the evaporation duct is best performed by making surface meteorological measurements and inferring the duct height from the meteorological processes occurring at the air/sea interface due to the turbulent nature of the troposphere at the ocean surface and the difficulty of measuring duct height using a low resolution radiosonde, rocketsonde, or a microwave refractometer.

The scattering problem was solved numerically in the presence of atmospheric duct by C. Bourlier et al [43]. The authors computed the field scattering due to highly conducting rough sea surface. A large-scale path-loss model was developed for the surface ducts based

on the parabolic equation (PE) method, in addition to a ray-optics (RO) method to analyse the delay spread and angle-of-arrival (AOA) of the ducting channel with the surface ducts. An analytical expression was developed for predicting the ranges of beamwidth that can be trapped by the surface ducts. Scattering of coherent and incoherent power components by a rough sea surface for certain wind speeds was provided, where strong fluctuations were observed for coherent power with large height while the incoherent power decreased. It was found that a longer surface was required to observe several bounces.

F. Ryan also presented in [44] a technique based on the parabolic wave equation (PWE) code for both the refractivity ducting and rough sea surface phenomena, in order to model maritime RF propagation over rough seas. It was found that the coordinate system used by the PWE method is conformal to the rough sea surface.

The calculation of the range at which the ducts modify the received power was introduced in [70]. The objective was to overcome the limitations of the refractivity from clutter (RFC) systems in retrieving the atmospheric ducts from the sea clutter echo of a radar in the open sea or coastal environment. The distance at which a ray reaches the ground in the presence of double ducts; namely evaporation and a surface-based duct, was calculated and validated with an example, which was found to be important to discriminate the ducts retrievable by an RFC system.

Yang et al. [71] analysed the statistical features and the physical mechanism of spatio-temporal distribution of the evaporation duct for the South China Sea based on high spatial

resolution of a climate database. The distribution features of the evaporation duct height (EDH) for different sea areas and months were obtained and proposed to be applied to ship borne radar and communication systems design. It was found that maximum EDH occurred in December (13.1 m) and the minimum EDH in October (9.9 m) for the middle part of South China Sea, where whole area had high EDH during the winter due to the stable condition with low relative humidity and low wind speed. The EDH remains above 10 m during summer and there was obvious decrease of EDH during spring. On the other hand, the maximum EDH was observed in September (12.0 m) while minimum EDH occurred in March (9.6 m) for the south part of South China Sea. The EDH increased rapidly in spring, while EDH was found to be below 10 m during winter time.

The positive air-sea temperature difference and high air temperature in June and July caused the high EDH. The unstable conditions and the low air temperature makes the EDH low during February. The EDH remained relatively stable all over the year in the Gulf of Thailand, since the air-sea temperature difference was negative and the wind speed was low all over the year. However, the low air temperature and low wind speed makes the EDH low during March. The unstable conditions in the north part of South China Sea during winter with the high wind speed and low relative humidity made the EDH high, while the stable conditions in summer with the high relative humidity made the EDH relatively low. On the other hand, the EDH reached the highest value during summer in the south part of South China Sea since the wind speed was found to be slow and the surface temperature was high. The high relative humidity and low surface temperature made the EDH low during March. It could be concluded that whenever surface or air temperature is

high and/or the relative humidity is low, the value of EDH is expected to be high and vice versa.

A MATLAB-based implementation of the parabolic equation (PE) was described in [72] using a software package, Evaporation Duct Propagation-Parabolic Equation (EDP-PE), for evaluating propagation loss on inhomogeneous atmosphere and a rough sea. The EDP-PE calculations were compared with the measurements, where good agreement could be found with calculated path loss for several evaporation duct profiles. The experiment was conducted at different frequencies and showed that the EDP-PE could predict, with reasonable good accuracy, field strengths for refractive environments and rough surfaces. The analysis of path losses showed clearly that signal strength was enhanced due to the influence of the evaporation duct.

Geoff et al. [73] described the implementation and performance of an over-the-horizon microwave link operating in 10.5 GHz band over seventy kilometres of ocean between the Australian mainland and an offshore site. The link used the ocean evaporation duct to propagate radio signals far beyond the optical line-of-sight limitation with an objective to open opportunities for high bandwidth linkages supporting a range of remote observation systems. The low-cost, low-power consumption microwave radio system was demonstrated to use the evaporation layer to transmit radio wave signals at 10.5 GHz over 78 km distance offshore on the Great Barrier Reef. It was concluded that further analysis was required to improve the signal strength and link stability of the experimental link.

The low-altitude over the-horizon propagation influenced by the evaporation duct was compared by Herbert et al. [74] for the frequency bands of 3, 9.6 and 18 GHz. The authors presented theoretical and experimental results for a 35 km over-water path, where the transmitters were located about 5 m above mean sea level and the receivers were located either 4-5 m or 18-19 m above sea level. A close agreement could be found between both theoretical and experimental results. It was concluded that substantial improvements in received signal levels are likely to be achieved by selecting two suitable frequencies in the 10-20 GHz range. The results indicated that frequency diversity can be used to give substantial improvements over a single-frequency system from the evaporation duct on over-the-horizon, over-water paths, such as using one frequency near 10 GHz and a second between 15 and 20 GHz, noting that each proposed application should be individually examined.

Jin-Peng et al. [75] introduced an estimation model for atmospheric refractivity structure based on multi-frequency radar sea returns, which was assessed using evaporation duct inversion processes. It was illustrated that the multi-frequency model was more robust in atmospheric refractivity structure inversion through the comparisons of evaporation duct height and strength errors predicted by multi-frequency and single-frequency estimation model.

2.4 Final Remarks

The background on refractivity relationships in accordance with meteorological parameters and along with characteristics of atmosphere were introduced in chapter 2. The components of wireless communication system were provided and the free path loss model was explained. The linear and exponential models of refractivity gradient evaluation were discussed and several propagation parameters were introduced including β_0, point refractivity gradient and Effective Earth Radius. The modified refractivity parameter and relevant atmospheric duct phenomena were introduced.

The research work and the analysis of refractivity and relevant propagation parameters were reviewed in the literature. Most of the studies were conducted in regions with temperate climate and some in a tropical one. Few studies are available for subtropical regions. Most of other studies were carried out using short-term meteorological data making the results' quality questionable. Different continuous and discontinuous models for the refractivity predictions were introduced. Linear and exponential models as well as direct and indirect refractivity estimations using various approaches were studied. The deterministic or artificial neural networks approaches from the received signal strength were not promising. The influence of ducting phenomena on path loss, scattering problem in the presence of duct, and over-the-horizon communication through the atmospheric ducts were investigated.

Based on the above, the artificial neural networks approach will not be investigated in this work. New indirect and discontinuous models will be studied at three layer within 1 km height of the atmosphere above the ground.

The specifications of weather stations and meteorological equipment used to gather the required data for the analysis are introduced in chapter 3, as well as the setup and installation procedure.

Chapter 3

SPECIFICATIONS OF WEATHER INSTRUMENTS AND WIRELESS EQUIPMENT SETUP AND INSTALLATION PROCEDURE

3.1 Introduction

There are several instruments and techniques to measure and calculate the refractive index of the air especially in the lowest layers of the troposphere. The common methods of refractivity measurement may lack adequate spatial or time resolution to map the behavior of the troposphere [55]. Some of these methods are:

- Refractometers: are precisely measuring the refractive index directly at the surface or higher fixed altitudes, but they are too expensive and heavy for many measurements.
- Radars: can be used to measure vertical refractivity profile by measuring time delay or the difference in time delay of electromagnetic waves reflected from the ground [56].
- GPS phase delay measurements: measures refractivity profile from variations in excess radio path length [57].

- Signal Strength Measurement: The refractivity is calculated from the diffraction losses or time delay of the propagating wave between transmitter and receiver of microwave link or other wireless systems [25, 26, 58, 76].
- Indirect semi-empirical formula for refractivity calculation: The refractivity profile can be determined from the climatic data collected from the atmosphere. This method is frequently used to obtain refractivity from the measured meteorological data of pressure, temperature, and humidity. As explained before, refractivity can be derived from experimental measurements, which is proposed by the ITU-R P.453-10 recommendation [12]. These meteorological data can be measured by air-borne radiosonde, and fixed weather stations with measuring sensors commonly installed at the ground and could be mounted at higher altitude on towers as well.

Other instruments can be used to measure the surface and upper-air meteorological data, temperature, pressure and humidity, such as refractometer, radar, barometer or radiosonde…etc, for both surface and upper-air data.

- Fixed Psychrometers and Barometers: installed at different heights of the tower to measure dry and wet temperatures and air pressure.
- Fixed surface weather stations: normally comprises of multiple sensors for measuring several atmospheric and soil data including, inter alia, temperature, pressure, relative humidity, wind speed and direction, average rain fall rate…etc.
- Radiosonde: for measuring upper-air meteorological data of temperature, pressure, dewpoint temperature, and wind speed and direction.

- Some types of radar for studying the lower atmosphere.
- Other methods might be accurate for upper-air data but rarely used due to their high costs such as using:
    - Small rocket or helicopter Probes
    - Satellite data.

The components and characteristics of the radiosonde and surface weather stations which are utilized in our experiments are explained further hereinafter.

The wireless experiments belong to the Emirates Telecommunication Corporation, Etisalat, which is the first leading Telecom operator in the country. A PTP microwave link is the wireless system used to measure the received signal strength and to study the fading situations. Two types of microwave links are commonly used:

a. Dual-Polarized Microwave Link.
b. Single Polarization Microwave Link (commercial MW network)

The measured signal strength for LOS microwave links with and without space diversity, which are selected to be operating in different frequency bands and atmospheric conditions (i.e. within coastal and inland areas) are studied. However, more links have been selected as candidate locations due to some limitations, which arose from the fact that these links are installed for business and commercial purposes and not dedicated for research. The criteria used to select the candidate links along with the experienced challenges and limitations, will be discussed in chapter 10. In this chapter, characteristics of the microwave

equipment and different link configurations are given. In addition, the installation procedure of a microwave link is explained based on operational experience.

3.2 Radiosonde (VAISALA RS92) for Measuring Upper-air Meteorological Data [77]

A radiosonde is a small instrument package attached to a weather balloon, see Figure 3.1. As the balloon ascends, the radiosonde takes a vertical profile of the atmosphere, up to around 30km, recording temperature, atmospheric pressure, relative humidity and wind velocity. A radio transmitter then transfers the data collected during the launch back to a computer for processing. These measurements serve as a reliable source for satellite data validation and are the fundamental backbone for weather forecasting and atmospheric modeling.

In the UAE, the radiosonde is operated by experts from Abu Dhabi airport. In normal cases, it is launched two times a day at the standard UT timing of 0:00 H and 12:00 H.

Figure 3.1: Vaisala RS92 Radiosonde with Ballon

There are many users of radiosonde worldwide which include national centers of meteorological and hydrological services, aviation authorities, defense forces, road authorities, the weather critical energy sector, life science and high-technology industries and building automation.

3.2.1 Vaisala Radiosonde RS92 [77]

Figure 3.2 shows the RS92-SGP unit in general and identifies its outer components.

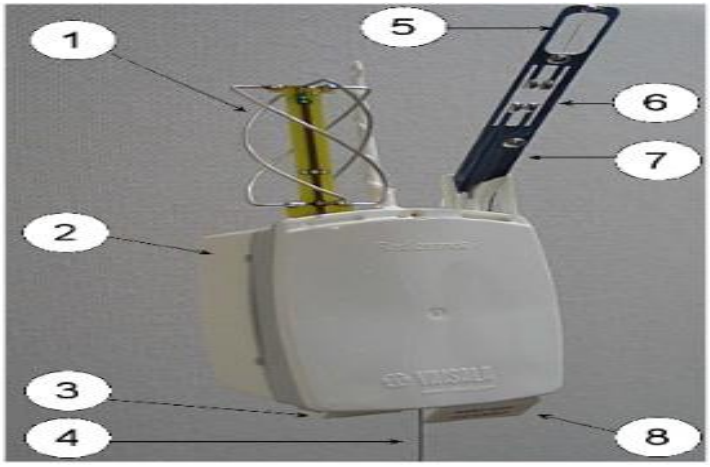

Figure 3.2: Vaisala RS92-SGP Unit [46]

As shown in Figure 3.2, the radiosonde RS92 consists of following components:

1. GPS Antenna
2. Battery Case
3. Additional Sensor Interface
4. Antenna
5. Temperature Sensor
6. Humidity Sensor
7. Sensor Boom
8. GC25 Interface for Calibration

3.2.2 Radiosonde Characteristic [77, 78]

The datasheet of the Vaisala RS92-SGP radiosonde with its technical details and characteristics are provided in Appendix B.

3.3 Surface Weather Stations for Measuring Surface Meteorological Data

Surface fixed weather stations are used to gather the weather parameters at the ground surface. They include multiple sensors to measure the required parameters. Figure 3.3 shows a standard surface station used in the experiments. In other manual surface stations, observers have to take the observations for the standard meteorological parameters and other data such as the occurrence of sand storm, fog and visibility evaluation, particularly at the airports. Among the multiple sensors shown in the figure, the measurements of the temperature, pressure and humidity sensors are to be gathered and analysed. Other parameters might be taken into consideration if data with acceptable resolution could be gathered.

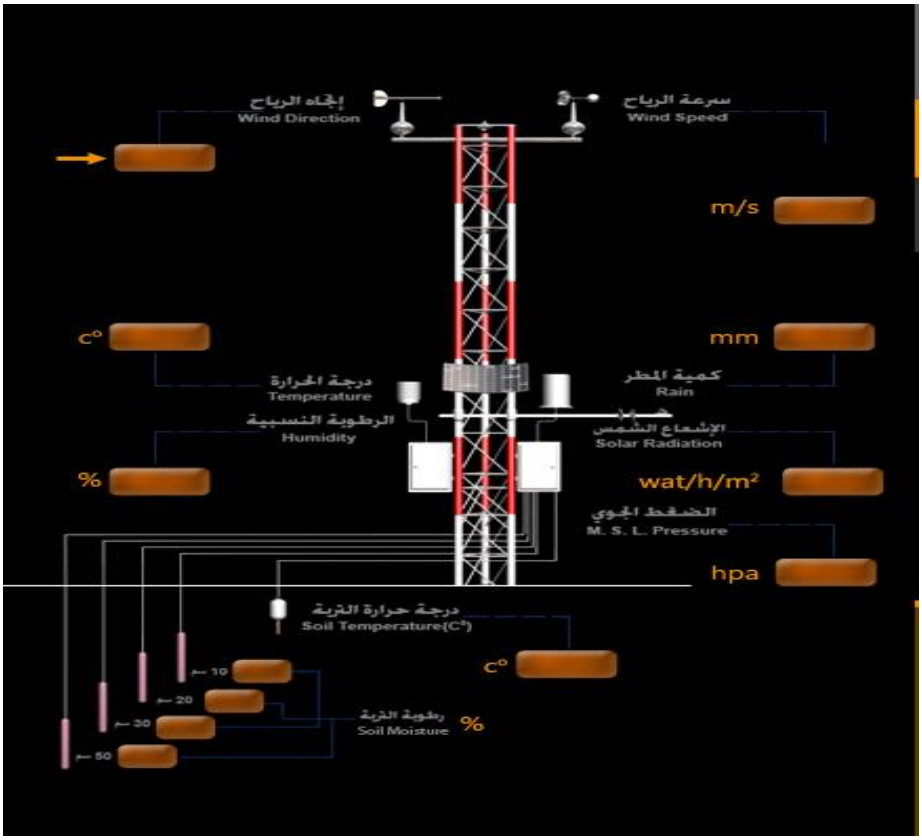

Figure 3.3: Surface Weather Station Installed in UAE

3.4 Point to Point Microwave Link Equipment

PTP microwave links are effective wireless solutions to carry the traffic from a point (A) to another far point (B) without a need for land cables, see Figure 3.4. The transmission medium of air is utilized to send and receive huge amount of data with high quality and negligible time for service outage. Wireless service providers such as mobile operators are using PTP microwave technologies to backhaul mobile stations and to connect the terminal base-stations to the base-station controllers. They can also be deployed by fixed network operators to provide direct services to their fixed customers. These wireless links could

provide cost effective and fast solutions to the service providers in new developing areas, where cable infrastructure is not available, or in developed areas, where there are limitations in rolling out copper or fiber land cables to new sites.

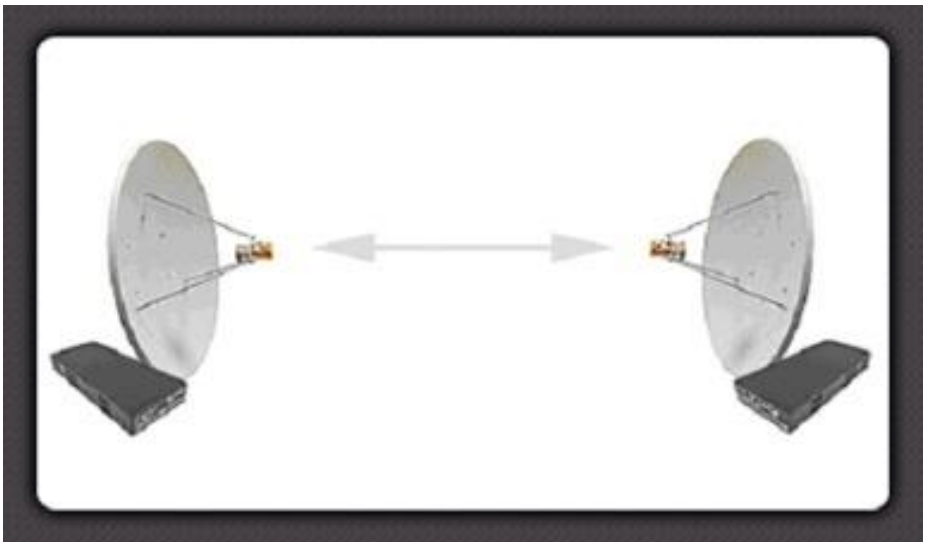

Figure 3.4: A Sample for a Line of Sight PTP Microwave Link

It is essential that wireless telecom operators select proper microwave technologies based on their capacity demands and the distance between the points of transmission and reception. For example; millimeter-wave links in the 70/80 GHz frequency bands can be used in the case that gigabit data throughput is required, but at the expense of the limit of maximum possible distance between the sites. Another solution to satisfy the requirement for large data transmission with longer distances is to use dual-polarized technology with links operating in different frequency bands.

3.4.1 Specifications and Radio Configurations of Utilized Microwave Equipment

The characteristics of microwave link equipment are vendor specific. Equipment specifications, such as receiver sensitivity, differ based on the assigned configuration to satisfy the commercial requirement. A large channel bandwidth and/or advanced modulation schemes could be used to provide relatively large data throughput. However, the receiver sensitivity will be less negative and accordingly shorter length of a microwave link could be obtained. Two important parameters should be determined accurately before designing and configuring microwave links:

- The required net data throughput to be transmitted over the link
- The target link availability with respect to the distance between the two sites of the link.

The higher the throughput required, the more bandwidth and modulation are needed. Accordingly, the noise level will increase and the threshold value of the receiver's sensitivity becomes more negative and the transmit power decreases as given in the following tables for two radio with the same frequency band and different configurations. This definitely reduces the range of distance between the two sites for the same target availability.

After defining these two factors, the link is designed considering the path loss and propagation conditions in the area under study. The channel bandwidth, antenna height and

size, modulation scheme and transmission power should be set accurately to ensure acceptable performance and reliability of the link.

In this project, several experiments were carried out to study the impact of different propagation phenomena on the variation of the received signal strength. Commercial PTP MW links with different specifications and configurations were installed all over the UAE and are utilized to gather the signal levels. They operate in different frequency bands such as 7, 15 and 23 GHz. The links were selected such that their locations have different geographical natures and accordingly cover several atmospheric conditions.

The tables from Table 3-1 to
Table 3-7 provide the specifications of the equipment used in these experiments.

Table 3-1: Equipment Specifications of 7GHz-QPSK-40Mbps Radio

Radio Configuration	7GHz-QPSK-40Mbps
Modulation	QPSK
Capacity/Interfaces	16E1
Data Rate Mbps	48.896
Channel Bandwidth (MHz)	28
Maximum Receive Signal (RX) for 10^{-3} BER (dBm)	-15
Maximum Receive Signal (RX) for 10^{-6} BER (dBm)	-15
Transmit Power (dBm)	29
Lower Frequency Limit (MHz)	7125
Upper Frequency Limit (MHz)	7750
RX Threshold at 10^{-3} BER (dBm) (SDH only)	-85.5
RX Threshold at 10^{-6} BER (dBm)	-84

Table 3-2: Equipment Specifications of 15GHz-32QAM-100Mbps Radio

Radio Configuration	15GHz-32QAM-100Mbps
Modulation	32 QAM
Capacity/Interfaces	48 E1
Data Rate Mbps	122.24
Channel Bandwidth (MHz)	28
Maximum Receive Signal (RX) for 10^{-3} BER (dBm)	-20
Maximum Receive Signal (RX) for 10^{-6} BER (dBm)	-20
Transmit Power (dBm)	21
Lower Frequency Limit (MHz)	14200
Upper Frequency Limit (MHz)	15350
RX Threshold at 10^{-3} BER (dBm) (SDH only)	-76.5
RX Threshold at 10^{-6} BER (dBm)	-75

Table 3-3: Equipment Specifications of 23GHz-QPSK-40Mbps Radio

Radio Configuration	23GHz-QPSK-40Mbps
Modulation	QPSK
Capacity/Interfaces	16E1
Data Rate Mbps	48.896
Channel Bandwidth (MHz)	28
Maximum Receive Signal (RX) for 10^{-3} BER (dBm)	-15
Maximum Receive Signal (RX) for 10^{-6} BER (dBm)	-15
Transmit Power (dBm)	24
Lower Frequency Limit (MHz)	21200
Upper Frequency Limit (MHz)	23600
RX Threshold at 10^{-3} BER (dBm) (SDH only)	-85
RX Threshold at 10^{-6} BER (dBm)	-83.5

Table 3-4: Equipment Specifications of 23GHz-16QAM-80Mbps Radio

Radio Configuration	23GHz-16QAM-80Mbps
Modulation	16QAM
Capacity/Interfaces	32E1
Data Rate Mbps	97.792
Channel Bandwidth (MHz)	28
Maximum Receive Signal (RX) for 10^{-3} BER (dBm)	-20
Maximum Receive Signal (RX) for 10^{-6} BER (dBm)	-20
Transmit Power (dBm)	22
Lower Frequency Limit (MHz)	21200
Upper Frequency Limit (MHz)	23600
RX Threshold at 10^{-3} BER (dBm) (SDH only)	-78
RX Threshold at 10^{-6} BER (dBm)	-76.5

Table 3-5: Equipment Specifications of 23GHz-32QAM-100Mbps Radio

Radio Configuration	23GHz-32QAM-100Mbps
Modulation	32QAM
Capacity/Interfaces	48E1
Data Rate Mbps	122.24
Channel Bandwidth (MHz)	28
Maximum Receive Signal (RX) for 10^{-3} BER (dBm)	-20
Maximum Receive Signal (RX) for 10^{-6} BER (dBm)	-20
Transmit Power (dBm)	19
Lower Frequency Limit (MHz)	21200
Upper Frequency Limit (MHz)	23600
RX Threshold at 10^{-3} BER (dBm) (SDH only)	-76.5
RX Threshold at 10^{-6} BER (dBm)	-75

Table 3-6: Equipment Specifications of 23GHz-128QAM-155Mbps

Radio Configuration	23GHz-128QAM-155Mbps
Modulation	128QAM
Capacity/Interfaces	STM-1
Data Rate Mbps	171.136
Channel Bandwidth (MHz)	28
Maximum Receive Signal (RX) for 10^{-3} BER (dBm)	-20
Maximum Receive Signal (RX) for 10^{-6} BER (dBm)	-20
Transmit Power (dBm)	19
Lower Frequency Limit (MHz)	21200
Upper Frequency Limit (MHz)	23600
RX Threshold at 10^{-3} BER (dBm) (SDH only)	-70.5
RX Threshold at 10^{-6} BER (dBm)	-69

Table 3-7: Equipment Specifications of 23GHz-QPSK-8Mbps Radio (Type 2)

Radio Configuration	23GHz-QPSK-8Mbps
Modulation	QPSK
Capacity/Interfaces	4E1
Data Rate Mbps	9.59576
Channel Bandwidth (MHz)	7
Maximum Receive Signal (RX) for 10^{-3} BER (dBm)	-15
Maximum Receive Signal (RX) for 10^{-6} BER (dBm)	-15
Transmit Power (dBm)	21.5
Lower Frequency Limit (MHz)	21200
Upper Frequency Limit (MHz)	23600
RX Threshold at 10^{-3} BER (dBm) (SDH only)	-86
RX Threshold at 10^{-6} BER (dBm)	-82.5

3.4.2 Link Installation Procedure

The following steps summarize the followed procedure by the telecom operators to install LOS PTP MW link:

a. Site Survey: Both sites of the microwave link are surveyed by the radio team before the installation in order to:

   - Confirm the availability of line of sight between the two sites.
   - Identify the minimum antenna heights required to maintain the line of sight.
   - Check the space availability and existing load on the tower.
   - Fix the antennas on the designed height to ensure the path clearance.

b. Link Design:

   In order to satisfy the required data capacity, the channel bandwidth and modulation scheme should be designed such that enough data throughput can be provided over the radio channel. The distance between the two sites and the predicted link availability should be taken into consideration as well. A margin of 25 to 30 dB of the received signal level above the minimum acceptable signal strength, defined by the equipment specification, is normally maintained. The predicted link availability needs to be also retained at 99.995 % or above. Accordingly, configurations of transmission power and antenna size have to be set properly.

c. Tower Structure:

   A tower with a suitable structure and enough length should be utilized to satisfy the antenna and LOS requirement:

   - Antenna size plays a vital role in selecting the tower structure. Small poles could carry small antennas with diameter of up to 0.6 m. Larger antennas

require stronger structure such as monopole or towers with multiple legs based on their sizes.

- If the LOS could not be obtained with the available tower structure due to its short length, it might be required to build a new tower or an additional mast on the existing structure, if logistically possible.

d. Antenna Installation and Alignment, see Figure 3.5: There are several methods; manually and automatically, to align the antennas with proper azimuth and tilting.

- A compass is normally required to determine the proper azimuth of the antenna according to the proposed values by the designers. A GPS-based compass is recommended in case of fixing the antennas over metal towers since magnetic-based compass cannot give accurate direction.
- A satellite finder is used to adjust the tilting of the antennas.

Figure 3.5: Fixed Antennas over the Top of the Tower

3.4.3 Setup of Dual Polarized Links

Figure 3.6 shows a possible setup for dual polarized protected microwave link using vertical (V) and horizontal (H) polarizations. The protection configuration comprises main and standby radios connected to one antenna for both polarizations. The Outdoor Unit (ODU) refers to the radio unit, where the transmission power and frequency channel are set. There will be 4 ODU units at each site, two for the main and standby links of each polarization. The traffic gets modulated in the indoor unit (IDU) and is then transferred through coaxial cable to the ODU.

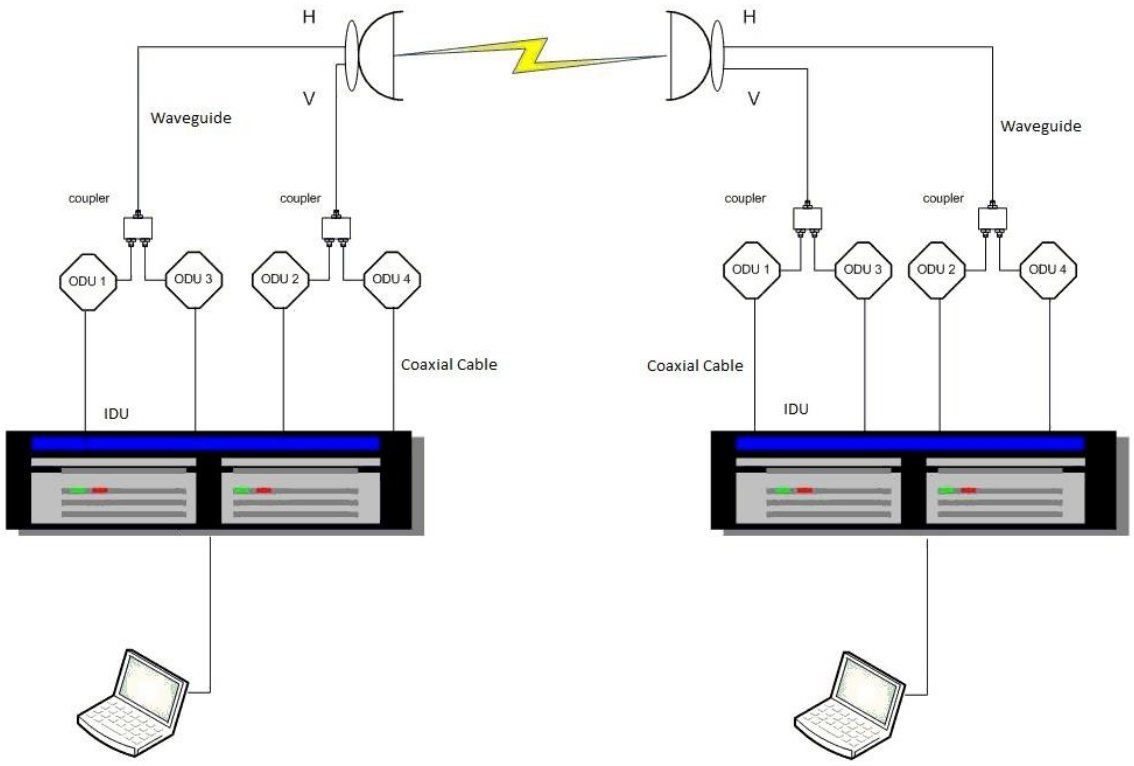

Figure 3.6: A Setup of Dual Polarized Protected Microwave Link

3.4.4 Remote Monitoring Systems and Connectivity

The microwave links are scattered all over the country; onshore and offshore. The links are connected through Etisalat network to a remote server in the data centre which is then connected to a local PC in order to monitor their performance and to gather the received signal strength, see Figure 3.7. In certain cases, equipment suppliers provide special software to access and monitor their links. The readings of the signal strength measurements at the sites of selected microwave links are being manually saved, on either daily or weekly basis according to the resolution. The default data resolution is a reading

every 15 min, which have to be saved on a weekly basis. However, other tools are utilized to gather higher resolution data, every 1 min, for some of the sites, which have to be collected and saved to a local PC on every day.

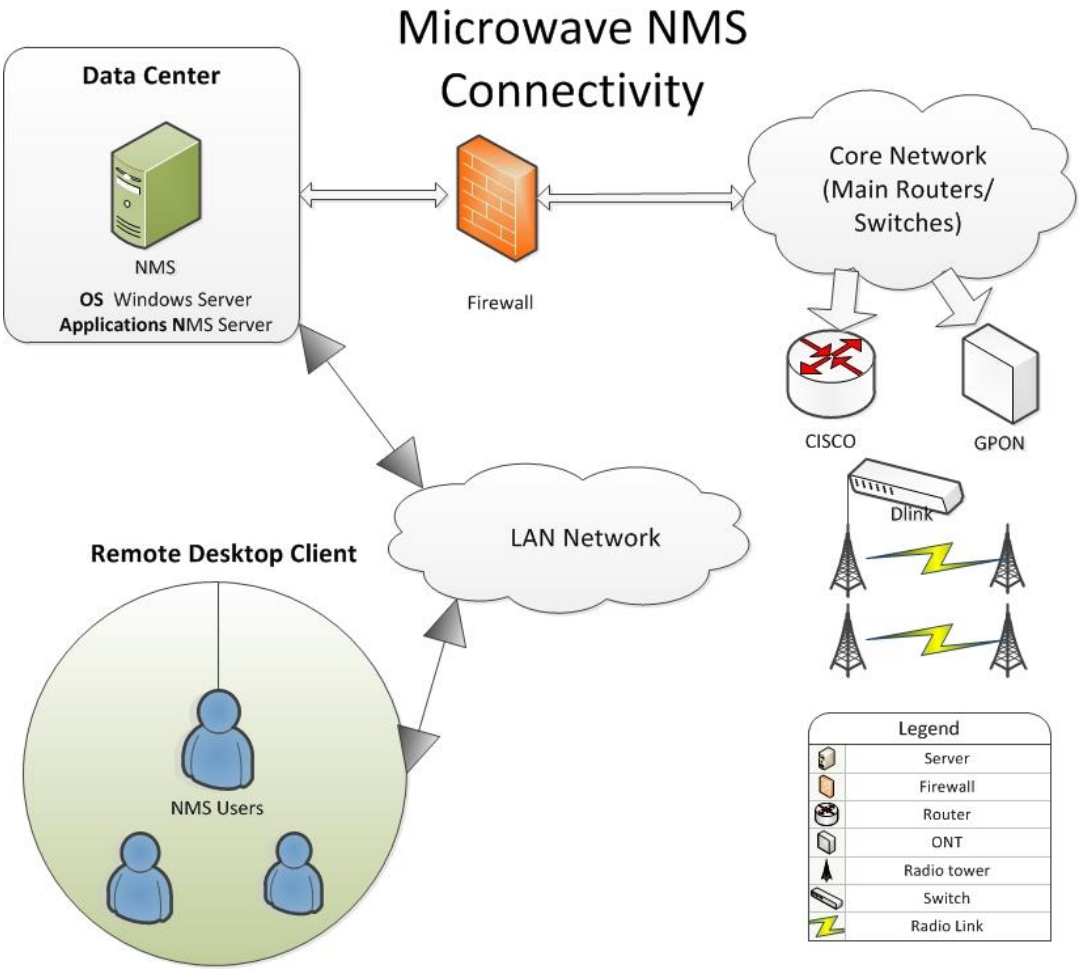

Figure 3.7: Remote Access Connectivity to the Microwave Links

3.5 Final Remarks

Chapter 3 discussed the specifications of weather stations and meteorological equipment. Several tools and instruments were introduced. Vaisala radiosonde equipment was used for upper-air meteorological measurements in only one location. Surface weather stations in many locations were used for gathering surface meteorological measurements. The characteristics of Vaisala radiosonde equipment and the surface weather stations were presented. The specifications of wireless PTP MW links were discussed. The radio configurations were presented including operating frequency bands, modulation schemes, link capacity, receiver's sensitivity and transmission power. The installation procedure and step-by-step procedure was explained in addition to the remote connectivity setup.

The types of meteorological and wireless measurement along with the procedure followed to process these gathered data for further analysis, will be discussed in chapter 4.

Chapter 4

DATA PROCESSING AND WIRELESS PREDICTION SOFTWARE

4.1 Introduction

The meteorological data and signal strength measurements have been gathered in UAE, which has subtropical climate and suffers from frequent anomalous propagation conditions. The meteorological data were collected from the weather stations of the national centre of meteorology, whereas the signal strength measurements have been gathered from the equipment of several LOS PTP MW links which are installed for commercial and business purposes.

The data have different formats since they have been gathered from several sources at many stages. ROAB software was used to process the radiosonde sounding in order to convert the codes of measurements into another format, which is easy to read. MATLAB software was used for further processing and analysing the gathered data and output files of the ROAB. Multiple MATLAB programs were developed to analyse the available sets of the meteorological data at each stage.

Commercial wireless planning and microwave designing software, ICS Telecom [79], has used to predict link availability, received power levels and signal fading, for each of the candidate LOS PTP MW links. The attenuation in the received signal strength was calculated considering different propagation conditions and fading phenomena in the experimental areas, based on the ITU-R recommendations and other standard models. The ICS Telecom models include, inter alia, the effects of multipath and signals' reflection, vertical rate of refractive index, effective earth radius factor, gas attenuation and diffraction losses when there is any obstacle cutting the first Fresnel zone during the path of the signal.

4.2 Meteorological Data and Field Measurement

Both signal strength measurements from several PTP microwave links and new meteorological data were gathered starting from October 2012 for the analysis of the fading situations and the propagation conditions which contributed to the signal attenuation.

4.2.1 Meteorological Data

Two types of measured weather data, surface and upper-air, gathered from many stations distributed all over the UAE were analysed. Historical long-term meteorological data were gathered to have strong background about the climate behaviour in the areas under study.

The data from three types of weather stations were gathered and utilized in this study. Manual surface stations exist only at airports, while automatic surface stations are widely available. Some of the meteorological parameters such as visibility and fog can be measured manually by professional observers only at the airports. There are six airport sites in UAE, all with surface manual weather stations, while only one radiosonde is available in Abu Dhabi. The radiosonde measures the meteorological data such as temperature, pressure, dewpoint and humidity at standard pressure levels over the atmosphere, such as the surface, 1000 mb, 900 mb, 850 mb, 800 mb, 700 mb, 600 mb, 500 mb, 400 mb, 300 mb, 250 mb, 200 mb, 150 mb and 100 mb. The raw radiosonde measurements are given in codes, which are known as sounding data. The sounding files are processed using ROAB software in order to convert it to a proper format that is easy to read and further process.

4.2.2 Surface data

Surface data are reported on hourly basis from airports' manual stations and automated observing platforms. The manual weather stations measure and register the occurrence of several atmospheric parameters including, inter alia, pressure, relative humidity, wind direction, wind speed, precipitation, fog, clouds, visibility and temperature. The manual surface weather stations are located in the six UAE airports as shown in Figure 4.1. The coordinates of these six sites are provided in Table 4-1.

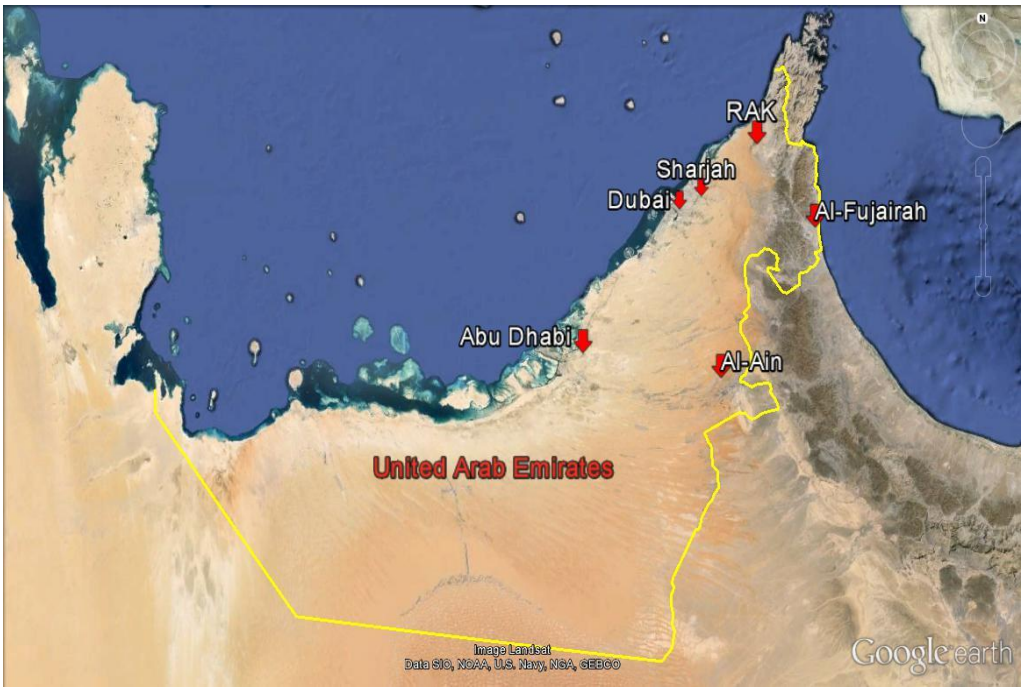

Figure 4.1: UAE Map with Locations of Six Surface Sites

Table 4-1: Sites' coordinates and altitudes of six manual surface weather stations

City	Site	Latitude [ºN]	Longitude [ºE]	Altitude (m)
Abu Dhabi	AUH	24.43	54.64	27
Dubai	DXB	25.25	55.36	36
Sharjah	SHJ	25.32	55.52	33
Ras Al-Khaimah	RAK	25.62	55.94	34
Al-Ain	AIN	24.26	55.62	262
Al-Fujairah	FUJ	25.11	56.33	21

The surface weather parameters are gathered for each of the six manual surface weather stations. There are 99 weather symbols with codes from 00 to 99, which are used in meteorology and divided into the following general groups [80]:

- Codes 00-09: No precipitation, fog, dust storm, sandstorm, drifting or blowing snow at the station at the time of observation or, except for 09 during the preceding hour.
- Codes 10-19: No precipitation at the station at the time of observation or, except 17, during the preceding hour.
- Codes 20-29: Precipitation, fog, ice fog, or thunderstorm at the station during the preceding hour but not at the time of observation.
- Codes 30-39: Dust storm, sandstorm, drifting or blowing snow.
- Codes 40-49: Fog at the time of observation.
- Codes 50-59: Drizzle.
- Codes 60-69: Rain.
- Codes 70-79: Solid precipitation not in showers.
- Codes 80-99: Showery precipitation, or precipitation with current or recent thunderstorm.

The weather symbols used in the meteorology with their descriptions are summarized in Appendix C.

The automatic weather stations provide most of these parameters except the incidence of some phenomena which require manual observations such as fog, cloud and visibility.

Details of automatic weather stations' locations are provided whenever used to evaluate relevant propagation parameters in this report.

4.2.3 Upper-air Radiosonde Data

Long-term radiosonde data recorded from two daily ascents, nominally at 00:00 and 12:00 UT, corresponding to 4:00 am and 4:00 pm local time of Abu Dhabi (UTC+4), are used for the analysis. However, some data are not available such as June 1998, April 2000, November 2005, June 2006 to November 2006 and January 2010 to May 2010 due to incomplete radiosonde ascents. From December 2006 to December 2008, the data for only one ascent, mostly at 00:00 UT, is available on daily basis.

The radiosonde is located in Abu Dhabi. The Gulf region is likely to experience abnormal propagation conditions such as ducting phenomenon due to its special climate, which is hot and humid over the course of the year. Radiosonde observations are made to determine the pressure, temperature, humidity, wind speed and direction, at standard pressure levels from the surface to the point where the sounding is terminated.

The possibility to add another radiosonde in the east coast region of UAE has been studied, however, it could not be accomplished during the study period due to its cost implication and technical constraints. The UAE east coast has unique climate as a mountainous coastal area with high probability of anomalous propagation and regularly observed interference between the radio networks in UAE and its neighbouring country, Oman. Based on the

operational experience, the upper-air data can be used within few hundreds kilometre from Abu Dhabi airport considering that the atmosphere is more horizontally homogenous in the upper levels.

4.2.4 Signal Strength Measurements

The resolutions of gathered field strength measurements differ according to the type of equipment and the available monitoring software capabilities of each equipment. The normal data resolution is a reading every 15 min, which needs to be saved manually to a local PC on a weekly basis. However, a higher resolution of one reading per minute could be obtained for few links using recently developed software. The number of sites with high resolution readings is very limited due to the huge bandwidth required to pull this traffic over Etisalat network which could get the network congested and the data should be saved manually to a local PC on every day. Data with even higher resolution of one reading per 10 seconds have been gathered for only one trial link in the city of Sharjah.

The signal strength measurements were gathered from single-polarized microwave links' technologies operating in 7, 15 and 23 GHz bands. The single-polarized links are permanent unless the business requirement changes since these links are installed originally for business and commercial purposes.

4.3 ROAB Software For Processing Radiosonde Soundings [81]

The RAwinsonde Observation program is the world's most powerful and innovative sounding software. It is a multi-functional sounding analysis program that can automatically decode data from 50 different formats and plots data on 12 interactive displays including skew-Ts, hodographs and cross-sections. It can create a variety of sounding diagrams, 3-D hodograms, time and distance based vertical cross-sections, mountain (lee) wave turbulence diagrams, and even produce forecast soundings. It produces displays of over 200 atmospheric parameters including temperature, pressure, humidity, icing, turbulence, wind shear, clouds, inversions plus a unique severe weather analysis table, a cloud parameter table, several thunderstorm analyses options, graphically interactive diagrams and more. The weather analysis software can be easily used.

4.3.1 Some of the key features of "RAOB" are:

- Advanced click and drag graphics screens with 3-D Hodogram.
- Allows detailed comparisons of one or two soundings and parameters.
- Process data above 100 mb and used for ozone and high-level analyses.
- Used for severe and aviation weather.
- Its modular design permits tailored functionality to customers in over 69 countries.

The ROAB display screen with multiple panels is shown in Figure 4.2.

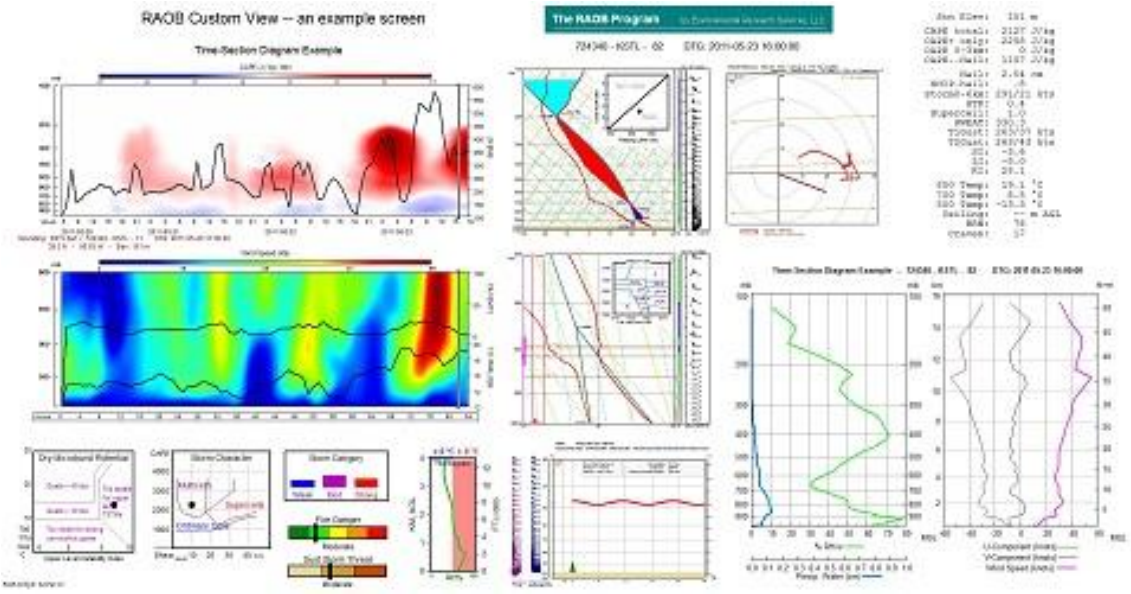

Figure 4.2: Multiple Panels Shown On One Screen Using RAOB

4.3.2 Processing Radiosonde Sounding Files Using RAOB

The RAOB 5.5 software have been used to import the sounding data created by the radiosonde, which contains the meteorological data of dry temperature, dewpoint temperature, atmospheric pressure, and humidity. The software has been used to convert the raw sounding files of the radiosonde for each ascent into readable text format with lists of data and exact measurements' dates and times in. The raw radiosonde sounding data have been measured for specific atmospheric pressures. The meteorological data at specific heights within the lowest 200 m above the ground may not be available all the time. The ROAB program has been widely used by the national meteorological centres across the world to process the raw sounding data in order obtain high resolution reliable meteorological data at the exact required heights within this most critical layer of the

troposphere for the operation of terrestrial wireless systems. This process could be time consuming since it is only possible to process the sounding data from one ascent at a time.

Each sounding is hydrostatically balanced to ensure accurate thermodynamic properties throughout the entire profile. Even the diagram's height scales are thermodynamically coupled so that the heights accurately represent the actual pressure level heights for each sounding. In other words, a unique height scale is created for each sounding. Additional accuracy is obtained by adjusting the gravity constant with respect to altitude and latitude. RAOB can find any sounding data elements for any pressure level and height using logarithmic interpolations when determining intermediate data.

The step by step procedure for processing the sounding data using RAOB is explained in Appendix D.

4.4 ICS Telecom for Link Design and Performance Prediction [7]

ICS Telecom is commercial software developed by a French company, ATD, for simulation, planning and optimization of radio networks, see Figure 4.3 for an example of ICS Telecom high resolution map. It enables planning engineers to plan and model radio communication networks efficiently and to manage network development. Technology-neutral, ICS Telecom also informs decisions made on spectrum management.

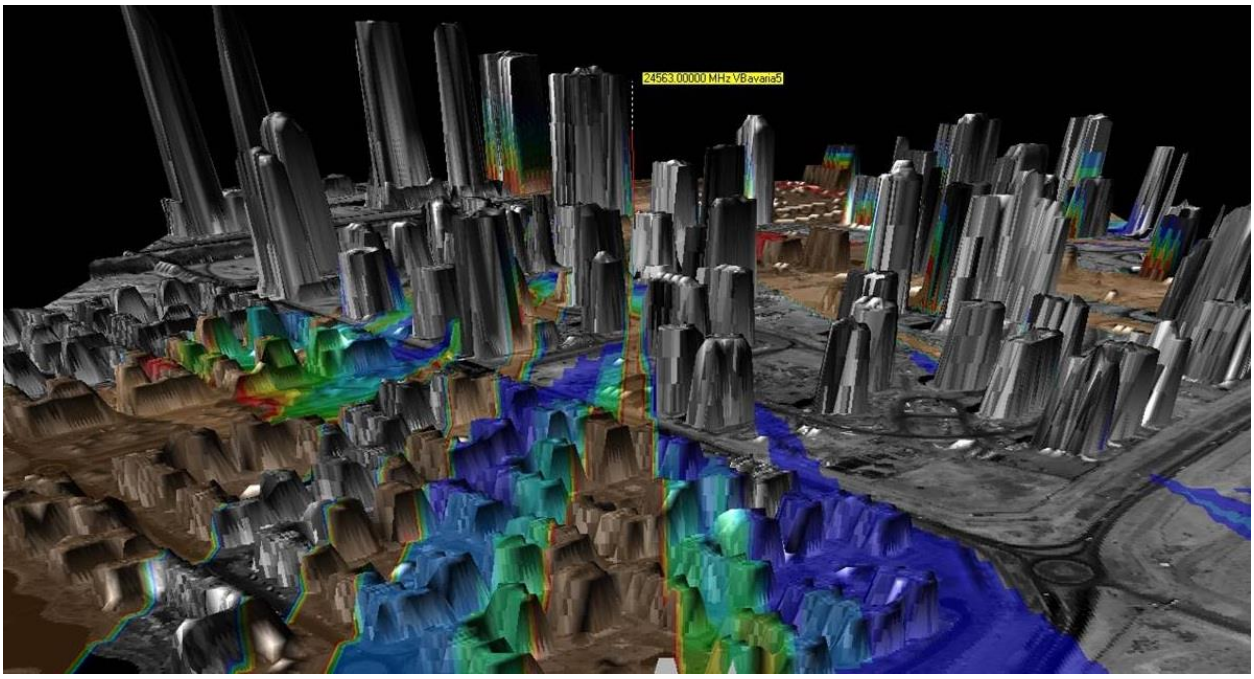

Figure 4.3: 3D High Resolution Maps of ICS Telecom

4.4.1 Features and Characteristics of ICS Telecom Planning Tool [79]

ICS Telecom is advance wireless planning software, which is widely used for planning, modelling, regulating radio communication and managing the spectrum in the frequency range 9 kHz to 400 GHz, by telecom regulators, systems integrators, network operators and consultants worldwide. It provides the required computational capabilities of connectivity, traffic flow and interference between the microwave stations, subscribers and nodes, and other assets within any wireless network. The tool considers such interaction in a technology, service and topology-neutral fashion, which is essential in today's mixed-technology world. ICS Telecom is the ideal tool for planning homogenous and heterogeneous wireless networks. Its statistics capability also allows virtual networks to be modelled.

ICS Telecom incorporates analysis methods from leading specialized organizations including the ITU. It covers spectrum-dependent technology and emerging technologies are added when methods are defined. Wireless networks' planning can be performed manually, or automatically on standalone machines or networked computers. It is mature software that is under continuous development to comprise new technologies and services. It is capable of modelling any size of radio system from intensive local area to extensive countrywide.

ICS Telecom enables the planning engineer to develop rapidly and economically wide networks. It has applications throughout all modern radio networks, both fixed and mobile

and across the frequency range 10kHz to 450GHz, including aeronautical systems, broadcast TV and radio, cellular and mobile broadband technologies (i.e. Tetra, 2G, 3G, 4G), fixed radio access, land mobile, marine systems, microwave bearer, mobile data, WiMAX, Fixed Wireless Access, terrestrial Digital Video Broadcasting (i.e. DVB-T, DVB-H), paging, radar, satellite, telemetry…etc. The wide range of functionalities makes it easy to simulate in detail any kind of technology on digital cartography. The tool offers planning, simulation and optimization capabilities for both PTP and point to multipoint (PMP) technologies. ICS Telecom is commonly used for the efficient design, frequency planning and interference management, as well as simulation of link budget and availability calculation of PTP MW links.

4.4.2 Step by Step Procedure of Microwave Link Design in ICS Telecom

The design and simulation of a microwave link can be done by applying the following steps manually or by importing an already existing external database:

1- Create a project with Cartographic Data

- Loading the cartographic data including digital terrain model layer with maximum possible resolution, clutter layer and image layer, see Figure 4.4. Accurate maps are important to calculate actual propagation losses and predict coverage maps in case of PMP technologies.

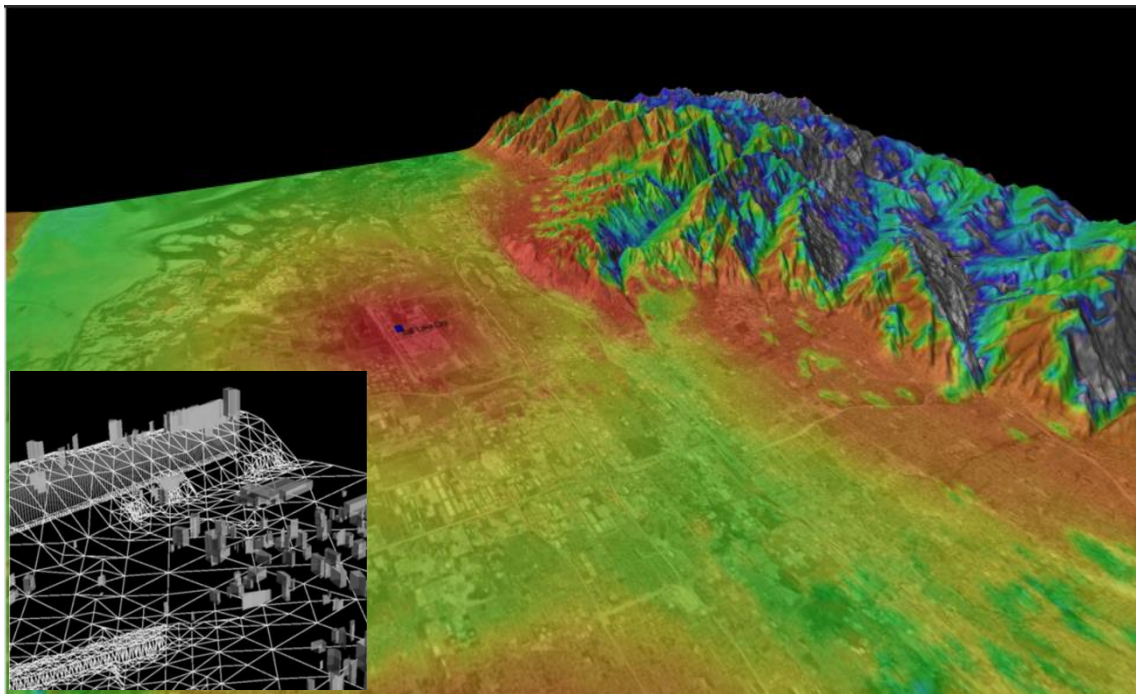

Figure 4.4: Digital Terrain Models

- If available, a high resolution building layer is highly recommended to be used for accurate predictions, see Figure 4.5. Otherwise, clutter layer is imported over the terrain model with assuming similar characteristics and heights for the same clutter types; such as agricultural, industrial, urban and dense urban areas.

Figure 4.5: Snapshots for Buildings in Abu Dhabi from Building Layer of ICS Telecom

2- Definition of Stations' Parameters:

- Positioning each of the two stations of the microwave link within the map and setting the coordinates. Different coordinate systems such as decimal degree, degree minute second…etc. can be used.
- Defining the stations' parameters including the transmission power, channel bandwidth, link throughput in Mbps, modulation scheme, cable losses.
- Loading the proper antenna pattern and setting correctly the antenna configurations such as height, gain, beamwidth and space diversity is used. ICS Telecom shows three dimension antennas pattern to predict the actual electric and magnetic fields and show the actual field coverage, see Figure 4.6. The azimuth and tilting of the antennas at both sites will be set automatically by the ICS Telecom once connected the two sites.

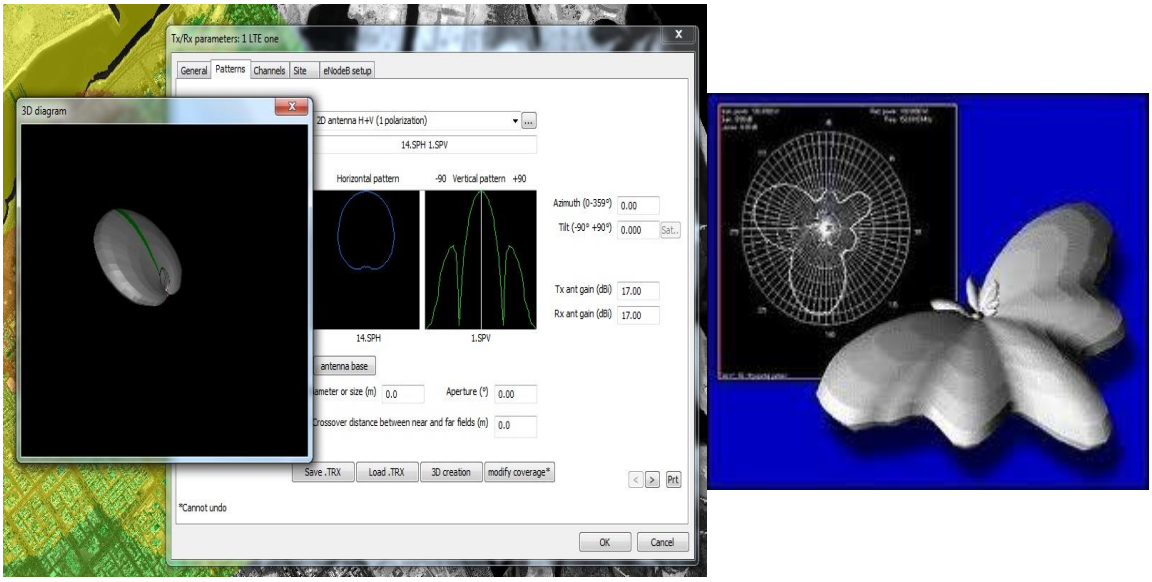

Figure 4.6: Antenna Pattern Drawn by ICS Telecom

3- Link Budget Calculation and Path Profile Development:

The field strength, propagation losses, fade margin, space diversity margin and link availability are calculated based on the recently developed models in the ITU recommendations and others considering the effects of different propagation phenomena such as diffraction, reflection, refraction and multipath. The path profile assists the planners in studying the line of sight availability between the sites and the clearance of the first Fresnel zone in case of designing line of sight microwave links, see Figure 4.7.

Figure 4.7: Path Profile of Microwave Link Developed by ICS Telecom

4- Frequency Assignment and Interference Analysis:

The planning tool has the capability to automatically assign frequency channels to the link's stations considering the predefined channel bandwidth and the existing assignment of the neighbouring microwave links. The co-channel and adjacent channels interference from and to the surrounding links are calculated, see Figure 4.8. The tool assigns the frequency channel with minimum predicted interference.

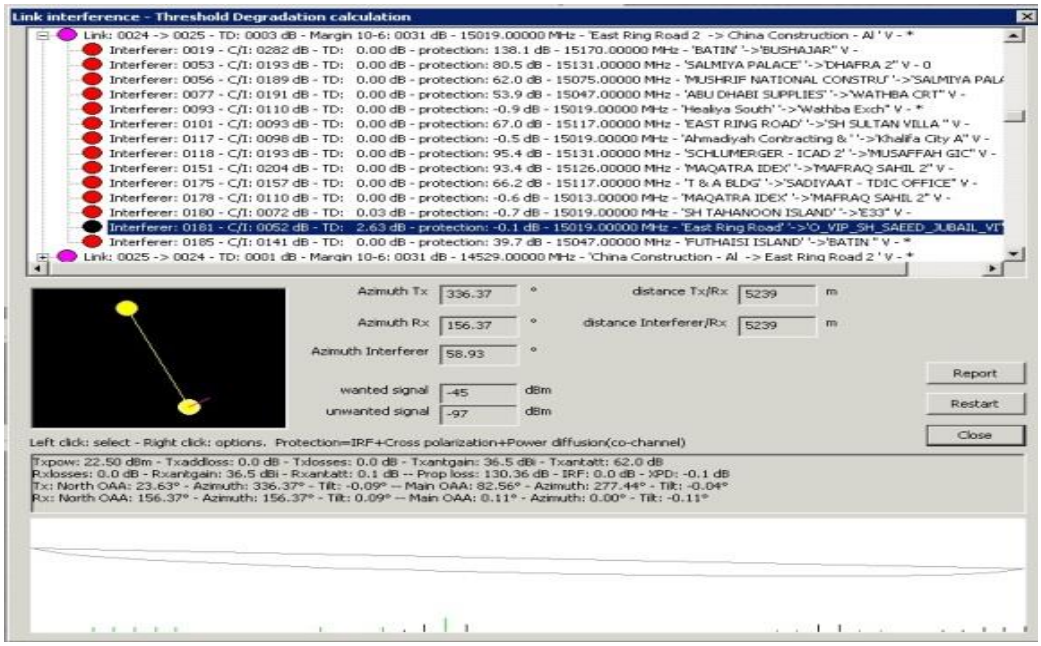

Figure 4.8: Results of Interference Calculation in ICS Telecom

4.5 Data Processing and Analysis Software (MATLAB)

MATLAB is a high-performance programming language for technical computing. It integrates computation, visualization, and programming in an easy-to-use environment where problems and solutions are expressed in familiar mathematical notation. Because of the huge amount of data which are being gathered for many locations in UAE, it is necessary to use MATLAB as a powerful tool to process and analyse them.

4.6 Final Remarks

The types of meteorological data along with utilized software and processing approaches were discussed. The raw hourly sounding data of radiosonde was processed using RAOB software, and the step by step procedure was explained.

Local meteorological measurements included dry and dewpoint temperatures, atmospheric pressure, relative humidity, wind speed, wind direction, rain rate and weather conditions. Wireless measurements from several microwave links operating in the Arab Gulf region were obtained.

The locations and altitudes of the radiosonde and six manual surface weather stations were provided. The weather codes could be registered manually at the six manual surface stations only. The data resolutions differed according to the source and type of data. The features of ICS Telecom software as well as the design and simulation procedures were discussed. The MATLAB software was used for data analysis and it was generally introduced.

Chapter 5 presents the initial analysis of refractivity and its vertical profiles based on fourteen years of meteorological data, from 1990 to 2003. More updated sets of data with higher resolution are gathered and analysed in the followings chapters.

Chapter 5

INITIAL ANALYSIS OF REFRACTIVITY RESULTS

5.1 Introduction

Refractivity has been initially analysed by processing fourteen years surface and upper-air metrological data collected at the airport of Abu Dhabi from 1990 to 2003 [5]. Raw data for different periods and resolutions have been considered at different stages of this project. The raw data have been converted to proper formats and ROAB software has been used to process and convert the radiosonde soundings into text formats that are easy to read and analyse. Multiple MATLAB programs have been developed to analyse the available sets of the meteorological data at each stage.

5.2 Initial Results of Vertical Refractive Index Rate in Abu Dhabi

The refractivity, N, and refractivity gradient, ΔN, are investigated using the linear model in three different layers of the lowest part of the atmosphere. Three sets of local radiosonde meteorological data have been utilized from chapter 5 to chapter 9, in order to calculate refractivity, N, and ΔN at 65 m, 100 m and 1 km layers of the atmosphere above the ground

in Abu Dhabi. Data set (1) is for fourteen years from 1990 to 2003. Data set (2) is for 9 years from 1997 to 2005, and has better resolution than data set (1). Third data set (3) is for seventeen years from 1997 to 2013 with the highest height resolution of radiosonde data. In this chapter, the refractivity profiles at 65 m and 1 km levels are calculated from the radiosonde measurements at standard pressures for the period from 1990 to 2003.

The standard deviation of refractivity, *N*, parameter is investigated. For n_t, n_p and n_{t_d} sample temperature, pressure and dewpoint temperature values spanning the range of values found in the seventeen years of data set (3), random offsets are added; using values chosen from a normal distribution corresponding to the accuracy quoted by the equipment manufacturer in Appendix B. The standard deviation in *N* parameter calculated from the noisy parameter values, σ_N, was evaluated at each sample point, resulting in an $n_t \times n_p \times n_{t_d}$ array of the standard deviation values.

Mesh plots of the minimum, maximum and mean σ_N across each dimension of the array are given in Figure 5.1 and Figure 5.2. Figure 5.1 shows σ_N values for the two dimensions of t and t_d parameters at a given p. It is observed that σ_N is most sensitive to the t_d parameter ranging from 1 around $t_d = 10^0\ C$ to 5 at $t_d = \pm 40^0\ C$. Sensitivity to the t parameter is relatively small ranging from $\sigma_N = 3.5$ to 4.5 at $t_d = \pm 40^0\ C$ across the range of $t = 0^0$ C to $50^0\ C$. Figure 5.2 shows σ_N values for the two dimensions of p and t_d parameters at a given t value. The σ_N is also found to be most sensitive to the t_d parameter ranging from 0.5 around $t_d = 5^0\ C$ to 3.5 at $t_d = \pm 40^0\ C$ for minimum σ_N

curve, and up to 5 at $t_d = \pm 40^0\ C$ in case of maximum σ_N curve. The sensitivity to the p parameter is found to be ranging from $\sigma_N = 3.5$ to 5 at $t_d = \pm 40^0\ C$ across the range of $p = 750$ hPa to 1050 hPa.

A range of 2σ was quoted by the equipment manufacturer in Appendix B, yielding to a maximum standard deviation of 10 N-units. Accordingly, the error in N parameter calculations are found to be ranging from 1 to 10 N-units subject to the values of the meteorological parameters, in particular t_d, at a given point of time.

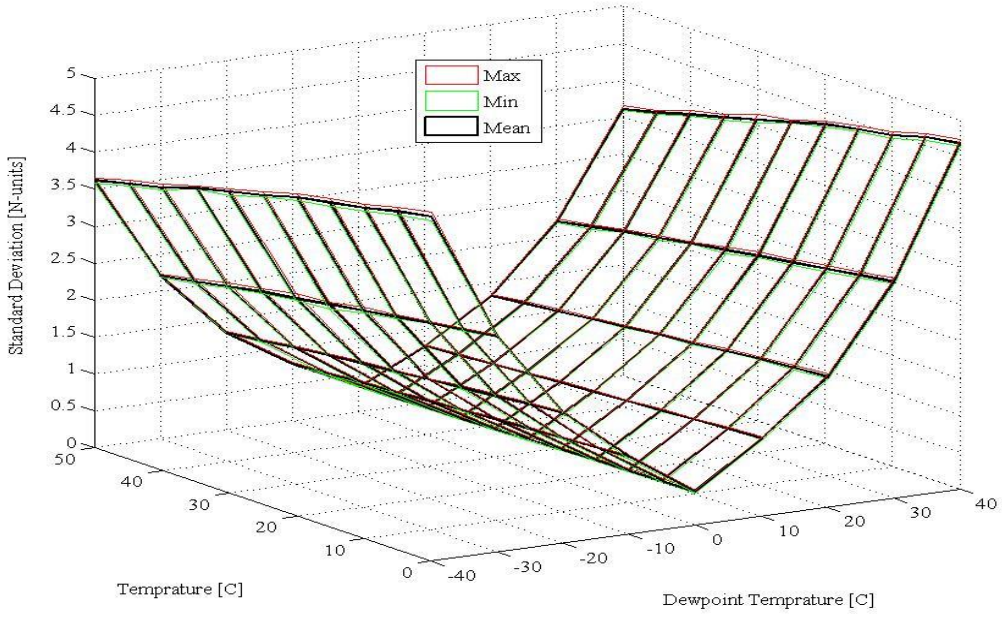

Figure 5.1: Minimum, maximum and mean $\boldsymbol{\sigma_N}$ for two dimensions of $\boldsymbol{t}$ and $\boldsymbol{t_d}$ parameters

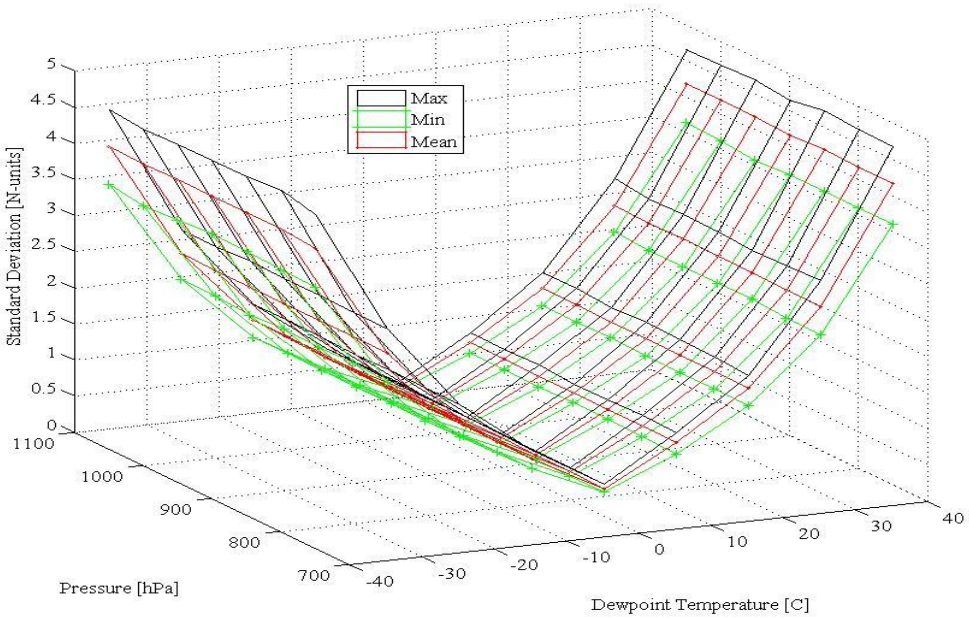

Figure 5.2: Minimum, maximum and mean $\boldsymbol{\sigma_N}$ for two dimensions of $\boldsymbol{p}$ and $\boldsymbol{t_d}$ parameters

5.2.1 Refractivity Gradient Calculations in First kilometre of Atmosphere

ΔN has been calculated in the first kilometre above the ground. The surface N_s is calculated at the lower height, h_s, while the upper height, h_1, is selected to be the point nearest to 1km height. ΔN, is calculated when 900 m < h_1 < 1100 m. The standard radiosonde data are not measured at fixed altitudes and accordingly the exact height may not be available in some occasions. The cumulative distributions for ΔN in the first kilometre are shown in Figure 5.3 for different times of the day. The gradient values oscillate between approximately -200 and 63 N/km, with a span of around 260 units. The long-term value of ΔN in the first kilometre was found to be around -72 N/km. The ITU proposes a value

of -40 N/km as the reference for the vertical refractivity gradient in the first kilometre of the standard atmosphere [32]. It is observed that there is a higher probability for larger negative values of refractivity gradient to be obtained during the morning time, at 0 H UT, when compared to the afternoon time, at 12 H UT, without any possibility for convergence between the two curves. There is also around 20 % probability that the refractivity gradient at the first kilometre of the atmosphere will exceed -100 N/km, while it is less than 1 % that the gradient value becomes positive.

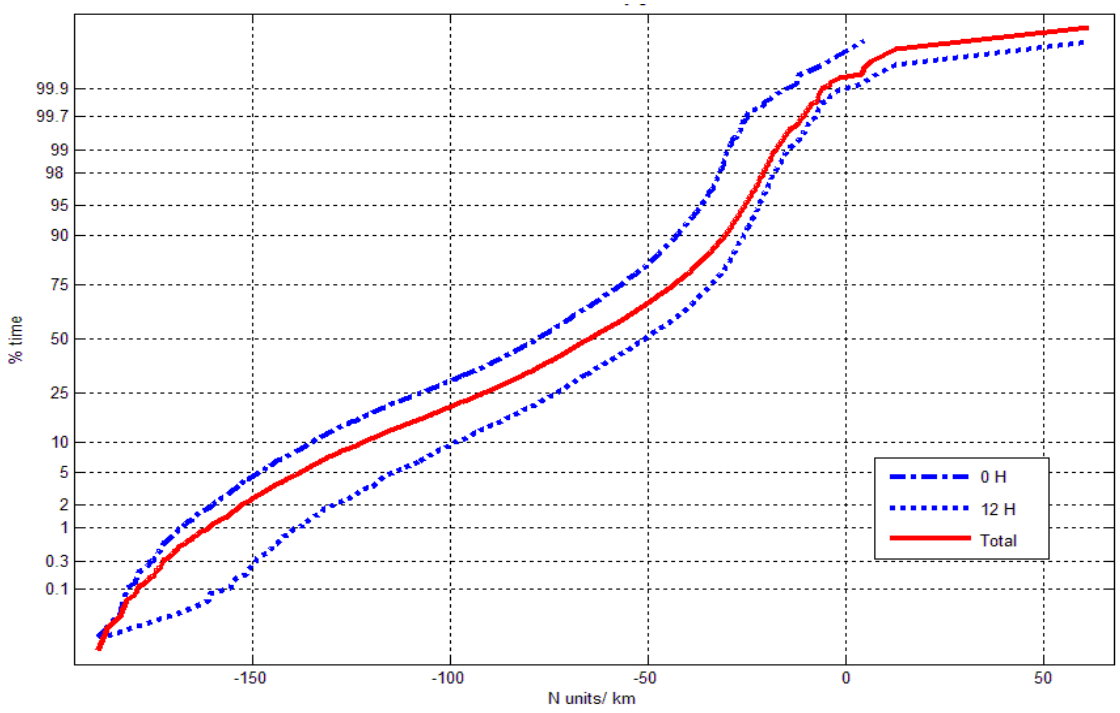

Figure 5.3: Cumulative distributions of refractivity gradient at 1 km from 1990 to 2003

The year to year variations were found to be not so significant. On the contrary, the monthly mean variations in the gradient's values were significant, where all values oscillated between approximately -50 and -110 N/km, with an exceptional value of -135 N-units/km for year 2003. The results are compared with the ITU maps of the ITU-R P.453-10 recommendation [12] in Table 5-1.

Table 5-1: Comparison of Monthly Mean Absolute Values of ΔN

Months	ITU Values [N/km]	Obtained Values [N/km]
February	70	53
May	80	77
August	90-100	89
November	70	60

The result of May is still in good coherence with the ITU maps. A difference of around 10 units is obtained for August and November. February has the most significant discrepancy of 17 units. It can also be seen that all ITU values for ΔN in the first kilometre are overestimated in comparison with the obtained results. Initial results of monthly and yearly variations of ΔN over the first kilometre in Abu Dhabi were presented in [5].

5.2.2 Refractivity Gradient Calculations in First 65 meters

Refractivity gradient over the first 65 m layer of the atmosphere above the surface has been evaluated, where h_1 corresponds to the value nearest to 65 m height, such that 60 m < h_1 < 70 m. Figure 5.4, displays the cumulative distribution of ΔN where its value varies between approximately -1400 and 400 N/km.

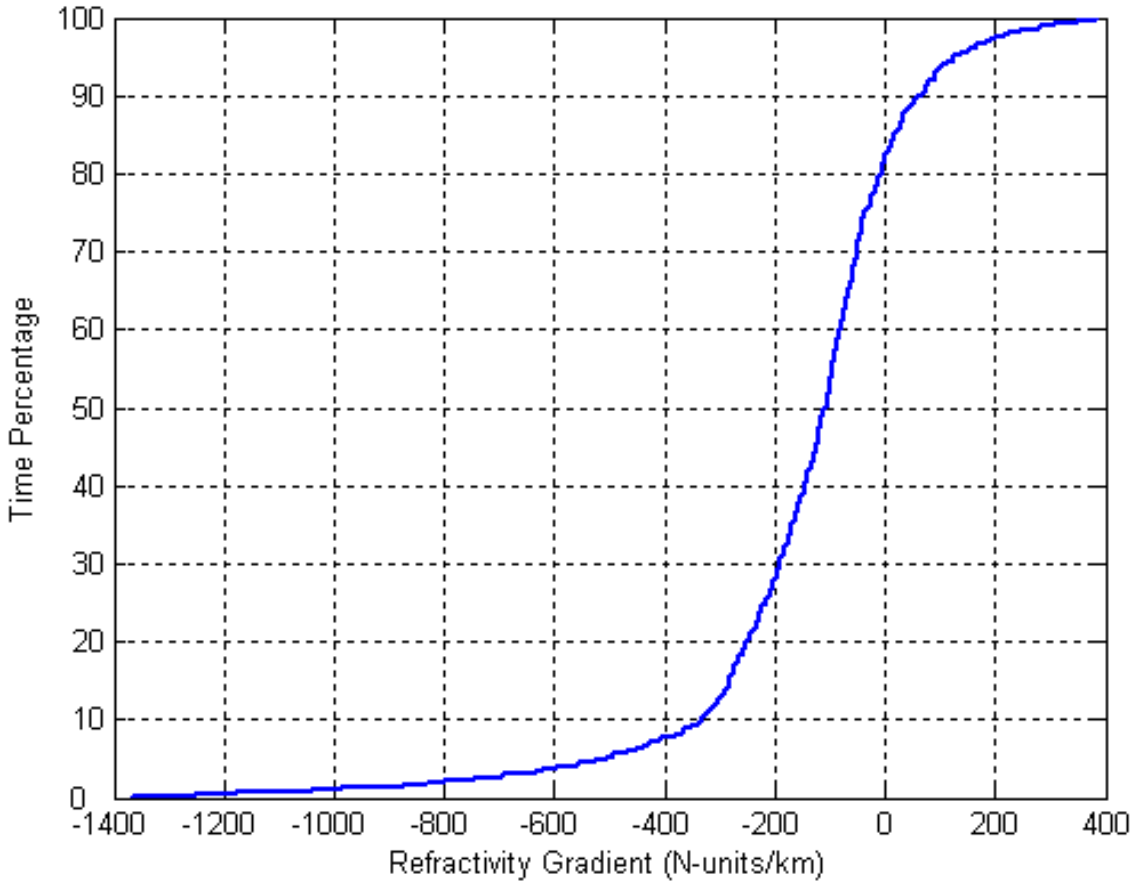

Figure 5.4: Cumulative distributions of refractivity gradient at 65 m

In Table 5-2, the obtained gradient values at 65 m height which have not been exceeded for different time percentages are compared with the estimated values by ITU [12]. The ITU data files have a resolution of 1.5^{o} in both latitude and longitude. Bilinear interpolation has been used to get the exact values of ΔN for Abu Dhabi.

Table 5-2: Values of ΔN at 65 m, Not Exceeded For Different Time Percentages

Time Percentages	ITU Values [N/km]	Obtained Values [N/km]
1 %	-952.42	- 1029
10 %	-553	-333.5
50 %	-92.824	-108
90 %	-4.38	63.6
99 %	38.86	293.6

The table shows optimistic ITU values for the percentages of 50 % and 90 %, while the obtained results indicate the occurrence of non-standard conditions with ΔN values exceed -100 N/km for 50 % of the time, and have higher positive values for 90 and 99 %.

5.3 Final Remarks

Fourteen years of surface and meteorological data, from 1990 to 2003, were utilized for the initial analysis of vertical refractivity profile. The monthly mean ΔN were provided for four reference months and compared with ITU maps. The monthly mean ΔN values were not in good coherence with ITU maps except for May.

The long-term value of ΔN in the first kilometre was around -72 N/km, which exceeded the ITU value of -40 N/km for reference standard atmosphere. The ΔN value for first 65 m not exceeded for 1 % of the time was found to be -1029 N/km at Abu Dhabi.

The ΔN analysis for the first 100 m in addition to the relevant statistics of β_0 parameter at Abu Dhabi and occurrence probabilities of relevant anomalous propagation conditions are

introduced in chapter 6. Due to the importance of the lowest 100 m layer of the atmosphere and considering the low resolution of the first data set, nine years of higher resolution meteorological data, from 1997 to 2005, are utilized for the analysis in chapter 6.

Chapter 6

STATISTICAL ANALYSIS OF ANOMALOUS PROPAGATION AND β0 PARAMETER

6.1 Introduction

The vertical refractivity profile in the first few hundred meters of the atmosphere, where terrestrial communication systems operate, is important for the analysis of these anomalous phenomena. Electromagnetic waves propagating through the lower layers of the atmosphere follow curved paths as a result of the variation of refractive index with height. The refractive index of air is dependent on temperature, pressure and humidity and thus varies with height. Anomalous propagation may occur due to nonstandard variation of vertical refractivity through different atmospheric layers. Few anomalous propagation studies are available for the Arabian Gulf region [4, 5, 82] compared with other temperate regions, although it is likely to experience abnormal conditions due to its special climate which is hot and humid, most of the year.

Nine years of local radiosonde meteorological data, from 1997 to 2005, have been used to calculate the vertical refractivity gradient, ΔN, in the first 100 meters above the ground

surface for Abu Dhabi. The data are recorded with good resolution from two daily ascents, nominally at 00:00 and 12:00 UT corresponding to 4:00 am and 4:00 pm local time. The ΔN values obtained are used to estimate the parameter β_0, which represents the probability of non-standard propagation. The β_0 statistics are derived from the cumulative distributions of the vertical ΔN. Hourly, monthly and yearly distributions of ΔN in the first 100 meters above the ground are given. Monthly and yearly variations of the mean of ΔN and β_0 are presented. The results obtained are compared with the β_0 values derived from ITU maps [12, 13], which are provided for different geographical locations where reliable local data are not available.

6.1.1 Refractivity Gradient in the Lowest Atmospheric Layer

The refractivity gradient, ΔN, statistics of the first 100 m from the surface may be used to estimate the occurrence probability of ducting and multipath conditions [12]. They have to be considered when studying the system performance of terrestrial line of sight communication. ΔN can be obtained from two refractivity values, N_s, surface refractivity, and N_1, refractivity at height h_1 above the ground level h_s, using the linear equation (2.27) [3-5].

The atmospheric radio refractivity, N, is calculated from atmospheric pressure (hPa), water vapour pressure (hPa) and absolute temperature (K) by the well-known formula (2.12) [11,

12]. The refractivity dry component can contribute up to 80 % of the overall value [29]. The vapour pressure, e, is derived from the dewpoint temperature, t_d, measured in degrees Celsius as follows:

$$e = 6.11\ x\ 10^{\left(\frac{7.5\ t_d}{237.3+\ t_d}\right)} \tag{6.1}$$

Other works have been conducted to study the feasibility of estimating the vertical refractivity gradient near the ground from measurements of electromagnetic wave strength and diffraction losses [25, 26], in particular when upper-air data are not available. An exponential model can also be used for quick, approximate estimates of refractivity gradient near the Earth's surface [12]. The vertical ΔN has usually a negative value since N decreases with altitude. If the gradient is less negative than usual, or even positive, sub-refraction occurs, where the ray bends less than usual towards the Earth, even bending upwards in the case of a positive gradient and the range reduces. Sub-refraction occurs when warm moist air flows over a cool ocean surface or over a cooler air mass just above the ocean surface [23, 24].

If the gradient is more negative than in a standard atmosphere, super-refraction takes place, with rays bending more than usual towards the Earth and propagating further than in standard conditions. Super-refraction occurs when temperature increases with height

and/or water vapour content decreases with height, where the signal propagates between the normal and critical gradient conditions. At a critical gradient value, ΔN = -157 N/km, the radius of curvature of the ray becomes equal to the Earth radius. The wave path approaches the Earth curvature and consequently the signal moves parallel to its surface [24]. Gradients, which are more negative than this critical value lead to ducting, and the signal becomes trapped in the boundary layer, propagating well beyond its usual range. Table 2-1 summarizes the limits considered for the refractive conditions in this study.

6.1.2 β_0 Statistics

β_0 is an important parameter in studies of clear air propagation and interference since it is commonly used to indicate the relative incidence of anomalous propagation. β_0 represents the percentage of time in which the value of ΔN is less than or equal to -100 N/km [12, 23, 29]. It is derived from ΔN statistics in the lowest 100 m of the atmosphere. The normal range of ΔN in the surface layer is between 0 and -100 N/km. In this chapter, "anomalous propagation" is defined as that occurring outside this normal range. Note that other references consider different values, such as -79 N/km, for the limit between the normal and non-standard propagation [24]. β_0 might relate, with reasonable accuracy, to the presence of ducting phenomenon where ΔN values exceed -157 N/km. It was observed [23] that β_0 is correlated to the latitude of the area under consideration, showing higher values in equatorial regions and lower toward the poles. In this work, β_0 is calculated from the occurrence probability of both super-refraction and ducting conditions.

6.2 Results and Analysis

Nine years of 10 m resolution meteorological data from 1997 to 2005 have been analysed in this study. Data are available for 5,391 radiosonde ascents. Due to low quality or incomplete ascents, data for June 1998, April 2000 and November 2005 are not available. A small number of abnormal values have been excluded owing to faulty readings from the instrument.

6.2.1 Refractivity Gradient calculations in the first 100 meters

The refractivity gradient, ΔN, has been evaluated using the linear equation approach. Since data at exact heights were not available, h_1, which was found to be 103 m, is selected to be the nearest point to 100 m height. In Figure 6.1 and Figure 6.2, the average seasonal and yearly variations of ΔN over the whole period of study are shown. The mean monthly variations are significant. Values oscillate between approximately -118 and -186 N/km, with a range of 68 units. The gradients are higher during summer months, May and June, while minimum values appear during winter months, January and December. This can be attributed to the decreasing vapour content and pressure and to the increasing temperature with height. Such ΔN trends explain the frequent interference cases even across national borders, which are most commonly experienced during the summer months in the Gulf

region. All monthly means are more negative than -100 N/km, which relates to the incidence of anomalous propagation.

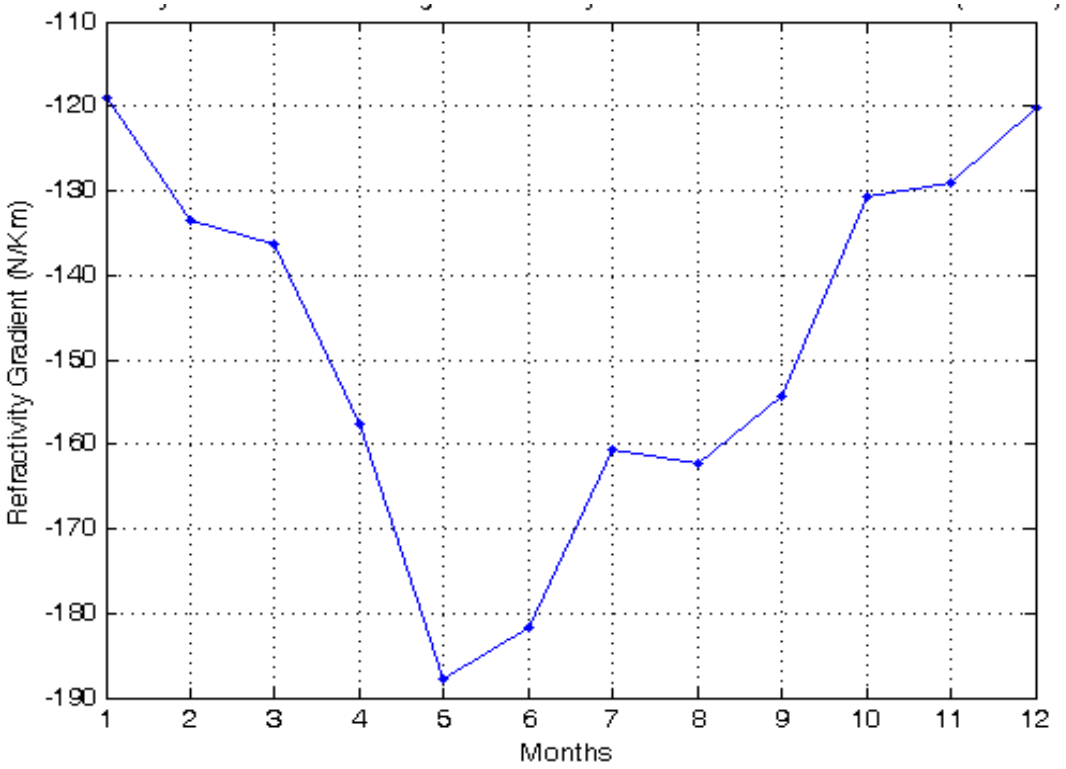

Figure 6.1: Mean monthly variations of the refractivity gradient, ΔN, at 100 m (1997 to 2005)

Year to year variations of the mean refractivity gradients with a span of 70 units, are given in Figure 6.2. It has been observed that the mean ΔN values have increased for the four years 2002, 2003, 2004 and 2005, with some exceptional values in the years 2003 and 2004. Whether this yearly increment is part of some short or longer-term climate cycle

cannot be reliably inferred from nine years' measurements, but may indicate an increasing probability of anomalous propagation occurrence in the Gulf region.

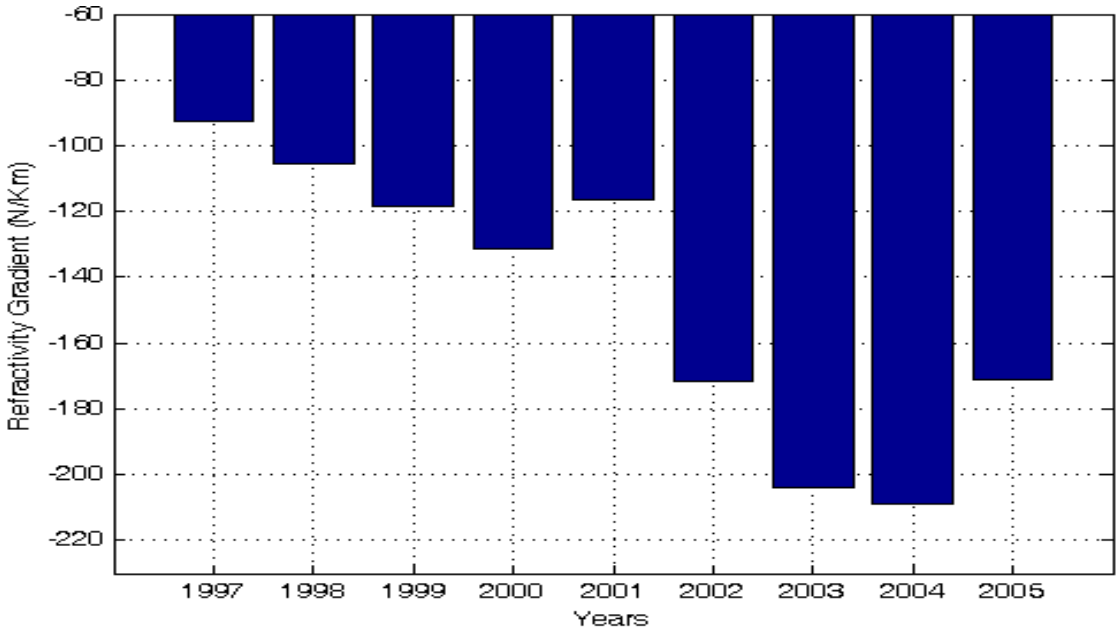

Figure 6.2: Mean yearly variations of the refractivity gradient, ΔN, at 100 m (1997 to 2005)

Cumulative distributions of ΔN over this period for different times of day are shown in Figure 6.3. The range of ΔN varied between approximately -1160 and 990 N/km, however for clarity only values between -1000 and 600 N/km are displayed. The long-term mean value of ΔN is -128.6 N/km, whereas the mean values at 00:00 and 12:00 UT are found to be -148.5 N/km and -113.9 N/km, respectively. The gradient values are more negative

during the morning. Meteorological phenomena following sunset, could be responsible for such a trend [29].

The vertical refractivity gradient in Abu Dhabi for the first kilometre of atmosphere has been found to vary between -200 and 63 N/km [4]. The ITU proposes a standard value of -40 N/km as the reference for the vertical refractivity gradient in the first kilometre [32]. It is clear from this study that the range of gradient variation in the lowest 100 m layer is much higher, which indicates that anomalous propagation is frequent in this critical atmospheric layer where most terrestrial wireless links operate.

The long-term occurrence probabilities of super-refraction and sub-refraction phenomena during the course of the year can be obtained from the "0 & 12H" curve in Figure 6.3, which corresponds to gradients exceeding -100 N/km and positive gradients above 0 N/km, respectively. The probabilities of super-refraction and sub-refraction conditions have been found to be around 23% and 9%, respectively.

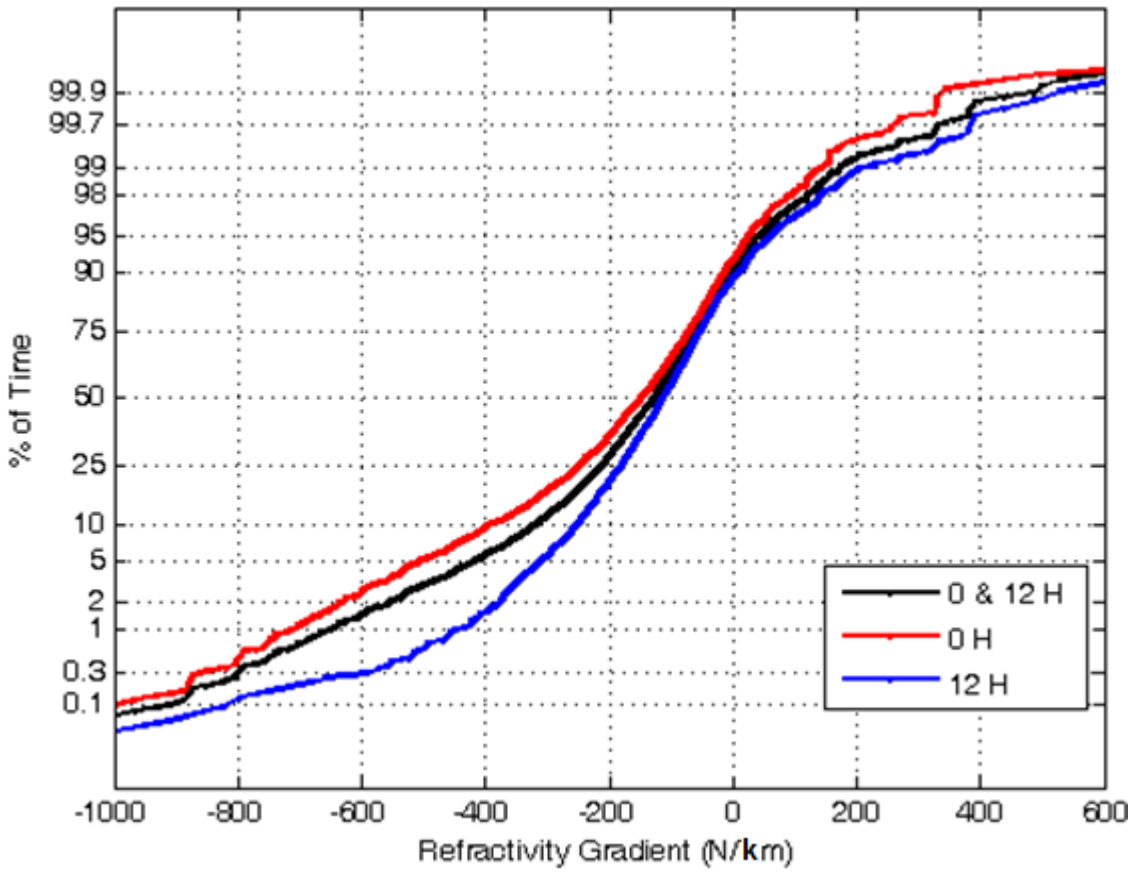

Figure 6.3: Cumulative distributions of refractivity gradient at 100 m

Monthly and yearly cumulative distributions of ΔN are given in Figure 6.4 and Figure 6.5. The cumulative distribution of each month is drawn in Figure 6.4 from all the data gathered for that calendar month during the entire period. There is a clear variation in the values during the course of the year. Summer months are more critical where the gradient varies over a wider range than in winter. Gradients with larger negative values have been obtained during the summer for higher percentages of time. Similar observations have been reported in [29, 42]. The monthly distribution curves converge around gradients between -50

and -90 N/km, and the time percentages change between 60 to 75% accordingly. It can be noticed that the probability of gradients less than or equal to -157 N/km, which indicates ducting occurrence, varies from 29% in January to 52% in May.

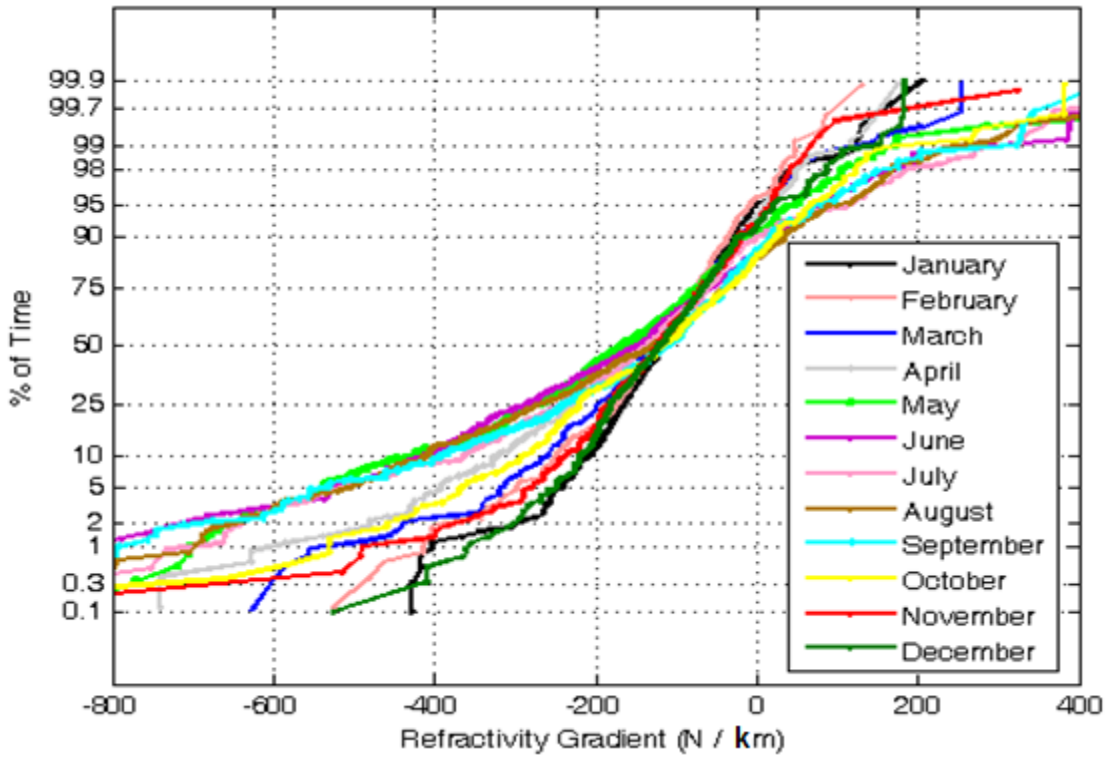

Figure 6.4: Monthly cumulative distributions of the refractivity gradient at 100 m

In Figure 6.5, it is evident that the yearly cumulative distributions have a fairly consistent form, however, the median value of ΔN increases systematically from year to year. The probability of anomalous propagation where ΔN exceeds -100 N/km also increases year on year.

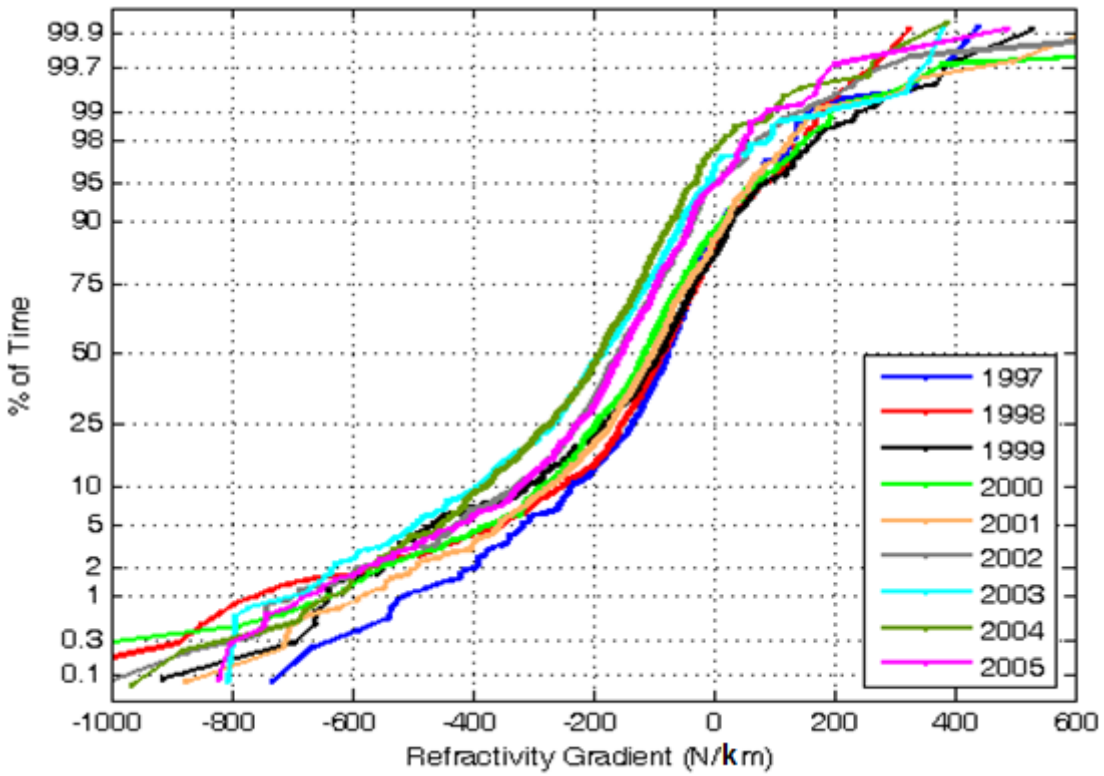

Figure 6.5: Yearly cumulative distributions of the refractivity gradient at 100 m

6.2.2 β_0 Calculations

Monthly and yearly variations of the β_0 parameter have been derived from cumulative distributions of ΔN at the lowest 100 m of the atmosphere. The long-term value of β_0 has been found to be 60.8% from the "0 & 12H" curve in Figure 6.3. This means that the value of refractivity gradient is expected to be less than or equal to -100 N/km for around 60% of the time. The values of β_0 obtained at 00:00 and 12:00 UT are 65.6% and 55.5% respectively, which indicate higher probability of anomalous propagation occurrence in the

early morning. This can explain the operational experience of intermittent outage due to high signal fading for some of the microwave links operating in UAE during the morning, mostly within the summer season.

Figure 6.6 shows monthly variations of β_0 obtained from the monthly cumulative distributions of the refractivity gradients in Figure 6.4. The value of β_0 fluctuates between 53% and 68%, with the highest value occurring in May. Generally, the summer months show higher probabilities of anomalous propagation than others.

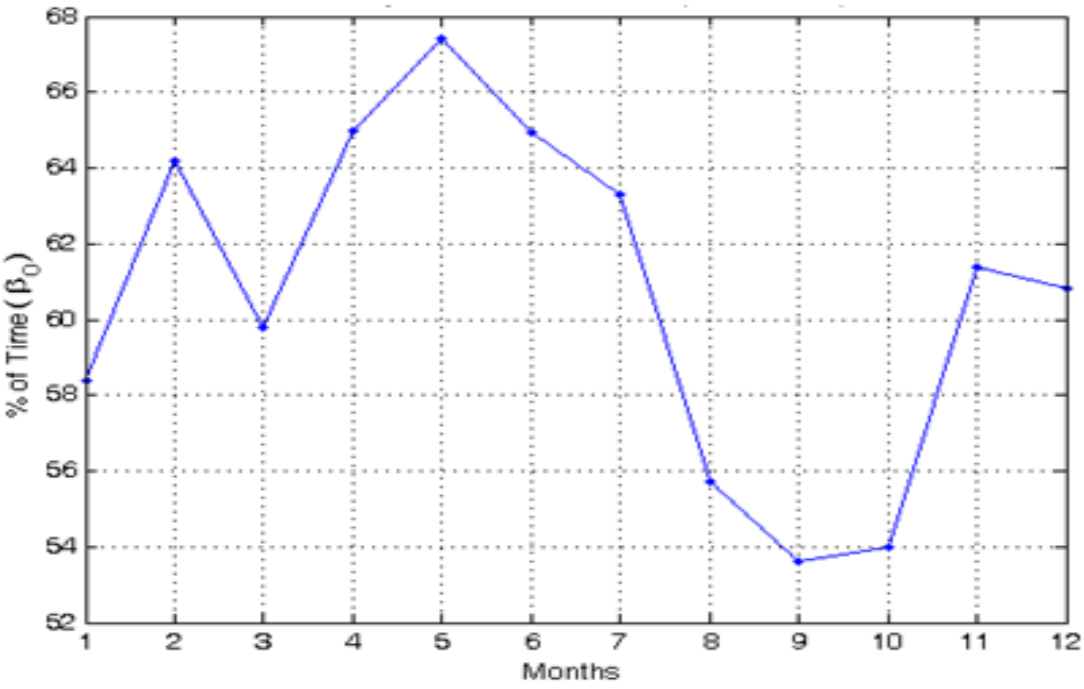

Figure 6.6: Monthly variations of β_0

The results obtained for the monthly variations of β_0 are compared with ITU maps [12] in Table 6-1. It is clear that the ITU values are not in good agreement with the results obtained in this study. The estimated ITU values are below those calculated in the case of February and November with differences of 34% and 21%, respectively, while they are overestimated for the months of May and August, with differences of 7% and 19%. This can be attributed to the fact that the ITU maps [12] were interpolated from radiosonde data from only 99 sites worldwide between 1955 and 1959. Differences have also been observed in other countries [29]. In addition, ITU curves and maps are usually derived from measurements performed largely in temperate regions of the world such as Europe, North America and Japan [15], which have different climatic conditions from the Gulf region. This would also suggest the necessity to revise these maps based on recently gathered long-term local meteorological data from more radiosonde sites, since they are being widely used for microwave link design.

Table 6-1: Values of β_0 compared with ITU maps

Months	ITU Values (%)	Obtained Values (%)
February	30	64
May	75	67
August	75	56
November	40	61

The annual variations of β_0 are given in Figure 6.7, which are obtained from the yearly cumulative distributions of the refractivity gradients in Figure 6.5. The variation is

significant where the percentages are increasing year by year; with a peak value shown for 2004.

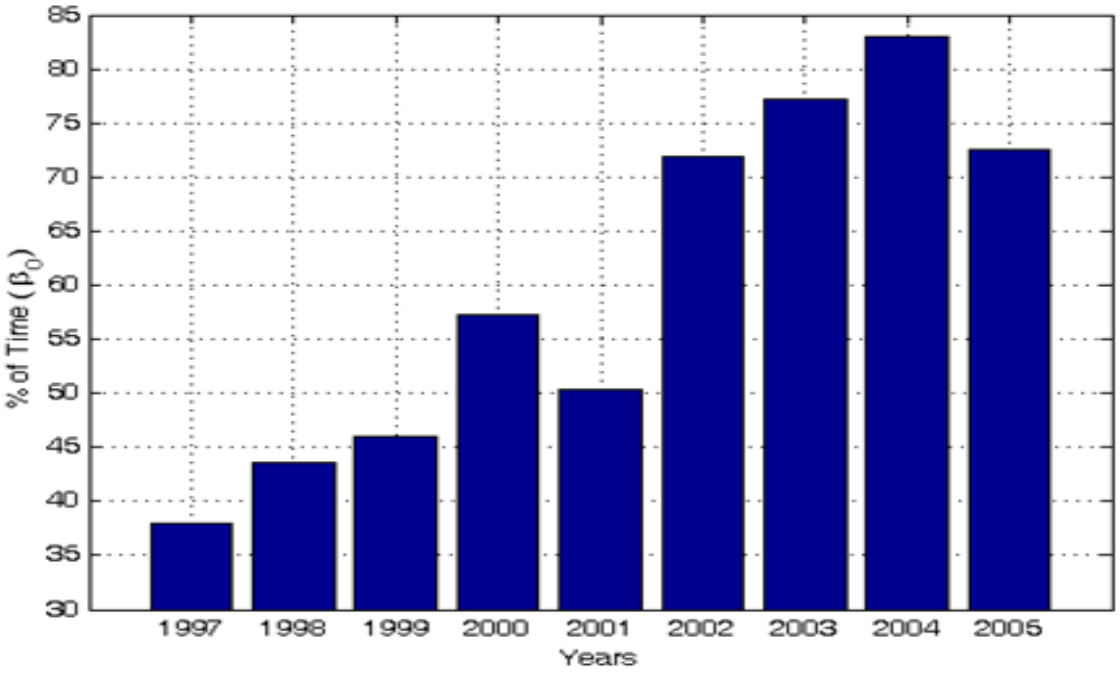

Figure 6.7: Year to year variations of β_0

6.3 Final Remarks

Local radiosonde data were used to obtain the refractivity gradient in the first hundred meters above the ground surface. The β_0 parameter has been calculated to indicate the probability of anomalous propagation such as ducting and multipath in Abu Dhabi. The results obtained for the long-term mean value of ΔN and β_0 were -128.6 N/km and 60.8%,

respectively. The monthly results of β_0 were not in good agreement with the values provided by the ITU maps. In general, the morning, and summer months, showed higher occurrence probability of nonstandard propagation conditions. Operational observations of the received signal strength, fading occurrence and interference cases for some of the microwave links operating in the UAE confirmed these findings. Since the calculations have been done using reliable local data, it is strongly recommended to adopt these values for better prediction of performance and reliability in the design and deployment of wireless communication systems working in this region. There is perhaps an opportunity to revise the ITU maps using the now abundant long-term local meteorological data which have been collected recently all over the world. Work will continue to report the fading occurrence based on real signal strength measurements and to study the occurrence of different ducting classes in UAE.

New approaches and algorithms will be presented in chapter 7 for the analysis of vertical atmospheric profile below 1 km using seventeen years of meteorological data, from 1997 to 2013.

Chapter 7

NEW APPROACHES AND ALGORITHMS FOR ANALYSIS OF VERTICAL ATMOSPHERIC PROFILE BELOW 1 KM

7.1 Introduction

The extent of ray-curvature is determined by the gradient of the refractive index, in N-units, versus height in km from the surface. This is known as the surface lapse rate, ΔN. The ITU has defined a reference atmosphere in the form of a negative exponential model and proposed a reference value of -40 N/km for the vertical ΔN over the first kilometre in temperate regions [32]. ITU has also published global contour maps for the refractive index at Earth's surface, N_s, and ΔN at specified altitudes [12].

It has been noted that surface meteorological data are widely available and the information about N_s is more readily available than the upper-air refractivity, N_h [83]. The shortage of upper-air data can be attributed to the operational and maintenance cost of radiosonde ascents compared with fixed surface weather stations. Some linear and exponential models [11, 12, 83] have been proposed to predict N_h at height h and vertical ΔN from the available

N_s data, where upper-air data are not available. It has been noted that most of these relations, in particular for ΔN, are derived from the refractivity analysis at the ground and 1 km height.

In this chapter, 17 years of high resolution surface and radiosonde meteorological data from 1997-2013 for the subtropical Gulf region are analysed. Radiosonde data recorded at Abu Dhabi. Relationships between the upper-air refractivity, N_h, and vertical refractivity gradient, ΔN, in the low troposphere and the commonly available data of surface refractivity, N_s are investigated. The measured refractivity parameters, N_s, N_h and ΔN, refer to the values obtained from the surface and radiosonde meteorological measurements, whereas predicted values of N_h and ΔN refer to those calculated from the measured N_s using the existing models in the literature. The measured ΔN is derived from the measured N_s and N_h parameters using the linear model. Root mean square errors, RMSE, and correlation between the measured parameters and between measured and predicted values will be presented.

A new approach is discussed to estimate N_h and ΔN from the analysis of the dry and wet components of N_s, which gives better results for certain cases. The relationships between dry, wet and net components N_s with both N_h and vertical ΔN are investigated. The investigation focusses on three layer heights at 65 m, 100 m and 1 km above ground level within the subtropical climate of the Arabian Gulf. These heights are common reference points in ITU-R models [12]. Cumulative distributions and scatter diagrams are presented.

The correlation between predicted and available radiosonde measurements for the components of N_s with both N_h and ΔN, as well as the root mean square errors, RMSE, are studied for each atmospheric layer. Where high correlations were found, empirical models are derived from best-fitting curves. New relationships are derived from the best fitting curves and compared with existing models. Results are compared with those obtained from existing linear and exponential models in the literature. The curve fitting analysis of the dry and wet components at each layer has not been reported before in the literature.

The height coefficient parameter of the ITU exponential model has also been investigated for all refractivity components in the three atmospheric layers. A considerable variation in the coefficient value is observed for each case. Correlation between the components of N_s with both N_h and ΔN are studied for each atmospheric layer.

7.1.1 Refractivity Models

The atmospheric radio refractivity, N, at any altitude is calculated from the meteorological measurements of total atmospheric pressure (hPa), water vapour pressure (hPa) and absolute temperature (K) using the well-known refractivity formula [11, 12]. The N parameter consists of two components, N_{D} and N_{W}, which are often referred to as the dry and wet air contributions to refractivity [11]. The dry component contributes around 60 to 80 % of the overall value [29]. The ITU provides a reference atmosphere for terrestrial

paths in the form of a negative exponential model (7.1) for the prediction of N_h at any height h (km) above mean sea level [12]:

$$N_h = N_0 \,.\, \mathrm{e}^{\left(\frac{-h}{h_0}\right)} \qquad (\mathrm{N-units}) \tag{7.1}$$

where N_o is refractivity extrapolated to sea level and h_o is the height coefficient which is referred to by ITU as the scale height of the model. The ITU provides global maps of N_o (derived using h_o = 9.5 km) and proposes an average global profile based on N_o and h_o, values of 315 N-units and 7.35 km, respectively [11, 12]. It has been noted [12] that h_o may vary from one region to another.

Other relationships have also been proposed to predict N_h from the surface data [11, 83]. The following exponential model (7.2) is further generalized to predict N_h from N_s considering "bulk" refractive index structure as opposed to short period random disturbances resulting from a variety of stochastic atmospheric processes [11]:

$$N_h = N_s \,.\, e^{\left[-\left(\frac{h-h_s}{h_o}\right)\right]} \qquad (\mathrm{N-units}) \tag{7.2}$$

7.1.2 Refractivity Gradient Models

The variation of ΔN is a function of climate, season, transient weather conditions across the day, clutter and terrain over the communication path. ΔN can be obtained from two refractivity values, N_s at the surface, h_s, and N_h at an altitude h, using the linear model, by dividing the refractivity difference (N_s - N_h) over (h_s - h) [3, 11, 38]. N_h usually decreases with altitude causing vertical ΔN to have negative values.

A close correlation has been observed between N_s and ΔN "near the ground", i.e. over the first few kilometres [11]. Several empirical equations have been derived to predict long-term mean values of ΔN for the first kilometre layer of atmosphere above the ground from measured N_s parameter, which are only applicable to average negative gradients close to the surface [11, 83]. If N_h is not readily available, the refractivity gradient near the Earth's surface can be predicted either by Equation (7.2), [11] or by applying the linear model for the measured N_s and the predicted N_h. Other models are also studied to predict the vertical ΔN near the ground from the measurements of electromagnetic wave strength and diffraction losses [25, 84]. For higher altitudes, different functions may be fitted as proposed by the three-part reference atmosphere model in Bean and Thayer's 1959 paper [11], which gives different expressions for the refractivity in the first kilometre, between 1 and 9 km and above 9 km. This has a drawback of introducing discontinuities in the ΔN profile. An exponential equation can also be used to directly relate ΔN with N_s as follows [11, 83]:

$$\Delta N = \ -a\ .\ e^{(k\ .N_s)}\ \text{(N/km)} \tag{7.3}$$

where a and k are the model coefficients. Another exponential decaying relationship, obtained from curve fitting analysis between N_s and ΔN, was proposed for the first kilometre, $\Delta N_{1\text{km}}$, [11, 82] as follows:

$$\Delta N_{1\text{km}} = a\ .(1 - e^{-bN_s})^c \qquad \text{(N/km)} \tag{7.4}$$

where a, b, and c are the model coefficients. In general, the values of coffecients of all the models are found to vary from one climate to another. Analyzing data for long periods may also provide more accurate values of the coeffecients. In order to extend these relations to other regions around the world, the correlation between long-term measured and predicted refractivity parameters need to be evaluated as well.

7.2 Analysis and Results

Seventeen years of high resolution meteorological data from 1997 till end of October 2013 have been analysed in this study. Due to low quality or incomplete ascents, data for June 1998, April 2000, November 2005, June 2006 to November 2006 and January 2010 to May

2010 are not available. From December 2006 to December 2008, the data of only one ascent, mostly at 00:00 UT, is available on daily basis. In addition, a small number of abnormal values have been excluded owing to faulty readings from the instrument.

Two approaches, direct and indirect, have been used to predict N_h and ΔN from the measured N_s values. In the direct approach, N_h and ΔN are directly predicted from measured N_s using the linear or exponential models. A new indirect approach is proposed by analyzing the dry and wet components of the refractivity parameters using various prediction models. In this indirect approach, the dry and wet components of N_h or ΔN are first estimated from corresponding components of measured N_s based on the correlations observed between different components. Then, the net values of the predicted parameters, $\Delta N_{(D+W)}$ and $N_{h\_(D+W)}$, are computed by summing both dry and wet terms.

7.2.1 ΔN Analysis at 65 m, 100 m and 1 km Layers

The measured refractivity, N, has been evaluated from the radiosonde measurements at the ground and at the three specified altitudes. Then, the measured ΔN is obtained from the measured N_s and N_h for each layer using the linear model. In Figure 7.1 and Figure 7.2, the average seasonal and yearly variations of ΔN over the whole period of study are shown for each of the three layers. The mean monthly variations are significant for all the layers, as shown in Figure 7.1. The gradient values at the 1 km layer, ΔN_{1km}, vary between -51 and -

99 N/km, whereas the gradients span from -68 to -158 N/km and from -68 to -156 N/km, in case of the 100 m layer, $\Delta N_{0.1\text{km}}$, and the 65 m layer, $\Delta N_{0.065\text{km}}$, respectively. The range of variation is found to be approximately 45 units for $\Delta N_{1\text{km}}$, 90 units for $\Delta N_{0.1\text{km}}$ and 88 units for $\Delta N_{0.065\text{km}}$.

Gradient values are smaller (i.e. more negative) during the summer months, May and June, than in winter months, January and December. This can be attributed to the decreasing vapour content and pressure with height and the observed temperature inversions (temperature increasing with height) during the night, particularly in summer. Such ΔN trends may explain the frequent interference cases even across national borders, which are commonly experienced by terrestrial communication systems operating in the Gulf region during the summer months [38]. For $\Delta N_{1\text{km}}$, no monthly mean is below -100 N/km, whereas $\Delta N_{0.1\text{km}}$ and $\Delta N_{0.065\text{km}}$ fall below this value for most months. In May, the monthly means of $\Delta N_{0.1\text{km}}$ and $\Delta N_{0.065\text{km}}$ even fall below the limit at which ducting phenomenon occurs, -157 N/km. Two peaks of $\Delta N_{0.1\text{km}}$ and $\Delta N_{0.065\text{km}}$ curves are observed in October, where both monthly mean values of $\Delta N_{0.1\text{km}}$ and $\Delta N_{0.065\text{km}}$ are found to be higher than $\Delta N_{1\text{km}}$. However, the curves were smoothed using linear interpolation, as shown in Figure 7.1. These two peaks at October can be attributed to a bias in the data due to having only early-morning radiosonde data for this month. In 2007 and 2008, the data for October are only available for at 00:00 UT (4 am local time). In the morning, it is observed that the temperature and the water vapour pressure, *e*, often increase with altitude in many cases, in particular within the 65 m and 100 m layers, while *e* decreases considerably at 1 km height. The early

morning / early evening effect on the gradient is clearly seen in the CDFs shown in Figure 7.3. Consequently, the wet components of N and ΔN increase with altitude and ΔN attains large positive gradients in both 65 m and 100 m layers, which relates to the incidence of sub-refraction phenomenon [23, 24, 38]. The linear ΔN model has the drawback, particularly for the altitudes 100 m and below, that a small difference between the two refractivity values may result in large disagreement in ΔN due to the low decimal number in the equation's denominator. Also, the data for October 2006 were not available, which may also affect the overall result.

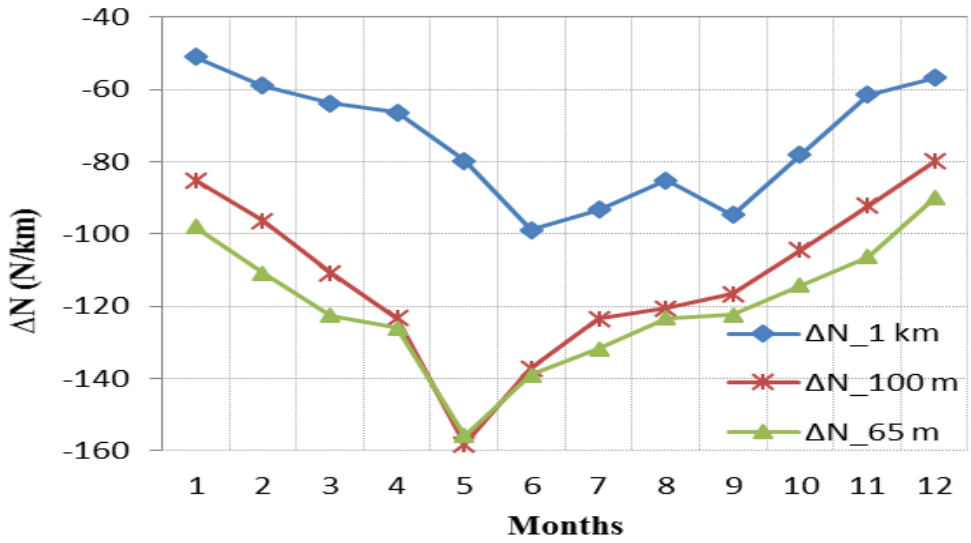

Figure 7.1: Mean monthly variations of ΔN (1997 to Oct. 2013)

Year to year variation of the mean ΔN at 1 km, 100 m and 65 m, with spans of 32, 209 and 298 N-units, respectively, are given in Figure 7.2. ΔN_{1km} shows no significant fluctuations,

while the values of $\Delta N_{0.1km}$ and $\Delta N_{0.065km}$ fluctuate from -1.5 to -210 N/km, and from 31 to -267 N/km, respectively. It can be observed that the mean $\Delta N_{0.1km}$ and $\Delta N_{0.065km}$ values decreased for the four years 2002, 2003, 2004 and 2005, with some exceptional values in the years 2003 and 2004. One reason for such trend is the considerable decrement of the water vapour content and pressure with higher altitudes that were observed over the course of these years. This yearly increment could be part of some short-term climate cycle, although a cyclical pattern cannot be reliably inferred from the currently available measurements. By contrast, the values of mean ΔN over each of the three layers were almost the highest during 2010, which can be attributed to the missing five months data, in particular the months of April and May, which contribute to lower gradient values. However, the curves were smoothed using linear interpolation, as shown in Figure 7.2.

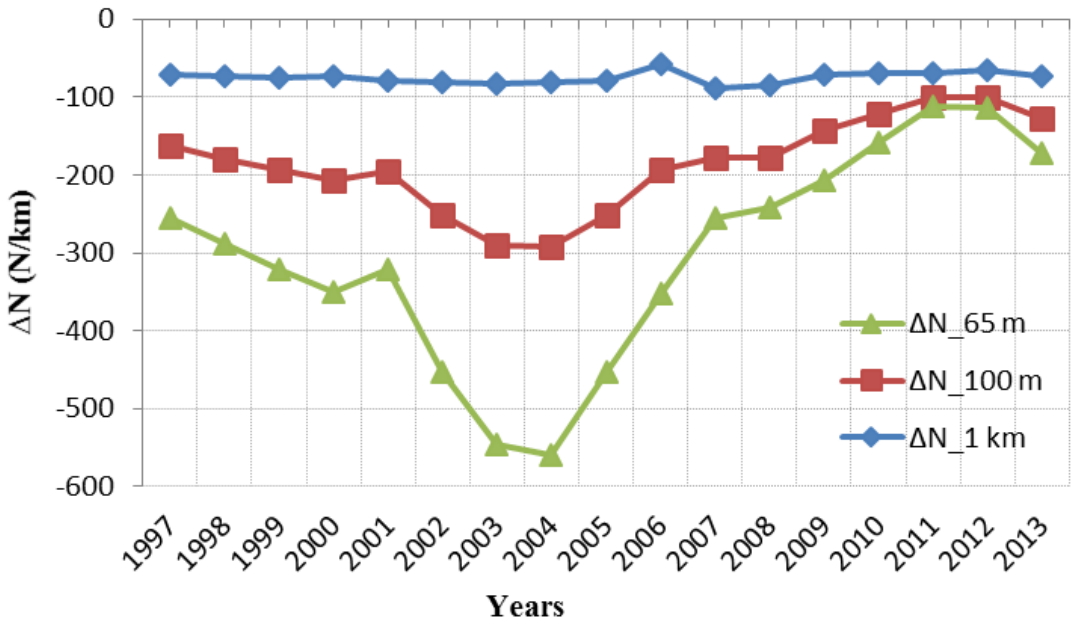

Figure 7.2: Mean yearly variations of ΔN (1997 to Oct. 2013)

Cumulative distributions of ΔN_{1km}, $\Delta N_{0.1km}$ and $\Delta N_{0.065km}$ for two times a day over the whole period are shown in Figure 7.3. The range of $\Delta N_{0.065km}$ varies between approximately -1947 and 1629 N/km, however only values between -1500 and 1500 N/km are displayed for clarity. The long-term mean values of ΔN_{1km}, $\Delta N_{0.1km}$ and $\Delta N_{0.065km}$ are -74.8, -109.6 and -116.4 N/km, respectively (well below the -40 of the ITU-R standard atmosphere), whereas the mean values at 00:00 and 12:00 UT are found to be -87.9 and -58.8 N/km for ΔN_{1km}, -138.7 and -74 N/km for $\Delta N_{0.1km}$, in addition to -134.9 and -93.7 N/km for $\Delta N_{0.065km}$.

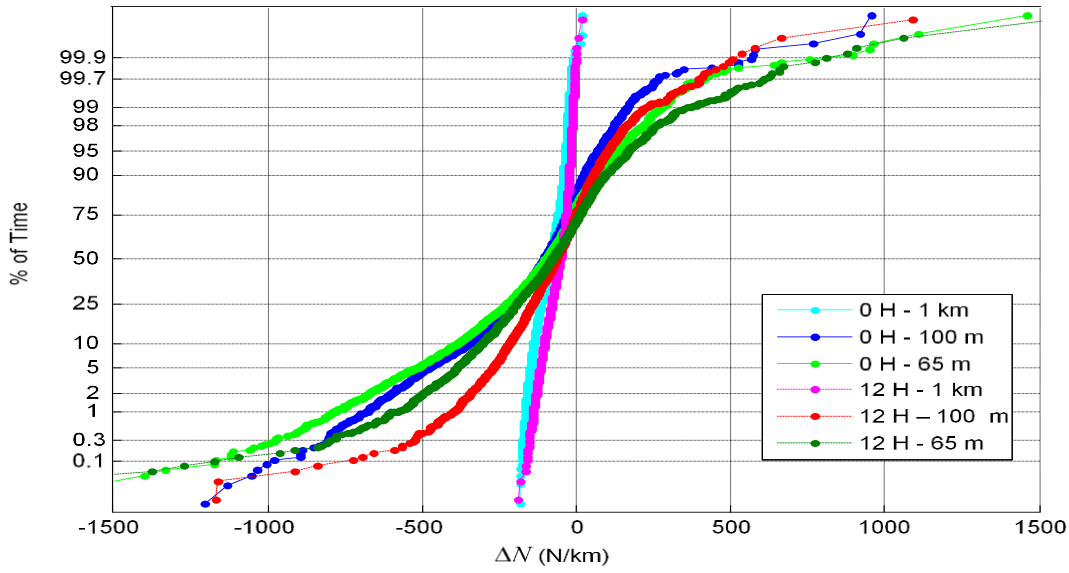

Figure 7.3: Hourly Cumulative distributions of ΔN (1997 to Oct. 2013), UT time

By comparing the 0 H and 12 H (UT) curves for each layer, it can be observed that the gradient values are lower during the morning. Meteorological phenomena following sunset

is responsible for such a trend [29], where vapour content considerably decreases with height, particularly during the summer season, while in Winter the moisture content may increase with altitude leading to higher positive values of $\Delta N_{0.1\text{km}}$ and $\Delta N_{0.065\text{km}}$ than 12:00 UT. Similar results were also reported in a previous study [38], however over a shorter period of years.

7.2.2 Correlation of Refractivity Components

The models introduced for predicting N_h and ΔN parameters from measured N_s, are examined and the predicted results are compared in terms of RMSE and correlation with the measured N_h and ΔN parameters. Table 7-1 summarizes the results of RMSE and correlation coefficients obtained for N_h and ΔN parameters using the exponential models (7.2) and (7.4), respectively, which give the best results in most cases, compared with other models. The exponential model (7.4) provides the best correlation and RMSE results for $\Delta N_{1\text{km}}$, whereas (7.2) gives the best results of N_h at the 65 m and 100 m layers.

Table 7-1: Correlation and RMSE Values of Existing Prediction Models for N_h and ΔN from N_s

Layer	N_h & ΔN	Correlation	RMSE
1 km	N_h	0.001	30.82
	ΔN_{1km}	0.86	18.77
100 m	N_h	0.87	15.18
	$\Delta N_{0.1km}$	0.29	151.7
65 m	N_h	0.91	12.59
	$\Delta N_{0.065km}$	0.24	196.2

No correlation has been found between N_h and N_s for the 1 km layer, while better correlation is observed for the other two layers, 100 m and 65 m. On the other hand, the correlation between ΔN_{1km} and N_s exceeds 0.85, whereas it is found to be poor in case of the 65 m and 100 m layers. In addition, the correlation between the dry, wet and net components of measured N_s and the corresponding components of the measured N_h and ΔN are also investigated for each of the three layers. Table 7-2 provides the results of correlation matrix for all the scenarios. The dry component of N_s, N_{s_D}, is in good correlation with the dry component of N_h, N_{h_D}, at all altitudes, N_{1km_D}, $N_{0.1km\_D}$ and $N_{0.065km\_D}$, where the maximum correlation is observed within the 65 m layer. The N_{s_D} is found to be much less correlated with the dry components of ΔN in the three layers; ΔN_{1km_D}, $\Delta N_{0.1km\_D}$ and $\Delta N_{0.065km\_D}$. The wet component of N_s, N_{s_W}, is well correlated with the wet component of N_h at the 100 m and 65 m altitudes, $N_{0.1km\_W}$ and $N_{0.065km\_W}$, while it is found to be only correlated with the wet component of ΔN at the 1 km layer, ΔN_{1km_W}.

Table 7-2: Correlation matrix of refractivity components at 1 km, 100 m and 65 m layers

	N_s	N_{s_D}	N_{s_W}
N_{1km}	0.001		
N_{1km_D}		0.84	
N_{1km_W}			0.15
$N_{0.1km}$	0.874		
$N_{0.1km\_D}$		0.96	
$N_{0.1km\_W}$			0.89
$N_{0.065km}$	0.91		
$N_{0.065km\_D}$		0.97	
$N_{0.065km\_W}$			0.92
ΔN_{1km}	-0.85		
ΔN_{1km_D}		-0.56	
ΔN_{1km_W}			-0.86
$\Delta N_{0.1km}$	-0.30		
$\Delta N_{0.1km\_D}$		-0.55	
$\Delta N_{0.1km\_W}$			-0.29
$\Delta N_{0.065km}$	-0.26		
$\Delta N_{0.065km\_D}$		-0.54	
$\Delta N_{0.065km\_W}$			-0.25

In general, no correlation could be obtained between either dry or wet components of N_s, and ΔN at the 100 m and 65 m layers. It is also noted that the correlation between the net parameters follows the correlation between their wet components. These observations seem to be reasonable since the wet term of refractivity is proportional to the water vapour content that varies significantly across these layers, in particular within the layers close to the ground, and gets more stable at around 1 km height. On the other hand, the dry term is proportional to the atmospheric pressure and inversely proportional to the dry temperature, which shows less variation over all atmospheric layers within the first kilometre.

The slope of the vertical refractivity curve at 1 km, which refers to ΔN_{1km}, is correlated with N_s since the variation of N_{1km} is very small compared with $N_{0.1km}$ and $N_{0.065km}$, which are directly correlated with N_s. No correlation is observed between N_s and gradients at the layers close to the ground, $\Delta N_{0.1km}$ and $\Delta N_{0.065km}$. Figure 7.4 describes this phenomenon, where at 1 km height the refractivity value does not change significantly with the variations in N_s, while $N_{0.1km}$ and $N_{0.065km}$ vary significantly with N_s. The slope, ΔN, is only correlated with N_s in case of the 1 km layer, ΔN_{1km}, since N_{1km} is assumed to have a stable value while N_s varies between the states S1 and S2.

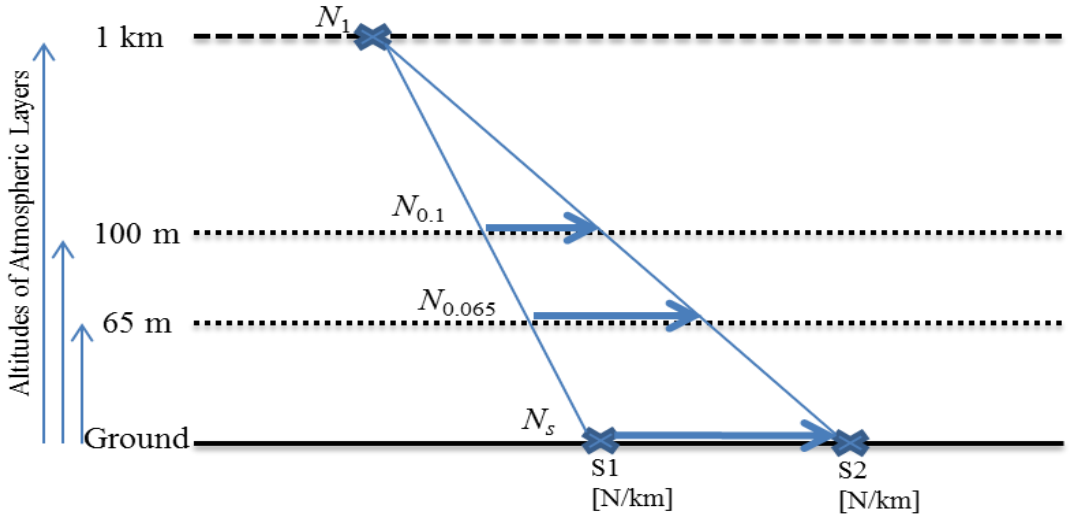

Figure 7.4: Description of Correlation Between N_s, N_h and ΔN

7.2.3 Curve Fitting Analysis and Algorithms

The scatter diagrams of all measured refractivity parameters and components are studied. Some figures of the correlated parameters and components are provided and empirical algorithms are derived from the best fitting curves. All relationships are evaluated based on the determination coefficients, correlation of the obtained results with the measured data and RMSE values.

As presented in Table 7-2, the correlation between N_s and ΔN_{1km} is dominated by the wet components of the two parameters, N_{s_W} and ΔN_{1km_W}, while $N_{s\_D,}$ is found to be correlated with N_{1km_D} rather than ΔN_{1km_D}.

The scatter diagram between the wet components, N_{s_W} and ΔN_{1km_W}, is shown in Figure 7.5. A third order polynomial relationship to predict ΔN_{1km_W} is obtained from the curve fitting analysis. The dry component of ΔN_{1km_D} is calculated using the linear model from the predicted N_{1km_D} and measured N_{s_D}. N_{1km_D} is predicted from measured N_{s_D} using equation (2). This new indirect approach for predicting $\Delta N_{1km(D+W)}$ has less RMSE value than the direct approach for predicting ΔN_{1km} from measured N_s using the linear model, as shown in Table 7-3.

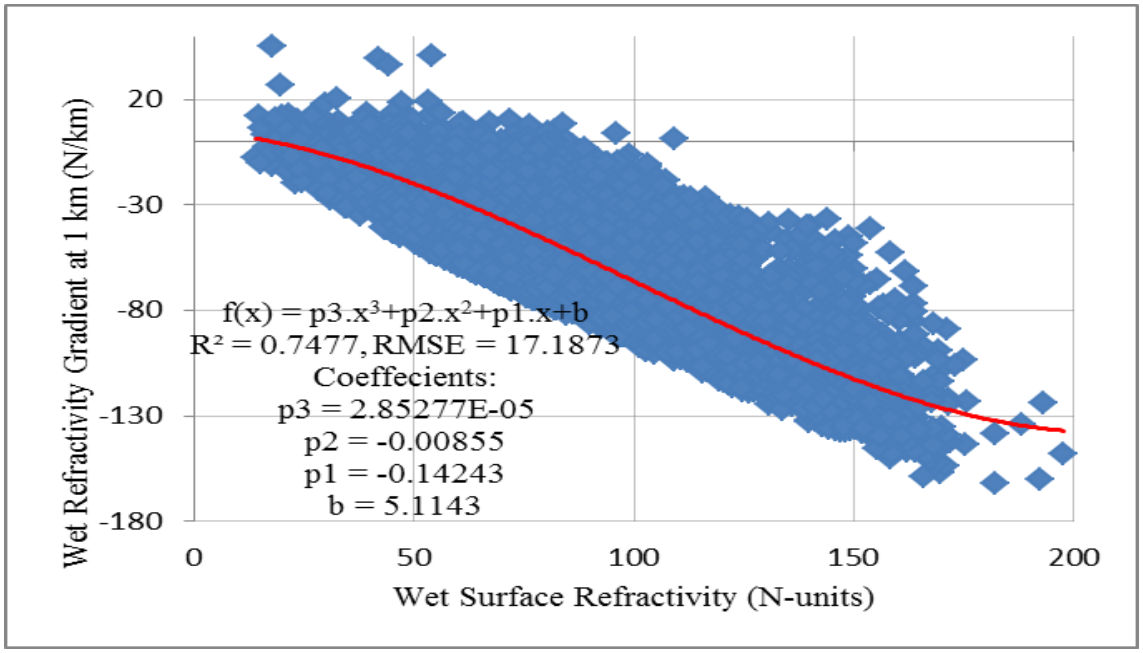

Figure 7.5: Correlation between N_{s_W} and ΔN_{1km_W}

Table 7-3: Comparison of two approaches for ΔN_{1km} prediction

	Correlation	**RMSE**
Direct Approach: ΔN_{1km} from measured N_s	0.85	30.8118
Indirect Approach: $\Delta N_{1km(D+W)}$ from Dry and Wet Components Analysis	0.85	19.3338

Multiple scatter diagrams are drawn for the dry, wet and net components of the measured N_h and ΔN against the corresponding measured N_s components at 65 m and 100 m atmospheric layers. Good correlation is observed between N_h and N_s components, while it is found to be poor between ΔN and N_s with large RMSE values regardless of the approach

or the prediction model to be used. This can be attributed to the sensitivity of ΔN to any small variation in the values of refractivity at these low altitudes. N_{h} has been predicted using the exponential model (2) considering both the direct and indirect approaches at the 65 m, $N_{0.065\mathrm{km}}$, and 100 m, $N_{0.1\mathrm{km}}$, layers. Due to the similarity of the N_h results at the 65 m and 100 m layers, the available data sets of these two layers are combined, $N_{0.065\&0.1\mathrm{km}}$, to develop a single model for the atmospheric layers below 100 m altitude from the ground. The correlation and RMSE values of the measured and predicted N_h, N_{h_D}, N_{h_W} and $N_{h\_(\mathrm{D+W})}$, are compared for each of the three data sets at 65 m, 100 m and their combined set. For all scenarios, RMSE results for $N_{h\_(\mathrm{D+W})}$ using the indirect approach are better than the results of N_h obtained directly from the measured N_s, while correlation results are almost the same.

The scatter diagram of N_h against N_s is given in Figure 7.6. Two exponential and third order polynomial relationships are obtained from the best fitting curves, which provide marginally better results in comparison with the other models. Both models have very similar results with marginal improvement for the polynomial model. However, the result from the polynomial is highly sensitive to the precision of the coefficients. The RMSE and correlation results obtained for the prediction of N_h from both direct and indirect approaches are similar. The following exponential model can be used for direct prediction of N_h below 100 m above the ground, where the values of the coefficients a and b are found to be 135.8 and 0.002609, respectively, for the area under study:

$$N_{0.065\&0.1km} = a \,.\, e^{(b \,.\, N_s)} \qquad (\mathrm{N-units}) \qquad (7.5)$$

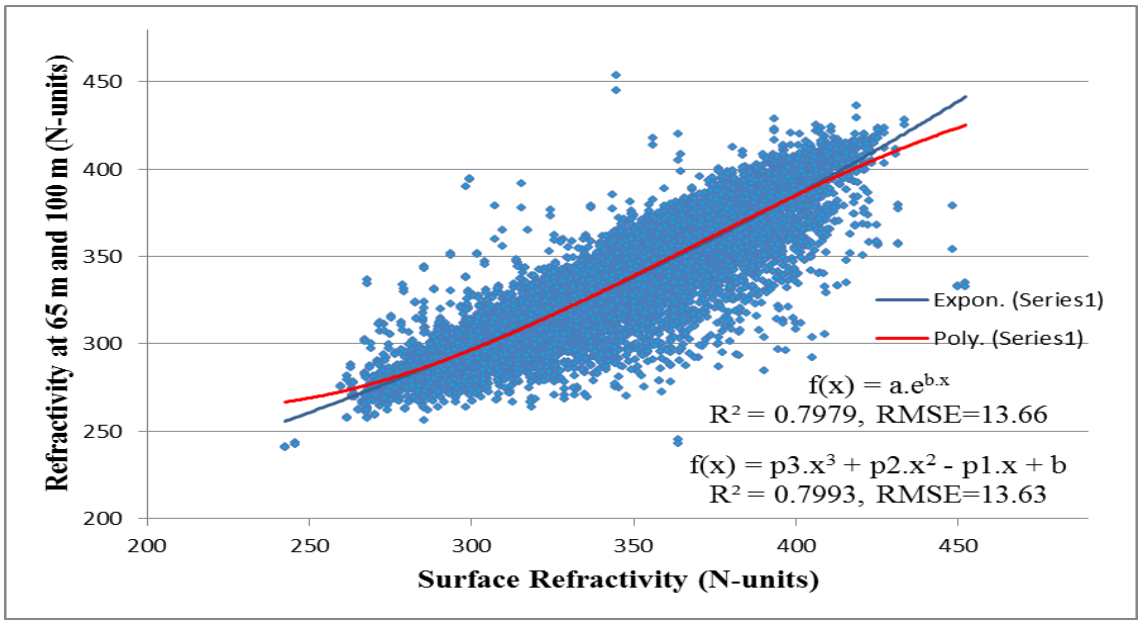

Figure 7.6: Correlation between N_s and $N_{0.065\&0.1km}$

7.3 Investigation of Height Coefficient in Arabian Gulf

The selection of the three atmospheric layers at 65 m, 100 m and 1 km above the ground for the investigation of ΔN statistics is due to their important contributions to several propagation studies [13, 30]. In addition, all terrestrial communication systems operate within these layers.

For comparison purposes and as explained before, N_h has been evaluated from N_s measurements at the three altitudes using the ITU exponential model. N_s values are

calculated from the surface radiosonde measurements. ΔN is then calculated for each layer using the linear and exponential models from N_s measurements as well.

The results of correlation between the predicted results, using exponential models, and the measured results, from radiosonde measurements, of the dry, wet and net components of N_h or ΔN parameters for each of the three layers are summarized in Table 7-1.

The value of h_o is found to vary slightly across different atmospheric layers and when the dry, wet and net components of each parameter are estimated for the same layer. In the subtropical Arabian Gulf region, h_o is found to be 3.9 km, 3 km and 2.8 km for 1 km, 100 m and 65 m layers, respectively, which give the minimum RMSE values in each scenario. No correlation has been found between N_h and N_s for the 1 km layer, while strong correlation is observed for the other two layers, 100 m and 65 m. On the other hand, the correlation between $\Delta N_{1\text{km}}$ and N_s in the 1 km layer exceeds 0.85 for all the models, whereas it is found to be weak in case of 65 m and 100 m layers.

The dry and wet components, N_{h_D} and N_{h_W}, can also be calculated from the corresponding components of N_s using the ITU exponential model and then $N_{h\_(\text{D+W})}$ is computed by summing both terms. Table 7-4 provides a comparison between the obtained correlation and RMSE results of the net, dry and wet components of N_h at the 65 m, $N_{0.065\text{km}}$, and 100 m, $N_{0.1\text{km}}$, layers. The correlation is calculated between the predicted values and the

available radiosonde measurements of each component. The data of these two layers are also combined, $N_{0.065\&0.1km}$, to form a consolidated set of data for the atmospheric layers below 100 m altitude from the ground. Different values of the height coefficient, h_o, are obtained during the calculation of each component, which provides the minimum RMSE value in each particular scenario. The value of h_o varies from 0.8 to 10 km, where the wet component takes smaller h_o value than the dry one.

It has been noted that the correlation and RMSE values of the four parameters, N_h, N_{h_D}, N_{h_W} and $N_{h\_(D+W)}$, are compared for each of the three data sets at 65 m, 100 m and their combination. For all scenario, the results of $N_{h\_(D+W)}$ are found to be better than the results of N_h obtained directly from the ITU exponential model, while the correlation between the predicted and measured N_h data are almost the same.

Table 7-4: Comparison of correlation and RMSE of N_h at 65 m and 100 m with different h_o values

N_h Component	h_o Value km	Correlation	RMSE
$N_{0.065km\_D}$	10	0.97	2.071
$N_{0.065km\_W}$	0.8	0.92	12.289
$N_{0.065km\_(D+W)}$	-	0.91	12.389
$N_{0.065km}$	2.8	0.91	12.586
$N_{0.1km\_D}$	9.1	0.96	2.486
$N_{0.1km\_W}$	0.9	0.89	14.317
$N_{0.1km\_(D+W)}$	-	0.87	14.869
$N_{0.1km}$	3	0.87	15.178
$N_{0.065\&0.1km\_D}$	9.3	0.96	2.290
$N_{0.065\&0.1km\_W}$	0.9	0.91	13.344
$N_{0.065\&0.1km\_(D+W)}$	-	0.89	13.685
$N_{0.065\&0.1km}$	2.3	0.88	15.649

7.4 Final Remarks

17 years of local radiosonde data from UAE were analysed to obtain the vertical refractivity profile for three critical atmospheric layers within the first kilometre above the ground. The correlation between N_s and either N_h or ΔN was found to depend predominantly on the wet components of these parameters.

For estimating ΔN at the three atmospheric layers, it was observed that the linear model resulted in somewhat lower RMSE values than the exponential one.

Based on the reduced RMSE, it is recommended to use the indirect approach to estimate N_h and ΔN from the analysis of dry and wet refractivity components, in particular at the 1 km layer. Marginal improvement was achieved for the 65 m and 100 m layers when N_h was predicted using the exponential model based on the indirect approach. Such multi-steps analysis may lead to slightly lower correlation, when compared with the measured data, than using the direct relations.

Although the use of more than one model to predict the refractivity at different atmospheric layers may introduce some discontinuities in its vertical profile, the RMSE values of the predicted N_h or ΔN were found to be reduced while the correlation between the measured and predicted values was marginally improved for certain parameters.

Third- and fourth-order polynomial models showed marginal improvements in terms of RMSE and correlation values for the prediction of N_h and ΔN parameters over the other models. However, it was noted that the results were very sensitive to the precision of the high order coefficients.

The variations of height coefficient in the ITU exponential models were evaluated considering the analysis of dry, wet and net components of N_h and ΔN at 1 km, 100 m and 65 m layers. The optimum values of the height coefficient parameter, h_o, were investigated and found to vary significantly for different components and atmospheric layers.

In chapter 8, new methodologies for predicting the vertical refractivity profile and relevant propagation parameters will be discussed using the same high resolution long-term data set.

Chapter 8

NEW METHODOLOGIES FOR PREDICTING REFRACTIVITY AND RELEVANT PROPAGATION PARAMETERS

8.1 Introduction

In this chapter, a new simplified approach is proposed to evaluate the vertical refractivity profile within the lowest 1 km of atmosphere from the analysis of surface refractivity, N_s, at areas where upper-air data are not available. Although radiosonde is commonly used for upper-air measurements, it should be noticed that the data accuracy is affected by sensors' uncertainties that can reach up to 0.5^0c, 5 % and 1 hPa for temperature, humidity and pressure parameters, respectively. Upper-air measurements from a surrounding radiosonde location with similar surface profile to these sites are utilized. The profiles of N_s and refractivity extrapolated to sea level, N_o, obtained from surface meteorological data using both fixed stations and radiosonde are investigated and compared. Vertical refractivity gradient, ΔN, is evaluated at the three atmospheric layers within the first kilometre above the ground in addition to propagation parameters relevant to each atmospheric layer. Different approaches are used at six sites for the analysis of three important parameters;

namely effective earth radius factor, k, anomalous propagation probability parameter, β_0, and point refractivity gradient at 65 m not exceeded for 1% of time, dN_1. The k-factor parameter is investigated using a new weighted average approach of ΔN at 65 m, 100 m and 1 km layers above the ground. The obtained results are compared with the latest ITU maps and tables for the same area.

Cumulative distributions in addition to the hourly, monthly and yearly variations are presented. The predicted results using the new models are compared with the values obtained from other available relationships in the literature. The correlation between predicted and actual available data for each parameter and the root mean square errors, RMSE, are compared as well.

8.1.1 Site Locations and Meteorological Data

Seventeen years of surface and radiosonde meteorological data from January 1st, 1997 to December 31st, 2013, have been used for the analysis. In certain periods, only one ascent was available per day, which mostly referred to 00:00 UT. The UAE is likely to experience abnormal propagation conditions such as ducting phenomenon. The climate is usually hot and humid over the course of the year. AIN site has lower humidity, while FUJ has a special climate nearby the tropical zone [5]. The geographical locations of the six sites are shown in UAE map in Figure 4.1.

The sites' coordinates and altitudes above the sea level are provided in Table 4-1. All the sites have similar height around 30 m above sea level, except AIN, which is located in a mountainous area.

Radiosonde data are available for 9462 radiosonde ascents. Due to low quality or incomplete ascents, data for June 1998, April 2000, November 2005, June 2006 to November 2006 and January 2010 to May 2010 are not available. From December 2006 to December 2008, the data of only one ascent, mostly at 00:00 UT, is available on daily basis. In addition, a small number of abnormal values have been excluded owing to faulty readings from the instrument, based on predefined ranges for the values of the parameters.

8.1.2 Models of Refractivity

The refractivity, N, in N-units consists of dry and wet components and can be evaluated at either the ground or higher altitudes using the expression (2.12) [11, 12].

In areas where radiosonde upper-air data are not available, several relationships can be used to predict N_h for the lowest part of troposphere at a certain altitude, h, from the surface refractivity, N_s, obtained from the commonly available surface meteorological measurements [11, 83]. The following ITU exponential model can be used to calculate N_h from the available surface data [11] using equation (7.2), where h_s is the surface altitude

from sea level and h_o is the height coefficient with respect to the sea level in km. Two values of h_o are used by ITU to evaluate the height profile of refractivity from the values extrapolated to sea level, N_o. The h_o value of 9.5 km was used to develop N_o maps by ITU, and 7.35 km is the global mean height profile recommended by ITU to be used for reference purpose where local reliable data are not available [12]. The N_o parameter can be estimated from N_s as follows:

$$N_o = N_s . \mathrm{e}^{\left[\frac{h_s}{h_o}\right]} \qquad (\mathrm{N-units}) \tag{8.1}$$

The vertical ΔN usually has a negative value causing the rays to bend towards the ground. In the linear model, ΔN can be obtained from two refractivity values, N_s at the surface, h_s, and N_h at an altitude h, by dividing the refractivity difference (N_s - N_h) over (h_s - h) [3, 11].

A close correlation is observed between N_s and N_h within the first 100 m of atmosphere and between N_s and ΔN at 1 km layer above ground. ΔN can be estimated from N_s using the following exponential decaying relationship for the first kilometre, ΔN:

$$\Delta N = a \,.\, (1 - e^{-b \,\cdot\, N_s})^c \qquad (\mathrm{N/km}) \tag{8.2}$$

where the values of coefficients a, b, and c are found to be -316.54734, 0.00958 and 37.85049, respectively. It is noted that these coefficients may vary from one place to another and for different study periods within the same location. Long-term data are required to provide accurate estimations. Other models are studied to also predict the vertical ΔN near the ground from the measurements of electromagnetic wave strength and diffraction losses [25, 84]. In order to extend these relations to other regions around the world, the correlation between the estimated data and the measured values needs to be evaluated.

8.1.3 Important Propagation Parameters

For microwave link design, some parameters must be set carefully as input data to optimize the link performance. Two of these parameters are quite important, the effective earth radius factor, k, which is commonly set as a standard value of 4/3, and point refractivity gradient not exceeded for 1% of time, $dN_{1\%}$, at 65 m layer of atmosphere [13]. Estimated values of anomalous propagation probability parameter, β_0 and $dN_{1\%}$ are provided by ITU tables for different geographical locations whenever reliable local data are not available [12].

8.1.3.1 Effective earth radius factor, *k,* and Anomalous propagation probability parameter, β_0

The *k*-factor is usually derived from the vertical ΔN in the first kilometre above the ground, ΔN_1, assuming that gradient of refraction index is constant with height, at least over the lower atmospheric layer up to 1 km, [24] and can be calculated from equation (2.35) [13]. Alternatively, a new weighted average approach of ΔN values at the three atmospheric layers of 1 km and below is used in this work to accurately evaluate *k*-factor considering the vertical variations of refractive index near the ground below 100 m, where most of the terrestrial wireless systems operate. The refractive conditions are related to the values of *k*-factor. The β_0 parameter represents occurrence probability of non-standard propagation and its statistics are derived from the cumulative distributions of the vertical ΔN at the first 100 m layer. β_0 is obtained from the percentage of time in which ΔN value is less than or equal to -100 N/km.

8.1.3.2 Point refractivity gradient, $dN_{1\%}$

$dN_{1\%}$ is the point ΔN value at the lowest 65 m of the atmosphere not exceeded for 1% of an average year [13, 85]. The accurate statistics of this parameter is essential for the prediction of PTP microwave links' availability.

8.1.4 New Methodology for Vertical ΔN Prediction

New approaches are used to simplify and improve the accuracy of vertical ΔN evaluation in areas where upper-air data are not available. In approach 1, only measured refractivity parameters at the surface and higher altitudes are utilized to estimate ΔN. The surface refractivity profiles for a number of sites are compared. For sites with similar surface conditions to a surrounding site with available radiosonde measurements, upper-air refractivity obtained from radiosonde can be utilized to estimate the vertical profile in the surrounding sites, where only surface data are available. This is based on the assumptions that most of the land and sea interactions occur at ground level, while the atmosphere gets more homogenous at higher altitudes and the vertical N_h is assumed to be more stable. Although poor correlation has been observed between N_s and ΔN at 65 m and 100 m layers compared with better correlation at 1 km, this new approach aims at improving the accuracy of estimated N_h values at these altitudes by using real radiosonde measurements in case of similar surface profiles. Consequently, the results of ΔN at these layers are expected to be improved as well, when the linear ΔN model is used. The sites can also be selected such that they are located within few hundred miles from a radiosonde location that have similar surface weather conditions. In this approach, the vertical profile at all sites are evaluated as follow:

a) The measured surface and upper-air data are obtained from radiosonde, which is available at the AUH site only. The measured ΔN at a particular altitude, h, is calculated using the linear model.

b) N_s is calculated from surface data measured using fixed surface stations at AUH and surrounding sites. The N_h parameter is obtained from radiosonde measurements available at the AUH site only. At 65 m and 100 m, N_h is utilized at the sites with similar surface refractivity profiles to AUH. At 1 km layer, N_h is applied for all six sites since the atmosphere get much more homogeneous at this high altitude. ΔN is then calculated from measured N_s and N_h using the linear model. Note that for the AUH site only, measured ΔN obtained using methods (a) and (b) are compared, in order to evaluate the radiosonde data accuracy. The flow diagram of this new approach is shown in Figure 8.1.

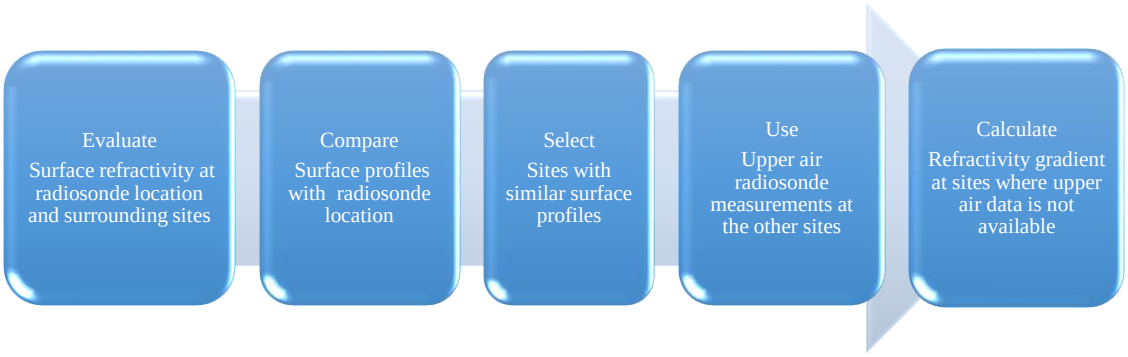

Figure 8.1: Flow diagram of Approach 1-(b)

In the second approach 2, ΔN is obtained from measured N_s at the surface and predicted N_h at higher altitudes. Empirical relationships are derived from radiosonde measurements at a single site. These models are used to predict the vertical refractivity profiles at the surrounding sites where only surface data are available. In this approach, ΔN is estimated from measured N_s and predicted N_h subject to the correlation observed between N_s and either N_h or ΔN at different altitudes as follows:

a) N_h is predicted using exponential model, e.g. equation (7.2), from measured N_s. Predicted ΔN is then calculated using the linear model. At 65 m and 100 m layers, it has been observed that N_s is correlated with N_h.

b) Predicted ΔN is directly estimated from measured N_s using the exponential model of equation (8.2). At 1 km layer, N_s is found to be correlated with ΔN.

The relationships between N_s and either N_h or ΔN for predicting the vertical refractivity profiles are investigated in comparison with the new approaches introduced in this study. The results of the new approaches and predicted N_h and ΔN are compared at certain sites to confirm the earlier correlation findings at different layers. To the best of our knowledge, the proposed approach to estimate the vertical refractivity profile based on analysis of the similarities in surface profiles, in addition to the use of weighted average approach to

evaluate the *k*-factor from mean and median of ΔN at different atmospheric layers, has not been investigated before.

8.2 Analysis and Results

ΔN statistics for the first three atmospheric layers above the ground, 65 m, 100 m and 1 km, where terrestrial communication systems operate, are important to be investigated due to their contributions to several propagation studies. For example; the first two layers, 65 m and 100 m, are essential for estimating the point refractivity gradient not exceeded for 1% of time, which is required for availability calculations for terrestrial microwave links [85], and the occurrence probability of ducting and multipath conditions [12, 13]. It is noticed that the extreme atmospheric stratification tends to occur in layers less than 100 m thickness, which can be extended horizontally over long distance at certain times. The 1 km layer analysis is important for the estimation of the effective Earth radius factor [13, 85]. These parameters have to be carefully considered when studying the performance of terrestrial line of sight communication systems.

8.2.1 Surface Refractivity Analysis

The analysis of surface refractivity, N_s, and its dry and wet components, N_{s_D} and N_{s_W}, in addition to the N_o analysis are based on the surface SYNOPS meteorological data measured

by the available fixed surface weather stations at all sites. The mean monthly distributions of N_s and its dry and wet components, N_{s_D} and N_{s_W}, respectively, over the whole period are shown in Figure 8.2, Figure 8.3 and Figure 8.4 for the six sites. In Figure 8.2, the dry refractivity component at all sites follows the same variation curve with almost the similar values. The monthly variations of N_{s_D} and N_{s_W} fluctuate from 250 to 272 with a span of 22 units. The monthly variation curves of N_s are dominated by the wet component, N_{s_W}, as clearly shown in Figure 8.3 and Figure 8.4. This variation is compensated by the inversely varying dry refractivity term, N_{s_D}. Figure 8.4 shows that N_s profiles in four sites; namely AUH, DXB, SHJ and RAK, are similar with peak values shown in summer season. The monthly means of N_s vary within a range of around 82 units at all sites where a maximum monthly difference of 62 units between the six sites is observed in August. The highest monthly values and variation of N_s are observed at FUJ site with a span of 61.6 units, from 333.5 up to 395.1 N-units. This can be attributed to its location as a coastal city nearby Oman Gulf within a mountainous area, with a humid climate. AIN site has lower N_s values and monthly variations than the other sites with a span of 21 units, from 313.2 up to 334.5 N-units. This trend is due to its location as an inland city at a distance of about 100 km away from the sea with dry and low humidity weather. Similar initial results were reported for the area under study [5].

For easy reference, the ITU provides global maps of the median value (50%) of N_{s_W} exceeded for the average year [12]. Table 8-1 provides the values of calculated N_{s_W} at the six sites in comparison with the ITU map for United Arab Emirates. In general, it has been

observed that ITU values underestimates N_{s_W} in the area under study, where the long-term median calculated values exceed 60 N-units for all sites.

Table 8-1: Comparison of calculated N_{s_W} exceeded for 50% of the year with ITU Map [12]

	N_{s_W} [N-units]
ITU values	60-75
AUH	81.2
DXB	81.7
SHJ	78.3
RAK	82.5
AIN	63.1
FUJ	93

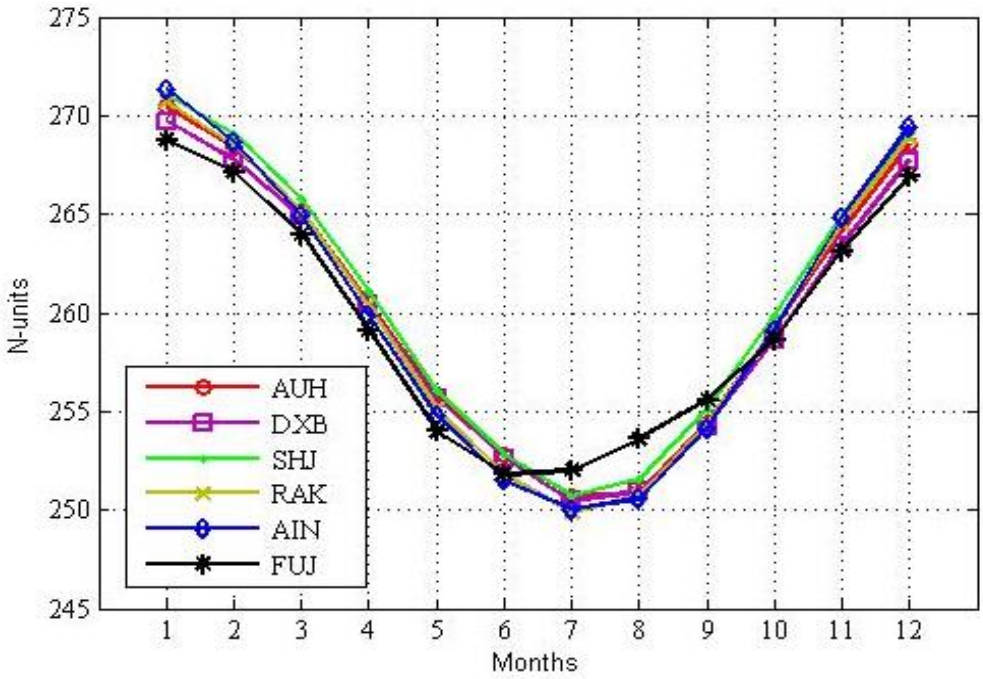

Figure 8.2: Mean monthly variations of dry component of surface refractivity, *N* (1997-2013)

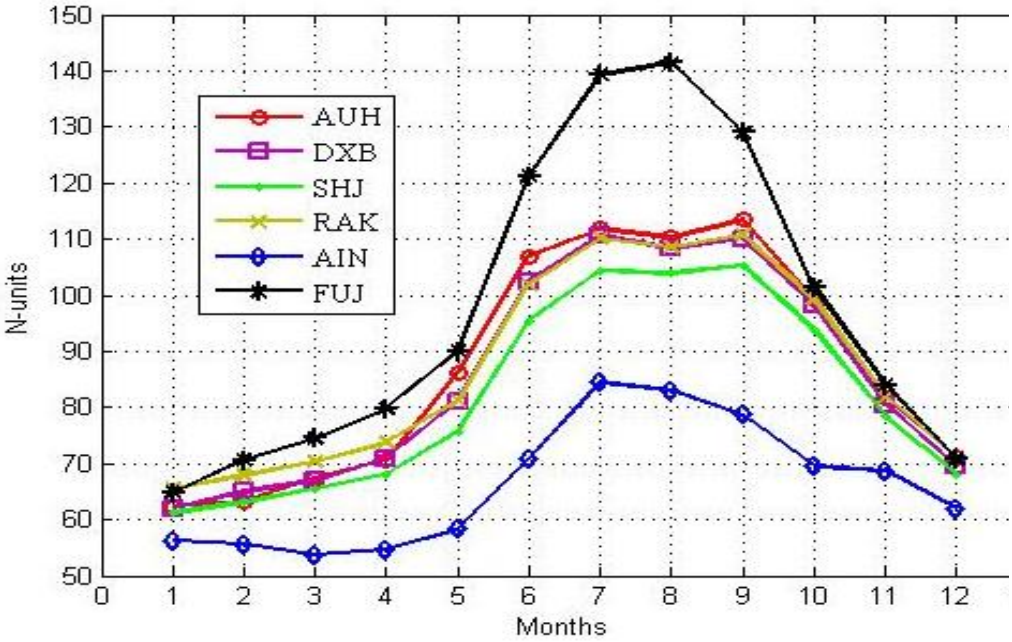

Figure 8.3: Mean monthly variations of wet component of N_s (1997-2013)

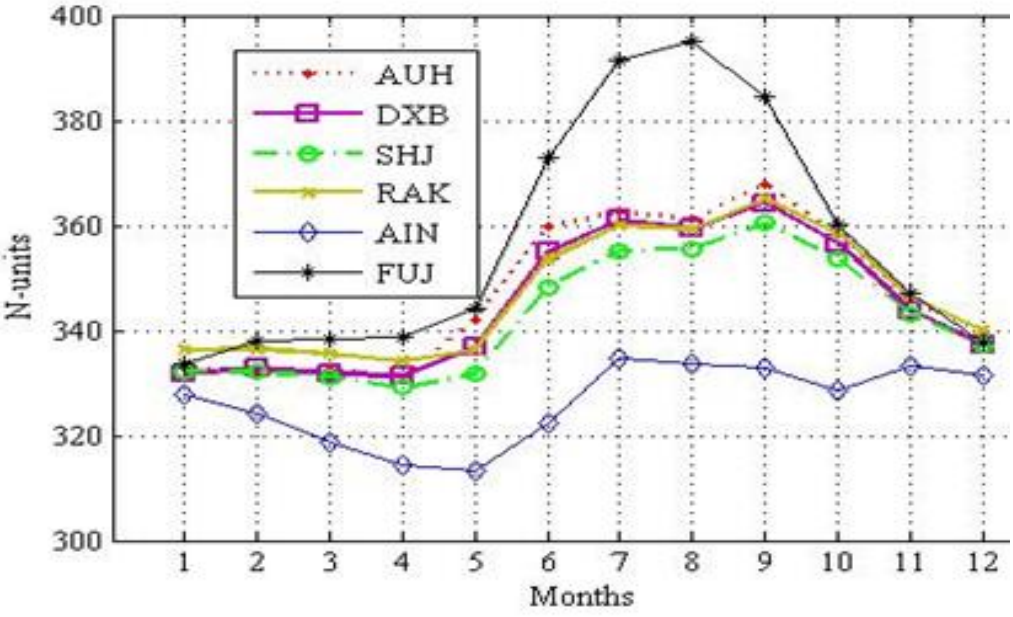

Figure 8.4: Mean monthly variations of surface refractivity, N (1997-2013)

The mean monthly N_o variations in the six sites are also compared with ITU maps [12] in Table 8-2. The ITU maps are derived using h_o = 9.5 km for the months of February and

August. N_o has been calculated using two values, 9.5 km and 7.35 km, of h_o parameter. For reference purpose, the ITU has also proposed an average global profile based on N_o and h_o values of 315 N-units and 7.35 km [12]. It has been noted that h_o value varies slightly across particular atmospheric layers which have marginal impact on the refractivity predictions.

The results for February are more consistent with the ITU values than August, except at certain sites such as AIN in case of February and FUJ in case of August. In August, the results at AUH, DXB, SHJ, and RAK are up to 14.2% less than ITU. AIN shows exceptional differences of 24.8 units and 55.4 units less than the ITU values for February and August, respectively. This can be attributed to the inland location with dry climate of the AIN site.

Figure 8.5 shows the average yearly variations of N_s at all sites over the whole period of seventeen years from 1997 to 2013, which are presented by numbers from 1 to 17 for simplicity. The yearly curves for AUH, DXB, SHJ and RAK follow a similar trend and the annual means are bounded within 12 units for most years. The year to year variation at these four sites is generally smooth with some peak values in 1998 at Abu Dhabi and 2003 at FUJ. AIN has the lowest values and the most significant variation within a range of around 23 units, from 313 up to 336 N-units. The highest N_s values are generally shown at FUJ, except in 1998.

The cumulative distributions of N_s at the six sites are given in Figure 8.6 over the whole period. The values vary from around 252 up to 601 N-units with a span of 349 units. N_s oscillates in an interval of 52 units from one site to another. The lowest and highest values for all time percentages are almost shown at AIN and FUJ, respectively, with some exceptional cases such as at AUH where values exceed 460 units for around 0.5% of the total time. This exceptional value at AUH can be attributed to the peak values observed in 1998.

Table 8-2: Comparison of calculated N_O with ITU maps [12]

	Coefficient h_o	February N_o	August N_o
ITU Maps	9.5	350	390
AUH	9.5	332.6	362.1
	7.35	332.9	362.4
DXB	9.5	333.8	360.3
	7.35	334.1	360.6
SHJ	9.5	333.1	356.5
	7.35	333.3	356.8
RAK	9.5	337.4	360.3
	7.35	337.7	360.6
AIN	9.5	325.2	334. 6
	7.35	325.5	334.9
FUJ	9.5	338.8	396.2
	7.35	339.1	396.6

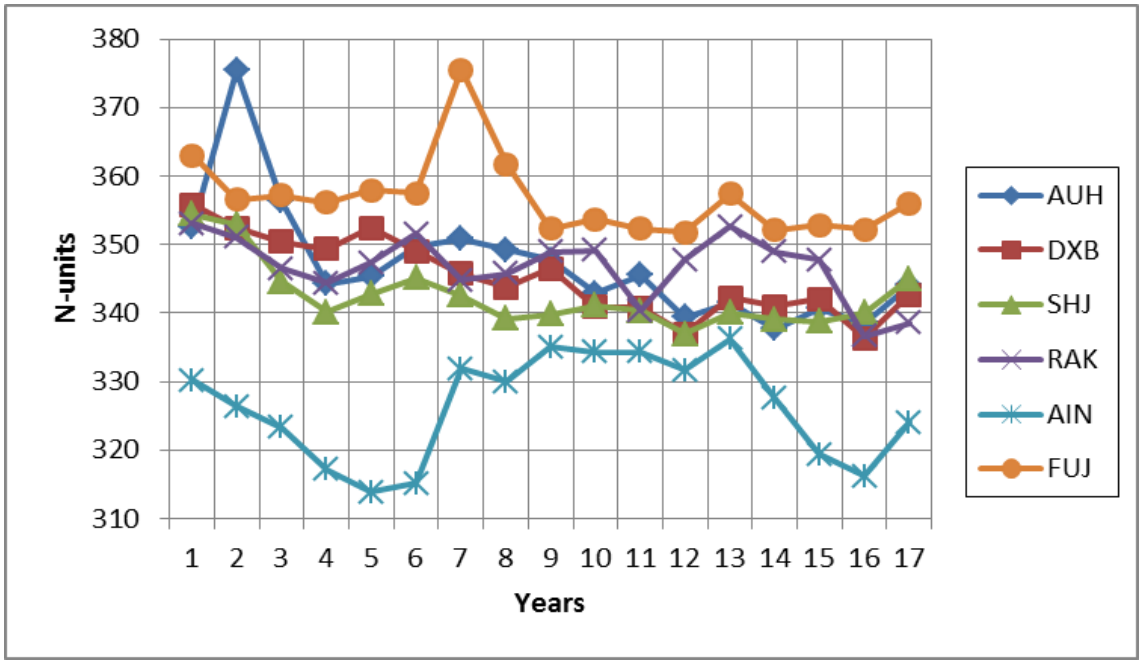

Figure 8.5: Mean yearly variations of surface refractivity, *N* (1997-2013)

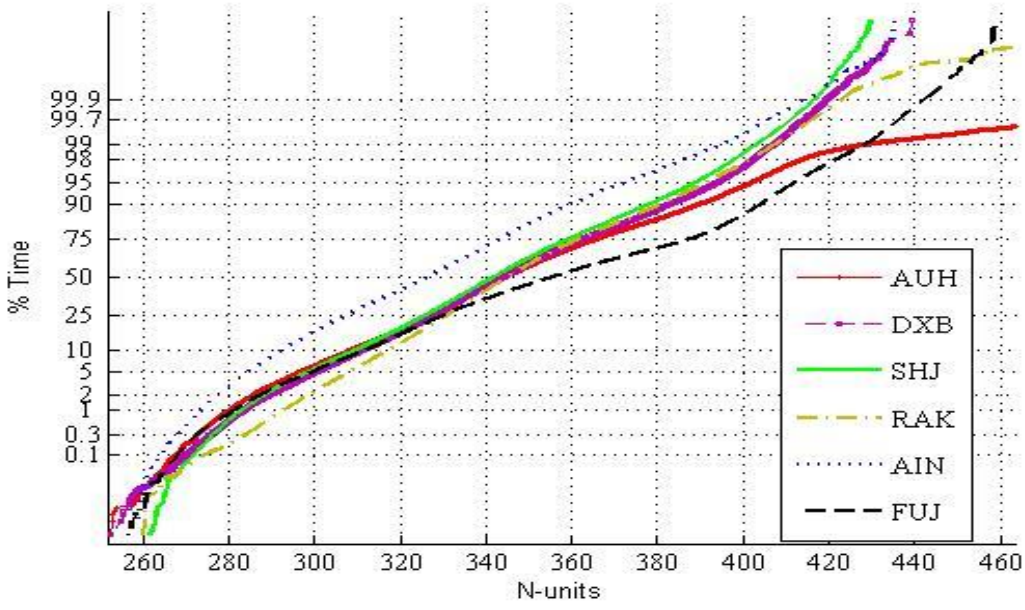

Figure 8.6: Cumulative distributions of surface refractivity, *N* (1997-2013)

The results obtained from the monthly, yearly and cumulative distributions show that the surface refractivity profile at four sites; namely AUH, DXB, SHJ and RAK, are similar. Accordingly, the vertical refractivity profiles at these sites are expected to be more consistent since the atmosphere is assumed to get more horizontally homogenous with height.

8.2.2 Comparison of Surface Measurements

The surface meteorological data can be measured using either surface weather stations or radiosonde at the ground. The radiosonde measurements at AUH site have been compared with the surface meteorological measurements using AUH surface weather station at only two times daily due to the radiosonde data availability. This is an indication for the radiosonde data accuracy compared with the stable fixed weather sensors at the ground. The monthly and cumulative distributions of measured N_s using both data types are shown in Figure 8.7 and Figure 8.8. Figure 8.7 shows that the monthly means of N_s measured from the surface station are larger than the values obtained from the radiosonde at all months, with a maximum difference of 8.5 units. The N_s values measured by the radiosonde are also found to be lower for all time percentages as shown in Figure 8.8. It has been found that the N_s value oscillates between 329.5 and 368.3 N-units for the surface station with a span of 38.8 units, whereas they vary from 325.5 to 359.8 N-units for the radiosonde.

Figure 8.9, Figure 8.10, Figure 8.11 and Figure 8.12 provide cumulative distributions of four surface meteorological parameters; namely atmospheric pressure, dry air temperature, relative humidity and water vapour pressure, measured by fixed surface station and radiosonde at AUH site. It is observed that the parameters measured by surface station has higher values for most time percentages, except for dry air temperature where radiosonde measurements are higher. This is the reason for obtaining higher N_s values for surface station at all-time percentages since the refractivity is directly proportional with pressure and vapour pressure while it is inversely proportional to the dry temperature.

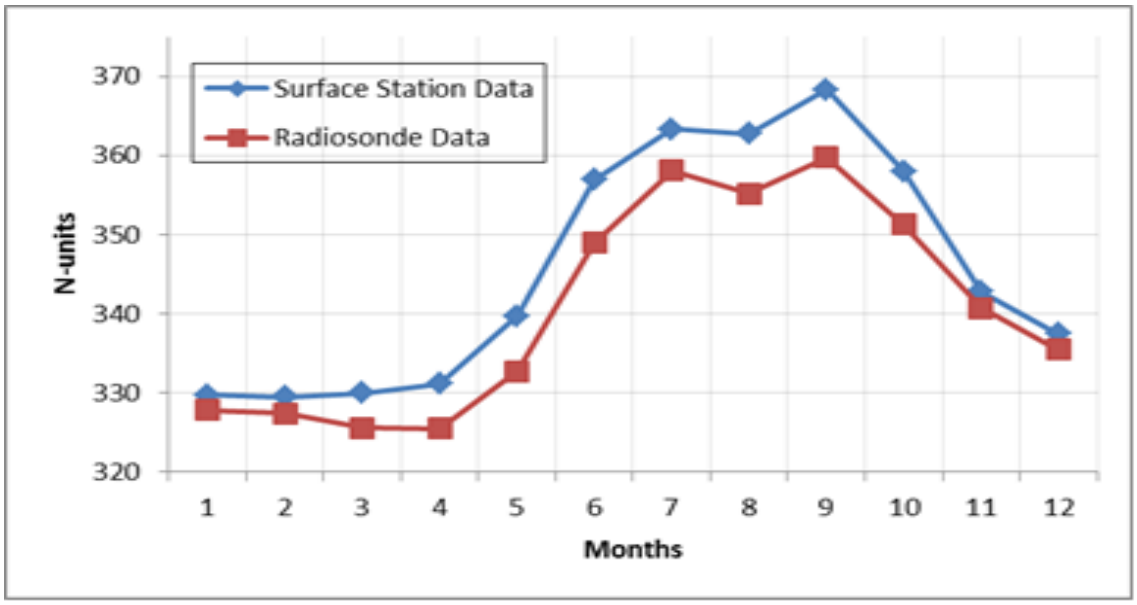

Figure 8.7: Cumulative distributions of surface refractivity calculated from fixed surface weather station and Radiosonde (1997-2013)

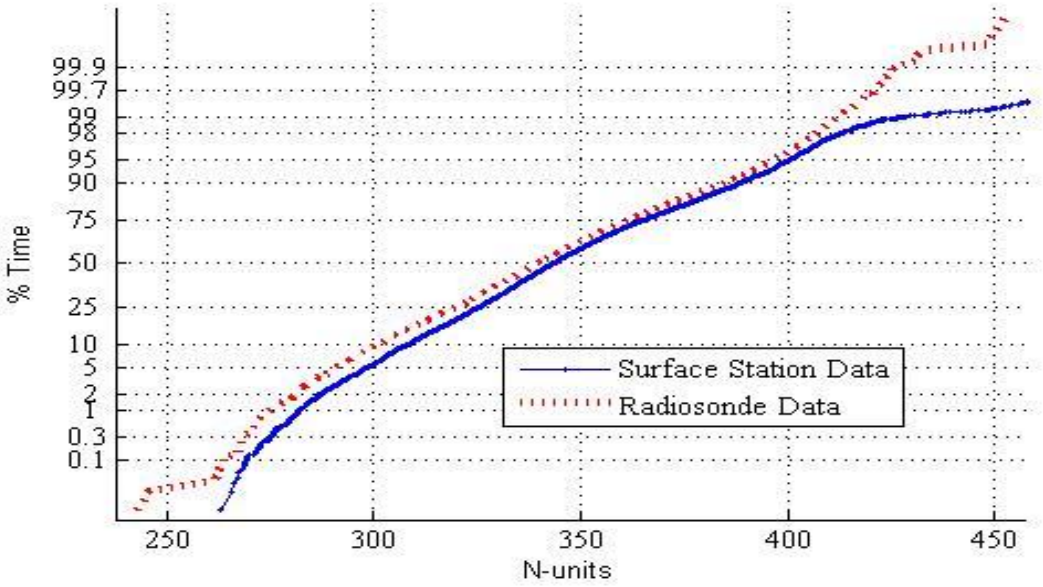

Figure 8.8: Cumulative distributions of surface refractivity calculated from fixed surface weather station and Radiosonde (1997-2013)

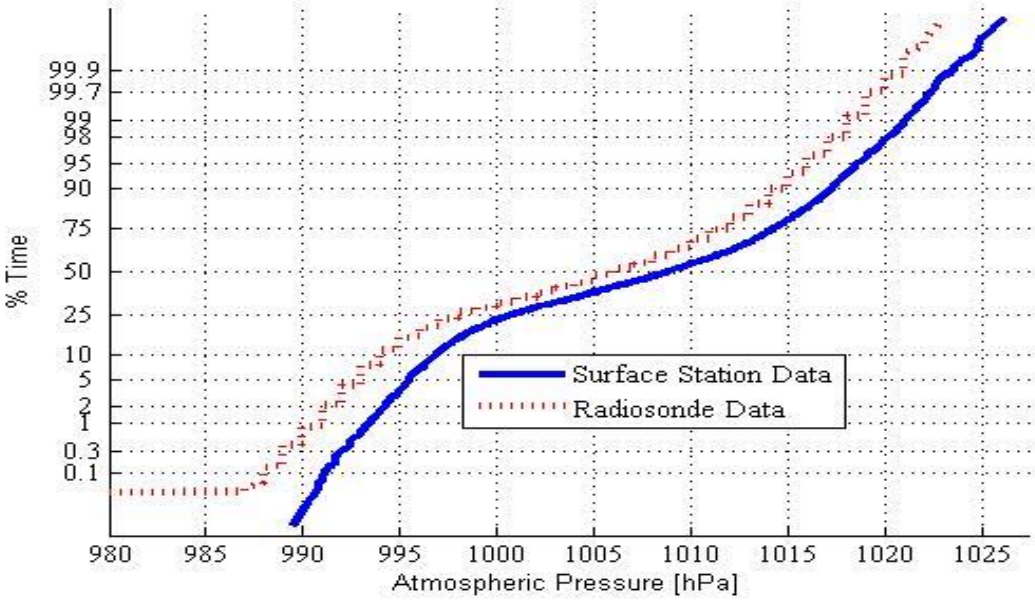

Figure 8.9: Cumulative distributions of surface Atmospheric Pressure at AUH

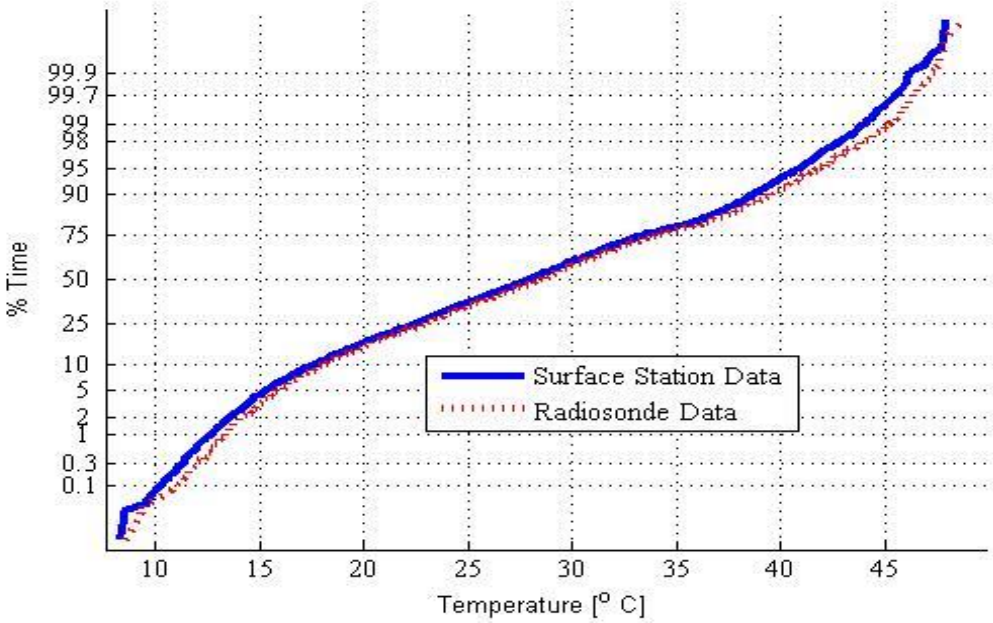

Figure 8.10: Cumulative distributions of surface dry air temperature at AUH

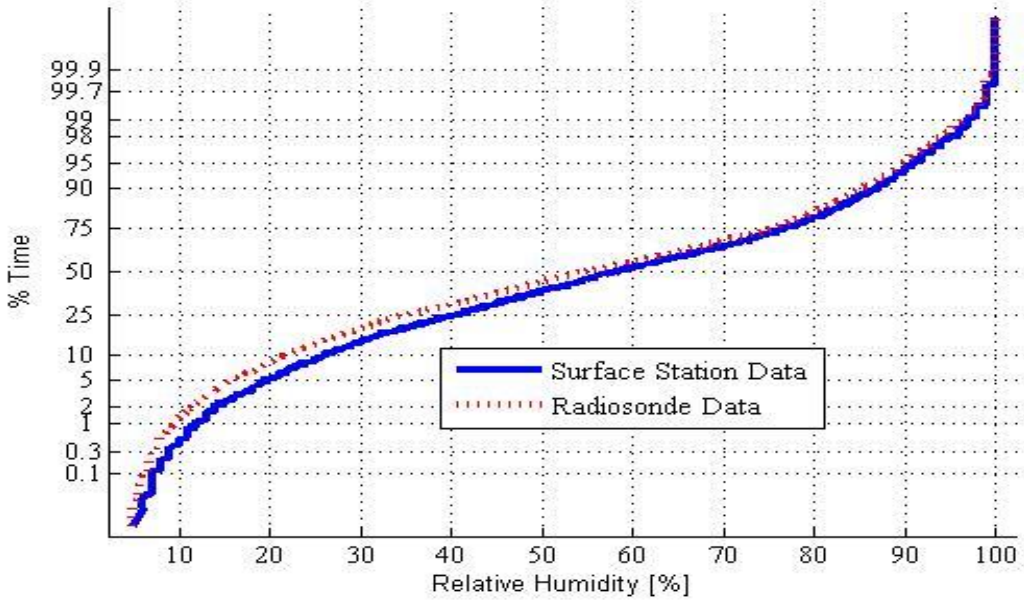

Figure 8.11: Cumulative distributions of surface relative humidity at AUH

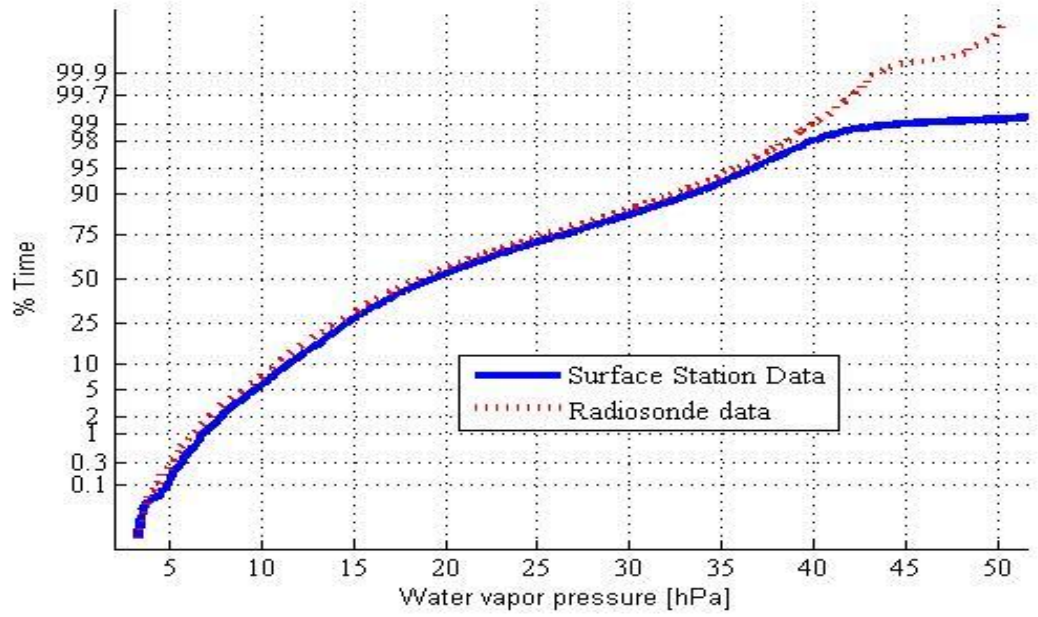

Figure 8.12: Cumulative distributions of surface water vapour pressure at AUH (1997-2013)

8.2.3 Refractivity Gradient Analysis

The ΔN parameter has been evaluated using different approaches. For the sites with similar surface refractivity profile to AUH, the same radiosonde data are utilized for upper layers. The measurement accuracy of surface weather stations is assumed to be higher than the radiosonde at the ground level. Consequently, the reference ΔN profile at the AUH site is calculated using approach 1-(b) from both the surface measurements at the ground and radiosonde measurements at higher altitudes. Figure 8.13, Figure 8.14 and Figure 8.15 provide comparisons of mean monthly variations of ΔN at 65 m ($\Delta N_{0.065}$), 100 m ($\Delta N_{0.1}$) and 1 km (ΔN_1) layers, using different approaches at the AUH site. The curves of ΔN_1

obtained from 1-(a) and 1-(b) approaches are more consistent with a maximum monthly difference of 8 units. The differences between ΔN values obtained using 1-(a) and 1-(b) approaches increase considerably up to 74 and 55 units at the 65 m and 100 m layers, respectively. The higher differences at the low altitudes can be attributed to the fact that any small change in N_s value results in large disagreement in ΔN due to the low decimal number in the denominator of the linear ΔN equation.

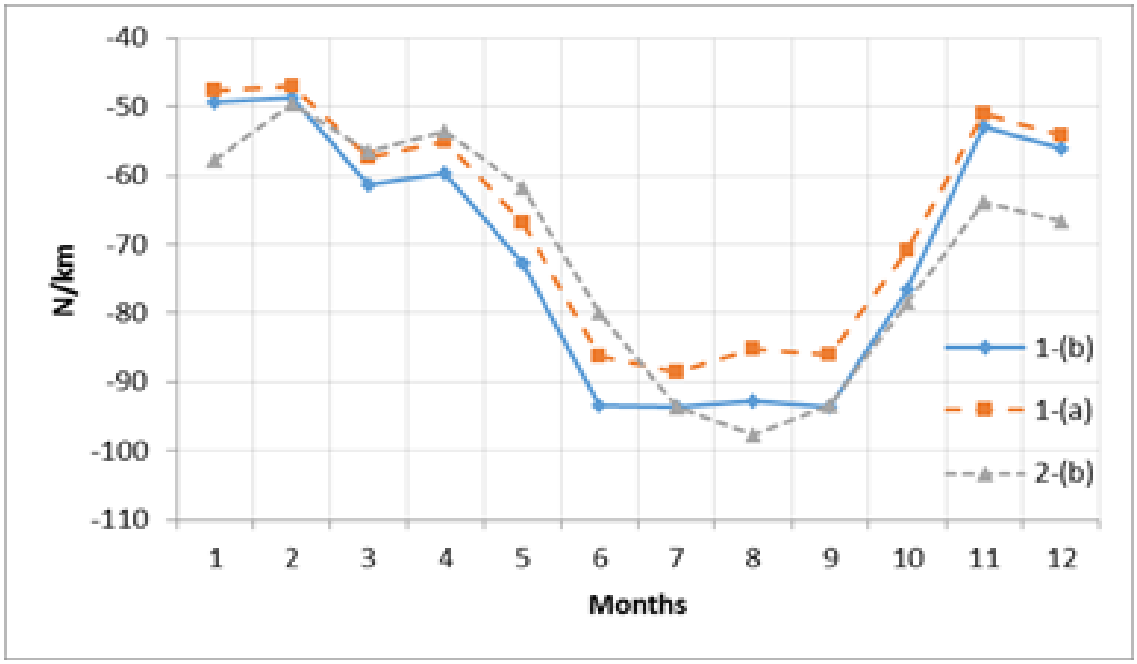

Figure 8.13: Comparison of mean monthly variations of ΔN at 1 km at AUH

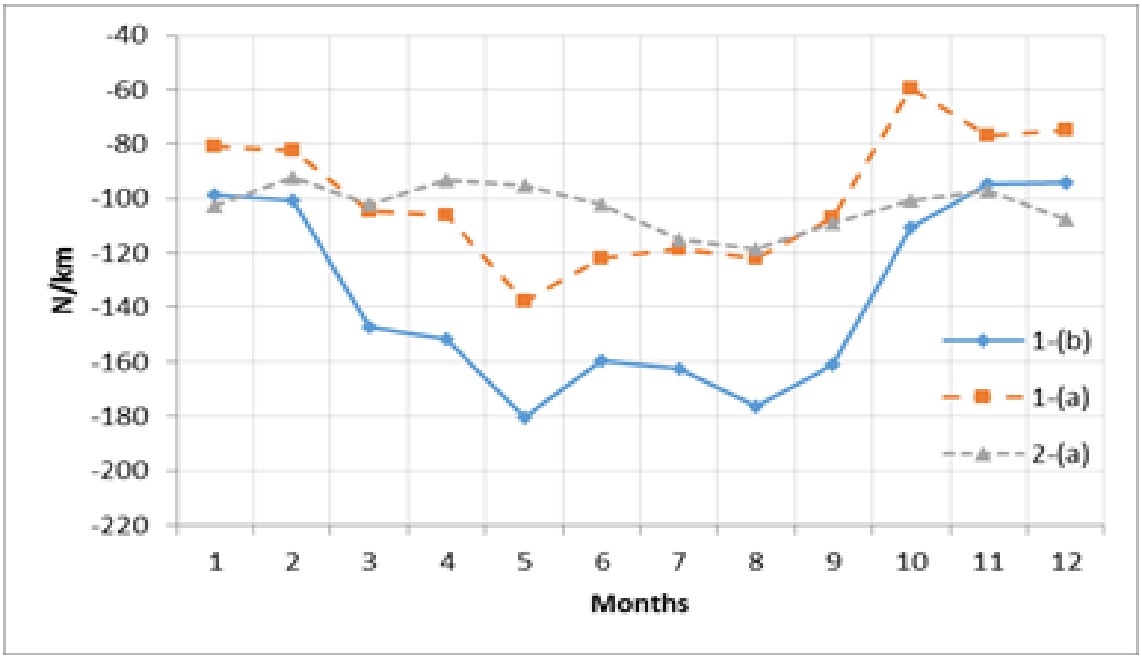

Figure 8.14: Comparison of mean monthly variations of Δ*N* at 100 m at AUH

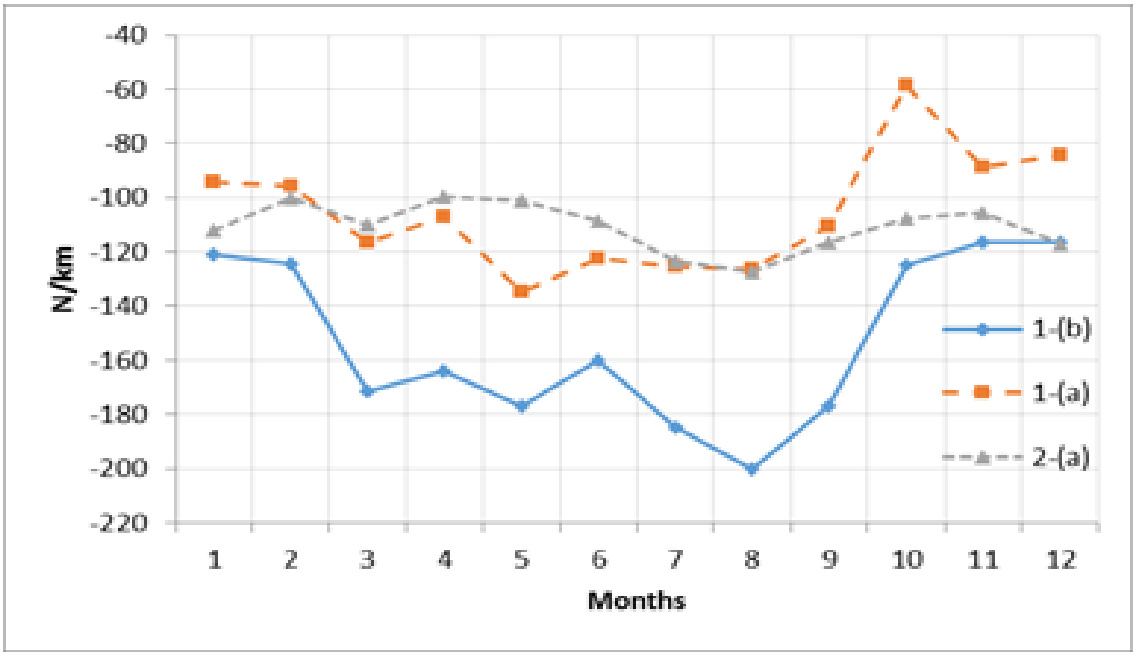

Figure 8.15: Comparison of mean monthly variations of Δ*N* at 65 m at AUH

The root mean square error, RMSE, and correlation coefficients are evaluated at the AUH site between the measured or predicted ΔN values using approaches 1-(a), 2-(a) and 2-(b) with reference to the measured ΔN using 1-(b) approach. Table 8-3 summarizes the obtained results. The correlation between ΔN and N_s at low altitudes, 65 m and 100 m, is found to be poor while good correlation is observed at 1 km height. A good correlation has also been observed at the 1 km layer between ΔN results obtained using approaches 1-(a), 2-(a) and 2-(b) with respect to the reference approach of 1-(b). At 1 km height, 2-(b) approach gives the highest correlation coefficient and minimum RMSE value noting that good correlation has been observed between ΔN and N_s, while 2-(a) gives the highest RMSE result. At 65 m and 100 m layers, 2-(a) approach shows marginal improvement compared to 2-(b), although poor correlation has been found between ΔN and N_s at these low altitudes.

Table 8-3: Correlation and RMSE Values of ΔN Results with Reference to Radiosonde data

Layer	Approach / Model	Correlation	RMSE
1 km	1-(a)	0.857	20.4
	2-(a)	0.859	35.2
	2-(b)	0.86	18.8
100 m	1-(a)	0.49	200.7
	2-(a)	0.41	216.8
	2-(b)	0.4	219.8
65 m	1-(a)	0.38	322.8
	2-(a)	0.4	337.9
	2-(b)	0.39	337.9

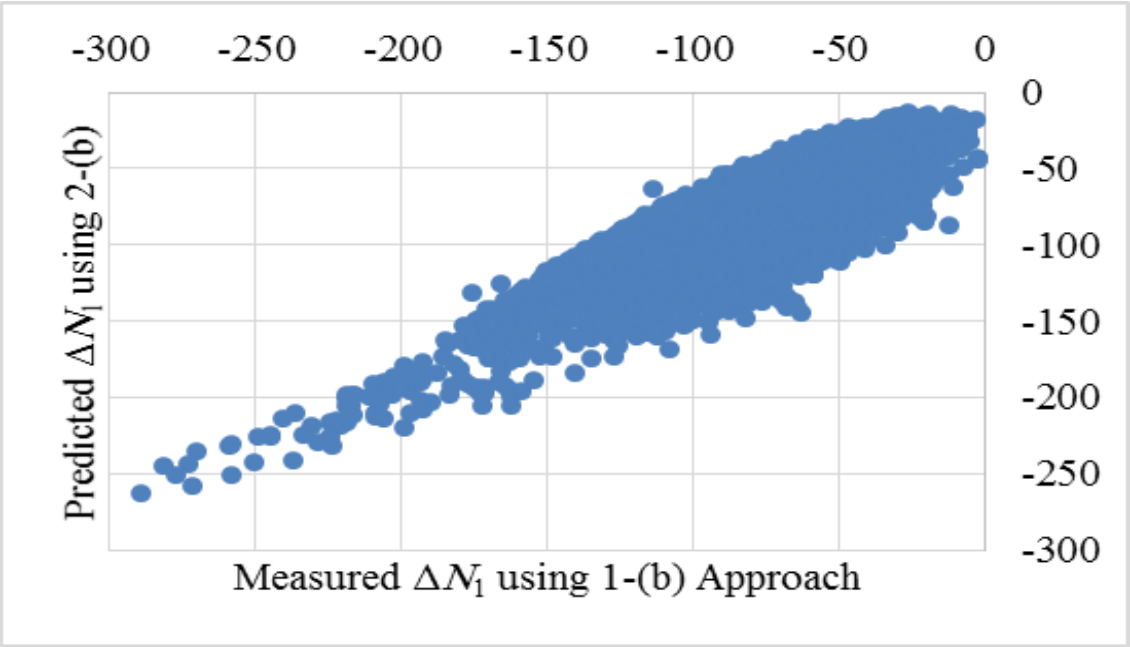

Figure 8.16: Scatter diagram for ΔN at 1 km at AUH, obtained using 1-(b) and 2-(b) approaches

Figure 8.16 shows the scatter diagram for the ΔN_1 values obtained using 1-(b) and 2-(b) approaches. The coefficient of determination is found to be 0.86, which means that significant correlation exists with minimum error. Figure 8.17 shows the mean monthly variations of ΔN_1 calculated using the 1-(b) approach for all six sites. The monthly ΔN values oscillate approximately between 125.5 and -48.8 N/km with a span of 76 units. In Figure 8.18, the mean monthly distributions of ΔN_1 obtained from the 2-(b) approach are provided. The ΔN_1 values range from -134 to -36.7 N/km with a span of 97.3 units. The curves of ΔN_1 are found to be similar to N_s at AUH, DXB, SHJ and RAK sites, where refractivity profiles are almost consistent with peak values shown in the summer. As shown

in Figure 8.17 and Figure 8.18, the ranges of monthly variations at these four sites are found to be around 49 units, from -97.7 to -48.8 N/km, and 51.9 units, from -101.5 to -49.6, for the approaches 1-(b) and 2-(b), respectively. The highest monthly variations of ΔN_1 has also been observed in the FUJ site within a span of 73.4 units, from -125.5 to -52 N/km, and an interval of 78.5 unites, from -134 to -55.4 N/km, using approaches 1-(b) and 2-(b), respectively. This can also be attributed to its special location and climate.

The lowest absolute ΔN_1 values are given during winter time with some exceptional cases such as May for AIN site in Figure 8.18 when the 2-(b) approach is used. On the other hand, the summer season shows the highest absolute ΔN_1 values at all sites, in particular for the months of June, July, August and September.

In Table 8-4, the absolute values of mean monthly ΔN_1 are compared with the corresponding values in the ITU maps [12] for the months of February, May, August and November. For the AUH, DXB, SHJ and RAK sites, the ΔN_1 results of May and August are more consistent with ITU values than February and November, when 1-(b) approach is used. The differences with ITU values are found to be up to 21.2 and 17.6 units, for February and November, respectively. Similar results have been reported before [5]. Higher inconsistencies have been observed for May and August using the 2-(b) approach, where the differences are found to be up to 25.5 and 11.5 units, respectively. All proposed ITU values for ΔN_1 are overestimated in comparison with the results obtained in this study.

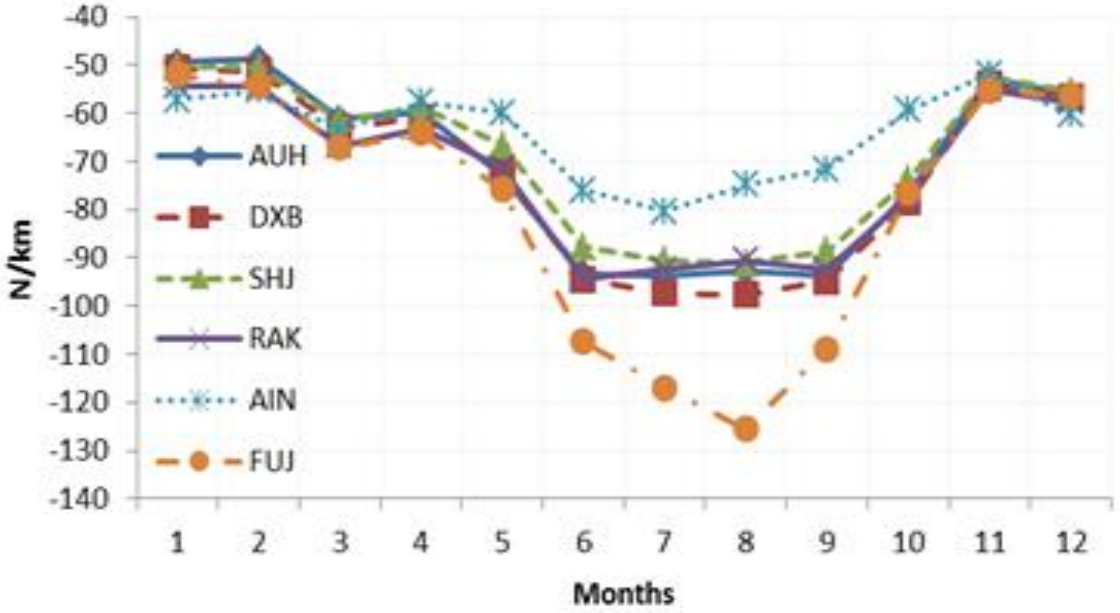

Figure 8.17: Comparison of mean monthly variations of ΔN_1 at all sites using 1-(b) (1997-2013)

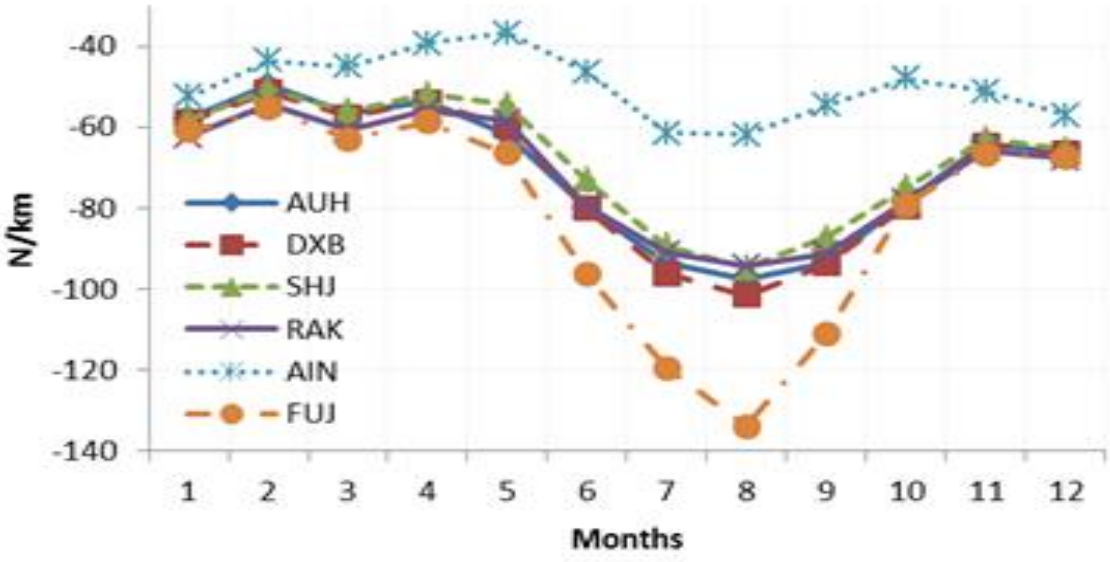

Figure 8.18: Comparison of mean monthly variations of ΔN_1 at all sites using 2-(b) (1997-2013)

Table 8-4: Comparison of absolute monthly ΔN_1 results using 1-(b) and 2-(b) approaches with ITU

	February		May		August		November	
Approach	1-(b)	2-(b)	1-(b)	2-(b)	1-(b)	2-(b)	1-(b)	2-(b)
ITU	70		80		90		70	
AUH	49	50	73	62	93	98	53	64
DXB	51	51	72	60	98	102	54	65
SHJ	51	51	67	55	91	95	52	63
RAK	54	54	71	59	91	94	55	66
AIN	55	44	60	37	75	62	52	51
FUJ	54	55	76	66	126	134	55	67

Figure 8.19 and Figure 8.20 show the mean monthly variations of ΔN at 100 m, $\Delta N_{0.1}$, using approaches 1-(b) and 2-(a), respectively, at the AUH, DXB, SHJ and RAK sites. Using 2-(a) at the four sites, low $\Delta N_{0.1}$ values are observed during winter and the highest absolute values are shown in summer season. The mean monthly distributions of $\Delta N_{0.065}$ at 65 m are provided in Figure 8.21 and Figure 8.22, which have similar seasonal variations using 2-(a) approach. When the 1-(b) approach is used, the monthly distributions of ΔN at 100 m and 65 m layers are not coherent at the four sites. However, the AUH and DXB sites have similar seasonal variations at all atmospheric layers when both approaches are used. Using 1-(b) approach, the ranges of $\Delta N_{0.1}$ and $\Delta N_{0.065}$ vary from -259.5 to -89 N/k and from -295 to -107.6 N/km, respectively. The maximum monthly differences between the four sites at 100 m and 65 m layers are found to be 83 and 103 units, respectively. This gives clear indication that the prediction of ΔN is much more complicated at lower altitudes.

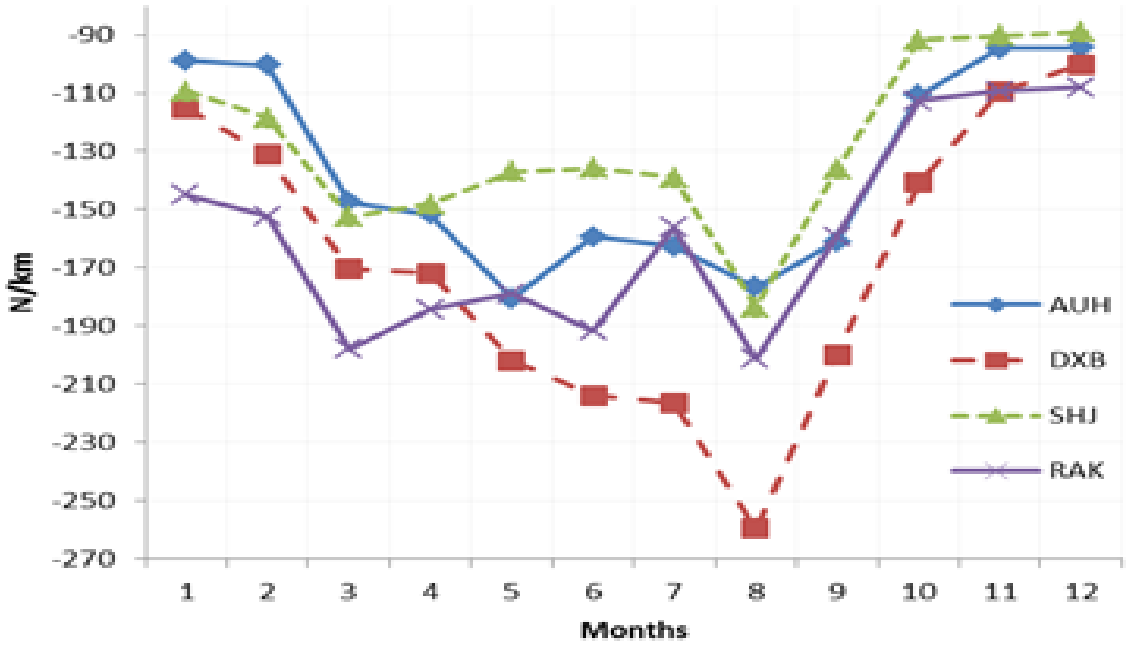

Figure 8.19: Comparison of mean monthly variations of $\Delta N_{0.1}$ at all sites using 1-(b) approach (1997-2013)

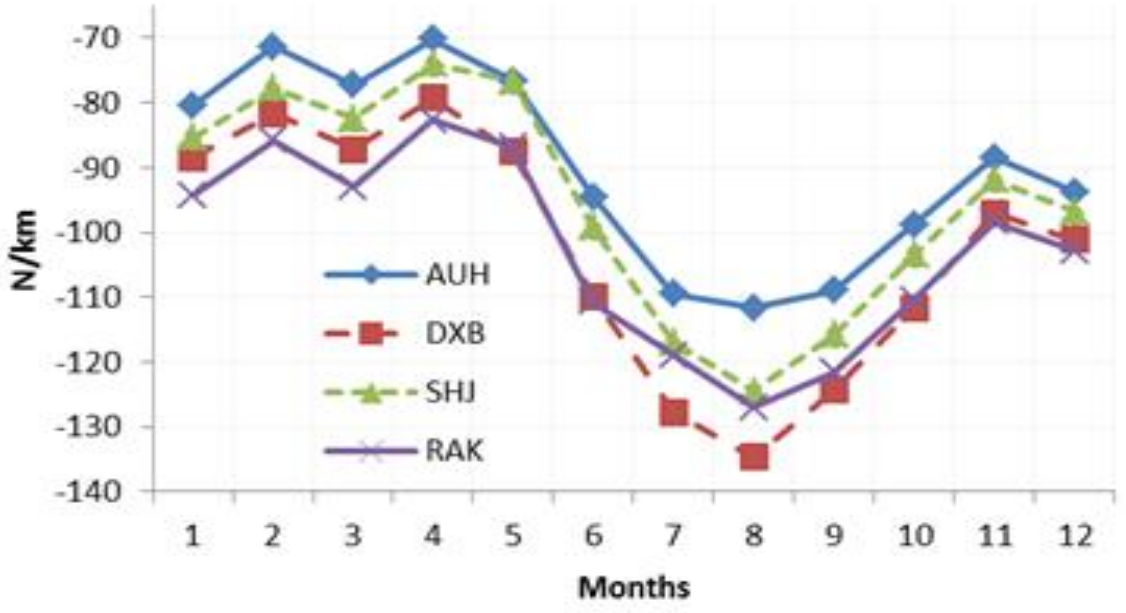

Figure 8.20: Comparison of mean monthly variations of $\Delta N_{0.1}$ at all sites using 2-(a) approach (1997-2013)

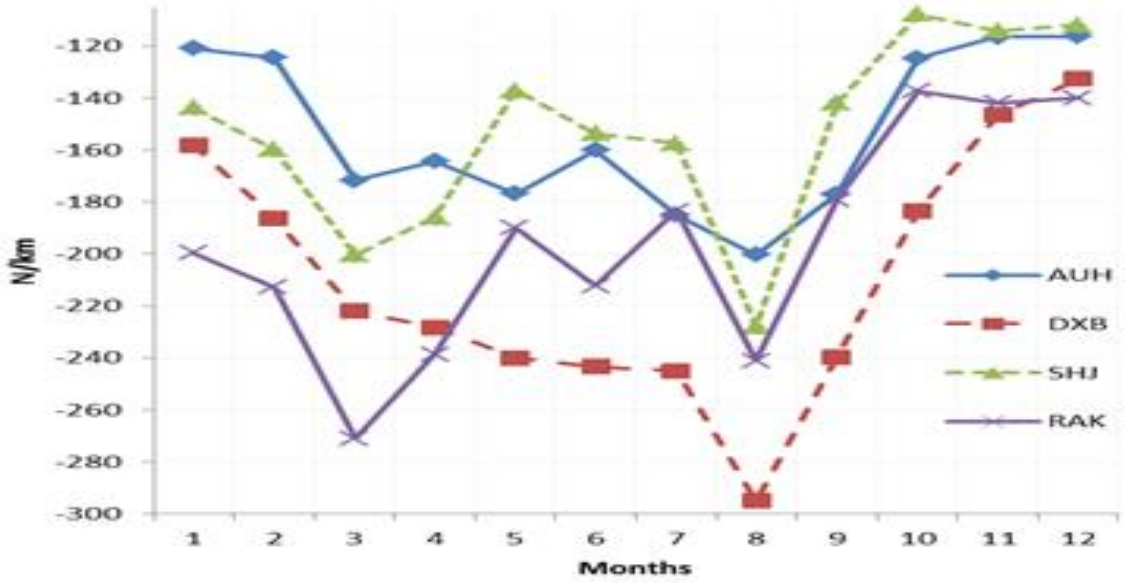

Figure 8.21: Comparison of mean monthly variations of $\Delta N_{0.065}$ at all sites using 1-(b) approach (1997-2013)

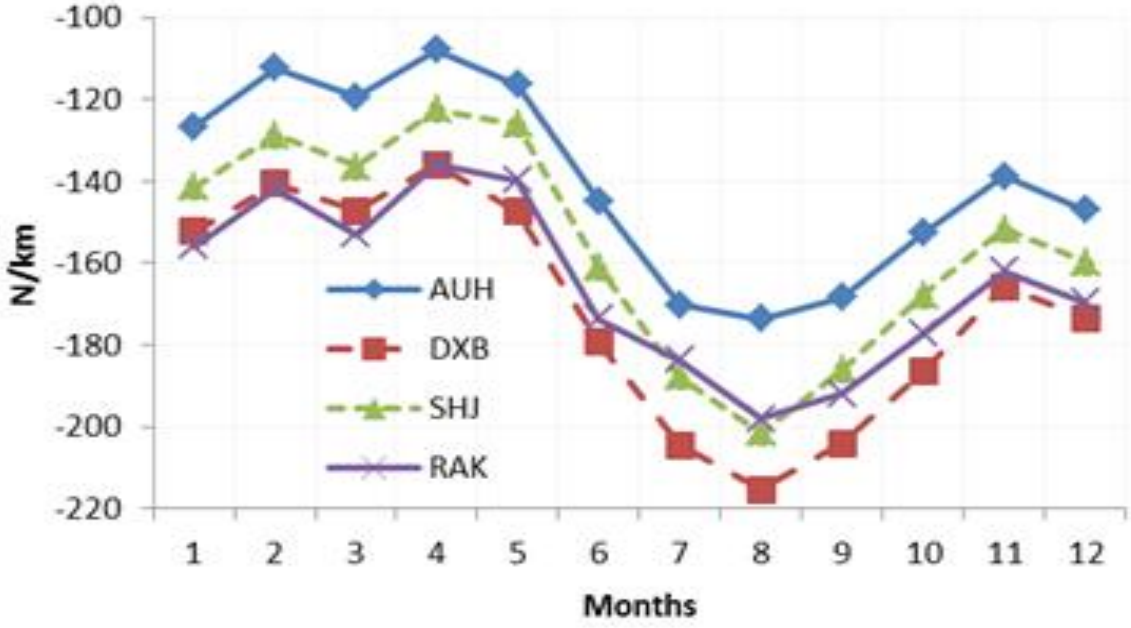

Figure 8.22: Comparison of mean monthly variations of $\Delta N_{0.065}$ at all sites using 2-(a) approach (1997-2013)

8.2.4 Analysis of *k*-factor Profile

The mean monthly ΔN_1 values at the AUH site vary between -97.62 and -47.1 N/km and the corresponding *k*-factor ranges between 1.43 to 2.64 when all three approaches of 1-(a), 1-(b) and 2-(b) are applied, as shown in Figure 8.23. The *k*-factor distributions at AUH using all approaches are found to always exceed the proposed ITU standard atmosphere value of 4/3.

Figure 8.24 and Figure 8.25 provide the mean monthly variation of *k*-factor at the six sites using the 1-(b) and 2-(b) approaches, respectively. Using the 1-(b) approach, the monthly values of *k*-factor at all sites oscillate from 1.45 to 2.65, with some exceptional results up to 4.98 in August for the FUJ site, whereas *k*-factor varies from 1.46 to 2.83 using the 2-(b) approach, with some exceptional values up to 6.81 at August for FUJ as well.

Table 8-5 summarizes the *k*-factor values obtained from the long-term mean and median results of ΔN_1 using three approaches of 1-(a), 1-(b) and 2-(b) at the six sites over the whole period from 1997-2013. At AUH, the long-term median values of ΔN_1 and *k*-factor using 1-(b) approaches are found to be -75.14 N/km and 1.92, respectively. The highest *k*-factor value of 2.4 is obtained at FUJ site based on ΔN_1 results. It has been noted that median *k*-factor is less than the mean value with approximately less than 0.2 units.

The *k*-factor has also been calculated from the mean Δ*N* values at 65 m and 100 m layers, where most of terrestrial wireless systems operate. A weighted average approach for evaluating mean and median Δ*N* among the three layers has been used for obtaining more appropriate *k*-factor value to be applied for the path clearance analysis of the microwave links operating within the first 150 m layer above the ground. For simplicity, similar weights have been assigned to the mean and median Δ*N* values at 65 m, 100 m and 1 km. As given in Table 8-5, the value of *k*-factor calculated from the long-term mean weighted average Δ*N* using the 1-(b) approach at the DXB site is found to be negative, which indicates the ducting occurrence in the area under study.

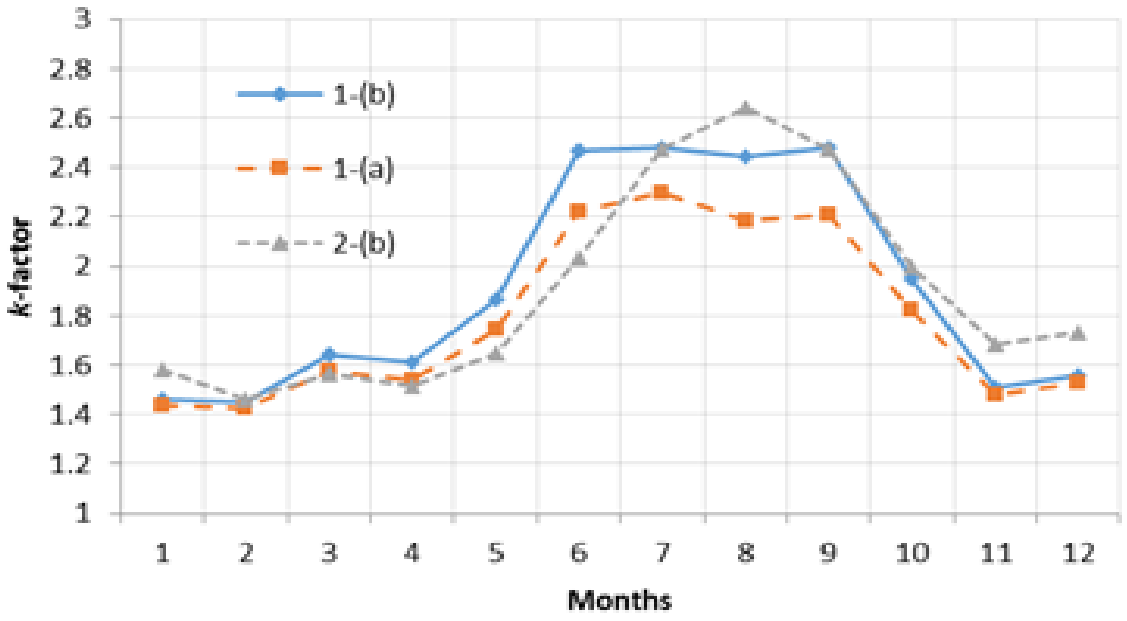

Figure 8.23: Comparison of monthly variations of *k*-factor at AUH based on 1-(a), 1-(b) and 2-(b) approaches (1997-2013)

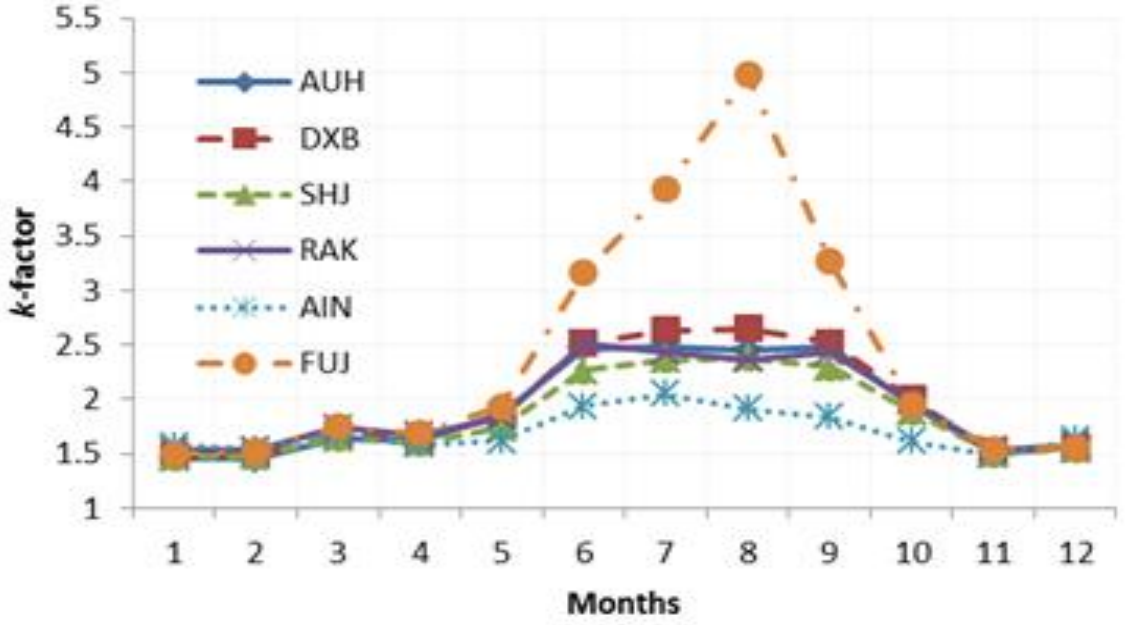

Figure 8.24: Comparison of monthly variations of *k*-factor at six sites based on 1-(b) approach (1997-2013)

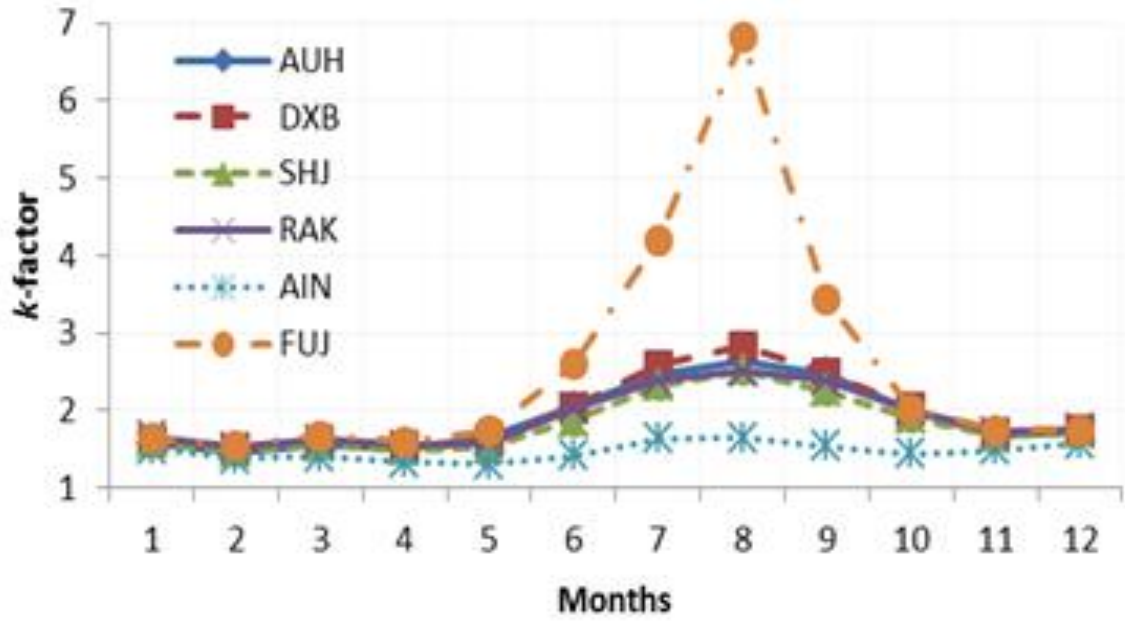

Figure 8.25: Comparison of monthly variations of *k*-factor at six sites based on 2-(b) approach (1997-2013)

Table 8-5: Comparison of ΔN_1 and *k*-factor results with ITU values for reference atmosphere

	Approach	Median	Mean	Median *k*-factor	Mean *k*-factor
ITU	-	-40		1.33	
From ΔN_1					
AUH	1-(a)	-71.11	-74.48	1.83	1.90
	1-(b)	-75.14	-79.60	1.92	2.03
	2-(b)	-74.88	-79.76	1.91	2.03
DXB	1-(b)	-78.15	-81.48	1.99	2.08
	2-(b)	-76.97	-80.67	1.96	2.06
SHJ	1-(b)	-74.14	-77.40	1.89	1.97
	2-(b)	-73.60	-76.63	1.88	1.95
RAK	1-(b)	-76.65	-79.85	1.95	2.04
	2-(b)	-75.39	-78.90	1.92	2.01
AIN	1-(b)	-64.96	-71.83	1.71	1.84
	2-(b)	-51.51	-55.85	1.49	1.55
FUJ	1-(b)	-84.14	-89.9	2.15	2.34
	2-(b)	-87.06	-91.63	2.24	2.4
From Weighted Average of ΔN_1, $\Delta N_{0.1}$ and $\Delta N_{0.065}$					
AUH	1-(a)	-81.35	-98.58	2.08	2.69
	1-(b)	-112.41	-143.8	3.52	11.85
	2-(b)	-74.12	-78.97	1.89	2.01
DXB	1-(b)	-144.25	-170.4	12.32	-11.69
	2-(b)	-76.13	-79.84	1.94	2.03
SHJ	1-(b)	-117.80	-128.4	4.01	5.49
	2-(b)	-72.81	-75.85	1.86	1.93
RAK	1-(b)	-145.49	-152.8	13.64	37.45
	2-(b)	-74.59	-78.07	1.91	1.99

8.3 $\Delta N_{0.1}$ at 100 m Layer and β_0 Analysis

The cumulative distributions of $\Delta N_{0.1}$ at the AUH site for different times using the 1-(a), 1-(b) and 2-(a) approaches are shown in Figure 8.26. $\Delta N_{0.1}$ values for all time percentages approximately oscillate between -1641 and 590 N/km for 1-(b) approach, and between -

1207 and 580 N/km for 1-(a) approach, with some exceptional values outside these ranges. The long-term β_0 values at AUH are found to be 45.3%, 57.3% and 56.5% using approaches 1-(a), 1-(b) and 2-(a), respectively. Considering the reference results of the 1-(b) approach, the value of $\Delta N_{0.1}$ is expected to be less than or equal to -100 N/km for around 57.3% of the time.

Figure 8.27 shows the monthly cumulative distributions of $\Delta N_{0.1}$ at AUH using 1-(b) approach. For 50% of the time, the summer season shows higher $\Delta N_{0.1}$ than winter with peak values obtained in May. The monthly β_0 variations obtained from $\Delta N_{0.1}$ distributions using approaches 1-(a) and 1-(b), are compared with ITU maps in Table 8-6. It has been noted that ITU values are not in good agreement with the results obtained in this study. With reference to the results of the 1-(b) approach, the estimated ITU values are below those calculated in the case of February and November with differences of around 46% and 23%, respectively, which are larger than the differences reported for the same months in an earlier study [38], which are 34% and 21%, respectively. Also, the ITU values are found to be overestimated for the months of May and August, with differences of 8.5% and 21.7%, compared with 7% and 19% reported for the same months before [38]. These differences have also been observed in other countries [29] and can be attributed to the fact that ITU maps [12] were interpolated from radiosonde data from only 99 sites worldwide between 1955 and 1959. In addition, ITU maps are usually derived from measurements performed largely in temperate regions of the world such as Europe, North America and Japan [15], which have different climatic conditions from the Gulf region.

The cumulative distributions of $\Delta N_{0.1}$ using the 1-(b) approach at the four sites with similar surface refractivity profiles are provided in Figure 8.28. The long-term β_0 values obtained using approach 1-(b) are found to be 57.3%, 62.1%, 56.5% and 60.9% at AUH, DXB, SHJ and RAK, respectively. The monthly β_0 variations at these four sites are compared in Figure 8.29. The monthly β_0 values at the four sites oscillate between 44.3% and 71.1%. Generally, summer months show higher probability of anomalous propagation at the four sites. RAK has the highest β_0 values for the first four months from January to April, while DXB site shows the highest probabilities of anomalous conditions for the remaining months from May to December.

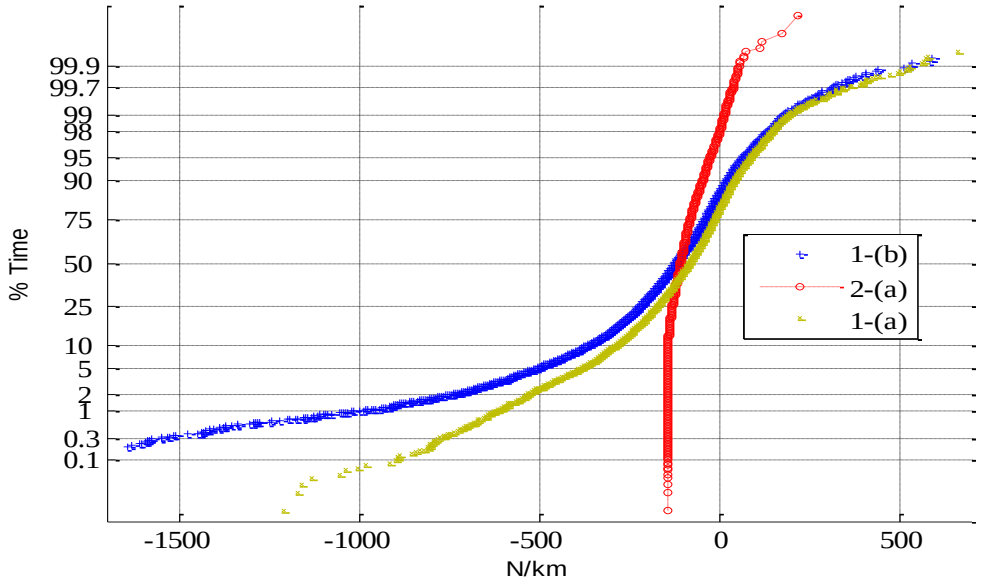

Figure 8.26: Comparison of cumulative distributions of $\Delta N0.1$ at AUH using 1-(a), 1-(b) and 2-(a) approaches (1997-2013)

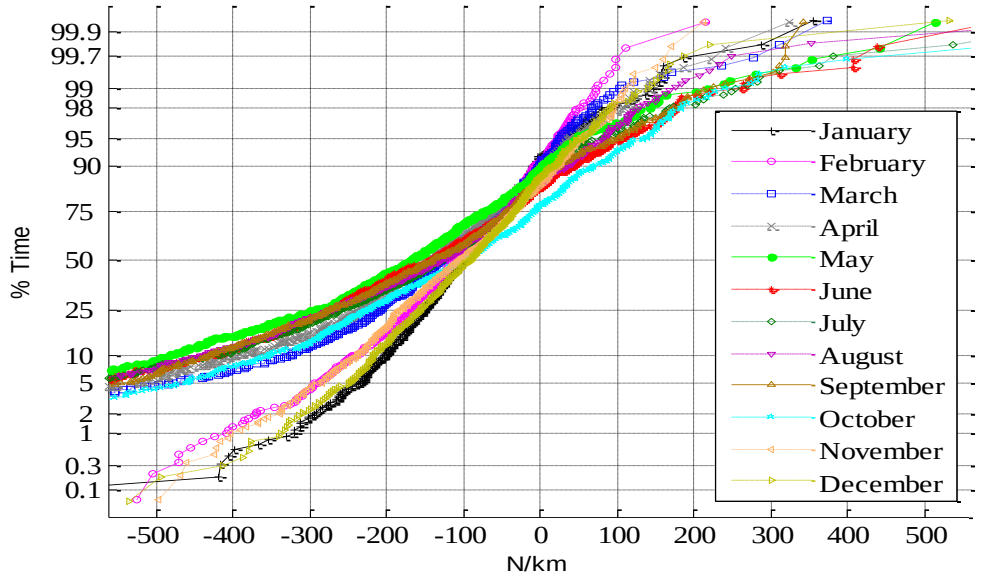

Figure 8.27: Monthly cumulative distributions of Δ*N0.1* at AUH using 1-(b) approach (1997-2013)

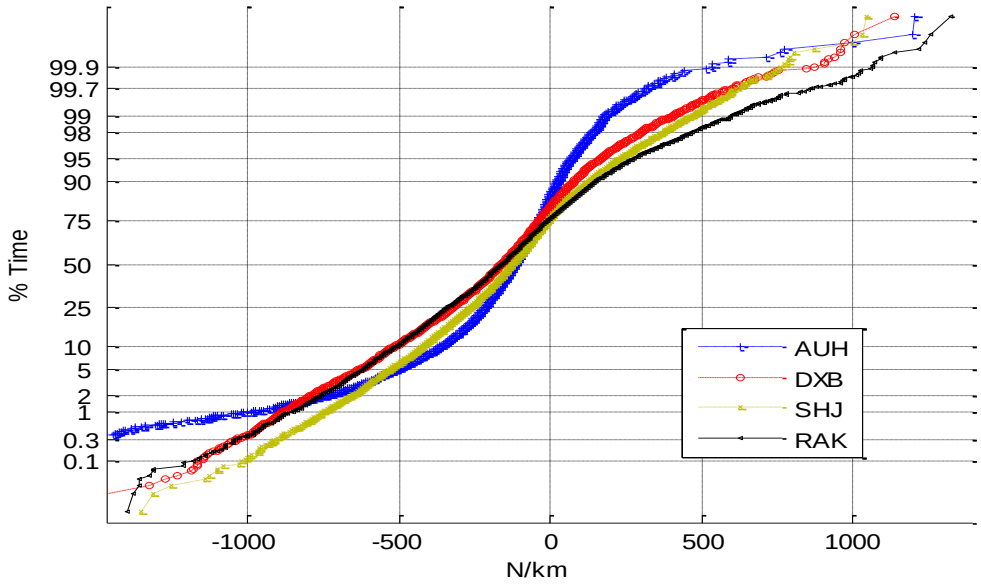

Figure 8.28: Comparison of cumulative distributions of Δ*N0.1* at 4 sites using 1-(b) approach (1997-2013)

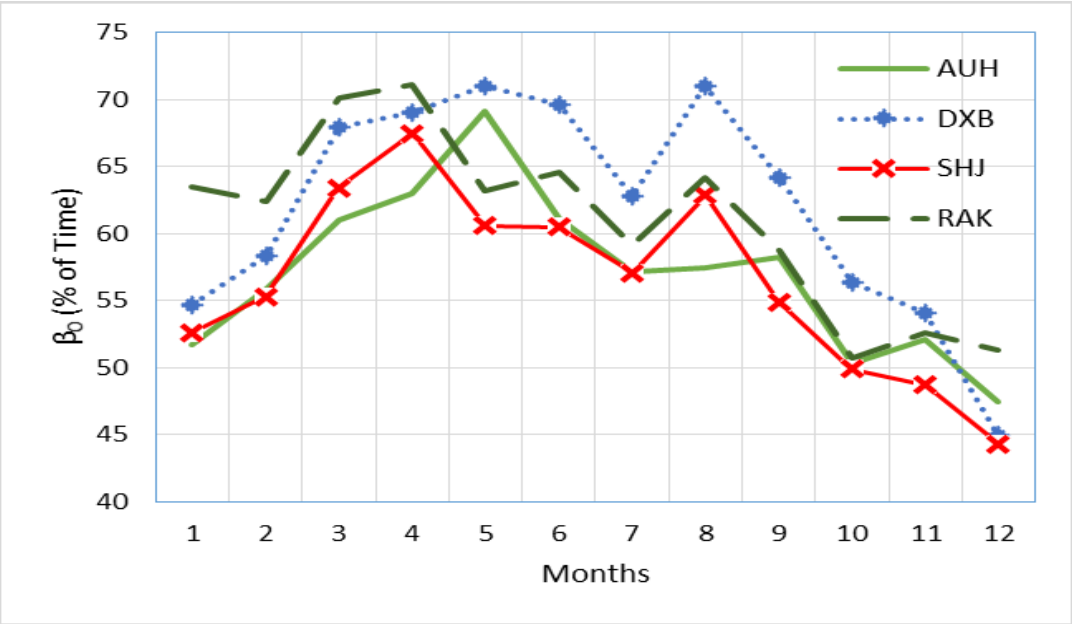

Figure 8.29: Monthly variations of β0

Table 8-7

Table 8-6 summarizes the monthly β_0 values obtained from the distributions of $\Delta N_{0.1}$ using different approaches at AUH site. The results are compared with ITU maps. The monthly β_0 results at the four sites using the 1-(b) approach are given in Table 8-7.

Table 8-6: Monthly β_0 values (%) using different approaches at AUH compared with ITU maps

Months	ITU Values	1-(a)	1-(b)
February	30	46.7	55.9
May	75	58	69.1
August	70	43.8	57.5
November	40	42.7	52.1

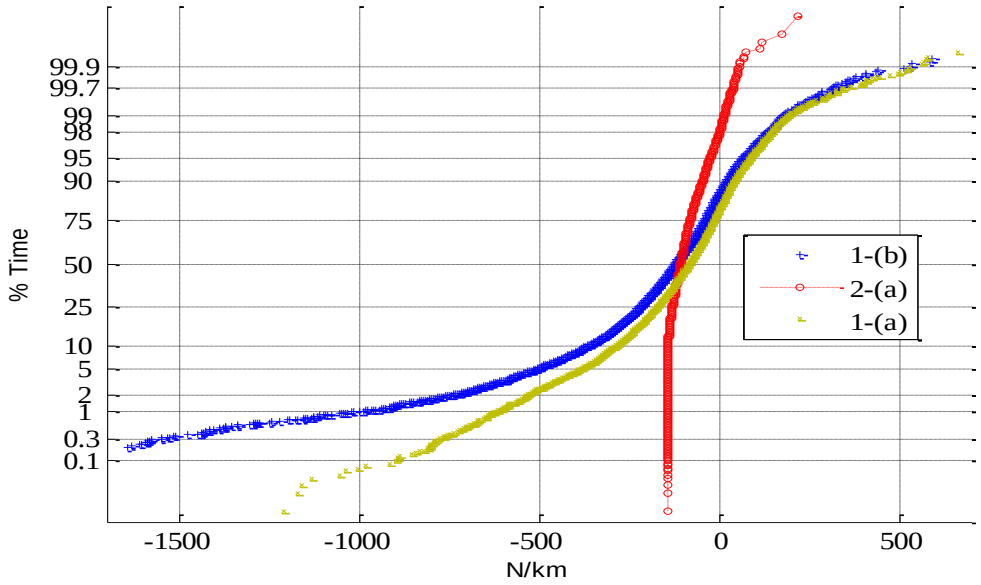

Figure 8.26: Comparison of cumulative distributions of $\Delta N_{0.1}$ at AUH using 1-(a), 1-(b) and 2-(a) approaches (1997-2013)

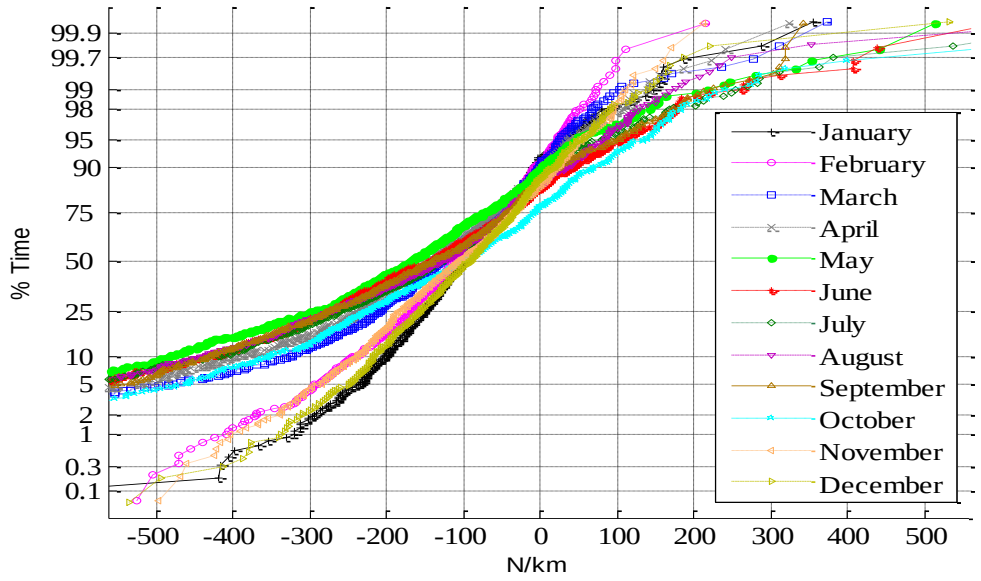

Figure 8.27: Monthly cumulative distributions of $\Delta N_{0.1}$ at AUH using 1-(b) approach (1997-2013)

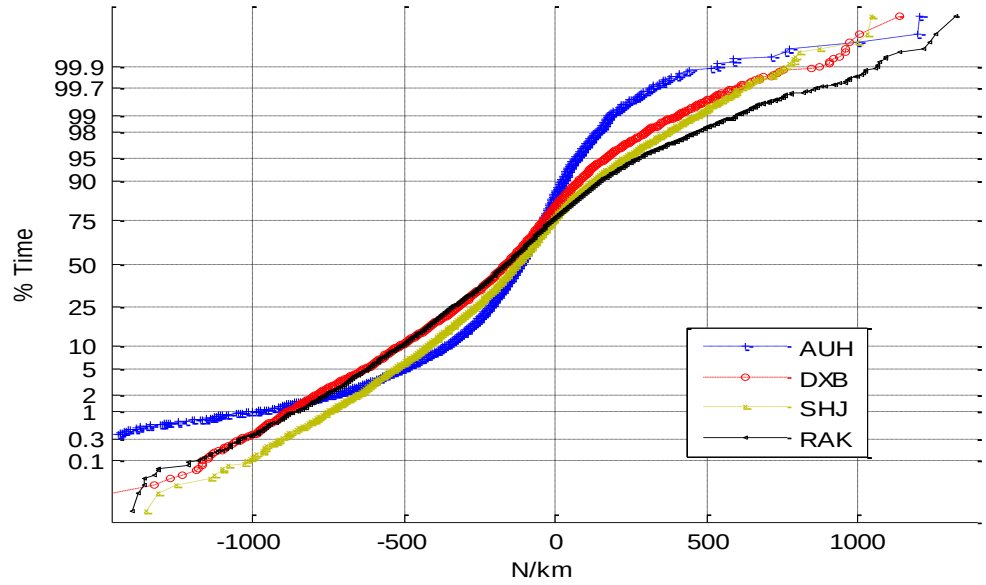

Figure 8.28: Comparison of cumulative distributions of $\Delta N_{0.1}$ at 4 sites using 1-(b) approach (1997-2013)

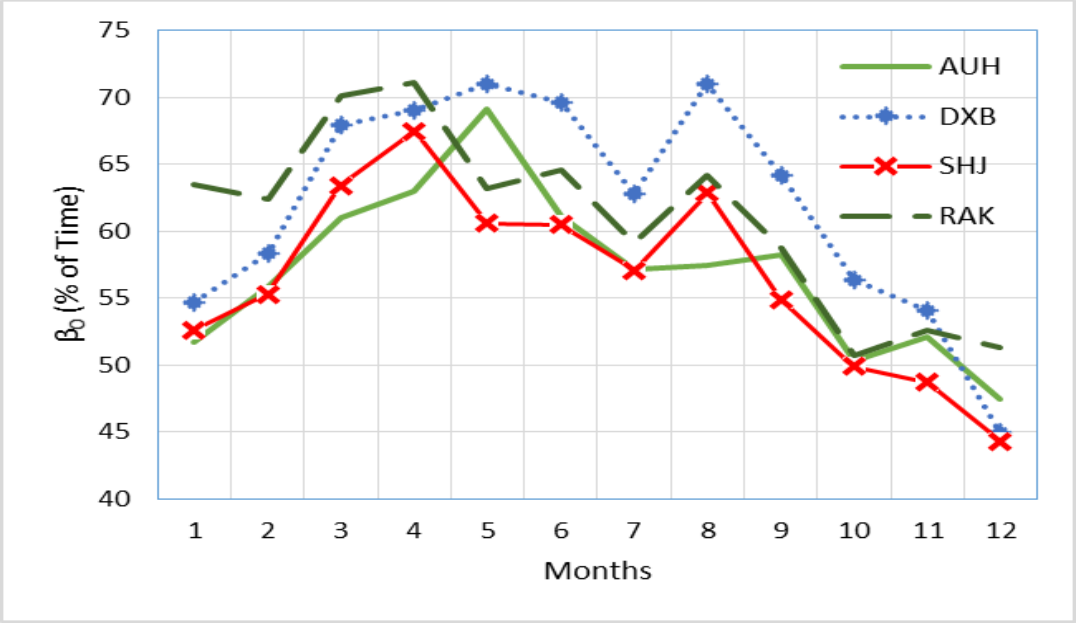

Figure 8.29: Monthly variations of β_0

Table 8-7: Monthly β_0 values (%) at 4 sites based on 1-(b) approach (1997-2013)

Months	AUH	DXB	SHJ	RAK
Jan	51.7	54.7	52.6	63.5
Feb	55.9	58.3	55.3	62.4
Mar	61	68	63.4	70.1
Apr	63	69	67.5	71.1
May	69.1	71	60.6	63.2
Jun	61.1	69.6	60.5	64.6
Jul	57.2	62.8	57.1	59.1
Aug	57.5	71	62.9	64.2
Sep	58.2	64.2	54.9	58.7
Oct	50.3	56.4	49.9	50.7
Nov	52.1	54.1	48.7	52.6
Dec	47.4	45	44.3	51.3

The monthly β_0 results at the four sites are compared with ITU maps [13] in Table 8-8. Generally, the ITU values are below-estimated for the months of February and November at the four sites, while they are overestimated for May and August.

Table 8-8: Comparison of monthly β_0 values (%) at 4 sites using 1-(b) approach with ITU maps

Months	ITU Values	AUH	DXB	SHJ	RAK
February	30	55.9	58.3	55.32	62.4
May	75	69.1	71.9	60.6	63.2
August	70	57.5	71.1	62.9	64.2
November	40	52.1	54.2	48.9	52.7

8.4 $\Delta N_{0.065}$ at 65 m Layer and Analysis of Point Refractivity Gradient ($dN_{1\%}$)

Figure 8.30 shows the cumulative distributions of $\Delta N_{0.065}$ using the 1-(a), 1-(b) and 2-(a) approaches at AUH. $\Delta N_{0.065}$ values for all time percentages approximately oscillates between -2750 and 1400 N/km for 1-(b) approach, and between -1860 and 1543 N/km for 1-(a) approach, with some exceptional values outside these ranges. The long-term value of $dN_{1\%}$ at AUH is found to be -722.5, -1604.5 and -228.2 N/km, using approaches 1-(a), 1-(b) and 2-(a), respectively.

The $\Delta N_{0.065}$ values calculated using approaches 1-(a) and 1-(b) for different time percentages at AUH are compared with ITU maps in Table 8-9. Bilinear interpolation has been used to get exact values of $\Delta N_{0.065}$ at AUH from the corresponding ITU data files for the given coordinates at different time percentages. The results are not in good concurrence with ITU values. Considering the absolute values of $\Delta N_{0.065}$ results, the ITU values are found to be overestimated for 10% while they are under-estimated for 90% and 99%. For 1% of time, the estimated ITU value is below the calculated value using the reference 1-(b) approach. Table 8-10 provides $\Delta N_{0.065}$ values obtained at AUH, DXB, SHJ and RAK sites, which have similar surface refractivity profiles, at different time percentages. The highest absolute $\Delta N_{0.065}$ values for 1% and 10% are shown in AUH and DXB, respectively, while RAK shows the top values for larger time percentages.

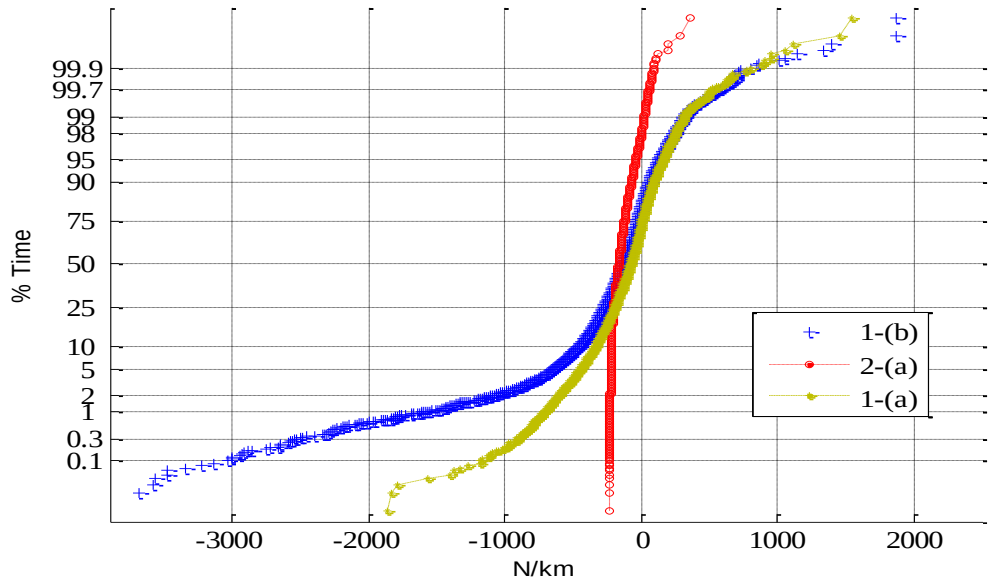

Figure 8.30: Comparison of cumulative distributions of $\Delta N_{0.065}$ at AUH using 1-(a), 1-(b) and 2-(a) approaches (1997-2013)

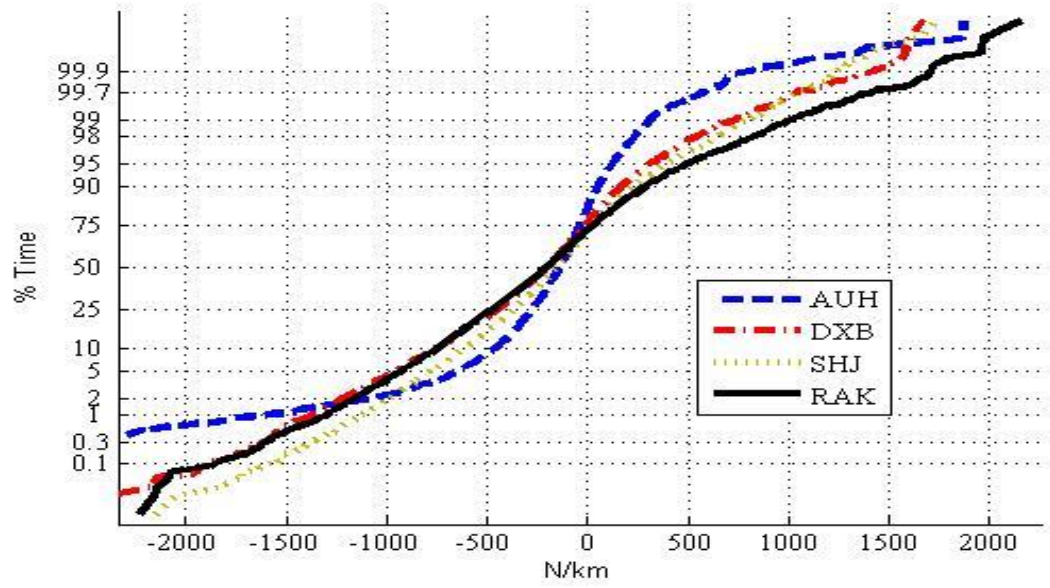

Figure 8.31: Comparison of cumulative distributions of $\Delta N_{0.065}$ at 4 sites using 1-(b) approach (1997-2013)

Table 8-9: Comparison of $\Delta N_{0.065}$ values (N/km) at AUH using 1-(a) and 1-(b) approaches with ITU maps

Time %	ITU values	1-(a)	1-(b)
1%	-952.42	-722.5	-1604.5
10%	-553	-344.9	-460.9
50%	-92.824	-89.8	-142
90%	-4.38	76.8	51.3
99%	38.86	305.4	307.6

Table 8-10: Values of $\Delta N_{0.065}$ not exceeded for different time percentages at 4 sites

Time %	AUH	DXB	SHJ	RAK
1%	-1604.5	-1378.8	-1122.3	-1300.1
10%	-460.9	-760.3	-616.3	-752.8
50%	-142	-198.6	-152.3	-202.7
90%	51.3	173.7	232.8	291.3
99%	307.6	733.6	803.7	1025.1

8.5 Final Remarks

Seventeen years of local surface and radiosonde meteorological data were used to study the vertical refractivity profile for three critical atmospheric layers within the first kilometre above the ground surface.

The surface meteorological measurements using the radiosonde were found slightly different from the measurements obtained from fixed weather stations which are usually more accurate due to higher stability.

The analysis of surface refractivity was used for the evaluation of vertical refractivity profile in areas where radiosonde data are not available, in particular for the first 100 m atmospheric layer and below. A new approach was proposed for utilizing the upper-air refractivity from a radiosonde site in the surrounding sites with similar surface conditions. For ΔN analysis at 1 km, the same approach was used for the sites where surface profiles are not so consistent with those from the radiosonde location assuming that the atmosphere gets increasingly horizontally homogeneous at higher altitudes. Exponential prediction models were also used for the ΔN prediction at all sites. The analysis of the given approaches for evaluating the mean vertical refractivity profiles showed that higher concurrency with radiosonde measurement could be obtained using the new proposed approach in this study. However, the range of variations was found to be higher for altitudes of 100 m and below. Some differences were observed in monthly refractivity gradient profiles at certain sites with similar mean surface profiles, in particular for low altitudes below 100 m. This could be attributed to the fact that the measurements at a given time were not necessary the same at these sites over the whole period, and that any small change in N_s value results in large disagreement in ΔN due to the low decimal number in the denominator of the linear ΔN equation for low heights.

A new approach was used to evaluate *k*-factor from the weighted average ΔN at the three layers, which is recommended to be applied in other areas. The *k*-factor value of -11.7 indicated the incidence of ducting phenomenon in the area under study. The β_0 analysis at four sites indicated that the probability of anomalous propagation exceeded 44% for all

months and reached up to 71 % at certain locations within the summer. The results obtained in this study for the Gulf region would suggest the necessity to revise the ITU maps, in particular for similar subtropical climate, based on recently gathered long-term local meteorological data from more radiosonde sites worldwide, since ITU values are being widely used for the design of wireless communication systems.

Based on the results presented in this work, it is recommended to apply similar approach to evaluate the vertical refractivity profiles in the surrounding areas to a radiosonde location and for areas with similar surface refractivity conditions.

The vertical profile evaluation is essential for the analysis of very critical atmospheric duct phenomena, particularly in the sub-tropical region under study. In chapter 9, various types and parameters of ducting phenomena will be investigated.

VOLUME II OF II

Chapter 9

INVESTIGATION OF DUCTING PHENOMENA AND TYPES OF ATMOSPHERIC DUCTS

9.1 Introduction

Tropospheric ducts can be associated with several reasons such as temperature inversions, subsidence in high pressure system, evaporation over water surfaces and weather fronts. Such phenomena are very common in the Arabian Gulf region causing cross borders interference since waves can propagate for very long distances.

The waves may be coupled into an atmospheric duct depending on the height of transmitting and receiving radio stations as well as the angle of incidence. The refractive index of atmosphere usually falls with higher altitudes due to the decreasing pressures and temperatures. As per Snell's law, the propagating signal get bent downward while moving from an atmospheric layer of refractive index, n_1, near the ground towards an upper layer

of index, n_2, such that $n_1 > n_2$. The incident and refracted rays as well as the angles made at the point of refraction with the normal to the boundary is shown in Figure 2.5.

The signal can be trapped within an atmospheric duct layer when angle of incidence with respect to the normal line is around 90^0, while the angle with the horizontal boundary is small enough, typically less than 1^0. Within a duct, the radio waves may get "bent" downwards and be able to propagate beyond the geometric horizon. However, the roughness of the duct can be an important factor such that the energy may be scattered out of the duct if the roughness is large compared with the signal wavelength. The duct thickness is important parameter where signals are trapped unless the wavelength is large compared with the thickness.

Subsidence in high pressure system can lead to elevated temperature inversions and ducts since the descending compressed air may get warmer than the lower air mass. This is usually experienced over large continents for long periods and expected at high altitudes above 1 km.

Strong rapid temperature inversions (temperature increases within small heights) can cause serious duct phenomena. In normal situations, the temperature usually falls about 1^0C per 100 m height. Temperature inversion may occur after sunset in clear nights when the air temperature rises with height while Earth is cooling rapidly by radiation and the air close to the ground. In desert areas, similar phenomena are experienced where the dry component

of refractivity dominates, due to the dry air causing the ducting to occur. In the case of significant water vapour, the condensation of the excess vapour, as fog, results in low vapour density and cold dry air near the ground with warmer moist air above. Accordingly, sub-refraction phenomenon may also occur, leading to multipath effects on LOS MW links. Surface ducts may occur within the first few hundred meters over coastal areas due to Earth advection phenomena when the advected warm air masses move from a warm ground surface over a cooler sea surface. This usually happens in early summer nights. The mixture of warm and cold moist air masses leads to significant gradients of relative humidity and temperature inversions. This is relatively common in the subtropical Arabian Gulf region, where UHF signals travels well beyond the horizon causing cross-border interference to neighbouring countries.

In surface ducts, the energy may be lost to the ground terrain (e.g. vegetation) as the lower boundary of the duct. Signals can propagate for long distances through elevated ducts considering sharp decrement in refractivity with height, however, path loss may increase when the receiving stations are below the duct layer.

In this chapter, the seventeen years of upper-air meteorological data from 1997-2013, obtained from the radiosonde at Abu Dhabi city, are analysed. The vertical profiles of upper-air refractivity, N_h, and modified refractivity, M_h, are investigated within the first 350 m of atmosphere above the ground surface, where most of terrestrial communication systems operates.

9.1.1 Modified Refractivity and Characteristics of Atmospheric Ducts

The description of atmospheric ducts' occurrence and structure, is an important element for predicting wireless systems performance operating in a subtropical region. Ducting phenomenon may cause deep slow fading or signal enhancements for terrestrial LOS radio links. The modified refractivity parameter, *M*, is commonly used in place of refractivity to examine the refractivity gradients and to describe their effect such as atmospheric ducts. The modified refractivity is defined as [12]:

$$M(h) = N(h) + 157 \, . \, h \tag{9.1}$$

where *M(h)*, in M-units, is the modified parameter of refractivity, *N(h)*, at certain height, *h*, given in kilometre.

Figure 9.1 describes three duct types; namely surface based, elevated-surface, and elevated ducts in terms of the modified refractivity as a function of height above ground [12], noting that evaporation duct profile is difficult to be obtained using radiosonde measurements. The ducts are characterized by their strength, S_s (M-units) or E_s (M-units), and their thickness, S_t (m) or E_t (m). Two additional parameters are used to characterize elevated ducts: namely, the base height of the duct E_b (m), and E_m (m), the height within the duct of maximum *M*.

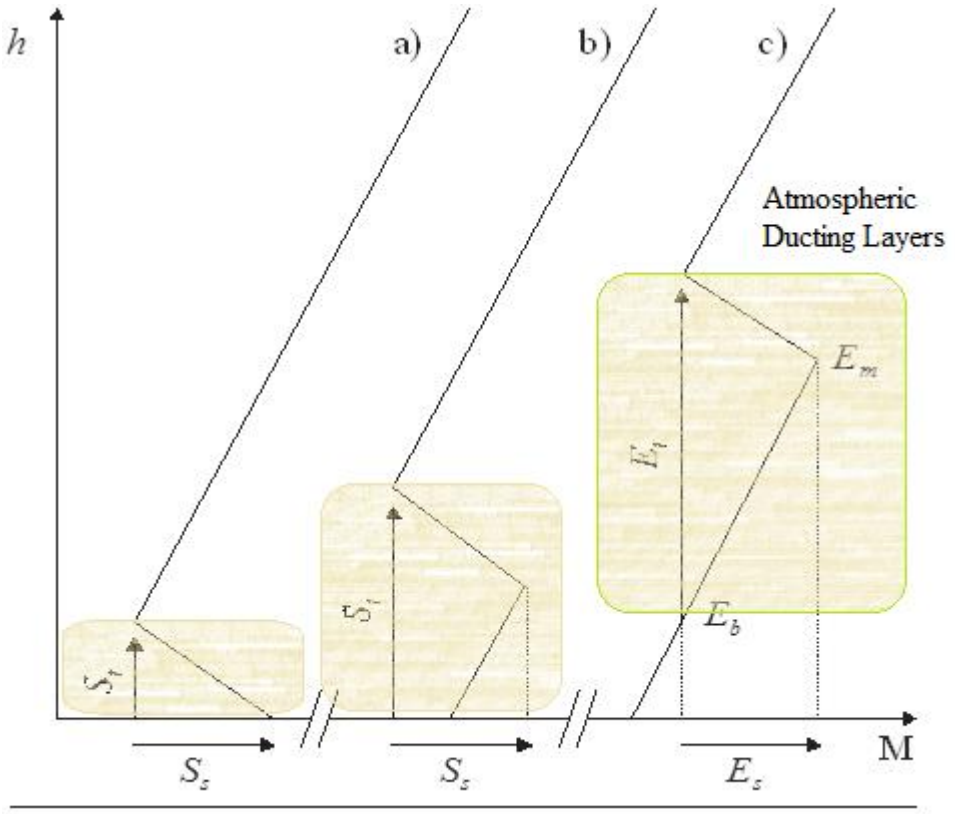

Figure 9.1: Definition of parameters describing a) surface, b) elevated surface and c) elevated ducts [12]

The characteristics of the three duct types are statistically analysed by investigating the mean hourly, monthly and yearly variations of each parameter. Two approaches are used to evaluate the average profile of atmospheric ducts and results are compared. In the first approach (1), the modified refractivity parameter is evaluated at each altitude and then values are averaged for each layer at a given time over the whole period. This approach considers the uncertainties in vertical radiosonde measurements due to the sensors' tolerance and accuracy.

In the second approach (2), the instantaneous hourly sets of *M* measurements are analysed. The mean variations of duct parameters are then calculated by averaging the values of each duct parameter on hourly, monthly or yearly basis.

9.1.2 Frequency dependency on duct thickness

The minimum signal wavelength (m) and frequency (Hz) that can be trapped by an atmospheric duct of a given thickness, *D*, is evaluated using the following empirical relationship [86]:

$$f_{min} = \left(\frac{3.6 * 10^{11}}{1^{\left(-\frac{3}{2}\right)}} \right) . D^{\frac{-3}{2}} \tag{9.2}$$

The list of the frequency bands defined by ITU [87] as well as the frequency ranges, signal wavelength and duct thickness required for trapping are summarized in Table **9-1**. The centimetric waves with 10 to 100 cm wavelengths operating in SHF band from 3 to 30 GHz can be trapped within atmospheric ducts of 5 to 24 m thickness.

Table 9-1: Frequency, wavelength and minimum trapping duct thickness

ITU Band Number	Band Symbols	Frequency range (lower limit exclusive, upper limit inclusive)	Metric Division	Wavelength (m)	Duct Thickness (m)
8	VHF	30 to 300 MHz	Metric waves	1 to 10	113-524
9	UHF	300 to 3 000 MHz	Decimetric waves	0.1 to 1	24-113
10	SHF	3 to 30 GHz	Centimetric waves	0.01 to 0.1	5-24
11	EHF	30 to 300 GHz	Millimetric waves	0.001 to 0.01	1-5

9.2 Results and Analysis

As explained in the previous chapters, some meteorological data are not available for the analysis due to low quality or incomplete ascents. A transmitter or receiver, which is placed in a surface duct, will experience significant signal enhancement, and long detection range. Omnidirectional sources will experience cylindrical spreading loses, and narrow radio beams will view the duct as a waveguide [86].

The vertical radio refractivity, N, modified parameter of refractivity, M, and refractivity gradient, ΔN, are evaluated for each 5 m of low atmosphere up to 350 m altitude above the ground using seventeen years of radiosonde meteorological data from 1997-2013. Three years' data from 1997 to 1999 are available with 10 m resolution, while data are obtained with 5 m resolutions for the remaining years. A linear interpolation is used to convert the

three years' data resolution from 10 m resolution to 5 m. The parameters of vertical *N*, *M*, duct strength, thickness and frequency of occurrence of the three duct types are studied.

The monthly occurrence probabilities of ducting phenomena over the whole study period are investigated from the monthly cumulative distributions of refractivity gradient at 100 m, $\Delta N_{0.1}$, given in Figure 8.27, where the gradient values exceed -157 N/km. The monthly ducting probabilities vary from 23.68% in January to 53.25% in May. Figure 9.2 shows the monthly probabilities of duct occurrence from 1997 to 2013.

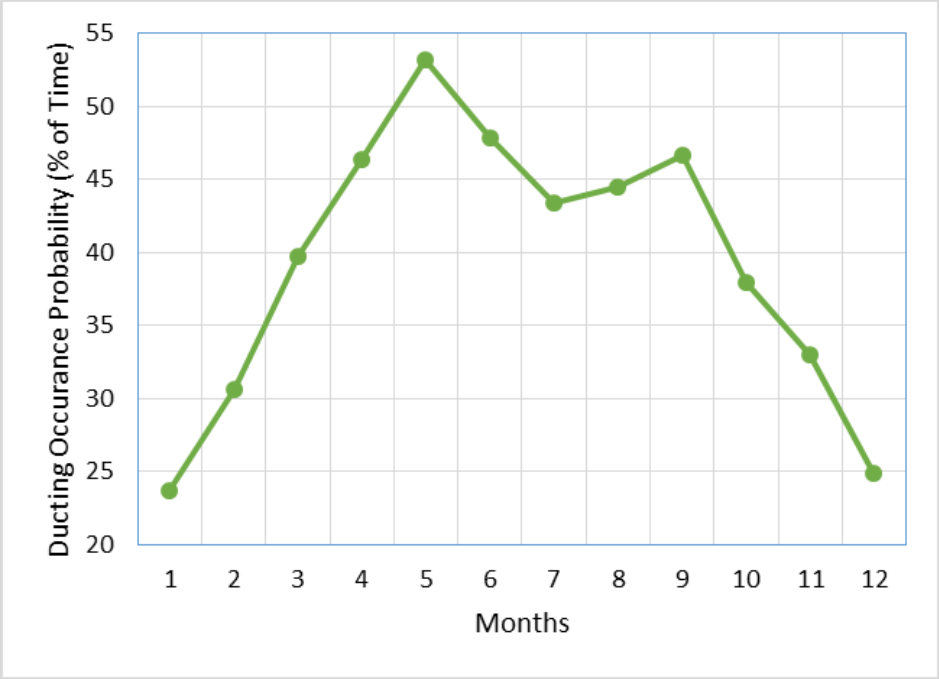

Figure 9.2: Monthly probabilities of atmospheric duct occurrence (1997-2013)

9.2.1 Duct analysis using approach (1)

The mean modified refractivity is evaluated using approach (1) on hourly, monthly and hourly basis from 1997 to 2013, in order to analyse the mean duct profiles in the area under study. Figure 9.3 shows the vertical variation of mean monthly modified refractivity parameter over the first 350 m above the ground. On monthly average basis, the surface duct is observed during the winter and spring seasons, while elevated duct is shown for the summer months, in particular for the mean months of June and July.

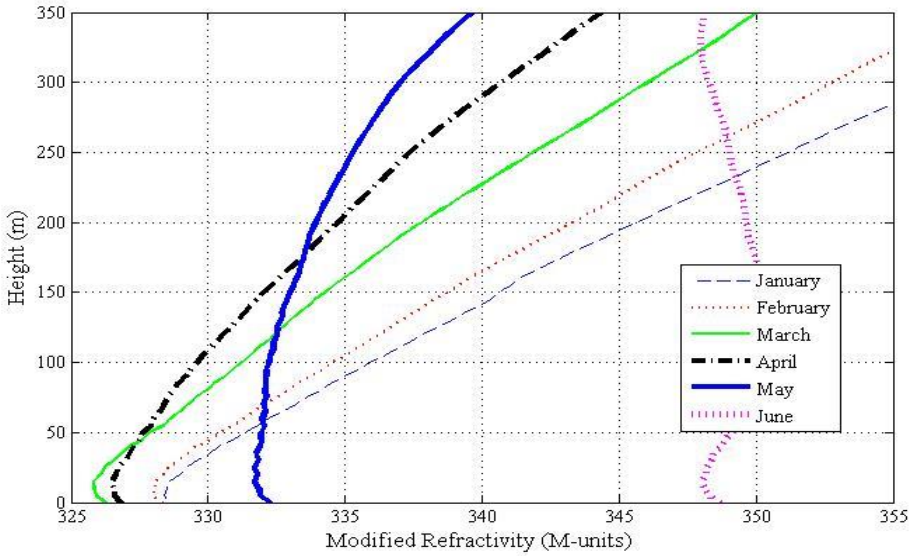

(a) Mean Months (January - June)

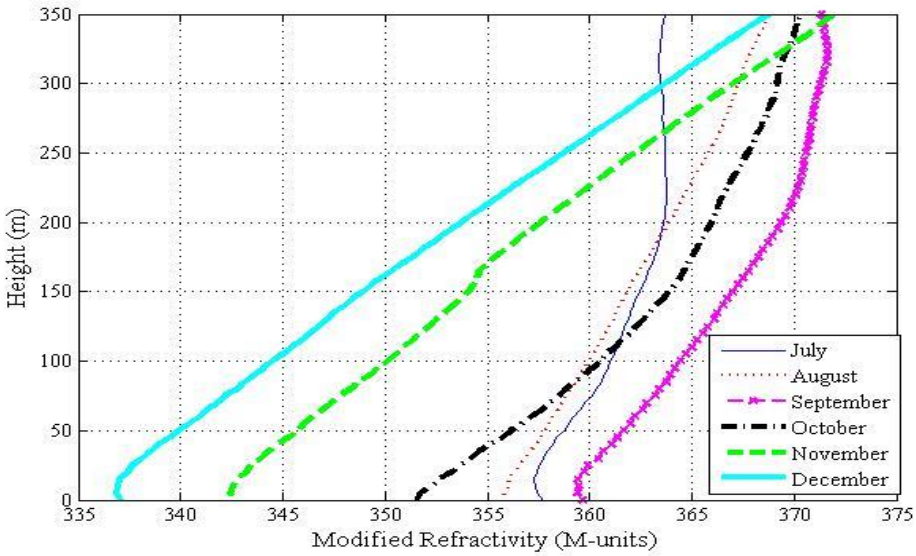

(b) Mean Months (June - December)

Figure 9.3: Mean monthly variations of vertical modified refractivity profile over 350 m above ground (1997 - 2013): (a) Mean months (January - June), (b) Mean months (June - December)

Figure 9.4 shows an example for the mean annual variations of vertical modified refractivity profile for the month of February over the whole period from 1997 to 2013. It has been noted that data for February 2010 are not available. In winter, surface duct is shown with average thickness below 25 m and around 40 m in 2005. Both elevated surface and elevated ducts are observed at higher altitudes for the years of 2005 and 2008.

The ITU has combined surface and elevated-surface ducts in the statistics, due to the rather few cases of elevated-surface ducts [12]. The mean vertical modified refractivity has also been analysed on hourly basis over the whole period. The mean monthly *M* profiles are studied for 0 H (00:00 UT), 12 H (12:00 UT) separately, as well as for the combined 0&12 H (00:00 and 12:00 UT) and the results are found to be almost similar. The obtained average values are compared with the ITU map as well [12]. The long-term mean statistics in addition to the minimum and maximum values of the mean hourly profiles for the surface based ducts, including surface and elevated-surface, in addition to the elevated ducts are given in Table 9-2 and Table 9-3, respectively.

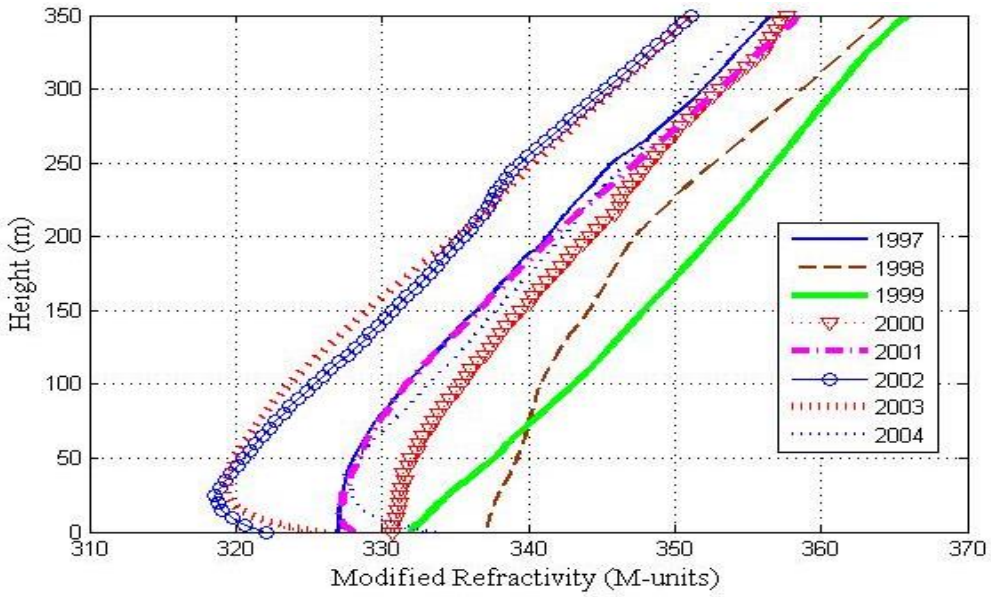

(a) February (1997 - 2004)

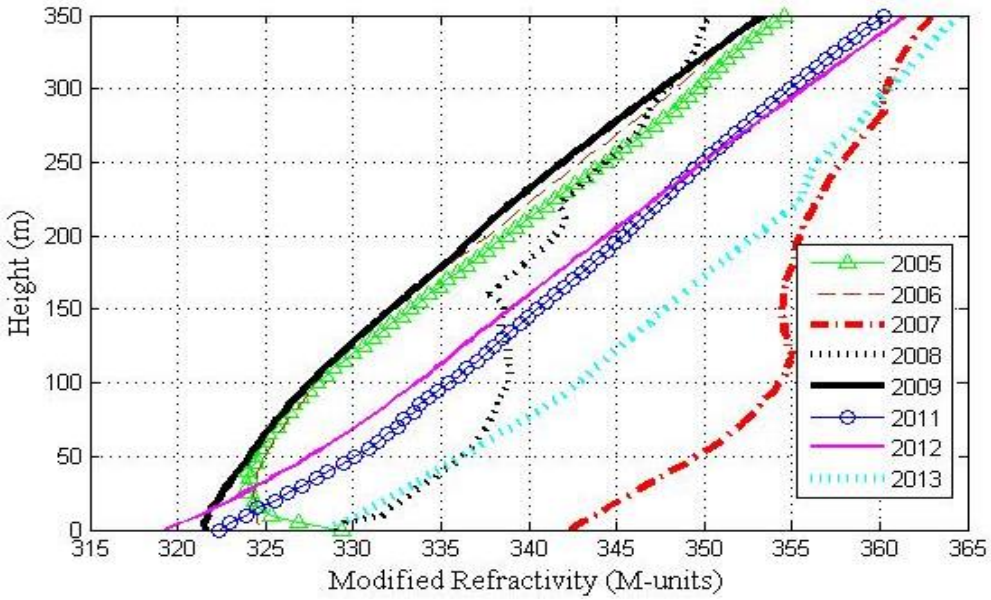

(b) February (2004 – 2013, except 2010)

Figure 9.4: Mean annual variations of vertical modified refractivity over 350 m above ground. (a) Mean Months (January - June), and (b) Mean Months (June - December)

Table 9-2: Long-term mean statistics of surface and elevated-surface duct characteristics (1997-2013) using approach (1) in comparison with ITU Maps

Duct Characteristics	Surface			Elevated-Surface			ITU Values
	Average	Min	Max	Average	Min	Max	
Occurrence Probability	39%			12%			35%
Mean Strength S_s (M-units)	7	0	17	10	0.25	32	25
Mean Thickness S_t (m)	73	5	301	262	15	350	200
Height of max M in Elevated-Surface Duct	-	-	-	86.4	10	290	-
Affected Frequency (GHz)	0.581	32.199	0.055	0.085	6.197	0.055	0.127

Table 9-3: Long-term mean statistics of elevated duct characteristics (1997-2013) using approach (1) in comparison with ITU Maps

Duct Characteristics	Elevated			ITU Values
	Average	Min	Max	
Occurrence Probability	21%			30%
Mean Strength E_s (M-units)	3	0.2	17	15
Mean Thickness E_t (m)	113	13	343	300
Mean Base Height of Elevated Duct E_b (m)	129	2	295	800
Mean Coupling Height E_m (m) / Height of Max M in Elevated Duct	180	5	340	800
Affected Frequency (GHz)	0.298	7.680	0.057	

The long-term average results obtained using approach (1) for all duct types are not in good coherence with ITU maps. The occurrence probabilities are found to be below-estimated for surface based ducts, including surface and elevated-surface, and overestimated for the

elevated duct considering that the occurrence probability of surface-elevated duct is part of the surface category.

The mean hourly profiles of modified refractivity has been analysed for each month of each year, such that the modified refractivity parameter is averaged for the given heights at either 0H, 12H or combined 0H an 12H (0H&12H) per each month over the whole study period. The number of occurrences for the values obtained for all duct parameters are provided in the following charts.

The hourly surface duct statistics for the mean strength and thickness parameters are given in Figure **9.5** and Figure **9.6**, respectively. The surface duct is found to be the most frequent duct type in the area under study. The surface duct strength is less than 15 M-units for around 72.6% of the events at 0H, while it is below 10 M-units for around 86% at 12H. The duct thickness at 12H is found to be less than 50 m for around 95.8% of time. At 0H, the occurrence probabilities exceed 50% for thickness values below 100 m, while 19.2% of the events are observed to be above 300 m.

The minimum signal frequencies that can be trapped are obtained from the duct thickness analysis that differ from 55 MHz to 32 GHz for the surface based ducts and from 57 MHz to 7.7 GHz for the elevated duct.

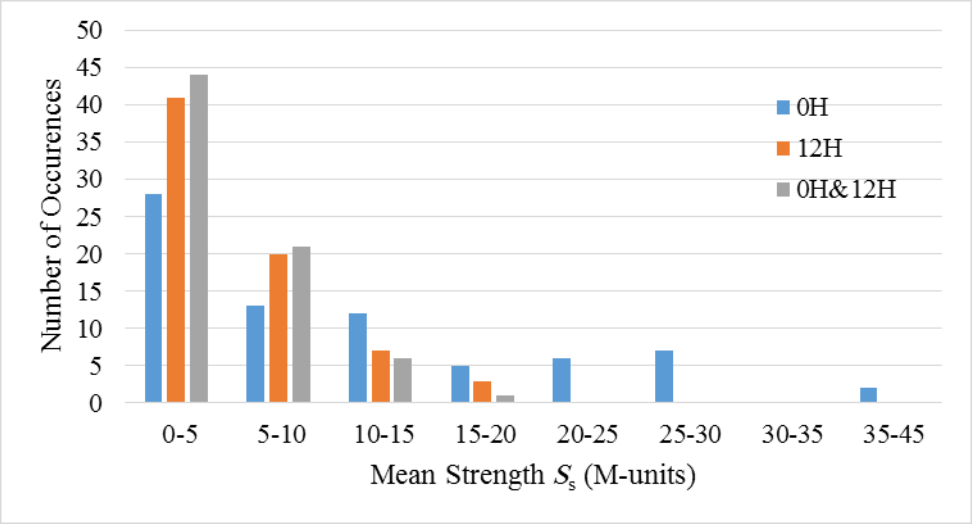

Figure 9.5: Surface duct strength, S_s (m), using approach (1)

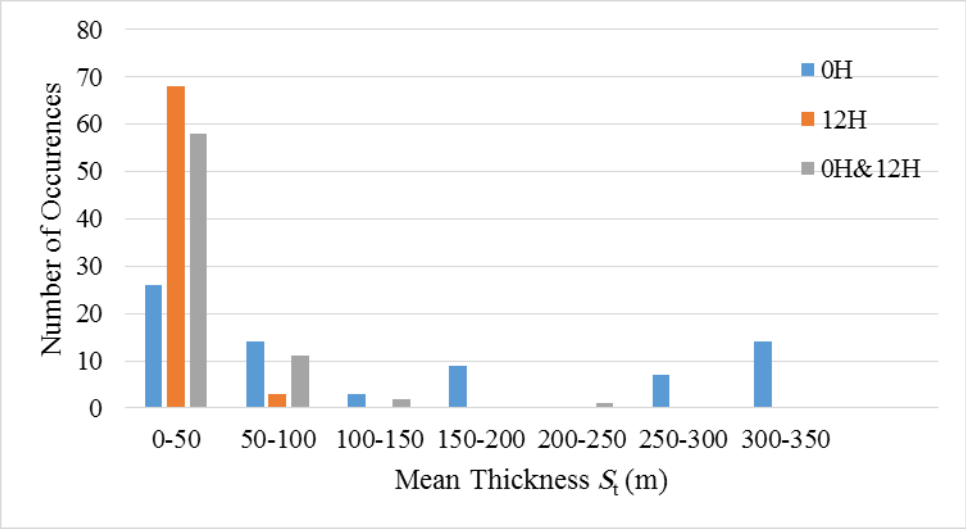

Figure 9.6: Surface duct thickness, S_t (m), using approach (1)

Figure **9.7**, Figure **9.8** and Figure **9.9** show the hourly statistics and number of occurrences for the mean strength, thickness and coupling height, respectively, of the surface-elevated duct. This duct category is the least frequent duct type with very few observations at 12H. The duct strength varies from 5 to 15 M-units for 63% of the events at 0H, where more

than 90% of the duct thickness observations are above 200 m with majority exceeds 300 m. The mean coupling height at 0H is below 100 m for more than 70% of the events, while the height is above 150 m for the majority of events in case of combined 0H&12H data sets.

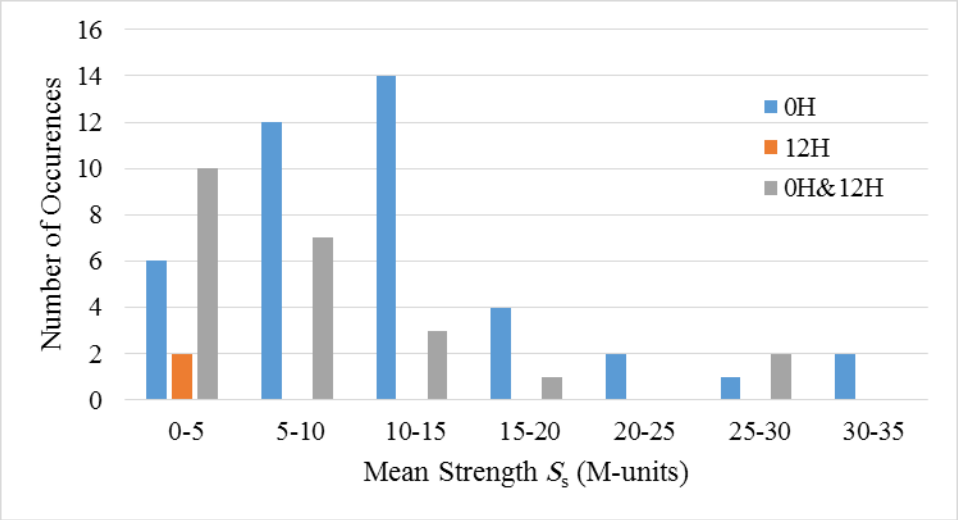

Figure 9.7: Surface-elevated duct strength, S_s (m), using approach (1)

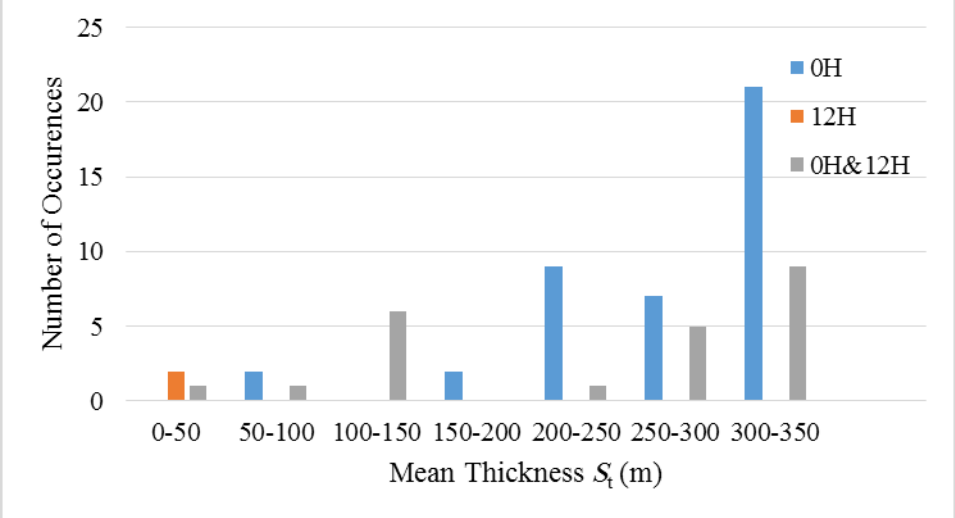

Figure 9.8: Surface-elevated duct thickness, S_t (m), using approach (1)

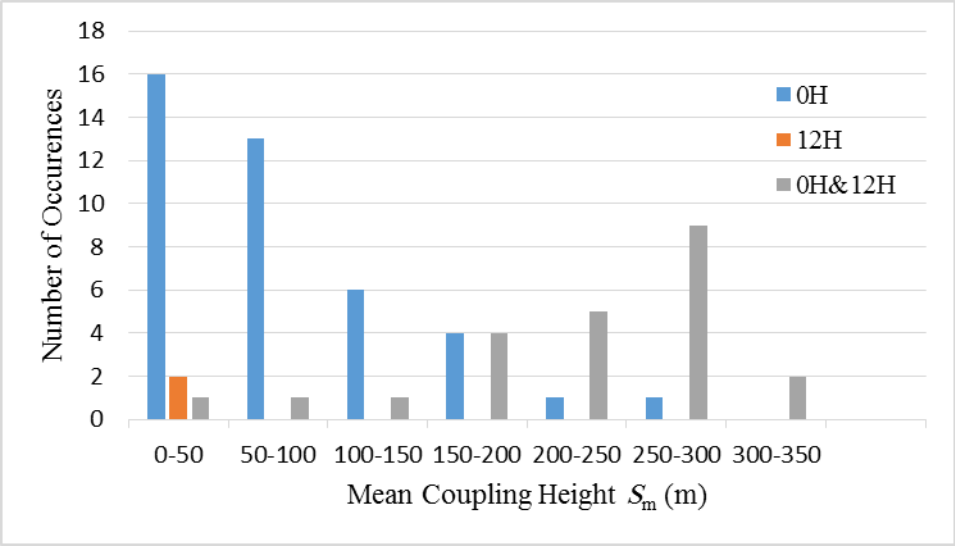

Figure 9.9: Surface-elevated duct height of max M , S_m (m), using approach (1)

The elevated duct occurrence statistics of the mean strength, thickness, base height and coupling height parameters are given in Figure **9.10**, Figure **9.11**, Figure **9.12** and Figure **9.13**, respectively. At 0H, the mean elevated duct strength is below 4 M-units for around 72% of the events, while the strength is found to be below 2 M-units for 77% of time at 12H. The combined 0H&12H modified refractivity profiles show that the elevated duct strength does not exceed 2 M-unit for 59% of events. For 12H and 0H&12H reference times, the duct thickness is below 100 m for around more than 57% of the events, except at 0H, where the thickness is found to be between 150 m and 200 m for around 24% of the time. The results of E_b parameter show that the heights are below 50 m or above 200 m for most of the events at 0H and 12H, respectively. The E_m height is found to vary significantly at 0H, while it is above 150 m for around 85% of events at 12H.

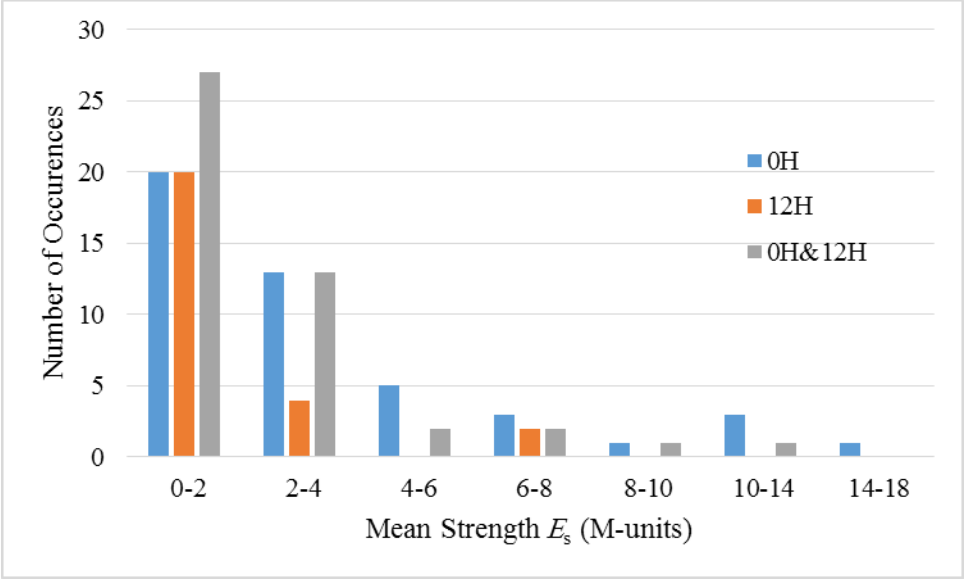

Figure 9.10: Elevated duct strength, E_s (m), using approach (1)

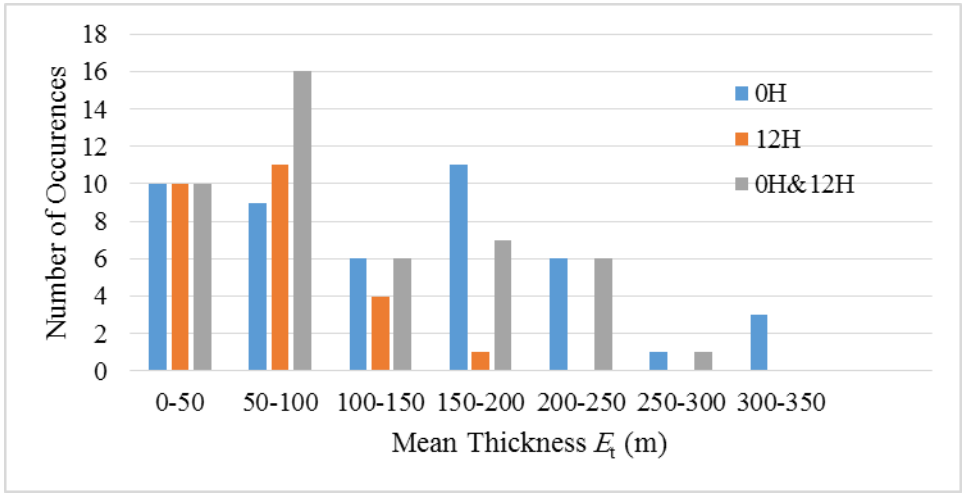

Figure 9.11: Elevated duct thickness, E_t (m), using approach (1)

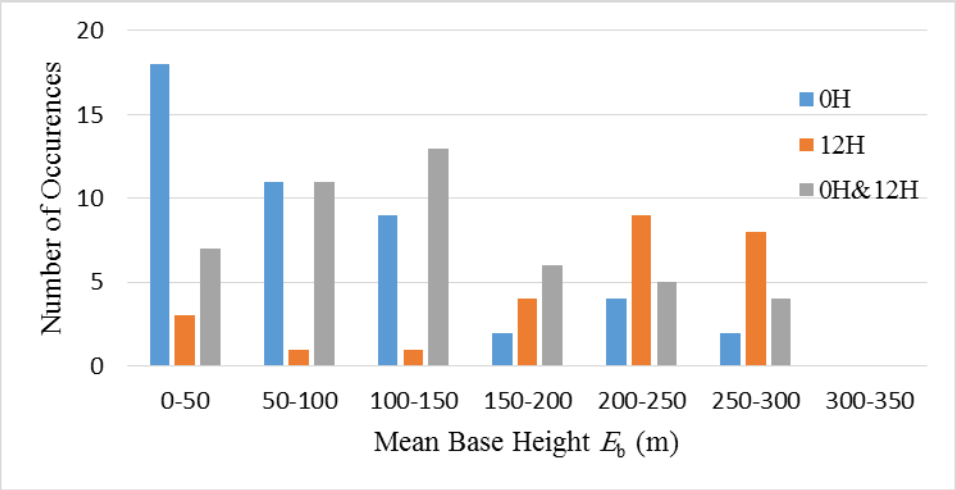

Figure 9.12: Base height of elevated duct, E_b (m), using approach (1)

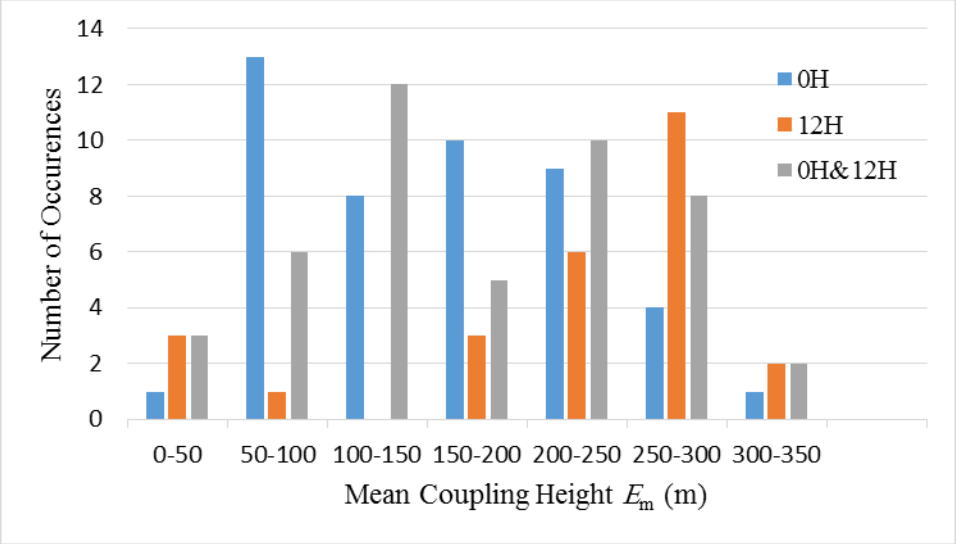

Figure 9.13: Mean coupling height, E_m (m), or height of max M, of elevated duct using approach (1)

9.2.2 Duct analysis using approach (2) and comparison with approach (1) results

The mean monthly distributions of the three duct types are evaluated using both introduced approached by averaging the modified refractivity parameters at the specified altitudes of 5 m resolution over each month for same time reference. The results of both approaches are compared at 0H for the month of July. In approach (1), the mean modified refractivity at the reference times are averaged for the given heights over the whole seventeen years. Then, the mean hourly *M* profiles are analysed to study duct characteristics. The mean M profiles at 0H of July from 1997 to 2013 is given in Figure **9.14**. Some curves show the possibility of having two duct types in the same given time. For 2013, the analysis of mean *M* profile shows the occurrence of two elevated ducts at 0H, while no duct phenomenon is observed from the mean *M* profile analysis at 12H. These results cannot be matched with the results obtained at 0H and 12H from the analysis of the instantaneous hourly *M* profiles using approach (2) given in Figure **9.16** and Figure **9.17**.

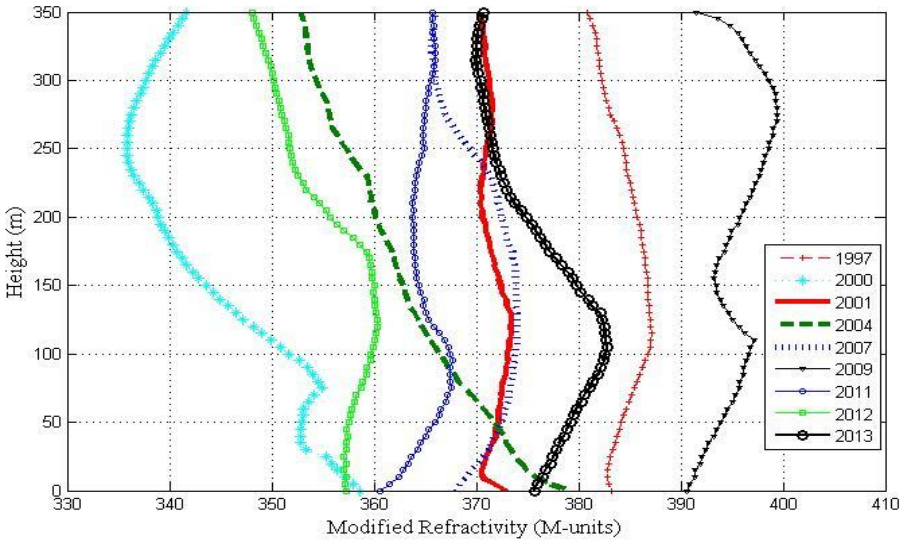

Figure 9.14: Mean annual variations of vertical modified refractivity over 350 m above ground for July at 0H for selected years from 1997 to 2013 using approach (1)

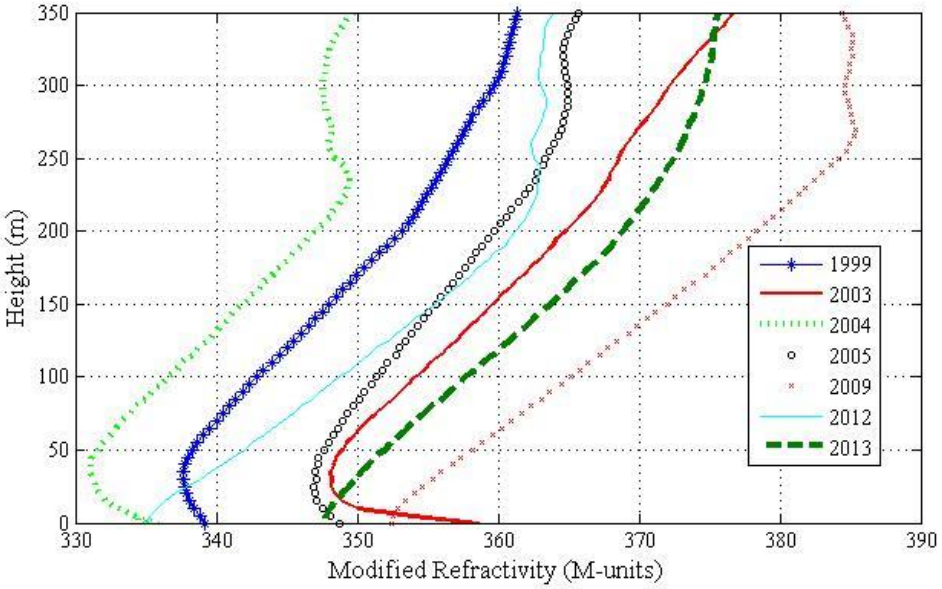

Figure 9.15: Mean annual variations of vertical modified refractivity over 350 m above ground for July at 12H for selected years from 1997 to 2013 using approach (1)

Using the approach (2), Figure **9.16** shows the instantaneous hourly *M* profiles at 0H for selected days in the month of July 2013. All duct types are observed with considerably larger duct thickness and strength for the elevated and surface-elevated ducts compared with approach (1). Although all duct types are obtained, the surface-based ducts are frequently observed at 12H compared with 0H. The duct parameters are found to vary over wide spans when the reliable measurements of *M* parameters at the given heights are utilized in approach (2) for studying the vertical *M* profiles at the reference times.

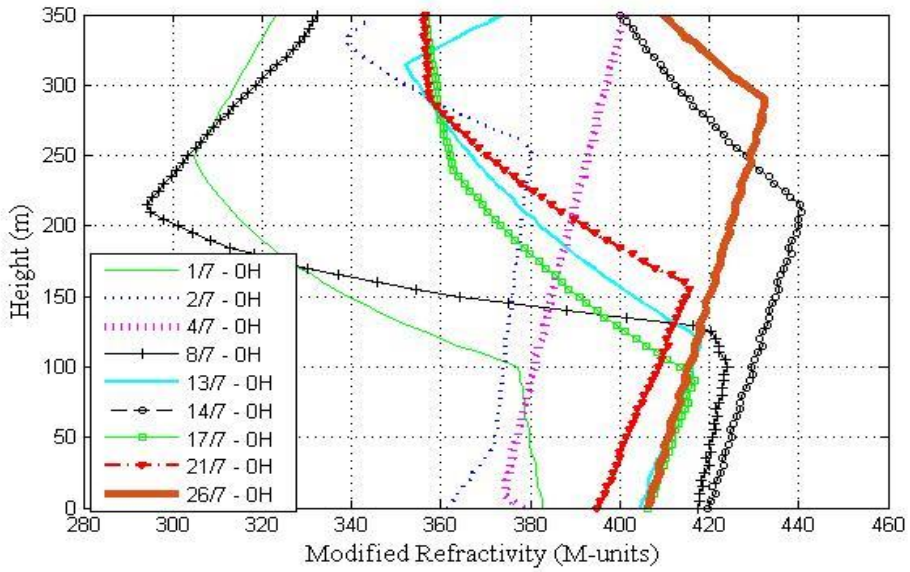

Figure 9.16: Instantaneous hourly variations of vertical modified refractivity over 350 m above ground for selected days of July 2013 at 0H using approach (2)

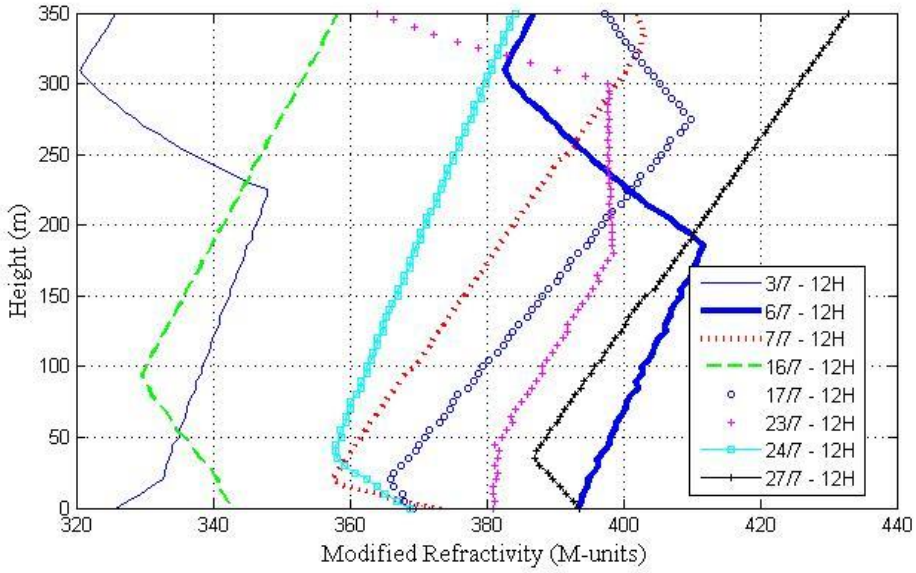

Figure 9.17: Instantaneous hourly variations of vertical modified refractivity over 350 m above ground for selected days of July 2013 at 12H using approach (2)

The statistics of duct parameters for July are compared using the approaches (1) and (2), considering all sets of data at 0H, 12H and 0H&12H. The mean July results using approach (1) from 1997 to 2013 for the surface (surface and elevated-surface) and elevated ducts are given in Table 9-4 and Table 9-5, respectively, based on the analysis of the mean hourly *M* profiles. The elevated duct occurrence probability is found to be more coherent with ITU maps compared with the surface-based ducts of July and the long-term mean duct statistics over the whole period. The results obtained for other parameters are still not in good coherent with ITU maps.

Table 9-4: Mean surface and surface-elevated duct statistics (1997-2013) using approach (1) compared with ITU Maps

Duct Characteristics	Surface			Elevated Surface			ITU Value
	Mean	Min	Max	Mean	Min	Max	
Occurrence Probability	34.50%			17.20%			35%
Mean Strength S_s (M-units)	7.45	0.31	26.27	11.65	0.29	31	25
Mean Thickness S_t (m)	102.8	15.0	350	323	220	350	200
Height of max *M* in Elevated-Surface Duct	-	-	-	130	50	260	-
Affected Frequency (GHz)	0.346	6.197	0.055	0.062	0.110	0.055	0.127

Table 9-5: Mean elevated duct statistics (1997-2013) using approach (1) compared with ITU Maps

Duct Characteristics	Elevated			ITU Values
	Mean	Min	Max	
Occurrence Probability	34.50%			30%
Mean Strength E_s (M-units)	2.72	0.16	17.17	15
Mean Thickness E_t (m)	113.4	13	343	300
Mean Base Height of Elevated Duct E_b (m)	128.7	2	295	800
Coupling Height E_m (m) / Height of Max *M* in Elevated Duct	179.51	5	340	800
Affected Frequency (GHz)	0.298	7.680	0.057	0.069

The duct statistics using the approach (2) for July 2013 are given in Table 9-6,

Table 9-7 and Table 9-8, and compared results obtained for the months of April, May and December 2013 as well. As given in Table 9-4, the ITU values of occurrence, strength and thickness of the surface based ducts are found to be 35%, 25 m and 200, respectively, leading to minimum frequency of 127 MHz to be trapped. In comparison with ITU maps, the occurrence probability of surface based ducts are found to be below-estimated for May and July, while over-estimated for December. The ITU values of the surface duct thickness are over-estimated for all months when compared with the mean monthly results obtained in this study. Similar observation for the duct strength, except for July, where ITU value is found to be below-estimated.

Table 9-6: Surface duct statistics using approach (2) compared with ITU Maps

(a) April and May 2013

Duct Characteristics	April 2013			May 2013		
	Mean	Min	Max	Mean	Min	Max
Occurrence	20.0%			32.3%		
Strength, S_s (M-units)	5.3	0.2	29.9	10.5	0.7	58.6
Thickness, S_t (m)	43.8	5.0	165.0	93.8	5.0	310.0
Affected Frequency (GHz)	1.244	32.199	0.170	0.397	32.199	0.066

(b) July and December 2013

Duct Characteristics	July 2013			Dec 2013		
	Mean	Min	Max	Mean	Min	Max
Occurrence	27.0%			4.8%		
Strength, S_s (M-units)	13.0	0.3	77.9	2.7	0.7	5.6
Thickness, S_t (m)	63.8	10.0	350.0	18.3	15.0	25.0
Affected Frequency (GHz)	0.706	11.384	0.055	4.586	6.197	2.880

Table 9-7: Surface-elevated duct statistics using approach (2) compared with ITU Maps

(a) April and May 2013

Duct Characteristics	April 2013			May 2013		
	Mean	Min	Max	Mean	Min	Max
Occurrence	11.7%			19.4%		
Strength, S_s (M-units)	17.2	2.3	38.8	38.3	4.2	75.1
Thickness, S_t (m)	178.3	55.0	290.0	240.4	100.0	350.0
Coupling Height, S_m (m) (Height of max M)	70.8	20.0	215.0	98.8	10.0	260.0
Affected Frequency (GHz)	0.151	0.883	0.073	0.097	0.360	0.055

(b) July and December 2013

Duct Characteristics	July 2013			Dec 2013		
	Mean	Min	Max	Mean	Min	Max
Occurrence	27.0%			6.5%		
Strength, S_s (M-units)	48.9	6.7	129.5	35.9	29.7	45.3
Thickness, S_t (m)	305.0	95.0	350.0	211.3	140.0	255.0
Coupling Height, S_m (m) (Height of max M)	138.5	15.0	250.0	93.8	30.0	145.0
Affected Frequency (GHz)	0.068	0.389	0.055	0.117	0.217	0.088

Table 9-8: Elevated duct statistics using approach (2) compared with ITU Maps

(a) April and May 2013

Duct Characteristics	April 2013			May 2013			ITU Values
	Mean	Min	Max	Mean	Min	Max	
Occurrence	16.7%			11.3%			30%
Strength, E_s (M-units)	13.5	1.2	30.8	9.4	0.7	28.1	15
Thickness, E_t (m)	203.1	31.0	338.0	155.4	48.0	307.0	300
Base Height of Elevated Duct, E_b (m)	64.4	6.0	319.0	83.1	2.0	302.0	800
Coupling Height, E_m (m) (Height of max M)	145.5	10.0	340.0	140.7	10.0	330.0	800
Affected Frequency (GHz)	0.124	2.086	0.058	0.186	1.083	0.067	0.069

(b) July and December 2013

Duct Characteristics	July 2013			Dec 2013			ITU Values
	Mean	Min	Max	Mean	Min	Max	
Occurrence	23.8%			4.8%			30%
Strength, E_s (M-units)	10.0	0.7	25.5	16.4	1.3	39.0	15
Thickness, E_t (m)	166.8	48.0	330.0	117.0	53.0	181.0	300
Base Height of Elevated Duct, E_b (m)	124.2	2.0	275.0	139.7	69.0	233.0	800
Coupling Height, E_m (m) (Height of max M)	218.3	10.0	315.0	168.3	95.0	280.0	800
Affected Frequency (GHz)	0.167	1.083	0.060	0.284	0.933	0.148	0.069

The hourly analysis of both surface and surface-elevated ducts shows higher occurrence probability during May and July, which exceeds 50% of the time, while probability is found to be around 10% for December. The hourly strengths of surface and surface-elevated ducts vary from 0.2 to 78 M-units and from 2.3 to 130 M-units, respectively. The mean monthly

strength oscillates from 2.7 M-units in December to 13 M-units in July. The hourly surface and surface-elevated duct thickness fluctuates in spans of 345 m, from 5 to 350 m, and 295 m, from 55 to 350 m, respectively. The mean monthly thickness of the surface duct is found to vary from 18.3 m in December to 93.8 in May, while the mean surface-elevated duct thickness varies from 178.3 m in April to 305 m in July. The duct thickness analysis shows that the minimum signal frequencies to be trapped within the surface based ducts differ from 55 MHz in July to 32 GHz in April for the surface duct and from 55 MHz to 880 MHz for the surface-elevated duct. These results show considerable differences when compared with the value calculated from proposed ITU thickness value of 127 MHz for the area under study. In case of the surface-elevated duct, the hourly coupling heights, S_m, is found to oscillate from 10 to 260 m, while the mean S_m varies from 70.8 m in April to 138.5 m in July.

The elevated duct occurrence is found to be higher in summer than in winter with time percentages of around 24 % and 5 % in July and December 2013, respectively. The hourly duct strength changes from 0.7 to 39 M-units. The mean monthly strength differs from 9.4 M-units in May to 16.4 M-units in December. The hourly duct thickness varies from 31 to 338 m, while the mean monthly thickness differs from 117 m in December to 203 in April. The minimum signal frequencies that can be trapped, which are calculated from the duct thickness analysis, vary from 58 MHz to 2.1 GHz in April.

The hourly occurrence statistics for the duct strength and thickness for the three duct types during the months of April, May, July and December are given in the following figures

from Figure **9.18** to Figure **9.41**. The surface duct statistics for the four months are displayed from Figure **9.18** to Figure **9.25**, while the surface-elevated duct statistics are given from Figure **9.26** to Figure **9.33**. It has been observed that surface duct thickness of more than 50% of observations in each month are found to be below 20 m resulting in high probability of trapping signal with frequencies from 4 to 32 GHz within the surface ducts in the area under study. The duct strength is found to be below 10 M-units for majority of observations.

The surface-elevated duct thickness is above 200 m for most the events, except at 0H in April where more observations obtained below 100 m. The duct strength is below 60 M-units for most of the events, which are higher than the surface duct strength observations.

The elevated duct occurrence statistics are shown from Figure **9.34** to Figure **9.41** for the four months. The obtained duct thickness is below 200 m for most of the events, except at 0H in April where more elevated duct observations obtained with thickness above 250 m.

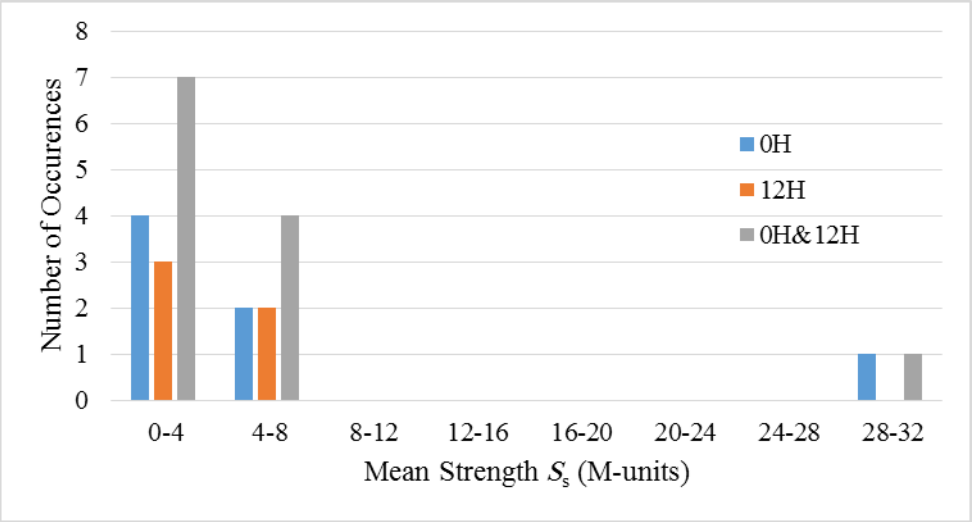

Figure 9.18: Hourly surface duct strength S_s (m) statistics, April 2013

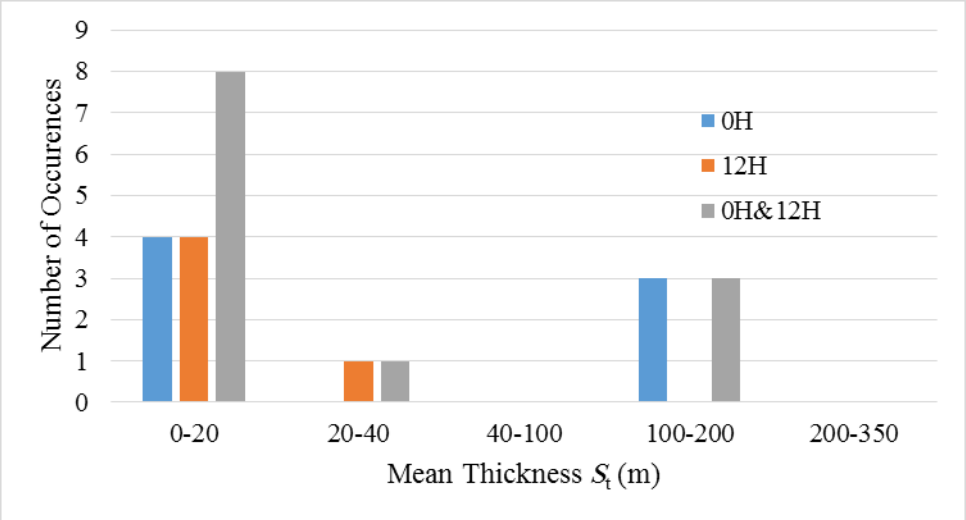

Figure 9.19: Hourly surface duct thickness S_t (m), April 2013

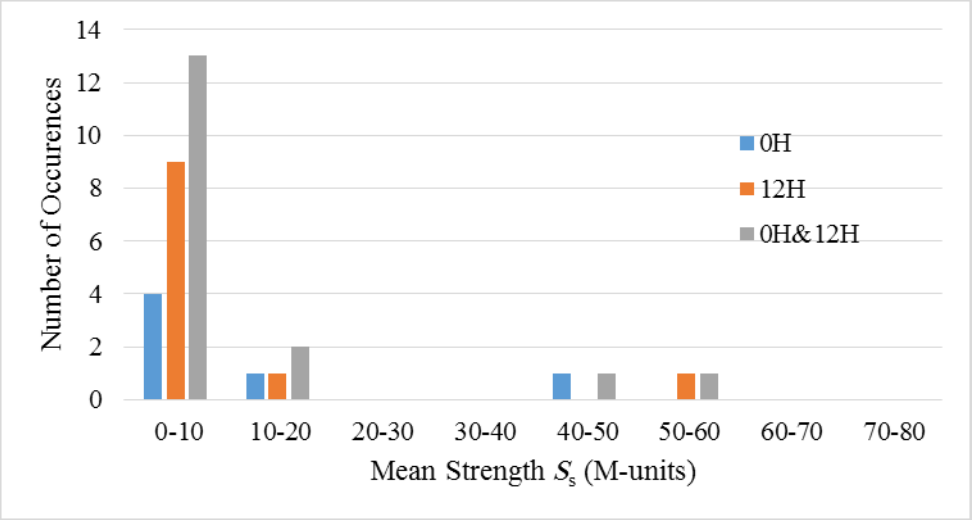

Figure 9.20: Hourly surface duct strength S_s (m) statistics, May 2013

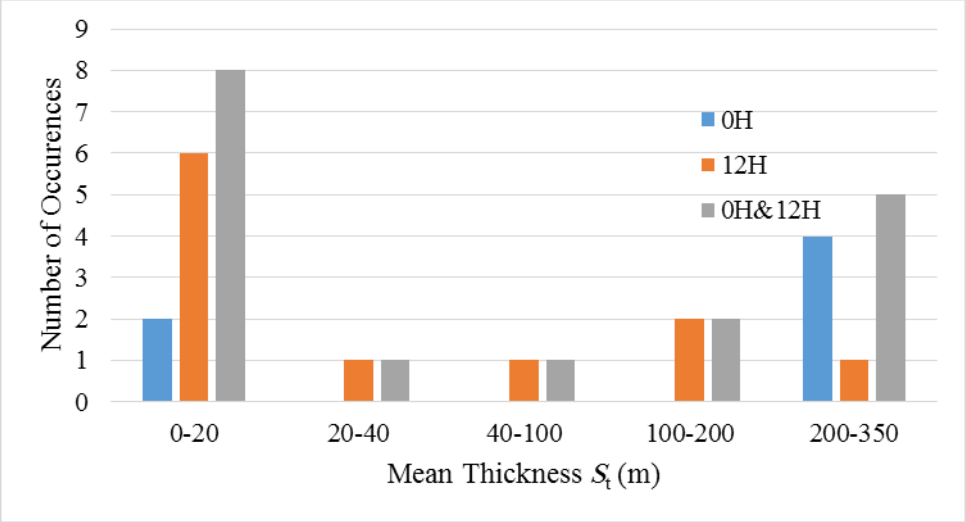

Figure 9.21: Hourly surface duct thickness S_t (m), May 2013

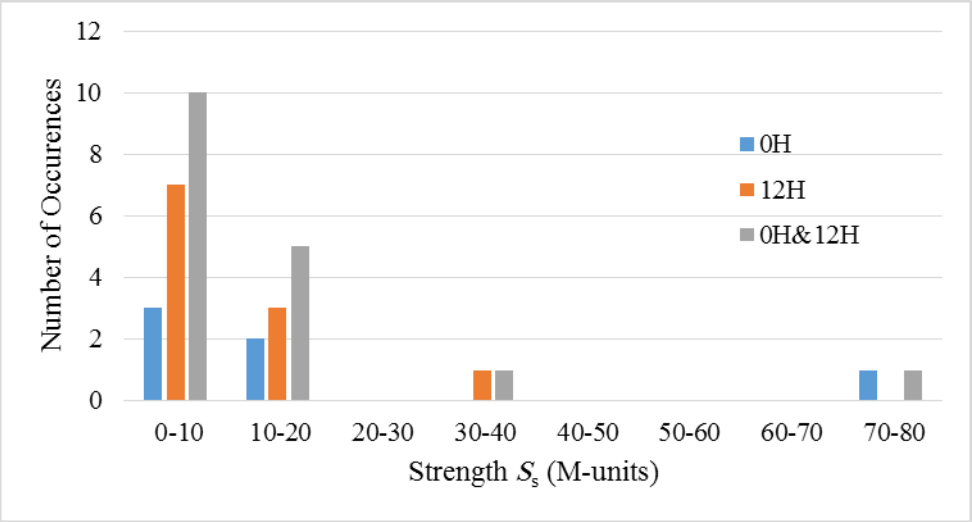

Figure 9.22: Hourly surface duct strength S_s (m) statistics, July 2013

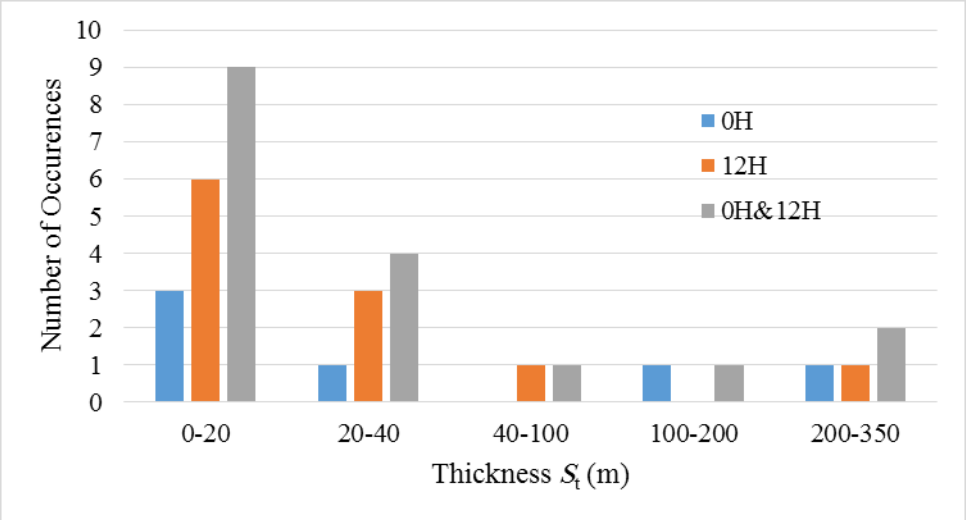

Figure 9.23: Hourly surface duct thickness S_t (m), July 2013

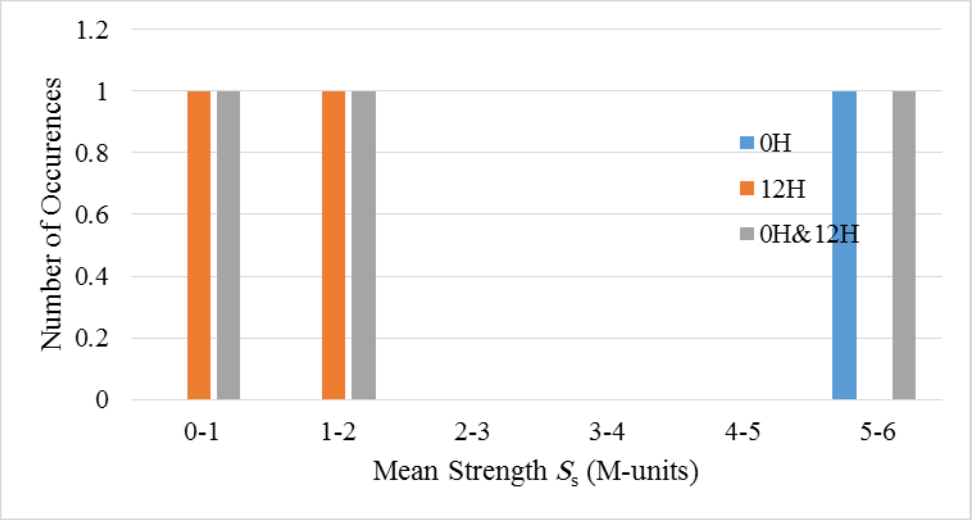

Figure 9.24: Hourly surface duct strength S_s (m) statistics, Dec. 2013

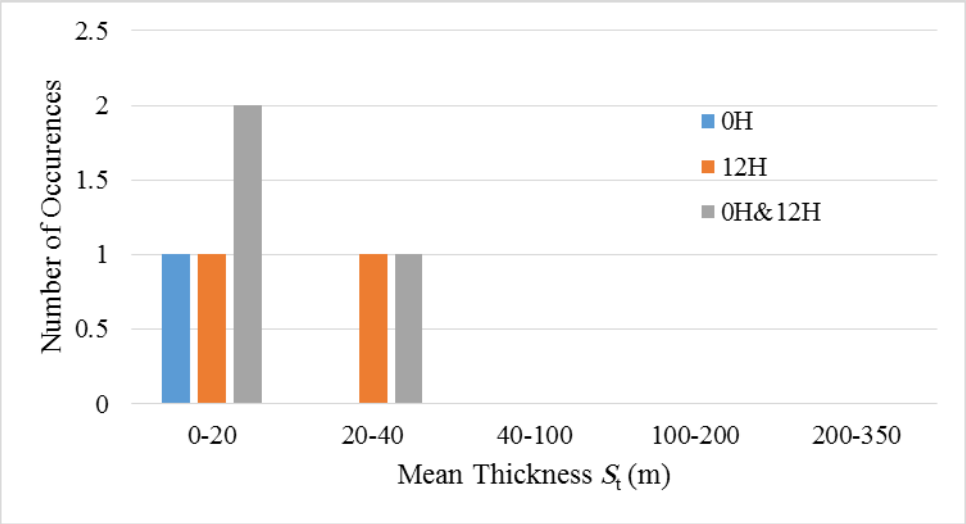

Figure 9.25: Hourly surface duct thickness S_t (m), Dec. 2013

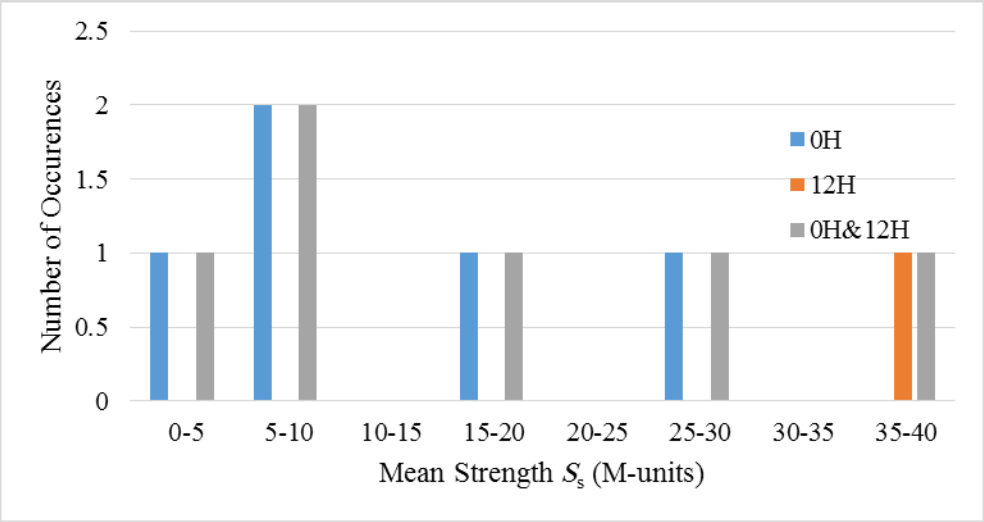

Figure 9.26: Hourly surface-elevated duct strength S_s (m) statistics, April 2013

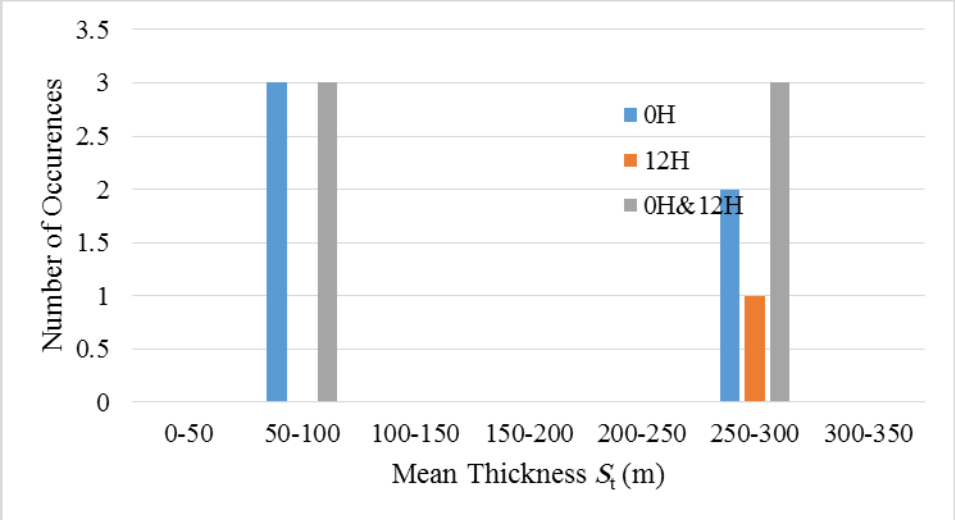

Figure 9.27: Hourly surface-elevated duct thickness S_t (m), April 2013

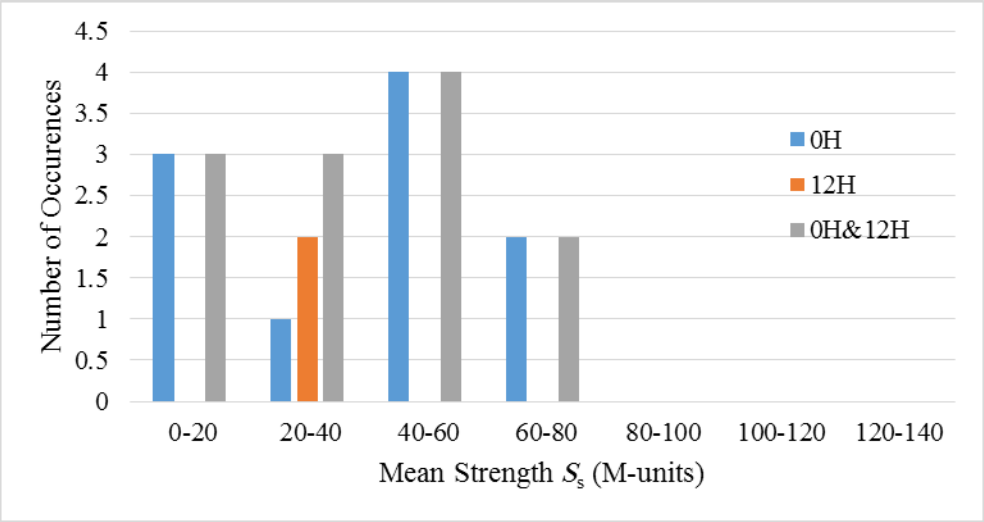

Figure 9.28: Hourly surface-elevated duct strength S_s (m) statistics, May 2013

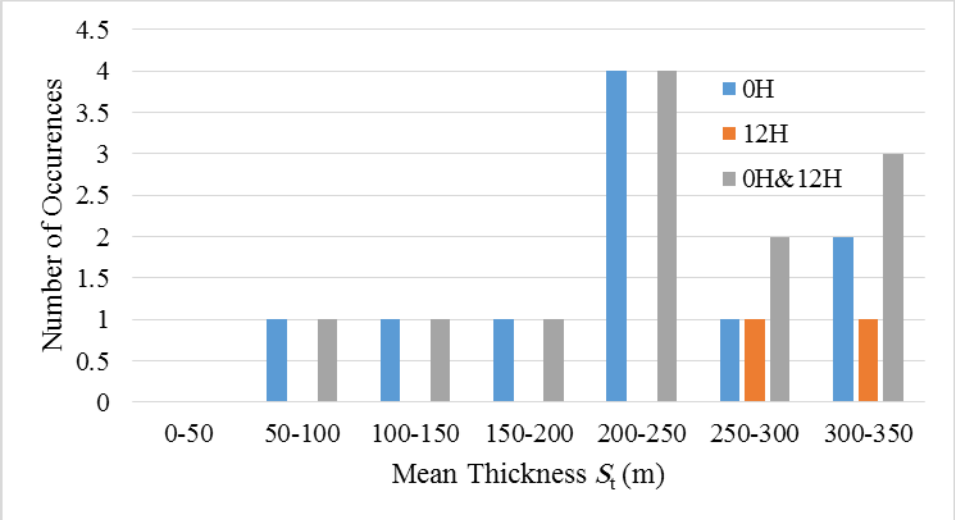

Figure 9.29: Hourly surface-elevated duct thickness S_t (m), May 2013

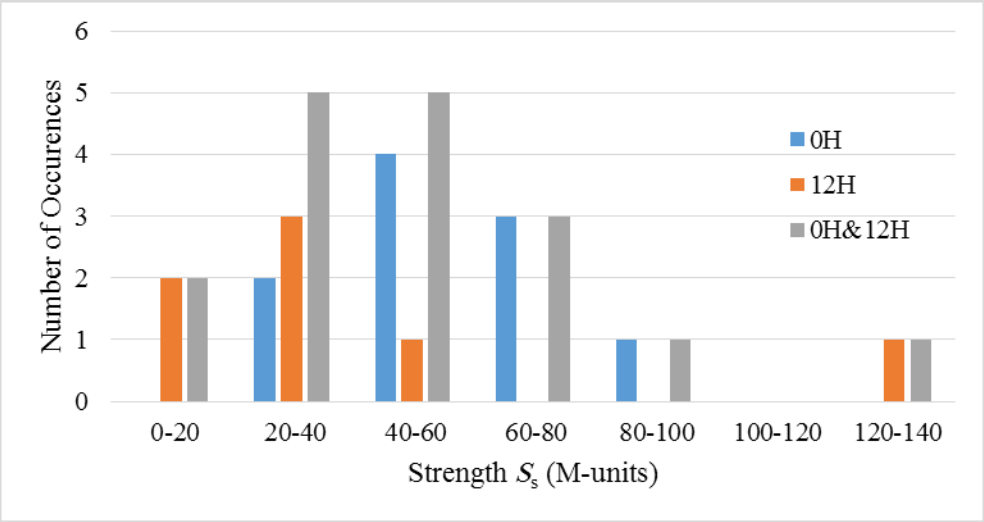

Figure 9.30: Hourly surface-elevated duct strength S_s (m) statistics, July 2013

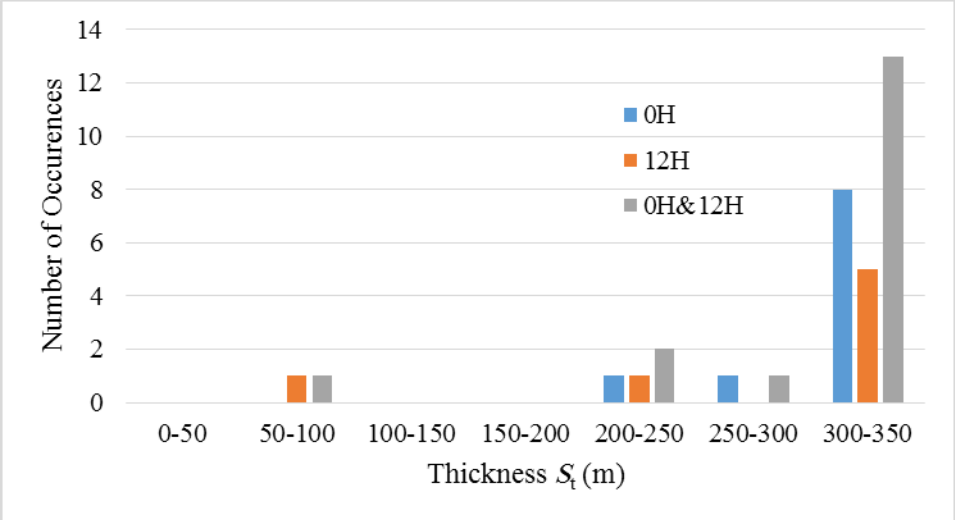

Figure 9.31: Hourly surface-elevated duct thickness S_t (m), July 2013

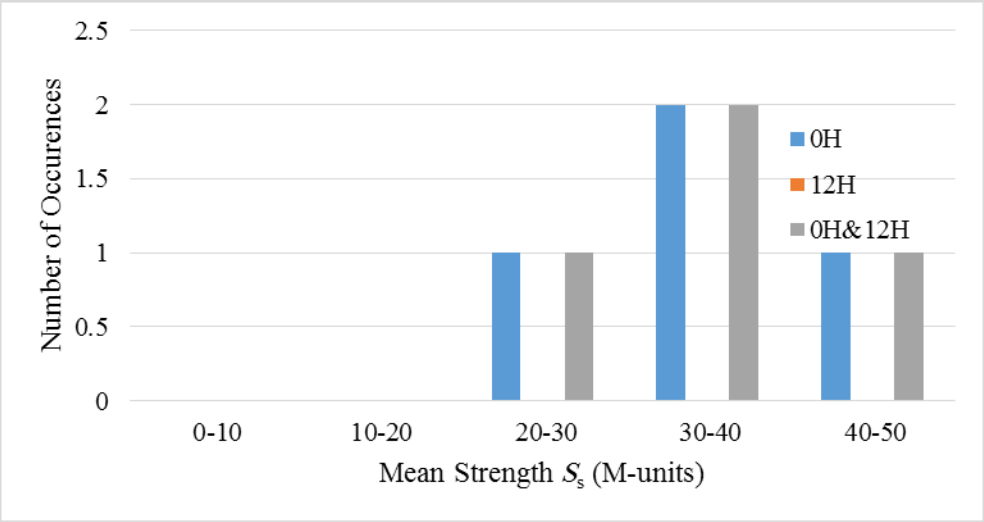

Figure 9.32: Hourly surface-elevated duct strength S_s (m) statistics, Dec 2013

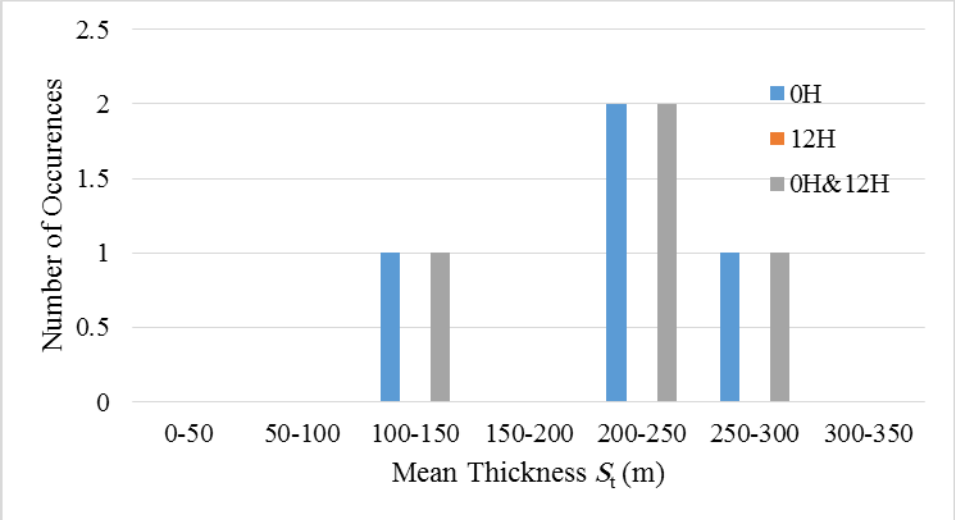

Figure 9.33: Hourly surface-elevated duct thickness S_t (m), Dec 2013

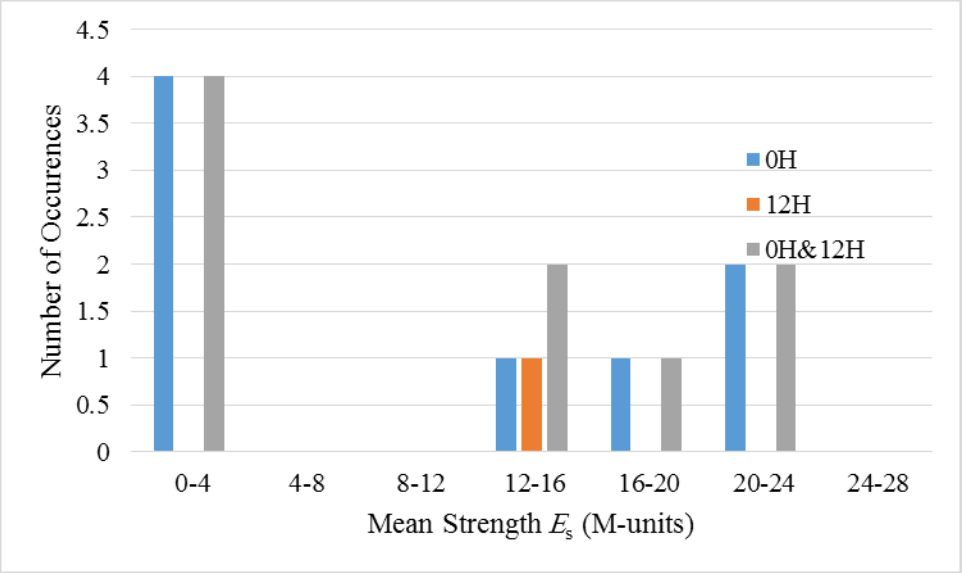

Figure 9.34: Hourly elevated duct strength S_s (m) statistics, April 2013

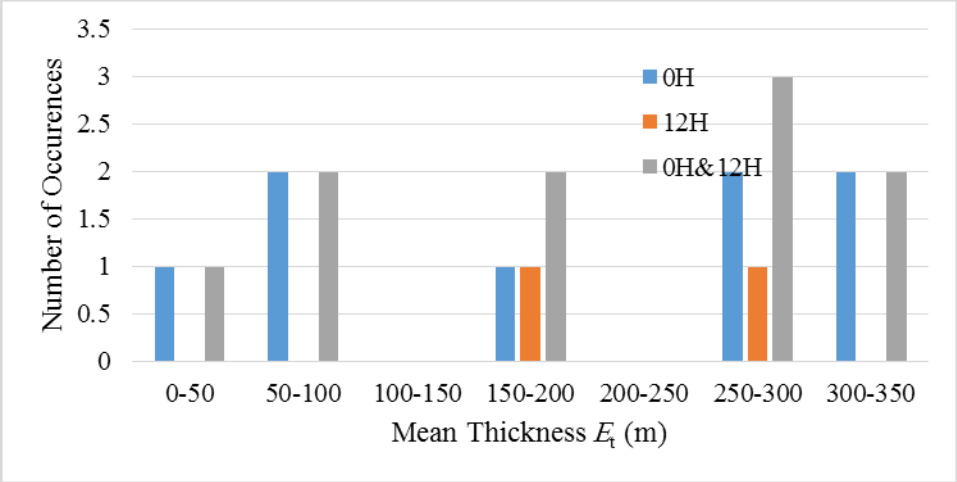

Figure 9.35: Hourly elevated duct thickness S_t (m), April 2013

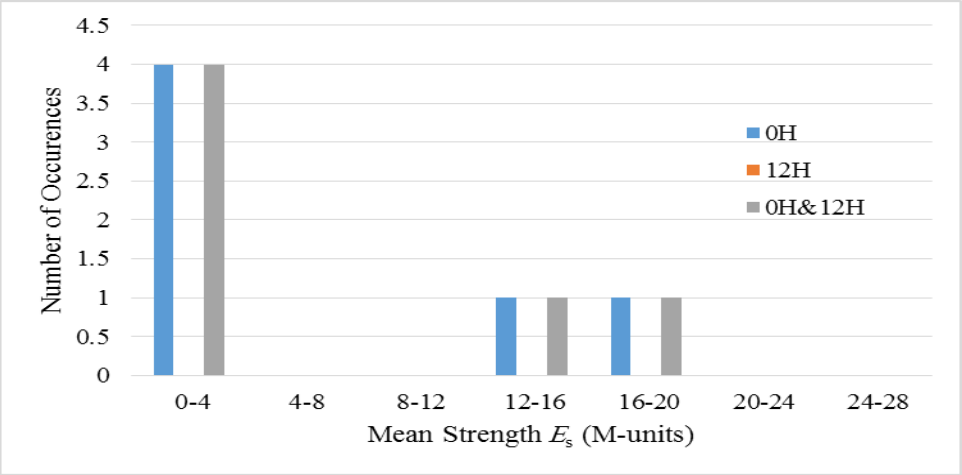

Figure 9.36: Hourly elevated duct strength S_s (m) statistics, May 2013

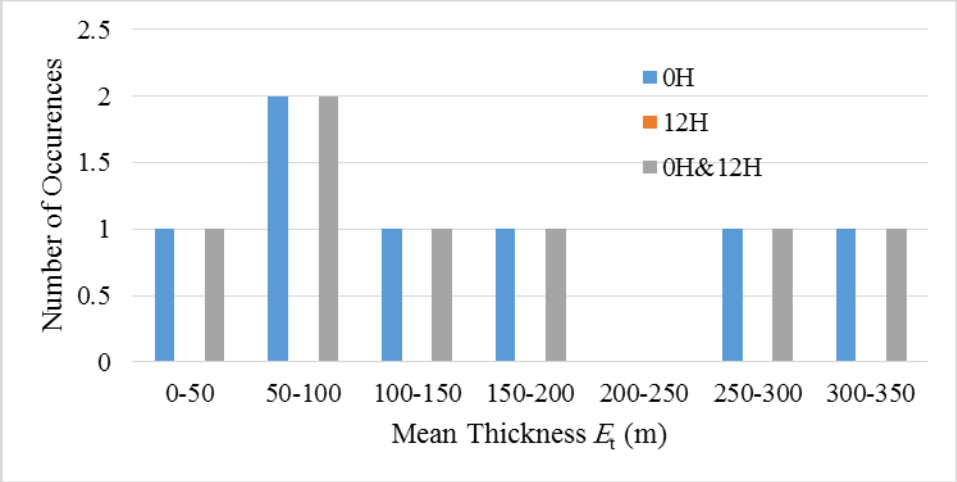

Figure 9.37: Hourly elevated duct thickness S_t (m), May 2013

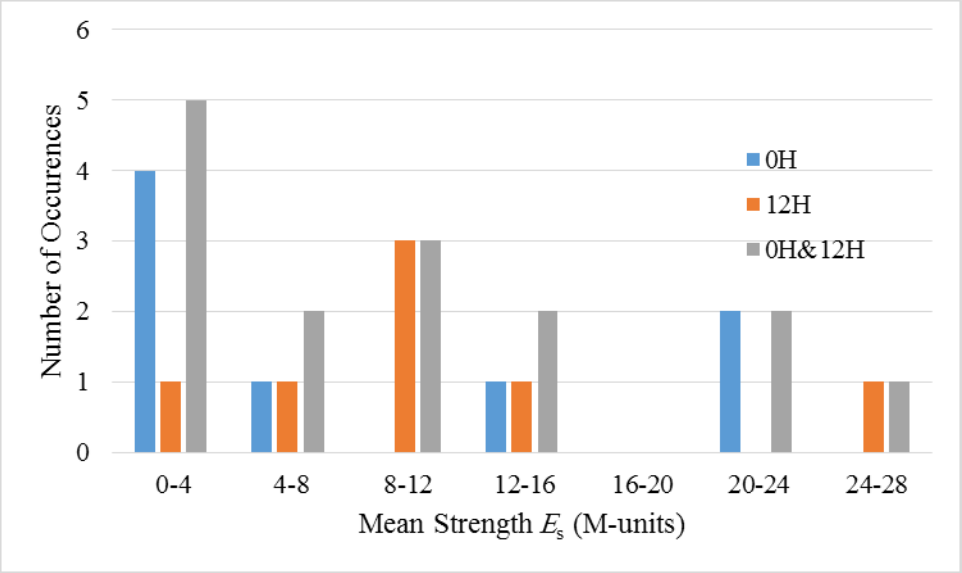

Figure 9.38: Hourly elevated duct strength S_s (m) statistics, July 2013

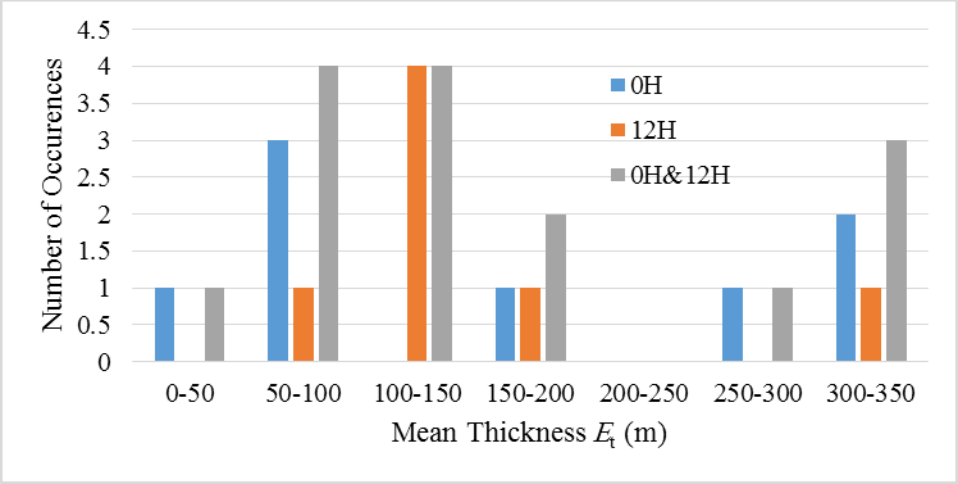

Figure 9.39: Hourly elevated duct thickness S_t (m), July 2013

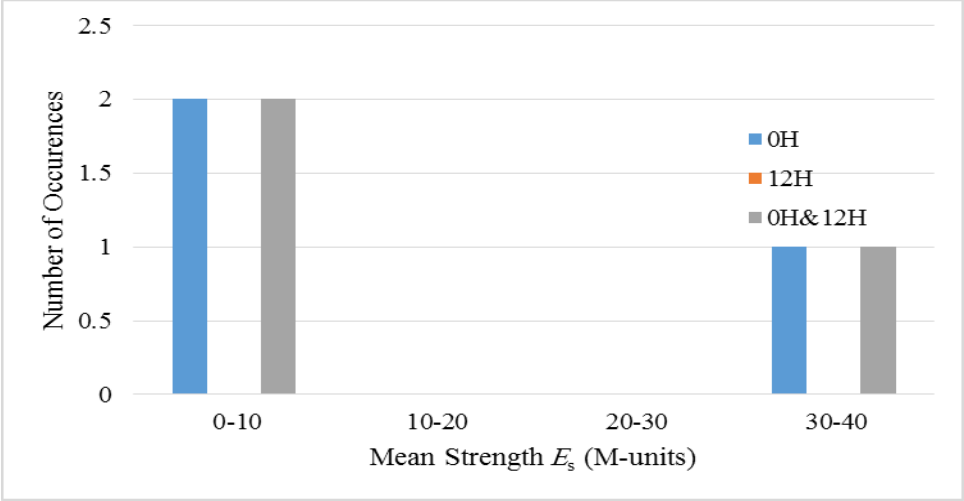

Figure 9.40: Hourly elevated duct strength S_s (m) statistics, Dec 2013

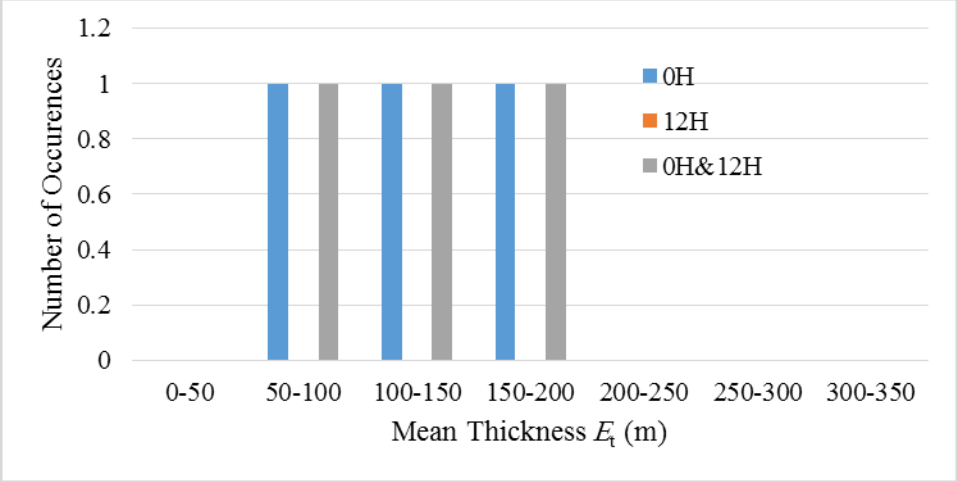

Figure 9.41: Hourly elevated duct thickness S_t (m), Dec 2013

9.3 Impact analysis of atmospheric ducts

The duct may have positive or negative consequences in the performance of the operating wireless systems. Trans-horizon links makes use of the duct phenomenon to strengthen the propagating signals over the horizon, in particular when both transmitter and receiver are

located within the atmospheric duct. On the other hand, the wave propagation over long distances may cause interference to other receivers located within the trapping duct layer. In addition, the receivers located outside the duct may suffer from considerable fading when the incident angle is below 1^0 with respect to the duct layer or within approximately 0.5^0 from the horizontal [88].

The following factors have to be considered and set carefully within areas with high probability of duct occurrence:

a) The dimensions of duct and its parameters during the system design, in particular the thickness and strength in case of surface based ducts, in addition to the base height for the elevated duct.

b) Antenna heights for both transmitter and receiver with respect to the frequently occurring duct type and considering the mostly experienced duct thickness.

c) Antenna tilt and elevation angle such that setting the incident angle with respect to the duct layer depending on the targeted application. For example, small angle has to be maintained with the horizontal boundary layer in case of trans-horizon link to make use of ducting phenomenon for propagating over long distances in which there is no line of sight between the antennas. In order to overcome the negative interference and fading impact of atmospheric duct, elevation angle with respect to the horizontal line has to exceed 0.5^0, preferably above 1^0, to avoid getting trapped by the duct.

d) Space diversity with properly setting diversity antenna heights with enough separation from the main antennas in order to ensure the constructive multipath effect rather than destructive one and to make use of signal strength improvement from the second path, in case of any signal diffraction on the main path.

e) Frequency band and the selected carriers within the band. The signal coupling within the atmospheric duct is related to its wavelength and the duct thickness. In case of interference of fading situations due to ducting, the designers can change the carrier frequency or shift to another band if technically or economically feasible.

f) Frequency diversity with enough frequency separation to overcome trapping or fading of one carrier by utilizing other carriers.

g) Activation of adaptive modulation configuration in order to ensure better service availability in addition to enhanced robustness and reliability of the link on the expense of throughput and capacity degradation in case of significant signal fading.

h) Reducing the capacity configurations and static modulation to enhance the system's reliability through improved power configurations and receiver sensitivity.

i) Use reliable area specific propagation parameters, whenever available, for designing wireless systems, such as *k*-factor to ensure energy path and Fresnel zone clearance and point refractivity gradient to ensure high link's availability and less service interruption or signal fluctuations.

j) Activation of automatic power control to manage transmission power to maintain the received signal strength at an acceptable level, as possible.

9.4 Final Remarks

The critical atmospheric ducting phenomenon were studied using seventeen years of high-resolution upper-air meteorological data from 1997 to 2013 in the subtropical Arabian Gulf region. Radiosonde data of 5 m vertical resolution was considered at Abu Dhabi. Three duct types were statistically analysed; namely surface, surface-elevated and elevated ducts, to dimension the duct parameters in the area under study. The duct could be formed due to several atmospheric phenomena considering that signal trapping was found to rely on the angle of incidence and the wavelength of propagating signals. Empirical equation was used to evaluate the minimum frequencies that could be trapped within each observed duct depending on the duct thickness dimensioning.

The vertical hourly profiles of the modified refractivity parameter has been developed over the entire study period and thoroughly analysed using two different approaches after evaluating the modified refractivity from the raw meteorological data. The ITU definitions for the three duct types and their parameters were considered as a reference for the analysis. In the first approach (1), the modified refractivity parameter was averaged for the given heights with respect to reference times, 0H, 12H or combined 0H&12H, as well as the reference monthly or yearly periods. The mean vertical *M* profile was then analysed for each reference period. In the second approach (2), hourly vertical *M* profiles were evaluated from the raw meteorological data and the analysed to dimension the duct parameters. The

obtained parameters for the same duct type were averaged to evaluate the monthly, yearly and long-term statistics.

It was noted that the duct occurrence probability exceeded 50% of the time during summer months. The surface based ducts; including both surface and surface-elevated, had higher occurrence probability in UAE and the Gulf region than the elevated duct. In winter, the average thickness of surface duct was below 25 m. The surface-based duct observations were higher at 12H compared with 0H.

The results obtained using both approaches for all duct types were not in good coherence with ITU maps considering that the surface-elevated duct is part of the surface based duct category. In comparison with ITU maps, the occurrence probability was found to be below-estimated for the surface based ducts and overestimated for the elevated duct, when using mean statistics approach (1). The surface duct strength was less than 15 M-units for more than 70% of time, while thickness was less than 50 m for more than 50% of time.

The approach (2) was applied on the data of April, May, July and December 2013. The surface duct thickness was found to be below 20 m for more than 50% of all studied months with trapping frequencies within the range from 4 to 32 GHz. The duct strength was below 10 M-units for majority of observations. The summer showed higher occurrence of elevated duct with around 24% in July 2013.

The analysis showed that VHF, UHF and SHF signals could be trapped through different duct types. The minimum signal frequencies that could be trapped were obtained using both approaches from the duct thickness analysis. The frequencies varied from 55 MHz to 32 GHz for the surface based ducts and from 57 MHz to 7.7 GHz for the elevated duct using approach (1). Similar result were obtained for surface based ducts using approach (2), while frequencies oscillated from 58 MHz to 2.1 GHz in case of the elevated duct.

The hourly, monthly and yearly distributions of duct parameters were investigated using the two approaches, including thickness and strength parameters for the three duct categories in addition to the coupling and base heights for the elevated ducts, and results were provided. The results obtained in this study makes the practical feasibility of using the mean long-term duct parameters of ITU maps is questionable for designing the wireless systems in various areas.

Several measures were introduced that could be practically implemented to manage the impact of ducting phenomena such as the selection of antenna height and elevation angle, operating frequency carrier and space diversity.

The impact of atmospheric ducts and other prevailing anomalous propagation conditions on the performance of operating wireless systems in the Arab Gulf region will be

investigated in chapter 10. The signal strength measurements are gathered from many PTP MW links and some fading events are examined.

Chapter 10

ANALYSIS OF WIRELESS SIGNAL STRENGTH MEASUREMENTS

10.1 Introduction

Microwave line-of-sight links are designed taking into account the curvature of rays in a stratified atmosphere over the curved earth [12, 24]. Variation of atmospheric parameters such as temperature and relative humidity dominate the vertical refractivity profile. The prevailing meteorological conditions in a specific region determine the extent of refraction. The analysis of reliable surface and upper-air meteorological data is essential to predict the fading and interference probabilities of the operating wireless systems in the area under study. Statistical analysis of refractivity and its vertical profile are essential for the prediction of anomalous propagation, such as sub- or super-refraction and ducting.

The predictions of received power levels, signal fading and link availability have been estimated using ICS Telecom planning software [79], for each of the candidate point to point LOS microwave links. The signal fading has been calculated considering different ITU-R recommendations and other standard propagation models. The effects of multipath and signals' reflection, vertical rate of refractive index, effective Earth radius factor, gas

attenuation and diffraction losses, have been taken into account. The path profiles have been drawn using 50 m resolution maps for UAE to ensure the clearance of the path according to the predefined antenna heights and the terrain type along the path. The calculated received power levels are compared to the actual measured signal strength considering the estimated attenuation values after analysing the meteorological data.

10.2 Selection Criteria of Microwave Links

A huge network of PTP MW links operating all over UAE within different frequency bands have been thoroughly studied to select the most feasible ones for our experiments. More than 2000 links have been initially analysed using the ICS Telecom. Several criteria have been used to select the candidate microwave links for this study. The main selection criteria are:

- Distance to Weather Station: The receiver site of the microwave link should be as close as possible to the surface or radiosonde weather stations in order to compare the analysed meteorological data with the field strength measurements.
- Capability for Remote Access: The possibility to access the links remotely by connecting the microwave equipment to remote computers through the highly secured network of Etisalat.
- Sites' Location: Spatial separation between the links considering different geographical natures and climates such as coastal, offshore and inland links.

- Frequency Bands: Links should be operating using different frequency channels to study the impact of the studied propagation parameters on the fading of signals with different frequencies and wavelengths.

The length of each microwave link has also been considered in the links' evaluation since the signals of long links are most likely to experience higher grades of refraction. However, the electromagnetic wave could also be exposed to different propagation phenomena over long distances which have to be studied carefully.

10.3 Challenges and Limitations

There are several challenges and limitations in the process of selecting the candidate microwave links and the management of their configurations for the research purpose. Some of these challenges are:

- Due to the cost implications of procuring several dedicated microwave links for the research purpose, the microwave links from the leading telecom operator in UAE have been utilized, which are originally installed for business reasons. The cost of installing a dedicated microwave link for research includes equipment, space rental at the towers, installation and maintenance, and frequency authorization costs. This could have the following drawbacks:

    - A link might be written-off and recovered due to several reasons:

        - Link's upgrade due to additional capacity requirement may require using new equipment with different frequency or which is not compatible with the remote access setup explained before.
        - The traffic can be provided to the site by another more stable technology such as fiber technology, which replaces the wireless solution. The microwave link solution is normally utilized to backhaul remote sites where cable infrastructure is not available.
        - Equipment failure and accordingly new equipment have to be used which might not be compatible with the current setup.

    - It might be required to change the link configuration during the study period due to any unexpected problem or to overcome intermittent outage errors due to signal fading.

- The difficulty incurred with the remote connectivity of the some potential candidate links. Some of the links which have been satisfying the previous criteria could not be selected because of the difficulty of accessing them remotely due to the following reasons:
    - There is no free port at the local Etisalat switch to connect the microwave equipment, at any of the two sites of the microwave link. For security reasons, adding a new switch to a site is a lengthy process that requires the involvement of several teams of the company.

    - The equipment is legacy and its hardware or software drivers are not compatible with the setup.

- The microwave links are not located at the same sites of the weather stations. Considering the current locations of the existing microwave links and weather stations, a microwave link is selected such that the distance to the nearest weather stations should be within 3 km.

- The resolutions of gathered data from various types of measurements are limited to the default available monitoring software of the equipment. The normal data resolution is a reading every 15 min, which needs to be saved manually to a local PC on a weekly basis. However, a higher resolution of a reading per each 1 min could be obtained for few links' sites using recently developed software. The following remarks should be considered for high resolution data:
    - Number of sites with high resolution readings is very limited due to huge bandwidth required to pull this traffic and accordingly the network gets congested.
    - Data should be saved manually to a local PC on every day.
    - Data with resolution of a reading per each 10 sec have been gathered for only one trial link in the city of Sharjah.

- Different types of microwave links have monitoring software with different capabilities. Old readings are overwritten with new data within short periods for some

candidate links. Although these links have succeeded in the evaluation stage and could be accessed remotely, they could not be selected due to the missing data. After investigation, some of the reasons for this problem are:

- Capacity and bandwidth of traffic channels are being wrongly utilized by other alarm data. For example, it was found that frequent alarms were sent over the network channels if any of the microwave equipment's ports are not used and not deactivated by the installation team.
- Limited capacity of the remote servers which are kept in the data center.

Some of the additional actions have been taken to overcome these limitations, such as:

- The links are being manually monitored on frequent basis to study any changes in the configurations and take them into account.
- Multiple candidate links, which are satisfying the criteria above, have been initially considered. The predictions of their link budgets and availability have been calculated using the ICS Telecom and provided in the relevant path profiles in the predictions' section below. The readings of their measurements are being gathered.

10.4 Links' Configurations and Performance Predictions of Candidate Microwave Links

The proper calculation of microwave link power budget is essential to guarantee a reliable and well performing wireless link in the real field. The design considers several

propagation parameters with values recommended by the ITU maps and table worldwide. The commercial ICS Telecom software is used to design and predict the performance of the microwave links for several scenarios and accordingly to find out the optimum link configurations. Figure 10.1 shows a sample radio channel for link budget calculation.

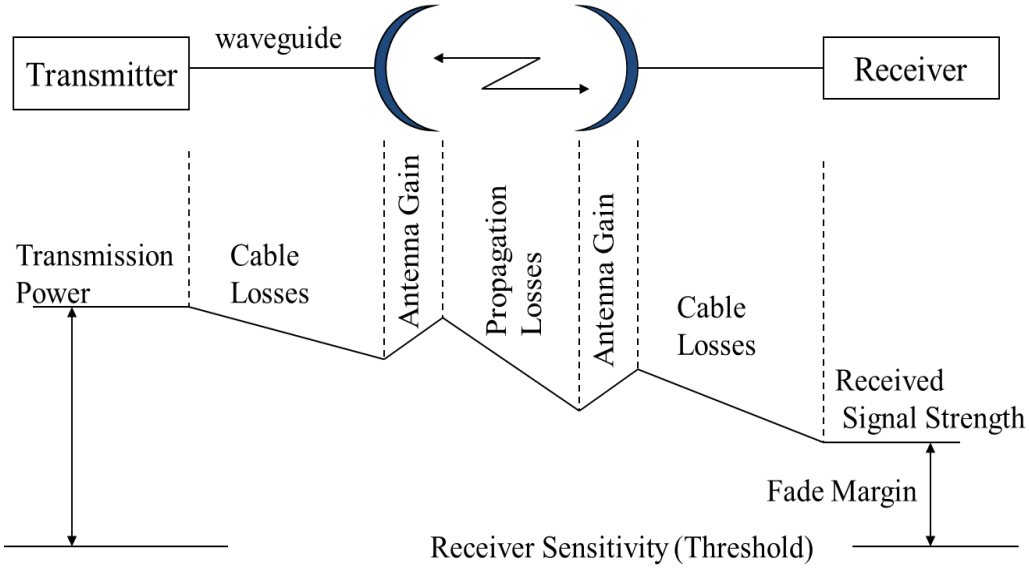

Figure 10.1: Link Budget of Typical Radio Link

10.4.1 Links' Configurations

Over 2000 microwave links have been studied against the predefined selection criteria. Twelve microwave links are considered as candidate links for further analysis that mostly satisfy the predefined conditions.

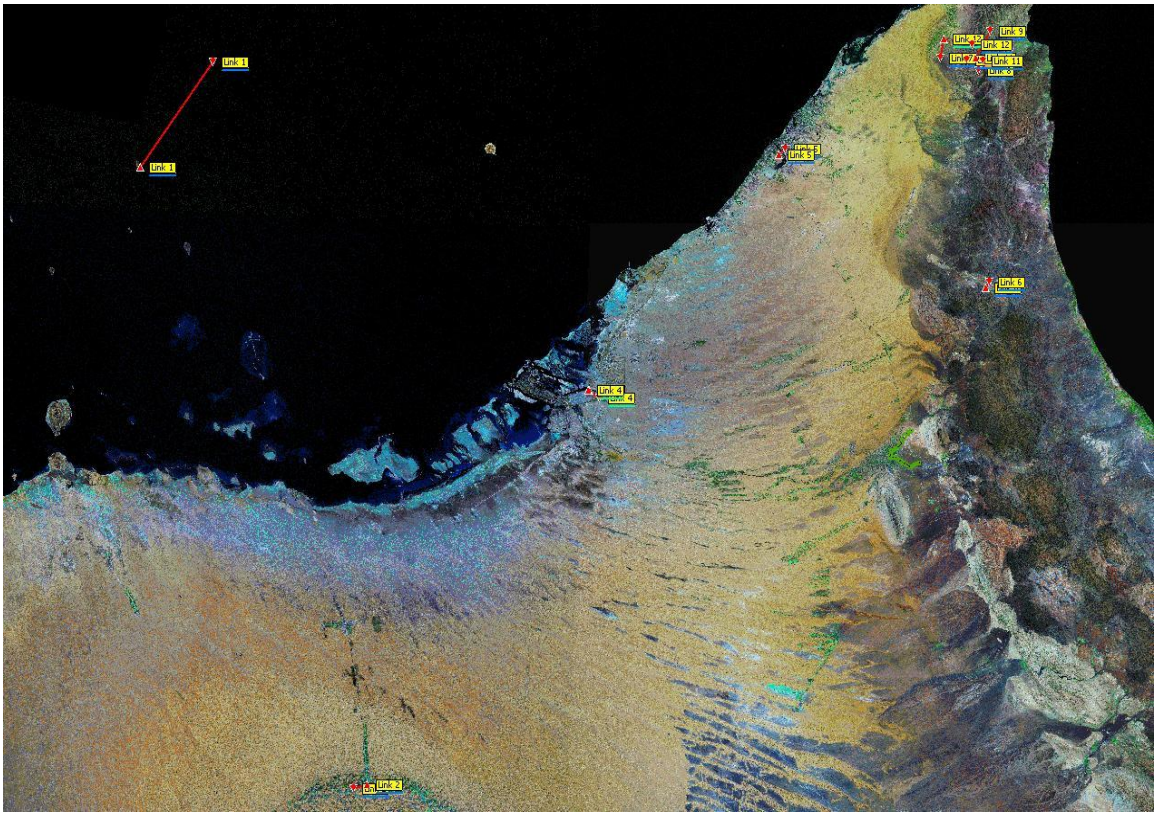

Figure 10.2: Links' Locations in UAE Map

The sites' locations of all candidate microwave links with longitude, latitude and altitude of each site above sea level, are listed in Table 10-1. Both latitudes and longitudes are given in decimal degree format.

The configurations of the 12 links including transmission power, assigned frequency channels, channel bandwidth, link capacity and distance between each pair of sites of all candidate microwave links are provided in Table 10-2.

Table 10-1: Locations of the Sites of Candidate Microwave Links

Link ID	Site ID	Location	Longitude (DEC)	Latitude (DEC)	Ground Altitude Above Sea Level (m)
Link 1	L1-S1	DAS Island	52.87994	25.14352	0
Link 1	L1-S2	Abu Albukhoosh Island	53.14695	25.49528	0
Link 2	L2-S1	Al Ain - LIWA_WEST	53.74594	23.11456	150
Link 2	L2-S2	Al Ain – LIWA	53.7977	23.12805	159
Link 3	L3-S1	Abu Dhabi - New ADIA	54.6487	24.4209	20
Link 3	L3-S2	Abu Dhabi	54.61	24.44525	3
Link 4	L4-S1	Abu Dhabi - New ADIA	54.6487	24.4209	20
Link 4	L4-S2	Abu Dhabi	54.6082	24.4435	4
Link 5	L5-S1	Dubai - Al Matar	55.3454	25.2495	4
Link 5	L5-S2	Dubai – SAMA	55.3222	25.2325	6
Link 6	L6-S1	Dubai - WADI HATTA HILL TOP	56.1162	24.7975	366
Link 6	L6-S2	Dubai - HATTA ROUNDABOUT	56.1311	24.8172	305
Link 7	L7-S1	NE – MATFAQ	55.9373	25.5553	44
Link 7	L7-S2	NE - AIRPORT RSU	55.95189	25.61808	44
Link 8	L8-S1	NE – TAWIYAN	56.07336	25.55583	158
Link 8	L8-S2	NE – FAGWA	56.08463	25.51479	272
Link 9	L9-S1	NE – TAWIYAN	56.07336	25.55583	158
Link 9	L9-S2	NE - JABR MOUNTAIN	56.12944	25.64694	1479
Link 10	L10-S1	NE - AL BAHAR CRUSHER	56.03868	25.54932	166
Link 10	L10-S2	NE – TAWIYAN	56.07336	25.55583	158
Link 11	L11-S1	NE – TAWIYAN	56.07336	25.55583	158
Link 11	L11-S2	NE – SUDANIYA	56.10083	25.54856	213
Link 12	L12-S1	NE - RAK AIRPORT	55.95189	25.61808	20
Link 12	L12-S2	NE – RAK	56.05772	25.60097	516

The antennas' configurations are given in Table 10-3 and Table 10-4. In Table 10-3, the configurations of the main antennas including the height above the ground, diameter and gain are provided for all links, while the azimuth and tilting are provided to site 1 of all candidate links. The configurations of the diversity antennas for the first four candidate links are presented in Table 10-4.

10.4.2 Path Profiles and Link Budget Calculations

The maps of the candidate links in addition to their path profiles and link budget calculations are provided in Appendix E. The maps show the areas where the links are located and the nearby weather stations. The calculations of link budget, fade margin, propagation losses and link availability are provided in the path profile figures in each direction. Two path profiles have been developed for each link in two directions, where each site becomes a transmitter in one direction and a receiver in the other one.

Some of these links are further analysed in the next section considering the comparison of the signal strength predictions using ICS Telecom software with the actual field strength measurements.

Table 10-2: Configurations of all Candidate Microwave Links (TX Power, Frequency, Bandwidth, Capacity and length)

Link ID	Site 1 ID	Site 2 ID	Equipment Configuration	S1 TX Power (dBm)	S2 TX Power (dBm)	S1 Frequency (MHz)	S2 Frequency (MHz)	Channel BW (kHz)	Link Capacity (Mbps)	Link Length (km)
Link 1	L1-S1	L1-S2	7GHz-40Mbps-QPSK	29	29	7442	7603	28000	40	47422.2
Link 2	L2-S1	L2-S2	23GHz-80Mbps-16QAM	9	9	23366	22134	28000	80	5481.79
Link 3	L3-S1	L3-S2	23GHz-80Mbps-16QAM	22	22	23366	22134	28000	80	4801.08
Link 4	L4-S1	L4-S2	23GHz 155Mbps-128QAM	19	19	23450	22218	28000	155	4770.76
Link 5	L5-S1	L5-S2	23GHz-100Mbps-32QAM	3	3	23422	22190	28000	100	3061.1
Link 6	L6-S1	L6-S2	23GHz-100Mbps-32QAM	2	2	21798	23030	28000	100	2663.39
Link 7	L7-S1	L7-S2	23GHz-40Mbps-QPSK	18	18	23366	22134	28000	40	7158.91
Link 8	L8-S1	L8-S2	23GHz-8Mbps-QPSK (Type 2)	23	23	22274	23506	7000	8	4731.17
Link 9	L9-S1	L9-S2	15GHz-100Mbps-32QAM	21	21	14529	15019	28000	100	11667
Link 10	L10-S1	L10-S2	23GHz-100Mbps-32QAM	10	10	23534	22302	28000	100	3471.35
Link 11	L11-S1	L11-S2	23GHz-100Mbps-32QAM	8	8	22246	23478	28000	100	2912.08
Link 12	L12-S1	L12-S2	23GHz-100Mbps-32QAM	19	19	22302	23534	28000	100	10796.5

Table 10-3: Configurations of Main Antennas of all Candidate Links

Link ID	Site 1 ID	Site 2 ID	S1 Antenna Height (m)	S2 Antenna Height (m)	S1 Ant. Diameter (m)	S2 Ant. Diameter (m)	S1 Gain (dB)	S2 Gain (dB)	S1 Ant. Azimuth°	S1 Ant. Tilt°
Link 1	L1-S1	L1-S2	75	56	3.6	3	46.3	44.9	36.34	-0.16
Link 2	L2-S1	L2-S2	65	43	0.6	0.6	40.1	40.1	75.2	-0.09
Link 3	L3-S1	L3-S2	15	13	0.6	0.6	40.1	40.1	305.68	-0.23
Link 4	L4-S1	L4-S2	30	30	0.6	0.6	40.1	40.1	303.02	-0.17
Link 5	L5-S1	L5-S2	37	17	0.6	0.6	40.1	40.1	231.63	-0.33
Link 6	L6-S1	L6-S2	30	30	0.6	0.6	40.1	40.1	34.29	-1.3
Link 7	L7-S1	L7-S2	22	50	0.6	0.6	40.1	40.1	12.09	0.01
Link 8	L8-S1	L8-S2	35	9	0.6	0.6	40.1	40.1	166.55	1.43
Link 9	L9-S1	L9-S2	47	9	0.6	0.6	36.5	36.5	29.44	6.26
Link 10	L10-S1	L10-S2	9	30	0.6	0.6	40.1	40.1	78.37	0.26
Link 11	L11-S1	L11-S2	50	9	0.6	0.6	40.1	40.1	105.95	0.29
Link 12	L12-S1	L12-S2	50	10	0.6	0.6	40.1	40.1	100.68	2.39

Table 10-4: Configurations of Diversity Antennas of Candidate Links

Link ID	Site 1 ID	Site 2 ID	S1 Diversity Height (m)	S2 Diversity Height (m)	S1 Div. Gain (dB)	S2 Div. Gain (dB)	S1 Ant. Polar	S2 Ant. Polar
Link 1	L1-S1	L1-S2	53	37	46	45	V	V
Link 2	L2-S1	L2-S2	46	28.5	40	40	V	V
Link 3	L3-S1	L3-S2	9.52	7.95	40	40	V	V
Link 4	L4-S1	L4-S2	25.1	24.9	40	40	V	V
Link 5	L5-S1	L5-S2	-	-	-	-	V	V
Link 6	L6-S1	L6-S2	-	-	-	-	V	V
Link 7	L7-S1	L7-S2	-	-	-	-	V	V
Link 8	L8-S1	L8-S2	-	-	-	-	V	V
Link 9	L9-S1	L9-S2	-	-	-	-	V	V
Link 10	L10-S1	L10-S2	-	-	-	-	V	V
Link 11	L11-S1	L11-S2	-	-	-	-	V	V
Link 12	L12-S1	L12-S2	-	-	-	-	V	V

10.5 Wireless Measurements and Events Analysis

The received signal strength variations of the candidate links were studied. Some events were analysed, where signal suffers from considerable fading, in accordance with the experienced propagation conditions such as ducting phenomena and prevailing meteorological conditions.

Due to some limitations, the sets of signal strength measurements differ according to the data resolution and measurement periods. Some measurements were taken instantaneously every 1 minute. The majority of measurements were gathered every 15 minutes such that the minimum and maximum readings were reported within this period. Few data were collected with higher resolution of every 10 seconds.

10.5.1 Analysis of Fading Events

Several fading events were investigated by calculating the differences between the received signal strength indicator (RSSI) measurements and the predicted values using ICS Telecom software considering no rain situation. Some of the events with absolute differences exceeding 10 dB for multiple contiguous measurements are analysed. The hourly weather codes are studied for the given period to identify the dominant weather conditions as the possible root cause of the experienced fading. These hourly code are manually observed at the surface weather stations given in Table 4-1.

Fading events are analysed at S1 and S2 sites of the links L3 in Figure **10.3** and Figure **10.4**, and in Figure **10.5** and Figure **10.6** for L4, respectively. The two links operate in the 23 GHz band. S1 and S2 sites of both links are found to be around 1.2 km and 4 km away from the AUH weather station, where surface and radiosonde measurements are available. Considerably high fading events are observed during the given period from 5 to 7 April 2013, where absolute differences from the predicted value vary from 1 dB to more than 52

dB. For example on 6/4/2013, the fading starts early morning at L1-S1 with the highest values observed at night time for all sites. Widespread dust in suspension in the air then dust or sand raised by the wind without well-developed dust whirl or sandstorm seen are observed at or near the station from 1 am till 4 pm. Slight intermittent rain and then a moderate thunderstorm with rain are experienced afterwards till evening. Table **10-5** provides comparison between the predicted RSSI values, with and without rain attenuation, using ICS Telecom software and the mean values of the total minimum and maximum readings of the 15 minutes resolution measurements for the main and diversity antennas of L3 and L4.

Table 10-5: Predicted and mean RSSI values at sites of L3 and L4

Link – Site	Predicted RSSI Value (No Rain)	Predicted RSSI Value (Rain)	Mean of min. RSSI readings (Main Antenna)	Mean of max. RSSI readings (Main Antenna)	Mean of min. RSSI readings (Diversity Antenna)	Mean of max. RSSI readings (Diversity Antenna)
L3-S1	-32.01	-39.25	-49.16	-44.73	-49.60	-44.97
L3-S2	-37.96	-44.58	-50.49	-45.59	-62.75	-56.40
L4-S1	-34.69	-41.41	-37.87	-36.62	-37.62	-36.41
L4-S2	-35.15	-42.5	-37.12	-35.83	-36.42	-35.17

Two surface duct events are observed at AUH site for the given period. At 0H on 5/4/2013, the duct strength and thickness are found to be 2.3 M-unit and 20 m, respectively, while the values at 12H on 7/8/2013 are 5.7 M-unit and 10 m, respectively. The frequency band, which is expected to be trapped by this surface duct ranges from 4 to 12 GHz.

The instantaneous RSSI measurements are gathered for other links with 1 minute resolution for the same period. The rain observations at the nearest weather stations and the distances to those stations are provided in Table **10-6**.

Table 10-6: Distances and rain observations at the nearest weather stations to the analysed links

Link-Site	Nearest weather station	Approximate distance to weather station	Recorded Rain Observation
L1-S1	DAS/ Bukhoosh	900 m / 47 km	No
L1-S2	Bukhoosh	100 m	No
L3-S1	AUH	1.2 km	Yes
L3-S2	AUH	4 km	Yes
L4-S1	AUH	1.2 km	Yes
L4-S2	AUH	4 km	Yes
L5-S1	DXB	1.2 km	Yes
L7-S2	RAK	1.8 km	Yes
L8-S1	Tawiyen	500 m	Yes
L11-S1	Tawiyen	500 m	Yes
L12-S1	RAK	1.8 km	Yes

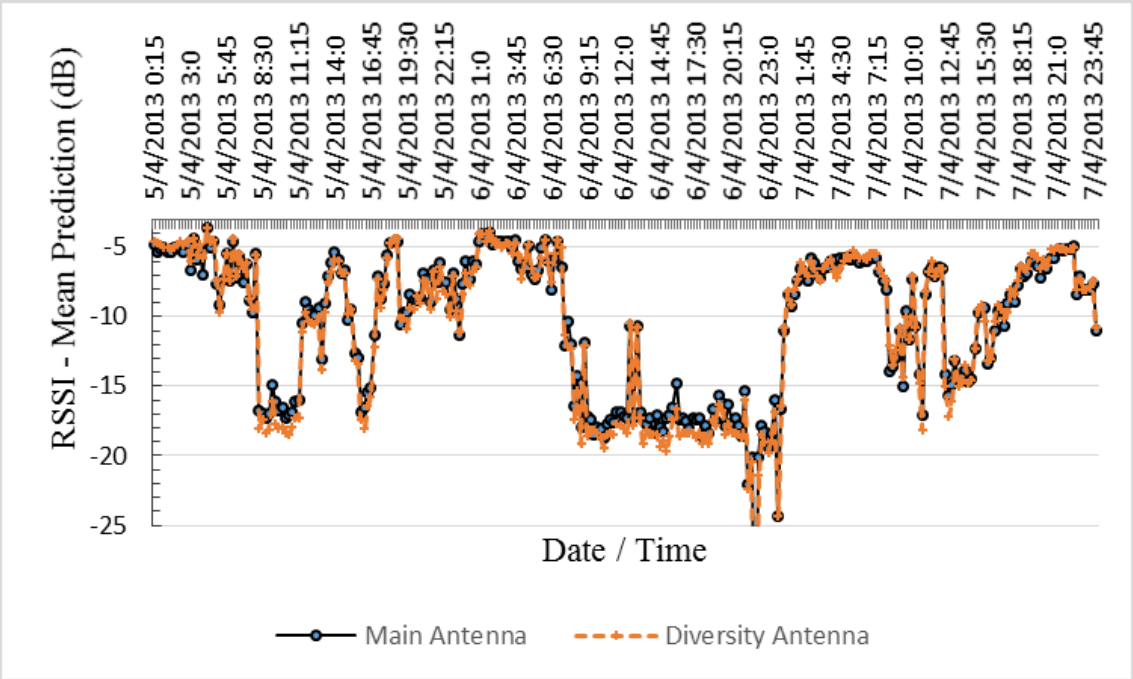

Figure 10.3: L3-S1 main and diversity antennas' RSSI measurements, 5-7/4/2013

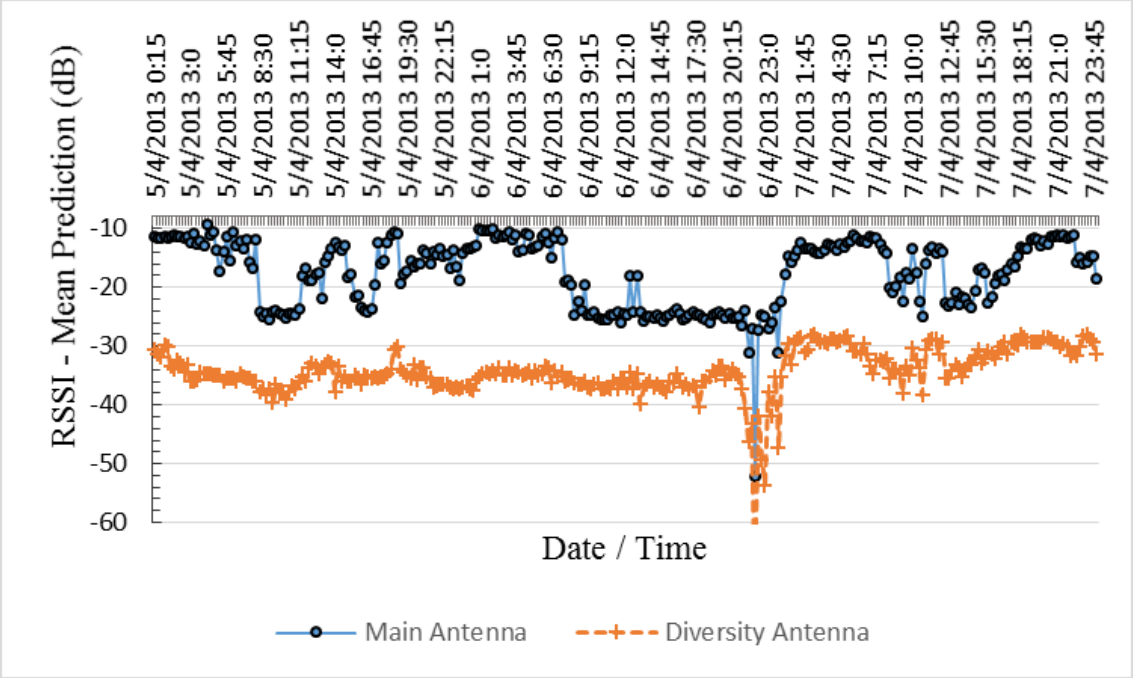

Figure 10.4: L3-S2 main and diversity antennas' fading, 5-7/4/2013

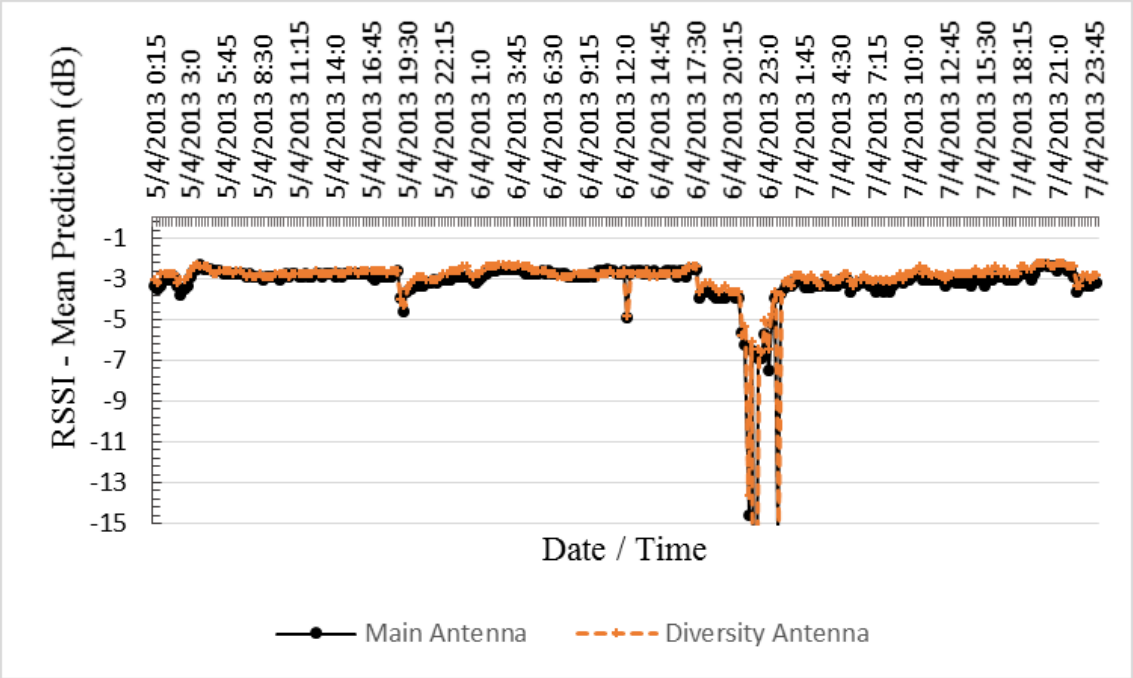

Figure 10.5: L4-S1 main and diversity antennas' fading, 5-7/4/2013

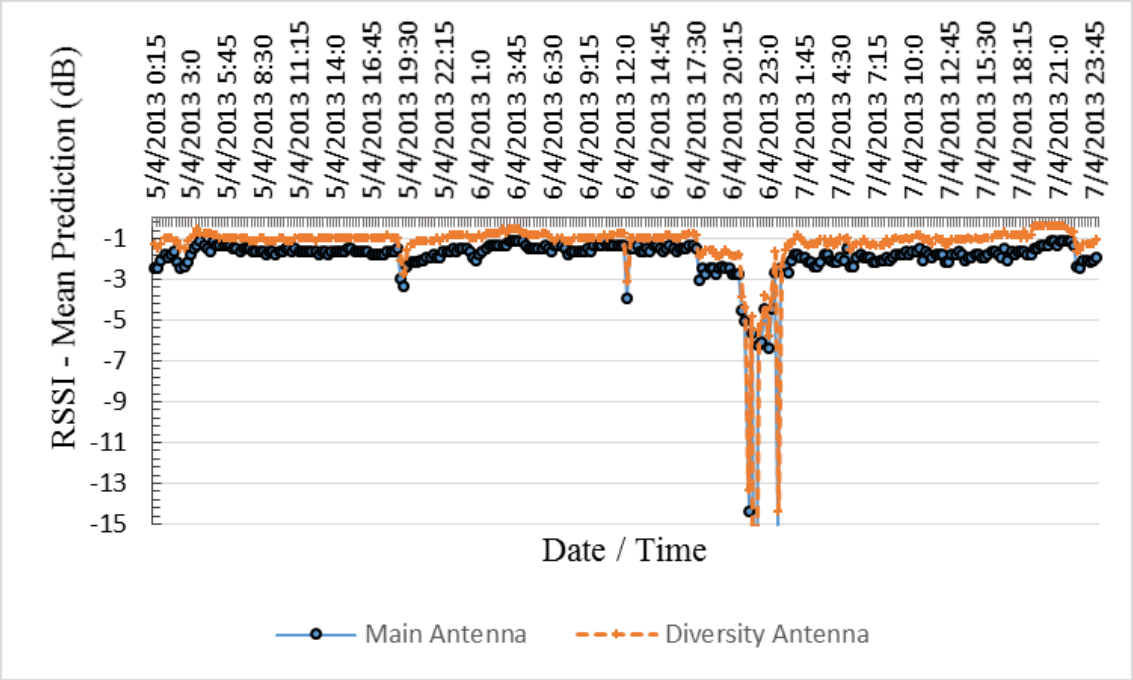

Figure 10.6: L4-S2 main and diversity antennas' fading, 5-7/4/2013

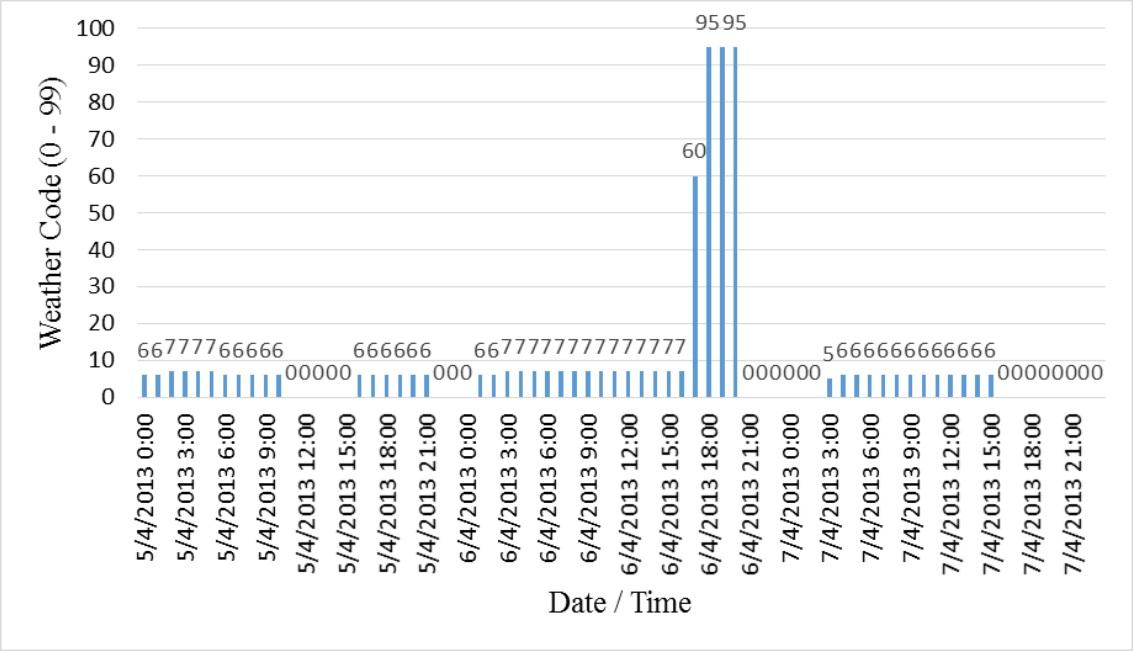

Figure 10.7: Hourly weather codes at AUH site, 5-7/4/2013

The rain events are observed at the weather stations near to the links L5, L7, L8, L11 and L12 for the same period. Similar fading events are experienced due to dust, sandstorm, thunderstorm and rain for the link L5-S1, L7-S2, L8-S1, L11-S1 and L12-S1. The differences between the RSSI measurements and the predicted values for these links, along with the observed weather codes or daily rain fall rate, are shown from Figure **10.8** up to Figure **10.15**. The description of the weather codes are provided in Appendix C. In general, severe fading is experienced with continuous and heavy rain compared with slight intermittent rain, which reaches up to -55 dB in case of L7-S2 and L12-S1, as displayed in Figure **10.10** and Figure **10.11**.

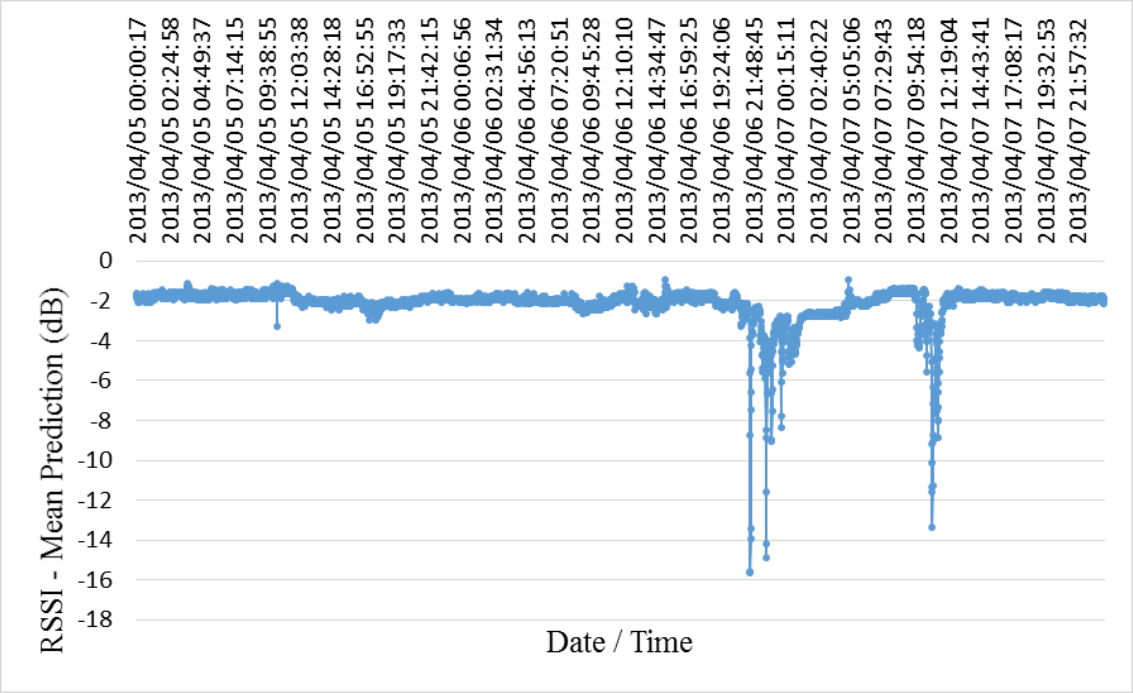

Figure 10.8: L5-S1 main antenna fading, 5-7/4/2013

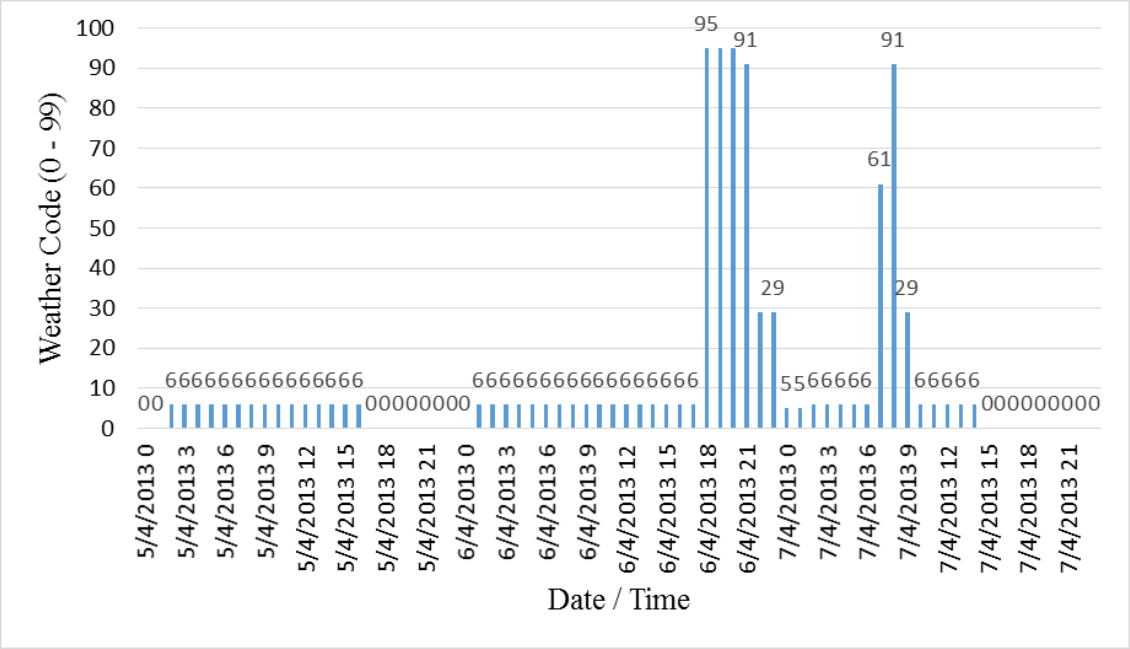

Figure 10.9: Hourly weather codes at DXB site, 5-7/4/2013

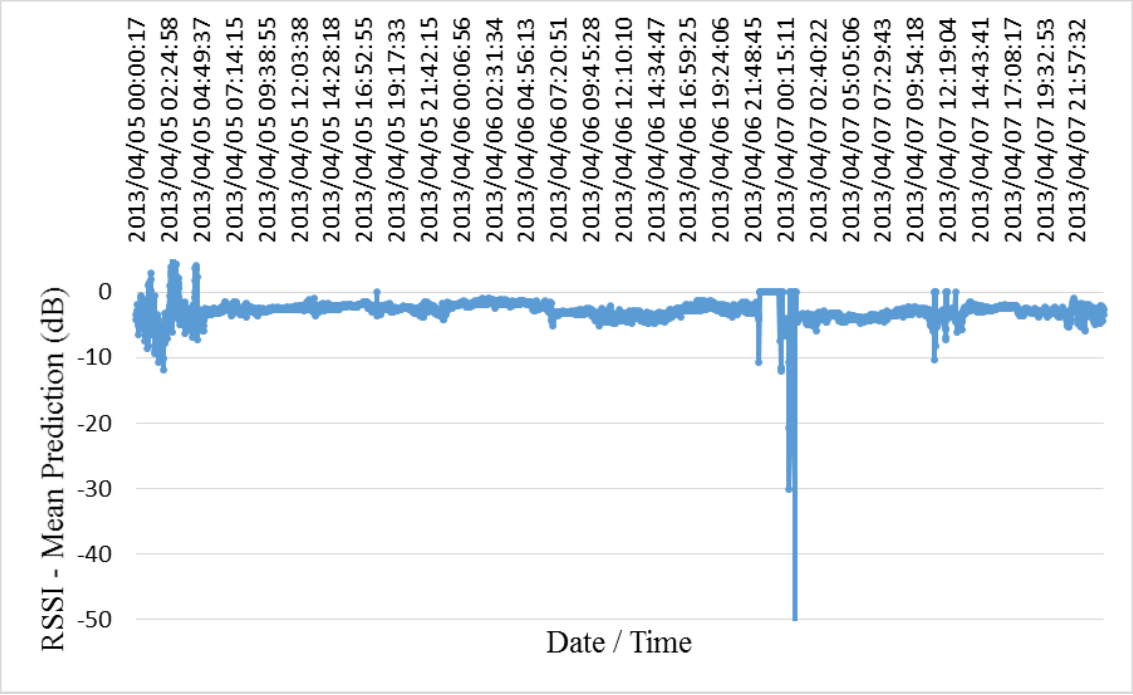

Figure 10.10: L7-S2 main antenna fading, 5-7/4/2013

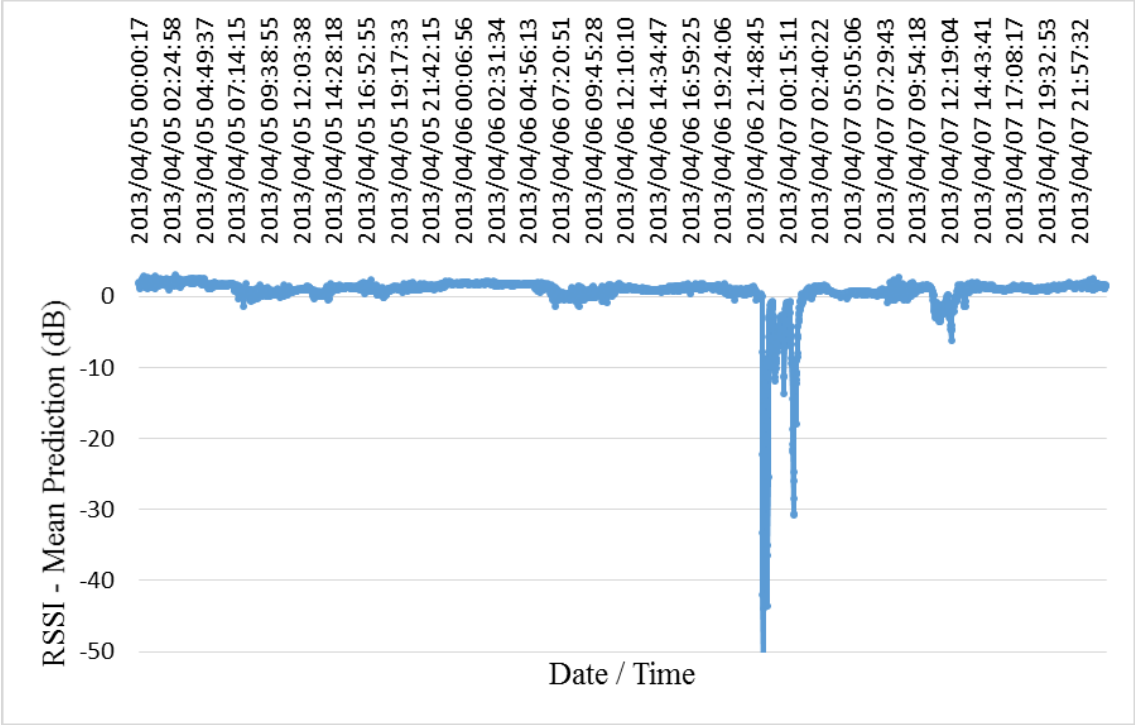

Figure 10.11: L12-S1 main antenna fading, 5-7/4/2013

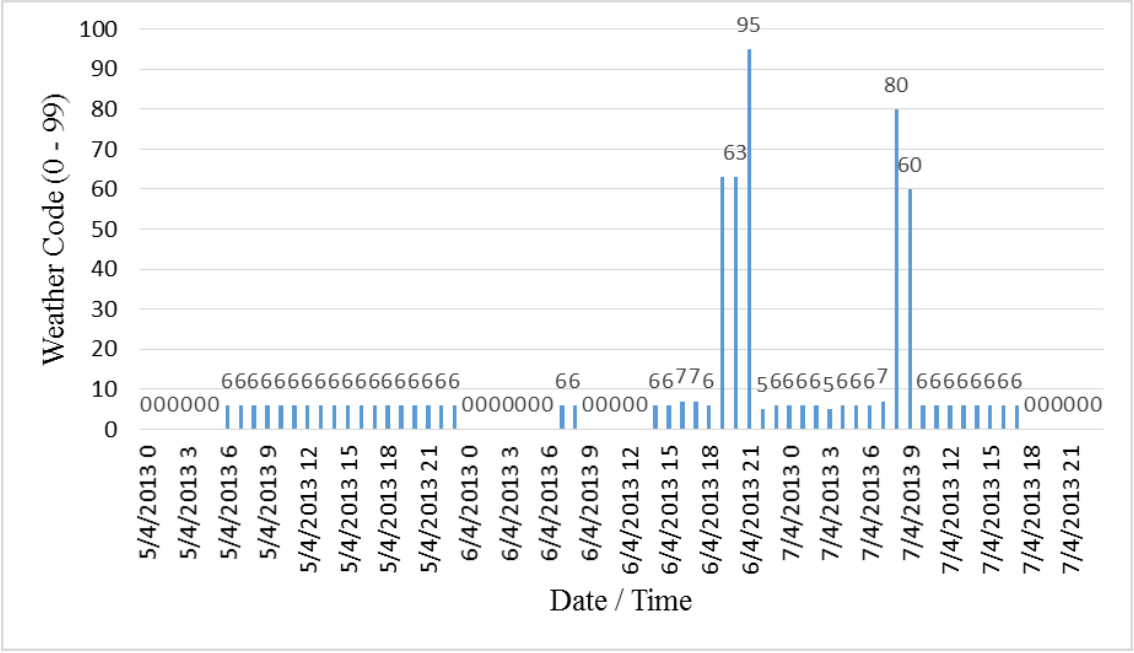

Figure 10.12: Hourly weather codes at RAK site, 5-7/4/2013

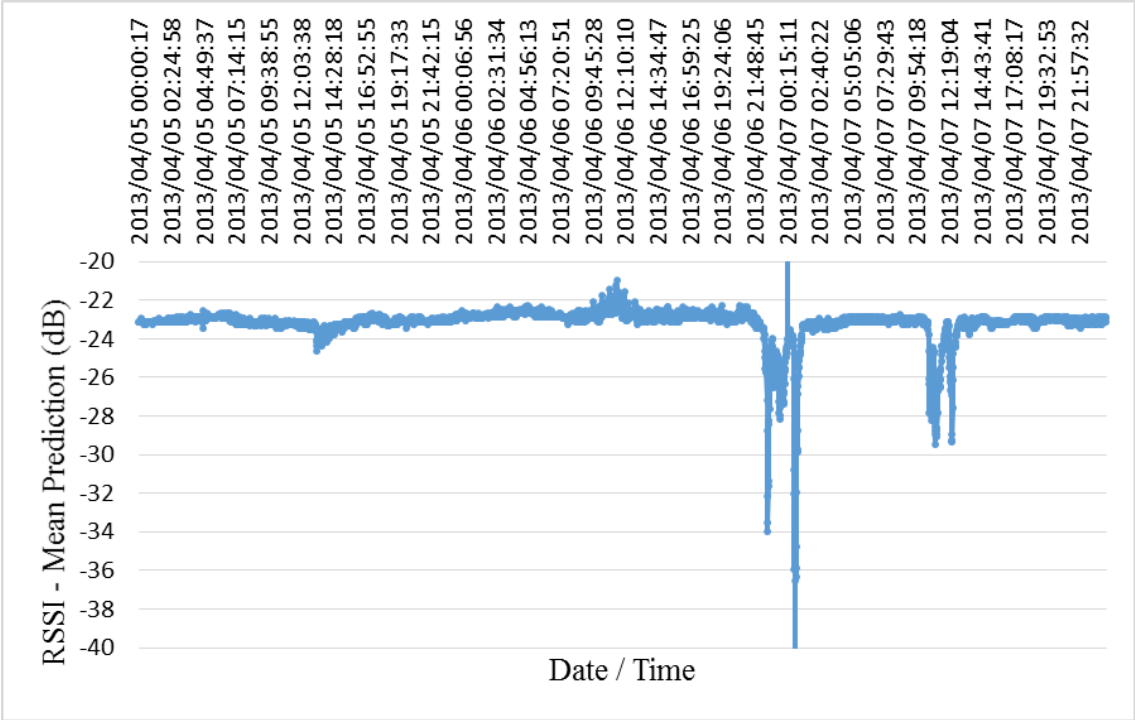

Figure 10.13: L8-S1 main antenna fading, 5-7/4/2013

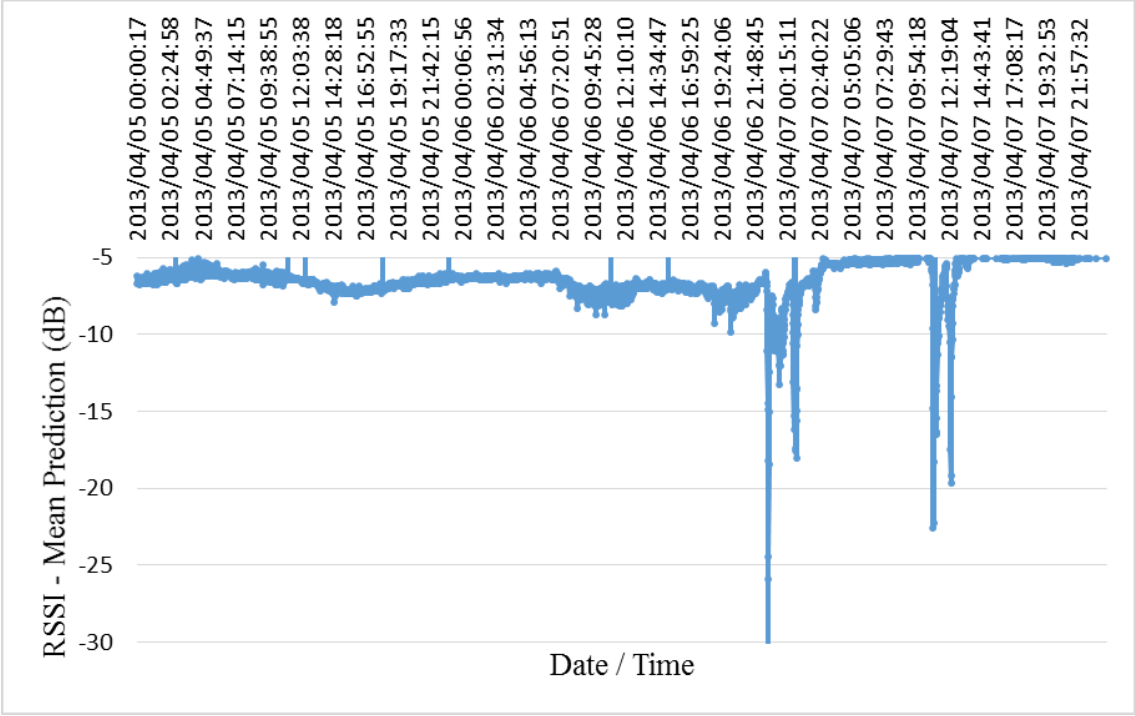

Figure 10.14: L11-S1 main antenna fading, 5-7/4/2013

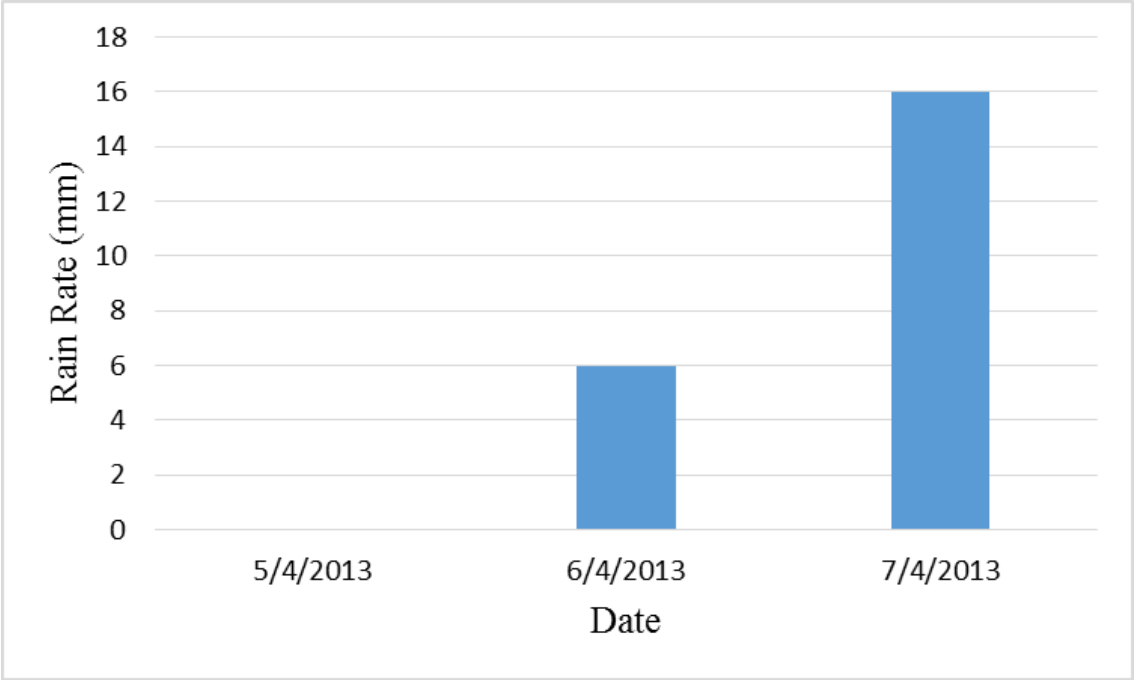

Figure 10.15: Cumulative rain rate at Tawiyen weather station, 5-7/4/2013

The RSSI measurements at S1 and S2 sites of the offshore link L1, operating in 7 GHz band, are found to vary significantly within a span of 50 dB, as shown in Figure **10.16** and Figure **10.17**. No rain data has been recorded for the given period. The readings at S1 and S2 of L1 are compared with the meteorological parameters and surface refractivity obtained from Bukhoosh weather station. The hourly variations of vapour pressure, relative humidity, dry temperature, wind speed, wind direction and solar radiation are provided in Figure **10.18**, Figure **10.19**, Figure **10.20**, Figure **10.21**, Figure **10.22** and Figure **10.23**, respectively. The hourly profile of surface refractivity is given in Figure **10.24**. The surface, upper and gradient of refractivity analysis for the first 65 m layer of the atmosphere are investigated for the same period at AUH site, where radiosonde data are available two times daily. The L1 RSSI fluctuations seem to be affected by the significant hourly oscillations of relative humidity, wind speed and consequently surface refractivity, as shown in Figure **10.19**, Figure **10.21** and Figure **10.24**, respectively. The correlation

between the RSSI measurements and readings of each individual parameter is found to be low where the coefficient does not exceed 0.4.

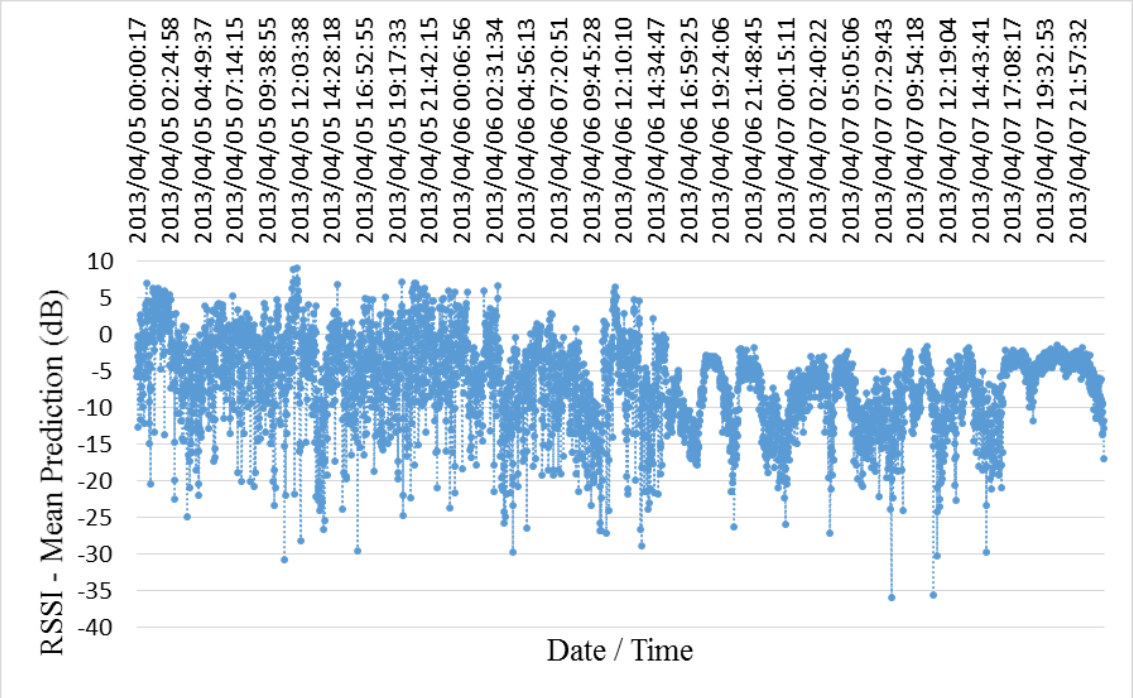

Figure 10.16: L1-S1 main antenna fading, 5-7/4/2013

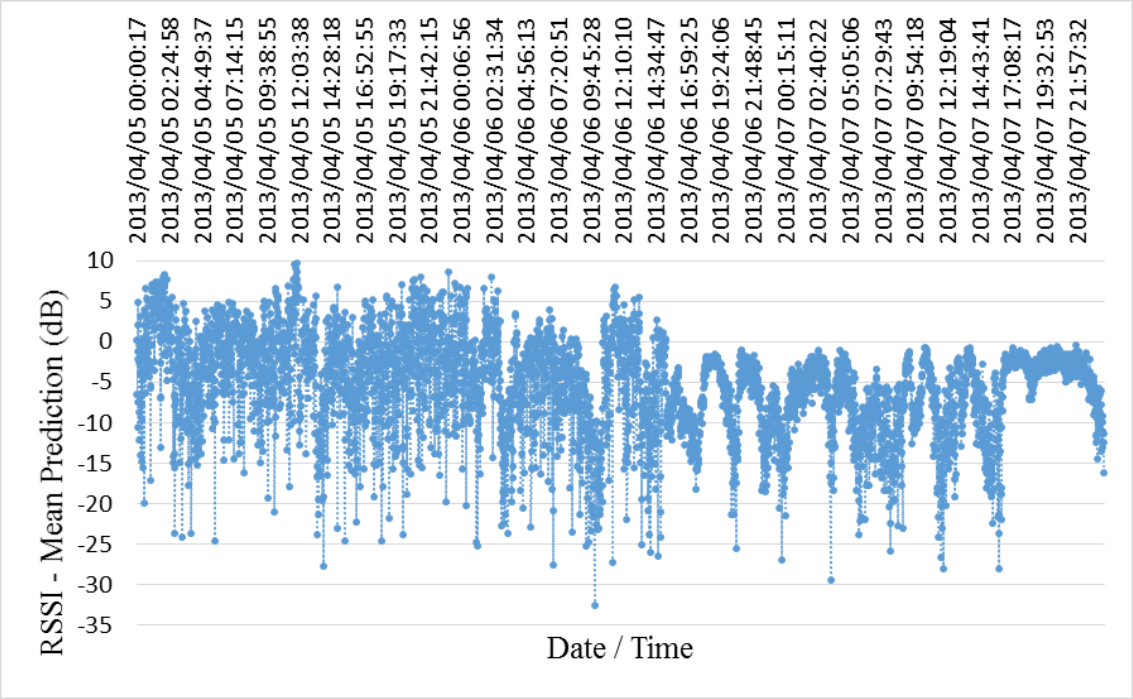

Figure 10.17: L1-S2 main antenna fading, 5-7/4/2013

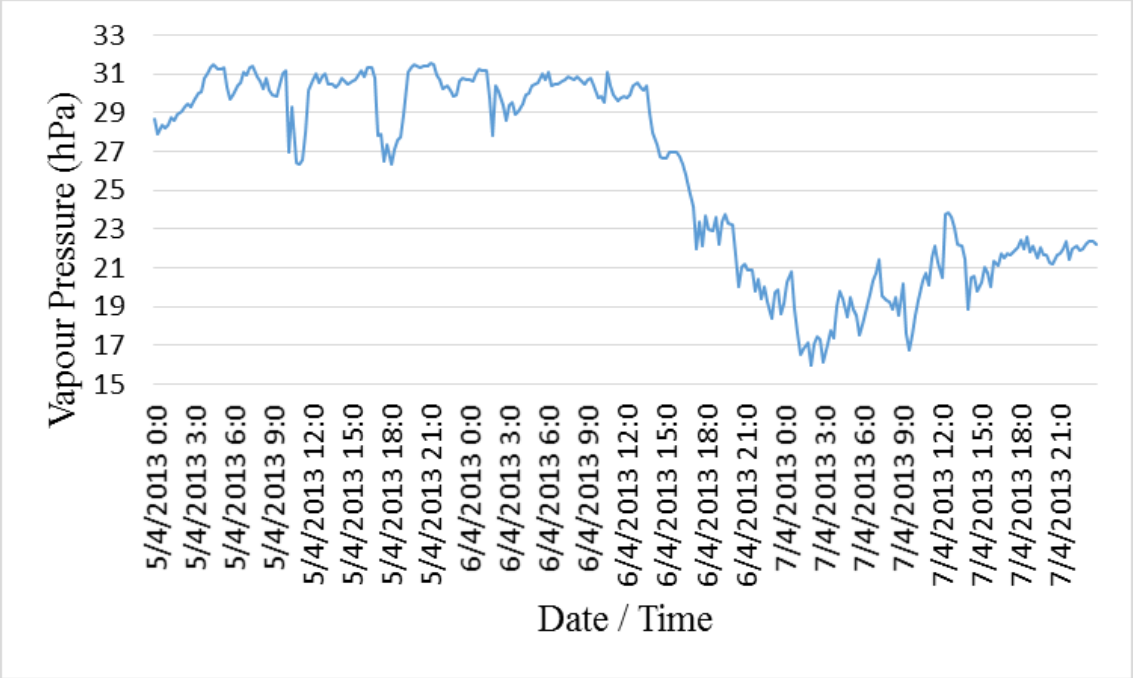

Figure 10.18: Hourly vapour pressure at Bukhoosh island weather station, 5-7/4/2013

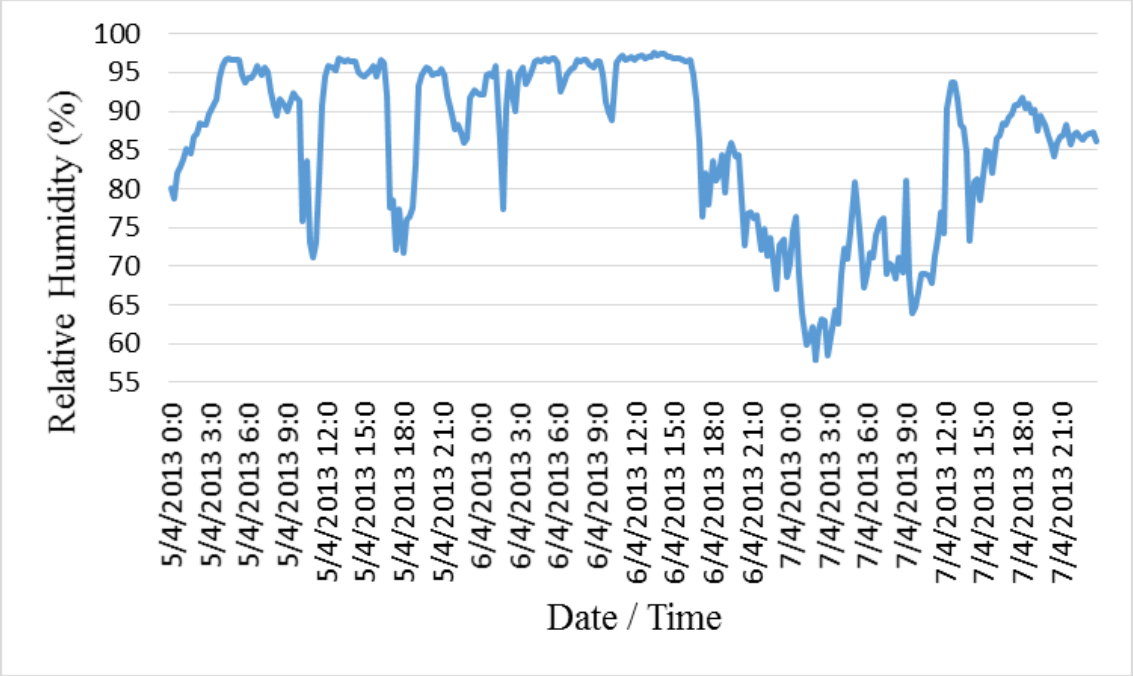

Figure 10.19: Hourly relative humidity at Bukhoosh island weather station, 5-7/4/2013

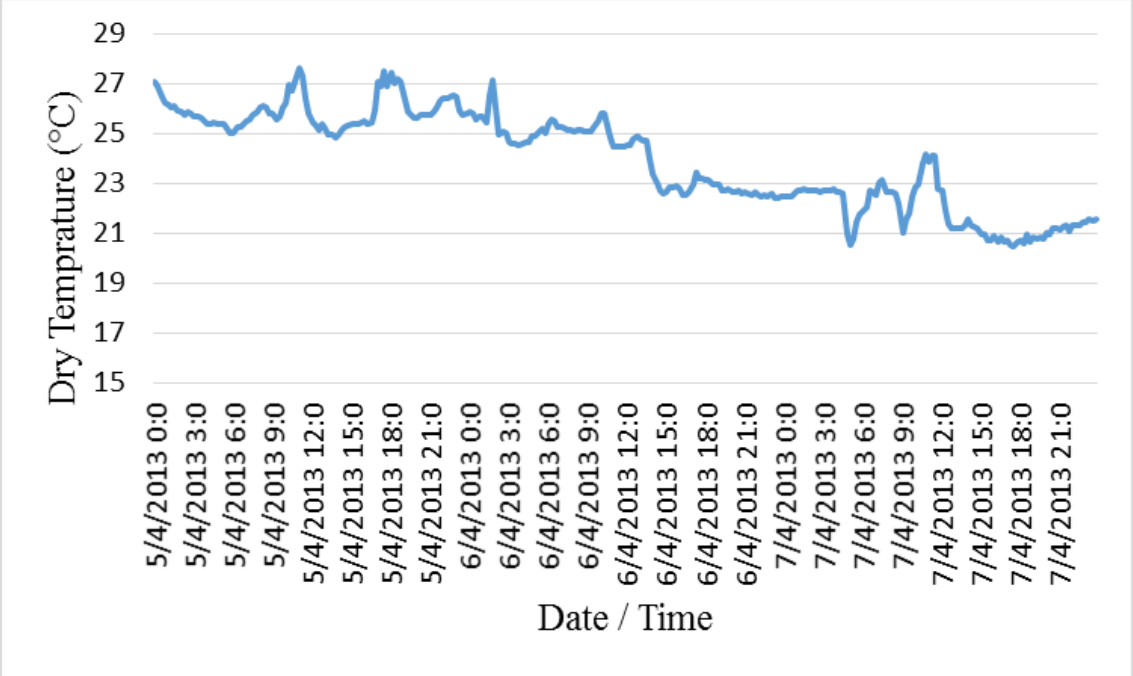

Figure 10.20: Hourly dry temperature at Bukhoosh island weather station, 5-7/4/2013

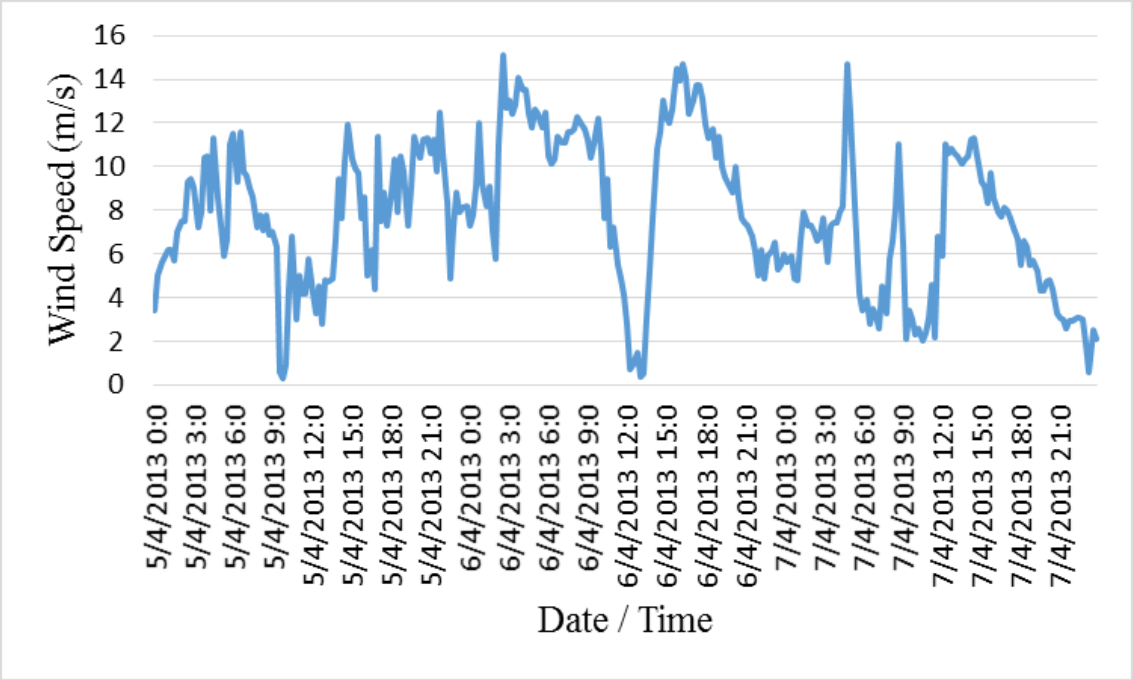

Figure 10.21: Hourly wind speed at Bukhoosh island weather station, 5-7/4/2013

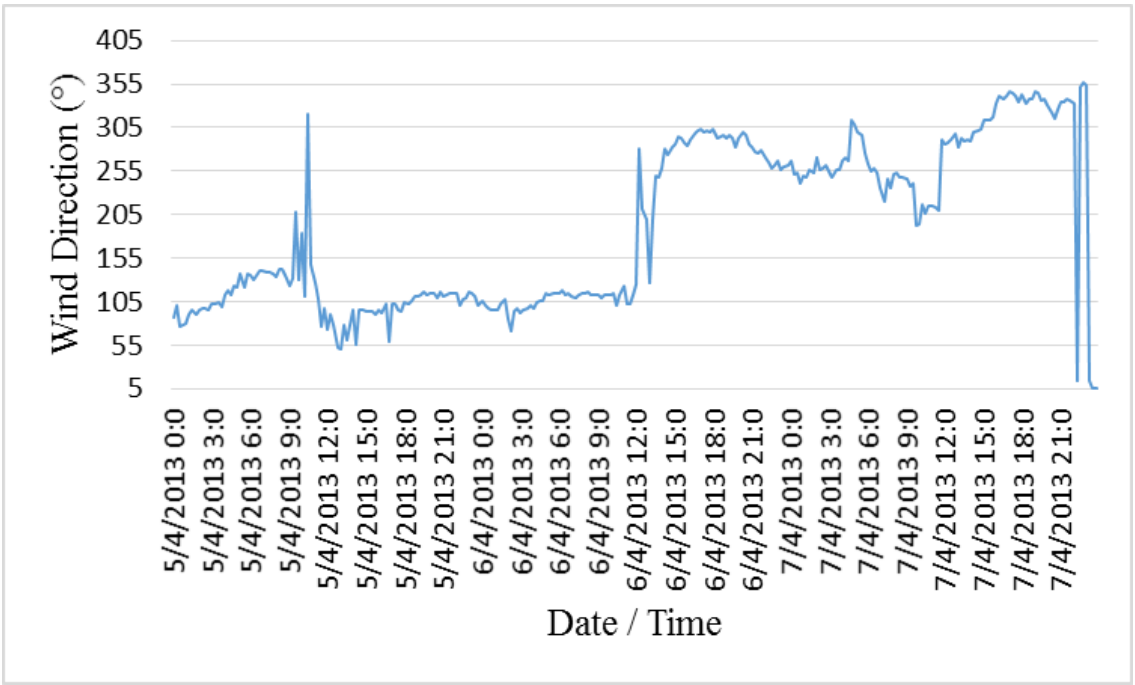

Figure 10.22: Hourly wind direction at Bukhoosh island weather station, 5-7/4/2013

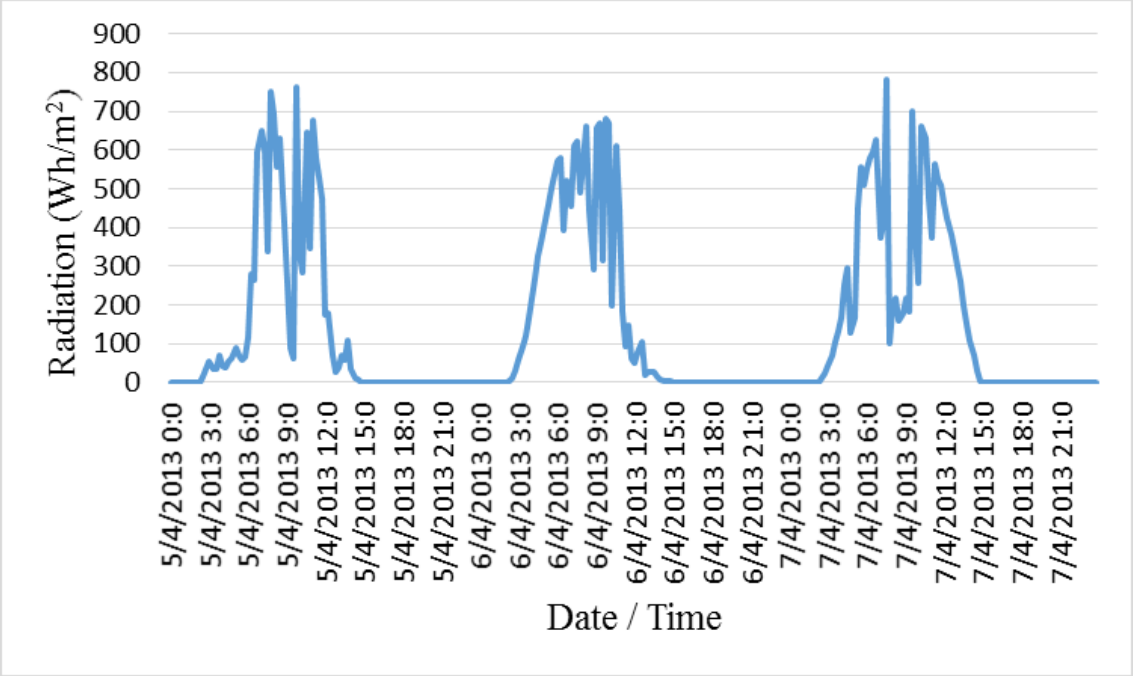

Figure 10.23: Hourly solar radiation at Bukhoosh island weather station, 5-7/4/2013

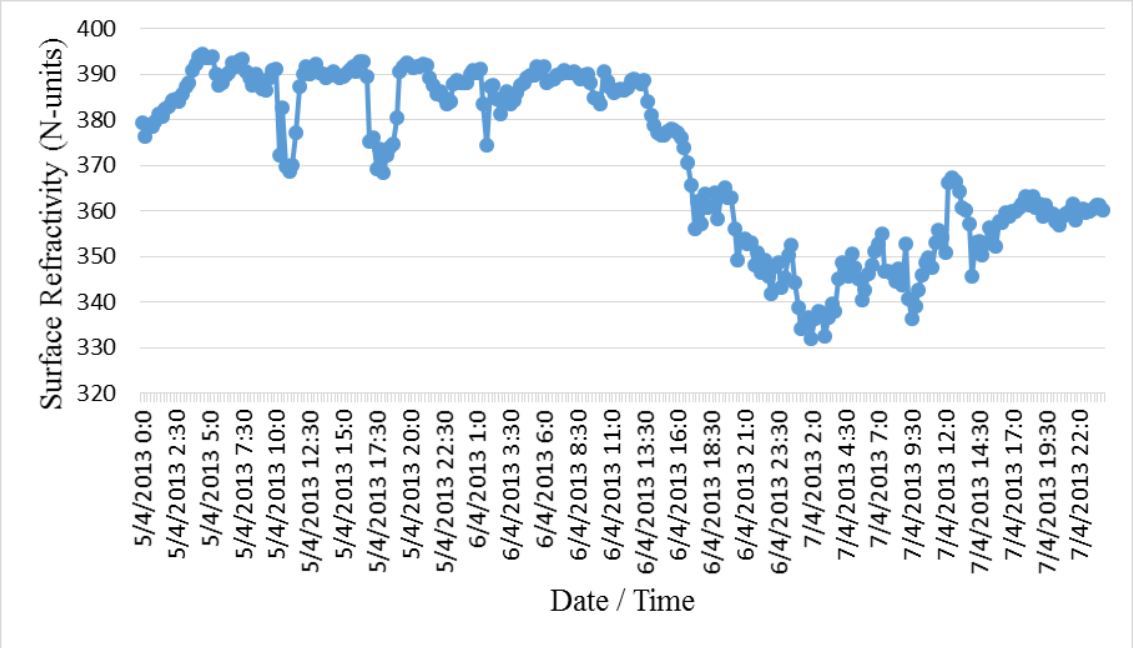

Figure 10.24: Hourly surface refractivity at Bukhoosh island weather station, 5-7/4/2013

The RSSI measurements at the offshore L1-S1 and L1-S2 sites are also compared with the surface and upper-air profiles of refractivity and meteorological parameters using the available radiosonde readings at the coastal AUH site. The hourly variations of surface refractivity obtained from the surface weather station, upper refractivity at 65 m obtained from the radiosonde measurements and the refractivity gradient at 65 m are provided in Figure **10.25**, Figure **10.26** and Figure **10.27**, respectively. Possible relationships between fading events and the vertical variations of various parameters within the first 65 m atmospheric layer are investigated, although the low radiosonde data resolution collected at two times daily. Several hourly inversions in the dry and dewpoint temperatures are observed in Figure **10.28** and Figure **10.29**, which contribute to the duct formation in the area under study. The vertical variations of wind speed, given in Figure **10.31**, may also contribute to the experienced fluctuations in the signals, which need further investigation based on long term wireless measurements.

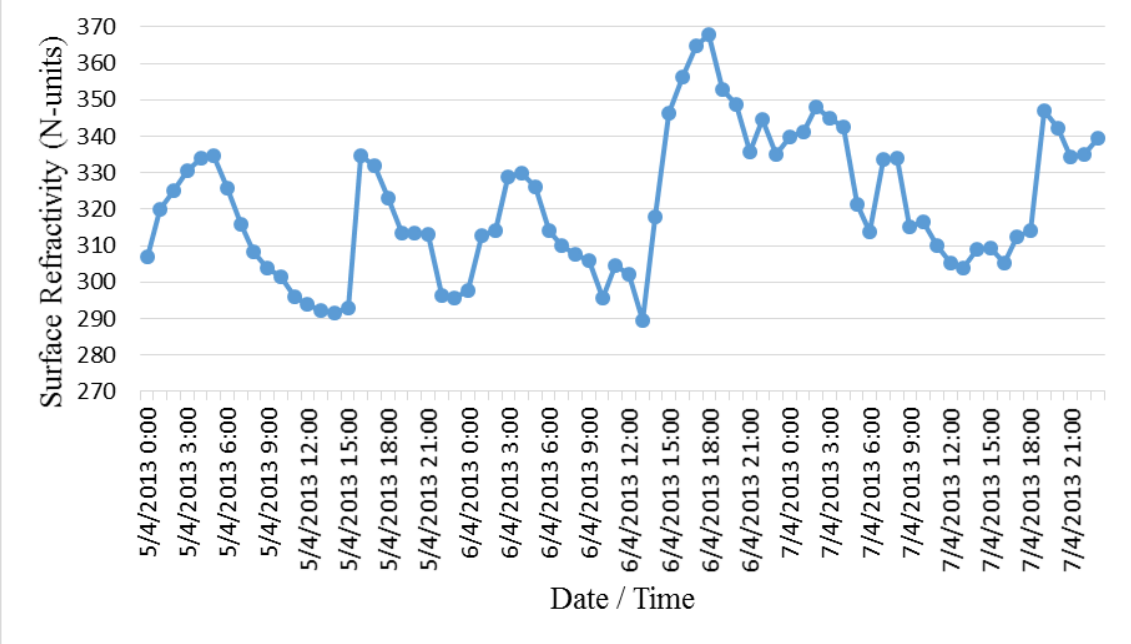

Figure 10.25: Hourly surface refractivity from AUH surface weather station, 5-7/4/2013

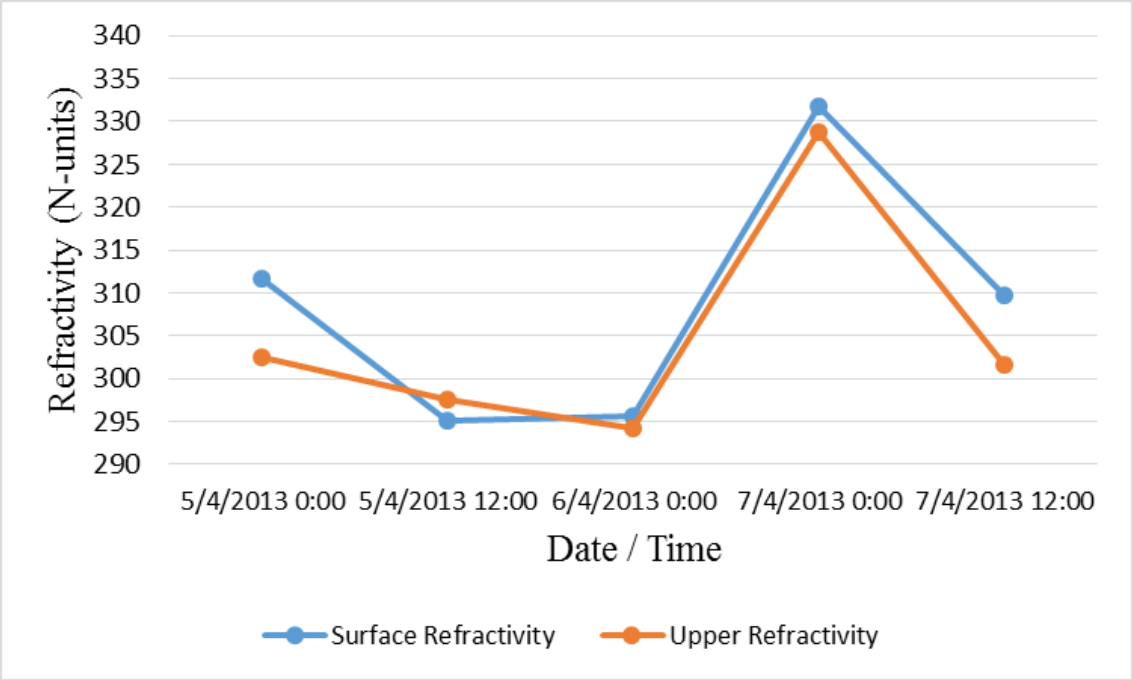

Figure 10.26: Surface and Upper (65 m) refractivity from AUH radiosonde data, 5-7/4/2013

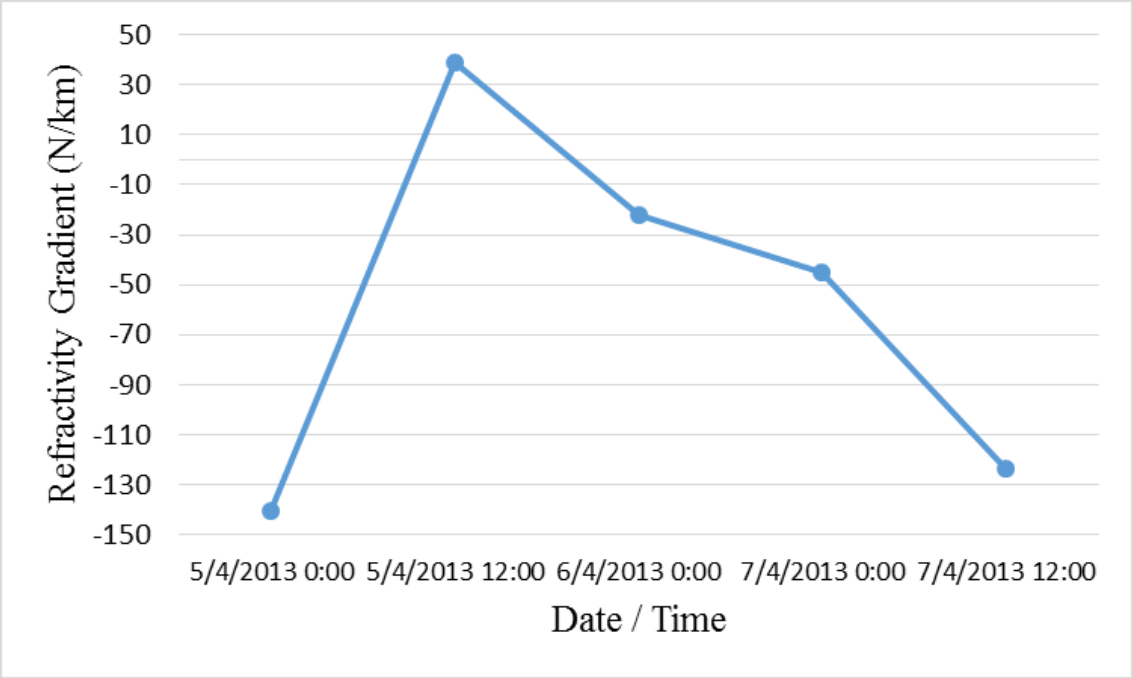

Figure 10.27: Refractivity gradient (65 m) at AUH site, 5-7/4/2013

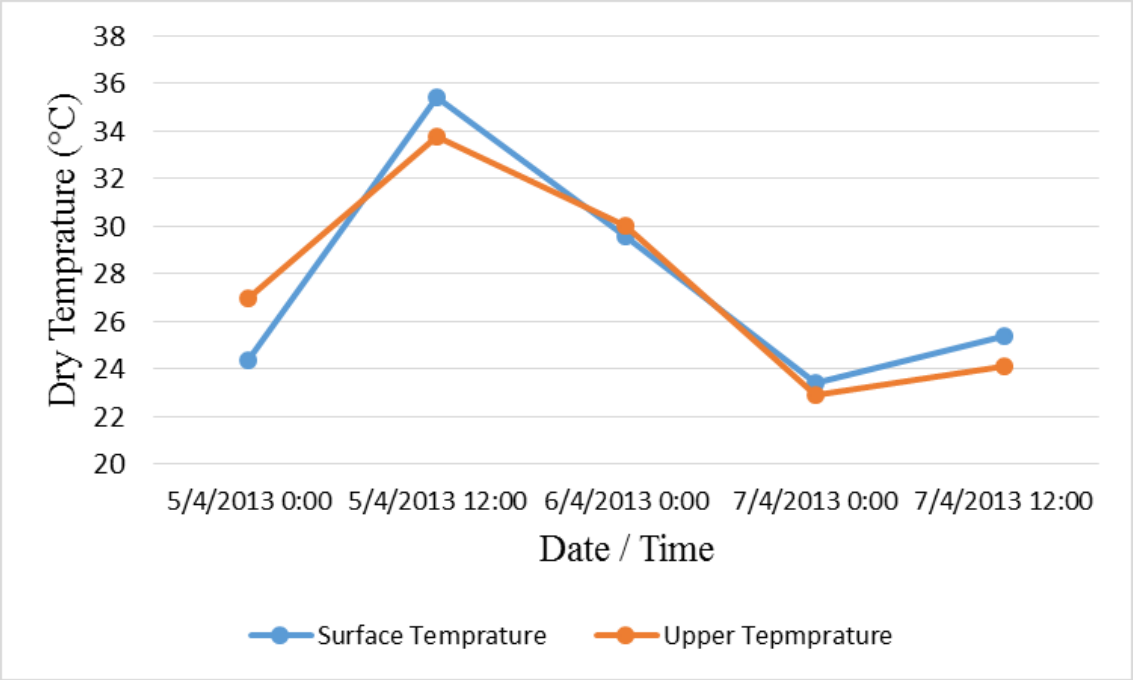

Figure 10.28: Surface and Upper (65 m) dry temperature at AUH site, 5-7/4/2013

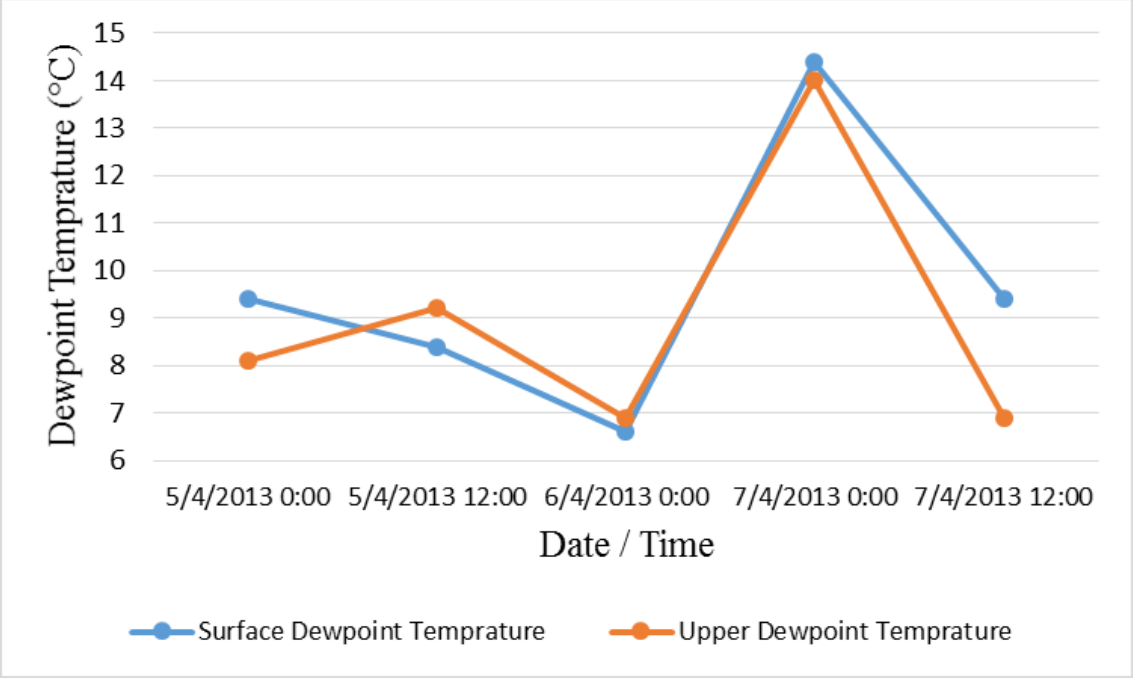

Figure 10.29: Surface and Upper (65 m) dewpoint temperature at AUH site, 5-7/4/2013

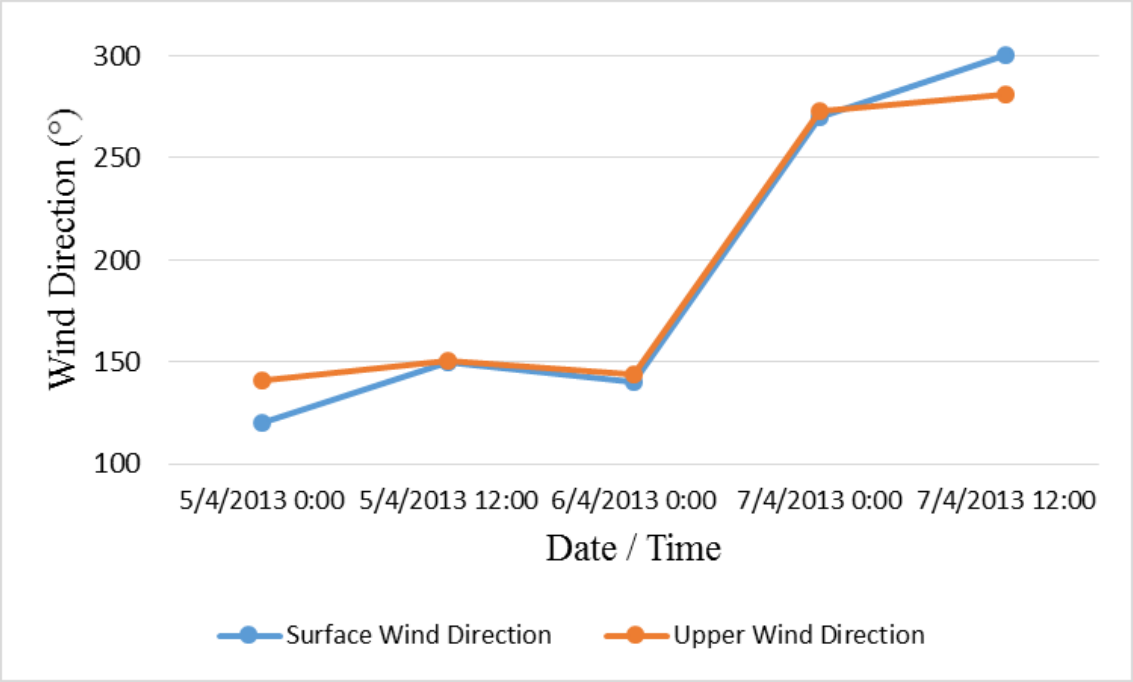

Figure 10.30: Hourly surface and upper-air (65 m) wind direction at AUH site, 5-7/4/2013

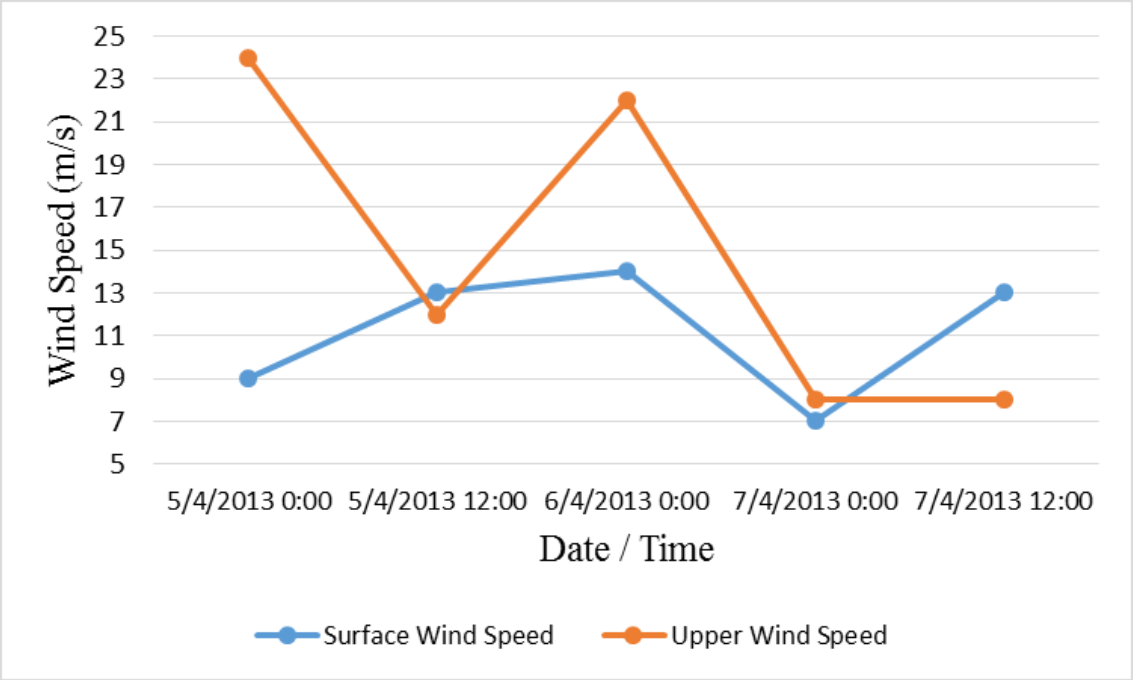

Figure 10.31: Hourly surface and upper-air (65 m) wind speed at AUH site, 5-7/4/2013

Table **10-7** provides comparison between the predicted RSSI values, with and without rain attenuation, using ICS Telecom software and the mean values of the total minimum and maximum readings of the 15 minutes resolution measurements for the main and diversity antennas of L1. The mean values of the minimum readings of both antennas are found to have considerable difference of around 19 dB.

Table 10-7: Predicted and mean RSSI values at sites of L1

Link – Site	Predicted RSSI Value (No Rain)	Predicted RSSI Value (Rain)	Mean of min. RSSI readings (Main Antenna)	Mean of max. RSSI readings (Main Antenna)	Mean of min. RSSI readings (Diversity Antenna)	Mean of max. RSSI readings (Diversity Antenna)
L1-S1	-23.9	-26.03	-43.65	-24.88	-43.89	-24.01
L1-S2	-23.71	-25.68	-44.36	-24.69	-44.95	-25.89

10.6 Simulations of Path Clearance and Link Availability

The impact of adopting ITU global values and the obtained results in this work for *k*-factor and $\Delta N_{0.065}$ not exceeded for 1% of time, known as dN_1, on the link performance is simulated using ICS Telecom. The path and Fresnel zone clearance is investigated using global ITU *k*-factor value of 4/3 and some of the results obtained in this study for different regions for AUH, DXB, SHJ, RAK, AIN and FUJ, which are 1.92, 1.96, 1.89, 1.95, 1.49 and 2.24, respectively. The predicted link's availability is also compared using ICS Telecom for different dN_1 values obtained from ITU maps and this study. It dN_1 values for AUH, DXB, SHJ and RAK are found to be -1604.5, -1378.8, -1122 and -1300, respectively.

The signal ellipsoid clearance is investigated for *k*-factor values of 1.33 and 1.92. The path profile and link budget of L1 link is studied from S1 to S2 for the clearance analysis. The

minimum required transmitting antenna height to ensure the ellipsoid clearance is examined assuming a fixed receiving antenna height of 37 m, and a transmitting antenna height of 53 m, as currently installed.

Figure 10.32 shows the profile from L1-S1 to L1-S2 for *k*-factor value of 1.33 with possible signal diffraction since the Fresnel zone is not 100 % clear for transmitting and receiving antenna height of 53 m and 37 m, respectively. The minimum transmitting antenna height required to ensure path clearance is found to be 78 m, assuming fixed receiving antenna height.

Figure 10.33 the path profile in case of adopting *k*-factor value of 1.92, noting that the minimum required transmitting antenna height is 54 m to ensure 100 % clearance of the Fresnel zone. Both scenarios for the minimum antenna heights' requirement in accordance with *k*-factor and effective earth radius values are summarized in Table **10-8**.

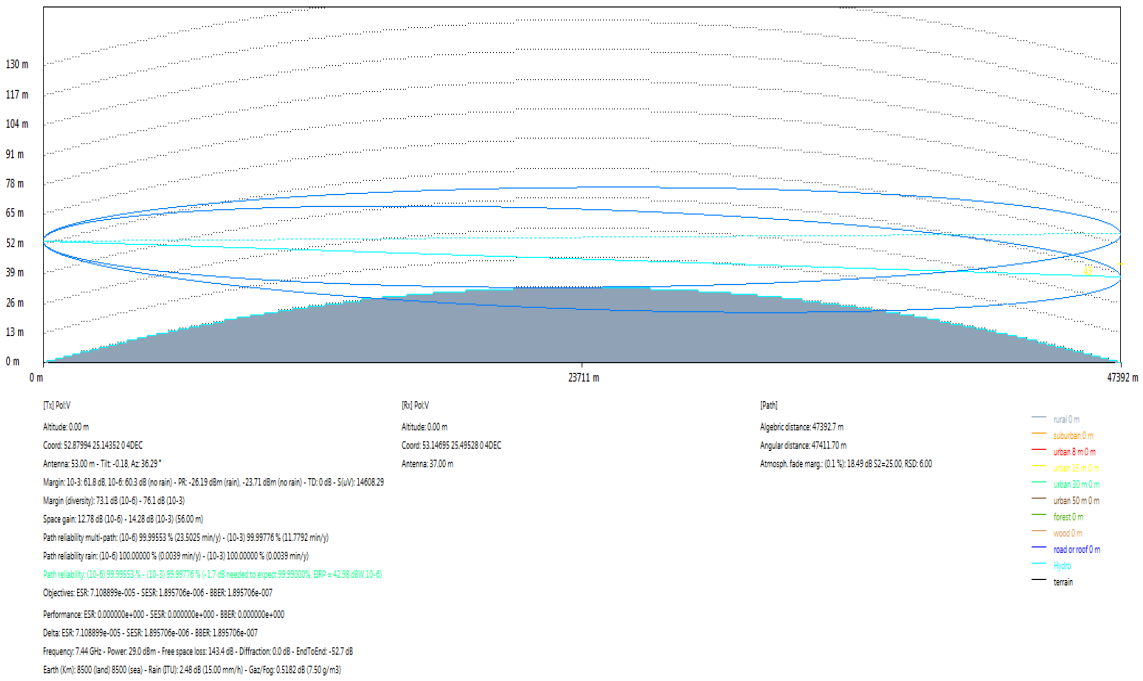

Figure 10.32: Ellipsoid clearance, *k* =1.33 and S2 antenna height = 37 m

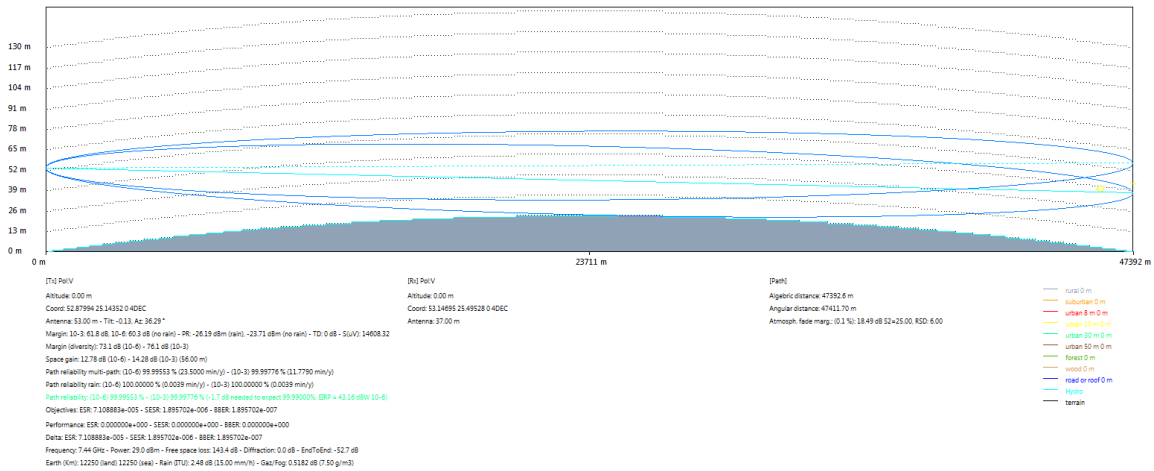

Figure 10.33: Ellipsoid clearance, k =1.92 and S2 antenna height = 37 m

Table 10-8: Minimum antenna heights at L1-S1 and L1-S2 for path clearance

Scenario	k-Factor	Effective Earth Radius (km)	Antenna Height required for Fresnel Zone clearance (m)
1	k = 1.33	8500	S1_Tx: 78 m S2_Rx: 37 m
2	k = 1.92	12250	S1_Tx: 54 m S2_Rx: 37 m

The prediction of link availability is evaluated for the same L1 link against two dN_1 values of -954.42 N/km and -1604.5 N/km for the same link. The link reliability also refers to the percentage of time the link is operating without severe degradation or outages. The targeted threshold link availability is assumed to be 99.999%. Figure 10.34 and Figure 10.35 provide the availability predictions, which are found to be 99.99999% (seven 9's) and 99.998% (four 9's) for the dN_1 values of -952.42 N/km and -1604.5 N/km, respectively.

The significant fluctuations in L1 RSSI measurements can be attributed to the antenna heights selection and availability prediction. The antenna height has to be raised at either the transmitting or the receiving antennas to ensure 100 % clearance of the Fresnel zone. The obtained dN_1 result in this study are not found so coherent with the proposed ITU values.

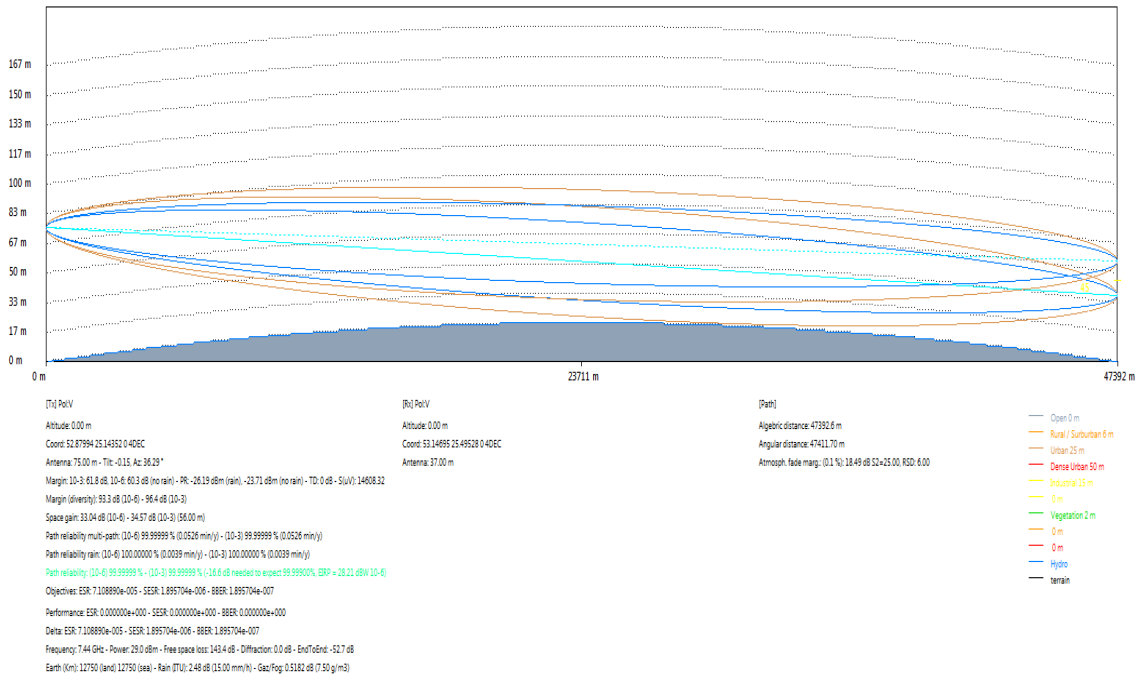

Figure 10.34: Link availability prediction, dN_1 = -952.42 N/km

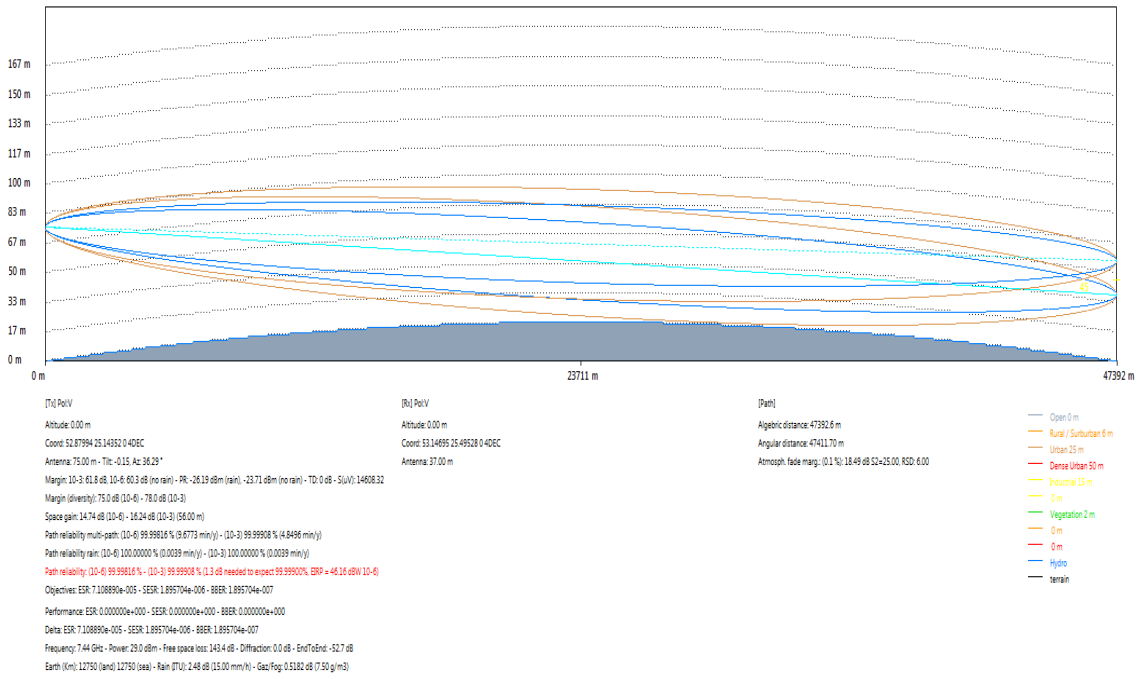

Figure 10.35: Link availability prediction, dN_1 = -1604.5 N/km

In general, there are many practical solutions that can be implemented to improve the link performance such as:

- Increasing the heights of either one or both transmitting and receiving antennas considering the limited tower heights to ensure clearance of the ellipsoid zones.
- Set the absolute elevation angle to more than 0.5^0 subject, as practically possible.
- Increase the transmission power to improve the link performance and availability, if possible, subject to the appropriate margin below receiver's saturation level.
- Activate adaptive modulation feature or implement lower static modulation scheme, which reduces link capacity, to improve link reliability.
- Installing bigger antennas with higher gain and directivity, subject to the tower load limitations.

10.7 Final Remarks

A network of more than 2000 point to point microwave links was studied based on predefined criteria to find out candidate links for comparing the link budget predictions with the actual field measurements.

The selection criteria took into account the operating frequency band of each link, locations of the receiving sites considering the clutter types, distances from receivers to the nearest weather stations, path length, and possibility for remotely accessing the link's signal strength measurements. Out of twelve candidate links for the study, RSSI measurements of eight links were analysed for some fading events.

Many challenges were raised due to the utilization of already established wireless and meteorological networks that were implemented for commercial or national purposes, but not intended for research. Some of these challenges related to the wireless measurements included the high cost for purchasing, implementing and maintaining new equipment dedicated for this research, systems' configurations and links' recovery were subject to the business requirement, remote connectivity for performance monitoring was hard for many links at the time of the study, and sites' locations. The data resolution was an additional limitation, where majority of data could be obtained with 15 minutes resolution while few data could be arranged with higher resolution up to 1 minute.

The link budget calculations for the selected links were carried out using commercial ICS Telecom planning software considering all links' parameters including exact locations, frequency carriers, channel bandwidth, power configuration, link capacity, and antenna configuration details. The maps showing the links' locations with respect to weather stations were provided. The path profiles were developed for all selected links for further analysis showing path length, LOS clearance and terrains between the sites.

The RSSI analysis showed considerable signal fading in comparison with the predicted values for most of the links. Some of the fading events were attributed to the observed dominating dust, sandstorm, thunderstorm and rain phenomena. Two offshore sites experienced severe signal fluctuations and fading events that could be associated with the oscillations of vapour pressure, wind speed and atmospheric refractivity.

The path clearance and link availability predictions were simulated using ICS Telecom software considering different values of k-factor and dN_1 propagation parameters. The results showed considerable differences in the predicted link's performance between the global ITU maps in comparison with the values introduced in chapter 8.

Chapter 11

CONCLUSIONS AND RECOMMENDATIONS

11.1 Overview

This chapter presents a summary of the work, the conclusions that are drawn from the work carried out in this thesis and finally some recommendations for further work.

11.2 Summary of Work

The prediction of certain propagation phenomena is a very complicated process due to the dynamic nature of meteorological and weather conditions and lack of data for upper atmospheric profiles in particular. The subtropical Arab Gulf region is one of the most critical areas with respect to the anomalous refraction conditions. Such areas needs extensive work to statistically dimension various non-standard propagation phenomena.

The anomalous refractive conditions and variations of the effective earth radius factor as well as their impact on the performance of operating microwave links in the subtropical Arabian Gulf region were studied. UAE was selected to conduct the experiments by utilizing the two networks of the weather stations and microwave links in the country, due

to its special climate which is hot and humid over the course of the year. Signal fluctuations and fading events were frequently occurring due to the commonly experienced anomalous propagation and severe variations of refractive conditions.

New empirical models and methodologies were developed in this research work to statistically analyse the dominating refractive conditions and relevant propagation parameters of clear air atmosphere and their fading impact on wireless communication systems using long-term field measurements of meteorological data and received signal strength. Some of the main achievements can be summarized as follows:

- New algorithms and approaches were developed to predict the vertical atmospheric profile where upper-air meteorological data are not available such as:
    - Empirical curve-fitting models were developed for evaluating the vertical upper refractivity and refractivity gradient profiles in the low troposphere with marginal improvement obtained for high order polynomial relationship.
    - A new approach was proposed to evaluate the refractivity from widely available surface meteorological data such that radiosonde data were utilized in the surrounding sites with similar surface conditions.
    - An indirect approach was suggested to estimate N_h and ΔN from the analysis of dry and wet refractivity components, which showed promising results for 1 km atmospheric layers and marginal improvement for 65 m and 100 m layers.

- A new weighted average approach was developed for evaluating the effective earth radius factor, *k*-factor parameter, from the analysis of three atmospheric layers namely; 65 m, 100 m and 1 km.
- A new approach was developed for analyzing mean duct statistics by averaging the modified refractivity parameter for given heights with respect to reference times to tackle the impact of uncertainties in meteorological measurements.
- It was proposed to adopt optimum height coefficient in the exponential models for different refractivity components and atmospheric layers rather than using fixed value.
- Some of the findings related to various propagation phenomena were validated using wireless signal strength measurements from different locations in UAE and the impact of other outputs on the performance of wireless systems were investigated.
- Different techniques for tackling the negative impact of anomalous propagation conditions were proposed from practical field experience.

The effective earth radius factor, point refractivity gradient, anomalous propagation conditions; such as sub-refraction, super-refraction, and different types of atmospheric ducts; such as surface-based and elevated ducts, were dimensioned and profiles were established for various areas with different locations and climates.

The background on refractivity relationships in accordance with meteorological parameters and the characteristics of atmosphere were introduced in chapter 2. The components of wireless communication system were provided and the parameters of free path loss model were explained. The linear and exponential models of refractivity gradient evaluation were discussed and several propagation parameters were introduced including β_0, point refractivity gradient and Effective Earth Radius. The modified refractivity parameter and different types of atmospheric duct phenomena were presented. The *k*-type fading due to refraction and diffraction interaction was discussed. The previous work in the literature regarding the analysis of these propagation parameters was investigated and also presented in chapter 2.

Different models were found in the literature for refractivity predictions, which had significant differences when applied and compared with the obtained measurements in the area under study. Linear and exponential models were investigated. Direct and indirect refractivity estimations using various approaches were studied, when reliable local meteorological data are not available.

The specifications of weather stations and meteorological equipment utilized in this work were discussed in chapter 3. Several tools and instruments were introduced. The characteristics of Vaisala radiosonde equipment, used for upper-air meteorological measurements, in addition to the surface weather stations, used for surface meteorological measurements, were presented. The configurations and specifications of wireless PTP MW links were discussed, considering various frequency bands, modulation schemes, link

capacity, receiver's sensitivity and transmission power. The installation procedure and the setup for remote connectivity to the links, based on operational field experience, was explained.

Multiple sets of local meteorological measurements were gathered, including dry and dewpoint temperatures, atmospheric pressure, relative humidity, wind speed, wind direction, rain rate and weather conditions. Field strength measurements were obtained from several microwave links. The types of meteorological and wireless measurements along with the processing approaches and the software used for processing them were discussed in chapter 4. The raw sounding data of radiosonde was processed using RAOB software. The step-by-step processing procedure of various meteorological data types was explained. The locations of the radiosonde and six manual surface weather stations were provided. The weather codes, registered manually at the six manual surface stations were presented. The resolutions of radiosonde data and wireless measurements were introduced. The capabilities and features of ICS Telecom commercial design software as well as the step-by-step procedure to create, design, and simulate performance of PTP MW links in ICS Telecom were explained. MATLAB software was used for data analysis.

Three critical atmospheric layers within the first kilometre of the low troposphere above the ground were studied, which are 65 m, 100 m and 1 km. The initial results of refractivity and its gradients in standard atmospheric layers above Earths' surface were presented in chapter 5, using radiosonde meteorological data in Abu Dhabi. Initial set of fourteen years surface and meteorological data were gathered from 1990 to 2003.

Initial β_0 parameter was evaluated in chapter 6 using nine years of local radiosonde data, from 1997 to 2005, to investigate the probability of anomalous propagation occurrence such as ducting and multipath in Abu Dhabi from the statistics of the refractivity gradient in the first hundred meters above the ground surface.

In chapter 7, seventeen years of local radiosonde data, from 1997 to 2013, were analysed to obtain the detailed vertical refractivity profile for the three atmospheric layers. The correlation between N_s and either N_h or ΔN depended predominantly on the wet components of these parameters. It was recommended to the application of indirect approach to estimate N_h and ΔN from the analysis of dry and wet refractivity components, in particular at the 1 km layer. Marginal improvement was achieved for the 65 m and 100 m layers for N_h prediction using the exponential model.

The same set of seventeen years data were used to investigate the surface and vertical refractivity profile in chapter 8. The surface measurements using fixed weather stations were expected to be more accurate when compared with the surface radiosonde measurement, due to higher stability of fixed stations. The evaluation of vertical refractivity profile for the critical atmospheric layers, in areas where radiosonde data are not available, from the analysis of surface refractivity was discussed. A new approach was proposed for utilizing the upper-air refractivity from a radiosonde site in the surrounding sites with similar surface conditions. This approach was used for ΔN analysis at 1 km at all the sites including sites with different surface profiles from the radiosonde location, as well

as exponential prediction models for the ΔN prediction at all sites. Higher concurrency with radiosonde measurement was obtained using the new proposed approach in this study with higher range of variations for 100 m altitude and below. The differences observed in monthly refractivity gradient profiles at sites with similar mean surface profiles is attributed to the fact that measurements at a given time were not necessary the same at these sites over the whole period. In addition, it was found that any small change in N_s value results in large disagreement in ΔN due to the low decimal number in the denominator of the linear ΔN equation for low heights. A new approach was used to evaluate *k*-factor from the weighted average ΔN at the three layers. Negative *k*-factor values were obtained, which indicated the incidence of ducting phenomenon in the area under study. It is recommended to apply similar approach to evaluate the vertical refractivity profiles in the surrounding areas to a radiosonde location and for areas with similar surface refractivity conditions.

Atmospheric duct was analysed in chapter 9 using the high-resolution seventeen years upper-air meteorological data with 5 m vertical resolution at Abu Dhabi. The surface, surface-elevated and elevated ducts' types were statistically analysed. The signal trapping was found to rely on the angle of incidence and the wavelength of propagating signals. Empirical equation was used to evaluate the minimum frequencies to be trapped from the duct thickness analysis. Two approaches were followed to analyse the vertical profiles of modified refractivity based on the ITU definitions of the three duct types. The modified refractivity parameter was averaged for the given heights with respect to reference times at the first approach (1) to overcome uncertainties and errors in the measurements. In the

second approach (2), the duct parameters were average after evaluating the hourly vertical *M* profiles from the raw meteorological data. The duct occurrence probability exceeded 50% of the summer time. The surface based ducts; including both surface and surface-elevated, had higher occurrence probability than the elevated duct, in particular at 12H. The approach (2) was applied on the data of April, May, July and December 2013, and the trapping frequencies were found to be within the range from 4 to 32 GHz. The duct strength was below 10 M-units for majority of observations. Higher occurrence of elevated duct was shown in summer.

The results for thickness and strength parameters for the three duct categories, in addition to the coupling and base heights for the elevated ducts, were provided. The practical feasibility of using the ITU mean long-term duct parameters for designing the wireless systems was found to be questionable.

Several practical measures were discussed to manage the impact of ducting phenomena such as the selection of antenna height and elevation angle, operating frequency carrier and space diversity.

In chapter 10, large number of more than 2000 LOS PTP radio Links were evaluated using ICS Telecom software according to predefined criteria and only 12 links were found to be candidate for further study. The operating frequency band of each link, locations of the receiving sites considering the clutter types, distances from receivers to the nearest weather stations, path length, and possibility for remotely accessing the link's signal strength measurements were considered in the links' selection. The maps of these links along with

the nearby weather stations and the path profiles were provided, showing path length, LOS clearance and terrains between the sites. The predictions of link budget including received signal strength, fade margin, propagation losses, and links' availability were presented considering exact locations, frequency carriers, channel bandwidth, power configuration, link capacity, and antenna configuration details. The RSSI measurements for eight out of the 12 candidate links were presented and some fading events were analysed.

Many challenges and limitations were experienced including fixed sites' locations and high cost of new equipment dedicated for this research noting that systems' configurations and links' recovery were subject to the business requirement. The remote connectivity for performance monitoring was not possible for many links. Majority of data could be obtained with 15 minutes resolution while few data had higher resolution up to 1 minute.

Operational observations of the received signal strength, fading occurrence and interference cases for some of the microwave links operating in the UAE confirmed the findings in this research work.

11.3 Conclusions

The concluding remarks for the accomplishments in this research work can be summarized as follow:

- In comparison with the ITU value of -40 N/km for the vertical refractivity gradient of reference standard atmosphere, the long-term mean value of ΔN in the first kilometre was found to be around -79.6 N/km at AUH, while the estimated values varied from -71.83 N/km at AIN, up to -89.9 N/km at FUJ. The monthly mean ΔN values were not in good coherence with ITU maps except for May and August at AUH and the surrounding sites. The ΔN value for the first 65 m of atmosphere above the ground not exceeded for 1 % of the time, known as dN_1 parameter, was found to be -1604 N/km at AUH. The values were adopted based on the results of 1-(b) approach.

- The long-term mean value of ΔN for the first 100 m and β_0 were found to be below -141.6 N/km and above 56.5%, respectively, at AUH, DXB, SHJ and RAK sites. The values were -159.6 N/km and 57.3%, respectively, at AUH. The monthly β_0 results were not in good agreement with the ITU maps. The results of refractivity gradient statistics presented that the range of gradient variations in the lowest 65 m and 100 m layers are much higher than the range for 1 km layer. These results indicated frequent occurrence of anomalous propagation in the critical 65 m and 100 m atmospheric layers, where most terrestrial wireless systems operate. In general, the morning, and summer months, showed higher occurrence probability of nonstandard propagation conditions. In comparison with other cumulative distribution curves for the 65 m and 1 km, the morning time showed higher probabilities for larger negative gradient values.

- It was found that the linear ΔN model resulted in somewhat lower RMSE values than the exponential one, at the three layers.

- It was noticed that indirect approach to estimate N_h and ΔN from the analysis of dry and wet refractivity components reduced the RMSE values, however, the multi-steps analysis may lead to slightly lower correlation, when compared with the measured data, than using the direct relations.

- The RMSE values of the predicted N_h or ΔN were reduced while the correlation between the measured and predicted values was marginally improved for certain parameters, when different models are used at the three layers. Third- and fourth-order polynomial models showed marginal improvements for N_h and ΔN predictions. However, the results were very sensitive to the precision of the high order coefficients. The optimum height coefficient in the exponential models was found to vary significantly for different components and atmospheric layers.

- The β_0 analysis at four sites indicated high probability of anomalous propagation for all months in the area under study, reaching up to 71 % at certain locations within the summer.

- The long-term median values of effective earth radius factor, *k*, varied from 1.71 at AIN to 2.15 at FUJ. The median *k*-factor value reached around 3.5 at AUH using the new weighted average approach.

- The atmospheric duct results were not in good coherence with ITU maps considering that the surface-elevated duct is part of the surface based duct category. The ITU below-estimated occurrence probability of the surface based ducts and overestimated probability of elevated duct, when approach (1) was used. The surface duct strength was less than 15 M-units for more than 70% of time, while thickness was less than 50 m and below 20 m for more than 50% of time using the approaches (1) and (2), respectively.

- The frequencies to be trapped in the duct were evaluated and found to vary from 55 MHz to 32 GHz for the surface based ducts using approaches (1) and (2). With regards to the elevated duct, the frequencies oscillated from 57 MHz to 7.7 GHz using approach (1) and from 58 MHz to 2.1 GHz in case of approach (2).

- The RSSI analysis showed considerable signal fading in comparison with the predicted values for most of the links. Some of the severe fading events could be attributed to the observed dominating dust, sandstorm, thunderstorm and rain phenomena.

- Two offshore sites experienced severe signal fluctuations and fading events that are associated with the oscillations of vapour pressure, wind speed and atmospheric refractivity, in addition to the possible diffraction due to the antenna heights. The path clearance and link availability predictions were simulated using ICS Telecom software considering different values of *k*-factor and dN_1 propagation parameters. The results showed considerable differences in the predicted link's performance between the global ITU maps in comparison with the values introduced in chapter 8.

- In general, it was found that the ITU values were not in good concurrence with many results obtained in this research work. This is due to the fact that ITU maps [12] were interpolated from radiosonde data from only 99 sites worldwide between 1955 and 1959. In addition, ITU curves and maps are usually derived from measurements performed largely in temperate regions of the world such as Europe, North America and Japan which have different climatic conditions from the Arab Gulf region.

11.4 Recommendations for Future Work

- It is strongly recommended to adopt the obtained results in this thesis in the design and deployment of wireless communication systems working in similar sub-

tropical regions for accurate prediction of systems' performance and reliability, since the calculations were carried out using long-term reliable local data.

- The results obtained in this study would suggest the necessity to revise the ITU maps for similar subtropical climate. The gathered long-term local meteorological data from more radiosonde sites worldwide can be utilized for this purpose.

- Additional radiosonde setups need to implemented in areas with different climates, such as in the east cost of UAE, which showed extreme surface results due to its unique hot and humid climate and the mountainous location in the tropical zone nearby Oman Gulf, where the gulf is opened to the Indian Ocean.

- The analysis of atmospheric ducts should be conducted on hourly basis for the complete study period in order to accurately evaluate all possible scenarios and to have solid understanding for the frequency of occurrence for each duct type. Development of algorithm for automatic evaluation of the parameters of each duct type from the values of vertical modified refractivity parameter will help saving considerably large processing time rather than the visual analysis of the hourly vertical refractivity profiles.

- Selection of additional MW links with various configurations that operate in different frequency bands will be very valuable if further upper-air meteorological data can be gathered in nearby locations. This study was conducted considering

case studies from the PTP MW network of the leading telecom operator in the region, Etisalat. However, other users are urged to carry out similar studies to ensure reliable performance of their wireless systems.

- Similar studies for other subtropical regions are essential to be conducted in many areas for developing appropriate methodologies, algorithms and profiles for such unique climate.

- The UAE Telecommunication Regulatory Authority (TRA) is advised to consider the results obtained in this research work in their evaluation of frequently experienced cross-border interference cases and to negotiate some of the proposed mitigation techniques in this work with neighbouring countries.

- Telecommunication Regulatory Authorities are urged worldwide to support the development of area specific propagation models within their countries and regions in coordination with the national centers of meteorology and users of wireless communication systems.

References

[1] UAE Map [Online]. Available: http://www.industradeservices.com/view_section.php?lang=0&id=0,62,74 [Accessed: 1/8/2015].

[2] L. E. Frenzel, *Communication Electronics*, 3rd ed: Mc Graw-Hill, 2001.

[3] Dominguez M. A., Benarroch A., and Riera J. M., "Refractivity Statistics in Spain: First Results," in *COST 255, CP52004*, May 1998.

[4] Abdulhadi Abu Al-mal and K. Al-Ansari, "Calculation of Effective Earth Radius and Point Refractivity Gradient in UAE," *International Journal of Antennas and Propagation*, vol. 2010, no. Article ID 245070, 2010.

[5] Kifah Al-Ansari, Abdulhadi AbuAl-Mal, and R. A. Kamel, "Statistical Analysis of Refractivity in UAE," *Internationl Symposium on Rainfall Rate and Radiowave Propagation, India, Published by American Institute of Physics Conference Proceedings*, vol. 923, no. pp. 232-247, 2007.

[6] T. S. Rappaport, *Wireless Communications*, 2nd ed.

[7] ATDI. Manuals of ICS Telecom Software For Radio Planning [Online]. Available: http://www.atdi.com/ [Accessed: 23 Feb. 2013].

[8] T. C. W. David, Y. K. Peng, C. L. Ying, C. C. Kee, and W. M. Jon, *Wireless Broadband Networks*: Wiley, 2009.

[9] R. Jain, "Channel Models: A Tutorial," WiMAX Forum, Feb. 2007.

[10] B. Gerard, *Microwave Engineering, Land & Space Radiocommunications*: John Wiley & Sons, 2008.

[11] I. R. Bureau, "Handbook on Radiometeorology," *International Telecommunication Union*, no., Geneva, 1996.

[12] I.-R. R. P.453-10, "The radio refractive index: its formula and refractivity data," *International Telecommunication Union, ITU*, no., 2012.

[13] I.-R. R. P.452-12, "Prediction Procedure for the Evaluation of Microwave Interference between stations on the surface of the earth at the frequencies above about 0.7 GHz," *International Telecommunication Union, ITU*, no., 2005.

[14] W. L. Patterson. Advanced Refractive Effects Prediction System (AREPS), Technical Document 3028 - Version 1.0 User's Manual [Online]. Available: file:///C:/Users/etisalat/Downloads/ADA348559.pdf [Accessed: April 1998].

[15] A. T. Adediji, M. O. Ajewole, and S. E. Falodun, "Distribution of radio refractivity gradient and effective earth radius factor (k-factor) over Akure, South Western Nigeria Original Research Article," *Journal of Atmospheric and Solar-Terrestrial Physics*, vol. 73, no. 16, pp. 2300-2304, Oct. 2011.

[16] I.-R. R. P.835-5, "Reference standard atmospheres," *International Telecommunication Union, ITU*, no., 2012.

[17] I.-R. R. P.836-4, "Water vapour: surface density and total columnar content," *International Telecommunication Union, ITU*, no., 2009.

[18] M. G. Lawrence, "The Relationship between Relative Humidity and the Dewpoint Temperature in Moist Air - A Simple Conversion and Applications," American Meteorological Society, 2005.

[19] W. Wagner and A. Pruß, "The IAPWS Formulation 1995 for the Thermodynamic Properties of Ordinary Water Substance for General and Scientific Use " *Journal of Physical and Chemical Reference Data*, vol. 31, no. 2, June 2002.

[20] X. Lin and K. G. Hubbard, "Uncertainties of Derived Dewpoint Temperature and Relative Humidity: Notes and Correspondence," American Meteorological Society, May 2004.

[21] M. G. Lawrence, "The Relationship between Relative Humidity and the Dewpoint Temperature in Moist Air - A Simple Conversion and Applications," in *American Meteorological Society*, 2005.

[22] S. S. MENTES and Z. KAYMAZ, "Investigation of Surface Duct Conditions over Istanbul, Turkey," *Journal of Applied Meteorology And Climatology*, vol. 46, no., 2006.

[23] T. G. Hayton and K. H. Craig, "Use of Radiosonde Data in Propagation Prediction," Presented at IEE. Available, [Accessed:

[24] M. I. Skolnik, *Introduction to Radar Systems*, 3rd ed: McGraw-Hill Inc., 2001.

[25] O. Jicha, P. Pechac, V. Kvicera, and M. Grabner, "Estimation of radio refractivity profile gradient from multiple LOS links using artificial neural networks — First results," in *Antennas and Propagation (EUCAP), 2012 6th European Conference on*, 2012, pp. 1174-1177.

[26] O. Jicha, P. Pechac, V. Kvicera, and M. Grabner, "Estimation of the Radio Refractivity Gradient From Diffraction Loss Measurements," *Geoscience and Remote Sensing, IEEE Transactions on*, vol. 51, no. 1, pp. 12-18, 2013.

[27] T. Tjelta and T. O. Breivik, "Measured attenuation data and predictions for a gigabit radio link in the 80 GHz band," in *Antennas and Propagation, 2009. EuCAP 2009. 3rd European Conference on*, 2009, pp. 657-661.

[28] I.-R. R. P.834-6, "Effects of Tropospheric Refraction On Radiowave Propagation," *International Telecommunication Union, ITU*, no., 2007.

[29] B. L. and S. H., "Refractivity Over France: First Results of ARGOS Experiment," *COST255, CP32003*, no., May 1997.

[30] I.-R. R. P.530-14, "Propagation data and prediction methods required for the design of terrestrial line-of-sight systems," *International Telecommunication Union, ITU*, no., 2012.

[31] A. T. Adediji and M. O. Ajewole, "Microwave anomalous propagation (AP) measurement over Akure South-Western Nigeria," *Journal of Atmospheric and Solar-Terrestrial Physics*, vol. 72, no. 5–6, pp. 550–555, April 2010.

[32] I.-R. R. PN.310-9, "Definitions of terms relating to propagation in non-ionized media," *International Telecommunication Union, ITU*, no., 1994.

[33] T. J. Afullo and P. K. Odedina, "On The K-Factor Distribution And Diffraction Fading For Southern Africa," *South African Institute Of Electrical Engineers*, vol. 97, no. pp. 172-181, June 2006.

[34] I. D. J.-E. f. S. A. t. t. I.-R. WP-3J, "Contribution To The Propagation Data Banks, Rain Rate and Slant-Path Rain Attenuation Data In Madrid," *International Telecommunication Union, ITU-R WP-3J Meeting*, no., Geneva, 2011.

[35] T. J. Afullo, T. Motsoela, and D. F. Molotsi, "Refractivity gradient and k-factor in Botswana," in *Proceeding of the Regional Workshop on Radio Communications in Africa*, 1999, pp. 107–110.

[36] G. B. a. P. A. Watson, *Atmospheric Modeling and Millimetre Wave Propagation*, 1st ed: Chapman & Hall, 1995.

[37] Simon R. Saunders and A. A. Zavala, *Antennas And Propagation For Wireless Communication Systems*, 2nd ed: John Wiley & Sons, Ltd, 2007.

[38] E. Dinc and O. B. Akan, "Channel Model for the Surface Ducts: Large-scale Path-Loss, Delay Spread, and AOA," *Antennas and Propagation, IEEE Transactions on*, vol. PP, no. 99, pp. 1-1, 2015.

[39] S. LYSTAD, "Investigation of surface refractivity and refractive gradients in the lower atmosphere of Norway," Presented at COST 235, CP 121. Available, [Accessed:

[40] K. H. Craig and T. G. Hayton, "Refractivity parameters from radiosonde data," Presented at AGARD Conf. On Propagation Assessment in Coastal Environments, CP 182. Available, [Accessed:

[41] A. K. P. Marsh, T. G. Hayton, and K. H. Craig, "Initial Comparison of Refractivity Parameters Derived from Radiosondes and Psychrometers in France," in *COST255, CP42010*, Oct. 1997.

[42] K. H. Craig and T. G. Hayton, "Investigation of β0 values derived from ten years radiosonde data at 26 stations," in *COST 235, CP 182*, Oct. 1993.

[43] C. Bourlier, L. Hongkun, and N. Pinel, "Low-Grazing Angle Propagation and Scattering Above the Sea Surface in the Presence of a Duct Jointly Solved by

Boundary Integral Equations," *Antennas and Propagation, IEEE Transactions on*, vol. 63, no. 2, pp. 667-677, 2015.

[44] F. Ryan, "Ducted millimeter wave propagation over rough seas using PWE," in *Radio Science Meeting (USNC-URSI NRSM), 2014 United States National Committee of URSI National*, 2014, pp. 1-1.

[45] F. Ryan, "MMW propagation in warm water evaporation ducts," in *Radio Science Meeting (USNC-URSI NRSM), 2013 US National Committee of URSI National*, 2013, pp. 1-1.

[46] G. Fedele, P. Lombardo, and D. Deli, "A phenomenological model for radar signal propagation in evaporation ducts," in *Radar Conference, 2000. The Record of the IEEE 2000 International*, 2000, pp. 515-520.

[47] B. R. Bean and G. D. Thayer, "Models of the Atmospheric Radio Refractive Index," *Proceedings of the IRE*, vol. 47, no. 5, pp. 740-755, 1959.

[48] J. H. Richter, "Sensing of radio refractivity and aerosol extinction," in *Geoscience and Remote Sensing Symposium, 1994. IGARSS '94. Surface and Atmospheric Remote Sensing: Technologies, Data Analysis and Interpretation., International*, 1994, vol. 1, pp. 381-385 vol.1.

[49] A. R. Lowry, C. Rocken, S. V. Sokolovskiy, and K. D. Anderson, "Vertical profiling of atmospheric refractivity from ground-based GPS," *Radio Science*, vol. 37, no. 3, pp. 13-1-13-19, 2002.

[50] R. M. Hodur, "The Naval Research Laboratory's Coupled Ocean/Atmosphere Mesoscale Prediction System (COAMPS)," *Monthly Weather Review*, vol. 125, no. 7, pp. 1414-1430, 1997.

[51] L. T. Rogers, C. P. Hattan, and J. K. Stapleton, "Estimating evaporation duct heights from radar sea echo," *Radio Science*, vol. 35, no. 4, pp. 955-966, 2000.

[52] P. Gerstoft, L. T. Rogers, J. L. Krolik, and W. S. Hodgkiss, "Inversion for refractivity parameters from radar sea clutter," *Radio Science*, vol. 38, no. 3, 2003.

[53] P. Valtr, P. Pechac, V. Kvicera, and M. Grabner, "Estimation of the Refractivity Structure of the Lower Troposphere From Measurements on a Terrestrial Multiple-Receiver Radio Link," *Antennas and Propagation, IEEE Transactions on*, vol. 59, no. 5, pp. 1707-1715, 2011.

[54] O. Jicha, P. Pechac, V. Kvicera, and M. Grabner, "Troposphere refraction state classification using measured attenuation of non-line-of-sight microwave links," in *Antennas and Propagation (EUCAP), Proceedings of the 5th European Conference on*, 2011, pp. 1626-1629.

[55] O. Jicha, P. Pechac, V. Kvicera, and M. Grabner, "On the Uncertainty of Refractivity Height Profile Measurements," *Antennas and Wireless Propagation Letters, IEEE*, vol. 10, no. pp. 983-986, 2011.

[56] B. L. Cheong, R. D. Palmer, C. D. Curtis, T.-Y. Yu, D. S. Zrnic, and D. Forsyth, "Refractivity retrieval using the phased-array radar: First results and potential for multimission operation," *IEEE Transaction on Geoscience and Remote Sensing*, vol. 46, no. 9, pp. 2527-2537, Sep. 2008.

[57] O. T. Davies, C. N. Mitchell, P. S. J. Spencer, J. D. Nash, R. J. Watson, and P. A. Watson, "Application of GPS phase delay measurements in radio science and atmospheric studies," *Microwaves, Antennas and Propagation, IEE Proceedings*, vol. 151, no. 1, pp. 1-6, 2004.

[58] R. J. Watson and C. J. Coleman, "The use of signals of opportunity for the measurement of atmospheric refractivity," in *Antennas and Propagation (EuCAP), 2010 Proceedings of the Fourth European Conference on*, 2010, pp. 1-5.

[59] I. Sirkova and M. Mikhalev, "Influence of Tropospheric Duct Parameters Changes on Microwave Path Loss," *Microwave Review*, vol. 9, no. 2, pp. 43-46, Dec. 2003.

[60] A. Kerans, A. Kulessa, G. Woods, and J. Hermann, "Evaporation Duct Statistics Around Australia and the West Pacific," in *AP2000*, 2000.

[61] J. M. Garcia-Rubia, J. M. Riera, P. Garcia-del-Pino, and A. Benarroch, "Propagation in the Ka Band: Experimental Characterization for Satellite Applications," *Antennas and Propagation Magazine, IEEE*, vol. 53, no. 2, pp. 65-76, 2011.

[62] I. D. J.-E. f. U. A. t. t. I.-R. WP-3J, "Test Results for Revised Sleet Attenuation Model," *International Telecommunication Union, ITU-R WP-3J Meeting*, no., Geneva, 2011.

[63] H. V. Hitney, J. H. Richter, R. A. Pappert, K. D. Anderson, and G. B. Baumgartner, Jr., "Tropospheric radio propagation assessment," *Proceedings of the IEEE*, vol. 73, no. 2, pp. 265-283, 1985.

[64] G. S. Woods, A. Ruxton, C. Huddlestone-Holmes, and G. Gigan, "High-Capacity, Long-Range, Over Ocean Microwave Link Using the Evaporation Duct," *Oceanic Engineering, IEEE Journal of*, vol. 34, no. 3, pp. 323-330, 2009.

[65] A. Iqbal and V. Jeoti, "Feasibility study of radio links using evaporation duct over sea off Malaysian shores," in *Intelligent and Advanced Systems (ICIAS), 2010 International Conference on*, 2010, pp. 1-5.

[66] S. D. Gunashekar, E. M. Warrington, and D. R. Siddle, "Long-term statistics related to evaporation duct propagation of 2 GHz radio waves in the English Channel," *Radio Science*, vol. 45, no. 6, p. RS6010, 2010.

[67] E. Dinc and O. Akan, "Beyond-line-of-sight communications with ducting layer," *Communications Magazine, IEEE*, vol. 52, no. 10, pp. 37-43, 2014.

[68] I. Sirkova, "Brief review on PE method application to propagation channel modeling in sea environment," in *Open Engineering*, vol. 2, 2012, pp. 19.

[69] O. Ozgun, G. Apaydin, M. Kuzuoglu, and L. Sevgi, "PETOOL: MATLAB-based one-way and two-way split-step parabolic equation tool for radiowave propagation over variable terrain," *Computer Physics Communications*, vol. 182, no. 12, pp. 2638-2654, 2011.

[70] R. Douvenot, V. Fabbro, and Y. Hurtaud, "The detectable double atmospheric ducts for RFC," in *Antennas and Propagation Society International Symposium (APSURSI), 2014 IEEE*, 2014, pp. 1616-1617.

[71] S. Yang, Y. Kunde, Y. Yixin, and M. Yuanliang, "Spatio-temporal distribution of evaporation duct for the South China Sea," in *OCEANS 2014 - TAIPEI*, 2014, pp. 1-6.

[72] Y. Pan and Y. Ma, "Modelling evaporation duct effects on microwave propagation with experiment validation," in *Antennas, Propagation & EM Theory, 2006. ISAPE '06. 7th International Symposium on*, 2006, pp. 1-4.

[73] G. Page, S. Bainbridge, and S. Gardner, "Implementation of low-cost, long-range microwave links on the Great Barrier Reef using evaporation duct transmission," in *OCEANS 2014 - TAIPEI*, 2014, pp. 1-4.

[74] H. V. Hitney and L. R. Hitney, "Frequency diversity effects of evaporation duct propagation," *Antennas and Propagation, IEEE Transactions on*, vol. 38, no. 10, pp. 1694-1700, 1990.

[75] Z. Jin-peng, W. Zhen-Sen, H. Rong-Xu, and W. Bo, "Estimating low-altitude atmospheric refractivity structure from multi-frequency radar returns," in *Antennas Propagation and EM Theory (ISAPE), 2010 9th International Symposium on*, 2010, pp. 682-685.

[76] R. J. Watson, B. Wiltshire, N. Dumont, and C. J. Coleman, "Measurement of atmospheric refractivity using signals of opportunity," in *Geoscience and Remote Sensing Symposium (IGARSS), 2012 IEEE International*, 2012, pp. 1964-1967.

[77] Vaisala Radiosonde RS92-SGP Mannual [Online]. Available: http://www.vaisala.com [Accessed: Feb. 2013].

[78] Main Parts of Radiosonde RS92-SGP [Online]. Available: http://alg.umbc.edu/umap/radiosonde/index.html [Accessed: Feb. 2013].

[79] ATDI. Mannuals of ICS Telecom Software For Radio Planning [Online]. Available: http://www.atdi.com/ [Accessed: 23 Feb. 2013].

[80] National Weather Service, Weather Symbols [Online]. Available: http://www.srh.weather.gov/jetstream/synoptic/sfc_plot_symbols.htm [Accessed: 8/8/2015].

[81] The Universal RAwinsonde OBservation (RAOB) Program [Online]. Available: http://www.raob.com/ [Accessed: Feb. 2013].

[82] K. Al Ansari and R. A. Kamel, "Correlation Between Ground Refractivity and Refractivity Gradient and Their Statistical and Worst Month Distributions in Abu

Dhabi," *Antennas and Wireless Propagation Letters, IEEE*, vol. 7, no. pp. 233-235, 2008.

[83] R. L. Freeman, *Radio System Design for Telecommunications*: John Wiley, 1997.

[84] S. Yang, Y. Kunde, M. Yuanliang, Y. Yixin, and S. Chao, "Short term forecast of the evaporation duct for the West Pacific Ocean," in *Oceans - San Diego, 2013*, 2013, pp. 1-4.

[85] H. J. Hansen, A. S. Kulessa, W. Marwood, M. Forrest, and O. Reinhold, "Over-the-horizon Ka band radio wave propagation studies in the coastal South Australian Spencer Gulf region," in *Radar (Radar), 2013 International Conference on*, 2013, pp. 69-74.

[86] E. L. Cairns-McFeeters, "Effects of surface-based ducts on electromagnetic systems," Master's Thesis, Naval Postgraduate School, Monterey, CA, USA, 1992.

[87] I. T. Union, "Radio Regulations Articles," in *ITU-R World Radiocommunication Conference 2012 (WRC-12)*, 2012.

[88] T. Manning, *Microwave Radio Transmission Design Guide*: ARTECH HOUSE, INC., 1999.

Author's Publication Records

Journals Papers:

1. AbouAlmal, A. ; Abd-Alhameed, R.A. ; Jones, S.M.R. ; Al-Ahmad, H., New Methodology for Predicting Vertical Atmospheric Profile and Propagation Parameters in Sub-tropical Arabian Gulf Region, IEEE Transactions on Antennas and Propagation, Volume: 63, Issue: 9, Publication Year: 2015 , Page(s): 1-6, DOI: 10.1109/TAP.2014.2360550

2. AbouAlmal, A. ; Abd-Alhameed, R.A. ; Jones, S.M.R. ; Al-Ahmad, H., New Approaches and Algorithms for the Analysis of Vertical Refractivity Profile below 1 km in a Subtropical Region, IEEE Transactions on Antennas and Propagation, Volume: 62, Issue: 12, Publication Year: 2014 , Page(s): 6501-6505

3. Abdulhadi AbouAlmal, Raed A. Abd-Alhameed, Kifah Al-Ansari, Hussein AlAhmad, James M Noras, Chan H See and Steve MR Jones, Statistical Analysis of Refractivity Gradient And β0 Parameter In The Gulf Region, IEEE Trans Antennas and Propagations, vol. 61, No. 12, Dec 2013, pp. 6250-6254.

Conferences Papers:

1. AbouAlmal, A. ; Abd-Alhameed, R.A. ; Jones, S.M.R. ; Al-Ahmad, H., New Methodology for Predicting Vertical Atmospheric Profile and Propagation Parameters in Sub-tropical Arabian Gulf Region, IEEE Transactions on Antennas and Propagation,

Volume: PP, Issue: 99, Publication Year: 2015 , Page(s): 1-6, DOI: 10.1109/TAP.2014.2360550

2. AbouAlmal, A. ; Abd-Alhameed, R.A. ; Jones, S.M.R. ; Al-Ahmad, H., New Approaches and Algorithms for the Analysis of Vertical Refractivity Profile below 1 km in a Subtropical Region, IEEE Transactions on Antennas and Propagation, Volume: 62, Issue: 12, Publication Year: 2014 , Page(s): 6501-6505

3. Abdulhadi AbouAlmal, Raed A. Abd-Alhameed, Kifah Al-Ansari, Hussein AlAhmad, James M Noras, Chan H See and Steve MR Jones, Statistical Analysis of Refractivity Gradient And β0 Parameter In The Gulf Region, IEEE Trans Antennas and Propagations, vol. 61, No. 12, Dec 2013, pp. 6250-6254.

4. AbouAlmal, H. Alhassan, H. Obeidat, R.A. Abd-Alhameed, S.M.R. Jones, and H Al-Ahmad, Surface Refractivity Profile and Validation of Measurements in Arabian Gulf Region, LAPC Conference, Nov 2015, in press.

5. AbouAlmal, H. Alhassan, R.A. Abd-Alhameed, S.M.R. Jones and H. AlAhmad, Investigation of Height Coefficient in Arabian Gulf, ITA 2015, EERT workshop, Wrexham, Wales, Sep 2015, in press.

6. Abdulhadi AbouAlmal, R.A.A. Abd-Alhameed, S.M.R. Jones, H Alahmad, Seasonal statistics of Anomalous Propagation in United Arab Emirates, 2014 Loughborough

Antennas and Propagation Conference (LAPC), 10 - 11 November 2014, UK, pp. 663-666. ISBN: 978-1-4799-3662-5/14

7. A AbouAlmal, R A Abd-Alhameed , S M R Jones, H Al Ahmad, New approach for predicting vertical refractivity profile in low troposphere in a subtropical region, The conference proceedings for the IET conference on Ninth CEM International Conference on Computation in Electromagnetics, Imperial College, London, UK, 31 March - 01 April 2014, session 3, P3-14; ISBN 978-1-84919-816-5, ISSN 0537-9989 Reference PEP0627U

8. M. AbouAlmal, M. Usman, R.A. Abd-Alhameed, H. Al-Ahmad, S.M.R. Jones and P.S. Excell, Initial Analysis Of K-Factor In The Gulf Region, Third International Workshop on Energy Efficient and Reconfigurable Transceivers (EERT): Towards a Green Wireless Internet, Proceedings of the fifth International Conference on Internet Technologies and Applications (ITA 13), Glyndŵr University, Wrexham, Wales, UK, Tuesday 10th – Friday 13th September 2013, pp. 415-420. ISBN 978-0-946881-81-9.

9. A AbouAlmal; Raed A Abd •]Alhameed; Abubakar Sadiq Hussaini; Tahereh S.Ghazaany; Sharon Zhu; Stephen M R Jones; Jonathan Rodriguez, Comparison of Three Vertical Refractivity Profiles In The Gulf Region, The 19th European Wireless Conference (EW 2013) in Guildford, United Kingdom from 16th to 18th April 2013, Special session 5: Green RF, Paper 2.

Appendix A:

List of Publications

New Methodology for Predicting Vertical Atmospheric Profile and Propagation Parameters in Subtropical Arabian Gulf Region

Abdulhadi AbouAlmal, Raed A. Abd-Alhameed, Steve M. R. Jones, and Hussain Al-Ahmad

***Abstract*—A new simplified approach is proposed to evaluate the vertical refractivity profile within the lowest 1 km of atmosphere from the analysis of surface refractivity N_s in areas where upper-air data are not available. Upper-air measurements from the nearest available radiosonde location with similar surface profile to these sites are utilized. The profiles of N_s and refractivity extrapolated to sea level N_o obtained from surface meteorological data using both fixed stations and radiosonde are investigated and compared. Vertical refractivity gradient ΔN is evaluated at three atmospheric layer heights within the first kilometer above the ground in addition to propagation parameters relevant to each atmospheric layer. At six sites, different approaches are compared for the analysis of three important parameters; namely effective earth radius factor k anomalous propagation probability parameter β_0 and point refractivity gradient at 65 m not exceeded for 1% of time dN_1 . The k-factor parameter is investigated using a new weighted average approach of ΔN at 65-m, 100-m, and 1-km layers above the ground. The results are compared with the latest ITU maps and tables for the same area.**

***Index Terms*—Anomalous propagation, atmospheric refraction, effective earth radius, point refractivity gradient, refractivity gradient β_0.**

I. Introduction

THE ANALYSIS of reliable meteorological data is essential to predict fading and interference probabilities that are dominated by atmospheric refraction in the area under study. The curvature of the propagation path is determined by the value of the effective earth radius factor, which is evaluated from the prevailing meteorological conditions; such as pressure, temperature, and relative humidity. The vertical refractivity profile is governed by the humidity gradients in the lowest layers of the troposphere and by the atmospheric pressure in the upper levels. However, the detailed profile is subject to random variation that is unpredictable in practice. Anomalous phenomena such as super-refraction and ducting may occur when large negative values of refractivity gradient ΔN are obtained, causing the curvature of radio signals to approach the Earth curvature or to be trapped for long distances [1]. Global contour maps and statistics are provided by ITU for the surface refractivity N_s and ΔN parameters at specified altitudes [2]. The ITU has defined a negative exponential model for the reference atmosphere and proposed a reference value of -40 N/km for the vertical ΔN over the first kilometer in temperate regions [3].

The surface meteorological data and N_s are widely available compared with the upper-air data and the point refractivity values at higher altitudes [4]. Although radiosonde is commonly used for upper-air measurements, the data accuracy is affected by sensors' uncertainties that can reach up to 0.5 °C, 5% and 1 hPa for temperature, humidity, and pressure parameters, respectively. Some linear and exponential models [2], [4], [5] have been proposed to estimate the vertical profile from existing N_s data. Several studies on refractivity analysis have been carried out for temperate climates all over the world [6]–[11], while a few are available for the unique subtropical climate of the Arabian Gulf region [12]–[17]. Three important atmospheric layers, namely 65-m, 100-m, and 1-km layers above the ground are analyzed and the relevant propagation parameters are derived for the design of terrestrial communication systems operating in such climate.

Cumulative distributions in addition to the hourly, monthly, and yearly variations are presented. The predicted results using the new models are compared with the values obtained from other relationships available in the literature. The correlation between predicted and actual available data for each parameter and the root-mean-square errors (RMSE) are compared.

A. Site Locations and Meteorological Data

Seventeen years of surface and radiosonde meteorological data from January 1, 1997 to December 31, 2013, have been gathered in the United Arab Emirates (UAE), for the analysis. The surface data are recorded hourly at six sites, whereas upper-air radiosonde data are obtained at one site from two daily ascents, nominally at 00:00 and 12:00 universal time (UT) which correspond to 4:00 A.M. and 4:00 P.M. local time. In certain periods, only one ascent was available per day, which mostly referred to 00:00 UT. The United Arab Emirates is located in the Arabian Gulf region, which is likely to experience abnormal propagation conditions such as ducting phenomenon

Manuscript received November 08, 2014; revised June 23, 2014; accepted June 28, 2015. Date of publication July 06, 2015; date of current version September 01, 2015.

A. AbouAlmal is with the Department of Engineering, Emirates Telecommunication Corporation, Etisalat 980, UAE.

A. AbouAlmal, R. A. Abd-Alhameed, and S. M. R. Jones are with the Antenna and Applied Electromagnetics Research Group, School of Engineering Design and Technology, University of Bradford, Bradford BD7 1DP, U.K. (e-mail: r.a.a.abd@bradford.ac.uk).

H. AlAhmad is with the Department of Electrical Engineering, Khalifa University of Science, Technology, and Research (KUSTAR), Sharjah 573, UAE.

Color versions of one or more of the figures in this paper are available online at http://ieeexplore.ieee.org.

Digital Object Identifier 10.1109/TAP.2015.2452937

Fig. 1. United Arab Emirates map with locations of six sites.

TABLE I
LOCATIONS OF SURFACE METEOROLOGICAL STATIONS

Site	Latitude (°N)	Longitude (°E)	Altitude (m)
AUH	24.43	54.64	27
DXB	25.25	55.36	36
SHJ	25.32	55.52	33
RAK	25.62	55.94	34
AIN	24.26	55.62	262
FUJ	25.11	56.33	21

due to its special climate, which is hot and humid over the course of the year. More details about the radiosonde and United Arab Emirates location are introduced in [12].

Abu Dhabi (AUH), Dubai (DXB), Sharjah (SHJ), and Ras Al-Khaimah (RAK) are four coastal sites located nearby the Arabian Gulf where the climate is usually hot and humid over the course of the year. Al-Ain (AIN) is an inland city with lower humidity. Al-Fujairah (FUJ) is coastal city nearby Oman Gulf that is also hot and humid but nearby the tropical zone where the gulf opens to the Indian Ocean. This location of Al-Fujairah results in a special climate in comparison with the other Emirates [14]. The geographical locations of the six sites are shown in United Arab Emirates map in Fig. 1.

The site coordinates and altitudes above the sea level are provided in Table I. All the sites have similar height around 30 m above sea level, except Al-Ain (AIN), which is located in a mountainous area.

Radiosonde data are available for 9462 radiosonde ascents. Due to low quality or incomplete ascents, data for June 1998, April 2000, November 2005, June 2006 to November 2006, and January 2010 to May 2010 are not available. From December 2006 to December 2008, the data of only one ascent, mostly at 00:00 UT, is available on daily basis. In addition, a small number of abnormal values have been excluded owing to faulty readings from the instrument.

B. Models of Refractivity

The refractivity N in N-units consists of dry and wet components and can be evaluated at either the ground or higher altitudes using the well-known expression [2], [5]. The dry component contributes to around 60%–80% of the overall value [9]. In the standard atmosphere, N decreases with altitude since the total pressure drops off rapidly while temperature decreases with height [18]. In areas where radiosonde upper-air data are not available, several relationships can be used to predict upper refractivity N_h at a certain altitude h from the surface refractivity N_s obtained from the commonly available surface meteorological measurements [4], [5]. ITU exponential models can be used to calculate N_h and refractivity values extrapolated to sea level N_o from the available surface data including N_s, the surface altitude from sea level h_s, and the height coefficient with respect to the sea level h_o in kilometer [2], [5]

$$N_h = N_s \cdot e^{\left[-\left(\frac{h-h_s}{h_o}\right)\right]} \text{ (N - units)}. \tag{1}$$

The vertical refractivity gradient $\Delta \boldsymbol{N}$ in N-units per km (N/km) usually has a negative value causing the rays to bend toward the ground. In the linear model, $\Delta \boldsymbol{N}$ can be obtained from two refractivity values, N_s at the surface h_s and N_h at an altitude h, by dividing the refractivity difference $(N_s - N_h)$ over $(h_s - h)$ [5], [19]. A close correlation is observed between N_s and N_h within the first 100 m of atmosphere and between N_s and $\Delta \boldsymbol{N}$ at 1-km layer above ground [17]. $\Delta \boldsymbol{N}$ can be estimated from N_s using the following exponential decaying relationship for the first kilometer $\Delta \boldsymbol{N}$ [17]

$$\Delta N = a. \cdot \left(1 - e^{-b.N_s}\right)^c \text{ (N/km)} \tag{2}$$

where the values of coefficients a, b, and c are found to be -316.54734, 0.00958, and 37.85049, respectively. It is noted that these coefficients may vary from one place to another and for different study periods within the same location. Long-term data are required to provide accurate estimations. Other models are studied to also predict the vertical $\Delta \boldsymbol{N}$ near the ground from the measurements of electromagnetic wave strength and diffraction losses [20], [21]. In order to extend these relations to other regions around the world, the correlation between the estimated data and the measured values needs to be evaluated.

C. Important Propagation Parameters

For microwave link design, some parameters must be set carefully as input data to optimize the link performance. Two of these parameters are particularly important, the effective earth radius factor k, which is commonly set as a standard value of 4/3, and point refractivity gradient not exceeded for 1% of time $\mathrm{d}N_{1\%}$ at 65-m layer of atmosphere [22]. Estimated values of $\mathrm{d}N_{1\%}$ and anomalous propagation probability parameter β_0 are provided by ITU tables for different geographical locations whenever reliable local data are not available [2].

1) Effective Earth Radius Factor k: The effective earth radius is the radius of a hypothetical spherical Earth, without atmosphere, for which propagation paths follow straight lines while the heights and ground distances being the same for actual Earth with atmosphere and constant vertical gradient of refractivity [1], [13]. The k-factor can be calculated from the rate of change of the refractive index with height and the actual Earth's radius a using Snell's law in spherical geometry, knowing that $N = (n-1) \times 10^6$, where a is given

by unit of nmi ($a = 6371$ km $= 3440$ nmi). The k-factor value must be multiplied by the actual Earth's radius a to plot the propagation paths as straight lines [1], [3]. The k-factor can be derived from the vertical refractivity gradient in the first kilometer above the ground ΔN_1 assuming that gradient of refractive index is constant with height, at least over the lower atmospheric layer up to 1 km [1], [22]. ITU suggests global standard values of ΔN_1 for reference atmosphere and corresponding k-factor, which are -40 N/km and 4/3, respectively [3]. As an alternative, a new weighted average approach of $\Delta \boldsymbol{N}$ values at the three atmospheric layers of 1 km and below is used in this work to accurately evaluate k-factor considering the vertical variations of refractive index near the ground below 100 m, where most terrestrial wireless systems operate. The refractive conditions are related to the values of k-factor. For example, if the ITU reference k-factor value of 4/3 is considered, which refers to a normal refraction condition in a standard atmosphere, the positive k-factor values below 4/3 indicates the incidence of subrefraction, where signals bend upward. The occurrence of super-refraction is indicated by positive k-factor values larger than 4/3. Negative values of k-factor refer to the incidence of ducting phenomenon, where the wireless signal gets trapped within two layers and travels for long distances over the horizon.

2) Anomalous Propagation Probability Parameter β_0*:* The vertical refractivity gradient, in the lowest 100 m of the troposphere above the ground surface, is an important parameter to estimate propagation effects such as ducting, surface reflection, and multipath on terrestrial line-of-sight links. The β_0 parameter represents occurrence probability of nonstandard propagation and its statistics are derived from the cumulative distributions of the vertical $\Delta \boldsymbol{N}$ at the first 100-m layer. β_0 is obtained from the percentage of time in which $\Delta \boldsymbol{N}$ value is less than or equal to -100N/km.

3) Point Refractivity Gradient "$\mathbf{dN}_{1\%}$*":* It is the point ΔN value at the lowest 65 m of the atmosphere not exceeded for 1% of an average year [22], [23], which is used for predicting microwave links' availability.

D. New Methodology for Vertical ΔN *Prediction*

New approaches are used to simplify and improve the accuracy of vertical $\Delta \boldsymbol{N}$ evaluation in areas where upper-air data are not available. In approach 1, only measured refractivity parameters at surface and higher altitudes are utilized to estimate $\Delta \boldsymbol{N}$. The surface refractivity profiles for a number of sites are compared. For sites with similar surface conditions to a site in the surrounding region with available radiosonde measurements, upper-air refractivity obtained from radiosonde can be utilized to estimate the vertical profile in the surrounding sites, where only surface data are available. This is based on the assumptions that most of the land and sea interactions occur at ground level, while atmosphere gets more horizontally homogenous at higher altitudes and the vertical N_h is assumed to be more stable. Although poor correlation has been observed between N_s and $\Delta \boldsymbol{N}$ at 65- and 100-m layers compared with good correlation at 1 km [17], this new approach aims at improving the accuracy of estimated N_h values at these altitudes by using real radiosonde measurements in case of similar surface profiles. Consequently, the results of $\Delta \boldsymbol{N}$ at these layers are expected to be improved as well, when the linear $\Delta \boldsymbol{N}$ model is used. The sites can be selected such that they are located within few hundred miles from a radiosonde location that have similar surface weather conditions. In this approach, vertical profile at all sites are evaluated as follows.

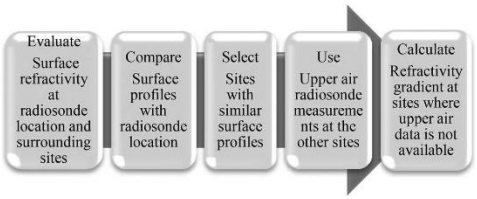

Fig. 2. Flow diagram of Approach 1-(b).

a) The measured surface and upper-air data are obtained from radiosonde, which is available at the AUH site only. The measured $\Delta \boldsymbol{N}$ at a particular altitude, h, is calculated using the linear model.
b) N_s is calculated from surface data measured using fixed surface stations at AUH and surrounding sites. The N_h parameter is obtained from radiosonde measurements available at the AUH site only. At 65 and 100 m, the measured N_h at AUH is utilized at the surrounding sites with similar surface refractivity profiles to AUH. At 1-km layer, N_h is applied for all six sites since the atmosphere gets much more homogeneous at this high altitude. $\Delta \boldsymbol{N}$ is then calculated from measured N_s and N_h using the linear model. Note that for the AUH site only, measured $\Delta \boldsymbol{N}$ obtained using methods 1) and 2) are compared, in order to evaluate the radiosonde data accuracy (Fig. 2).

In the second approach 2, $\Delta \boldsymbol{N}$ is obtained from measured N_s at the surface and predicted N_h at higher altitudes using empirical relationships, which are derived from radiosonde measurements at a single site. These models are used to predict the vertical refractivity profiles at the surrounding sites where only surface data are available. In this approach, $\Delta \boldsymbol{N}$ is estimated from measured N_s and predicted N_h subject to the correlation observed between N_s and either N_h or $\Delta \boldsymbol{N}$ at different altitudes [17] as follows.

a) N_h is predicted using exponential model, e.g. (1), from measured N_s. Predicted $\Delta \boldsymbol{N}$ is then calculated using the linear model. At 65- and 100-m layers, it has been observed that N_s is correlated with N_h.
b) Predicted $\Delta \boldsymbol{N}$ is directly estimated from measured N_s using exponential model (2). At 1-km layer, N_s is found to be correlated with $\Delta \boldsymbol{N}$.

The relationships between N_s and either N_h or $\Delta \boldsymbol{N}$ for predicting the vertical refractivity profiles are investigated in comparison with the new approaches introduced in this study. The results of the new approaches and predicted N_h and $\Delta \boldsymbol{N}$ are compared at certain sites to confirm the earlier correlation findings at different layers. To the best of our knowledge, the proposed approach to estimate the vertical refractivity profile

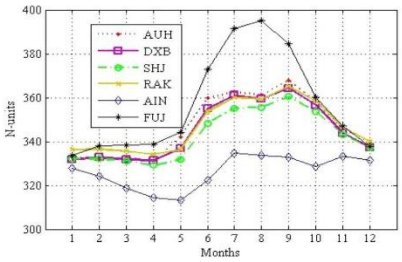

Fig. 3. Mean monthly variations of surface refractivity N_s (1997–2013).

based on analysis of the similarities in surface profiles, in addition to the use of weighted average approach to evaluate the k-factor from mean and median of ΔN at different atmospheric layers, has not been investigated before.

II. Analysis and Results

ΔN statistics for the first three atmospheric layers above the ground, 65 m, 100 m, and 1 km, where terrestrial communication systems operate, are important to be investigated due to their contributions to several propagation studies. For example; the first two layers, 65 and 100 m, are essential for estimating the point refractivity gradient not exceeded for 1% of time, which is required for availability calculations for terrestrial microwave links [23], and the occurrence probability of ducting and multipath conditions [2], [22]. It is noticed that the extreme atmospheric stratification tends to occur in layers less than 100-m thickness, which can be extended horizontally over long distance at certain times. The 1-km layer analysis is important for the estimation of the effective Earth radius factor [22], [23]. These parameters have to be carefully considered when studying the performance of terrestrial line of sight communication systems.

A. Surface Refractivity Analysis

The analysis of surface refractivity N_s and its dry and wet components N_{s_D} and N_{s_w} in addition to the N_o analysis are based on the surface SYNOPS meteorological data measured by the available fixed surface weather stations at all sites. The mean monthly distributions of N_s over the whole period is shown in Fig. 3 for the six sites. The dry refractivity component N_{s_D} at all sites follows the same monthly variation curve with similar values fluctuating from 250 to 272 with a span of 22 units. The monthly variation curves of N_s are dominated by the wet component N_{s_w}, which is compensated by the inversely varying dry refractivity term N_{s_D}. Fig. 3 shows that N_s profiles in four sites; namely AUH, DXB, SHJ, and RAK, are similar with peak values shown in summer season. The monthly means of N_s vary within a range of around 82 units at all sites where a maximum monthly difference of 62 units between the six sites is observed in August. The highest monthly values and variation of N_s are observed at FUJ site

TABLE II
Comparison of Calculated N_{s_w} Exceeded for 50% of the Year With ITU Map [2]

	$N_{s\ w}$ (N-units)
ITU values	60–75
AUH	81.2
DXB	81.7
SHJ	78.3
RAK	82.5
AIN	63.1
FUJ	93

TABLE III
Comparison of Calculated N_o With ITU Maps [2]

	Coefficient h_o	February N_o	August N_o
ITU maps	9.5	350	390
AUH	9.5	332.6	362.1
	7.35	332.9	362.4
DXB	9.5	333.8	360.3
	7.35	334.1	360.6
SHJ	9.5	333.1	356.5
	7.35	333.3	356.8
RAK	9.5	337.4	360.3
	7.35	337.7	360.6
AIN	9.5	325.2	334. 6
	7.35	325.5	334.9
FUJ	9.5	338.8	396.2
	7.35	339.1	396.6

with a span of 61.6 units, from 333.5 up to 395.1 N-units. This can be attributed to its location as a coastal city nearby Oman Gulf within a mountainous area, with a humid climate. AIN site has lower N_s values and monthly variations than the other sites with a span of 21 units, from 313.2 up to 334.5 N-units. This trend is due to its location as an inland city at a distance of about 100 km away from the sea with dry and low humidity weather. Similar initial results were reported for the area under study [14].

For easy reference, the ITU provides global maps of the median value (50%) of N_{s_w} exceeded for the average year [2]. Table II provides the values of calculated N_{s_w} at the six sites in comparison with the ITU map for United Arab Emirates. In general, it has been observed that ITU values underestimate $N_{\mathrm{s\_w}}$ in the area under study, where the long-term median calculated values exceed 60 N-units for all sites.

The mean monthly N_o variations in the six sites are also compared with ITU maps [2] in Table III. The ITU maps are derived using $h_o = 9.5$ km for the months of February and August. N_o has been calculated using two values 9.5 and 7.35 km of h_o parameter. For reference purpose, the ITU has also proposed an average global profile based on N_o and h_o values of 315 N-units and 7.35 km [2]. It has been noted that h_o value varies slightly across particular atmospheric layers, which have marginal impact on the refractivity predictions. The results for the winter season, February, are more consistent with the ITU values than the summer, August, except at certain sites such as AIN in case of February and FUJ in case of August. In August, the results at AUH, DXB, SHJ, and RAK are up to 14.2% less than ITU. AIN shows exceptional differences of 24.8 and 55.4

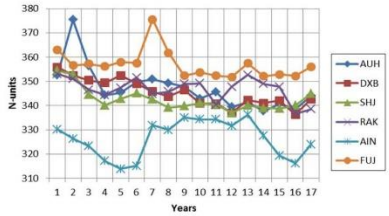

Fig. 4. Mean yearly variations of surface refractivity N_s (1997–2013).

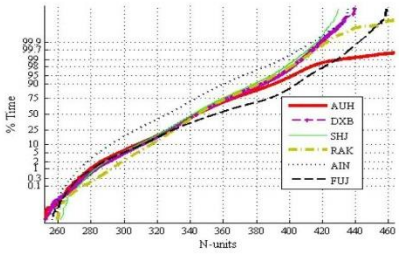

Fig. 5. Cumulative distributions of surface refractivity N_s (1997–2013).

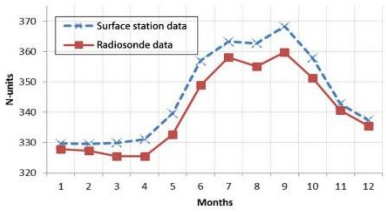

Fig. 6. Mean monthly variations of surface refractivity N_s calculated from fixed surface weather station and radiosonde (1997–2013).

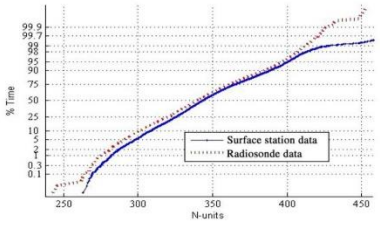

Fig. 7. Cumulative distributions of surface refractivity calculated from fixed surface weather station and Radiosonde (1997–2013).

units less than the ITU values for February and August, respectively. This can be attributed to the inland location with dry climate of the AIN site.

Fig. 4 shows the average yearly variations of N_s at all sites over the whole period from 1997 to 2013. The yearly curves for AUH, DXB, SHJ, and RAK follow a similar trend and the annual means are bounded within 12 units for most years. The year to year variation at these four sites is generally smooth with some peak values in 1998 at AUH and 2003 at FUJ. AIN has the lowest values and the most significant variation within a range of around 23 units, from 313 up to 336 N-units. The highest N_s values are generally shown at FUJ, except in 1998.

The cumulative distributions of N_s at the six sites are given in Fig. 5 over the whole period. The values vary from around 252 up to 601 N-units with a span of 349 units. N_s oscillates in an interval of 52 units from one site to another. Almost the lowest and highest values for all time percentages are shown at AIN and FUJ, respectively, apart from some exceptional cases such as at AUH where values exceed 460 units for around 0.5% of the total time. This exceptional value at AUH can be attributed to the peak values observed in 1998.

The results obtained from the monthly, yearly, and cumulative distributions show that the surface refractivity profile at four sites; namely AUH, DXB, SHJ, and RAK, are similar. Accordingly, the vertical refractivity profiles at these sites are expected to be more consistent since the atmosphere is assumed to get more horizontally homogenous with height.

B. Comparison of Surface Measurements

The surface meteorological data can be measured using either surface weather stations or radiosonde at the ground. The radiosonde measurements at AUH site have been compared with the surface meteorological measurements using AUH surface weather station at only two times daily due to the radiosonde data availability. This is an indication for the radiosonde data accuracy compared with the stable fixed weather sensors at the ground. The monthly and cumulative distributions of measured N_s using both data types are shown in Figs. 6 and 7. Fig. 6 shows that the monthly means of N_s measured from the surface station are larger than the values obtained from the radiosonde at all months, with a maximum difference of 8.5 units within a span of 2.5%. The N_s values measured by the radiosonde are also found to be lower for all time percentages as shown in Fig. 7. It has been found that the N_s value oscillates between 329.5 and 368.3 N-units for the surface station with a span of 38.8 units, whereas they vary from 325.5 to 359.8 N-units for the radiosonde.

The cumulative distributions of four surface meteorological parameters; namely atmospheric pressure, dry air temperature, relative humidity, and water vapour pressure, measured by fixed surface station and radiosonde are analyzed at AUH site. The parameters measured by surface station has higher values for most time percentages, except for dry air temperature where radiosonde measurements are higher. This is the reason for obtaining higher N_s values for surface station at all-time percentages since the refractivity is directly proportional with pressure and vapor pressure while it is inversely proportional to the dry temperature.

C. Refractivity Gradient Analysis

The ΔN parameter has been evaluated using different approaches. For the sites with similar surface refractivity profile

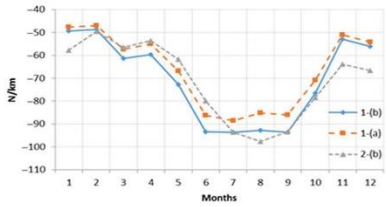

Fig. 8. Comparison of mean monthly variations of $\Delta \boldsymbol{N}$ at 1 km at AUH.

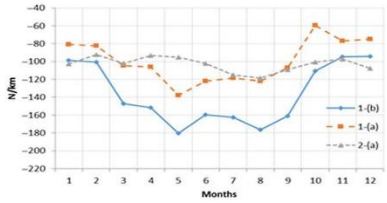

Fig. 9. Comparison of mean monthly variations of $\Delta \boldsymbol{N}$ at 100 m at AUH.

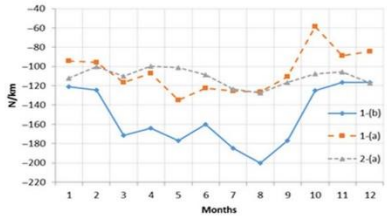

Fig. 10. Comparison of mean monthly variations of $\Delta \boldsymbol{N}$ at 65 m at AUH.

to AUH, the same radiosonde data are utilized for upper layers. The measurement accuracy of surface weather stations is assumed to be higher than the radiosonde at the ground level. Consequently, the reference ΔN profile at the AUH site is calculated using approach 1-(b) from both the surface measurements at the ground and radiosonde measurements at higher altitudes. Figs. 8–10 provide comparisons of mean monthly variations of ΔN at 65 m ($\Delta \mathrm{N}_{0.065}$), 100 m ($\Delta N_{0.1}$), and 1 km ($\Delta N_1$) layers, using different approaches at the AUH site. The curves of ΔN_1 obtained from 1-(a) and 1-(b) approaches are more consistent with a maximum monthly difference of 8 units. The differences between ΔN values obtained using 1-(a) and 1-(b) approaches increase considerably up to 74 and 55 units at the 65 and 100 m layers, respectively. The higher differences at the low altitudes can be attributed to the fact that any small change in N_s value results in large disagreement in $\Delta \boldsymbol{N}$ due to the low decimal number in the denominator of the linear $\Delta \boldsymbol{N}$ equation.

The RMSE and correlation coefficients are evaluated at AUH site between the measured or predicted ΔN values using approaches 1-(a), 2-(a), and 2-(b) with reference to the measured ΔN using 1-(b) approach. Table IV summarizes the

TABLE IV
CORRELATION AND RMSE VALUES OF ΔN RESULTS WITH REFERENCE TO RADIOSONDE DATA

Layer	Approach/model	Correlation	RMSE
1 km	1-(a)	0.857	20.4
	2-(a)	0.859	35.2
	2-(b)	0.86	18.8
100 m	1-(a)	0.49	200.7
	2-(a)	0.41	216.8
	2-(b)	0.4	219.8
65 m	1-(a)	0.38	322.8
	2-(a)	0.4	337.9
	2-(b)	0.39	337.9

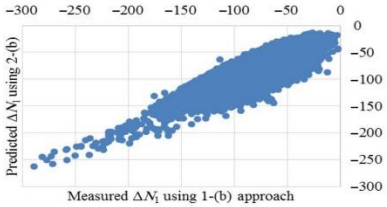

Fig. 11. Scatter diagram for $\Delta \boldsymbol{N}$ at 1 km at AUH, obtained using 1-(b) and 2-(b) approaches.

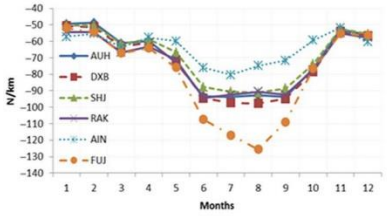

Fig. 12. Comparison of mean monthly variations of ΔN_1 at all sites using 1-(b) (1997–2013).

obtained results. The correlation between ΔN and N_s at low altitudes, 65 and 100 m, is found to be poor while good correlation is observed at 1 km height. Similar results have been reported [17]. At 1 km height, 2-(b) approach gives the highest correlation coefficient and minimum RMSE value noting that good correlation has been observed between ΔN and N_s, whereas 2-(a) gives the highest RMSE result. At 65 and 100 m layers, 2-(a) approach shows marginal improvement compared to 2-(b), although poor correlation has been found between ΔN and N_s at these low altitudes [17].

Fig. 11 shows the scatter diagram for the ΔN_1 values obtained using 1-(b) and 2-(b) approaches. The coefficient of determination is found to be 0.86, which means that significant correlation exists with minimum error. Fig. 12 shows the mean monthly variations of ΔN_1 calculated using the 1-(b) approach for all six sites. The monthly ΔN values oscillate approximately between 125.5 and -48.8 N/km with a span of 76 units. Fig. 13 shows the mean monthly distributions of ΔN_1 obtained using 2-(b). The ΔN_1 values range from -134 to -36.7 N/km with a span of 97.3 units. The curves of ΔN_1 are found to be

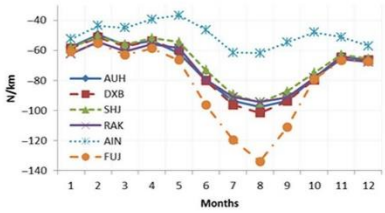

Fig. 13. Comparison of mean monthly variations of ΔN_1 at all sites using 2-(b) (1997–2013).

TABLE V
COMPARISON OF ABSOLUTE MONTHLY ΔN_1 RESULTS USING 1-(B) AND 2-(B) APPROACHES WITH ITU

	February		May		August		November	
Approach	1-(b)	2-(b)	1-(b)	2-(b)	1-(b)	2-(b)	1-(b)	2-(b)
ITU	70		80		90		70	
AUH	49	50	73	62	93	98	53	64
DXB	51	51	72	60	98	102	54	65
SHJ	51	51	67	55	91	95	52	63
RAK	54	54	71	59	91	94	55	66
AIN	55	44	60	37	75	62	52	51
FUJ	54	55	76	66	126	134	55	67

similar to N_s at AUH, DXB, SHJ, and RAK sites, where refractivity profiles are almost consistent with peak values shown in the summer. The ranges of monthly variations at these four sites are found to be around 49 units, from -97.7 to -48.8 N/km, and 51.9 units, from -101.5 to -49.6, for approaches 1-(b) and 2-(b), respectively. The highest monthly variations of ΔN_1 has also been observed in the FUJ site within a span of 73.4 units, from -125.5 to -52 N/km, and an interval of 78.5 units, from -134 to -55.4 N/km, using approaches 1-(b) and 2-(b), respectively. This can also be attributed to its special location and climate.

The lowest absolute ΔN_1 values are given during winter time with some exceptional cases such as May for AIN site in Fig. 13 when the 2-(b) approach is used. On the other hand, the summer season shows the highest absolute ΔN_1 values at all sites, in particular for the months of June, July, August, and September.

In Table V, the absolute values of mean monthly ΔN_1 are compared with the corresponding values in the ITU maps [2] for the months of February, May, August, and November. For the AUH, DXB, SHJ, and RAK sites, the ΔN_1 results of May and August are more consistent with ITU values than February and November, when the 1-(b) approach is used. The differences with ITU values are found to be up to 21.2 and 17.6 units, for February and November, respectively. Similar results have been reported before [14]. Higher inconsistencies have been observed for May and August using the 2-(b) approach, where the differences are found to be up to 25.5 and 11.5 units, respectively. All proposed ITU values for ΔN_1 are overestimated in comparison with the results obtained in this study.

Figs. 14 and 15 show the mean monthly variations of ΔN at 100 m $\Delta N_{0.1}$ using approaches 1-(b) and 2-(a), respectively, at the AUH, DXB, SHJ, and RAK sites. Using 2-(a) at the four sites, low $\Delta N_{0.1}$ values are observed during winter and the

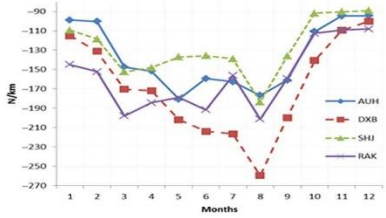

Fig. 14. Comparison of mean monthly variations of $\Delta N_{0.1}$ at all sites using 1-(b) approach (1997–2013).

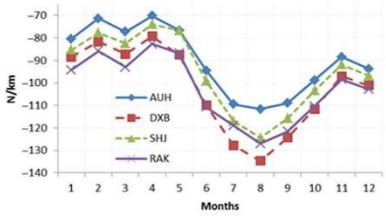

Fig. 15. Comparison of mean monthly variations of $\Delta N_{0.1}$ at all sites using 2-(a) approach (1997–2013).

highest absolute values are shown in summer season. Similarly, the mean monthly distributions of $\Delta N_{0.065}$ at 65 m have similar seasonal variations using the 2-(a) approach. When the 1-(b) approach is used, the monthly distributions of ΔN at 100 and 65 m layers are not coherent at the four sites. However, the AUH and DXB sites have similar seasonal variations at all atmospheric layers when both approaches are used. Using the 1-(b) approach, the ranges of $\Delta N_{0.1}$ and $\Delta N_{0.065}$ vary from -259.5 to -89 N/k and from -295 to -107.6 N/km, respectively. The maximum monthly differences between the four sites at 100 and 65 m layers are found to be 83 and 103 units, respectively. This gives a clear indication that the prediction of ΔN is much more complicated at lower altitudes.

D. Analysis of k-Factor Profile

The mean monthly ΔN_1 values at the AUH site vary between -97.62 and -47.1 N/km and the corresponding k-factor ranges between 1.43 to 2.64 when all three approaches, 1-(a), 1-(b), and 2-(b) are applied, as shown in Fig. 16. The k-factor distributions at AUH using all approaches are found to always exceed the proposed ITU standard atmosphere value of 4/3.

Fig. 17 provides the mean monthly variation of k-factor at the six sites using the 1-(b) approach. The monthly values of k-factor at all sites oscillate from 1.45 to 2.65, with some exceptional results up to 4.98 in August for the FUJ site Using the 2-(b) approach, the k-factor is found to vary from 1.46 to 2.83 with some exceptional values up to 6.81 at August for FUJ as well.

Table VI summarizes the k-factor values obtained from the long-term mean and median results of ΔN_1 using three approaches, 1-(a), 1-(b), and 2-(b) at the six sites over the whole

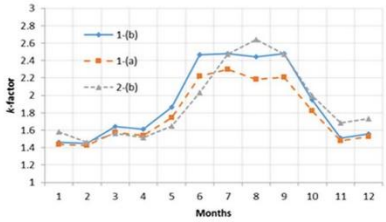

Fig. 16. Comparison of monthly variations of k-factor at AUH based on 1-(a), 1-(b) and 2-(b) approaches (1997–2013).

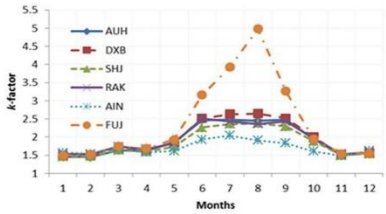

Fig. 17. Comparison of monthly variations of k-factor at six sites based on 1-(b) approach (1997–2013).

TABLE VI
COMPARISON OF ΔN_1 AND k-FACTOR RESULTS WITH ITU VALUES FOR REFERENCE ATMOSPHERE

	Approach	Median	Mean	Median k-factor	Mean k-factor
ITU	–	−40		1.33	
From Δ N1					
AUH	1-(a)	−71.11	−74.48	1.83	1.90
	1-(b)	−75.14	−79.60	1.92	2.03
	2-(b)	−74.88	−79.76	1.91	2.03
DXB	1-(b)	−78.15	−81.48	1.99	2.08
	2-(b)	−76.97	−80.67	1.96	2.06
SHJ	1-(b)	−74.14	−77.40	1.89	1.97
	2-(b)	−73.60	−76.63	1.88	1.95
RAK	1-(b)	−76.65	−79.85	1.95	2.04
	2-(b)	−75.39	−78.90	1.92	2.01
AIN	1-(b)	−64.96	−71.83	1.71	1.84
	2-(b)	−51.51	−55.85	1.49	1.55
From weighted average of Δ N1, Δ N0.1 and Δ N0.065					
AUH	1-(a)	−81.35	−98.58	2.08	2.69
	1-(b)	−112.41	−143.8	3.52	11.85
	2-(b)	−74.12	−78.97	1.89	2.01
DXB	1-(b)	−144.25	−170.4	12.32	−11.69
	2-(b)	−76.13	−79.84	1.94	2.03
SHJ	1-(b)	−117.80	−128.4	4.01	5.49
	2-(b)	−72.81	−75.85	1.86	1.93
RAK	1-(b)	−145.49	−152.8	13.64	37.45
	2-(b)	−74.59	−78.07	1.91	1.99
FUJ	1-(b)	−81.35	−98.58	2.08	2.69
	2-(b)	−112.41	−143.8	3.52	11.85

period from 1997 to 2013. At AUH, the long-term median values of ΔN_1 and k-factor using the 1-(b) approach are found to be -75.14 N/km and 1.92, respectively. The highest k-factor value of 2.4 is obtained at FUJ site based on ΔN_1 results. It has been noted that median k-factor is less than mean value by approximately 0.2.

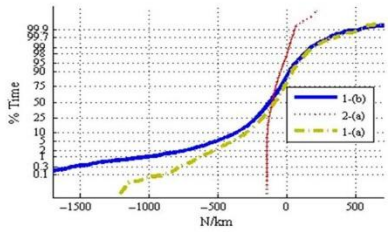

Fig. 18. Comparison of cumulative distributions of $\Delta N_{0.1}$ at AUH using 1-(a), 1-(b) and 2-(a) approaches (1997–2013).

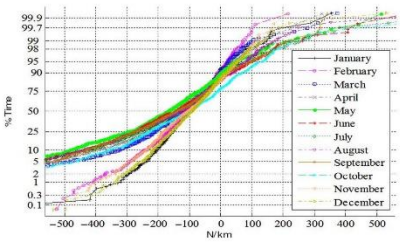

Fig. 19. Monthly cumulative distributions of $\Delta N_{0.1}$ at AUH using 1-(b) approach (1997–2013).

The k-factor has also been calculated from the mean ΔN values at 65- and 100-m layers, where most of terrestrial wireless systems operate. A weighted average approach for evaluating mean and median ΔN among the three layers has been used for obtaining more appropriate k-factor value to be applied for the path clearance analysis of microwave links operating within the first 150-m layer above the ground. Antennas on these microwave systems are found to be fixed at around 55–150-m height above the sea level. For simplicity, similar weights have been assigned to the mean and median ΔN values at 65 m, 100 m and 1 km. As given in Table VI, the value of k-factor calculated from the long-term mean weighted average ΔN using the 1-(b) approach at the DXB site is found to be negative, which indicates the prevalence of ducting in the area under study.

E. $\Delta N_{0.1}$ at 100-m Layer and β_0 Analysis

The cumulative distributions of $\Delta N_{0.1}$ at the AUH site for different times using the 1-(a), 1-(b), and 2-(a) approaches are shown in Fig. 18. $\Delta N_{0.1}$ values for all time percentages approximately oscillate between -1641 and 590 N/km for the 1-(b) approach, and between -1207 and 580 N/km for the 1-(a) approach, with some exceptional values outside these ranges. The long-term β_0 values at AUH are found to be 45.3%, 57.3%, and 56.5% using approaches 1-(a), 1-(b), and 2-(a), respectively. Considering the reference results for the 1-(b) approach, the value of $\Delta N_{0.1}$ is expected to be less than or equal to -100 N/km for around 57.3% of the time.

Fig. 19 shows the monthly cumulative distributions of $\Delta N_{0.1}$ at AUH using the 1-(b) approach. For 50% of the time, the

TABLE VII
MONTHLY β_0 VALUES (%) USING DIFFERENT APPROACHES AT AUH COMPARED WITH ITU MAPS

Months	ITU values	1-(a)	1-(b)
February	30	46.7	55.9
May	75	58	69.1
August	70	43.8	57.5
November	40	42.7	52.1

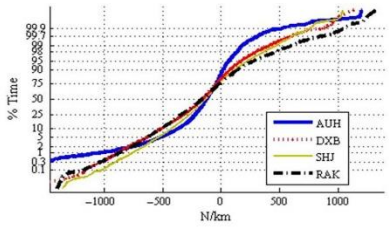

Fig. 20. Comparison of cumulative distributions of $\Delta N_{0.1}$ at four sites using 1-(b) approach (1997–2013).

summer season shows higher $\Delta N_{0.1}$ than winter with peak values obtained in May. The monthly β_0 variations obtained from $\Delta N_{0.1}$ distributions using approaches 1-(a) and 1-(b) are compared with ITU maps in Table VII. It has been noted that ITU values are not in good agreement with the results obtained in this study. With reference to the results of the 1-(b) approach, the estimated ITU values are below those calculated in the case of February and November with differences of around 46% and 23%, respectively, which are larger than the differences reported for the same months in an earlier study [24], which are 34% and 21%, respectively. Also, the ITU values are found to be overestimated for the months of May and August, with differences of 8.5% and 21.7%, compared with 7% and 19% reported for the same months before [24]. These differences have also been observed in other countries [9] and can be attributed to the fact that ITU maps [2] were interpolated from radiosonde data from only 99 sites worldwide between 1955 and 1959. In addition, ITU maps are usually derived from measurements performed largely in temperate regions of the world such as Europe, North America, and Japan [25], which have different climatic conditions from the Gulf region.

The cumulative distributions of $\Delta N_{0.1}$ using the 1-(b) approach at the four sites with similar surface refractivity profiles are provided in Fig. 20. The long-term β_0 values obtained using approach 1-(b) are found to be 57.3%, 62.1%, 56.5%, and 60.9% at AUH, DXB, SHJ, and RAK, respectively. The monthly β_0 variations at these sites are compared in Fig. 21. The monthly β_0 values oscillate between 44.3% and 71.1%. Generally, summer months show higher probability of anomalous propagation at all sites. RAK has the highest β_0 values for the first four months from January to April, while DXB site shows the highest probabilities of anomalous conditions for the remaining months from May to December. Table VIII summarizes the monthly β_0 values obtained from the distributions of $\Delta N_{0.1}$ at the four sites using the 1-(b) approach.

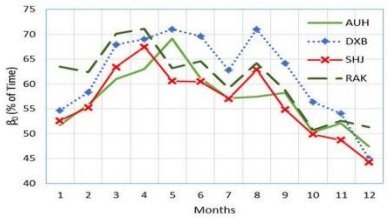

Fig. 21. Monthly variations of β_0.

TABLE VIII
MONTHLY β_0 VALUES (%) AT FOUR SITES BASED ON 1-(B) APPROACH (1997–2013)

Months	AUH	DXB	SHJ	RAK
January	51.7	54.7	52.6	63.5
February	55.9	58.3	55.3	62.4
March	61	68	63.4	70.1
April	63	69	67.5	71.1
May	69.1	71	60.6	63.2
June	61.1	69.6	60.5	64.6
July	57.2	62.8	57.1	59.1
August	57.5	71	62.9	64.2
September	58.2	64.2	54.9	58.7
October	50.3	56.4	49.9	50.7
November	52.1	54.1	48.7	52.6
December	47.4	45	44.3	51.3

TABLE IX
COMPARISON OF MONTHLY β_0 VALUES (%) AT FOUR SITES USING 1-(B) APPROACH WITH ITU MAPS

Months	ITU values	AUH	DXB	SHJ	RAK
February	30	55.9	58.3	55.32	62.4
May	75	69.1	71.9	60.6	63.2
August	70	57.5	71.1	62.9	64.2
November	40	52.1	54.2	48.9	52.7

The monthly β_0 results at the four sites are compared with ITU maps [22] in Table IX. Generally, the ITU values are underestimated for the months of February and November at the four sites, while they are overestimated for May and August.

The cumulative distributions of $\Delta N_{0.065}$ are obtained using the 1-(a), 1-(b), and 2-(a) approaches at AUH. $\Delta N_{0.065}$ values for all time percentages approximately oscillates between -2750 and 1400 N/km for the 1-(b) approach, and between -1860 and 1543 N/km for the 1-(a) approach, with some exceptional values outside these ranges. The long-term value of $dN_{1\%}$ at AUH is found to be -722.5, -1604.5, and -228.2 N/km, using approaches 1-(a), 1-(b), and 2-(a), respectively.

F. $\Delta N_{0.065}$ at 65-m Layer and Analysis of Point Refractivity Gradient ($dN_{1\%}$)

The $\Delta N_{0.065}$ values calculated using approaches 1-(a) and 1-(b) for different time percentages at AUH are compared with ITU maps in Table X. Bilinear interpolation has been used to get exact values of $\Delta N_{0.065}$ at AUH from the corresponding

TABLE X
COMPARISON OF $\Delta N_{0.065}$ VALUES (N/KM) AT AUH USING 1-(A) AND 1-(B) APPROACHES WITH ITU MAPS

Time (%)	ITU values	1-(a)	1-(b)
1	−952.42	−722.5	−1604.5
10	−553	−344.9	−460.9
50	−92.824	−89.8	−142
90	−4.38	76.8	51.3
99	38.86	305.4	307.6

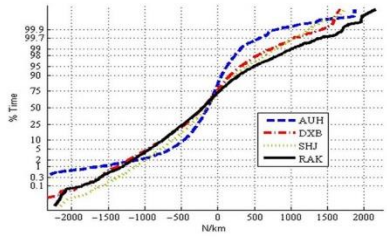

Fig. 22. Comparison of cumulative distributions of $\Delta N_{0.065}$ at four sites using 1-(b) approach (1997–2013).

TABLE XI
VALUES OF $\Delta N_{0.065}$ NOT EXCEEDED FOR DIFFERENT TIME PERCENTAGES AT FOUR SITES

Time (%)	AUH	DXB	SHJ	RAK
1	−1604.5	−1378.8	−1122.3	−1300.1
10	−460.9	−760.3	−616.3	−752.8
50	−142	−198.6	−152.3	−202.7
90	51.3	173.7	232.8	291.3
99	307.6	733.6	803.7	1025.1

ITU data files for the given coordinates at different time percentages. The results are not in good concurrence with ITU values. Considering the absolute values of $\Delta N_{0.065}$ results, the ITU values are found to be overestimated for 10% of time, while they are under-estimated for 90% and 99%. For 1% of time, the estimated ITU value is below the calculated value using the reference 1-(b) approach. The cumulative distributions of $\Delta N_{0.065}$ using the 1-(b) approach at the sites with similar surface refractivity profiles are provided in Fig. 22. Table XI provides $\Delta N_{0.065}$ values obtained at AUH, DXB, SHJ, and RAK sites at different time percentages. The highest absolute $\Delta N_{0.065}$ values for 1% and 10% are shown in AUH and DXB, respectively, while RAK shows the top values for larger time percentages.

III. CONCLUSION

Seventeen years of local surface and radiosonde meteorological data were used to study the vertical refractivity profile for three critical atmospheric layers within the first kilometer above the ground surface.

The surface meteorological measurements using the radiosonde were found to be slightly different from the measurements obtained from fixed weather stations, which are usually more accurate due to higher stability.

A new approach was proposed for utilizing the upper-air refractivity from a radiosonde site in the surrounding sites with similar surface conditions. The analysis of surface refractivity was used for the evaluation of vertical refractivity profile in areas where radiosonde data are not available. For ΔN analysis at 1 km, the same approach was used for the sites where surface profiles were not so consistent with those from the radiosonde location assuming that the atmosphere gets increasingly horizontally homogeneous at higher altitudes. Exponential prediction models were also used for the ΔN prediction at all sites. The analysis of the given approaches for evaluating the mean vertical refractivity profiles showed that higher concurrency with radiosonde measurement could be obtained using the new proposed approach in this study. However, the range of variation was found to be higher for altitudes of 100 m and below. Some differences were observed in monthly refractivity gradient profiles at certain sites with similar mean surface profiles, in particular for low altitudes below 100 m. This could be attributed to the fact that the measurements at a given time were not necessarily the same at these sites over the whole period, and that any small change in N_s value results in large disagreement in ΔN due to the low decimal number in the denominator of the linear ΔN equation for low heights.

A new approach was used to evaluate k-factor from the weighted average ΔN at three layers, which is recommended to be applied in other areas. The mean k value of -11.7 indicated the prevalence of the ducting phenomenon in one area under study.

The results obtained in this study can be useful for areas with a subtropical climate, where weather is hot and humid over the year. The proposed approaches can also be applied in other areas with different climates. The vertical refractivity gradients in areas where upper-air measurements are not available can be evaluated from the analysis of surface refractivity profiles. The upper-air data are measured at a single radiosonde site and used in surrounding areas with similar surface profiles. In addition, the new weighted average approach at various atmospheric layers can be applied to estimate effective earth radius factor.

The β_0 analysis at four sites indicated that the probability of anomalous propagation exceeded 44% for all months and reached up to 71% at certain locations within the summer.

The results obtained in this study for the Gulf region would also suggest the necessity to revise the ITU maps, in particular for similar subtropical climate, based on recently gathered long-term local meteorological data from more radiosonde sites worldwide, since ITU values are being widely used for the design of wireless communication systems.

Based on the results presented in this work, it is recommended to apply similar approach to evaluate the vertical refractivity profiles in the areas surrounding a radiosonde location and for areas with similar surface refractivity conditions.

ACKNOWLEDGMENT

The authors would like to express their gratitude to the National Center of Meteorology in the United Arab Emirates for providing the raw meteorological data used in this work

and the Radio Frequency and Computational Electromagnetics Research Group of Bradford University in providing the software requirements.

REFERENCES

[1] M. I. Skolnik, *Introduction to Radar Systems*, 3rd ed. New York, NY, USA: McGraw-Hill, 2001.

[2] International Telecommunication Union, "The radio refractive index: Its formula and refractivity data," Recommendation ITU-R P.453-10, 2012.

[3] International Telecommunication Union, "Definitions of terms relating to propagation in non-ionized media," Recommendation ITU-R PN.310-9, 1994.

[4] R. L. Freeman, *Radio System Design for Telecommunications*. Hoboken, NJ, USA: Wiley, 1997.

[5] I. R. Bureau, *Handbook on Radiometeorology*. Geneva, Switzerland: International Telecommunication Union, 1996.

[6] T. G. Hayton and K. H. Craig, "Use of radiosonde data in propagation prediction," presented at the *IEE, Savoy Place*, London WC2R OBL, UK, 1996.

[7] S. Lystad, "Investigation of surface refractivity and refractive gradients in the lower atmosphere of Norway," presented at the *COST 235, CP 121*, Mar. 1993.

[8] A. K. P. Marsh, T. G. Hayton, and K. H. Craig, "Initial comparison of refractivity parameters derived from radiosondes and psychrometers in France," *COST255, CP42010*, Oct. 1997.

[9] L. Blanchard and H. Sizun, "Refractivity over France: First results of ARGOS experiment," in *COST255, CP32003*, May 1997.

[10] K. H. Craig and T. G. Hayton, "Investigation of $\beta 0$ values derived from ten years radiosonde data at 26 stations," presented at the *COST 235, CP 182*, Oct. 1993.

[11] K. H. Craig and T. G. Hayton, "Refractivity parameters from radiosonde data," in *Proc. AGARD Conf. Propag. Assess. Coastal Environ.*, 1994, pp. 1–12.

[12] A. AbouAlmal, R. A. Abd-Alhameed, K. Al-Ansari, H. AlAhmad, C. H. See, and S. M. Jones, "Statistical analysis of refractivity gradient and β_0 parameter in the gulf region," *IEEE Trans. Antennas Propag.*, vol. 61, no. 12, pp. 6250–6254, 2013.

[13] A. Abu Al-mal and K. Al-Ansari, "Calculation of effective earth radius and point refractivity gradient in UAE," *Int. J. Antennas Propag.*, vol. 2010, 2010, 4 pp., Article ID: 245070.

[14] K. Al-Ansari, A. AbuAl-Mal, and R. A. Kamel, "Statistical Analysis of Refractivity in UAE," in *Proc. Int. Symp. Rainfall Rate Radiowave Propag.*, 2007, vol. 923, pp. 232–247.

[15] K. Al Ansari and R. A. Kamel, "Correlation between ground refractivity and refractivity gradient and their statistical and worst month distributions in Abu Dhabi," *IEEE Antennas Wireless Propag. Lett.*, vol. 7, pp. 233–235, Aug. 2008.

[16] A. AbouAlmal *et al.*, "Comparison of three vertical refractivity profiles in the Gulf Region," in *Proc. 19th Eur. Wireless Conf. (EW)*, 2013, pp. 1–4.

[17] A. AbouAlmal, R. A. Abd-Alhameed, S. M. R. Jones, and H. Al-Ahmad, "New approaches and algorithms for the analysis of vertical refractivity profile below 1 km in a subtropical region," *IEEE Trans. Antennas Propag.*, vol. 62, no. 12, pp. 6501–6505, 2014.

[18] S. S. Mentes and Z. Kaymaz, "Investigation of surface duct conditions over Istanbul, Turkey," *J. Appl. Meteorol. Climatol.*, vol. 46, 2006.

[19] M. A. Dominguez, A. Benarroch, and J. M. Riera, "Refractivity statistics in Spain: First results," in *COST 255, CP52004*, May 1998.

[20] O. Jicha, P. Pechac, V. Kvicera, and M. Grabner, "Estimation of the radio refractivity gradient from diffraction loss measurements," *IEEE Trans. Geosci. Remote Sens.*, vol. 51, pp. 12–18, 2013.

[21] O. Jicha, P. Pechac, V. Kvicera, and M. Grabner, "Estimation of radio refractivity profile gradient from multiple LOS links using artificial neural networks—First results," in *Proc. 6th Eur. Conf. Antennas Propag. (EUCAP)*, 2012, pp. 1174–1177.

[22] International Telecommunication Union. "Prediction procedure for the evaluation of microwave interference between stations on the surface of the earth at the frequencies above about 0.7 GHz," Recommendation ITU-R P.452-12, 2005.

[23] International Telecommunication Union. "Propagation data and prediction methods required for the design of terrestrial line-of-sight systems," Recommendation ITU-R P.530-14, 2012.

[24] A. AbouAlmal *et al.*, "Statistical analysis of refractivity gradient and $\beta 0$ parameter in the Gulf region," *IEEE Trans. Antennas Propag.*, vol. 61, no. 12, pp. 6250–6254, Dec. 2013.

[25] A. T. Adediji, M. O. Ajewole, and S. E. Falodun, "Distribution of radio refractivity gradient and effective earth radius factor (k-factor) over Akure, South Western Nigeria Original Research Article," *J. Atmos.Solar Terr. Phys.*, vol. 73, pp. 2300–2304, Oct. 2011.

Abdulhadi AbouAlmal received the Bachelor's degree in communication engineering from Ajman University of Science and Technologies (AUST), Ajman, UAE, in 2007, and the Master's degree in engineering systems management from the American University of Sharjah (AUS), Sharjah, UAE, in 2011. He is currently pursuing the Ph.D. degree in wireless communication at the University of Bradford, Bradford, U.K.

After obtaining the undergraduate degree, he joined the Research Unit of Sharjah University and the Schools of Engineering in AUS and AUST universities, as a Research and Teaching Assistant for around two years. Since 2008, he has been with the Emirates Telecommunication Corporation, ETISALAT, as a Manager of Wireless Networks Planning and then as the Section Head of Radio Access Transformation, Technology Standardization and Spectrum Management. He has worked on a wide variety of projects in the areas of wave propagation, radio access technologies development (e.g., for 5G and IoT/M2M) and cost modeling of telecom networks and services. He used to be the coordinator of ETISALAT, UAE, and Arab Spectrum Management Group in the world conferences, Study Groups 3 and 5 meetings of the International Telecommunication Union (ITU) and 3GPP RAN meetings. He is the author and co-author of journal and conference papers and his research interests include modeling and optimization of wireless networks deployment, wave propagation, microwave fading.

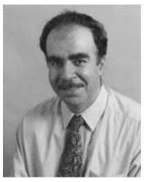

Raed A. Abd-Alhameed received the Ph.D. degree in antennas and propagations from the University of Bradford, Bradford, U.K., in 1997.

He is a Professor of radio frequency, antennas and computational electromagnetic techniques with the University of Bradford. He has over 20 years research experience and has authored over 400 academic journal and conference papers; in addition, he is the coauthor of three books and several book chapters. He is a Principal Investigator for the EPSRC-funded project "Multi-Band Balanced Antennas with Enhanced Stability and Performance for Mobile Handsets." He has also been named a Co-Investigator in several funded research projects including: 1) nonlinear and demodulation mechanisms in biological tissue (Department of Health, Mobile Telecommunications and Health Research Programme) and 2) assessment of the potential direct effects of cellular phones on the nervous system (EU: collaboration with six other major research organizations across Europe). He is the Leader for several successful knowledge transfer programmes such as with Pace plc, YW plc, Seven Technologies Group Ltd., Emkay Ltd., Two World Ltd., and IETG Ltd. He is also a Research Visitor at Wrexham University, Wrexham, Wales, since September 2009, covering the wireless and communications research areas. His research interests include hybrid electromagnetic computational techniques, EMC, antenna design, low SAR antennas for mobile handset, bioelectromagnetics, RF mixers, active antennas, beam steering antennas, MIMO antennas, Energy efficient PAs, RF predistorter design including biological cell modeling for breast cancer applications.

Prof. Abd-Alhameed is the Chair of several successful workshops on Energy Efficient and Reconfigurable Transceivers (EERT): Approach toward Energy Conservation and CO_2 Reduction. He is also invited as Keynote Speaker for several International conferences such as, ICST, ITA and EPC; in addition he also Chaired many research sessions. He has been a Guest Editor for the *IET Science, Measurements, and Technology Journal* since 2009. He is a Fellow of the Institution of Engineering and Technology, Fellow of Higher Education Academy, and a Chartered Engineer. He was awarded the Business Innovation Award for his successful KTP with Pace on the design and implementation of MIMO antenna systems; and recently Excellence in KTP project with Seven Technologies Group Ltd.

Steve M. R. Jones received the B.A. degree in physics (hons) from the University of East Anglia, U.K., in 1975 and the Ph.D. degree from the University of Bradford, Bradford, U.K., in 1994.

He is a Senior Lecturer in Telecommunications and the Head of Electrical Engineering with the School of Electrical Engineering and Computer Science, Faculty of Engineering and Informatics, University of Bradford. Since 1987, he has worked on a wide variety of projects in the area of satellite slant-path propagation and mobile radio propagation (notably Copernicus, Mobile VCE, and TEAMS projects). His research interests include multiple-antenna technologies, signal processing, and propagation modeling for broadband wireless access systems.

Prof. Jones served as an Associate Editor for the IEEE TRANSACTIONS ON ANTENNAS AND PROPAGATION from 2004 to 2008.

Hussain Al-Ahmad (S'78–M'83–SM'90) received the Ph.D. degree in signal processing from the University of Leeds, Leeds, U.K., in 1984.

He was with the University of Portsmouth, Portsmouth, U.K., Leeds Beckett University, Leeds, U.K., Kuwaiti Faculty of Technological Studies, University of Bradford, Bradford, U.K., and Etisalat University College, Sharjah, UAE. Currently, he is a Full Professor with the Department of Electrical and Computer Engineering, Khalifa University of Science, Technology and Research, Sharjah, UAE. He is the author and coauthor of 115 journal and conference papers. He has supervised successfully 30 Ph.D. and Master students in the U.K. and UAE. His research interests include signal and image processing.

Prof. Al-Ahmad is a Fellow of the IET, Chartered Engineer, member of BCS, Chartered IT Professional, and a Fellow of the Royal Photographic Society. He is the Vice Chair of the IEEE UAE Section and Chair of the IEEE UAE Education Chapter. He was the Secretary of the IEEE Kuwaiti section, the Chair of the IEEE UAE computer chapter and Vice Chair of the IEEE UAE signal processing and communication chapter. He has delivered short courses and seminars in Europe, Middle East, and Korea. He was a member of the Technical Program Committees of many IEEE conferences such as EDUCON, ICECS, ICSPC, ISSPIT, and ICIP.

[15] S. Yaoming and C. J. Scheytt, "Low-power 60 GHz receiver front-end with a variable-gain LNA in SiGe BiCMOS technology," in *Proc. IEEE Bipolar/BiCMOS Circuits and Technol. Meeting*, Oct. 2010, pp. 192–195.
[16] B. Allen and M. Ghavami, *Adaptive Array Systems: Fundamentals and Applications*, 1st ed. Hoboken, NJ, USA: Wiley, 2005, ch. 2.
[17] H. Oraizi and M. Fallahpour, "Array pattern synthesis with mutual coupling consideration," in *Proc. Int. Symp. on Telecommunications*, Aug. 2008, pp. 77–82.

New Approaches and Algorithms for the Analysis of Vertical Refractivity Profile Below 1 km in a Subtropical Region

Abdulhadi AbouAlmal, Raed A. Abd-Alhameed, Stephen M. R. Jones, and Hussein AlAhmad

***Abstract*—In this communication, 17 years of high resolution surface and radiosonde meteorological data from 1997–2013 for the subtropical Gulf region are analysed. Relationships between the upper air refractivity, N_h, and vertical refractivity gradient, ΔN, in the low troposphere and the commonly available data of surface refractivity, N_s are investigated. A new approach is discussed to estimate N_h and ΔN from the analysis of the dry and wet components of N_s, which gives better results for certain cases. Results are compared with those obtained from existing linear and exponential models in the literature. The investigation focusses on three layer heights at 65 m, 100 m and 1 km above ground level. Correlation between the components of N_s with both N_h and ΔN are studied for each atmospheric layer. Where high correlations were found, empirical models are derived from best-fitting curves.**

***Index Terms*—Microwave links, radio refractive index, refractivity gradient, standard atmosphere.**

I. Introduction

Microwave line-of-sight links are designed taking into account the curvature of rays in a stratified atmosphere over the curved earth [1], [2]. Variation of atmospheric parameters such as temperature and relative humidity dominate the vertical refractivity profile. The prevailing meteorological conditions in a specific region determine the extent of refraction. Statistical analysis of refractivity and its vertical profile are essential to the prediction of fading and anomalous propagation, such as sub- or super-refraction and ducting, as well as interference probabilities from reliable surface and upper-air meteorological data. The extent of ray-curvature is determined by the gradient of the refractive index, in N-units, versus height in km from the surface. This is known as the surface lapse rate, ΔN. The ITU has defined a reference atmosphere in the form of a negative exponential model and proposed a reference value of -40 N/km for the vertical ΔN over the first kilometer in temperate regions [3]. ITU has also published global contour maps for the refractive index at Earth's surface, N_s, and ΔN at specified altitudes [2].

It has been noted that surface meteorological data are widely available and the information about N_s is more readily available than the upper air refractivity, N_h [4]. The shortage of upper air data can be attributed to the operational and maintenance cost of radiosonde ascents compared with fixed surface weather stations. Some linear and exponential models [2], [4], [5] have been proposed to predict N_h at height h and vertical ΔN from the available N_s data, where upper air data are not available. It has been noted that most of these relations, in particular for ΔN, are derived from the refractivity analysis at the ground and 1 km height. Several refractivity studies are available, e.g., [6]–[11], while only a few are available for the Arabian Gulf region [12]–[16], where high incidence of anomalous propagation conditions are reported.

The vertical refractivity profile in the first few hundred meters of the atmosphere, where terrestrial communication systems operate, is important for the analysis of these anomalous phenomena. In this study, the relationships and correlation between dry, wet and net components of N_s with the corresponding components of either N_h or ΔN are investigated at 65 m, 100 m and 1 km layers above the ground, which are common reference altitudes proposed by ITU [2]. To the best of our knowledge, the curve fitting analysis of the dry and wet components at each layer has not been reported before. Cumulative distributions and scatter diagrams are presented. New relationships are derived from the best fitting curves and compared with existing models.

Long-term radiosonde data recorded at Abu Dhabi, the capital of UAE, from two daily ascents, nominally at 00:00 and 12:00 UT, have been used for the analysis corresponding to 4:00 am and 4:00 pm local time. In certain periods, only one ascent was available per day, usually at 00:00 UT. More details about the radiosonde and the special climate of Arabian Gulf area were recently introduced in [12]. In this communication, the measured refractivity parameters, N_s, N_h and ΔN, refer to the values obtained from the surface and radiosonde meteorological measurements, whereas predicted values of N_h and ΔN refer to those calculated from the measured N_s using the models in Sections I.A and I.B. The measured ΔN is derived from the measured N_s and N_h parameters using the linear model. Root mean square errors, RMSE, and correlation between the measured parameters and between measured and predicted values are presented, using the formulations as defined in MATLAB R2009a.

A. Refractivity Models

The atmospheric radio refractivity, N, at any altitude is calculated from the meteorological measurements of total atmospheric pressure (hPa), water vapor pressure (hPa) and absolute temperature (K) using the well-known refractivity formula [2], [5]. The N parameter consists of two components, N_D and N_W, which are often referred to as the dry and wet air contributions to refractivity [5]. The dry component contributes around 60 to 80% of the overall value [9]. The ITU provide a reference atmosphere for terrestrial paths in the form of a negative exponential model for prediction of N_h at any height h (km) above mean sea level [2]:

$$N_h = N_0 \cdot e^{(-h/h_0)} \quad (\text{N} - \text{units}) \tag{1}$$

Manuscript received March 16, 2014; revised August 12, 2014; accepted September 11, 2014. Date of publication September 26, 2014; date of current version November 25, 2014. This work was supported in part by the Engineering and Physical Sciences Research Council (EPSRC), U.K. under Grant EP/E022936 and in part by the Technology Strategy Board of the Knowledge Transfer Programme KTP008734.

A. AbouAlmal is with the Engineering Department, Emirates Telecommunication Corporation, Etisalat, UAE and also with the Antenna and Applied Electromagnetics Research Group, School of Electrical Engineering and Computer Science Bradford University, Bradford, West Yorkshire, BD7 1DP, U.K. (e-mail: eng_abdulhadi@yahoo.com).

R. A. Abd-Alhameed and S. M. R. Jones are with the Antenna and Applied Electromagnetics Research Group, School of Electrical Engineering and Computer Science Bradford University, Bradford, West Yorkshire, BD7 1DP, U.K. (e-mail: r.a.a.abd@bradford.ac.uk).

H. AlAhmad is with the Electrical Engineering Department, Khalifa University of Science, Technology & Research, Sharjah, UAE.

Color versions of one or more of the figures in this communication are available online at http://ieeexplore.ieee.org.

Digital Object Identifier 10.1109/TAP.2014.2360550

where N_o is refractivity extrapolated to sea level and h_o is the height coefficient which is referred to by ITU as the scale height of the model. The ITU provides global maps of N_o (derived using $\mathbf{ho = 9.5\ km}$) and proposes an average global profile based on N_o and h_o, values of 315 **N**-units and 7.35 km, respectively [2], [5]. It has been noted [2] that h_o may vary from one region to another.

Other relationships have also been proposed to predict N_h from the surface data [4], [5]. The following exponential model is further generalized to predict N_h from N_s considering "bulk" refractive index structure as opposed to short period random disturbances resulting from a variety of stochastic atmospheric processes [5]:

$$N_h = N_s \cdot e^{[-((h-h_s)/h_o)]} \quad (\mathrm{N-units}). \tag{2}$$

B. Refractivity Gradient Models

The variation of ΔN is a function of climate, season, transient weather conditions across the day, clutter and terrain over the communication path. In the standard atmosphere, N_h decreases with altitude since the total pressure decreases more rapidly than temperature with height [17]. The vertical ΔN usually has a negative value causing the rays to bend towards the earth and to propagate beyond the geometric horizon. ΔN can be obtained from two refractivity values, N_s at the surface, h_s, and N_h at an altitude h, using the linear model, by dividing the refractivity difference $(N_s - N_h)$ over $(h_s - h)$ [5], [12], [18].

A close correlation has been observed between N_s and ΔN "near the ground", i.e., over the first few kilometers [5]. Several empirical equations have been derived to predict long-term mean values of ΔN for the first kilometer layer of atmosphere above the ground from measured N_s parameter, which are only applicable to average negative gradients close to the surface [4], [5]. If N_h is not readily available, the refractivity gradient near the Earth's surface can be predicted either by differentiating (2), [5] or by applying the linear model for the measured N_s and the predicted N_h. Other models are also studied to predict the vertical ΔN near the ground from the measurements of electromagnetic wave strength and diffraction losses [19], [20]. For higher altitudes, different functions may be fitted as proposed by the three-part reference atmosphere model in Bean and Thayer's 1959 paper [5], which gives different expressions for the refractivity in the first kilometer, between 1 and 9 km and above 9 km. This has a drawback of introducing discontinuities in the ΔN profile. An exponential equation can also be used to directly relate ΔN with N_s as follows [4], [5]:

$$\Delta N = -a \cdot e^{(k \cdot N_s)} \quad \left(\frac{\mathrm{N}}{\mathrm{km}}\right) \tag{3}$$

where **a** and **k** are the model coefficients. Another exponential decaying relationship, obtained from curve fitting analysis between N_s and ΔN, was proposed for the first kilometer, $\Delta N_{1\ \mathrm{km}}$, [5], [15] as follows:

$$\Delta N_{1\ \mathrm{km}} = a \cdot (1 - e^{-bN_s})^c \quad \left(\frac{\mathrm{N}}{\mathrm{km}}\right) \tag{4}$$

where **a**, **b**, and **c** are the model coefficients, which are found to be -477.45, 0.00736, and 22.297, respectively, in this study. In general, the values of coefficients of all the models are found to vary from one climate to another. Analyzing data for long periods may also provide more accurate values of the coefficients. In order to extend these relations to other regions around the world, the correlation between long-term measured and predicted refractivity parameters need to be evaluated as well.

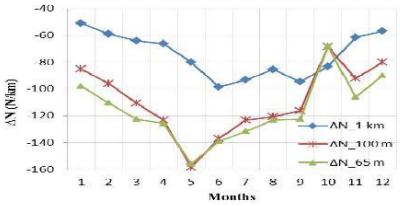

Fig. 1. Mean monthly variations of ΔN (1997 to Oct. 2013).

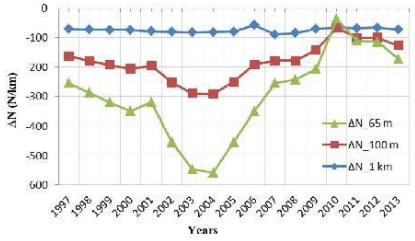

Fig. 2. Mean yearly variations of ΔN (1997 to Oct. 2013).

II. Analysis and Results

Seventeen years of high resolution meteorological data from 1997 till end of October 2013 have been analyzed in this study. Due to low quality or incomplete ascents, data for June 1998, April 2000, November 2005, June 2006 to November 2006 and January 2010 to May 2010 are not available. From December 2006 to December 2008, the data of only one ascent, mostly at 00:00 UT, is available on daily basis. In addition, a small number of abnormal values have been excluded owing to faulty readings from the instrument.

Two approaches, direct and indirect, have been used to predict N_h and ΔN from the measured N_s values. In the direct approach, N_h and ΔN are directly predicted from measured N_s using the linear or exponential models. A new indirect approach is proposed by analyzing the dry and wet components of the refractivity parameters using various prediction models. In this indirect approach, the dry and wet components of N_h or ΔN are first estimated from corresponding components of measured N_s based on the correlations observed between different components. Then, the net values of the predicted parameters, $\Delta N_{(\mathrm{D+W})}$ and $N_{h\_(\mathrm{D+W})}$, are computed by summing both dry and wet terms.

A. ΔN Analysis at 65 m, 100 m and 1 km Layers

The measured refractivity, N, has been evaluated from the radiosonde measurements at the ground and at the three specified altitudes. Then, the measured ΔN is obtained from the measured N_s and N_h for each layer using the linear model. In Figs. 1 and 2, the average seasonal and yearly variations of ΔN over the whole period of study are shown for each of the three layers. The mean monthly variations are significant for all the layers, as shown in Fig. 1. The gradient values at the 1 km layer, $\Delta N_{1\ \mathrm{km}}$, vary between -51 and -99 **N/km**, whereas the gradients span from -68 to -158 **N/km** and from -68 to -156 **N/km**, in case of the 100 m layer, $\Delta N_{0.1\ \mathrm{km}}$, and the 65 m layer, $\Delta N_{0.065\ \mathrm{km}}$, respectively. The range of variation is found to be approximately 45 units for $\Delta N_{1\ \mathrm{km}}$, 90 units for $\Delta N_{0.1\ \mathrm{km}}$ and 88 units for $\Delta N_{0.065\ \mathrm{km}}$.

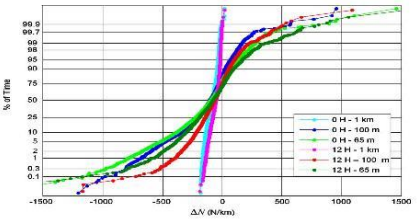

Fig. 3. Hourly Cumulative distributions of ΔN (1997 to Oct. 2013).

Gradient values are lower (i.e., higher in magnitude, but negative) during summer months, May and June, than in winter months, January and December. This can be attributed to the decreasing vapor content and pressure with height and the observed temperature inversions (temperature increasing with height) during the night, particularly in summer. Such ΔN trends may explain the frequent interference cases even across national borders, which are commonly experienced by terrestrial communication systems operating in the Gulf region during the summer months [12]. Occurrence of ΔN exceeding -100 N/km is related to the incidence of anomalous propagation [2], [6], [9], [12]. For $\Delta N_{1\text{ km}}$, no monthly mean is below -100 N/km, whereas $\Delta N_{0.1\text{ km}}$ and $\Delta N_{0.065\text{ km}}$ fall below this value for most months. In May, the monthly means of $\Delta N_{0.1\text{ km}}$ and $\Delta N_{0.065\text{ km}}$ even fall below the limit at which ducting phenomenon occurs, -157 N/km. The two peaks of $\Delta N_{0.1\text{ km}}$ and $\Delta N_{0.065\text{ km}}$ in October, where both monthly mean values of $\Delta N_{0.1\text{ km}}$ and $\Delta N_{0.065\text{ km}}$ are found to be higher than $\Delta N_{1\text{ km}}$, can be attributed to a bias in the data due to having only early-morning radiosonde data for this month. In 2007 and 2008, the data for October are only available for at 00:00 UT (4 am local time). In the morning, it is observed that the temperature and the water vapor pressure, e, often increase with altitude in many cases, in particular within the 65 m and 100 m layers, while e decreases considerably at 1 km height. The early morning/early evening effect on the gradient is clearly seen in the CDFs shown in Fig. 3. Consequently, the wet components of N and ΔN increase with altitude and ΔN attains large positive gradients in both 65 m and 100 m layers, which relates to the incidence of sub-refraction phenomenon [1], [6], [12]. The linear ΔN model has the drawback, particularly for the altitudes 100 m and below, that a small difference between the two refractivity values may result in large disagreement in ΔN due to the low decimal number in the equation's denominator. Also, the data for October 2006 were not available, which may also affect the overall result.

Year to year variation of the mean ΔN at 1 km, 100 m and 65 m, with spans of 32, 209 and 298 N-units, respectively, are given in Fig. 2. $\Delta N_{1\text{ km}}$ shows no significant fluctuations, while the values of $\Delta N_{0.1\text{ km}}$ and $\Delta N_{0.065\text{ km}}$ fluctuate from -1.5 to -210 N/km, and from 31 to -267 N/km, respectively. It can be observed that the mean $\Delta N_{0.1\text{ km}}$ and $\Delta N_{0.065\text{ km}}$ values decreased for the four years 2002, 2003, 2004 and 2005, with some exceptional values in the years 2003 and 2004. One reason for such trend is the considerable decrement of the water vapor content and pressure with higher altitudes that were observed over the course of these years. This yearly increment could be part of some short-term climate cycle, although a cyclical pattern cannot be reliably inferred from the currently available measurements. By contrast, the mean ΔN over each of the three layers showed almost the highest values during 2010, which could be due to the missing five months data, in particular the months of April and May, which contribute to lower gradient values as shown above in Fig. 1.

TABLE I
CORRELATION AND RMSE VALUES OF EXISTING PREDICTION MODELS FOR N_h AND ΔN FROM N_s

Layer	N_h&ΔN	Correlation	RMSE
1 km	N_h	0.001	30.82
	$\Delta N_{1\text{km}}$	0.86	18.77
100 m	N_h	0.87	15.18
	$\Delta N_{0.1\text{km}}$	0.29	151.7
65 m	N_h	0.91	12.59
	$\Delta N_{0.065\text{km}}$	0.24	196.2

Cumulative distributions of $\Delta N_{1\text{ km}}$, $\Delta N_{0.1\text{ km}}$ and $\Delta N_{0.065\text{ km}}$ for different times of day over the whole period are shown in Figs. 3. The range of $\Delta N_{0.065\text{ km}}$ varies between approximately -1947 and 1629 N/km, however only values between -1500 and 1500 N/km are displayed for clarity. The long-term mean values of $\Delta N_{1\text{ km}}$, $\Delta N_{0.1\text{ km}}$ and $\Delta N_{0.065\text{ km}}$ are -74.8, -109.6 and -116.4 N/km, respectively (well below the -40 of the ITU-R standard atmosphere), whereas the mean values at 00:00 and 12:00 UT are found to be -87.9 and -58.8 N/km for $\Delta N_{1\text{ km}}$, -138.7 and -74 N/km for $\Delta N_{0.1\text{ km}}$, in addition to -134.9 and -93.7 N/km for $\Delta N_{0.065\text{ km}}$.

By comparing the 0 H and 12 H curves for each layer, it can be observed that the gradient values are lower during the morning. Meteorological phenomena following sunset, could be responsible for such a trend [9], where vapor content considerably decreases with height, particularly during the summer season, while in Winter the moisture content may increase with altitude leading to higher positive values of $\Delta N_{0.1\text{ km}}$ and $\Delta N_{0.065\text{ km}}$ than 12:00 UT. Similar results were also reported in a previous study [12], however over a shorter period of years.

B. Correlation of Refractivity Components

The models introduced in Section I (Parts A and B) for predicting N_h and ΔN parameters from measured N_s, are examined and the predicted results are compared in terms of RMSE and correlation with the measured N_h and ΔN parameters. Table I summarizes the results of RMSE and correlation coefficients obtained for N_h and ΔN parameters using the exponential models (2) and (4), respectively, which give the best results in most cases, compared with other models. The h_o value is found to be 3.9 km, 3 km and 2.8 km for 1 km, 100 m and 65 m layers, respectively, for which minimum RMSE values can be obtained in each scenario. The exponential model (4) provides the best correlation and RMSE results for $\Delta N_{1\text{ km}}$, whereas (2) gives the best results of N_h at the 65 m and 100 m layers.

No correlation has been found between N_h and N_s for the 1 km layer, while strong correlation is observed for the other two layers, 100 m and 65 m. On the other hand, the correlation between $\Delta N_{1\text{ km}}$ and N_s exceeds 0.85, whereas it is found to be poor in case of the 65 m and 100 m layers. In addition, the correlation between the dry, wet and net components of measured N_s and the corresponding components of the measured N_h and ΔN are also investigated for each of the three layers. Table II provides the results of correlation matrix for all the scenarios. The dry component of N_s, N_{s_D}, is in good correlation with the dry component of N_h, N_{h_D}, at all altitudes, $N_{1\text{ km\_D}}$, $N_{0.1\text{ km\_D}}$ and $N_{0.065\text{ km\_D}}$, where the maximum correlation is observed within the 65 m layer. The N_{s_D} is found to be much less correlated with the dry components of ΔN in the three layers; $\Delta N_{1\text{ km\_D}}$, $\Delta N_{0.1\text{ km\_D}}$ and $\Delta N_{0.065\text{ km\_D}}$. The wet component of N_s, N_{s_W}, is well correlated with the wet component of N_h at the 100 m and 65 m altitudes, $N_{0.1\text{ km\_W}}$ and $N_{0.065\text{ km\_W}}$, while it is found to be only correlated with the wet component of ΔN at the 1 km layer, $\Delta N_{1\text{ km\_W}}$.

In general, no correlation could be obtained between either dry or wet components of N_s, and ΔN at the 100 m and 65 m layers. It is

TABLE II
CORRELATION MATRIX OF REFRACTIVITY COMPONENTS AT 1 KM, 100 M AND 65 M LAYERS.

	N_s	N_{s_D}	N_{s_W}
N_{1km}	0.001		
N_{1km_D}		0.84	
N_{1km_W}			0.15
$N_{0.1km}$	0.874		
$N_{0.1km\_D}$		0.96	
$N_{0.1km\_W}$			0.89
$N_{0.065km}$	0.91		
$N_{0.065km\_D}$		0.97	
$N_{0.065km\_W}$			0.92
ΔN_{1km}	-0.85		
ΔN_{1km_D}		-0.56	
ΔN_{1km_W}			-0.86
$\Delta N_{0.1km}$	-0.30		
$\Delta N_{0.1km\_D}$		-0.55	
$\Delta N_{0.1km\_W}$			-0.29
$\Delta N_{0.065km}$	-0.26		
$\Delta N_{0.065km\_D}$		-0.54	
$\Delta N_{0.065km\_W}$			-0.25

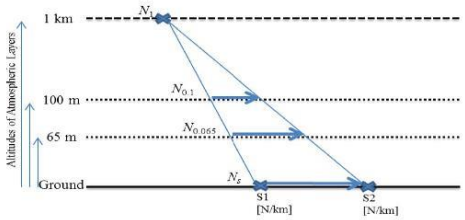

Fig. 4. Description of Correlation Between N_s, N_h and ΔN.

also noted that the correlation between the net parameters follows the correlation between their wet components. These observations seem to be reasonable since the wet term of refractivity is proportional to the water vapor content that varies significantly across these layers, in particular within the layers close to the ground, and gets more stable at around 1 km height, while the dry term is proportional to the atmospheric pressure and inversely proportional to the dry temperature, which show less variation over all atmospheric layers within the first kilometer.

The slope of the vertical refractivity curve at 1 km, which refers to $\Delta N_{1\text{ km}}$, is correlated with N_s since the variation of $N_{1\text{ km}}$ is very small compared with $N_{0.1\text{ km}}$ and $N_{0.065\text{ km}}$, which are directly correlated with N_s. No correlation is observed between N_s and gradients at the layers close to the ground, $\Delta N_{0.1\text{ km}}$ and $\Delta N_{0.065}$. Fig. 4 describes this phenomenon, where at 1 km height the refractivity value does not change significantly with the variations in N_s, while $N_{0.1\text{ km}}$ and $N_{0.065\text{ km}}$ vary significantly with N_s. The slope, ΔN, is only correlated with N_s in case of the 1 km layer, $\Delta N_{1\text{ km}}$, since $N_{1\text{ km}}$ is assumed to have a stable value while N_s varies between the states S1 and S2.

C. Curve Fitting Analysis and Algorithms

The scatter diagrams of all measured refractivity parameters and components are studied. Some figures of the correlated parameters and components are provided and empirical algorithms are derived from the best fitting curves. All relationships are evaluated based on the determination coefficients, correlation of the obtained results with the measured data and RMSE values.

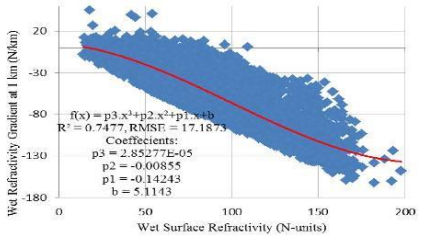

Fig. 5. Correlation between N_{s_W} and $\Delta N_{1\text{ km\_W}}$.

TABLE III
COMPARISON OF TWO APPROACHES FOR $\Delta N_{1\text{ km}}$ PREDICTION

	Correlation	RMSE
Direct Approach: ΔN_{1km} from measured N_s	0.85	30.8118
Indirect Approach: $\Delta N_{1km(D+W)}$ from Dry and Wet Components Analysis	0.85	19.3338

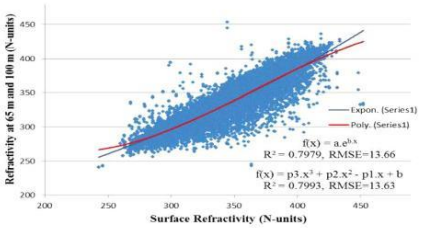

Fig. 6. Correlation between N_s and $N_{0.065\&0.1\text{ km}}$.

As presented in Table II, the correlation between N_s and $\Delta N_{1\text{ km}}$ is dominated by the wet components of the two parameters, N_{s_W} and $\Delta N_{1\text{ km\_W}}$, while N_{s_D}, is found to be correlated with $N_{1\text{ km\_D}}$ rather than $\Delta N_{1\text{ km\_D}}$.

The scatter diagram between the wet components, N_{s_W} and $\Delta N_{1\text{ km\_W}}$, is shown in Fig. 5. A third order polynomial relationship to predict $\Delta N_{1\text{ km\_W}}$ is obtained from the curve fitting analysis. The dry component of $\Delta N_{1\text{ km\_D}}$ is calculated using the linear model from the predicted $N_{1\text{ km\_D}}$ and measured N_{s_D}. $N_{1\text{ km\_D}}$ is predicted from measured N_{s_D} using (2). This new indirect approach for predicting $\Delta N_{1\text{ km(D+W)}}$ has less RMSE value than the direct approach for predicting $\Delta N_{1\text{ km}}$ from measured N_s using the linear model, as shown in Table III.

Multiple scatter diagrams are drawn for the dry, wet and net components of the measured N_h and ΔN against the corresponding measured N_s components at 65 m and 100 m atmospheric layers. Good correlation is observed between N_h and N_s components, while it is found to be poor between ΔN and N_s with large RMSE values obtained regardless of the approach or the prediction model to be used. This can be attributed to the sensitivity of ΔN to any small variation in the values of refractivity at these low altitudes. N_h has been predicted using the exponential model (2) considering both the direct and indirect approaches at the 65 m, $N_{0.065\text{ km}}$, and 100 m, $N_{0.1\text{ km}}$, layers. Due to the similarity of the N_h results at the 65 m and 100 m layers, the available data sets of these two layers are combined, $N_{0.065\&0.1\text{ km}}$, to

develop a single model for the atmospheric layers below 100 m altitude from the ground. The correlation and RMSE values of the measured and predicted N_h, N_{h_D}, N_{h_W} and $N_{h\_(D+W)}$, are compared for each of the three data sets at 65 m, 100 m and their combined set. For all scenarios, RMSE results for $N_{h\_(D+W)}$ using the indirect approach are better than the results of N_h obtained directly from the measured N_s, while correlation results are almost the same.

The scatter diagram of N_h against N_s is given in Fig. 6. Two exponential and third order polynomial relationships are obtained from the best fitting curves, which provide marginally better results in comparison with the other models. Both models have very similar results with marginal improvement for the polynomial model. However, the result from the polynomial is highly sensitive to the precision of the coefficients. The RMSE and correlation results obtained for the prediction of N_h from both direct and indirect approaches are similar. The following exponential model can be used for direct prediction of N_h below 100 m above the ground, where the values of the coefficients a and b are found to be 135.8 and 0.002609, respectively, for the area under study:

$$N_{0.065\&0.1\ \mathrm{km}} = a \cdot e^{(b \cdot N_s)} \quad (\mathrm{N-units}). \tag{5}$$

III. Conclusions

17 years of local radiosonde data from UAE were analysed to obtain the vertical refractivity profile for three critical atmospheric layers within the first kilometer above the ground. The correlation between N_s and either N_h or ΔN was found to depend predominantly on the wet components of these parameters.

For estimating ΔN at the three atmospheric layers, it was observed that the linear model resulted in somewhat lower RMSE values than the exponential one.

Based on the reduced RMSE, it is recommended to use the indirect approach to estimate N_h and ΔN from the analysis of dry and wet refractivity components, in particular at the 1 km layer. Marginal improvement was achieved for the 65 m and 100 m layers when N_h was predicted using the exponential model (2) based on the indirect approach. Such multi-steps analysis may lead to slightly lower correlation, when compared with the measured data, than using the direct relations.

Although the use of more than one model to predict the refractivity at different atmospheric layers may introduce some discontinuities in its vertical profile, the RMSE values of the predicted N_h or ΔN were found to be reduced while the correlation between the measured and predicted values was marginally improved for certain parameters.

Third- and fourth-order polynomial models showed marginal improvements in terms of RMSE and correlation values for the prediction of N_h and ΔN parameters over the other models. However, it was noted that the results were very sensitive to the precision of the high order coefficients.

Acknowledgment

The authors would like to express their gratitude to the National Center of Meteorology in UAE for providing the raw meteorological data used in this work.

References

[1] M. I. Skolnik, *Introduction to Radar Systems*, 3rd ed. New York, NY, USA: McGraw-Hill, 2001.

[2] The Radio Refractive Index: Its Formula and Refractivity Data International Telecommunication Union, 2012, ITU-R Recommendation P.453-10.

[3] Definitions of Terms Relating to Propagation in Non-Ionized Media International Telecommunication Union, ITU, 1994, ITU-R Recommendation PN.310-9.

[4] R. L. Freeman, *Radio System Design for Telecommunications*, 3rd ed. Hoboken, NY, USA: Wiley, 2007.

[5] Handbook on Radiometeorology. Geneva, ITU R Bureau, International Telecommunication Union, 1996.

[6] T. G. Hayton and K. H. Craig, "Use of radiosonde data in propagation prediction," presented at the Inst. Elect. Eng., London, U.K., 1996.

[7] S. Lystad, Investigation of surface refractivity and refractive gradients in the lower atmosphere of Norway CP 121, COST 235, Mar. 1993.

[8] A. K. P. Marsh, T. G. Hayton, and K. H. Craig, Initial comparison of refractivity parameters derived from radiosondes and psychrometers in France CP42010, COST 255, Oct. 1997.

[9] L. Blanchard and H. Sizun, Refractivity over France: First results of ARGOS experiment CP32003, COST 255, May 1997.

[10] K. H. Craig and T. G. Hayton, Investigation of $\beta 0$ values derived from ten years radiosonde data at 26 stations CP 182, COST 235, Oct. 1993.

[11] K. H. Craig and T. G. Hayton, "Refractivity parameters from radiosonde data," in *Proc. AGARD Conf. On Propagation Assessment in Coastal Environments*, Germany, 1994, pp. 1–12.

[12] A. AbouAlmal, R. A. Abd-Alhameed, K. Al-Ansari, H. Al-Ahmad, C. H. See, S. M. R. Jones, and J. M. Noras, "Statistical analysis of refractivity gradient and $\beta 0$ parameter in the Gulf Region," *IEEE Trans. Antennas Propag.*, vol. 61, pp. 6250–6254, 2013.

[13] A. Abu Al-mal and K. Al-Ansari, "Calculation of effective earth radius and point refractivity gradient in UAE," *Int. J. Antennas Propag.*, vol. 2010, 2010 [Online]. Available: http://www.hindawi.com/journals/ijap/2010/245070/

[14] K. Al-Ansari, A. AbuAl-Mal, and R. A. Kamel, "Statistical analysis of refractivity in UAE," in *Proc. Int. Symp. on Rainfall Rate and Radiowave Propagation*, 2007, vol. 923, pp. 232–247.

[15] K. Al Ansari and R. A. Kamel, "Correlation between ground refractivity and refractivity gradient and their statistical and worst month distributions in Abu Dhabi," *IEEE Antennas Wireless Propag. Lett.*, vol. 7, pp. 233–235, 2008.

[16] A. AbouAlmal, R. A. Abd-Alhameed, A. S. Hussaini, T. Ghazaany, Z. Sharon, S. M. R. Jones, and J. Rodriguez, "Comparison of three vertical refractivity profiles in the Gulf Region," in *Proc. 19th Eur. Wireless Conf.*, 2013, pp. 1–4.

[17] S. S. Mentes and Z. Kaymaz, "Investigation of surface duct conditions over Istanbul, Turkey," *J. Appl. Meteor. Climat.*, vol. 46, no. 3, pp. 318–337, 2006.

[18] M. A. Dominguez, A. Benarroch, and J. M. Riera, Refractivity statistics in Spain: First results CP52004, COST 255, May 1998.

[19] O. Jicha, P. Pechac, V. Kvicera, and M. Grabner, "Estimation of the radio refractivity gradient from diffraction loss measurements," *IEEE Trans. Geosci. Remote Sensing*, vol. 51, pp. 12–18, 2013.

[20] O. Jicha, P. Pechac, V. Kvicera, and M. Grabner, "Estimation of radio refractivity profile gradient from multiple LOS links using artificial neural networks—First results," in *Proc. 6th Eur. Conf. on Antennas and Propagation*, 2012, pp. 1174–1177.

TABLE I
MEAN AND VARIANCE OF THE ERROR BETWEEN THE UTD-PO AND THE FRESNEL INTEGRAL RESULTS AND THE MEASUREMENTS (dB)

	Mean Error		Variance	
	Vertical Pol.	Horizontal Pol.	Vertical Pol.	Horizontal Pol.
UTD-PO	0.50	0.85	0.11	0.09
Fresnel	0.48	1.01	0.07	0.16

shows a smaller error than the method based on a Fresnel surface integral when horizontal polarization is considered.

V. CONCLUSIONS

A new method based on a hybrid UTD-PO formulation for the evaluation of the propagation loss due to the diffraction that takes place at the top of a rectangular obstacle that is illuminated from a low source has been presented. The proposed solution shows less mathematical complexity than other existing techniques, and comparison with measurements and a method based on the evaluation of a Fresnel surface integral shows solid agreement.

REFERENCES

[1] J. H. Whitteker, "Diffraction over a flat-topped terrain obstacle," *Inst. Elect. Eng. Proc. H.*, vol. 137, no. 2, pp. 113–116, 1990.

[2] J. Gong, T. S. M. Maclean, and Z. Wu, "Radiowave propagation over rectangular plateau," *Electron. Lett.*, vol. 25, no. 11, pp. 707–709, 1989.

[3] C. J. Haslett and M. O. Al-Nuaimi, "Prediction of diffracted field strength in the shadow of a flat roofed building," *Electron. Lett.*, vol. 27, no. 11, pp. 950–951, 1991.

[4] J.-V. Rodriguez, J.-M. Molina-Garcia-Pardo, and L. Juan-Llácer, "A new solution expressed in terms of UTD coefficients for the multiple diffraction of spherical waves by a series of buildings," *Radio Sci.* , vol. 42, 2007, RS4011, DOI: 10.1029/2006RS003464..

[5] R. G. Kouyoumjian and P. H. Pathak, "A uniform geometrical theory of diffraction for an edge in a perfectly conducting surface," *Proc. IEEE*, vol. 62, no. 11, pp. 1448–1461, 1974.

[6] L. Juan-Llácer and J. L. Rodriguez, "A UTD-PO solution for diffraction of plane waves by an array of perfectly conducting wedges," *IEEE Trans. Antennas Propag.*, vol. 50, no. 9, pp. 1207–1211, 2002.

[7] S. R. Saunders and F. R. Bonar, "Explicit multiple building diffraction attenuation function for mobile radio wave propagation," *Electron. Lett.*, vol. 27, no. 14, pp. 1276–1277, Jul. 1991.

[8] M.-T. Martínez-Inglés, C. Garcia-Pardo, J. Pascual-Garcia, J.-M. Molina-Garcia-Pardo, J.-V. Rodriguez, J. Reig, and L. Juan-Llácer, "Initial experimental characterization of the millimeter-wave radio channel," in *Eur. Conf. on Antennas and Propagation*, Prague, Czech Republic, Mar. 2012, pp. 23–30.

[9] G. Millington, R. Hewitt, and F. Immirzi, "Double knife edge diffraction in field strength predictions," *Proc. Inst. Elect. Eng.*, vol. 16, pp. 419–429, 1962.

Statistical Analysis of Refractivity Gradient and β_0 Parameter in the Gulf Region

Abdulhadi AbouAlmal, Raed A. Abd-Alhameed, Kifah Al-Ansari, Hussein AlAhmad, Chan H. See, Steve M. R. Jones, and James M. Noras

***Abstract*—In this communication, nine years of local radiosonde meteorological data, from 1997 to 2005, have been used to calculate the vertical refractivity gradient, ΔN, in the lowest atmospheric layer above the ground surface. The values obtained are used to estimate the parameter β_0, which represents the probability of non-standard propagation. Hourly, monthly and yearly distributions of ΔN in the first 100 meters above the ground are given. Monthly and yearly variations of the mean of ΔN and β_0 are provided and the β_0 values are compared with the ITU maps.**

***Index Terms*—Anomalous propagation, atmospheric refraction, β_0, refractivity gradient.**

I. INTRODUCTION

Electromagnetic waves propagating through the lower layers of the atmosphere follow curved paths as a result of the variation of refractive index with height. The refractive index of air is dependent on temperature, pressure and humidity and thus varies with height. As a reference point, the ITU has defined a negative exponential "standard atmosphere" and published maps showing variations in refractive index at the Earth's surface [1]. The gradient of refractive index in N-units versus height (in km) at the surface is known as the surface lapse rate ΔN. ITU maps [1] also provide ΔN data at specified altitudes. Anomalous propagation may occur due to nonstandard variation of vertical refractivity through different atmospheric layers. Several studies related to the refractivity analysis are available [2]–[7]. Only a few studies are available for the Gulf region although it is likely to experience abnormal conditions due to its special climate which is hot and humid, most of the year. Initial results of the statistical analysis of surface refractivity, ΔN in the first kilometer, k-factor and point refractivity gradient in United Arab Emirates (UAE) have been discussed previously in [8], [9]. The UAE is situated on the northeastern part of the Gulf, along the tropic of Cancer. Abu Dhabi, capital of UAE, is a coastal city located at 24.52° N latitude and 54.98° E longitude, with an altitude of 27 m above sea level. Its climate is subtropical and arid due to its location

Manuscript received November 12, 2012; revised June 06, 2013; accepted July 15, 2013. Date of publication August 28, 2013; date of current version November 25, 2013.

A. AbouAlmal is with the Antenna and Applied Electromagnetics Research Group, School of Engineering Design and Technology Bradford University, Bradford, West Yorkshire, BD7 1DP, U.K. and also with the Wireless Network Planning, Engineering Department, Emirates Telecommunication Corporation, Etisalat, UAE (e-mail: eng_abdulhadi@yahoo.com).

R. A. A. Abd-Alhameed, C. H. See, S. M. R. Jones, and J. M. Noras are with the Antenna and Applied Electromagnetics Research Group, School of Engineering Design and Technology Bradford University, Bradford, West Yorkshire, BD7 1DP, U.K. (e-mail: r.a.a.abd@bradford.ac.uk; chsee2@bradford.ac.uk).

K. Al-Ansari and H. AlAhmad are with Electrical Engineering Department, Khalifa University of Science, Technology & Research (KUSTAR), Sharjah, UAE.

C. H. See is with the Antenna and Applied Electromagnetics Research Group, School of Engineering Design and Technology Bradford University, Bradford, West Yorkshire, BD7 1DP, U.K. and also with Engineering, Sport and Science (ESS) Academic Group, University of Bolton, Bolton, BL3 5AB, U.K. (e-mail: c.see@bolton.ac.uk).

Color versions of one or more of the figures in this communication are available online at http://ieeexplore.ieee.org.

Digital Object Identifier 10.1109/TAP.2013.2279999

within the Northern desert belt, which is warm and sunny throughout the year. From May to September, the temperature and humidity are high with an average temperature above 40°C and sandstorms occur intermittently. Winter can be windy with brief and irregular rainfall.

Long-term radiosonde data recorded with good resolution from two daily ascents, nominally at 00:00 and 12:00 UT, have been used for the analysis corresponding to 4:00 am and 4:00 pm local time. A radiosonde is an airborne weather station coupled with a radio transmitter which makes measurements of temperature, air pressure, humidity, and wind speed and direction, and transmits the measurements back to the ground. A Vaisala RS92 Radiosonde, which offers high level performance of meteorological measurements and GPS capabilities with a reliable telemetry link, has been used for gathering the meteorological data.

This study was conducted to investigate ΔN in the lowest part of the atmosphere, and to derive β_0 values for Abu Dhabi. The β_0 statistics are derived from the cumulative distributions of the vertical ΔN. Hourly, seasonally and yearly distributions of ΔN and β_0 variations are presented. The results obtained are compared with the β_0 values derived from ITU maps [1], [10], which are provided for different geographical locations where reliable local data are not available.

A. Refractivity Gradient in the Lowest Atmospheric Layer

ΔN statistics of the first 100 m from the surface may be used to estimate the occurrence probability of ducting and multipath conditions [1]. They have to be considered when studying the system performance of terrestrial line of sight communication. The atmospheric radio refractivity, N, is calculated by the following well known formula [1], [11]:

$$N = N_{dry} + N_{wet} = \frac{77.6}{T}\left(P + 4810\frac{e}{T}\right) \quad \text{(N-Units)} \qquad (1)$$

where P is the total atmospheric pressure (hPa), e is the water vapor pressure (hPa) and T is the absolute temperature (K). The dry component of refractivity is the most important; it contributes around 60% to 80% of the overall value [5]. The atmospheric pressure and temperature are directly sensed during the radiosonde balloon ascents, while the vapor pressure is derived from the dewpoint as follows [12]:

$$e = 6.11 \times 10^{(7.5T_d/237.7+T_d)} \quad \text{(hPa)} \qquad (2)$$

where T_d is the dewpoint temperature measured in degrees Celsius.

ΔN can be obtained from two refractivity values, N_s, surface refractivity, and N_1, refractivity at any height h_1 within the 1 km layer above the ground level h_s, using the following linear equation [13]:

$$\Delta N = (N_s - N_1)/(h_s - h_1) \quad \text{(N/km)}. \qquad (3)$$

Other works have been conducted to study the feasibility of estimating the vertical refractivity gradient near the ground from measurements of electromagnetic wave strength and diffraction losses [14], [15], in particular when upper air data are not available. An exponential model can also be used for quick, approximate estimates of refractivity gradient near the Earth's surface [1]. In the standard atmosphere, N decreases with altitude since the total pressure drops off rapidly while temperature decreases with height [16]. Consequently, the vertical refractivity gradient usually has a negative value causing rays to bend towards the earth and obtaining propagation beyond the geometric horizon. If the gradient is more (i.e., less negative) than usual, or even positive, sub-refraction occurs, where the ray bends less than usual towards the earth, even bending upwards in the case of a positive gradient and the range reduces. Sub-refraction occurs when warm moist air flows over a cool ocean surface or over a cooler air mass just above the ocean surface [2], [17].

TABLE I
SUMMARY OF REFRACTIVE PROPAGATION CONDITIONS

Refractive Conditions	Gradients (N/km)
Sub-refraction	Positive Gradients
No Refraction	0
Normal Refraction	0 to -100
Super-refraction	-100 to -157
Trapping or Ducting	-157 to $-\infty$

If the gradient is less than in a standard atmosphere (i.e., more negative), super-refraction takes place, with rays bending more than usual towards the earth and propagating further than in standard conditions. Super-refraction occurs when temperature increases with height and/or water vapor content decreases with height, where the signal propagates between the normal and critical gradient conditions. At a critical gradient value, $\Delta N = -157$ N/km, the radius of curvature of the ray becomes equal to the Earth radius. The wave path approaches the Earth curvature and consequently the signal moves parallel to its surface [17]. Gradients more negative than this critical value lead to ducting, in which the signal becomes trapped in the boundary layer, propagating well beyond its usual range. Table I summarizes the limits considered for the refractive conditions in this study.

B. β_0 Statistics

β_0 is an important parameter in studies of clear air propagation and interference since it is commonly used to indicate the relative incidence of anomalous propagation. β_0 represents the percentage of time in which the value of ΔN is less than or equal to -100 N/km [1], [2], [5]. It is derived from ΔN statistics in the lowest 100 m of the atmosphere. The normal range of ΔN in the surface layer is between 0 and -100 N/km. In this communication, "anomalous propagation" is defined as that occurring outside this normal range. Note that other references consider different values, such as -79 N/km, for the limit between the normal and non-standard propagation [17]. β_0 might relate, with reasonable accuracy, to the presence of ducting phenomenon where ΔN values do not exceed -157 N/km. It was observed [2] that β_0 is correlated to the latitude of the area under consideration, showing higher values in equatorial regions and lower toward the poles. In this work, β_0 is calculated from the occurrence probability of both super-refraction and ducting conditions.

II. RESULTS AND ANALYSIS

Nine years of high resolution meteorological data from 1997 to 2005 have been analyzed in this study. Data are available for 5,391 radiosonde ascents. Due to low quality or incomplete ascents, data for June 1998, April 2000 and November 2005 are not available. A small number of abnormal values have been excluded owing to faulty readings from the instrument.

A. Refractivity Gradient Calculations in the First 100 Meters

The refractivity gradient, ΔN, has been evaluated using (3). h_1 is selected to be the nearest point to 100 m height, which was found to be 103 m since data at the exact height were not available. In Figs. 1 and

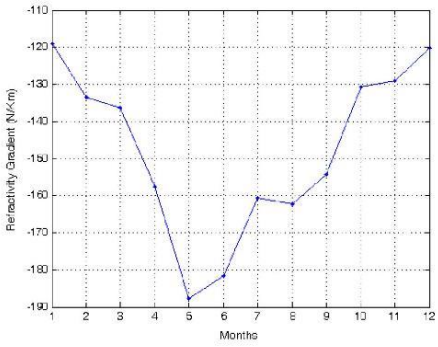

Fig. 1. Mean monthly variations of the refractivity gradient, ΔN, at 100 m (1997 to 2005).

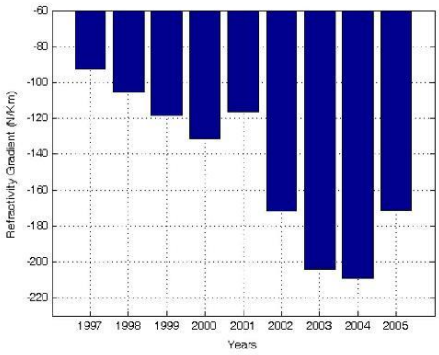

Fig. 2. Mean yearly variations of the refractivity gradient, ΔN, at 100 m (1997 to 2005).

2, the average seasonal and yearly variations of ΔN over the whole period of study are shown. The monthly variations are significant. Values oscillate between approximately -118 and -186 N/km, with a range of 68 units. The gradient values are lower (i.e., more negative) during summer months, May and June, than winter months, January and December. This can be attributed to the decreasing vapor content and pressure and to the increasing temperature with height. Such ΔN trends explain the frequent interference cases even across national borders, which are most commonly experienced during the summer months in the Gulf region. All monthly means do not exceed -100 N/km, which relates to the incidence of anomalous propagation as explained in Section I.B above.

Year to year variations of the mean refractivity gradients with a span of 70 units, are given in Fig. 2. It has been observed that the mean ΔN values have increased for the four years 2002, 2003, 2004 and 2005, with some exceptional values in the years 2003 and 2004. Whether or not this yearly increment is part of some short or longer-term climate cycle cannot be reliably inferred from nine years' measurements, but may indicate an increasing probability of anomalous propagation occurrence in the Gulf region.

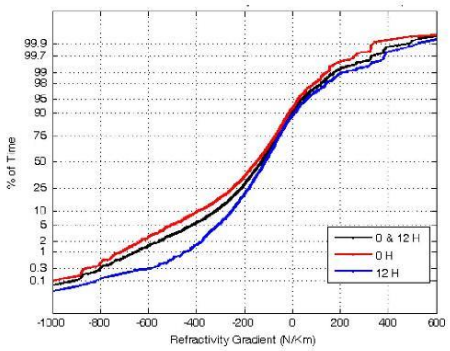

Fig. 3. Cumulative distributions of refractivity gradient at 100 m.

Cumulative distributions of ΔN over this period for different times of day are shown in Fig. 3. The range of ΔN varied between approximately -1160 and 990 N/km, however for clarity only values between -1000 and 600 N/km are displayed. The long-term mean value of ΔN is -128.6 N/km, whereas the mean values at 00:00 and 12:00 UT are found to be -148.5 N/km and -113.9 N/km, respectively. The gradient values are less (i.e., more negative) during the morning. Meteorological phenomena following sunset, could be responsible for such a trend [5].

In a previous study [9], the vertical refractivity gradient was evaluated in Abu Dhabi for the first kilometer of atmosphere and found to vary between -200 and 63 N/km. The ITU proposes a standard value of -40 N/km as the reference for the vertical refractivity gradient in the first kilometer [18]. The range of gradients in the lowest 100 m layer is rather below this value, which indicates that anomalous propagation is frequent in this critical atmospheric layer where most terrestrial wireless links operate.

The long-term probabilities of super-refraction and sub-refraction phenomena during the course of the year can be obtained from the "0 & 12H" curve as in Fig. 3. These two refractive conditions correspond to range of gradients given in Table I, which are -100 to -157 N/km and positive gradient above 0 N/km respectively. The probabilities of super-refraction and sub-refraction conditions have been found to be around 23% and 9%, respectively.

Monthly and yearly cumulative distributions of ΔN are given in Figs. 4 and 5. The cumulative distribution of each month is drawn in Fig. 4 from all the data gathered for that calendar month during the entire period.

In Fig. 5, it is evident that the yearly cumulative distributions have a fairly consistent form, however, the median value of ΔN increases systematically from year to year. The probability of anomalous propagation where ΔN do not exceed -100 N/km also increases annually. However, there is a clear variation in the values during the course of the year as displayed in Fig. 4. Summer months are more critical where the gradient varies over a wider range than in winter. Gradients with lower values have been obtained during the summer for higher percentages of time. Similar observations have been reported in [5], [6]. The monthly distribution curves converge around gradients between -50 and -90 N/km, and the time percentages change between 60 to 75% accordingly. It can be noticed that the probability of gradients less than or equal to -157 N/km, which indicates ducting occurrence, varies from 29% in January to 52% in May.

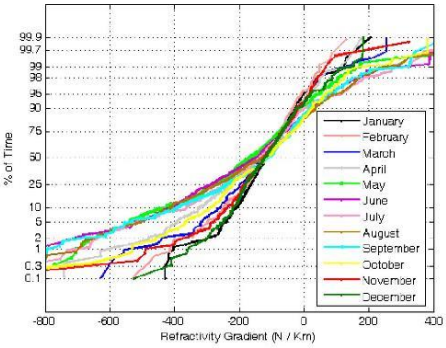

Fig. 4. Monthly cumulative distributions of the refractivity gradient at 100 m.

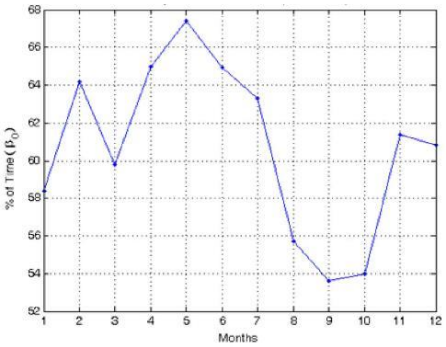

Fig. 6. Monthly variations of β_0.

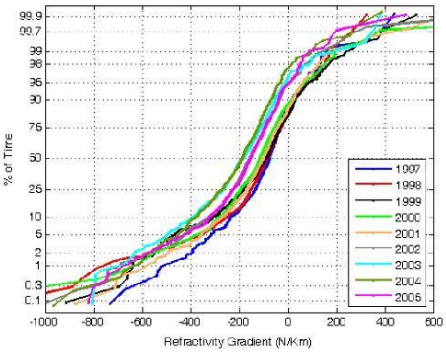

Fig. 5. Yearly cumulative distributions of the refractivity gradient at 100 m.

B. β_0 *Calculations*

Hourly, monthly and yearly variations of the β_0 parameter have been derived from cumulative distributions of ΔN at the lowest 100 m of the atmosphere. It corresponds to the probability at which the value of ΔN is less than or equal to -100 N/km, causing the incidence of non-standard conditions such as super-refraction and ducting. The long-term value of β_0 has been found to be 60.8% from the "0 & 12H" curve in Fig. 3. This means that the value of refractivity gradient is expected to be less than or equal to -100 N/km for around 60% of the time. The values of β_0 obtained at 00:00 and 12:00 UT are 65.6% and 55.5% respectively, which indicate higher probability of anomalous propagation occurrence in the early morning. This can explain the operational experience of intermittent outage due to high signal fading for some of the microwave links operating in UAE during the morning, mostly within the summer season.

Fig. 6 shows monthly variations of β_0 obtained from the monthly cumulative distributions of the refractivity gradients in Fig. 4. The value of β_0 fluctuates between 53% and 68%, with the highest value occurring in May. Generally, the summer months show higher probabilities of anomalous propagation than others.

The results obtained for the monthly variations of β_0 are compared with ITU maps [1] in Table II. It is seen that the ITU values are not in good agreement with the results obtained in this study. The estimated ITU values are below those calculated in the case of February and November with differences of 34% and 21%, respectively, while they are overestimated for the months of May and August, with differences of 7% and 19%. This can be attributed to the fact that the ITU maps [1] were interpolated from radiosonde data from only 99 sites worldwide between 1955 and 1959. Differences have also been observed in other countries [5]. In addition, ITU curves and maps are usually derived from measurements performed largely in temperate regions of the world such as Europe, North America and Japan [19], which have different climatic conditions from the Gulf region. This would also suggest the necessity to revise these maps based on recently gathered long-term local meteorological data from more radiosonde sites, since they are being widely used for microwave link design.

TABLE II
VALUES OF β_0 COMPARED WITH ITU MAPS

Months	ITU Values (%)	Obtained Values (%)
February	30	64
May	75	67
August	75	56
November	40	61

The annual variations of β_0 are given in Fig. 7, obtained from the yearly cumulative distributions of the refractivity gradients in Fig. 5. The variation is significant where the percentages are increasing year by year; with a peak value shown for 2004.

III. CONCLUSION

Local radiosonde data were used to obtain the refractivity gradient in the first hundred meters above the ground surface. The β_0 parameter has been calculated to indicate the probability of anomalous propagation such as ducting and multipath in Abu Dhabi. The results obtained for the long-term mean value of ΔN and β_0 were -128.6 N/km and 60.8%, respectively. The monthly results of β_0 were not in good agreement with the values provided by the ITU maps.

Monthly values of β_0 averaged over the nine years of this study showed the ITU values to be somewhat conservative during the summer months, but to significantly underestimate the severity during the winter months. However, year-to-year variations showed that in

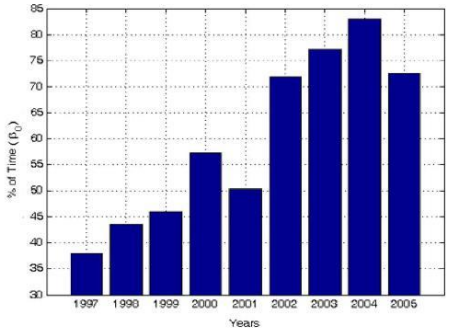

Fig. 7. Year to year variations of β_0.

two out of the nine years, the annual average value of β_0 exceeded the ITU figure for the worst month. This is consistent with operational observations of the received signal strength, fading occurrence and interference cases for some of the microwave links operating in the UAE, which confirmed the high probability of anomalous phenomena over the course of the year, exceeding 50% even during the winter, and in particular during the early morning time.

Since local data are now available for the UAE region, it is strongly recommended that link designs for this region take account of the annual and seasonal variations reported here. This will enable better prediction of performance and reliability in the design and deployment of wireless communication systems working in this region.

There is perhaps an opportunity to revise the ITU maps using the now abundant long-term local meteorological data which have been collected recently all over the world. Work will continue to report the fading occurrence based on real signal strength measurements and to study the occurrence of different ducting classes in UAE.

ACKNOWLEDGMENT

The authors would like to express their gratitude to the National Center of Meteorology in UAE for providing the meteorological data used in this work.

REFERENCES

[1] ITU-R Recommendation P.453-10: The radio refractive index: its formula and refractivity data, International Telecommunication Union, 2012.
[2] T. G. Hayton and K. H. Craig, "Use of radiosonde data in propagation prediction," presented at the IEE, Savoy Place, WC2R OBL, London, U.K., 1996.
[3] L. S. , "Investigation of surface refractivity and refractive gradients in the lower atmosphere of Norway," COST 235, CP 121 Mar. 1993.
[4] A. K. P. Marsh, T. G. Hayton, and K. H. Craig, "Initial comparison of refractivity parameters derived from radiosondes and psychrometers in France," COST255, CP42010 Oct. 1997.
[5] B. L. and S. H. , "Refractivity over France: First results of ARGOS experiment," COST255, CP32003 May 1997.
[6] K. H. Craig and T. G. Hayton, "Investigation of $\beta 0$ values derived from ten years radiosonde data at 26 stations," COST 235, CP 182 Oct. 1993.
[7] K. H. Craig and T. G. Hayton, "Refractivity parameters from radiosonde data," in *Proc. AGARD Conf. on Propagation Assessment in Coastal Environments*, Germany, 1994, pp. 1–12.
[8] K. Al-Ansari, A. AbuAl-Mal, and R. A. Kamel, "Statistical analysis of refractivity in UAE," in *Proc. Int. Symp. on Rainfall Rate and Radiowave Propagation*, India, 2007, vol. 923, pp. 232–247.
[9] A. A. Al-Mal and K. Al-Ansari, "Calculation of effective earth radius and point refractivity gradient in UAE," *Int. J. Antennas Propag.*, vol. 2010, 2010.
[10] ITU-R Recommendation P.452-12: Prediction Procedure for the Evaluation of Microwave Interference between stations on the surface of the earth at the frequencies above about 0.7 GHz, International Telecommunication Union, ITU, 2005.
[11] "Handbook on Radiometeorology," ITU R Bureau, International Telecommunication Union. Geneva, 1996.
[12] Apr. 2013 [Online]. Available: http://www.johnsnhweather.com/formulas/vaporPressure.html
[13] M. A. Dominguez, A. Benarroch, and J. M. Riera, "Refractivity statistics in Spain: First results," COST 255, CP52004 May 1998.
[14] O. Jicha, P. Pechac, V. Kvicera, and M. Grabner, "Estimation of the radio refractivity gradient from diffraction loss measurements," *IEEE Trans. Geosci. Remote Sensing*, vol. 51, pp. 12–18, 2013.
[15] O. Jicha, P. Pechac, V. Kvicera, and M. Grabner, "Estimation of radio refractivity profile gradient from multiple LOS links using artificial neural networks #x2014; first results," in *Proc. 6th Eur. Conf. on Antennas and Propagation (EUCAP)*, 2012, pp. 1174–1177.
[16] S. S. Mentes and Z. Kaymaz, "Investigation of surface duct conditions over Istanbul, Turkey," *J. Appl. Meteorol. Climat.*, vol. 46, 2006.
[17] M. I. Skolnik, *Introduction to Radar Systems*, 3rd ed. New York, NY, USA: McGraw-Hill, 2001.
[18] ITU-R Recommendation PN.310-9: Definitions of terms relating to propagation in non-ionized media, International Telecommunication Union, ITU, 1994.
[19] A. T. Adediji, M. O. Ajewole, and S. E. Falodun, "Distribution of radio refractivity gradient and effective earth radius factor (k-factor) over Akure, South Western Nigeria original research article," *J. Atmos. Solar-Terrest. Phys.*, vol. 73, pp. 2300–2304, Oct. 2011.

Appendix B:

Datasheet of Vaisala Radiosonde RS92-SGP

VAISALA www.vaisala.com

Vaisala Radiosonde RS92-SGP

Benefits

- World's highest level of PTU measurement performance
- Code correlating GPS technology for continuous wind data availability
- Stable transmission complies with ETSI standard EN 302 054

Proven PTU measurement performance

The all-digital Vaisala Radiosonde RS92-SGP offers the world's highest level of PTU measurement performance: the sum of the excellent individual performance of the Vaisala pressure, temperature and humidity sensors employed.

Code correlating GPS

The Vaisala Radiosonde RS92-SGP has a reliable code correlating GPS receiver. This receiver has a very fast search engine which ensures that all satellites in view are tracked. The GPS signal filtering and amplifying produce an excellent signal-to-noise ratio: the RS92-SGP is largely immune to radar or other sources of RF interference. If a malfunction occurs, an independent watchdog function instantly resets the radiosonde to minimize the tracking gap. The result: you receive continuous wind data with high resolution – from radiosonde release to bursting height.

Fully digital data transmission

The Vaisala Radiosonde RS92-SGP's fully digital data transmission offers important advantages over analog data transmission. Data availability during a sounding is excellent and telemetry errors are always detected. The digital transmitter also consumes less power than an analog transmitter and more channels are available in the meteorological frequency band.

Complies with ETSI standard for 400 MHz band

The RS92-SGP is fully compliant with the European ETSI standard for digital radiosondes operating in the 400 MHz band, EN 302 054. This standard aims to regulate usage of the 400 MHz meteorological band in order to universally improve meteorological data availability.

Vaisala ground check set GC25

Ground checking of the Vaisala Radiosonde RS92-SGP is done with the Vaisala Ground Check Set GC25 and the sounding system. The sounding system reads the calibration coefficient automatically via a telemetry link. The GC25 is used to recondition the humidity sensor, removing any chemical contaminants and ensuring excellent humidity measurement accuracy. Setting the transmitter frequency is a simple matter of scrolling in the display to the correct frequency.

CAL-4 calibrated

The RS92-SGP's PTU sensors are calibrated in the CAL-4 calibration machine. Designed by Vaisala and built in-house, CAL-4 is the world's most advanced calibration machine for the mass production of PTU sensors.

Technical data

Meteorological sensors

TEMPERATURE SENSOR	TYPE: CAPACITIVE WIRE
Measurement range	+60 °C to -90 °C
Response time (63.2%, 6 m/s flow)	
1000 hPa	< 0.4 s
100 hPa	< 1 s
10 hPa	< 2.5 s
Resolution	0.1 °C
Accuracy	
Total uncertainty in sounding*	0.5 °C
Repeatability in calibration**	0.15 °C
Reproducibility in sounding***	
1080 - 100 hPa	0.2 °C
100 - 20 hPa	0.3 °C
20 - 3 hPa	0.5 °C

HUMIDITY SENSOR	TYPE: THIN-FILM CAPACITOR, HEATED TWIN SENSOR
Measurement range	0 to 100 %RH
Resolution	1 %RH
Response time	
6 m/s, 1000 hPa, +20 °C	< 0.5 s
6 m/s, 1000 hPa, -40 °C	< 20 s
Accuracy	
Total uncertainty in sounding*	5 %RH
Repeatability in calibration**	2 %RH
Reproducibility in sounding***	2 %RH

PRESSURE SENSOR	TYPE: SILICON
Measurement range	1080 hPa to 3 hPa
Resolution	0.1 hPa
Accuracy	
Total uncertainty in sounding*	
1080 - 100 hPa	1 hPa
100 - 3 hPa	0.6 hPa
Repeatability in calibration**	
1080 - 100 hPa	0.4 hPa
100 - 3 hPa	0.3 hPa
Reproducibility in sounding***	
1080 - 100 hPa	0.5 hPa
100 - 3 hPa	0.3 hPa

Dimensions and Weight

Dimensions	220 x 80 x 75 mm
Weight with lithium battery (RS92-SGPL)	Typically 160 g [1]
Weight with alkaline (dry-cell) batteries (RS92-SGPD, RS92-SGPA)	Typically 280 - 290 g [1]

[1] Weight does not include rigging, unwinder, parachute etc.

Battery

Order codes with different battery types	
RS92-SGPD	alkaline (dry-cell), 9 V nominal
RS92-SGPL	lithium, 9V nominal
RS92-SGPA	dry-cell for AUTOSONDE, 9 V nominal
Operating time	135 min

Telemetry

Transmitter type	Synthesized
Frequency band	403 MHz
Tuning range	400 - 406 MHz
Frequency stability, 90 % probability	± 2 kHz
Deviation, peak-to-peak	4.8 kHz
Emission bandwidth	According to EN 302 054
Output power (high-power mode)	60 mW min
Modulation	GFSK
Data downlink	2400 bit/s, digital
Measurement cycle	1 s

Code correlating GPS receiver (SA Off, PDOP<4)

Number of channels	12
Positioning uncertainty, horizontal	10 m
Positioning uncertainty, vertical	20 m
Velocity measurement uncertainty***	0.15 m/s
Directional measurement uncertainty****	2 degrees

* 2-sigma (k=2) confidence level (95.5 %), cumulative uncertainty including:
- Repeatability
- Long-term stability
- Effects due to measurement conditions
- Dynamic effect (such as response time)
- Effects due to measurement electronics

For humidity T > -60 °C
For pressure T < 35 °C

** Standard deviation of differences between two successive repeated calibrations, k=2 confidence level

*** Standard deviation of differences in twin soundings

**** Standard deviation of differences in twin soundings, wind speed above 3 m/s

Note: The pressure, temperature and humidity performance specifications given above are valid only when the Vaisala Ground Check Set GC25 is used to perform the ground check, including reconditioning of the humidity sensor.

Note: Selective Availability (SA) was switched off 1st May, 2000. Position Dilution of Precision (PDOP) describes the effect of current GPS satellite geometry on radiosonde wind-finding accuracy.

VAISALA

For more information, visit www.vaisala.com or contact us at sales@vaisala.com

Appendix C:

Weather Symbols (00-99)

Weather symbols (00-49) [80]:

00	01	02	03	04	05	06	07	08	09
									
Cloud development NOT observed or NOT observable during past hour (not plotted)	Clouds generally dissolving or becoming less developed during past hour (not plotted)	State of sky on the whole unchanged during past hour (not plotted)	Clouds generally forming or developing during past hour (not plotted)	Visibility reduced by smoke	Haze	Widespread dust in suspension in the air, not raised by wind at or near the station at the time of observation	Dust or sand raised by the wind at or near the station at the time of the observation, but no well-developed dust whirl(s), and no sandstorm seen: or, in the case of ships, blowing spray at the station	Well developed dust whirl(s) or sand whirl(s) seen at or near the station during the preceding hour or at the time of observation, but no dust storm or sandstorm	Dust storm or sandstorm within sight at the time of observation, or at the station during the preceding hour

10	11	12	13	14	15	16	17	18	19
									
Mist	Patches of shallow fog at station, NOT deeper than 6 feet on land	More or less continuous shallow fog at station, NOT deeper than 6 feet on land	Lighting visible, no thunder heard	Precipitation within sight, but NOT reaching the ground	Precipitation within sight, reaching ground or the surface of the sea, but distant, i.e. estimated to be more than 3 miles from the station	Precipitation within sight, reaching the ground or the surface of the sea, near to (within 3 miles), but not at the station	Thunder heard, but no precipitation at the station	Squall(s) within sight during past hour	Funnel cloud(s) / Tornado(s) during the preceding hour or at time of observation

20	21	22	23	24	25	26	27	28	29
									
Drizzle (not freezing) or snow grains not falling as shower(s) ended in the past hour	Rain (not freezing) not falling as shower(s) ended in the past hour	Snow not falling as shower(s) ended in the past hour	Rain and snow or ice pellets not falling as shower(s) ended in the past hour	Freezing drizzle or freezing rain not falling as shower(s) ended in the past hour	Shower(s) of rain ended in the past hour	Shower(s) of snow, or of rain and snow ended in the past hour	Shower(s) of hail, or of rain and hail ended in the past hour	Fog or ice fog ended in the past hour	Thunderstorm (with or without precipitation) ended in the past hour

30	31	32	33	34	35	36	37	38	39
									
Slight or moderate dust storm or sandstorm (has decreased during the preceding hour)	Slight or moderate dust storm or sandstorm (no appreciable change during the preceding hour)	Slight or moderate dust storm or sandstorm (has begun or increased during the preceding hour)	Severe dust storm or sandstorm has decreased during the preceding hour	Severe dust storm or sandstorm has no appreciable change during the preceding hour	Severe dust storm or sandstorm has begun or increased during the preceding hour	Slight or moderate drifting snow (generally below eye level)	Heavy drifting snow (generally below eye level)	Slight or moderate blowing snow (generally above eye level)	Heavy blowing snow (generally above eye level)

40	41	42	43	44	45	46	47	48	49
									
Fog at a distance at the time of observation, but not at the station during the preceding hour, the fog or ice fog extending to a level above that of the observer	Fog in patches	Fog sky visible (has become thinner during preceding hour)	Fog sky obscured (has become thinner during preceding hour)	Fog sky visible (no appreciable change during the preceding hour)	Fog sky obscured (no appreciable change during the preceding hour)	Fog sky visible (has begun or has become thicker during the preceding hour)	Fog sky obscured (has begun or has become thicker during the preceding hour)	Fog, depositing rime ice, sky visible	Fog, depositing rime ice, or ice fog, sky obscured

Weather symbols (50-99) [80]:

50	51	52	53	54	55	56	57	58	59
									
Drizzle, not freezing, intermittent (slight at time of observation)	Drizzle, not freezing, continuous (slight at time of observation)	Drizzle, not freezing, intermittent (moderate at time of observation)	Drizzle, not freezing, continuous (moderate at time of observation)	Drizzle, not freezing, intermittent (heavy at time of observation)	Drizzle, not freezing, continuous (heavy at time of observation)	Drizzle, freezing, slight	Drizzle, freezing, moderate or heavy	Drizzle and rain, slight	Drizzle and rain, moderate or heavy

60	61	62	63	64	65	66	67	68	69
									
Rain, not freezing, intermittent (slight at time of observation)	Rain, not freezing, continuous (slight at time of observation)	Rain, not freezing, intermittent (moderate at time of observation)	Rain, not freezing, continuous (moderate at time of observation)	Rain, not freezing, intermittent (heavy at time of observation)	Rain, not freezing, continuous (heavy at time of observation)	Rain, freezing, slight	Rain, freezing, moderate or heavy	Rain or drizzle and snow, slight	Rain or drizzle and snow, moderate or heavy

70	71	72	73	74	75	76	77	78	79
									
Intermittent fall of snowflakes (slight at time of observation)	Continuous fall of snowflakes (slight at time of observation)	Intermittent fall of snowflakes (moderate at time of observation)	Continuous fall of snowflakes (moderate at time of observation)	Intermittent fall of snowflakes (heavy at time of observation)	Continuous fall of snowflakes (heavy at time of observation)	Ice needles (with or without fog)	Snow grains (with or without fog)	Isolated star-like snow crystals (with or without fog)	Ice pellets (sleet)

80	81	82	83	84	85	86	87	88	89
									
Rain shower(s), slight	Rain shower(s), moderate or heavy	Rain shower(s), violent	Shower(s) of rain and snow mixed, slight	Shower(s) of rain and snow mixed, moderate or heavy	Snow shower(s), slight	Snow shower(s), moderate or heavy	Shower(s) of snow pellets or small hail, slight with or without rain or rain and snow mixed	Shower(s) of snow pellets or small hail, moderate or heavy with or without rain or rain and snow mixed	Shower(s) of hail, with or without rain or rain and snow mixed, not associated with thunder, slight

90	91	92	93	94	95	96	97	98	99
									
Shower(s) of hail, with or without rain or rain and snow mixed, not associated with thunder, moderate or heavy	Thunderstorm during the preceding hour but not at time of observation with slight rain at time of observation	Thunderstorm during the preceding hour but not at time of observation with moderate or heavy rain at time of observation	Thunderstorm during the preceding hour but not at time of observation with slight snow, or rain and snow mixed, or hail at time of observation	Thunderstorm during the preceding hour but not at time of observation with moderate or heavy snow, or rain and snow mixed, or hail at time of observation	Thunderstorm, slight or moderate, without hail but with rain and or snow at time of observation	Thunderstorm, slight or moderate, with hail at time of observation	Thunderstorm, heavy, without hail but with rain and or snow at time of observation	Thunderstorm combined with dust storm or sandstorm at time of observation	Thunderstorm, heavy, with hail at time of observation

Appendix D:

Step by Step Procedure for Processing Sounding Data using RAOB

1. Install the ROAB software and start the program.

The sounding raw data represented by codes, are imported to ROAB.

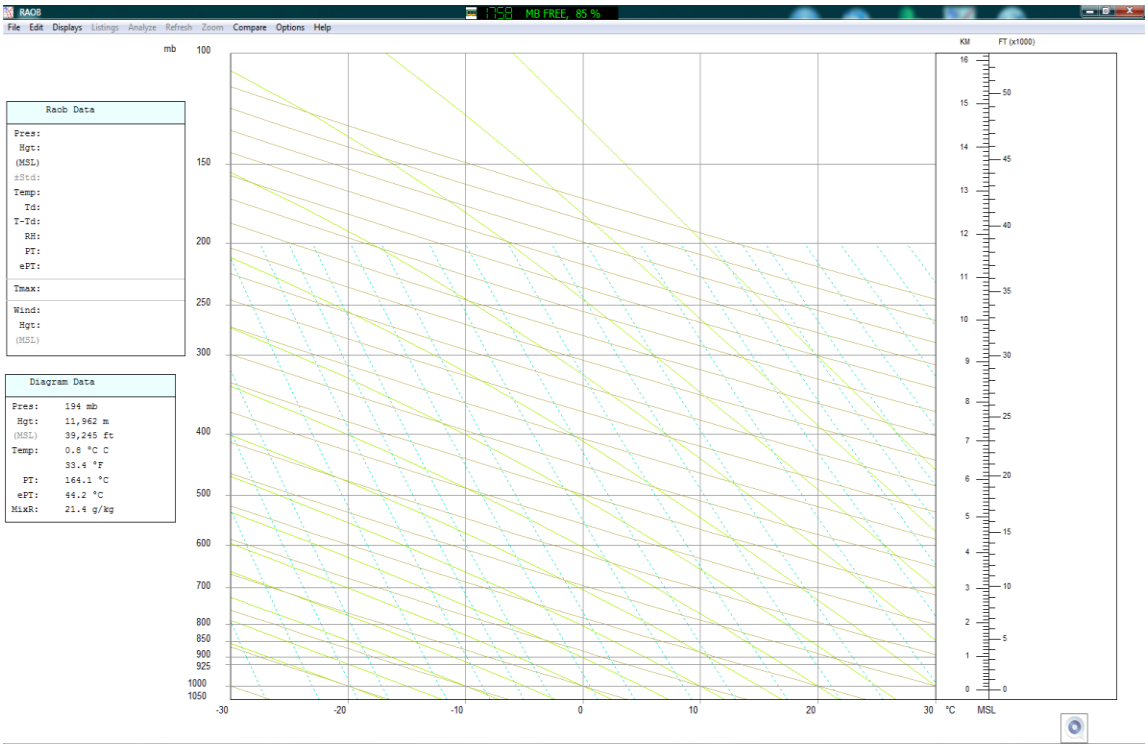

Step 1 – Start the RAOB Software

2. On the left most corner of the ROAB screen, go to File → Open Sounding

Select the raw text file that need to be processed and then click ‘Open’. If the sounding file has the data for a list of ascents, the user needs to select one at a time. The list for a month would ideally show from 56 to 62 sounding listings, 2 ascents/ day at 0:00 H and 12:00 H UT. Then the exact ascents need to be selected in order for further analysis.

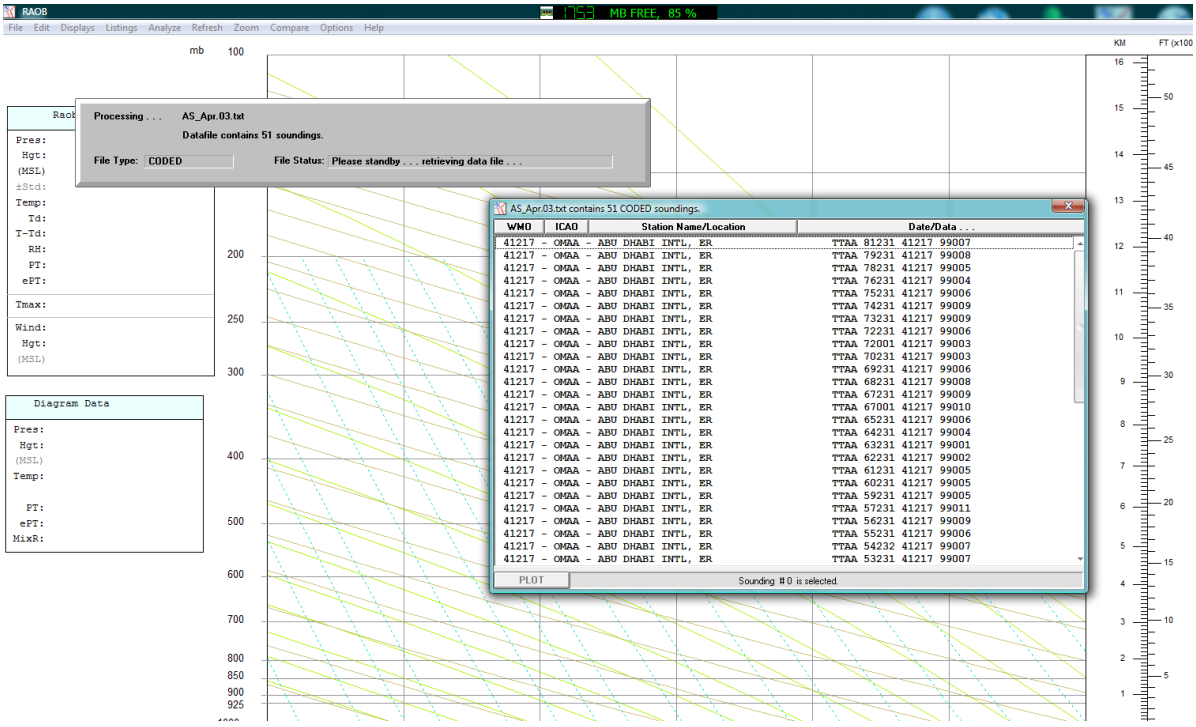

Step 2 – Open Radiosonde Sounding Files

3. Click on the observation curve to find the corresponding values. Analysis of the observations is displayed.

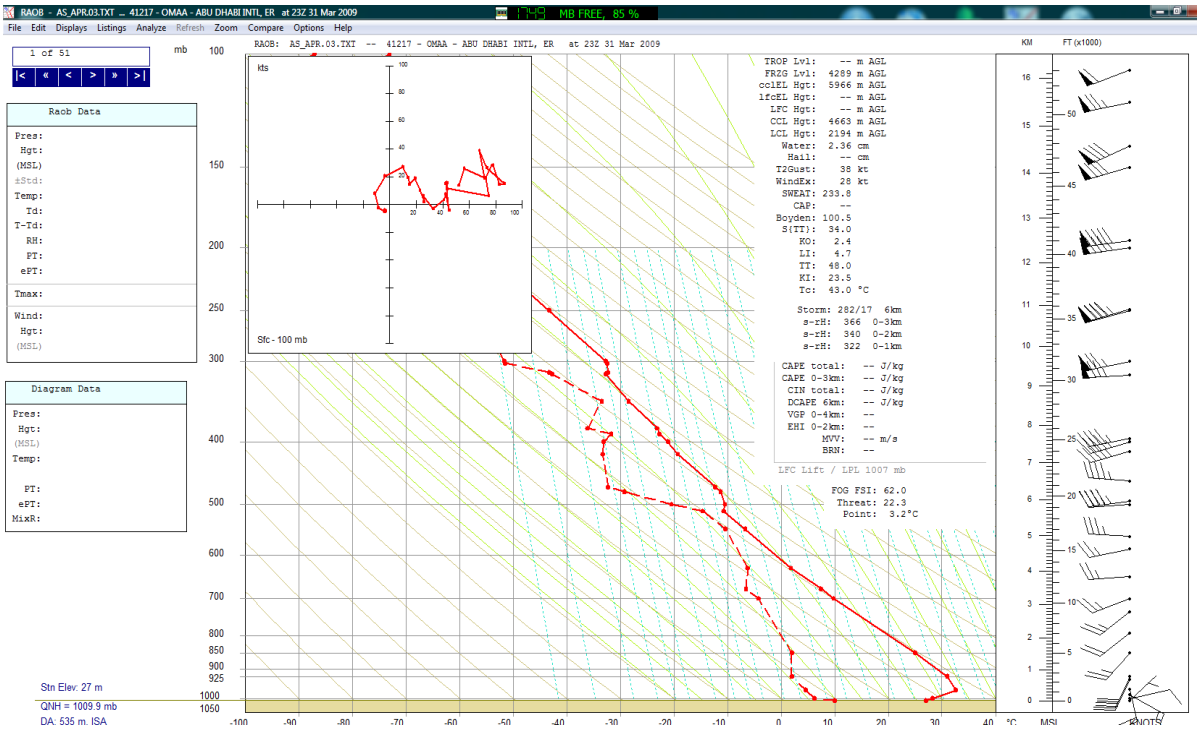

Step 3 - Review RAOB Analysis for Radiosonde Soundings' Observations

4. On the top menu bar, press the “listings” to generate another matrix obtained from the coded sounding data. Then press on the “Interval Listing” tab to set the required height interval of the meteorological data.

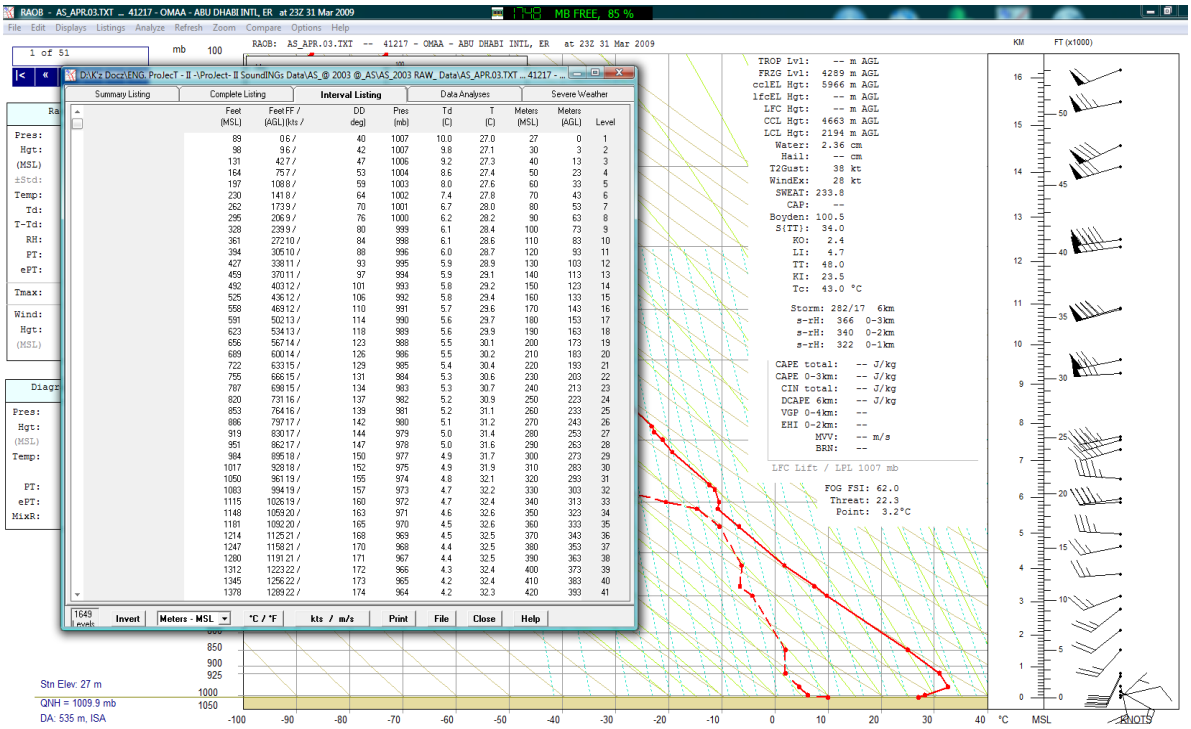

Step 4 – Select Interval Listings

5. The height interval is set in meter or foot with respect to the ground or sea levels.

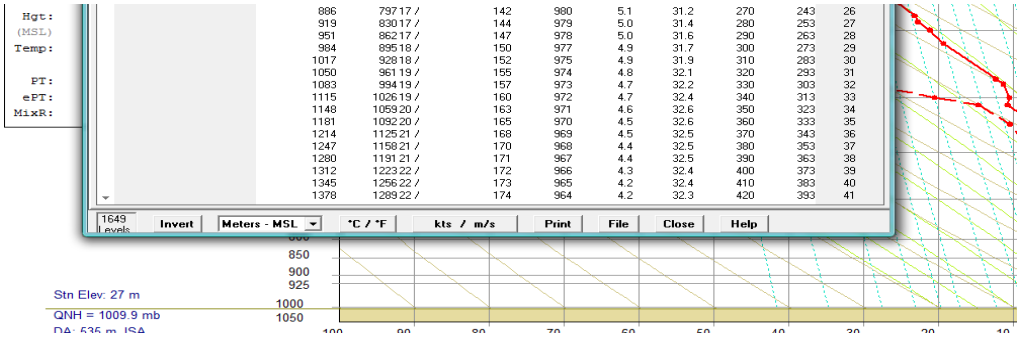

Step 5 - Height Interval Screen

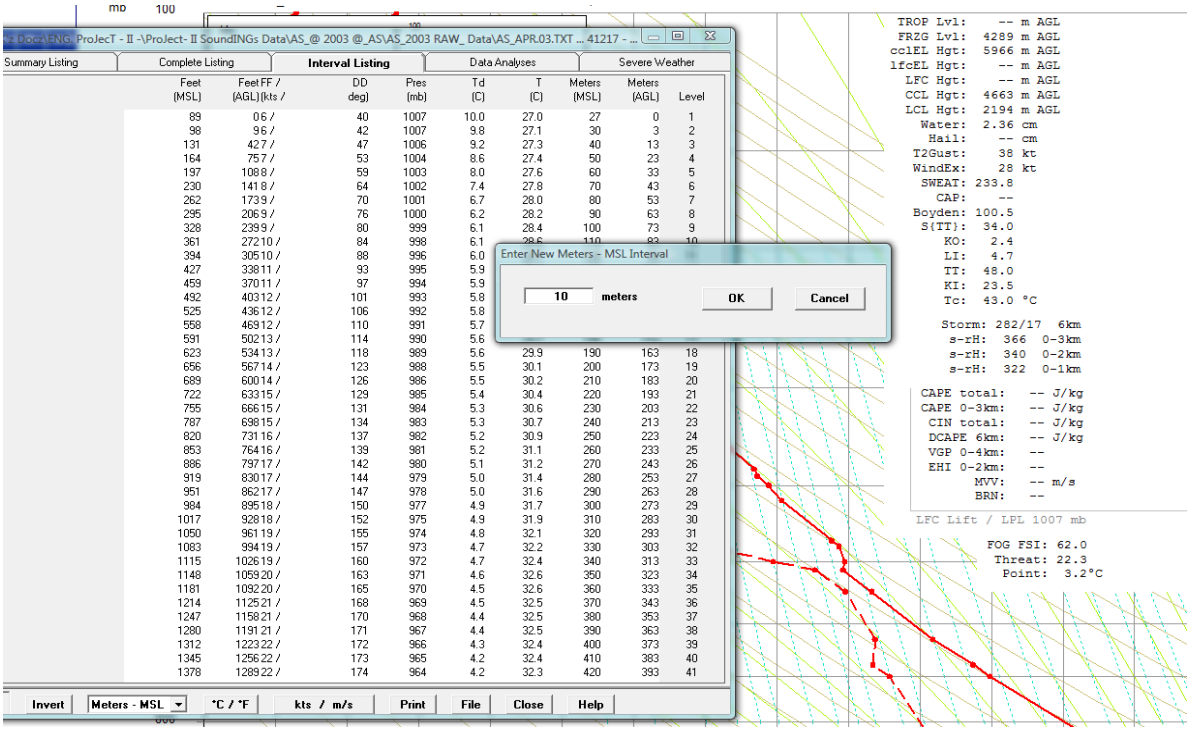

Step 5 – Define Height Interval

6. Finally, the processed meteorological data can be saved in text or notepad formats.

Appendix E:

Path Profiles and Link Budget Calculations of 12 Candidate MW Links

Link 1 path profile and link budget calculation

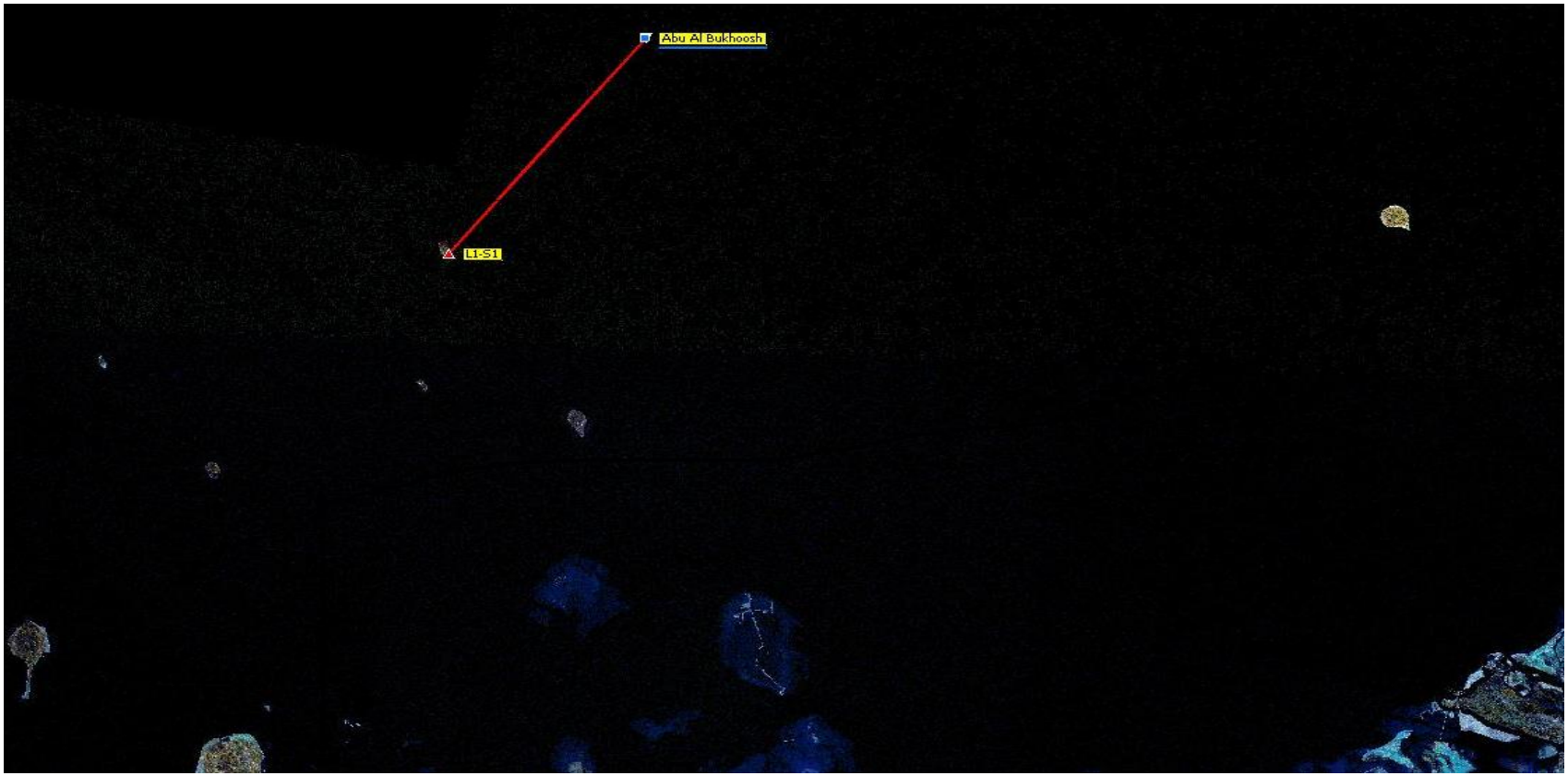

Link 1 location with surface weather station at Bukhoosh Island

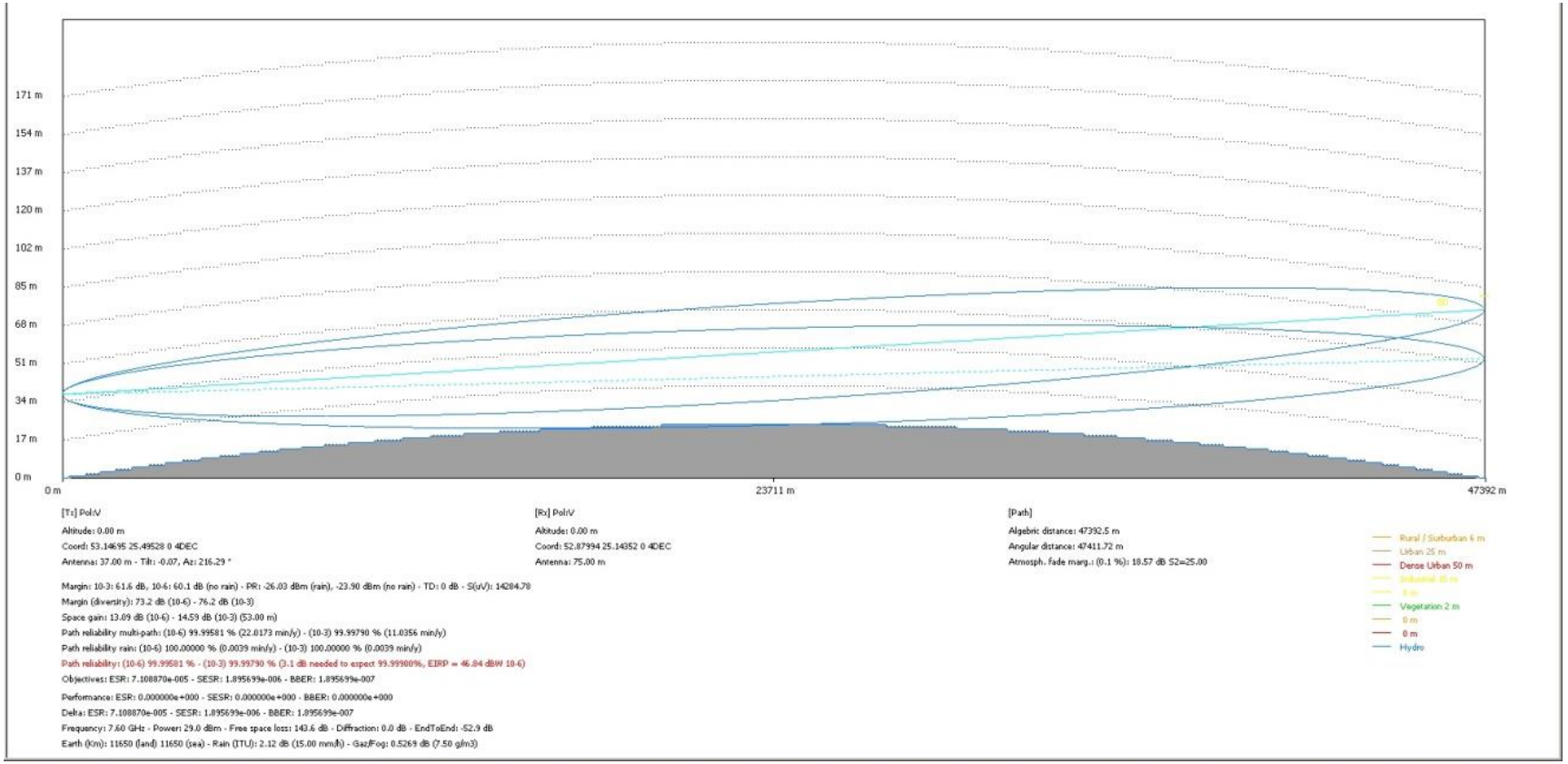

Link 1 Path Profile and Link Budget Calculation at S1 (from L1-S2 to L1-S1)

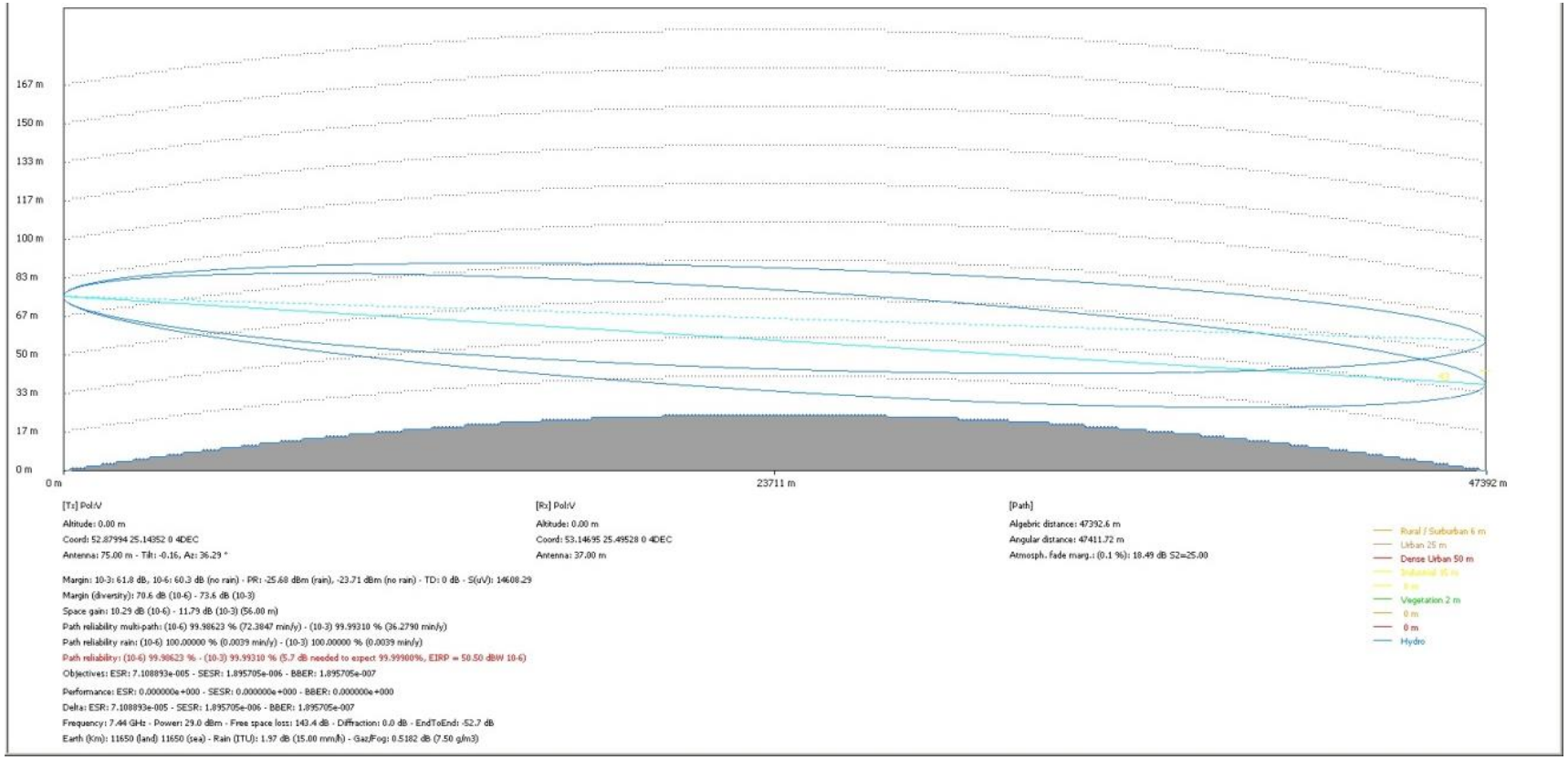

Link 1 Path Profile and Link Budget Calculation at S2 (from L1-S1 to L1-S2)

Link 2 path profile and link budget calculation

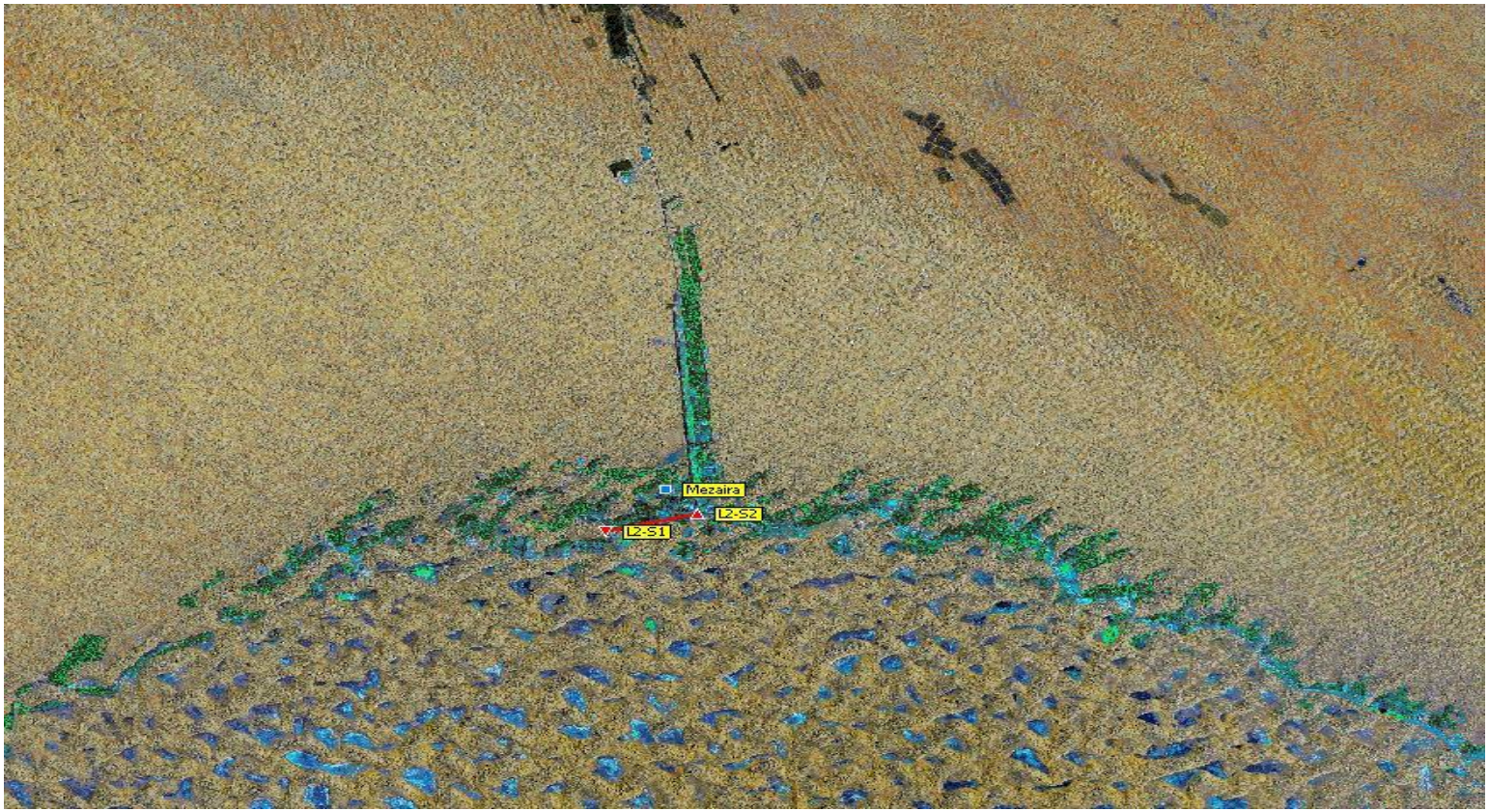

Link 2 location with nearby weather station

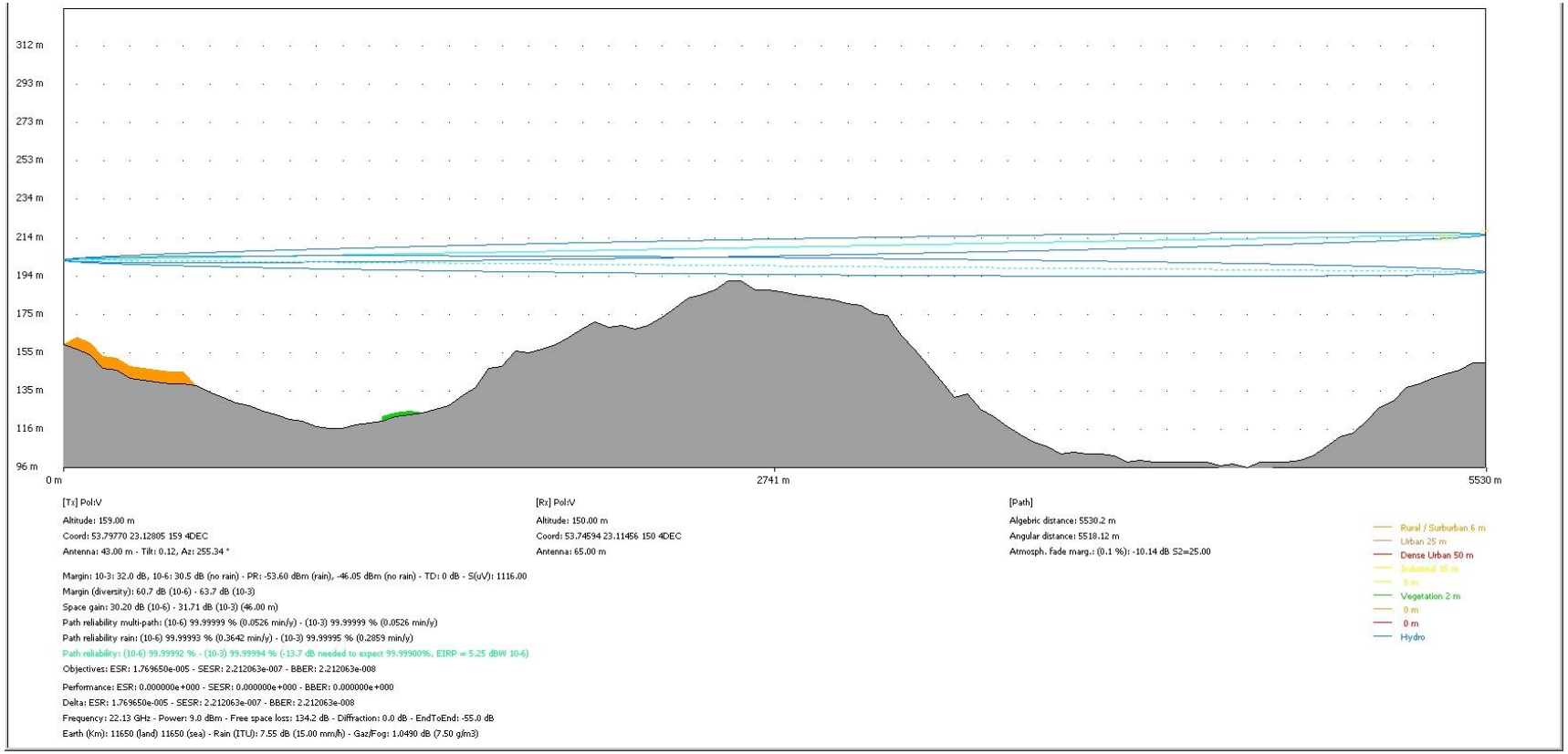

Link 2 Path Profile and Link Budget Calculation at S1 (from L2-S2 to L2-S1)

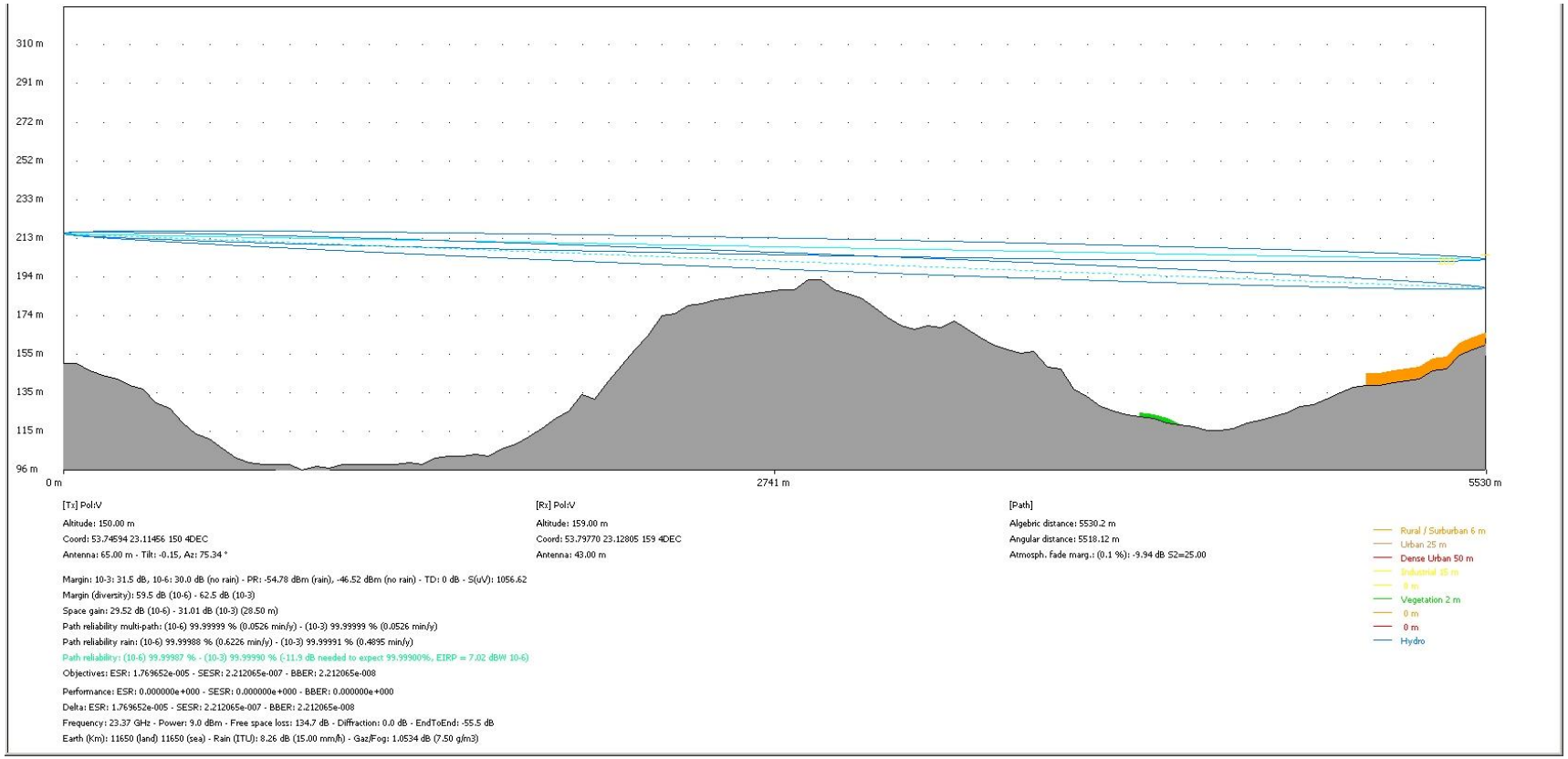

Link 2 Path Profile and Link Budget Calculation at S2 (from L2-S1 to L2-S2)

Link 3 Path Profile and Link Budget calculation

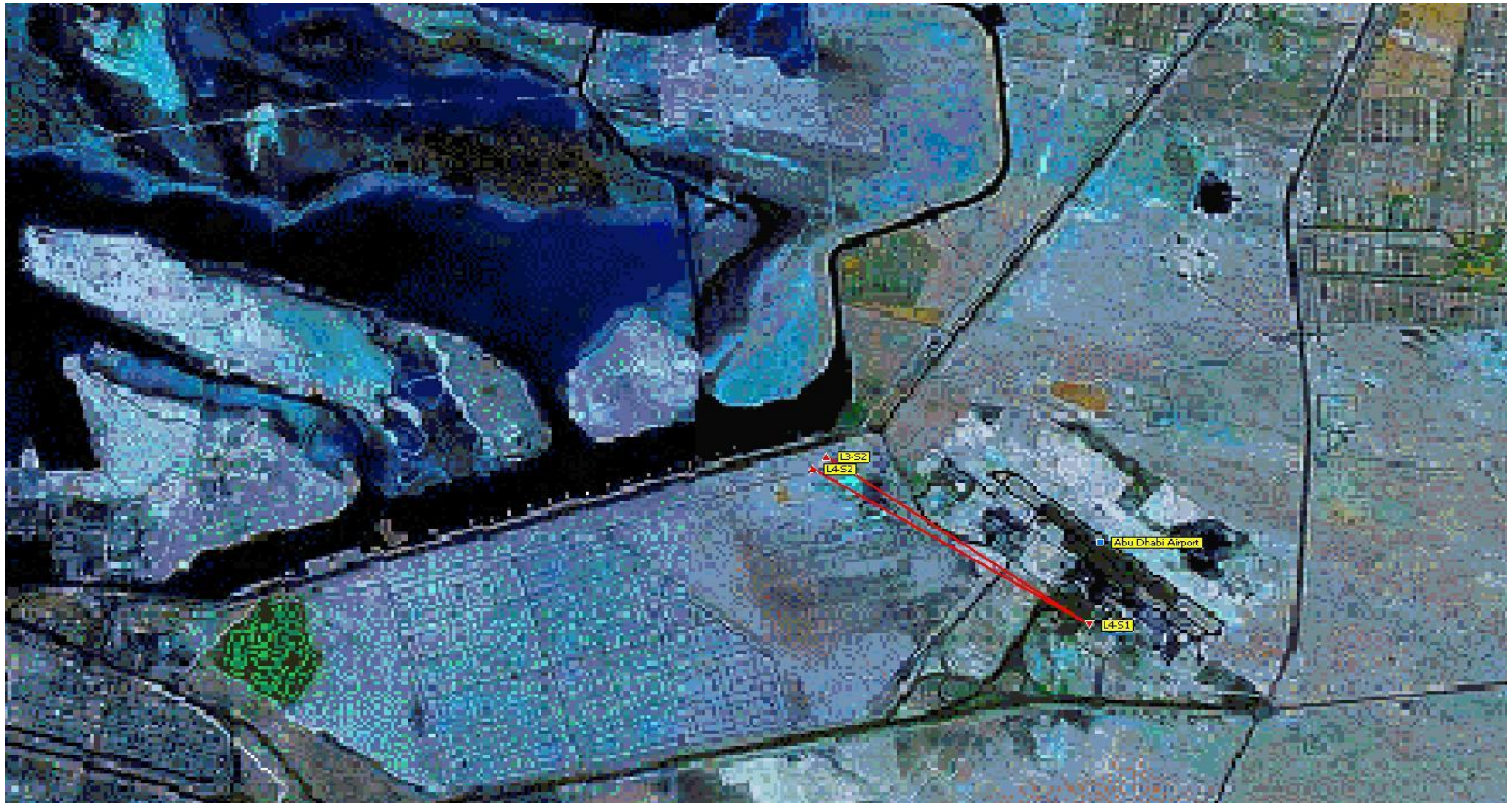

Locations of links 3 and 4 with nearby weather stations

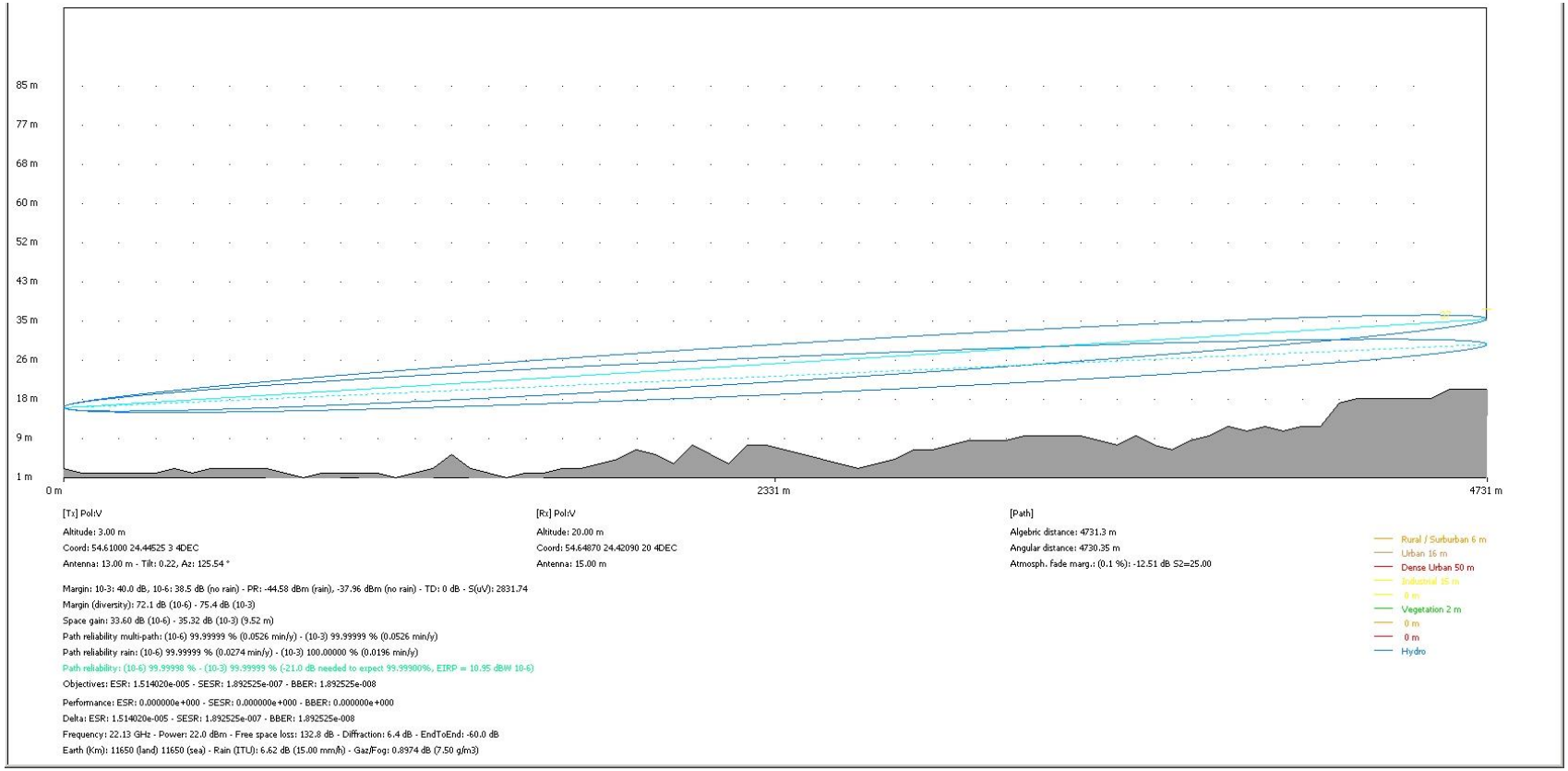

Link 3 Path Profile and Link Budget Calculation at S1 (from L3-S2 to L3-S1)

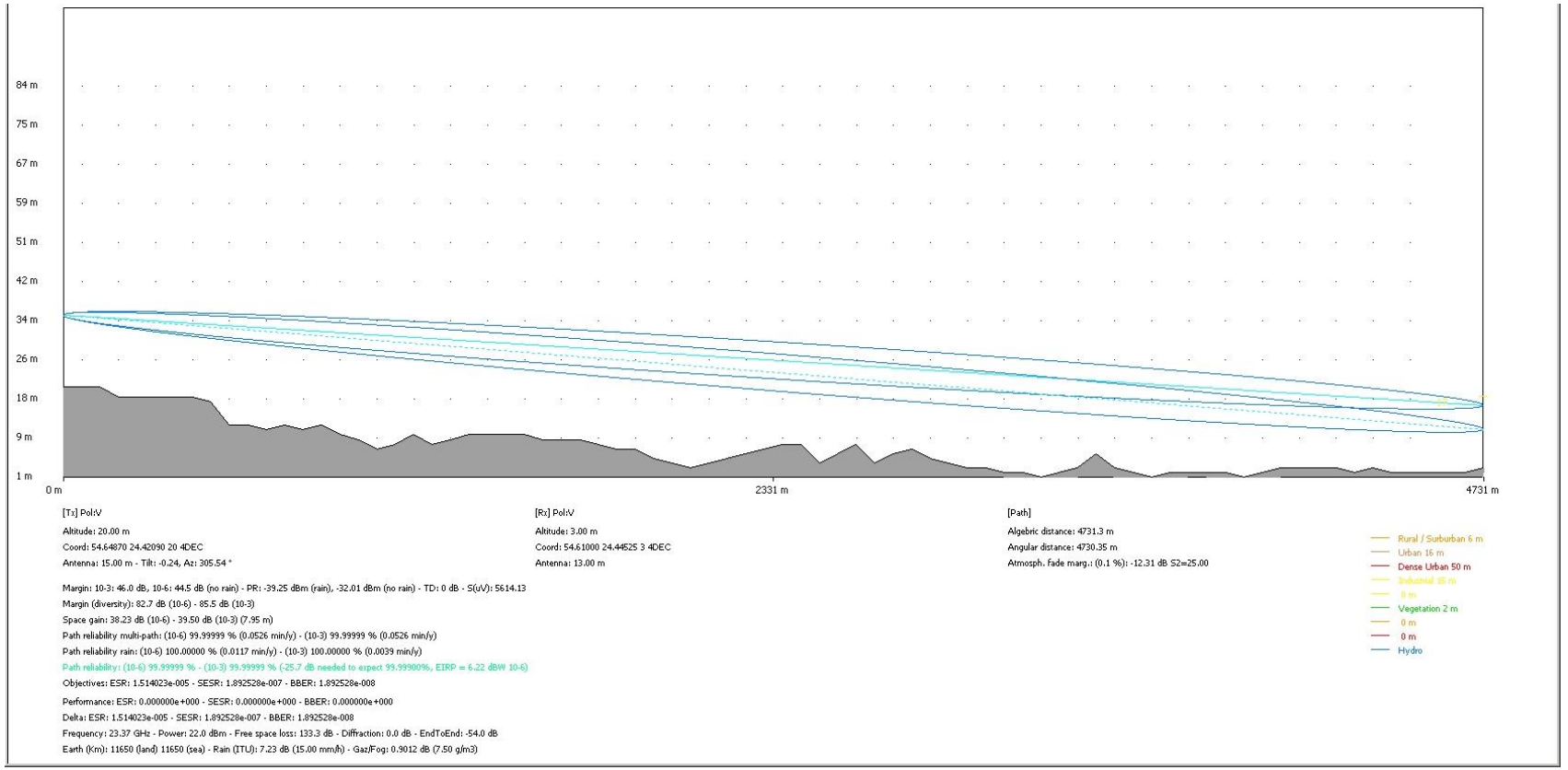

Link 3 Path Profile and Link Budget Calculation at S2 (from L3-S1 to L3-S2)

Link 4 Path Profile and Link Budget calculation

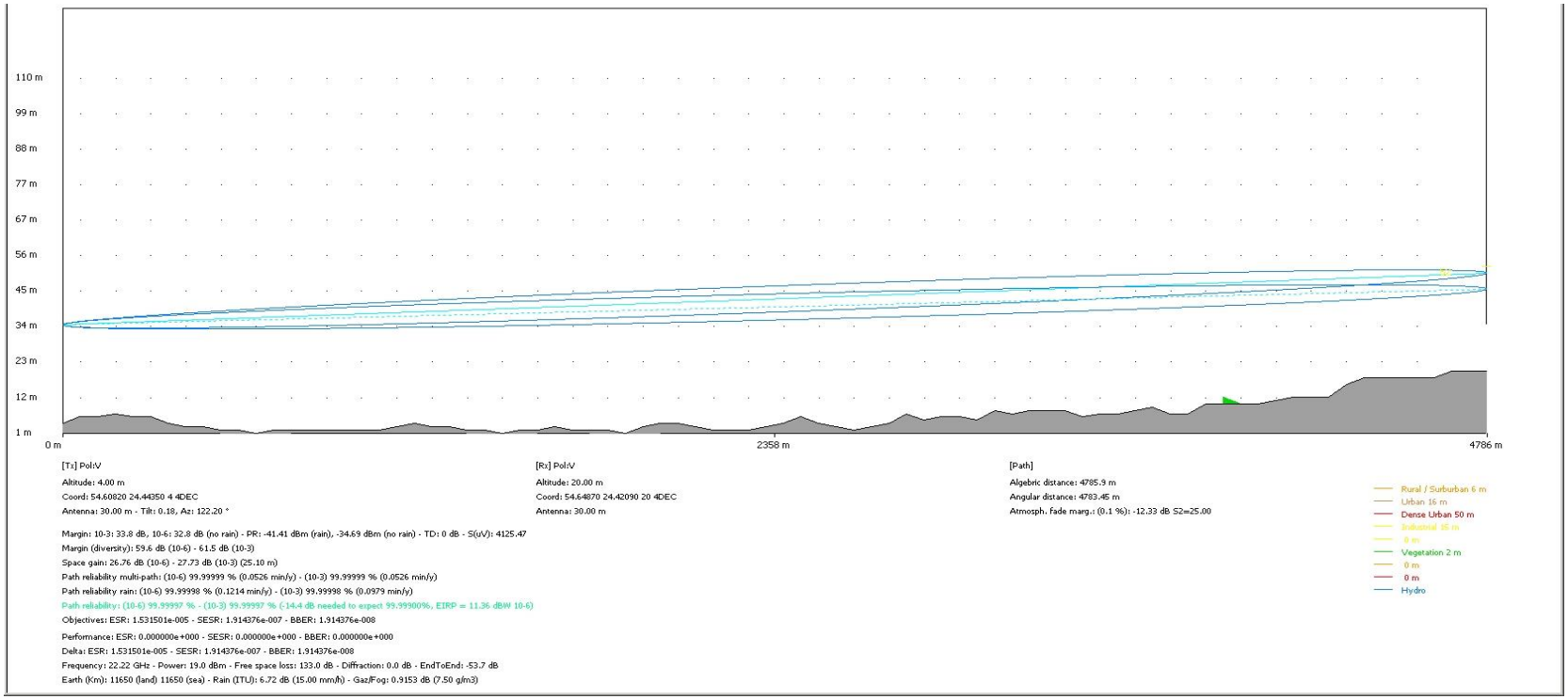

Link 4 Path Profile and Link Budget Calculation at S1 (from L4-S2 to L4-S1)

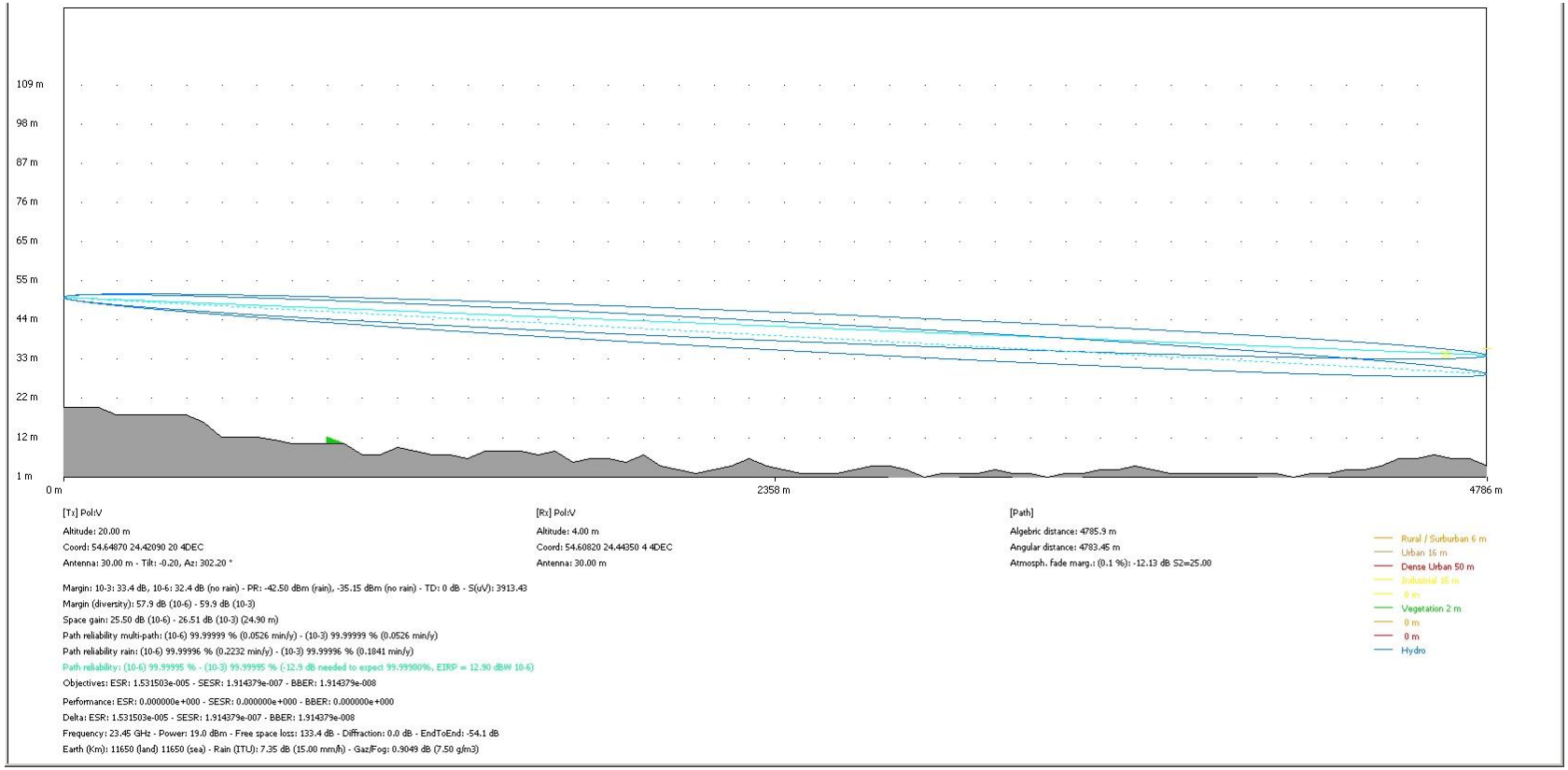

Link 4 Path Profile and Link Budget Calculation at S2 (from L4-S1 to L4-S2)

Link 5 Path Profile and Link Budget calculation

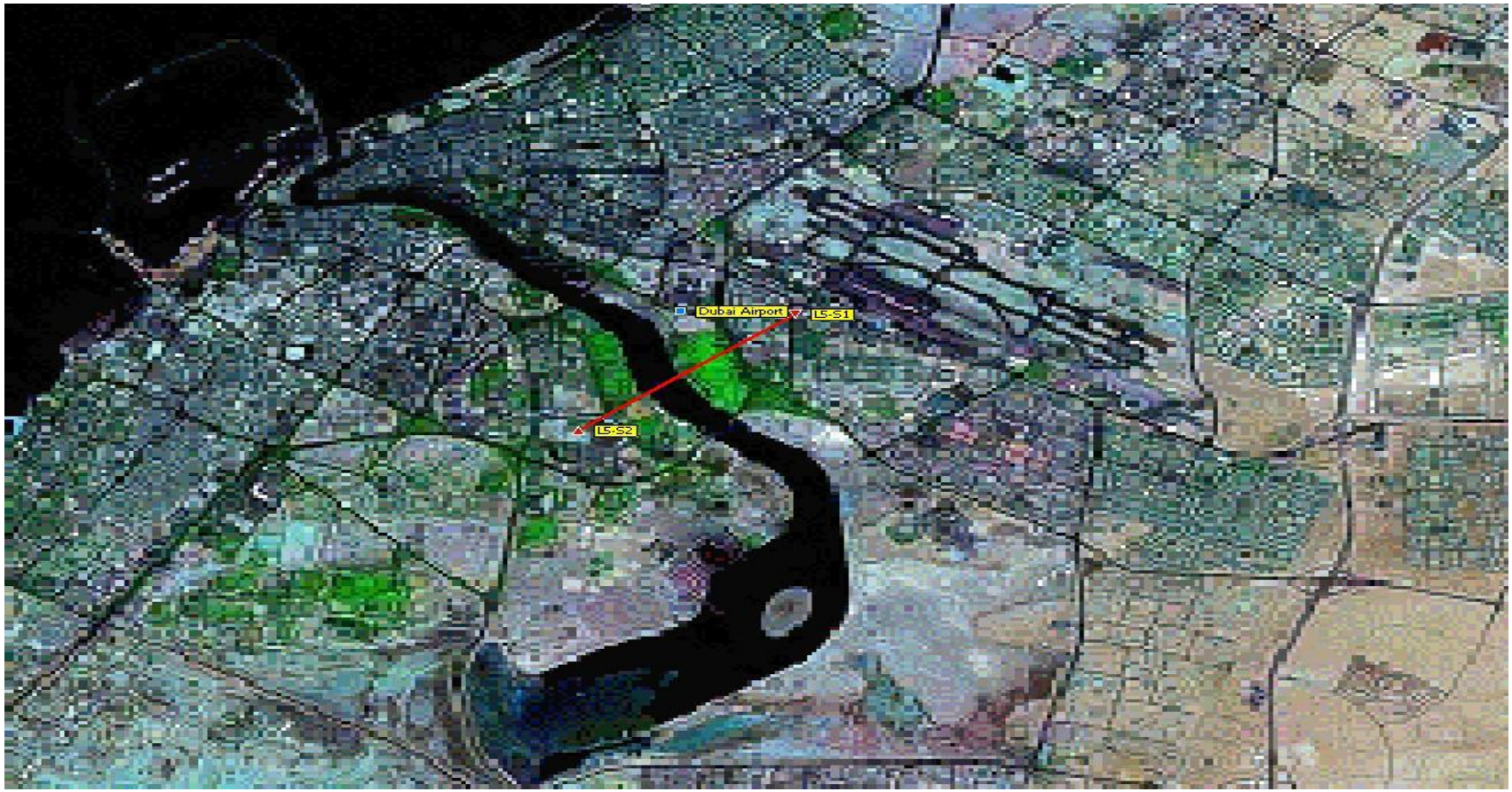

Location of link 5 with nearby weather station

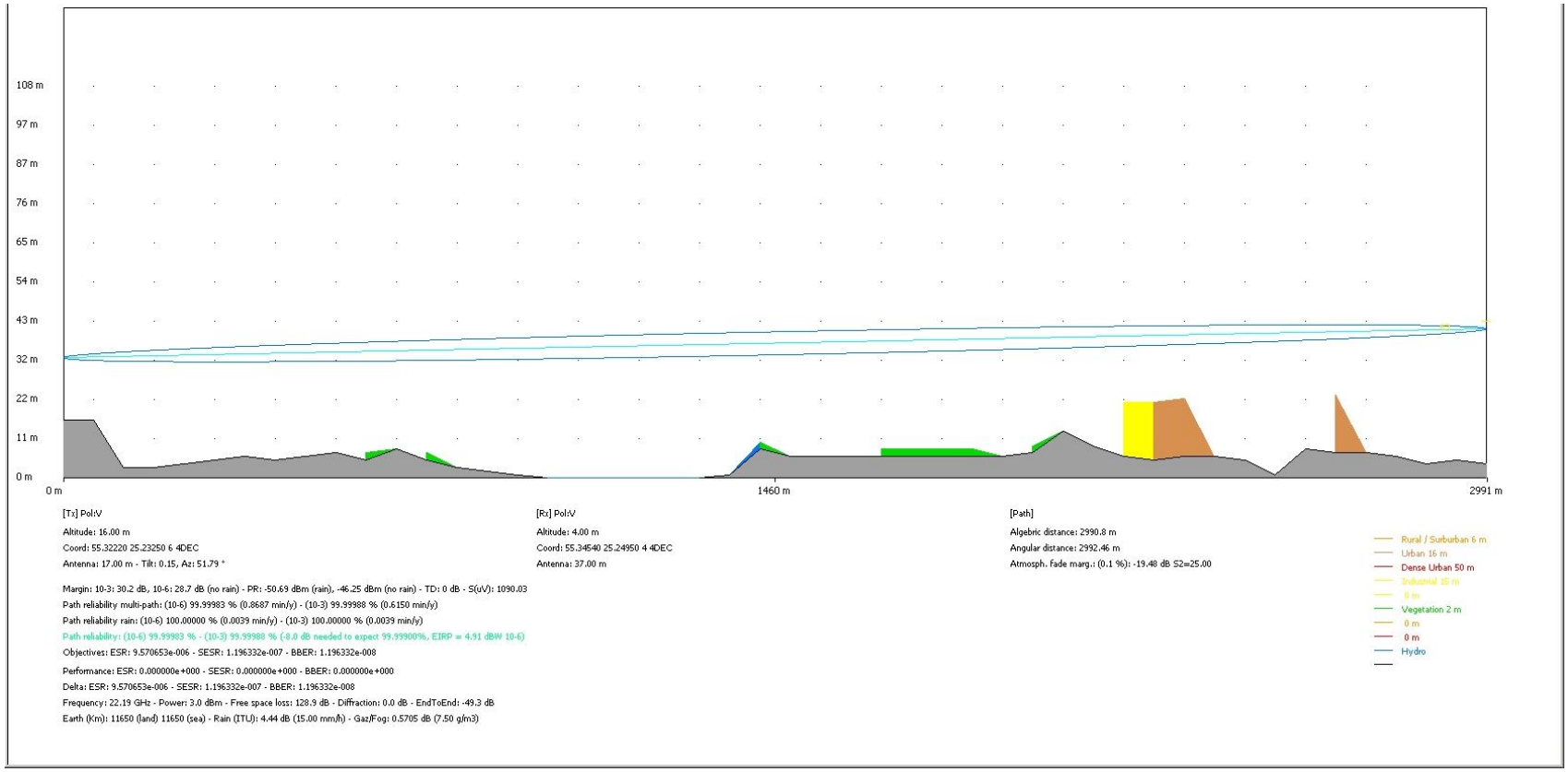

Link 5 Path Profile and Link Budget Calculation at S1 (from L5-S2 to L5-S1)

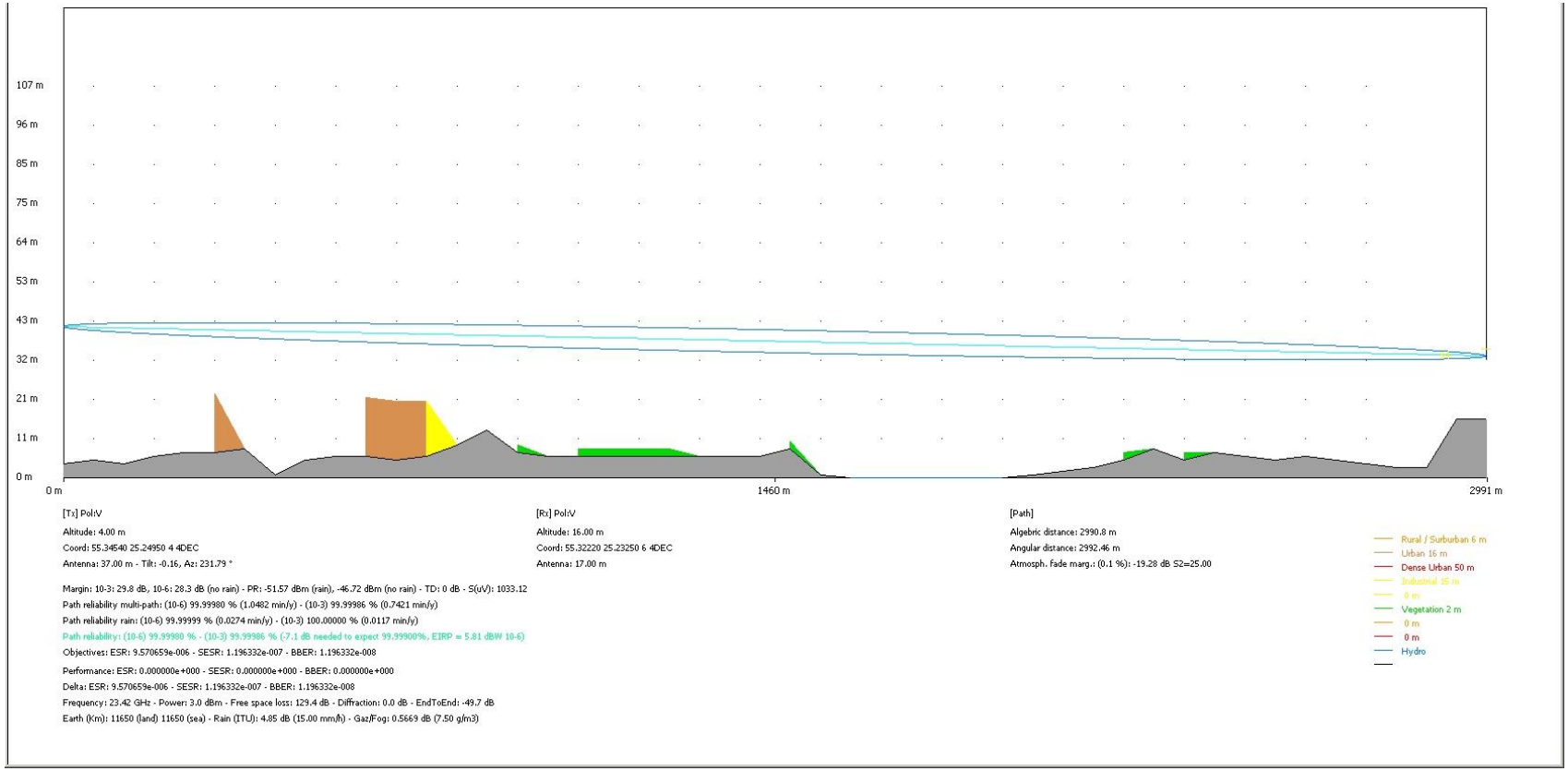

Link 5 Path Profile and Link Budget Calculation at S2 (from L5-S1 to L5-S2)

Link 6 Path Profile and Link Budget calculation

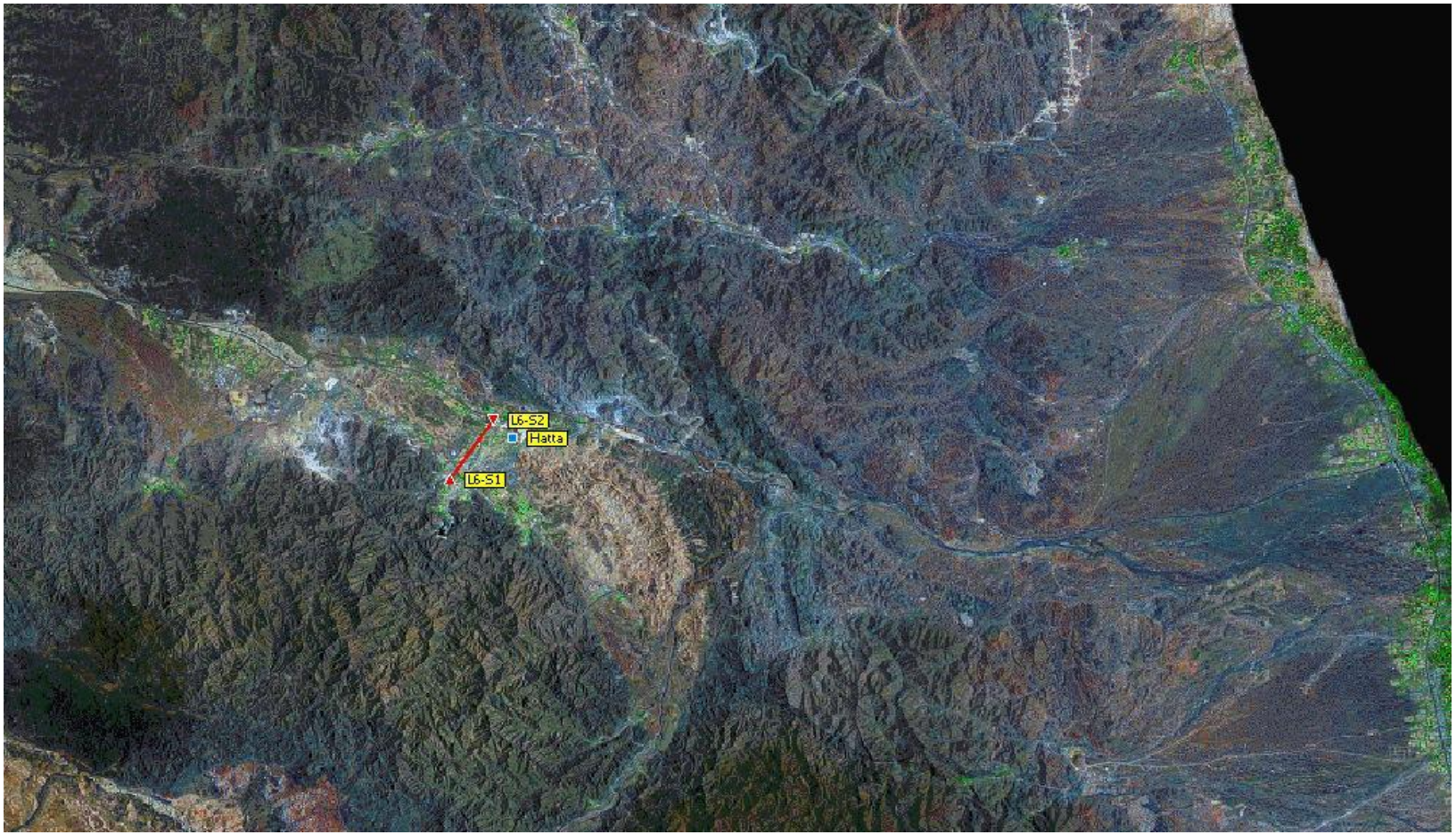

Location of link 6 with nearby weather station

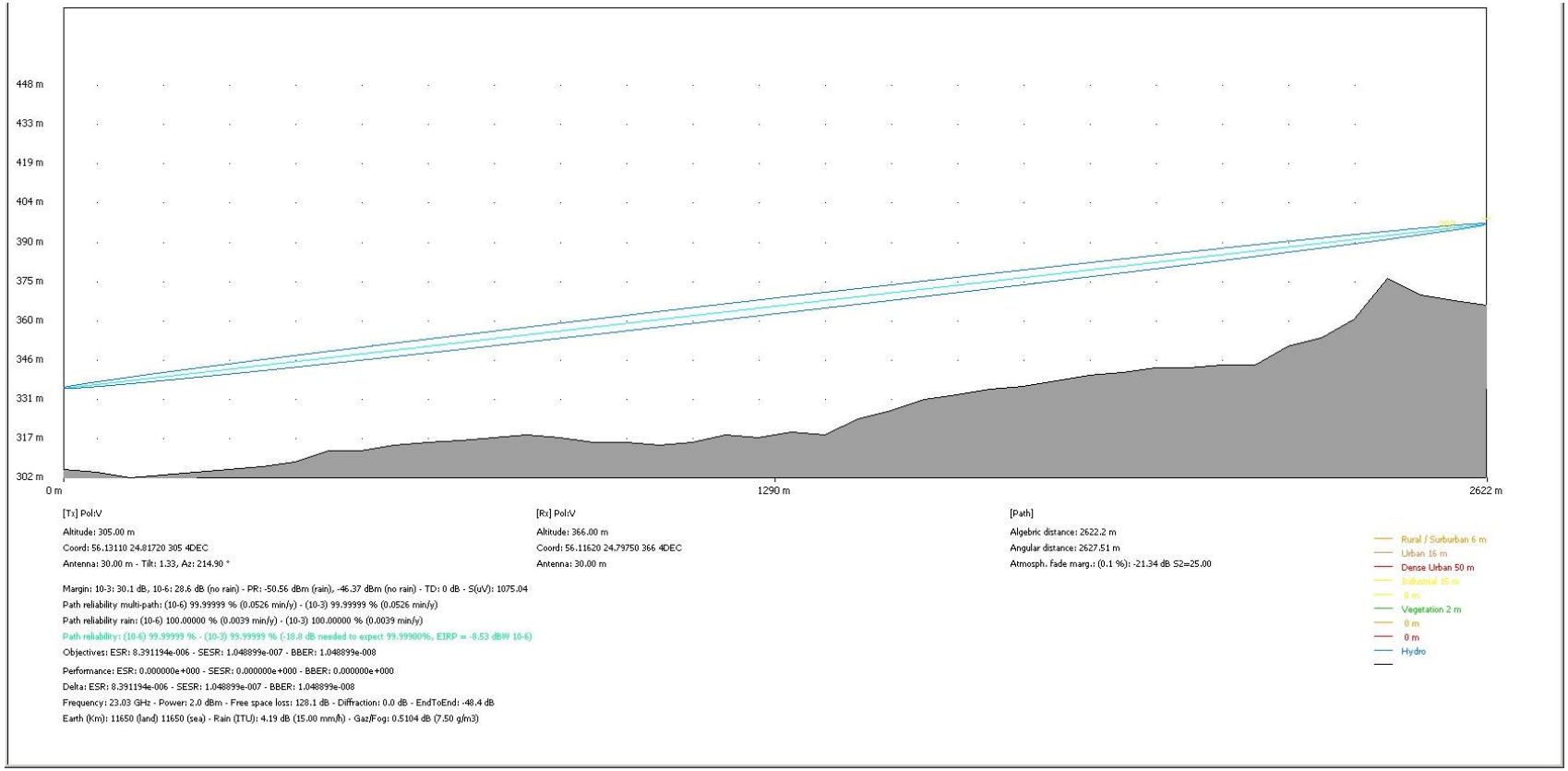

Link 6 Path Profile and Link Budget Calculation at S1 (from L6-S2 to L6-S1)

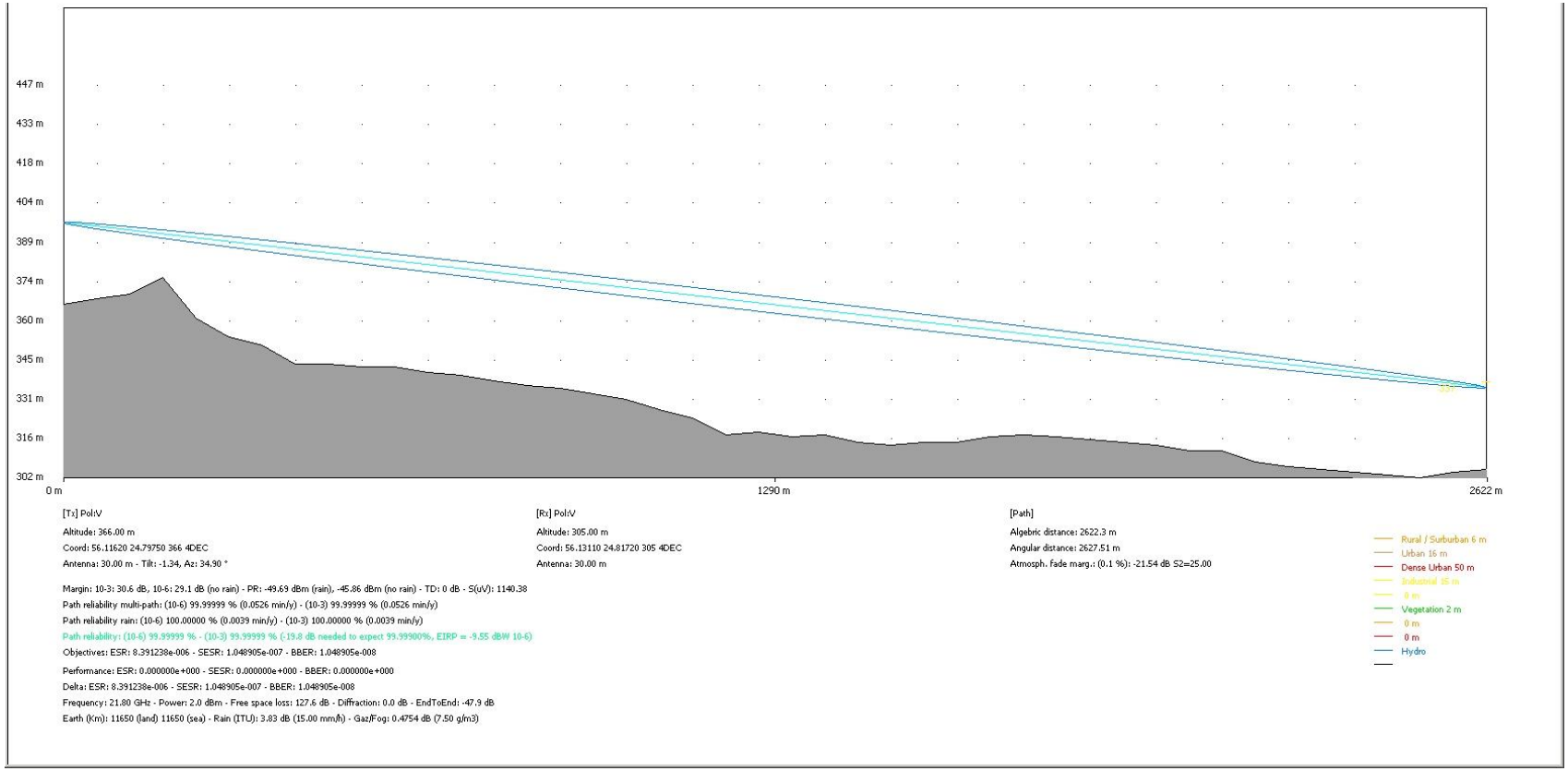

Link 6 Path Profile and Link Budget Calculation at S2 (from L6-S1 to L6-S2)

Link 7 Path Profile and Link Budget calculation

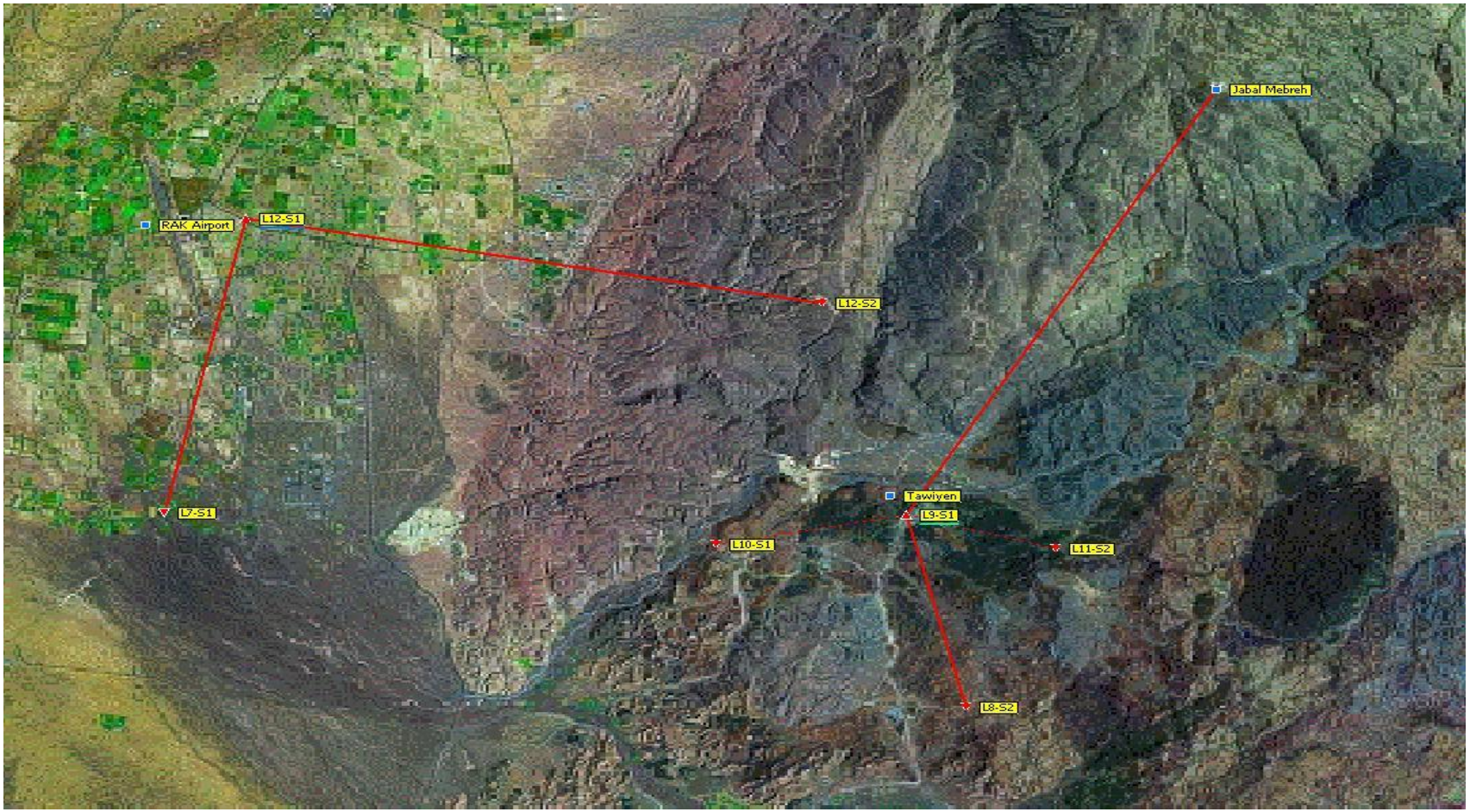

Locations of links 7 - 12 with nearby weather stations

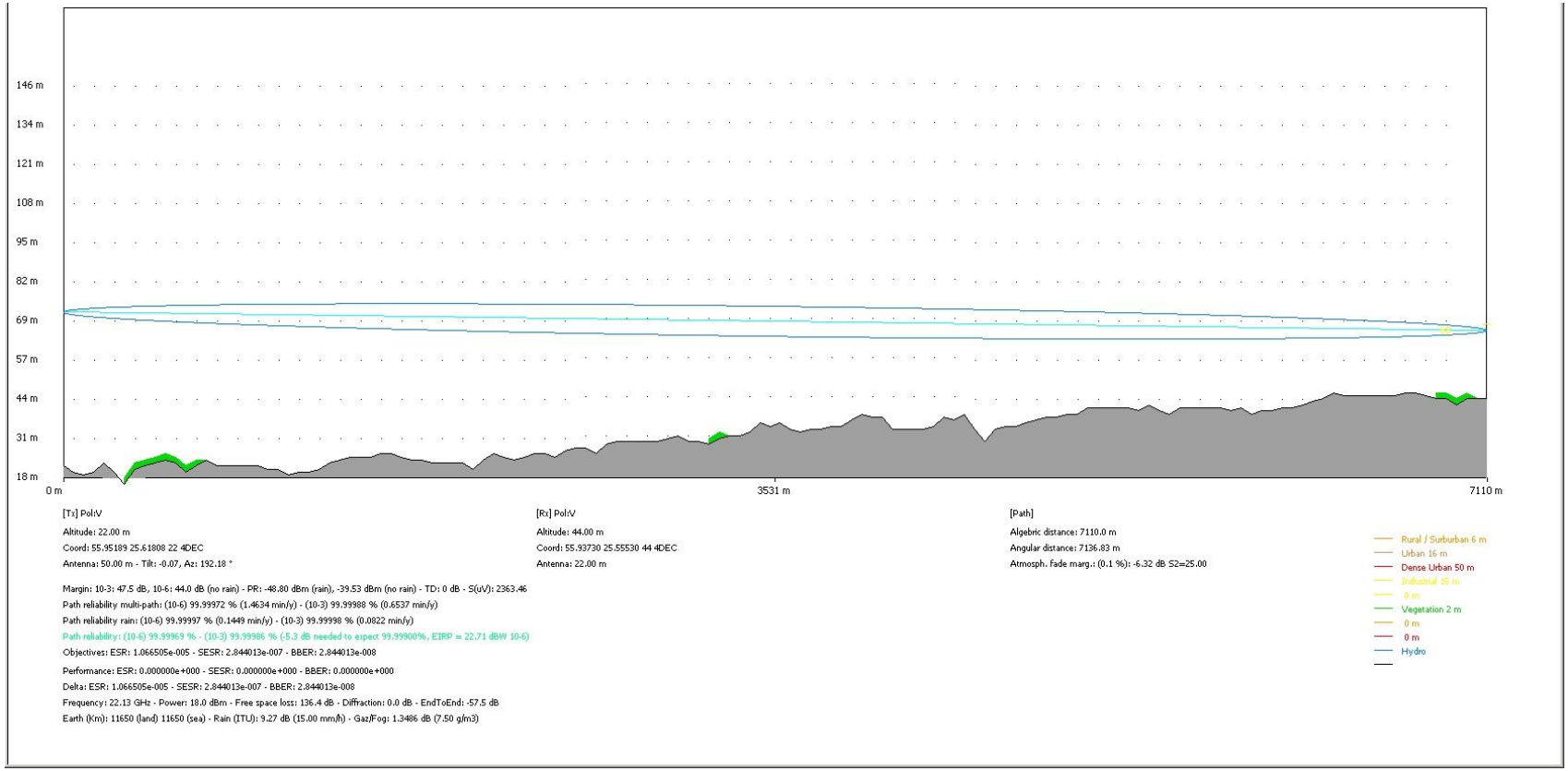

Link 7 Path Profile and Link Budget Calculation at S1 (from L7-S2 to L7-S1)

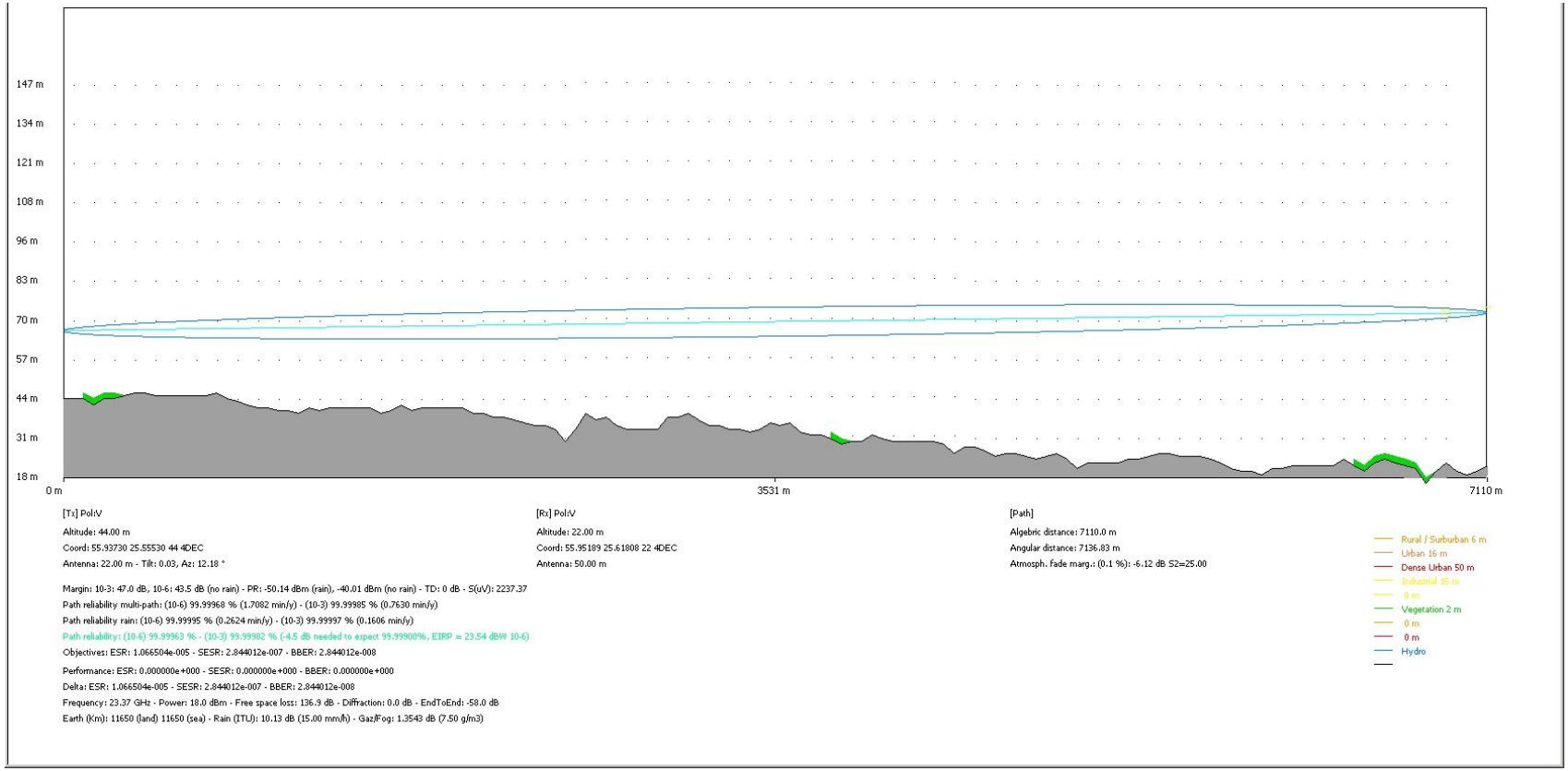

Link 7 Path Profile and Link Budget Calculation at S2 (from L7-S1 to L7-S2)

Link 8 Path Profile and Link Budget calculation

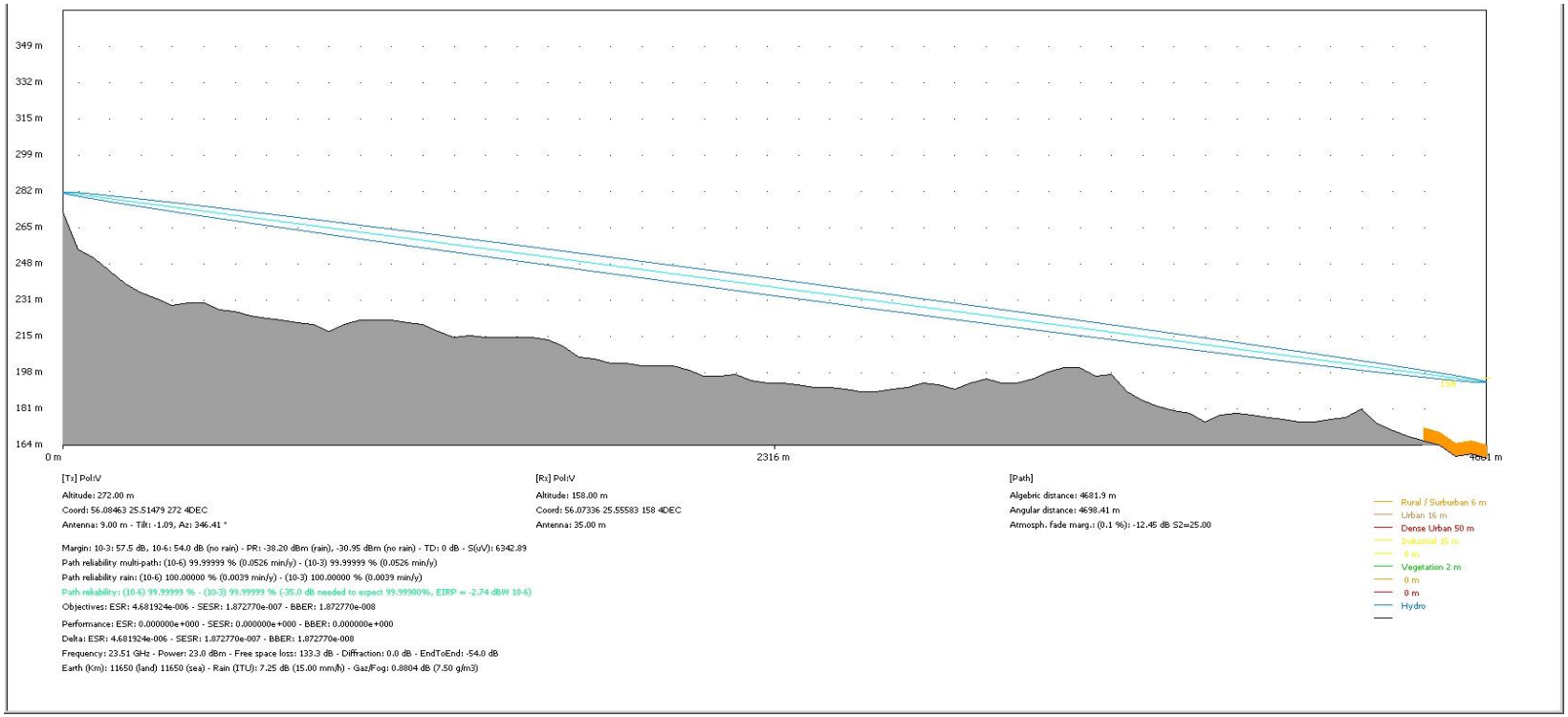

Link 8 Path Profile and Link Budget Calculation at S1 (from L8-S2 to L8-S1)

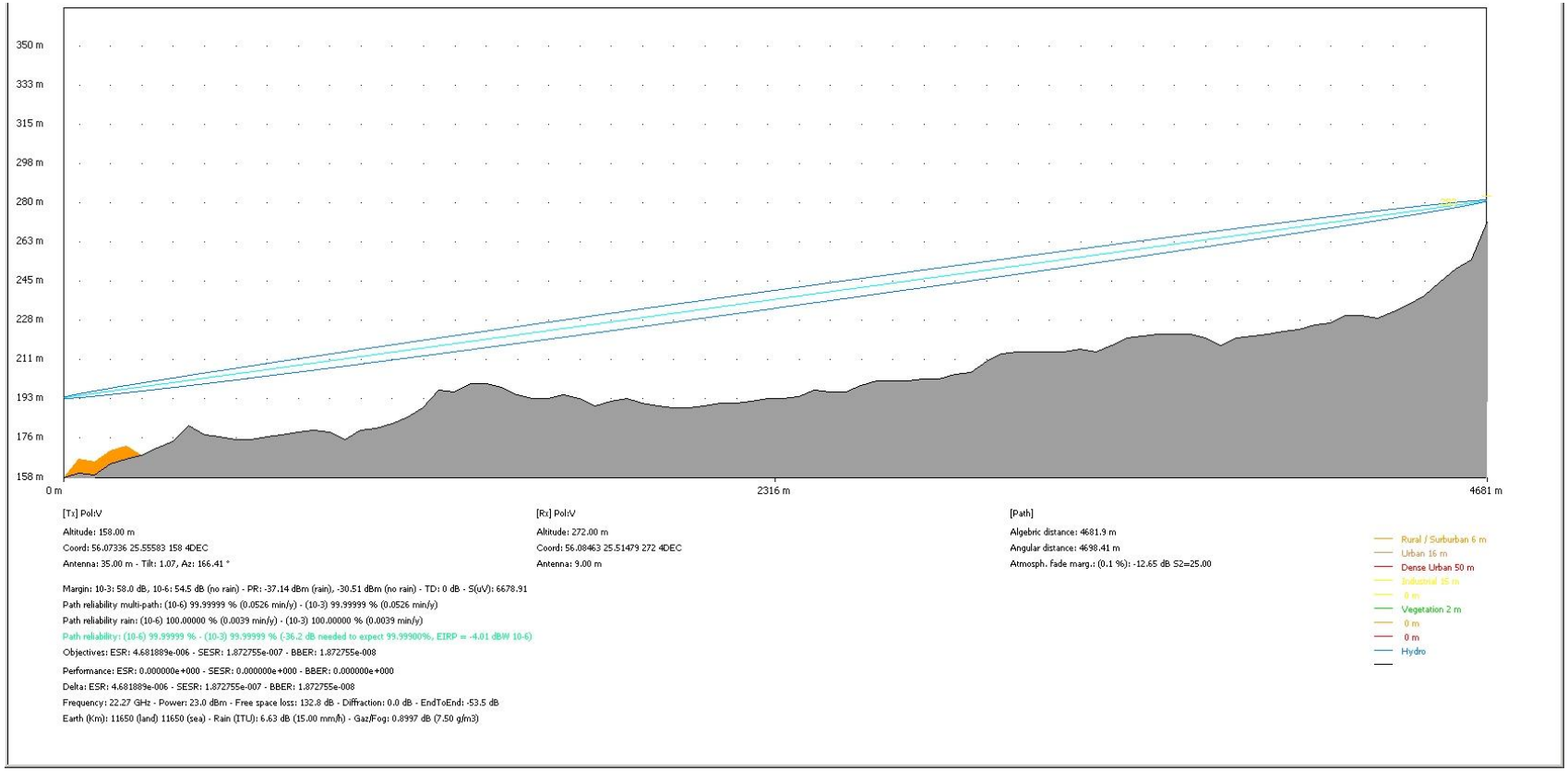

Link 8 Path Profile and Link Budget Calculation at S2 (from L8-S1 to L8-S2)

Link 9 Path Profile and Link Budget calculation

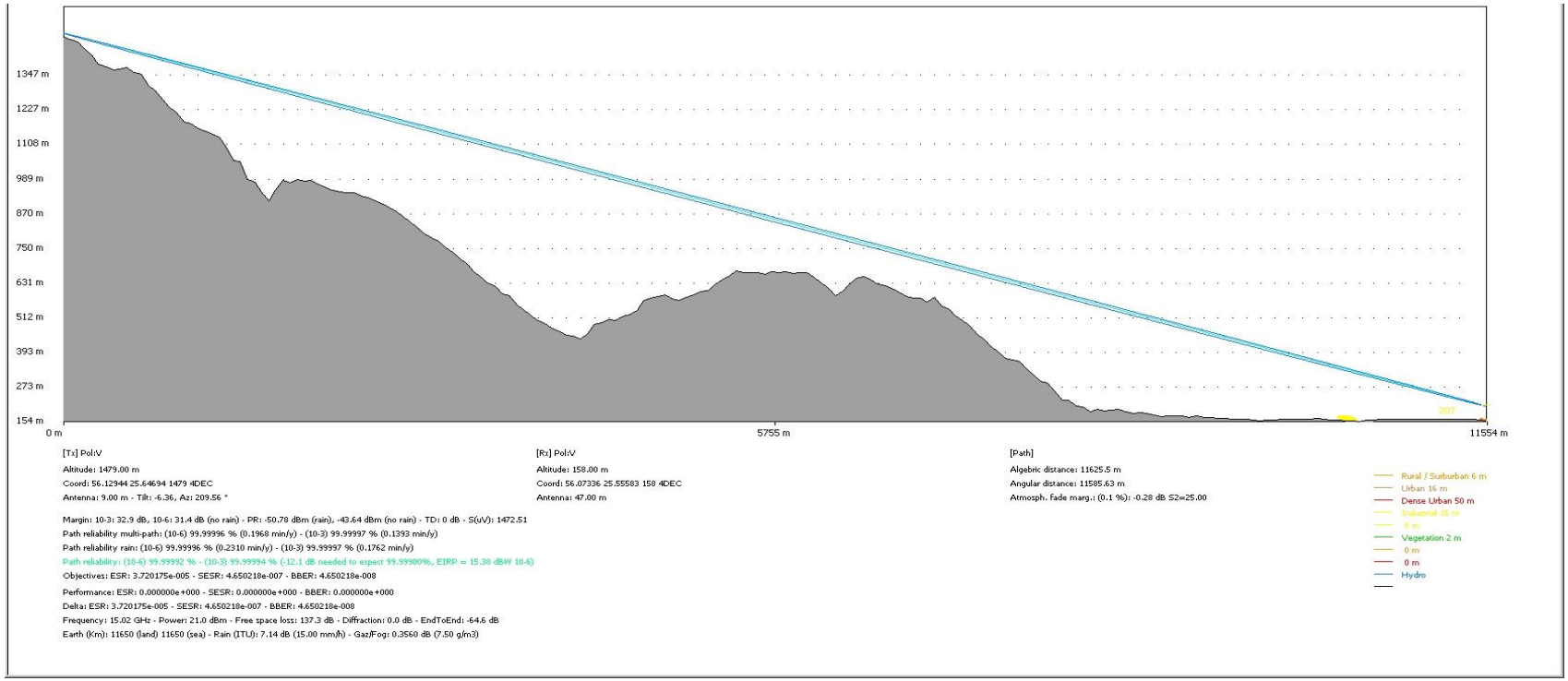

Link 9 Path Profile and Link Budget Calculation at S1 (Link From L9S2 to L9S1)

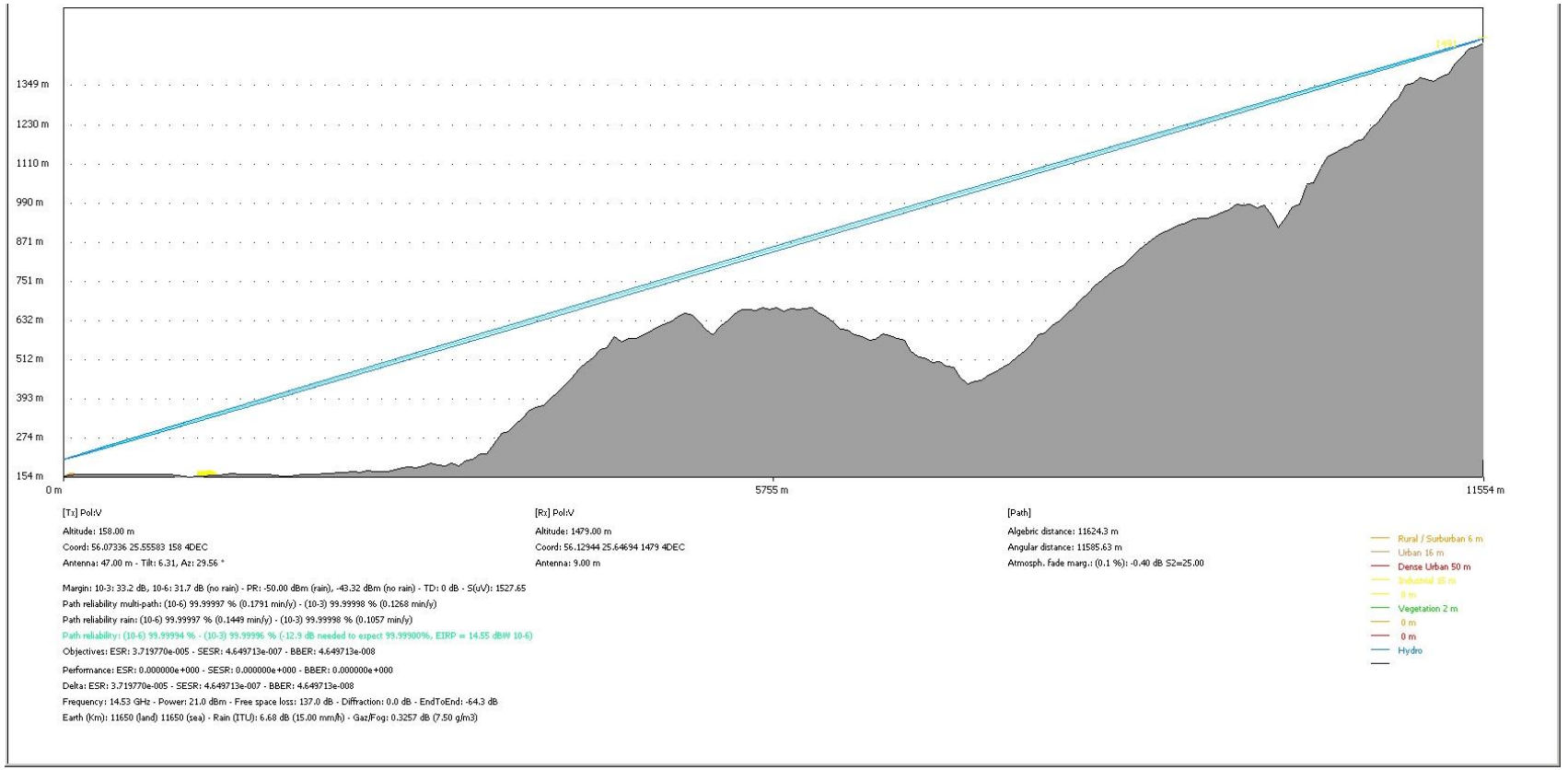

Link 9 Path Profile and Link Budget Calculation at S2 (from L9-S1 to L9-S2)

Link 10 Path Profile and Link Budget calculation

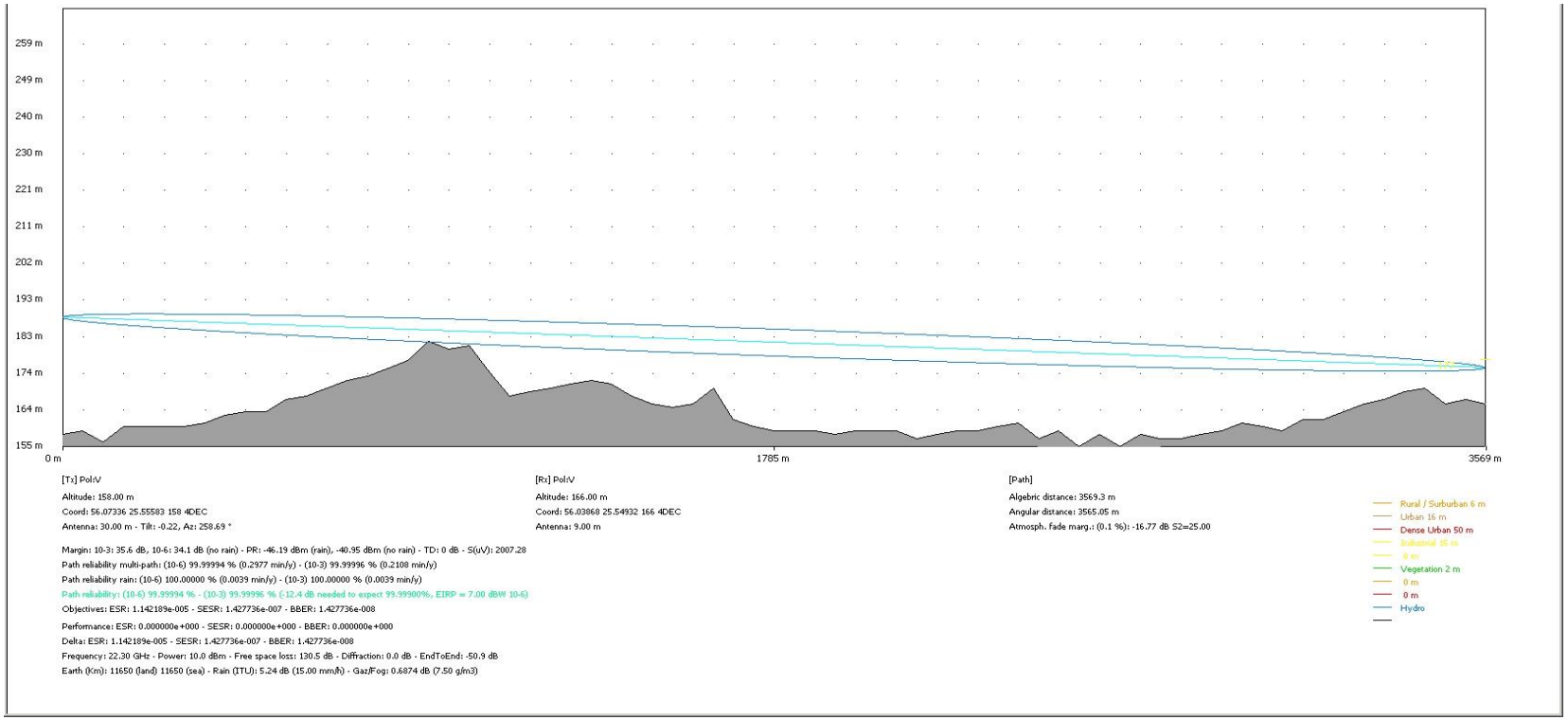

Link 10 Path Profile and Link Budget Calculation at S1 (from L10-S2 to L10-S1)

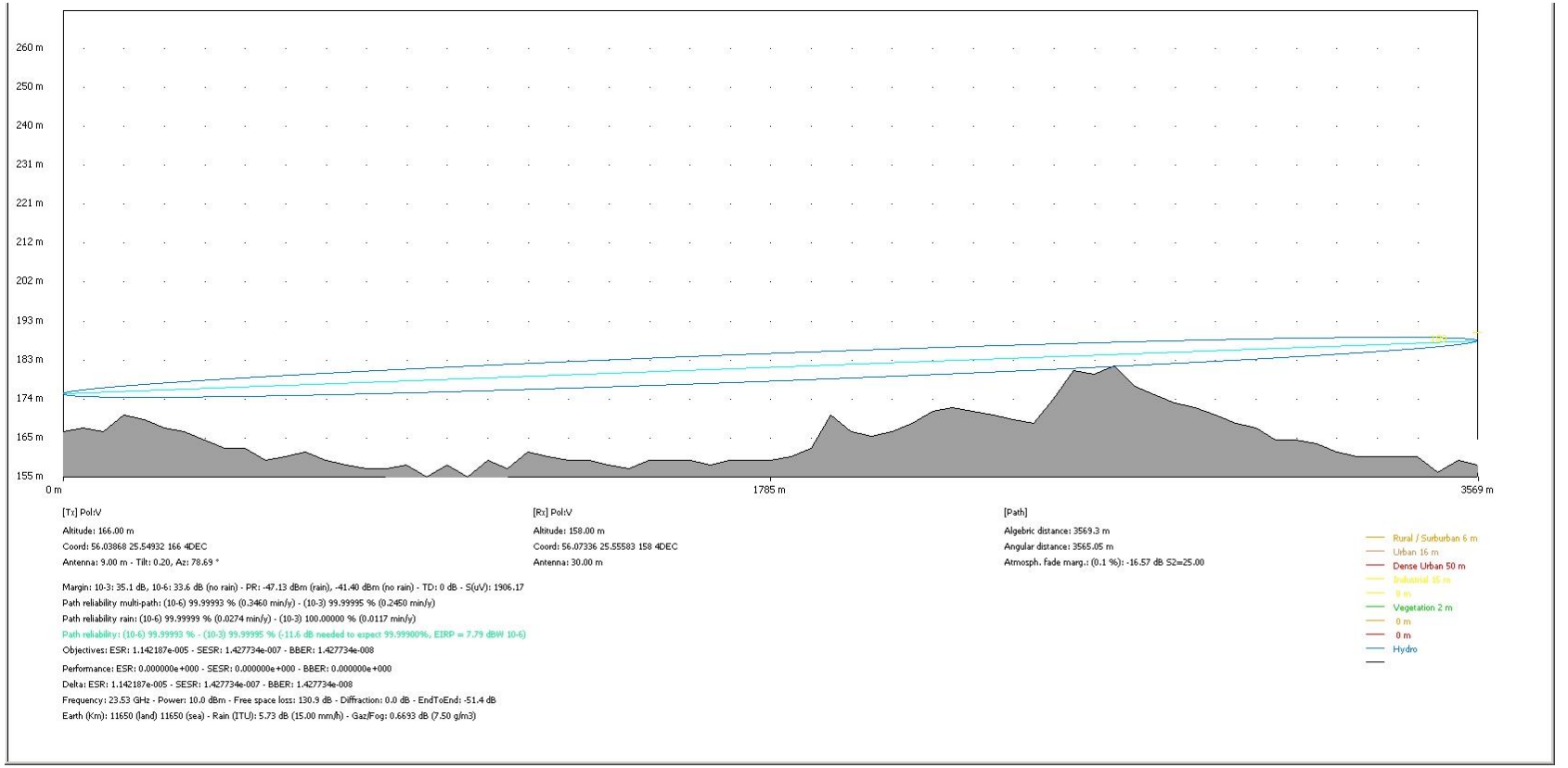

Link 10 Path Profile and Link Budget Calculation at S2 (from L10-S1 to L10-S2)

Link 11 Path Profile and Link Budget calculation

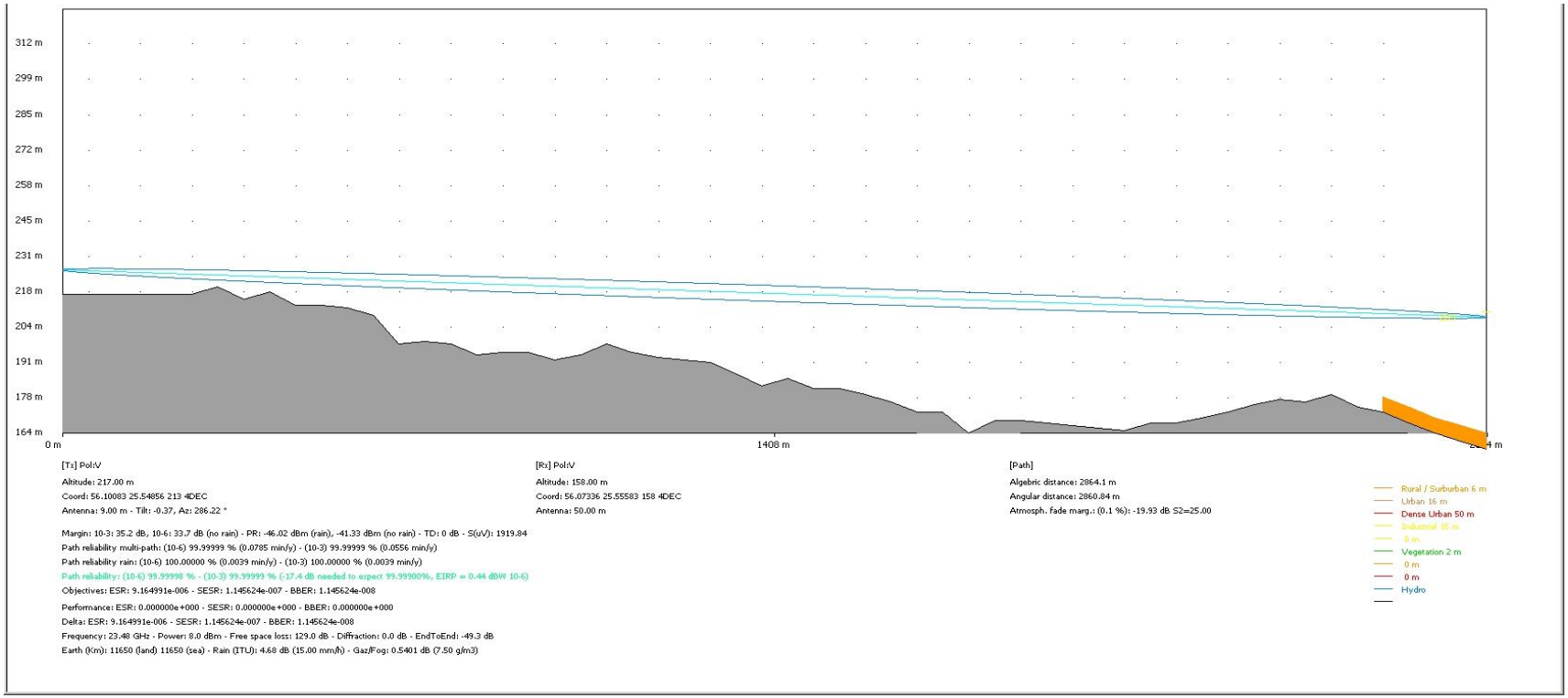

Link 11 Path Profile and Link Budget Calculation at S1 (from L11-S2 to L11-S1)

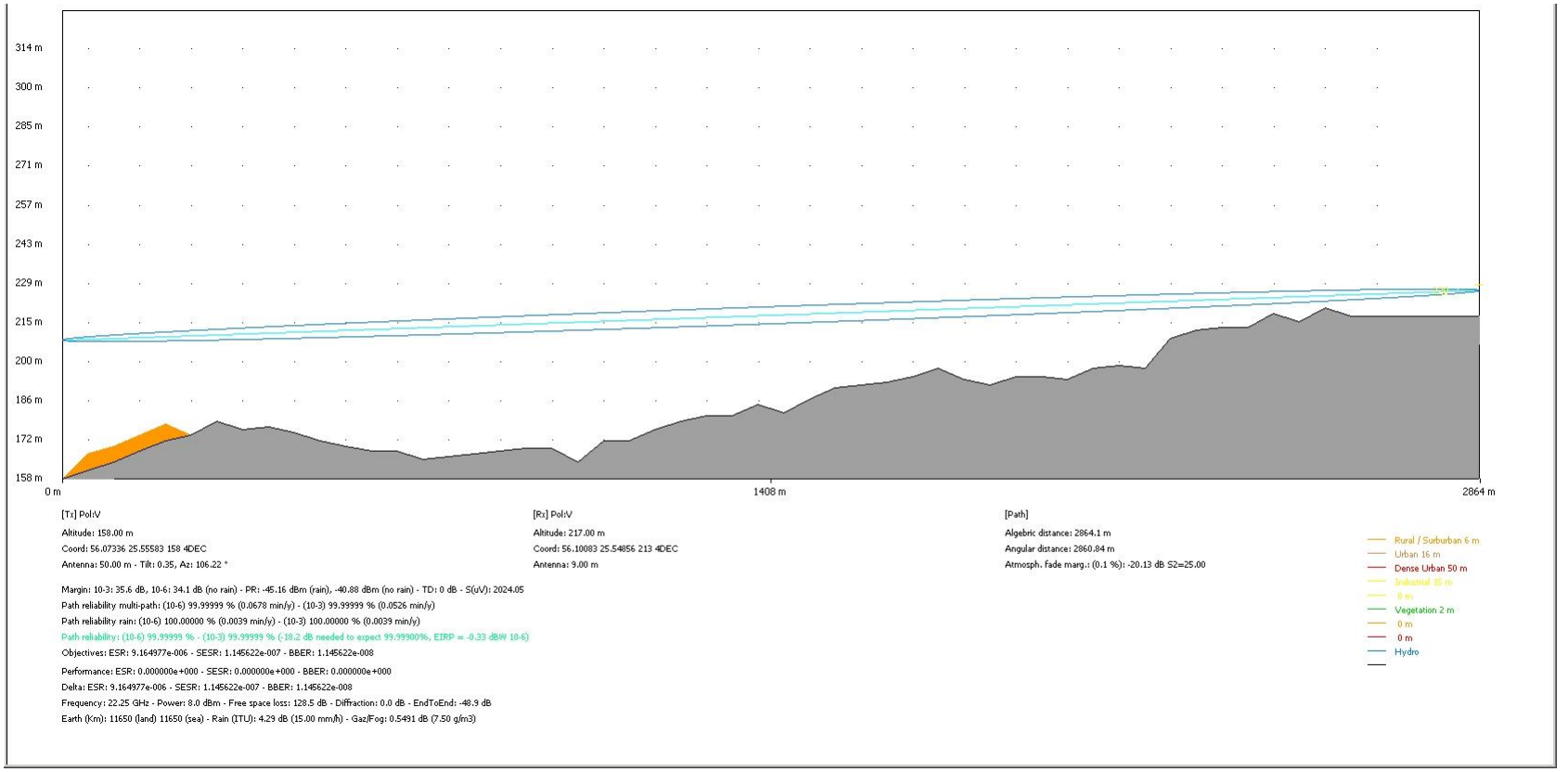

Link 11 Path Profile and Link Budget Calculation at S2 (from L11-S1 to L11-S2)

Link 12 Path Profile and Link Budget calculation

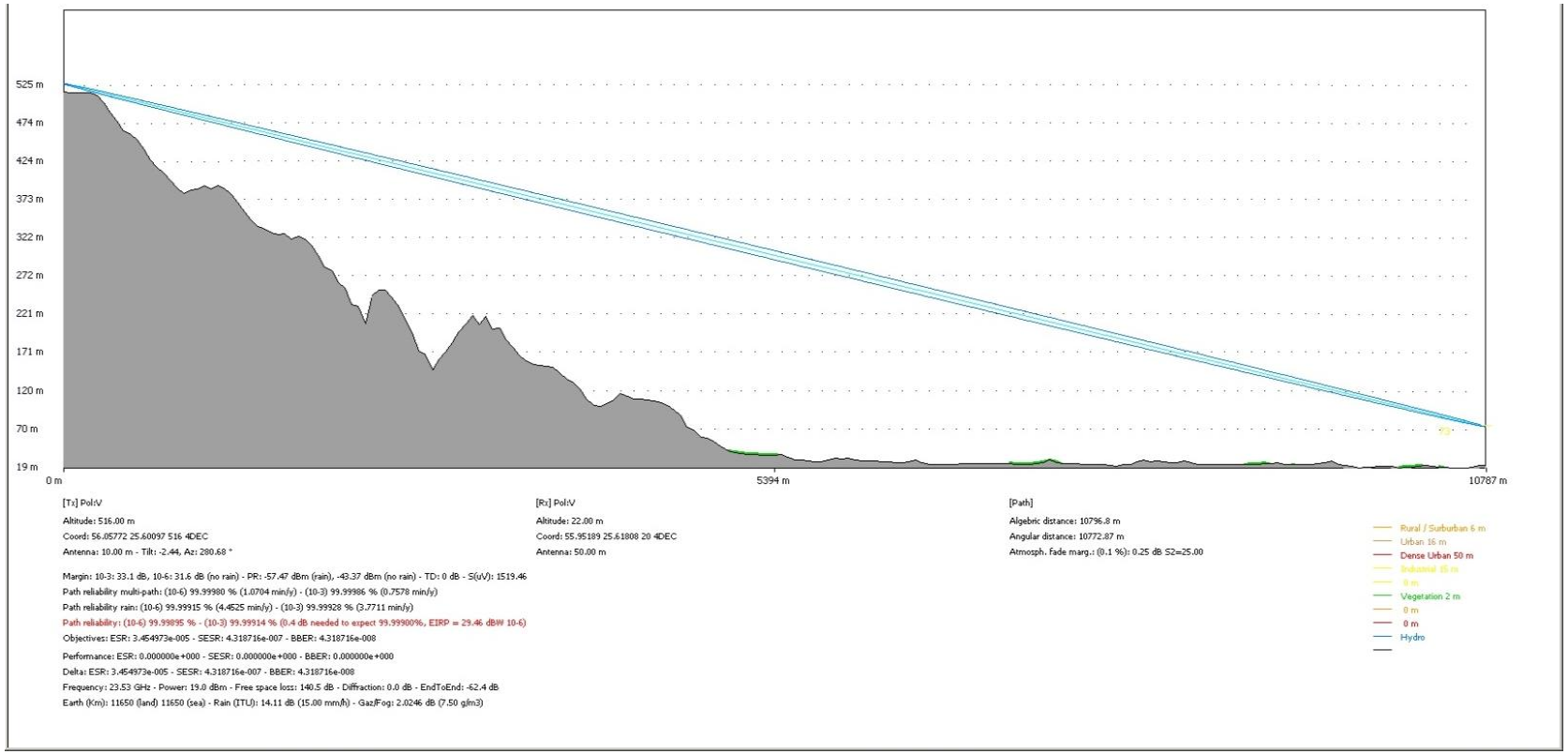

Link 12 Path Profile and Link Budget Calculation at S1 (from L12-S2 to L12-S1)

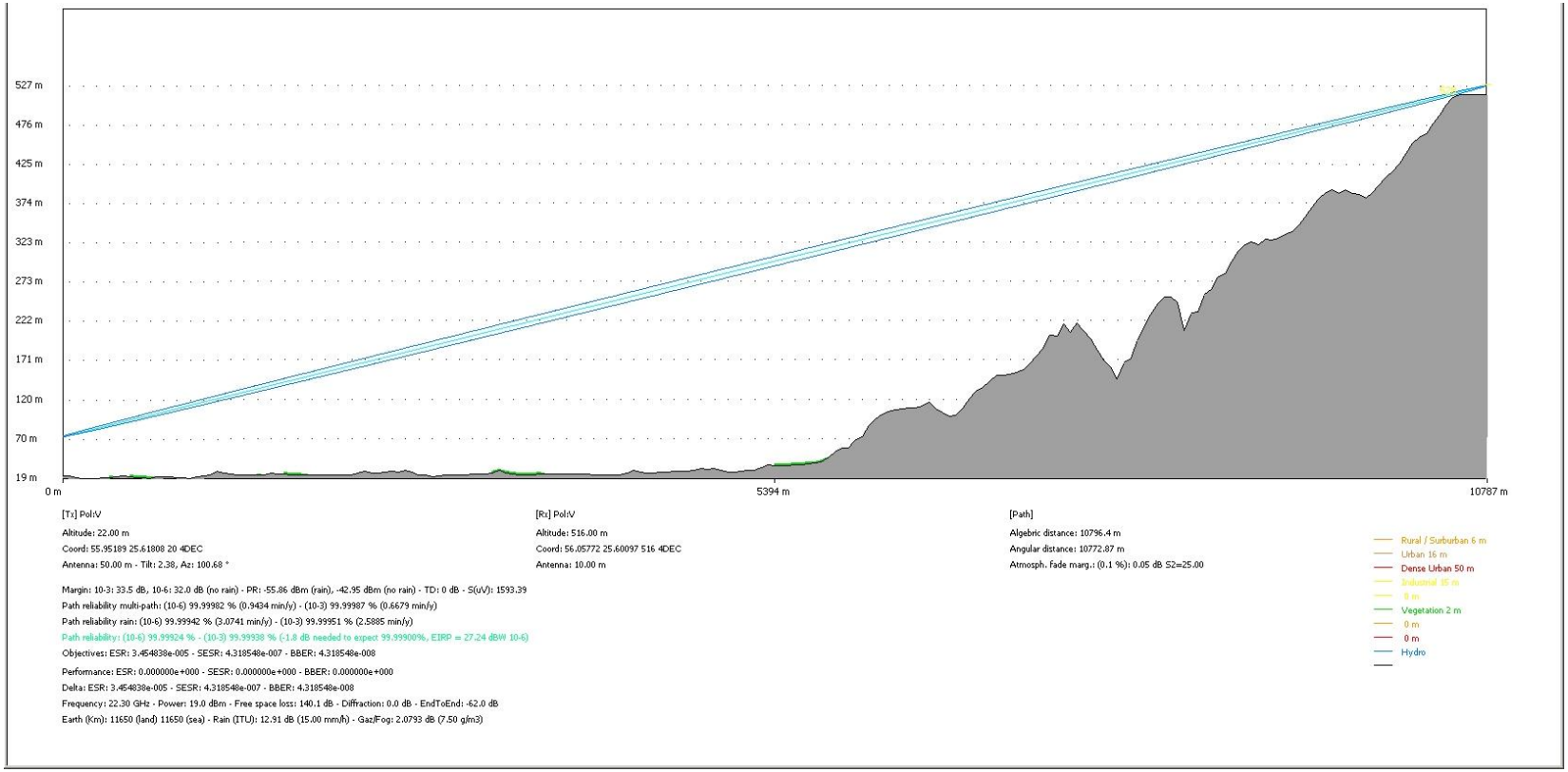

Link 12 Path Profile and Link Budget Calculation at S2 (from L1-2S1 to L12-S2)